Isabel B. Valente
António Ventura Gouveia
Salvador J. E. Dias   *Editors*

Proceedings of the 3rd RILEM Spring Convention and Conference (RSCC 2020)

Volume 2: New Materials and Structures for Ultra-durability

Proceedings of the 3rd RILEM Spring Convention and Conference (RSCC 2020)

RILEM BOOKSERIES

Volume 33

RILEM, The International Union of Laboratories and Experts in Construction Materials, Systems and Structures, founded in 1947, is a non-governmental scientific association whose goal is to contribute to progress in the construction sciences, techniques and industries, essentially by means of the communication it fosters between research and practice. RILEM's focus is on construction materials and their use in building and civil engineering structures, covering all phases of the building process from manufacture to use and recycling of materials. More information on RILEM and its previous publications can be found on www.RILEM.net.

Indexed in SCOPUS, Google Scholar and SpringerLink.

More information about this series at http://www.springer.com/series/8781

Isabel B. Valente · António Ventura Gouveia ·
Salvador J. E. Dias
Editors

Proceedings of the 3rd RILEM Spring Convention and Conference (RSCC 2020)

Volume 2: New Materials and Structures for Ultra-durability

Springer

Editors
Isabel B. Valente
ISISE, Civil Engineering
University of Minho
Guimarães, Portugal

António Ventura Gouveia
ISISE, Civil Engineering
Polytechnic Institute of Viseu
Viseu, Portugal

Salvador J. E. Dias
ISISE, Civil Engineering
University of Minho
Guimarães, Portugal

Committee

Executive Chair

Eduardo B. Pereira, ISISE, University of Minho, Portugal

Vice-chair

Fábio Figueiredo

Honorary Chair

Joaquim A. O. Barros

Topic 1: Strategies for a Resilient Built Environment

Topic Lead

Daman Panesar, University of Toronto, Canada

Topic Scientific Committee

Cise Unluer, Nanyang Technological University, Singapore
Cristina Zanotti, The University of British Columbia, Canada
Daniel Straub, Technical University of Munich, Germany
Fausto Minelli, University of Brescia, Italy
Guillaume Habert, ETH Zurich, Switzerland
Manu Santhanam, IIT Madras, Chennai, India
Miguel Ferreira, VTT Technical Research Centre of Finland, Finland
Antonio Caggiano, Darmstadt University of Technology, Germany
Carlos Bettencourt, LNEC, Portugal
Carlos Chastre Rodrigues, Universidade NOVA de Lisboa, Portugal
Daniel Oliveira, University of Minho, Portugal
Jorge Branco, University of Minho, Portugal
José Matos, University of Minho, Portugal
Klaas van Breugel, Delft TU, The Netherlands
Luc Tarweve, University of Ghent, Belgium
Marko Bartolac, University of Zagreb, Croatia
Mette Geiker, Norwegian University of Science and Technology, Norway
Paulo Cachim, Universidade de Aveiro, Portugal

Preface

The world is changing fast and getting confronted with many challenges that could impact the well-being and happiness of society. Among the most severe are rapid urbanization, climate change, and resource scarcity.

In this scenario, the construction industry is transforming itself and the challenge of current civil engineering is to find a proper balance between increasing the lifespan of structures as much as resources and technology available allow and keeping the overall costs (construction, exploitation, and recycling) both affordable and sustainable to the society. This change presents engineers and designers with an opportunity to redefine the methods and materials with which new civil engineering projects are undertaken. Engineers must look to innovations, taking into account resilience to natural hazards, efficiency in design, sustainability, and durability of materials and structures, while cultivating new structural concepts.

This transformation in the construction industry should be supported by the most updated research developed concerning the best use of materials and the design and execution of constructions that are more eco-efficient and durable over time. Conference segment *New Materials and Structures for Ultra-durability* provided a forum for presenting and discussing the most updated topics related to the use of waste materials, fiber reinforced concrete, phase change materials, self-healing capability of cementitious composites, geopolymer concrete, carbon textile reinforced composites, alternative cementitious materials, cementitious materials with natural fibers, alkali sensitivity, and more. It also covers advances in the structural application of new materials, as for example, the use of FRC in wind towers, composite floor systems, and urban furniture, or the use of geopolymer concrete in structures.

The Editors of the segment *New Materials and Structures for Ultra-durability* wish to appreciate and acknowledge all the efforts made by the authors to produce innovative research and high-quality papers. We are sure that the group of

42 papers included in this volume will be a valued reference in this field. Together with the other volumes from the RSC2020 conference, the present book will form a suitable base for discussion and suggestions for future development and research.

Guimarães, Portugal   Isabel B. Valente
Viseu, Portugal   António Ventura Gouveia
Guimarães, Portugal   Salvador J. E. Dias

Contents

RILEM Publications

The following list is presenting the global offer of RILEM Publications, sorted by series. Each publication is available in printed version and/or in online version.

RILEM Proceedings (PRO)

PRO 1: Durability of High Performance Concrete (ISBN: 2-912143-03-9; e-ISBN: 2-351580-12-5; e-ISBN: 2351580125); *Ed. H. Sommer*

PRO 2: Chloride Penetration into Concrete (ISBN: 2-912143-00-04; e-ISBN: 2912143454); *Eds. L.-O. Nilsson and J.-P. Ollivier*

PRO 3: Evaluation and Strengthening of Existing Masonry Structures (ISBN: 2-912143-02-0; e-ISBN: 2351580141); *Eds. L. Binda and C. Modena*

PRO 4: Concrete: From Material to Structure (ISBN: 2-912143-04-7; e-ISBN: 2351580206); *Eds. J.-P. Bournazel and Y. Malier*

PRO 5: The Role of Admixtures in High Performance Concrete (ISBN: 2-912143-05-5; e-ISBN: 2351580214); *Eds. J. G. Cabrera and R. Rivera-Villarreal*

PRO 6: High Performance Fiber Reinforced Cement Composites—HPFRCC 3 (ISBN: 2-912143-06-3; e-ISBN: 2351580222); *Eds. H. W. Reinhardt and A. E. Naaman*

PRO 7: 1st International RILEM Symposium on Self-Compacting Concrete (ISBN: 2-912143-09-8; e-ISBN: 2912143721); *Eds. Å. Skarendahl and Ö. Petersson*

PRO 8: International RILEM Symposium on Timber Engineering (ISBN: 2-912143-10-1; e-ISBN: 2351580230); *Ed. L. Boström*

PRO 9: 2nd International RILEM Symposium on Adhesion between Polymers and Concrete ISAP '99 (ISBN: 2-912143-11-X; e-ISBN: 2351580249); *Eds. Y. Ohama and M. Puterman*

PRO 10: 3rd International RILEM Symposium on Durability of Building and Construction Sealants (ISBN: 2-912143-13-6; e-ISBN: 2351580257); *Ed. A. T. Wolf*

PRO 11: 4th International RILEM Conference on Reflective Cracking in Pavements (ISBN: 2-912143-14-4; e-ISBN: 2351580265); *Eds. A. O. Abd El Halim, D. A. Taylor and El H. H. Mohamed*

PRO 12: International RILEM Workshop on Historic Mortars: Characteristics and Tests (ISBN: 2-912143-15-2; e-ISBN: 2351580273); *Eds. P. Bartos, C. Groot and J. J. Hughes*

PRO 13: 2nd International RILEM Symposium on Hydration and Setting (ISBN: 2-912143-16-0; e-ISBN: 2351580281); *Ed. A. Nonat*

PRO 14: Integrated Life-Cycle Design of Materials and Structures—ILCDES 2000 (ISBN: 951-758-408-3; e-ISBN: 235158029X); (ISSN: 0356-9403); *Ed. S. Sarja*

PRO 15: Fifth RILEM Symposium on Fibre-Reinforced Concretes (FRC)—BEFIB'2000 (ISBN: 2-912143-18-7; e-ISBN: 291214373X); *Eds. P. Rossi and G. Chanvillard*

PRO 16: Life Prediction and Management of Concrete Structures (ISBN: 2-912143-19-5; e-ISBN: 2351580303); *Ed. D. Naus*

PRO 17: Shrinkage of Concrete—Shrinkage 2000 (ISBN: 2-912143-20-9; e-ISBN: 2351580311); *Eds. V. Baroghel-Bouny and P.-C. Aïtcin*

PRO 18: Measurement and Interpretation of the On-Site Corrosion Rate (ISBN: 2-912143-21-7; e-ISBN: 235158032X); *Eds. C. Andrade, C. Alonso, J. Fullea, J. Polimon and J. Rodriguez*

PRO 19: Testing and Modelling the Chloride Ingress into Concrete (ISBN: 2-912143-22-5; e-ISBN: 2351580338); *Eds. C. Andrade and J. Kropp*

PRO 20: 1st International RILEM Workshop on Microbial Impacts on Building Materials (CD 02) (e-ISBN 978-2-35158-013-4); *Ed. M. Ribas Silva*

PRO 21: International RILEM Symposium on Connections between Steel and Concrete (ISBN: 2-912143-25-X; e-ISBN: 2351580346); *Ed. R. Eligehausen*

PRO 22: International RILEM Symposium on Joints in Timber Structures (ISBN: 2-912143-28-4; e-ISBN: 2351580354); *Eds. S. Aicher and H.-W. Reinhardt*

PRO 23: International RILEM Conference on Early Age Cracking in Cementitious Systems (ISBN: 2-912143-29-2; e-ISBN: 2351580362); *Eds. K. Kovler and A. Bentur*

PRO 24: 2nd International RILEM Workshop on Frost Resistance of Concrete (ISBN: 2-912143-30-6; e-ISBN: 2351580370); *Eds. M. J. Setzer, R. Auberg and H.-J. Keck*

PRO 25: International RILEM Workshop on Frost Damage in Concrete (ISBN: 2-912143-31-4; e-ISBN: 2351580389); *Eds. D. J. Janssen, M. J. Setzer and M. B. Snyder*

PRO 26: International RILEM Workshop on On-Site Control and Evaluation of Masonry Structures (ISBN: 2-912143-34-9; e-ISBN: 2351580141); *Eds. L. Binda and R. C. de Vekey*

PRO 27: International RILEM Symposium on Building Joint Sealants (CD03; e-ISBN: 235158015X); *Ed. A. T. Wolf*

PRO 28: 6th International RILEM Symposium on Performance Testing and Evaluation of Bituminous Materials—PTEBM'03 (ISBN: 2-912143-35-7; e-ISBN: 978-2-912143-77-8); *Ed. M. N. Partl*

PRO 29: 2nd International RILEM Workshop on Life Prediction and Ageing Management of Concrete Structures (ISBN: 2-912143-36-5; e-ISBN: 2912143780); *Ed. D. J. Naus*

PRO 30: 4th International RILEM Workshop on High Performance Fiber Reinforced Cement Composites—HPFRCC 4 (ISBN: 2-912143-37-3; e-ISBN: 2912143799); *Eds. A. E. Naaman and H. W. Reinhardt*

PRO 31: International RILEM Workshop on Test and Design Methods for Steel Fibre Reinforced Concrete: Background and Experiences (ISBN: 2-912143-38-1; e-ISBN: 2351580168); *Eds. B. Schnütgen and L. Vandewalle*

PRO 32: International Conference on Advances in Concrete and Structures 2 vol. (ISBN (set): 2-912143-41-1; e-ISBN: 2351580176); *Eds. Ying-shu Yuan, Surendra P. Shah and Heng-lin Lü*

PRO 33: 3rd International Symposium on Self-Compacting Concrete (ISBN: 2-912143-42-X; e-ISBN: 2912143713); *Eds. Ó. Wallevik and I. Níelsson*

PRO 34: International RILEM Conference on Microbial Impact on Building Materials (ISBN: 2-912143-43-8; e-ISBN: 2351580184); *Ed. M. Ribas Silva*

PRO 35: International RILEM TC 186-ISA on Internal Sulfate Attack and Delayed Ettringite Formation (ISBN: 2-912143-44-6; e-ISBN: 2912143802); *Eds. K. Scrivener and J. Skalny*

PRO 36: International RILEM Symposium on Concrete Science and Engineering —A Tribute to Arnon Bentur (ISBN: 2-912143-46-2; e-ISBN: 2912143586); *Eds. K. Kovler, J. Marchand, S. Mindess and J. Weiss*

PRO 37: 5th International RILEM Conference on Cracking in Pavements—Mitigation, Risk Assessment and Prevention (ISBN: 2-912143-47-0; e-ISBN: 2912143764); *Eds. C. Petit, I. Al-Qadi and A. Millien*

PRO 38: 3rd International RILEM Workshop on Testing and Modelling the Chloride Ingress into Concrete (ISBN: 2-912143-48-9; e-ISBN: 2912143578); *Eds. C. Andrade and J. Kropp*

PRO 39: 6th International RILEM Symposium on Fibre-Reinforced Concretes—BEFIB 2004 (ISBN: 2-912143-51-9; e-ISBN: 2912143748); *Eds. M. Di Prisco, R. Felicetti and G. A. Plizzari*

PRO 40: International RILEM Conference on the Use of Recycled Materials in Buildings and Structures (ISBN: 2-912143-52-7; e-ISBN: 2912143756); *Eds. E. Vázquez, Ch. F. Hendriks and G. M. T. Janssen*

PRO 41: RILEM International Symposium on Environment-Conscious Materials and Systems for Sustainable Development (ISBN: 2-912143-55-1; e-ISBN: 2912143640); *Eds. N. Kashino and Y. Ohama*

PRO 42: SCC'2005—China: 1st International Symposium on Design, Performance and Use of Self-Consolidating Concrete (ISBN: 2-912143-61-6; e-ISBN: 2912143624); *Eds. Zhiwu Yu, Caijun Shi, Kamal Henri Khayat and Youjun Xie*

PRO 43: International RILEM Workshop on Bonded Concrete Overlays (e-ISBN: 2-912143-83-7); *Eds. J. L. Granju and J. Silfwerbrand*

PRO 44: 2nd International RILEM Workshop on Microbial Impacts on Building Materials (CD11) (e-ISBN: 2-912143-84-5); *Ed. M. Ribas Silva*

PRO 45: 2nd International Symposium on Nanotechnology in Construction, Bilbao (ISBN: 2-912143-87-X; e-ISBN: 2912143888); *Eds. Peter J. M. Bartos, Yolanda de Miguel and Antonio Porro*

PRO 46: Concrete Life'06—International RILEM-JCI Seminar on Concrete Durability and Service Life Planning: Curing, Crack Control, Performance in Harsh Environments (ISBN: 2-912143-89-6; e-ISBN: 291214390X); *Ed. K. Kovler*

PRO 47: International RILEM Workshop on Performance Based Evaluation and Indicators for Concrete Durability (ISBN: 978-2-912143-95-2; e-ISBN: 9782912143969); *Eds. V. Baroghel-Bouny, C. Andrade, R. Torrent and K. Scrivener*

PRO 48: 1st International RILEM Symposium on Advances in Concrete through Science and Engineering (e-ISBN: 2-912143-92-6); *Eds. J. Weiss, K. Kovler, J. Marchand, and S. Mindess*

PRO 49: International RILEM Workshop on High Performance Fiber Reinforced Cementitious Composites in Structural Applications (ISBN: 2-912143-93-4; e-ISBN: 2912143942); *Eds. G. Fischer and V. C. Li*

PRO 50: 1st International RILEM Symposium on Textile Reinforced Concrete (ISBN: 2-912143-97-7; e-ISBN: 2351580087); *Eds. Josef Hegger, Wolfgang Brameshuber and Norbert Will*

PRO 51: 2nd International Symposium on Advances in Concrete through Science and Engineering (ISBN: 2-35158-003-6; e-ISBN: 2-35158-002-8); *Eds. J. Marchand, B. Bissonnette, R. Gagné, M. Jolin and F. Paradis*

PRO 52: Volume Changes of Hardening Concrete: Testing and Mitigation (ISBN: 2-35158-004-4; e-ISBN: 2-35158-005-2); *Eds. O. M. Jensen, P. Lura and K. Kovler*

PRO 53: High Performance Fiber Reinforced Cement Composites—HPFRCC5 (ISBN: 978-2-35158-046-2; e-ISBN: 978-2-35158-089-9); *Eds. H. W. Reinhardt and A. E. Naaman*

PRO 54: 5th International RILEM Symposium on Self-Compacting Concrete (ISBN: 978-2-35158-047-9; e-ISBN: 978-2-35158-088-2); *Eds. G. De Schutter and V. Boel*

PRO 55: International RILEM Symposium Photocatalysis, Environment and Construction Materials (ISBN: 978-2-35158-056-1; e-ISBN: 978-2-35158-057-8); *Eds. P. Baglioni and L. Cassar*

PRO 56: International RILEM Workshop on Integral Service Life Modelling of Concrete Structures (ISBN 978-2-35158-058-5; e-ISBN: 978-2-35158-090-5); *Eds. R. M. Ferreira, J. Gulikers and C. Andrade*

PRO 57: RILEM Workshop on Performance of cement-based materials in aggressive aqueous environments (e-ISBN: 978-2-35158-059-2); *Ed. N. De Belie*

PRO 58: International RILEM Symposium on Concrete Modelling—CONMOD'08 (ISBN: 978-2-35158-060-8; e-ISBN: 978-2-35158-076-9); *Eds. E. Schlangen and G. De Schutter*

PRO 59: International RILEM Conference on On Site Assessment of Concrete, Masonry and Timber Structures—SACoMaTiS 2008 (ISBN set: 978-2-35158-061-5; e-ISBN: 978-2-35158-075-2); *Eds. L. Binda, M. di Prisco and R. Felicetti*

PRO 60: Seventh RILEM International Symposium on Fibre Reinforced Concrete: Design and Applications—BEFIB 2008 (ISBN: 978-2-35158-064-6; e-ISBN: 978-2-35158-086-8); *Ed. R. Gettu*

PRO 61: 1st International Conference on Microstructure Related Durability of Cementitious Composites 2 vol., (ISBN: 978-2-35158-065-3; e-ISBN: 978-2-35158-084-4); *Eds. W. Sun, K. van Breugel, C. Miao, G. Ye and H. Chen*

PRO 62: NSF/ RILEM Workshop: In-situ Evaluation of Historic Wood and Masonry Structures (e-ISBN: 978-2-35158-068-4); *Eds. B. Kasal, R. Anthony and M. Drdácký*

PRO 63: Concrete in Aggressive Aqueous Environments: Performance, Testing and Modelling, 2 vol., (ISBN: 978-2-35158-071-4; e-ISBN: 978-2-35158-082-0); *Eds. M. G. Alexander and A. Bertron*

PRO 64: Long Term Performance of Cementitious Barriers and Reinforced Concrete in Nuclear Power Plants and Waste Management—NUCPERF 2009 (ISBN: 978-2-35158-072-1; e-ISBN: 978-2-35158-087-5); *Eds. V. L'Hostis, R. Gens and C. Gallé*

PRO 65: Design Performance and Use of Self-consolidating Concrete—SCC'2009 (ISBN: 978-2-35158-073-8; e-ISBN: 978-2-35158-093-6); *Eds. C. Shi, Z. Yu, K. H. Khayat and P. Yan*

PRO 66: 2nd International RILEM Workshop on Concrete Durability and Service Life Planning—ConcreteLife'09 (ISBN: 978-2-35158-074-5; ISBN: 978-2-35158-074-5); *Ed. K. Kovler*

PRO 67: Repairs Mortars for Historic Masonry (e-ISBN: 978-2-35158-083-7); *Ed. C. Groot*

PRO 68: Proceedings of the 3rd International RILEM Symposium on 'Rheology of Cement Suspensions such as Fresh Concrete (ISBN 978-2-35158-091-2; e-ISBN: 978-2-35158-092-9); *Eds. O. H. Wallevik, S. Kubens and S. Oesterheld*

PRO 69: 3rd International PhD Student Workshop on 'Modelling the Durability of Reinforced Concrete (ISBN: 978-2-35158-095-0); *Eds. R. M. Ferreira, J. Gulikers and C. Andrade*

PRO 70: 2nd International Conference on 'Service Life Design for Infrastructure' (ISBN set: 978-2-35158-096-7, e-ISBN: 978-2-35158-097-4); *Eds. K. van Breugel, G. Ye and Y. Yuan*

PRO 71: Advances in Civil Engineering Materials—The 50-year Teaching Anniversary of Prof. Sun Wei' (ISBN: 978-2-35158-098-1; e-ISBN: 978-2-35158-099-8); *Eds. C. Miao, G. Ye and H. Chen*

PRO 72: First International Conference on 'Advances in Chemically-Activated Materials—CAM'2010' (2010), 264 pp., ISBN: 978-2-35158-101-8; e-ISBN: 978-2-35158-115-5; *Eds. Caijun Shi and Xiaodong Shen*

PRO 73: 2nd International Conference on 'Waste Engineering and Management—ICWEM 2010' (2010), 894 pp., ISBN: 978-2-35158-102-5; e-ISBN: 978-2-35158-103-2, *Eds. J. Zh. Xiao, Y. Zhang, M. S. Cheung and R. Chu*

PRO 74: International RILEM Conference on 'Use of Superabsorsorbent Polymers and Other New Addditives in Concrete' (2010) 374 pp., ISBN: 978-2-35158-104-9; e-ISBN: 978-2-35158-105-6; *Eds. O.M. Jensen, M.T. Hasholt, and S. Laustsen*

PRO 75: International Conference on 'Material Science—2nd ICTRC—Textile Reinforced Concrete—Theme 1' (2010) 436 pp., ISBN: 978-2-35158-106-3; e-ISBN: 978-2-35158-107-0; *Ed. W. Brameshuber*

PRO 76: International Conference on 'Material Science—HetMat—Modelling of Heterogeneous Materials—Theme 2' (2010) 255 pp., ISBN: 978-2-35158-108-7; e-ISBN: 978-2-35158-109-4; *Ed. W. Brameshuber*

PRO 77: International Conference on 'Material Science—AdIPoC—Additions Improving Properties of Concrete—Theme 3' (2010) 459 pp., ISBN: 978-2-35158-110-0; e-ISBN: 978-2-35158-111-7; *Ed. W. Brameshuber*

PRO 78: 2nd Historic Mortars Conference and RILEM TC 203-RHM Final Workshop—HMC2010 (2010) 1416 pp., e-ISBN: 978-2-35158-112-4; *Eds. J. Válek, C. Groot and J. J. Hughes*

PRO 79: International RILEM Conference on Advances in Construction Materials Through Science and Engineering (2011) 213 pp., ISBN: 978-2-35158-116-2, e-ISBN: 978-2-35158-117-9; *Eds. Christopher Leung and K.T. Wan*

PRO 80: 2nd International RILEM Conference on Concrete Spalling due to Fire Exposure (2011) 453 pp., ISBN: 978-2-35158-118-6; e-ISBN: 978-2-35158-119-3; *Eds. E.A.B. Koenders and F. Dehn*

PRO 81: 2nd International RILEM Conference on Strain Hardening Cementitious Composites (SHCC2-Rio) (2011) 451 pp., ISBN: 978-2-35158-120-9; e-ISBN: 978-2-35158-121-6; *Eds. R.D. Toledo Filho, F.A. Silva, E.A.B. Koenders and E.M.R. Fairbairn*

PRO 82: 2nd International RILEM Conference on Progress of Recycling in the Built Environment (2011) 507 pp., e-ISBN: 978-2-35158-122-3; *Eds. V.M. John, E. Vazquez, S.C. Angulo and C. Ulsen*

PRO 83: 2nd International Conference on Microstructural-related Durability of Cementitious Composites (2012) 250 pp., ISBN: 978-2-35158-129-2; e-ISBN: 978-2-35158-123-0; *Eds. G. Ye, K. van Breugel, W. Sun and C. Miao*

PRO 84: CONSEC13—Seventh International Conference on Concrete under Severe Conditions—Environment and Loading (2013) 1930 pp., ISBN: 978-2-35158-124-7; e-ISBN: 978-2- 35158-134-6; *Eds. Z.J. Li, W. Sun, C.W. Miao, K. Sakai, O.E. Gjorv and N. Banthia*

PRO 85: RILEM-JCI International Workshop on Crack Control of Mass Concrete and Related issues concerning Early-Age of Concrete Structures—ConCrack 3—Control of Cracking in Concrete Structures 3 (2012) 237 pp., ISBN: 978-2-35158-125-4; e-ISBN: 978-2-35158-126-1; *Eds. F. Toutlemonde and J.-M. Torrenti*

PRO 86: International Symposium on Life Cycle Assessment and Construction (2012) 414 pp., ISBN: 978-2-35158-127-8, e-ISBN: 978-2-35158-128-5; *Eds. A. Ventura and C. de la Roche*

PRO 87: UHPFRC 2013—RILEM-fib-AFGC International Symposium on Ultra-High Performance Fibre-Reinforced Concrete (2013), ISBN: 978-2-35158-130-8, e-ISBN: 978-2-35158-131-5; *Eds. F. Toutlemonde*

PRO 88: 8th RILEM International Symposium on Fibre Reinforced Concrete (2012) 344 pp., ISBN: 978-2-35158-132-2; e-ISBN: 978-2-35158-133-9; *Eds. Joaquim A.O. Barros*

PRO 89: RILEM International workshop on performance-based specification and control of concrete durability (2014) 678 pp., ISBN: 978-2-35158-135-3; e-ISBN: 978-2-35158-136-0; *Eds. D. Bjegović, H. Beushausen and M. Serdar*

PRO 90: 7th RILEM International Conference on Self-Compacting Concrete and of the 1st RILEM International Conference on Rheology and Processing of Construction Materials (2013) 396 pp., ISBN: 978-2-35158-137-7; e-ISBN: 978-2-35158-138-4; *Eds. Nicolas Roussel and Hela Bessaies-Bey*

PRO 91: CONMOD 2014—RILEM International Symposium on Concrete Modelling (2014), ISBN: 978-2-35158-139-1; e-ISBN: 978-2-35158-140-7; *Eds. Kefei Li, Peiyu Yan and Rongwei Yang*

PRO 92: CAM 2014—2nd International Conference on advances in chemically-activated materials (2014) 392 pp., ISBN: 978-2-35158-141-4; e-ISBN: 978-2-35158-142-1; *Eds. Caijun Shi and Xiadong Shen*

PRO 93: SCC 2014—3rd International Symposium on Design, Performance and Use of Self-Consolidating Concrete (2014) 438 pp., ISBN: 978-2-35158-143-8; e-ISBN: 978-2-35158-144-5; *Eds. Caijun Shi, Zhihua Ou and Kamal H. Khayat*

PRO 94 (online version): HPFRCC-7—7th RILEM conference on High performance fiber reinforced cement composites (2015), e-ISBN: 978-2-35158-146-9; *Eds. H.W. Reinhardt, G.J. Parra-Montesinos and H. Garrecht*

PRO 95: International RILEM Conference on Application of superabsorbent polymers and other new admixtures in concrete construction (2014), ISBN: 978-2-35158-147-6; e-ISBN: 978-2-35158-148-3; *Eds. Viktor Mechtcherine and Christof Schroefl*

PRO 96 (online version): XIII DBMC: XIII International Conference on Durability of Building Materials and Components (2015), e-ISBN: 978-2-35158-149-0; *Eds. M. Quattrone and V.M. John*

PRO 97: SHCC3—3rd International RILEM Conference on Strain Hardening Cementitious Composites (2014), ISBN: 978-2-35158-150-6; e-ISBN: 978-2-35158-151-3; *Eds. E. Schlangen, M.G. Sierra Beltran, M. Lukovic and G. Ye*

PRO 98: FERRO-11—11th International Symposium on Ferrocement and 3rd ICTRC—International Conference on Textile Reinforced Concrete (2015), ISBN: 978-2-35158-152-0; e-ISBN: 978-2-35158-153-7; *Ed. W. Brameshuber*

PRO 99 (online version): ICBBM 2015—1st International Conference on Bio-Based Building Materials (2015), e-ISBN: 978-2-35158-154-4; *Eds. S. Amziane and M. Sonebi*

PRO 100: SCC16—RILEM Self-Consolidating Concrete Conference (2016), ISBN: 978-2-35158-156-8; e-ISBN: 978-2-35158-157-5; *Ed. Kamal H. Kayat*

PRO 101 (online version): III Progress of Recycling in the Built Environment (2015), e-ISBN: 978-2-35158-158-2; *Eds I. Martins, C. Ulsen and S. C. Angulo*

PRO 102 (online version): RILEM Conference on Microorganisms-Cementitious Materials Interactions (2016), e-ISBN: 978-2-35158-160-5; *Eds. Alexandra Bertron, Henk Jonkers and Virginie Wiktor*

PRO 103 (online version): ACESC'16—Advances in Civil Engineering and Sustainable Construction (2016), e-ISBN: 978-2-35158-161-2; *Eds. T.Ch. Madhavi, G. Prabhakar, Santhosh Ram and P.M. Rameshwaran*

PRO 104 (online version): SSCS'2015—Numerical Modeling—Strategies for Sustainable Concrete Structures (2015), e-ISBN: 978-2-35158-162-9

PRO 105: 1st International Conference on UHPC Materials and Structures (2016), ISBN: 978-2-35158-164-3; e-ISBN: 978-2-35158-165-0

PRO 106: AFGC-ACI-fib-RILEM International Conference on Ultra-High-Performance Fibre-Reinforced Concrete—UHPFRC 2017 (2017), ISBN: 978-2-35158-166-7; e-ISBN: 978-2-35158-167-4; *Eds. François Toutlemonde and Jacques Resplendino*

PRO 107 (online version): XIV DBMC—14th International Conference on Durability of Building Materials and Components (2017), e-ISBN: 978-2-35158-159-9; *Eds. Geert De Schutter, Nele De Belie, Arnold Janssens and Nathan Van Den Bossche*

PRO 108: MSSCE 2016—Innovation of Teaching in Materials and Structures (2016), ISBN: 978-2-35158-178-0; e-ISBN: 978-2-35158-179-7; *Ed. Per Goltermann*

PRO 109 (2 volumes): MSSCE 2016—Service Life of Cement-Based Materials and Structures (2016), ISBN Vol. 1: 978-2-35158-170-4; Vol. 2: 978-2-35158-171-4; Set Vol. 1&2: 978-2-35158-172-8; e-ISBN : 978-2-35158-173-5; *Eds. Miguel Azenha, Ivan Gabrijel, Dirk Schlicke, Terje Kanstad and Ole Mejlhede Jensen*

PRO 110: MSSCE 2016—Historical Masonry (2016), ISBN: 978-2-35158-178-0; e-ISBN: 978-2-35158-179-7; *Eds. Inge Rörig-Dalgaard and Ioannis Ioannou*

PRO 111: MSSCE 2016—Electrochemistry in Civil Engineering (2016); ISBN: 978-2-35158-176-6; e-ISBN: 978-2-35158-177-3; *Ed. Lisbeth M. Ottosen*

PRO 112: MSSCE 2016—Moisture in Materials and Structures (2016), ISBN: 978-2-35158-178-0; e-ISBN: 978-2-35158-179-7; *Eds. Kurt Kielsgaard Hansen, Carsten Rode and Lars-Olof Nilsson*

PRO 113: MSSCE 2016—Concrete with Supplementary Cementitious Materials (2016), ISBN: 978-2-35158-178-0; e-ISBN: 978-2-35158-179-7; *Eds. Ole Mejlhede Jensen, Konstantin Kovler and Nele De Belie*

PRO 114: MSSCE 2016—Frost Action in Concrete (2016), ISBN: 978-2-35158-182-7; e-ISBN: 978-2-35158-183-4; *Eds. Marianne Tange Hasholt, Katja Fridh and R. Doug Hooton*

PRO 115: MSSCE 2016—Fresh Concrete (2016), ISBN: 978-2-35158-184-1; e-ISBN: 978-2-35158-185-8; *Eds. Lars N. Thrane, Claus Pade, Oldrich Svec and Nicolas Roussel*

PRO 116: BEFIB 2016—9th RILEM International Symposium on Fiber Reinforced Concrete (2016), ISBN: 978-2-35158-187-2; e-ISBN: 978-2-35158-186-5; *Eds. N. Banthia, M. di Prisco and S. Soleimani-Dashtaki*

PRO 117: 3rd International RILEM Conference on Microstructure Related Durability of Cementitious Composites (2016), ISBN: 978-2-35158-188-9; e-ISBN: 978-2-35158-189-6; *Eds. Changwen Miao, Wei Sun, Jiaping Liu, Huisu Chen, Guang Ye and Klaas van Breugel*

PRO 118 (4 volumes): International Conference on Advances in Construction Materials and Systems (2017), ISBN Set: 978-2-35158-190-2; Vol. 1: 978-2-35158-193-3; Vol. 2: 978-2-35158-194-0; Vol. 3: ISBN:978-2-35158-195-7; Vol. 4: ISBN:978-2-35158-196-4; e-ISBN: 978-2-35158-191-9; *Ed. Manu Santhanam*

PRO 119 (online version): ICBBM 2017—Second International RILEM Conference on Bio-based Building Materials, (2017), e-ISBN: 978-2-35158-192-6; *Ed. Sofiane Amziane*

PRO 120 (2 volumes): EAC-02—2nd International RILEM/COST Conference on Early Age Cracking and Serviceability in Cement-based Materials and Structures, (2017), Vol. 1: 978-2-35158-199-5, Vol. 2: 978-2-35158-200-8, Set: 978-2-35158-197-1, e-ISBN: 978-2-35158-198-8; *Eds. Stéphanie Staquet and Dimitrios Aggelis*

PRO 121 (2 volumes): SynerCrete18: Interdisciplinary Approaches for Cementbased Materials and Structural Concrete: Synergizing Expertise and Bridging Scales of Space and Time, (2018), Set: 978-2-35158-202-2, Vol.1: 978-2-35158-211-4, Vol.2: 978-2-35158-212-1, e-ISBN: 978-2-35158-203-9; *Eds. Miguel Azenha, Dirk Schlicke, Farid Benboudjema, Agnieszka Knoppik*

PRO 122: SCC'2018 China—Fourth International Symposium on Design, Performance and Use of Self-Consolidating Concrete, (2018), ISBN: 978-2-35158-204-6, e-ISBN: 978-2-35158-205-3; *Eds. C. Shi, Z. Zhang, K. H. Khayat*

PRO 123: Final Conference of RILEM TC 253-MCI: Microorganisms-Cementitious Materials Interactions (2018), Set: 978-2-35158-207-7, Vol.1: 978-2-35158-209-1, Vol.2: 978-2-35158-210-7, e-ISBN: 978-2-35158-206-0; *Ed. Alexandra Bertron*

PRO 124 (online version): Fourth International Conference Progress of Recycling in the Built Environment (2018), e-ISBN: 978-2-35158-208-4; *Eds. Isabel M. Martins, Carina Ulsen, Yury Villagran*

PRO 125 (online version): SLD4—4th International Conference on Service Life Design for Infrastructures (2018), e-ISBN: 978-2-35158-213-8; *Eds. Guang Ye, Yong Yuan, Claudia Romero Rodriguez, Hongzhi Zhang, Branko Savija*

PRO 126: Workshop on Concrete Modelling and Material Behaviour in honor of Professor Klaas van Breugel (2018), ISBN: 978-2-35158-214-5, e-ISBN: 978-2-35158-215-2; *Ed. Guang Ye*

PRO 127 (online version): CONMOD2018—Symposium on Concrete Modelling (2018), e-ISBN: 978-2-35158-216-9; *Eds. Erik Schlangen, Geert de Schutter, Branko Savija, Hongzhi Zhang, Claudia Romero Rodriguez*

PRO 128: SMSS2019—International Conference on Sustainable Materials, Systems and Structures (2019), ISBN: 978-2-35158-217-6, e-ISBN: 978-2-35158-218-3

PRO 129: 2nd International Conference on UHPC Materials and Structures (UHPC2018-China), ISBN: 978-2-35158-219-0, e-ISBN: 978-2-35158-220-6

PRO 130: 5th Historic Mortars Conference (2019), ISBN: 978-2-35158-221-3, e-ISBN: 978-2-35158-222-0; *Eds. José Ignacio Álvarez, José María Fernández, Íñigo Navarro, Adrián Durán, Rafael Sirera*

PRO 131 (online version): 3rd International Conference on Bio-Based Building Materials (ICBBM2019), e-ISBN: 978-2-35158-229-9; *Eds. Mohammed Sonebi, Sofiane Amziane, Jonathan Page*

PRO 132: IRWRMC'18—International RILEM Workshop on Rheological Measurements of Cement-based Materials (2018), ISBN: 978-2-35158-230-5, e-ISBN: 978-2-35158-231-2; *Eds. Chafika Djelal, Yannick Vanhove*

PRO 133 (online version): CO2STO2019—International Workshop CO2 Storage in Concrete (2019), e-ISBN: 978-2-35158-232-9; *Eds. Assia Djerbi, Othman Omikrine-Metalssi, Teddy Fen-Chong*

PRO 134: 3rd ACF/HNU International Conference on UHPC Materials and Structures—UHPC'2020, ISBN: 978-2-35158-233-6, e-ISBN: 978-2-35158-234-3; *Eds. Caijun Shi and Jiaping Liu*

RILEM Reports (REP)

Report 19: Considerations for Use in Managing the Aging of Nuclear Power Plant Concrete Structures (ISBN: 2-912143-07-1); *Ed. D. J. Naus*

Report 20: Engineering and Transport Properties of the Interfacial Transition Zone in Cementitious Composites (ISBN: 2-912143-08-X); *Eds. M. G. Alexander, G. Arliguie, G. Ballivy, A. Bentur and J. Marchand*

Report 21: Durability of Building Sealants (ISBN: 2-912143-12-8); *Ed. A. T. Wolf*

Report 22: Sustainable Raw Materials—Construction and Demolition Waste (ISBN: 2-912143-17-9); *Eds. C. F. Hendriks and H. S. Pietersen*

Report 23: Self-Compacting Concrete state-of-the-art report (ISBN: 2-912143-23-3); *Eds. Å. Skarendahl and Ö. Petersson*

Report 24: Workability and Rheology of Fresh Concrete: Compendium of Tests (ISBN: 2-912143-32-2); *Eds. P. J. M. Bartos, M. Sonebi and A. K. Tamimi*

Report 25: Early Age Cracking in Cementitious Systems (ISBN: 2-912143-33-0); *Ed. A. Bentur*

Report 26: Towards Sustainable Roofing (Joint Committee CIB/RILEM) (CD 07) (e-ISBN 978-2-912143-65-5); *Eds. Thomas W. Hutchinson and Keith Roberts*

Report 27: Condition Assessment of Roofs (Joint Committee CIB/RILEM) (CD 08) (e-ISBN 978-2-912143-66-2); *Ed. CIB W 83/RILEM TC166-RMS*

Report 28: Final report of RILEM TC 167-COM 'Characterisation of Old Mortars with Respect to Their Repair (ISBN: 978-2-912143-56-3); *Eds. C. Groot, G. Ashall and J. Hughes*

Report 29: Pavement Performance Prediction and Evaluation (PPPE): Interlaboratory Tests (e-ISBN: 2-912143-68-3); *Eds. M. Partl and H. Piber*

Report 30: Final Report of RILEM TC 198-URM 'Use of Recycled Materials' (ISBN: 2-912143-82-9; e-ISBN: 2-912143-69-1); *Eds. Ch. F. Hendriks, G. M. T. Janssen and E. Vázquez*

Report 31: Final Report of RILEM TC 185-ATC 'Advanced testing of cement-based materials during setting and hardening' (ISBN: 2-912143-81-0; e-ISBN: 2-912143-70-5); *Eds. H. W. Reinhardt and C. U. Grosse*

Report 32: Probabilistic Assessment of Existing Structures. A JCSS publication (ISBN 2-912143-24-1); *Ed. D. Diamantidis*

Report 33: State-of-the-Art Report of RILEM Technical Committee TC 184-IFE 'Industrial Floors' (ISBN 2-35158-006-0); *Ed. P. Seidler*

Report 34: Report of RILEM Technical Committee TC 147-FMB 'Fracture mechanics applications to anchorage and bond' Tension of Reinforced Concrete Prisms—Round Robin Analysis and Tests on Bond (e-ISBN 2-912143-91-8); *Eds. L. Elfgren and K. Noghabai*

Report 35: Final Report of RILEM Technical Committee TC 188-CSC 'Casting of Self Compacting Concrete' (ISBN 2-35158-001-X; e-ISBN: 2-912143-98-5); *Eds. Å. Skarendahl and P. Billberg*

Report 36: State-of-the-Art Report of RILEM Technical Committee TC 201-TRC 'Textile Reinforced Concrete' (ISBN 2-912143-99-3); *Ed. W. Brameshuber*

Report 37: State-of-the-Art Report of RILEM Technical Committee TC 192-ECM 'Environment-conscious construction materials and systems' (ISBN: 978-2-35158-053-0); *Eds. N. Kashino, D. Van Gemert and K. Imamoto*

Report 38: State-of-the-Art Report of RILEM Technical Committee TC 205-DSC 'Durability of Self-Compacting Concrete' (ISBN: 978-2-35158-048-6); *Eds. G. De Schutter and K. Audenaert*

Report 39: Final Report of RILEM Technical Committee TC 187-SOC 'Experimental determination of the stress-crack opening curve for concrete in tension' (ISBN 978-2-35158-049-3); *Ed. J. Planas*

Report 40: State-of-the-Art Report of RILEM Technical Committee TC 189-NEC 'Non-Destructive Evaluation of the Penetrability and Thickness of the Concrete Cover' (ISBN 978-2-35158-054-7); *Eds. R. Torrent and L. Fernández Luco*

Report 41: State-of-the-Art Report of RILEM Technical Committee TC 196-ICC 'Internal Curing of Concrete' (ISBN 978-2-35158-009-7); *Eds. K. Kovler and O. M. Jensen*

Report 42: 'Acoustic Emission and Related Non-destructive Evaluation Techniques for Crack Detection and Damage Evaluation in Concrete'—Final Report of RILEM Technical Committee 212-ACD (e-ISBN: 978-2-35158-100-1); *Ed. M. Ohtsu*

Report 45: Repair Mortars for Historic Masonry—State-of-the-Art Report of RILEM Technical Committee TC 203-RHM (e-ISBN: 978-2-35158-163-6); *Eds. Paul Maurenbrecher and Caspar Groot*

Report 46: Surface delamination of concrete industrial ffloors and other durability related aspects guide—Report of RILEM Technical Committee TC 268-SIF (e-ISBN: 978-2-35158-201-5); *Ed. Valerie Pollet*

Nonlinear Analysis of Offshore Wind Towers in Prefabricated Segments of Prestressed Fibre Reinforced Concrete

Fabio P. Figueiredo [ID]**, Joaquim A. O. Barros** [ID]**, and A. Ventura-Gouveia** [ID]

Abstract This paper presents the nonlinear finite element analysis of a new concept of offshore wind tower made by prefabricated prestressed fibre reinforced concrete (FRC) segments that are assembled to form the final structure. Fibre reinforcement aims to eliminate conventional passive steel reinforcement in order to avoid corrosion concerns and decrease the thickness of the segments. The first stage of the design approach consists on an analytical model that optimizes the geometry of the eolic tower by considering the relevant loading cases, the properties of the developed FRC, the resisting stress levels of the constituent materials and the frequency and lateral deformability of the tower. By determining the thickness and radius along with the height of the tower, this model can provide the solution of minimum FRC volume for the eolic tower. In the second stage of the design approach, the optimum solution from the previous design stage is simulated by a finite element approach that considers the geometric and material nonlinear features. This paper describes the main relevant aspects of this design methodology.

Keywords Fibre reinforced concrete · Nonlinear finite element · Offshore wind tower

1 Introduction

Wind power has grown fast in the last two decades. Global wind-generation capacity has increased by thirty per cent over the past decade [1]. This type of renewable energy has become attractive not only because costs are falling, but especially because it is greener and can deliver a more environmentally friend solution. Modern wind turbines are typically a horizontal-axis machine with a

F. P. Figueiredo (✉) · J. A. O. Barros
University of Minho, Braga, Portugal
e-mail: f.figueiredo@civil.uminho.pt

A. Ventura-Gouveia
Polytechnic Institute of Viseu, Viseu, Portugal

1

three-bladed rotor mounted upwind on a tower. The tower heights of wind turbines have increased during recent years to capture the more energetic winds that occur at higher elevations. These structures can range from 60 to 200 m.

This research investigates a new concept of offshore wind tower made by pre-fabricated prestressed fibre reinforced concrete (FRC) segments that are assembled to form the final structure. This new system allows the construction of towers of relatively low self-weight and high stiffness, which can deliver better structural behaviour than actual solutions, as well as higher durability, lower construction time, manufacturing and maintenance costs.

This paper describes the properties of the developed FRC and the finite element analyses carried out to investigate the influence of the tower's geometry and material properties of FRC on the local and global behaviour of this structure, in the context of its aimed functioning for serviceability and ultimate limit state conditions.

2 Material Properties

A FRC was produced according to the mixture composition given in Table 1, where W/C abbreviates water (W) to cement (C) ratio. Superplasticizer Sika® 3005 (SP) has been used to assure the required self-compactibility requirements due to the low water content. A crushed granite coarse aggregate was used with a maximum aggregate size of 12 mm. The mix included 60 kg/m^3 of hooked-end steel fibres of length (l_f) and diameter (d_f) of 33 mm and 0.55 mm, respectively, aspect ratio (l_f/d_f) of 60, and tensile strength of about 1100 MPa. The fresh concrete behaviour was determined by the Abrams cone slump test in the inverted position according to EFNARC [2] recommendations. The spread diameter was approximately 590 mm.

Six cylinders, 150 × 300 mm, were tested at 28 days. The average compressive strength and modulus of elasticity were 72 MPa and 42.15 GPa, respectively. The coefficients of variation (CoV) were 8.23% and 0.26%, respectively.

In order to assess the influence of fibre distribution and orientation, four-point notched beam bending tests were carried out according to the Italian standard [UNI-11039, 2003] in specimens (240 × 60 × 60 mm, with a notch of 10 mm depth and 2 mm width) extracted from a shell type panel [3]. The average force versus crack tip mouth displacement (F-CTOD) for the series with fibre orientation intervals [0–15°], [15–45°], [45–75°] and [75–90°] is represented in Fig. 1a, while

Table 1 Mix design of steel fibre reinforced self-compacting concrete per m^3

Cement [kg]	Water [kg]	W/C [–]	SP [kg]	Filler [kg]	Fine sand [kg]	Coarse sand [kg]	Coarse aggregate [kg]	Fibre [kg]
412	124	0.30	7.83	353	237	710	590	60
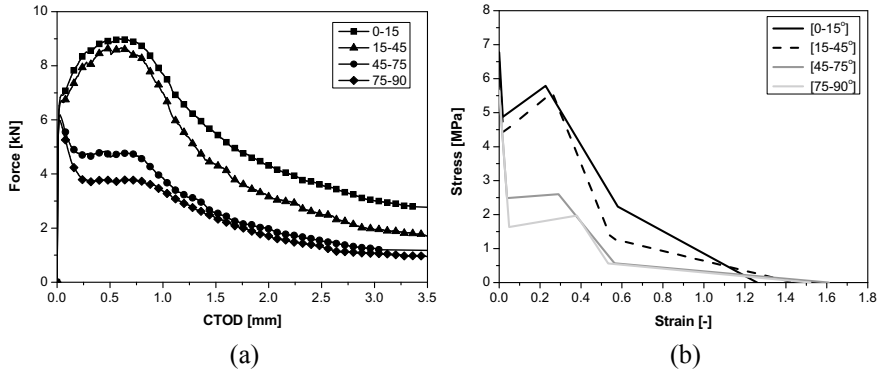
Fig. 1 **a** Force versus crack tip mouth displacement response for the series of fibre orientation: [0–15°], [15–45°], [45–75°] and [75–90°], and **b** corresponding post-cracking tensile stress–strain relationships obtained by inverse analysis

the corresponding quadrilinear tensile stress vs crack normal tensile strain diagrams, obtained from the inverse analysis [4], are shown in Fig. 1b, whose defining values are included in Table 2. These diagrams will define the fracture mode I parameters used in the material nonlinear analysis carried out in this work.

3   Structural Concept

The 5 MW turbine consists of a 3-bladed, 126 m diameter rotor, pitch regulated constant speed turbine. The support structure is a monopole with a hub height of 90 m above mean sea level and 20 m below the sea level. The tower is assembled by stacking ten prefabricated prestressed fibre reinforced concrete segments measuring 11 m each. Figure 2 shows the schematic representation of the offshore wind turbine and the applied loads considered in this study.

The geometry of the tower was defined by a simplified optimisation approach [5] so that the material in use and the stresses in the structure do not exceed a maximum level. The prestressing force applied in each segment was assumed equal to 5% of the concrete compressive strength. An algorithm to find the best linear variation of

Table 2 Mix design of steel fibre reinforced self-compacting concrete per m^3

β	α_1 [–]	α_2 [–]	α_3 [–]	ξ_1 [–]	ξ_2 [–]	ξ_3 [–]	f_{ct} [MPa]	G_f^I [N/mm]
[0–15°]	0.72	0.85	0.33	0.014	0.18	0.46	6.77	6.00
[15–45°]	0.68	0.86	0.20	0.014	0.18	0.38	6.50	5.10
[45–75°]	0.44	0.46	0.10	0.024	0.18	0.35	5.65	2.70
[75–90°]	0.29	0.35	0.10	0.032	0.25	0.35	5.64	2.20
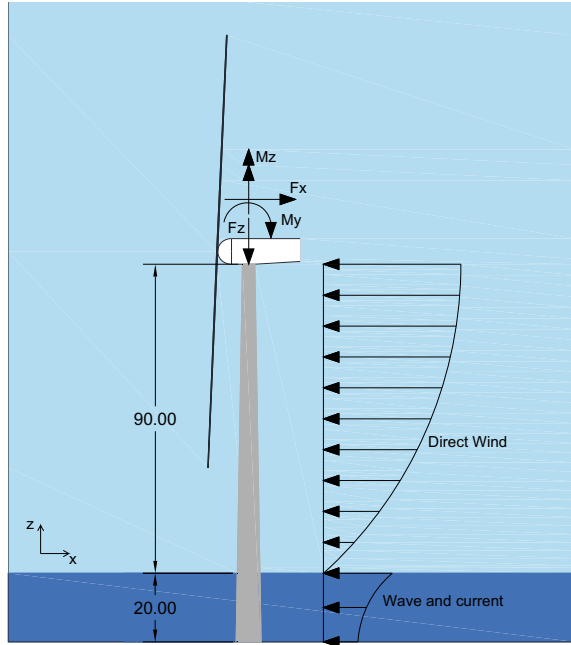
tower diameter, $D(z)$, and thickness, $t(z)$, was implemented in a code written in Python. The program analyses different cases, i.e. it varies the tower diameter and thickness, to find the optimised solution for the problem. A case is considered a candidate solution only if all sections of the tower are satisfied in terms of strength and geometry restrictions criteria.

The diameter of the tower, after the optimisation process, was 3.6 and 7.2 m at the top and bottom respectively. The thickness of the tower wall varies linearly from 0.4 m at the top to 0.6 m at the bottom of the tower.

An initial estimation of a wind tower loading, including the major loads it will withstand during its design life, is a significant requirement for engineering practitioners. In this respect, a simplified approach for the design of support structures for offshore wind turbines is adopted in this paper. The loads considered herein consist of forces acting on the top of the structure due to wind passing throughout the rotor, wind pressure on the tower structure, waves slamming the tower, and loads produced by water currents on the tower structure (see Fig. 2). However, other load cases should be considered in the final design, such as fatigue installation and transportation, control system faults, maintenance and repair and testing. Further discussions on these cases are available in [1, 6].

Since it was not possible to obtain precise information about loads from turbine wind towers manufacturers, they were extrapolated from a 3 MW wind turbine [7] and presented in Table 3. The axial forces acting on the tower are the prestressing and gravitational loads. The wind pressure on the tower, wave and current loads

Table 3 5 MW wind turbine loads

Parameter	SLS	ULS
Horizontal shear force Fx (kN)	690	1585
Moment My (kN m)	1600	3677
Torque Mz (kN m)	1010	1789

were applied as shown in Fig. 2. The wind profile was calculated using the following equation:

$$f_{wi}(z) = 0.5\, C_a \rho_{air} D(z)\, u(z)^2 \tag{1}$$

where f_{wi} [N/m] is the wind load per unit of length; ρ_{air} [kg/m^3] is the density of air, C_a [–] is the aerodynamic drag coefficient (shape, surface dependent), $D(z)$ [m] is the diameter of the tower cross-section at elevation z and $u(z)$ [m/s] is the mean wind speed at elevation z. The wave and current loads were obtained using the semi-empirical Morison's equation:

$$f_M(z) = f_i(z) + f_d(z) \tag{2}$$

where the first term $f_i\,(z)$ represents the hydrodynamic inertial load [N/m] and the second term $f_d\,(z)$ is the hydrodynamic drag load [N/m]. More information can be found elsewhere [5].

Design of wind turbines in compliance with standards requires that the structure shall satisfy ultimate, accidental, fatigue and serviceability limit state design conditions, ULS, ALS, FLS and SLS), respectively [8]. However, in this example, only the most unfavourable combination for the ULS is considered. The load combination given by DNV [8] is calculated using the following expression:

$$F = 1.0\, G + 1.35\, E \tag{3}$$

where G are the permanent loads and E are the environment loads.

4 Finite Element Analysis

This section describes the finite element model used in all analyses performed in this research. The models considered the geometry and loads defined in the pre-design stage explained in the previous section. The analyses were performed using the finite element package FEMIX [9].

As mentioned before, this initial study aims to investigate the influence of the tower's geometry and material properties (mainly the tensile performance) on the global behaviour of the structure. Therefore, the model does not consider

the connections between the prefabricated prestressed fibre reinforced concrete (FRC) segments, which is a topic treated in another publication being prepared in parallel [10].

The tower was modelled using twenty-node solid finite elements with $3 \times 3 \times 3$ Gauss–Legendre integration scheme. The prestressed cables were modelled using 2-nodes perfect bounded 3D embedded cables elements with two integration points. The boundary condition was assumed fixed at the bottom. The final finite element mesh was created using 3530 elements.

The cables were modelled as a linear-elastic material with Poison's coefficient equal to 0.2 and elasticity modulus of 200 GPa. The number of cables in each prefabricated segment was variable. It was defined so that the applied prestress force was 5% of the concrete compressive strength.

The behaviour of the FRC was modelled using the 3D multi-directional fixed smeared crack model available in FEMIX 4.0, see Ventura-Gouveia [11] for more information. The fracture mode I in this model is simulated by a quadrilinear tensile-softening diagram, whose defining values are provided in Table 2.

Five loads cases and two loads combinations were considered. Initially, self-weight, prestresses forces, nacelle and rotor mass were applied to the structure. Next, wind turbine, direct wind, current and waves forces were introduced in small steps up to the stage where the ultimate limit state capacity is reached.

Fibre orientation can significantly influence the tensile and bending behaviours of FRC. Therefore, four analyses considering only the material non-linear behaviour were performed to investigate the impact of fibre orientation on tower behaviour. The models have the same geometry (as defined in the previous section), mesh, loads and boundary conditions. The only difference between the four models was the concrete tensile behaviour, which was changed according to the data presented in Table 2. Figure 3 shows the results of the comparison between the four models considering the fracture mode I parameters for FRC with fibre orientations in the intervals: [0–15º], [15–45º], [45–75º] and [75–90º] (see Table 2).

Up to about 1500 kN all models presented equal linear behaviour since up to this load level they are only submitted to axial loads, therefore no cracking has occurred. After the application of the remaining loads, i.e. wind turbine, direct wind, current and waves forces, the models showed a nonlinear behaviour due to the crack formation.

Note that the models considering fibres oriented at [0–15°] and [15–45°] presented similar behaviours, with [0–15°] performing slightly better. Both models were able to resist the load applied ($\sim$2000 kN). The models considering fibre orientations at [45–75°] and [75–90°] failed before the application of the total load due to the localization of a failure macro-crack. This behaviour was expected as fibres oriented at such angles do not contribute effectively to increase the concrete tensile strength [12].

For assessing the relative influence of material and geometric nonlinearity on the structural behaviour of the tower being analysed, the following analyses were performed by considering the FRC with tensile properties corresponding to [0–15º] fibre orientation interval: (i) FRC is considered linear and geometric nonlinearity is

Fig. 3 Fibre orientation comparison. Total horizontal force versus the displacement at the top of the tower
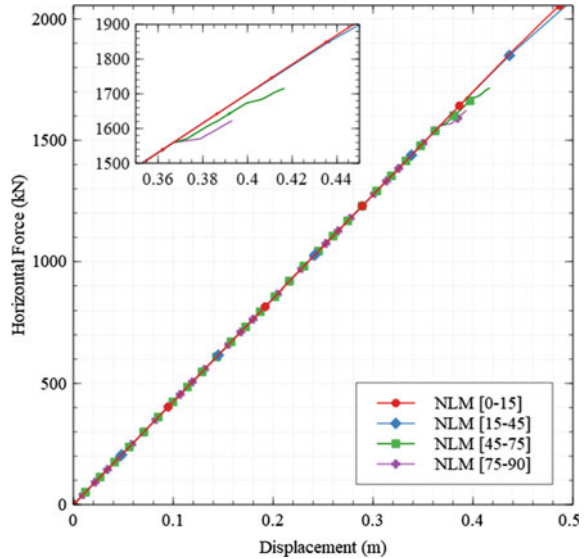
not included (LIN); (ii) FRC is linear and geometric nonlinearity is included (NLG); (iii) FRC is nonlinear and geometric nonlinearity is not considered (NLM); (iv) Both types of nonlinearities are considered (NLMG) (Fig. 4).

A simulation considering a plain concrete of the same strength class of FRC was also adopted to analyse the influence of fibre reinforcement. However, no convergence was possible to ensure after crack initiation due to abrupt macro-crack localization. Up to the maximum applied load, the difference between a linear analysis (LIN) and a material nonlinear analysis (NLM) is not significant in terms of maximum lateral deflection, since at this maximum load level the maximum crack width is limited to 0.3 mm. Therefore, due to the reduced crack width of all the cracks formed, the relative loss of stiffness of the tower is marginal. On the other hand, the consideration of the geometric non-linearity increased the displacement at the top of the tower by 6% (NLG) and 10% (NLGM).

The last study investigated the effect of reducing the concrete volume (and moment of inertia) of the tower. Two additional analyses were performed. In the first one, the wall thickness of the tower was reduced linearly from top to bottom in 25% (NLMG-25) and in the second one, it was reduced in 50% (NLMG-50). For all models, the radius of the towers was kept the same, i.e. 1.8 m and 3.6 m at the top and bottom, respectively. Also, material and geometric nonlinearities were considered and a FRC fibre orientation of [0–15°] was used.

The response in terms of horizontal force versus deflection of the towers at the top is compared with the original model (NLMG-00) in Fig. 5. A decrease of the wall thickness in 25% (NLMG-25) and 50% (NLMG-50) corresponds to a reduction of concrete volume of, respectively, 23% and 47% and in terms of the moment of inertia of 20% (NLMG-25) and 43% (NLMG-50).

Fig. 4 Effect of material and geometric nonlinearity response of the tower in terms of total horizontal force versus the displacement at the top of the tower
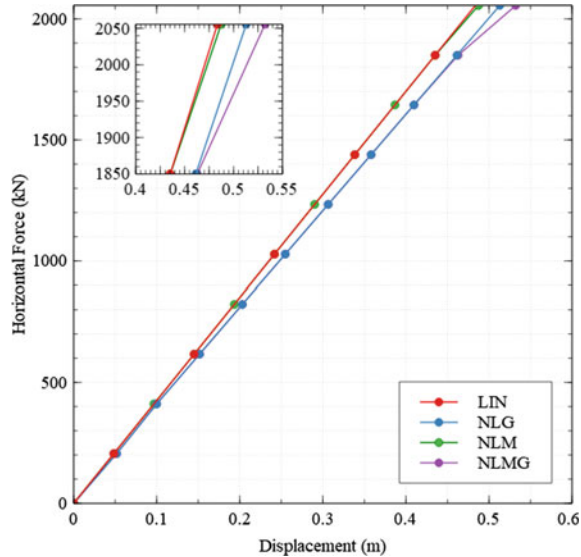
Figure 5 shows that the reduction of wall thickness by 25% and 50% increased the displacement at the top of the tower by 73% and 94%, respectively. The dashed horizontal lines in Fig. 5 indicates the maximum force corresponding to the serviceability limit state combination. According to available research, below to this crack width limit the corrosion of steel fibres, even in maritime environmental conditions, is not sufficient to compromise the structural performance of the SFRC [13].

The stresses (S_z) at the concrete and the crack pattern obtained by the analyses can be seen in Fig. 6. The highest concrete compressive stress is of the order of 32.9 MPa at the tower with a reduction of 50% (NLMG-50), Fig. 6a. It can also be seen that more cracks are developed by reducing the wall of the structure. However, the number of cracks does not increase significantly when the thickness of the wall is reduced from 25 to 50%, Fig. 6b. The maximum crack width was 0.2 mm ($\sim$2055 kN), 0.3 mm ($\sim$2080 kN) and 0.4 mm ($\sim$1850 kN) for NLMG-00, NLMG-25 and NLMG-50 respectively.

The natural frequencies are also affected by the reduction of volume/moment-of-inertia of the tower. The rotor is the most visible and present source of excitation in a wind turbine system. It creates peaks in excitation at frequencies of the rotor speed range (1P) and blade passing speed range (3P for a three-bladed rotor). Thus, the tower should be designed such that its first natural frequency does not coincide with either 1P or 3P excitation to avoid resonance. It is recommended that the lowest frequencies differ from at least $\pm$10% of the 1P and 3P rotor frequencies at nominal power [14].

The frequencies of the towers analysed in the study were calculated using the in-house FEM-based software for dynamic analysis of frame type structures.
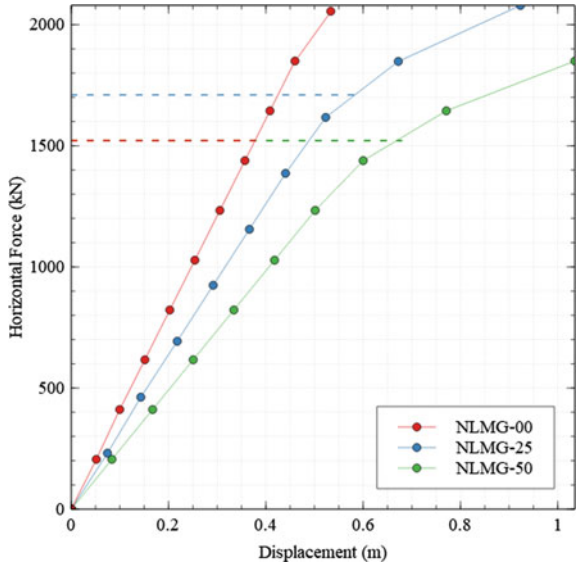
Fig. 5 Effect of the moment of inertia reduction on the behaviour of the tower in terms of total horizontal force versus the displacement at the top of the tower
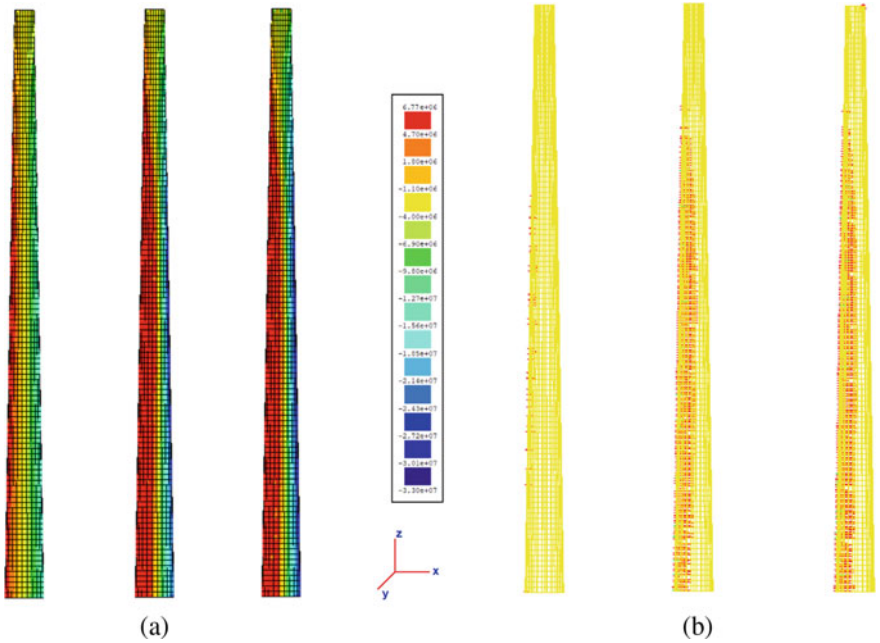
Fig. 6 **a** Stress S_z results in Pa for NLMG-00, NLMG-25 and NLMG-50, respectively. **b** Crack pattern for NLMG-00, NLMG-25 and NLMG-50, respectively

The structures were modelled as a cantilever beam with an added mass applied at the top to represent the nacelle and rotor masses. The finite element mesh was made of hundred 2D-Timoshenko beam elements. The estimated first natural frequencies for 0% (NLM-00), 25% (NLM-25) and 50% (NLM-50) of the moment of inertia reduction were 0.338 Hz, 0.320 Hz and 0.289 Hz, respectively. These frequencies do not coincide with either the rotor speed range (1P) or blade passing speed range (3P), which are 0.187 Hz and 0.560 Hz, respectively.

5   Conclusions

This paper presented the nonlinear finite element analysis of a new concept of offshore wind tower made by prefabricated prestressed fibre reinforced concrete (FRC) segments that are assembled to form the final structure. Three studies were carried out to investigate the impact of the fibre orientation in the FRC, nonlinearities (material and geometric) and moment of inertia of the tower section in the global behaviour of the structure.

The analyses performed clearly showed the importance of considering the geometric and material nonlinearities to analyse this type of structures. The consideration of both nonlinearities increased the displacement at the top of the tower by 10% at the load level corresponding to serviceability limit design state conditions.

The results obtained in this initial study also indicates the potential of the proposed solution. The analyses showed that, by using fibre reinforcement, it is possible to eliminate conventional passive steel reinforcement and decrease the thickness of the wall of the segments considerably compared to conventional solutions. However, it is necessary to optimise the prefabrication process to guarantee that the fibres are oriented between 0° and 45°. The influence of the assembling process of the prestressed FRC segments on the global and local (stress gradients in the corresponding connections) behaviour must be also addressed.

References

1. Schaarup, J., Krogh, T.: DNV-Risø 'Guidelines for Design of Wind Turbines'. Risø vinddag, Denmark (2002)
2. EFNARC: The European Guidelines for Self-Compacting Concrete: Specification, Production and Use. UK (2005)

3. Abrishambaf, A., Barros, J.A.O., Cunha, V.M.C.F.: Time-dependent flexural behaviour of cracked steel fibre reinforced self-compacting concrete panels. Cem. Concr. Res. **72**, 21–36 (2015)
4. Abrishambaf, A.: Creep behaviour of cracked steel fibre reinforced self-compacting concrete laminar structures. Ph.D. Thesis, University of Minho (2015)
5. Figueiredo, F.P., Hassanabadi, M.E., Barros, J.A.O., Ventura-Gouveia, A.: Simplified Design Approach of Offshore Wind Towers Report. University of Minho, Portugal (2018)
6. Arany, L., Bhattacharya, S., Adhikari, S., Hogan, S.J., Macdonald, J.H.G.: An analytical model to predict the natural frequency of offshore wind turbines on three-spring flexible foundations using two different beam models. Soil Dyn. Earthq. Eng. **74**, 40–45 (2015)
7. Ma, H., Yang, J., Chen, L.: Numerical analysis of the long-term performance of offshore wind turbines supported by monopoles. Ocean Eng. **136**, 94–105 (2017)
8. DNV: DNV-OS-J101 Design of Offshore Wind Turbine Structures (2014)
9. Barros, J.A.O.: Debilites and strengths of FEM-based constitutive models for the material nonlinear analysis of steel fiber reinforced concrete structures. In: Saouma, V., Bolander, J., Landis, E. (eds.) 9th International Conference on Fracture Mechanics of Concrete and Concrete Structures, FraMCoS-9. California, May 29–June 1 (2016)
10. Gowda, C.C., Figueiredo, F.F, Barros, J.A.O., Ventura-Gouveia, A.: Numerical analyses of the connections between representative SFRC prestressed rings of off-shore wind towers. In: 3rd RILEM Spring Convention. Springer, Portugal (2020)
11. Ventura-Gouveia, A.: Constitutive models for the material nonlinear analysis of concrete structures including time-dependent effects. Ph.D. Thesis, University of Minho (2011)
12. Lameiras, R.M., Barros, J.A.O., Azenha, M.A.D.: Influence of casting condition on the anisotropy of the fracture properties of Steel Fibre Reinforced Self-Compacting Concrete (SFRSCC). Cement Concr. Compos. **59**, 60–76 (2015)
13. Frazão, C.M.V., Barros, J.A.O., Bogas, J.A.B.A.: Durability of recycled steel fiber reinforced concrete in chloride environment. Fibers J. **7**(12) (2019)
14. Det Norske Veritas: Guidelines Design of Wind Turbines, 2nd edn. DNV/Riso, Denmark (2002)

Early Age Temperature Control in Mass Concrete Through Incorporation of Dispersed Phase Change Materials (PCMs)

Mohammad Kheradmand, Romeu Vicente, Miguel Azenha, and José Luís Barroso de Aguiar

Abstract There is a frequent need to take measures for temperature control in massive concrete structures, as to avoid thermal cracking risk at early ages (induced by temperature gradients inherent to hydration heat release). This research work has explored a procedure for temperature control through the incorporation of phase change materials (PCMs) in laboratory environment (mortar testing). Indeed, PCM's have the potential to store and release heat energy during phase change from solid to liquid, or vice versa. By choosing a PCM with a melting range between casting temperature and the expected peak temperature, it is possible to attenuate the temperature rise rate in concrete through heat storage (the melting process is endothermic). This paper presents and discusses an experimental work focused on the thermo-physical properties and thermal performance analysis of mortar with direct incorporation of pristine PCM (with a melting temperature of 34 °C and latent heat capacity of 240 J/g) in three volume fractions of 0, 10 and 20% in mixture compositions (volumetric percentage replacement with regard to sand particles), cast into partially insulated cubes with 320 mm^3 size. The thermal performance tests revealed the impact of the PCM in the thermal behavior of the cast element, by reducing the maximum peak temperatures in comparison with the reference case (without PCM). Mechanical tests were also performed and revealed that, as expected, their compressive and flexural strength are reduced. Nonetheless, the observed reduction might still be compatible with structural applications in specific contexts, even for the case of high PCM content incorporation (20%).

M. Kheradmand (✉) · R. Vicente
RISCO, Department of Civil Engineering, University of Aveiro, Aveiro, Portugal
e-mail: mohammadkheradmand@hotmail.com

R. Vicente
e-mail: romvic@ua.pt

M. Azenha
ISISE, Department of Civil Engineering, University of Minho, Braga, Portugal
e-mail: miguel.azenha@civil.uminho.pt

J. L. B. de Aguiar
CTAC, Department of Civil Engineering, University of Minho, Braga, Portugal
e-mail: aguiar@civil.uminho.pt

1 Introduction

In concrete, the stress developed at early ages can lead to cracking due to the restrained volume changes, originally associated to the autogenous shrinkage and thermal expansion/contraction [1]. Early age cracking of concrete [2] may reduce performance levels for serviceability and durability [3]. Several measures can be taken to help to mitigate early age cracking, particularly at the definition of mix constituents and mix proportioning: using specific cement or admixtures [4], and phase change materials (PCMs) as additives [5–9].

The principle of operation of PCMs [10] through heat storage in the scope of concrete applications can be explained with the following example: in a concrete mixture containing PCM, when the increasing core temperature of concrete (induced by cement hydration heat) reaches the melting point of the PCM, it endures the corresponding phase change and absorbs heat (endothermic process). Therefore, while the heat storage capacity of PCM still exists, concrete temperature tends to remain in the vicinity of the PCM's melting point [5], therefore limiting the temperature rise, and inherently leading to smaller thermal cracking risk.

There are several methods of incorporation of PCM into mortar proposed in the literature, such as: suspension of phase change material (SPCM) in combination with water [6], self-compacting concrete cubes containing PCMs (dispersed form of incorporation) [11], concrete containing porous aggregates incorporated with PCMs (in the form of vacuum impregnation) [12], mortar and concrete mixes blended with microencapsulated PCM (by direct incorporation) [13], footing member and bridge pier containing PCM (added into the mixture) [14], and cement based materials incorporating microencapsulated PCM [15]. Regardless of the incorporation method, the selection of the PCM to incorporate is mostly related to two key characteristics [16]: the specific enthalpy and phase change temperature range.

The present work presents a study of thermal and mechanical behaviour of a mortar in which the volume of sand is partially replaced by PCM (directly incorporated into the mixture). Apart from the study of the reference case (no PCM added), two volumetric ratios of replacement of sand by PCM are considered: 10% and 20%.

2 Experimental Program

2.1 *Materials*

The PCM selection was based on the typical temperature development for concrete structures. The initial selection of PCM melting temperature range was limited to

30–40 °C, which is a range that is usually attained during curing of most massive concrete structures, when the surrounding boundary temperature is ∼20 °C [17]. The average hydration heat of cement is 300 kJ/kg, therefore, the selected PCM needs to have high latent heat capacity [3]. For the experimental testing carried out, commercial PCM "RT35HC" (from Rubitherm paraffin RT series) [18] was selected for this study that has a latent heat capacity of 240 kJ/kg and melting temperature ranges between 34 and 36 °C. Portland cement type I class 42.5R was used as a binder from the SECIL company, Portugal. River sand was used as aggregate. The fineness modulus of the sand was 3.2.

2.2   Development of Mortars

The mix design of the investigated mortars together with their adopted designations are listed in Table 1. This study includes a reference mortar (REFM) and two mortar systems named as PCMM10 and PCMM20, which incorporate respectively 10% and 20% Vol. of PCM dispersed in the mixture (ratios defined in regard to the volume of sand). Figure 1, shows a illustrative scheme on the comparison between the cross section structure of the PCM mortars dispersed PCM and reference mortar. This figure presents the effect of the PCM incorporation on the specific configuration of the mortar systems, i.e. possibly of homogeneity of dispersed form of the PCM particles.

3   Strategies and Test Procedures

3.1   Characterization of the Mortars

3.1.1   Flow Table Test

The flow table test was used to maintain the mortar workable according to the flow value based on diameter of standard frustum. The workability tests were conducted through flow table test based on the European standard EN 1015-3 [19]. The mortar

Table 1 Mix design of reference mortar and mortars with grated PCM

Components (kg/m^3)	Reference mortar	PCM mortar	
	REFM	PCMM10	PCMM20
Cement type I—42.5R	500	500	500
Water	245	265	285
Sand	1579	1435.5	1315.8
PCM	0	41.7	76.5

Fig. 1 Illustrative scheme of the internal structure of reference (left), dispersed PCM (right) mortars
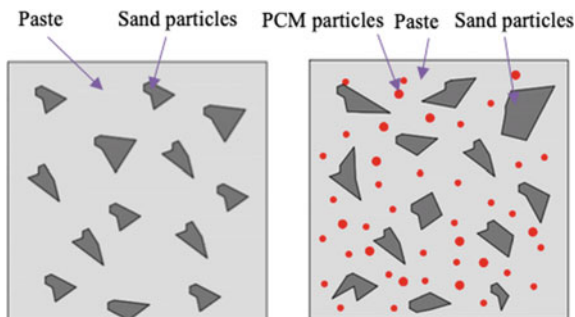
was considered workable only when the value of 140 ± 5 mm was monitored/recorded for proposed mortar.

3.1.2 Density

For the density measurement, three specimens were considered for each type of mortar. The test was made following recommendations of EN1015:10 [20]. Firstly, the specimens were casted into prism moulds (with dimensions of 160 mm × 40 mm × 40 mm). Then, the specimens were kept sealed with a plastic wrap at room temperature (20 ± 1 °C) for 24 h. Then, the specimens were submerged at 20 ± 1 °C for 7 days. Finally, the specimens were dried at 70 °C until recording constant weight for each specimen. The density of the specimens was calculated directly. The average density of different formulations is reported.

3.1.3 Flexural Strength

Flexural strength testing was performed at age of 28 days following European standard EN1015-11 [21]. Three prism specimens with dimensions of 40 mm 40 mm × 160 mm were prepared and sealed by plastic wrap at room temperature (20 °C) until testing. A three-point loading method was deployed using apparatus model SHIMADZU-AG-IC with the capacity of 100 kN. Average of the measured valued was used on the analysis. For the flexural strength measurement, three specimens were considered for each type of mortar and average values are reported.

3.1.4 Compressive Strength

The compressive strength tests were performed to evaluate the effect of the PCM on the mechanical strength of the mortars taken from ruptured specimens in flexural strength testing. For each mortar mixture, three specimens were tested at the age of 28 days. The testing recommendations of EN1015-11 [21] were followed. All the

specimens were kept sealed with a plastic wrap in laboratory environment until testing (28 days). Then, the compressive strength tests were carried out using apparatus model SHIMADZU-AG-IC with 100 kN capacity. The average of the measured values was used for the analysis.

3.2 Field Thermal Analysis of the Mortars

3.2.1 Thermal Energy Storage

A total number of 3 specimens were prepared for differential scanning calorimetry (DSC) testing. This includes a representative specimen of each mortar containing PCM (PCMM10 and PCMM20), one specimen for reference mortar (REFM) and one specimen was also taken from bulk PCM (RT35HC). The specimen preparation for DSC testing is shown in Fig. 2. All test samples were obtained from mortar cast prism molds with dimensions of 40 mm × 40 mm × 160 mm, which were cured for 28 days before preparation for DSC testing (Fig. 2a). Central part of the prism was cut out, resulting in a slice with size of 40 mm × 40 mm × 4 mm (Fig. 2b). A small sub sample with dimensions about 4 mm × 4 mm × 1 mm was extracted and submitted to DSC testing (Fig. 2c). The detained classification of the type of specimen as well as weight of the samples for DSC testing is presented in Table 2.

In performed DSC analyses (Perkin Elmer model AD-4), the system measures the difference in the amount of heat required to increase the temperature of a material sample (sample pan) and an empty sample (reference pan) as a function of temperature. The DSC equipment has an accuracy of ±0.3 °C. The specific heat and the specific enthalpy was determined following the methodology detailed in [16]. The phase change and temperature were obtained from the DSC heat fluxes
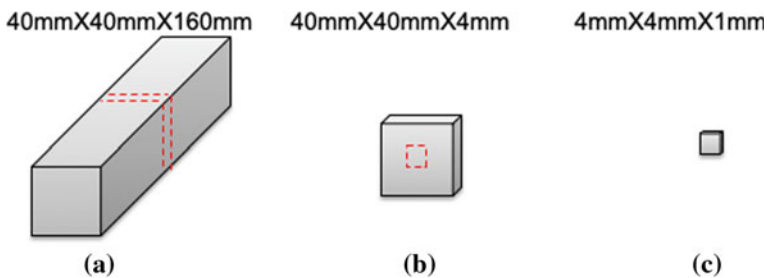
Fig. 2 Schematic of specimen preparation for DSC test: **a** fabricated sample in the shape of prism cured for 28 days; **b** the thin layer of 4 mm width were cut from the middle of the prism in the form of slice; **c** finalized sample for DSC testing, extracted from the center of the slice

Table 2 Identification of the samples taken and weight for DSC testing

Samples	Names	Weight of specimen for DSC testing (mg)
Mortar with 10% PCM	PCMM10	16.202
Mortar with 20% PCM	PCMM20	15.860
Conventional mortar	REFM	16.401
Pristine PCM	RT35HC	7.564

signal response by integration. The volumetric heat capacity of the material is calculated by multiplying the density and specific heat capacity according to Eq. (1):

$$C_{pv} = C_p \times Rho \tag{1}$$

Such value ascribes the ability of the material in terms of energy storage in a certain volume while undergoing a given temperature change. The theoretical latent heat capacity of these PCM mortars was also determined as Eq. (2):

$$H(T) = H_{pcm} \times \left(W_{pcm}\%/100\right) \tag{2}$$

where $H(T)$ is the calculated latent heat of the mortar (J/g), H_{pcm} is the latent heat of the PCM, W_{pcm} is the weight percentage of the PCM in the matrix.

3.2.2 Design of the Specimen Prototypes

In order to assess the effect of different quantities of dispersed PCM into the mortar, for measuring early age temperature, three cubic specimens were casted. The cubes for the testing REFM, PCMM10 and PCMM20 mixtures, have dimensions of $200 \times 200 \times 200$ mm^3, as presented in Fig. 3. Lateral faces, base and top of the element were insulated with 40 mm thick extruded polystyrene (XPS) and 20 mm thick plywood formworks. The casting process and the experiments themselves took place in controlled conditions, inside a climatic chamber to guarantee a constant temperature of 20 °C and relative humidity of 50%. Data acquisition started at the end of casting operations. Regarding the experimental monitoring equipment, a temperature sensor type K with a precision of ±1.1 °C was placed at the geometrical centre of the mortar. A total of three experiments were conducted by submitting the specimens to the climatic chamber room with constant temperature of 20 °C with during 4 days. The temperature sensor was connected to the data logger (AGILENT 34970A) with a acquisition period of 15 min. The physical arrangement of this setup can be observed in Fig. 4.
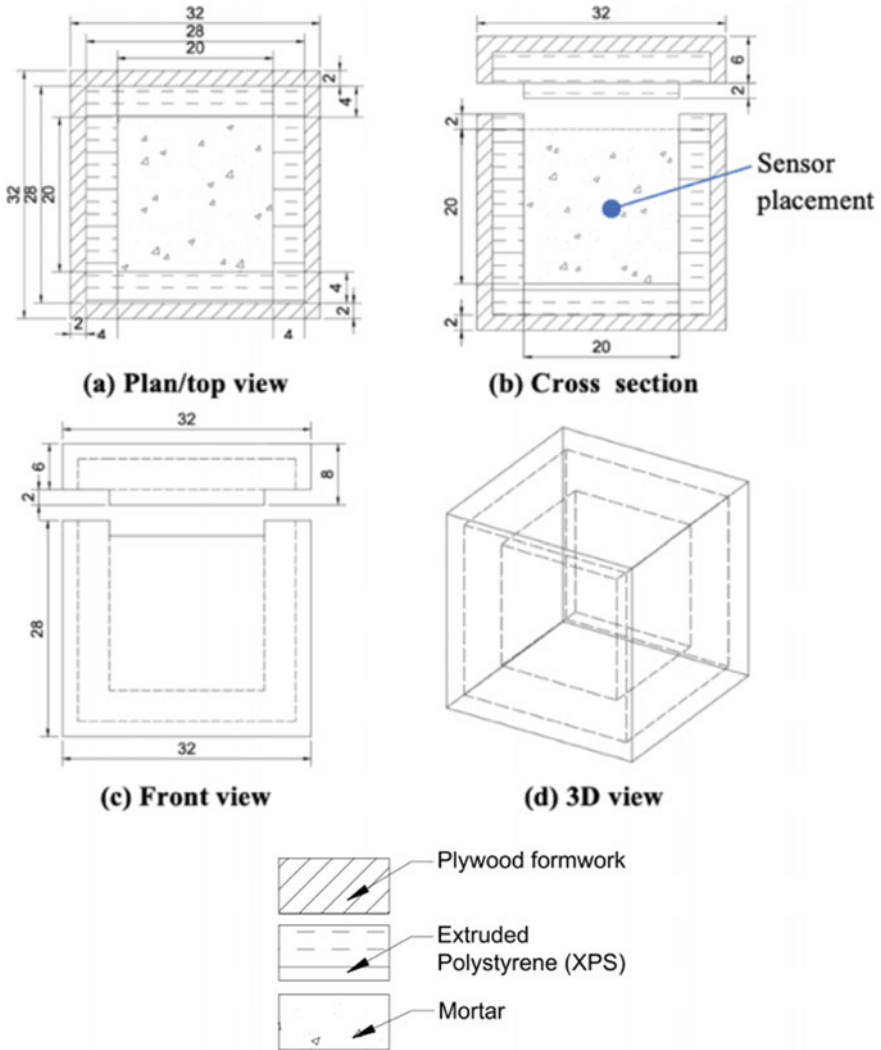
Fig. 3 Schematic representation of the experimental set up for reference mortar (REFM) and distributed form of grated pristine PCM mortars (PCMM10 and PCMM20): mixtures and sensor location. Units [cm]

4 Results and Discussion

4.1 Physical and Mechanical Performance

The workability test proved that the incorporation of the PCM leads to an increase in water content by 8% and 16% for the PCMM10 and PCMM20, respectively.
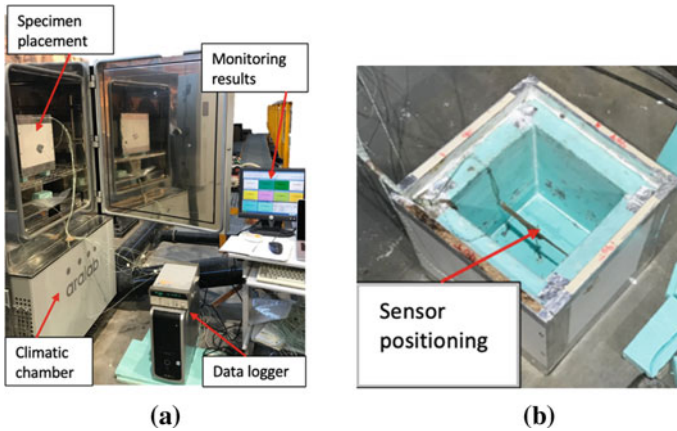
Fig. 4 **a** Photo of the prototype within climatic chamber before starting the test; **b** position of the temperature sensor for REFM, PCMM10 and PCMM20 cases

This is maybe due to the particle size distribution of the PCMs in the mixture compared to the sand particles.

The density values for the REFM, PCMM10 and PCMM20 were 2188 kg/m^3, 1904 kg/m^3, 1870 kg/m^3, respectively. The density of the mortars with PCM are 13% and 17% lower than that of reference mortar (REFM) for the MPCMM10 and MPCMM20, respectively. This is attributed to the density of the PCM, which is lower than the sand particles.

Figure 5a shows the compressive strength values for different specimens at 28 days of age. PCM mortars have lower compressive strength than the reference mortar, REFM. The strength of the PCMM10 and PCMM20 was reduced about 19% and 50%, respectively, when compared with REFM. A similar trend was observed for the flexural strength of the mortars with PCM (shown in Fig. 5b). The flexural strength reduces for the cases of MPCMM10 and MPCMM20 by 24% and 42%, respectively, when compared with REFM.
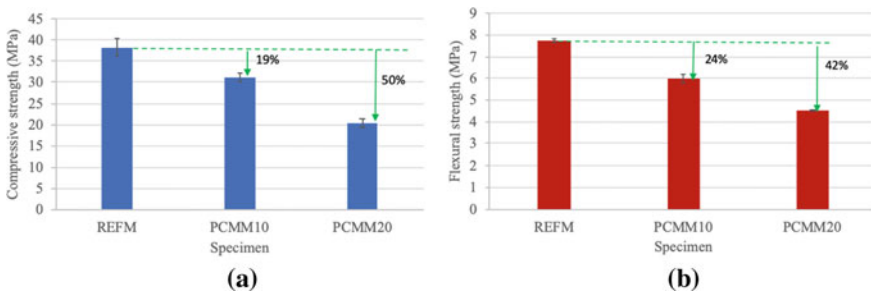
Fig. 5 Strength performance of different mortars and average with standard deviation of the measured values: **a** compressive strength; **b** flexural strength

4.2 Thermal Performance

4.2.1 DSC Analysis

The results of DSC testing on the pristine PCM (RT35HC), REFM, PCMM10 and PCMM20 specimens are shown in Fig. 6. The absence of phase change can be confirmed for the case of REFM. The melting peak temperatures were obtained by 38.2 °C, 36.8 °C and 37.8 °C for pristine PCM (RT35HC), REFM, PCMM10 and PCMM20, respectively. The peak temperatures of PCM and PCMM20 are in a similar fashion. While, the tendency is though less clear because the PCMM10 involved smaller quantity of the PCM. The results suggested that the PCM peak temperature shifts in the direction of the imposed flux, thus, showing higher peaks for mortars containing more PCM incorporation. The DSC thermograms have been zoomed to clearly visualize the peak values in the case of mortars with PCM.

Figure 7 shows the volumetric heat capacity calculation for the studied mortars. Volumetric specific heat capacity indicates the ability of the material in terms of energy storage in a certain volume while experiencing a given temperature change.

The high thermal capacity indicates a material is characterized by high thermal mass and high thermal conductivity. In general, it can be stated that, the PCM mortars have higher thermal inertia than that of the reference mortar, thus, higher potential for attenuating the effect of hydration heat of cement based material.

Figure 8a shows the values of the specific enthalpy of mortars. It can be observed that the specific enthalpy values increased with incorporation of more PCM quantity. It is also interesting to calculate the specific enthalpy values through extrapolation in order to predict the energy performance of PCM mortar. Figure 8b shows the estimated specific enthalpy for mortars (based on the characteristics of the PCM and its volume within each mortar) in which the values are in the same magnitude as those already obtained experimentally (less than 10% difference). These results confirm the expectable proportionality between specific enthalpy of PCM and mortar containing PCM, based on the mass fraction of the PCM.
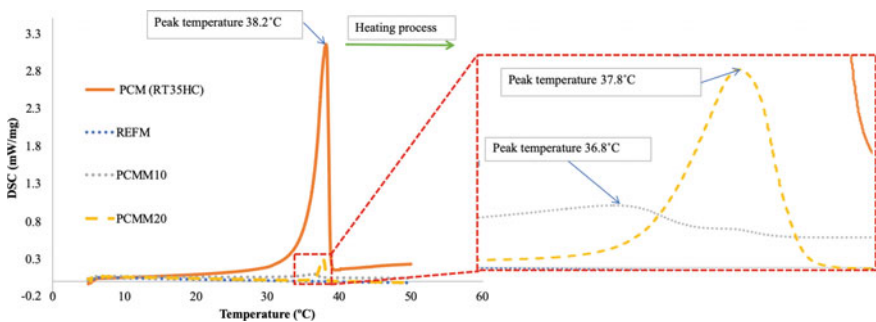
Fig. 6 DSC thermograms for mortars with and without PCM plus pristine PCM at the rate of 2 ° C/min
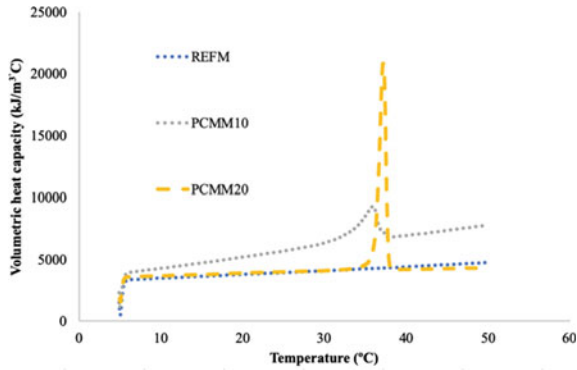
Fig. 7 Results for volumetric specific heat capacities of mortars
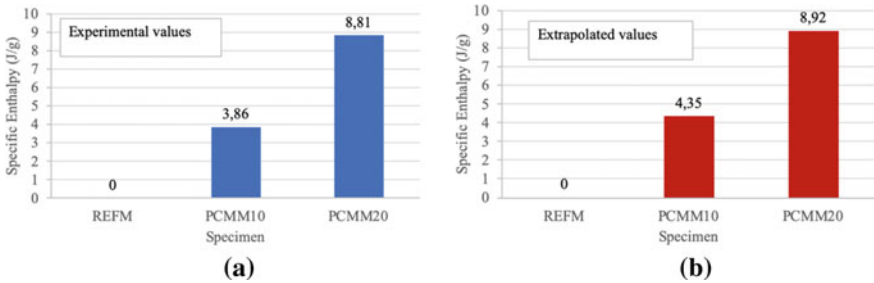
Fig. 8 a Measured specific enthalpy values of the mortars with PCM; **b** extrapolated specific enthalpy values

4.2.2 Transient Behavior of Cube Specimen

Temperature values measured in the geometrical center of the specimens are presented in Fig. 9. It can be noted that the temperature rises after casting of the mortar continues up to about 1 day and then, reduces until the end of testing. It is interesting to note that the peak temperature recorded for the cases with PCM is lower than that of REFM. as expected, the specimen with more PCM shows a lower peak temperature. It is also noticeable that, the phase change temperature of the PCM ranges between 33 and 36 °C, flatting the temperature evolution in the cooling phase. The peak temperatures reduction was recorded by 5 °C and 9 °C for the PCMM10 and PCMM20, respectively, when compared with REFM.

Fig. 9 Interior temperature of the cubic specimens: comparison between REFM, PCMM10 and PCMM20
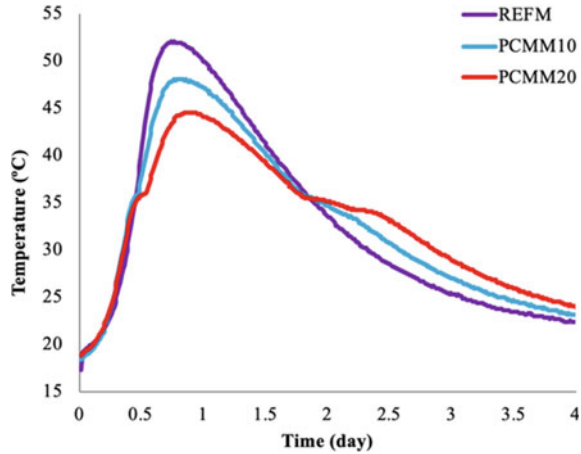
5   Conclusions

In this study, mortars incorporated with PCM have been developed and experimentally characterized. Based on the experimental campaign results, the following main conclusions can be drawn:

- The addition of the dispersed form of PCM into the mortar has led to 13% and 17% reduction of the density, when compared with the reference mortar.
- Addition of PCM leads to reduction of mechanical properties. However, it may still be compatible in structural applications.
- The DSC test results showed that the specific enthalpy is proportional to the mass fraction of PCM in the mortar sample as compared to the behavior of the pristine PCM sample. The numerical estimation of enthalpy values for PCM mortars matched the measured values quite closely, indicating the applicability of the estimation procedure.
- Thermal performance of the transient test has demonstrated the reduction of temperature rise, enhancing thermal capacity of the mortars with PCM.

References

1. Bilčík, J., Sonnenschein, R., Gažovičová, N.: Causes of early-age thermal cracking of concrete foundation slabs and their reinforcement to control the cracking. Slovak J. Civil Eng. **25**(3), 8–14 (2017)
2. Nicholas, J., Carino, J.R.: Clifton, prediction of cracking in reinforced concrete structures. NISTIR Report No.5634, 51 p. (1995)
3. Neville, A.M.: Properties of Concrete, 5th edn, 2865 p. Pearson Education, Limited (2011)
4. Sant, G.N.: Fundamental Investigations Related to the Mitigation of Volume Changes in Cement-Based Materials at Early Ages. Purdue University (2009)

5. Bentz, D.P., Turpin, R.: Potential applications of phase change materials in concrete technology. Cement Concr. Compos. **29**(7), 527–532 (2007)
6. Qian, C., Gao, G., Zhu, C., Guo, Z.: Influence of phase change materials on temperature rise caused by hydration heat evolution of cement-based materials. Mag. Concr. Res. **62**(11), 789–794 (2010)
7. Fernandes, F., Manari, S., Aguayo, M., Santos, K., Oey, T., Wei, Z., Falzone, G., Neithalath, N., Sant, G.: On the feasibility of using phase change materials (PCMs) to mitigate thermal cracking in cementitious materials. Cement Concr. Compos. **51**, 14–26 (2014)
8. Qian, C., Gao, G.: Reduction of interior temperature of mass concrete using suspension of phase change materials as cooling fluid. Constr. Build. Mater. **26**(1), 527–531 (2012)
9. Thaicham, P., Gadi, M.B., Riffat, S.B.: An investigation of microencapsulated phase change material slurry as a heat-transfer fluid in a closed-loop system (2004)
10. Duffie, J.A., Beckman, W.A.: Solar Engineering of Thermal Processes. Wiley (2013)
11. Hunger, M., Entrop, A., Mandilaras, I., Brouwers, H., Founti, M.: The behavior of self-compacting concrete containing micro-encapsulated phase change materials. Cement Concr. Compos. **31**(10), 731–743 (2009)
12. Zhang, D., Li, Z., Zhou, J., Wu, K.: Development of thermal energy storage concrete. Cem. Concr. Res. **34**(6), 927–934 (2004)
13. Jayalath, A., San Nicolas, R., Sofi, M., Shanks, R., Ngo, T., Aye, L., Mendis, P.: Properties of cementitious mortar and concrete containing micro-encapsulated phase change materials. Constr. Build. Mater. **120**, 408–417 (2016)
14. Kim, Y.-R., Khil, B.-S., Jang, S.-J., Choi, W.-C., Yun, H.-D.: Effect of barium-based phase change material (PCM) to control the heat of hydration on the mechanical properties of mass concrete. Thermochim. Acta **613**, 100–107 (2015)
15. Šavija, B., Schlangen, E.: Use of phase change materials (PCMs) to mitigate early age thermal cracking in concrete: theoretical considerations. Constr. Build. Mater. **126**, 332–344 (2016)
16. Kheradmand, M., Azenha, M., de Aguiar, J.L.B., Krakowiak, K.J.: Thermal behaviour of cement based plastering mortar containing hybrid microencapsulated phase change materials. Energy Build. **84**, 526–536 (2014)
17. Azenha, M. Â. D.: Numerical Simulation of the Structural Behavior of Concrete since its Early Ages. Ph.D. Thesis, University of Porto (2009)
18. RUBITHERM®: Technologies GmbH PCM Technology and Development (2017). https://www.rubitherm.eu/en/about-us.html
19. EN 1015-3: Methods of Test for Mortar for Masonry—Part 3: Determination of Consistence of Fresh Mortar (by Flow Table), European Committee for Standardization (CEN) (2004)
20. EN 1015-10: Methods of Test for Mortar for Masonry, European Committee for Standardization (CEN) (2006)
21. B. EN. 1015-11: Methods of Test for Mortar for Masonry–Part 11: Determination of Flexural and Compressive Strength of Hardened Mortar, European Committee for Standardization, Brussels (1999)

Determination of Autogenous Self-healing Capability of Cementitious Composites Through Non-destructive Testing

Gürkan Yıldırım, **Oğuzhan Öztürk**, **Hüseyin Ulugöl**,
Muhammed Hatem, and **Mustafa Şahmaran**

Abstract Unlike conventional concrete and fiber reinforced concrete, Engineered Cementitious Composites (ECC) display closely spaced multiple microcracks through strain/deflection-hardening response when subjected to tension-based loadings. These multiple microcracks allow ECC to be characterized with inherent autogenous self-healing capability. With the emergence of cement-based composites exhibiting multiple tight cracking, possibility for favoring the intrinsic self-healing behavior increased. Self-healing phenomenon in cementitious composites is being studied extensively nowadays. Although, great number of tests utilized to evaluate the self-healing mechanism in cementitious composites, implementation can be time consuming in some occasions and results from different tests may not always well-suit. Thus, different from other studies in literature, direct electrical impedance (EI) measurements were used in the present study to evaluate the self-healing performance of ECC mixtures along with rapid chloride permeability test (RCPT) and resonant frequency (RF) measurements. Experimental results revealed that EI testing is rather easy to perform and takes very limited time but it seems that the method itself is markedly influenced by anything modifying ionic state of specimens. Therefore, it looks like a hard task to very accurately assess the self-healing performance of ECC specimens considering the fact that both ongoing hydration and calcium carbonate precipitation which are regarded to be the main mechanisms contributing to the autogenous self-healing significantly changes the specimens' pore solution chemistry. Well-fitting exponential relationship exists between EI and RCPT measurements at different ages regardless of the mixture and specimen type. However, results from RF tests do not correlate either with EI or RCPT results which is attributed to the different parameters having

G. Yıldırım
Kırıkkale University, Kırıkkale, Turkey

O. Öztürk
Konya Technical University, Konya, Turkey

H. Ulugöl (✉) · M. Şahmaran
Hacettepe University, Ankara, Turkey

M. Hatem
Ankara University, Ankara, Turkey

paramount influence on the individual tests. Although results from different tests do not always correlate well among themselves, three different tests used for the present study are capable of monitoring the self-healing behavior with differing efficiencies.

1 Introduction

Concrete materials and structures are expected to be durable during their service life For example, European Standards obligate 75-years of service life for large-scale public constructions [1]. However, mechanical loads and environmental effects may reduce the expected service life of concrete and necessitate repair and maintenance process [2]. Crack formation is inevitable in concrete's service life and is a phenomenon that introduces a deterioration process which is detrimental for the cement-based materials. This deterioration arises from durability problems such as rebar corrosion, freeze–thaw cycles, alkali-silica reaction and sulfate attacks. Additionally, cracking may lead to loss of cross-sectional area due to spalling. Moreover, these durability issues may stimulate each other. For this reason, cracking is a basic problem that triggers many different types of durability problems. To that end, limiting the crack formation of brittle concrete-like materials is of great interest.

Self-healing is a practical way of healing and repairing cracks. There are various self-healing methods that requires different techniques and matrices. One of the most popular and practical self-healing methods is autogenous self-healing. This technique differs from the others and do not require internal triggering mechanism such as capsules, bacteria or expanding agents. Engineered Cementitious Composites (ECC), which is a material favoring intrinsic autogenous healing due to inherent tight microcracking behavior under excessive loading, were introduced by Li et al. in the late 1990s [3]. So far, various studies related to intrinsic autogenous healing have been conducted [4–10]. Besides, studies about assessment methods of self-healing have been published in the literature [11].

This study concentrated on direct electrical impedance (EI) measurements to evaluate the amount of autogenous self-healing. Additionally, results were verified with non-destructive test (NDT) methods; rapid chloride permeability test (RCPT) and resonant frequency (RF) test.

2 Experimental Investigation

2.1 Materials and Mixture Designs

In this study, two different ECC mixtures were designed with two different pozzolanic materials (PMs). Mixture produced with fly ash (Class-F [FA-F]) was labeled as F_ECC while mixture incorporating slag (GGBFS) was labeled as S_ECC. All mixtures were produced with CEM I 42.5 R general-use ordinary Portland cement (PC, similar to ASTM Type I cement), silica sand with maximum aggregate size of 0.4 mm, polyvinyl-alcohol (PVA) fibers with a diameter of 39 mm, length of 8 mm, nominal tensile strength of 1610 MPa and specific gravity of 1.3, water and polycarboxylic-ether based high range water reducing admixture (HRWRA) with a solid content of 40%. Table 1 shows the chemical and physical properties of materials. Water to cementitious material ratio and pozzolanic material to Portland cement ratio of all specimens were 0.27 and 1.2 respectively. PVA fibers were used on a volumetric basis by 2% and the amount of HRWRA used in the mixtures was based on the achievement of reasonable fresh properties. Mixture designs for one cubic meter are shown in Table 2.

2.2 Specimen Preparation and Initial Pre-loading

Cylindrical specimens with a diameter of 100 mm and a height of 200 mm were produced and after the initial curing of 28 days, disc specimens were cut by diamond blade saw to obtain specimens for non-destructive tests. 28 days of initial curing was carried out in plastic bags at relative humidity of 95% and temperature of 23 ± 2 °C. Non-destructive tests were conducted on pre-loaded specimens after

Table 1 Chemical and physical properties of materials

Chemical composition	FA-F	GGBFS	PC
CaO	3.48	35.09	61.43
SiO_2	60.78	37.55	20.77
Al_2O_3	21.68	10.55	5.55
Fe_2O_3	5.48	0.28	3.35
MgO	1.71	7.92	2.49
SO_3	0.34	2.95	2.49
Available alkalis as Na_2O_{eq}	2.02	0.94	0.70
Loss on ignition	1.57	2.79	2.20
$SiO_2 + Al_2O_3 + Fe_2O_3$	87.94	48.38	29.37
Physical Properties			
Specific gravity	2.10	2.79	3.06
Blaine fineness (m^2/kg)	269	425	325

Table 2 Mixture designs of specimens

Mixture	Amount of ingredients (kg/m^3)						
	PC	FA	GGBFS	Water	PVA	Sand	HRWRA
F_ECC	566	680	–	331	26	453	5.1
S_ECC	593	–	712	347	26	474	6.0

applying splitting tensile loading. Pre-loading was performed by deformation of 70% of the splitting tensile deformation capacity at 28 days, as can be seen in Fig. 1. While determining the splitting tensile deformation capacity at 28 days, a closed-loop controlled material testing system at a loading rate of 0.005 mm/s was used. Sound specimens were also tested to compare the experimental results.

Widths of microcracks were measured shortly after pre-loading by a microscope with a maximum enlargement ratio of 125x. Initial measurements of EI, RCPT and RF were recorded after 28 day-curing. Following NDT measurements were recorded at 15-days intervals until the end of 90 days of further curing. This further curing was provided by a curing cabinet with a relative humidity of 90% and temperature of 50 °C.

2.3 Assessment Methods for Self-healing

Electrical impedance (EI) measurements were carried out by a concrete resistivity meter with a uniaxial configuration. The test setup of resistivity meter can be found in the study of Spragg et al. [12]. Disc specimens having 50 mm height were perpendicularly put between the set of plate electrodes to measure EI precisely

Fig. 1 Multiple microcracks over an ECC specimen after pre-loading
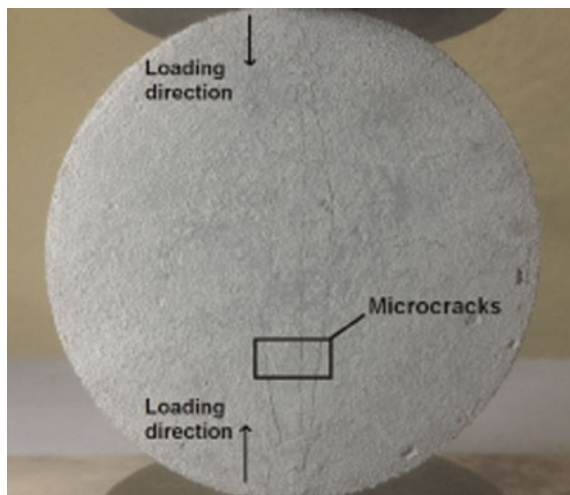
(Fig. 2a). Water-saturated sponges (having 150 mm diameter and 10 mm height) were placed top and bottom of disc specimen to provide sufficient electrical contact between the electrodes and specimens. Concrete resistivity meter works on frequencies between 1 Hz and 30,000 Hz. However, according to Hou [13], AC current should be at least 1 Hz to limit polarization effect. Accordingly, EI tests were conducted at 1 Hz in the present study. EI specimens were left in laboratory conditions at relative humidity of 50% and temperature of 23 °C for 24 h to avoid affecting results by excessive moisture presence in microcracks.

Resonant frequency measurements were recorded according to ASTM C 215 [14] after EI tests. RF device with a frequency range between 10 Hz and 40,000 Hz was arranged to obtain measurements. During RF measurements, frequency spectrums were applied by using impacts of three different hardened steel balls with diameters of 8, 12 and 14 mm. The spectrums recorded through the hardened balls were analyzed by the measurement device. After that, average of RF values in Hertz (Hz) were recorded.

Rapid chloride permeability test (RCPT) was conducted according to ASTM C 1202 [15] to support the EI and RF results. RCPT does not represent the real-time field conditions since there is no concrete material in the field with a 60 V voltage on it and therefore does not give direct information about the permeability of concrete as expected from the test's name, although it can be used for relative comparison of samples under the same conditions. Additionally, there are many studies in the literature in which RCPT is used as, if not for testing of chloride ion resistance, a supporting test method assessing the rate and amount of not only autogenous self-healing [16–18] but also bacteria-based self-healing [19]. Therefore, RCPT was performed on specimens to see whether to harmonize EI and RF results or not. In this context, disc specimens were placed between two cells with a potential difference of 60 V. One of these two cells contains 3.0% salt (NaCl) solution and the other one contains 0.3 M sodium hydroxide (NaOH) solution. Each RCP test lasted 6 h and total amount of current passed through the specimens was recorded in Coulombs. RCPT suggests about chloride ion penetration resistance in the presence of electrical current thus overall permeability can
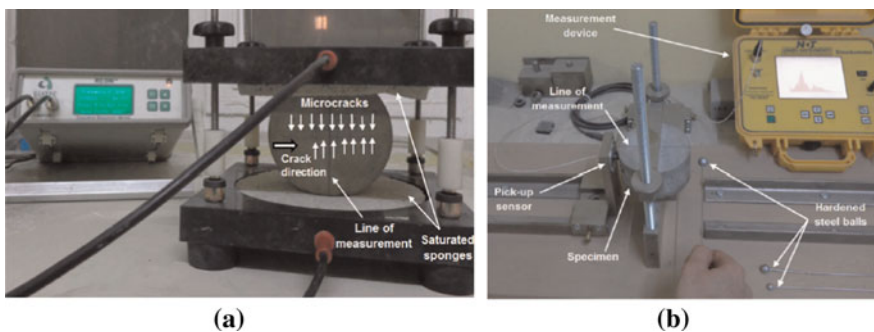
Fig. 2 Non-destructive test methods **a** RCPT, **b** RF

be associated with electrical current results. Although some studies exist in the literature about correlation between RCPT and EI test results [20–22], there is no study concentrated on self-healing performance through these two test methods.

3   Results and Discussion

3.1   *Electrical Impedance (EI) Results*

Table 3 presents electrical impedance (EI) results of both sound and pre-loaded specimens. It is clearly seen from Table 3 that EI results were between 6.77 and 8.19 kΩ for sound F_ECC specimens and 10.4 and 12.2 kΩ for sound S_ECC specimens. Taking into account individual EI results from separate specimens of the same mixture, it can be seen that results were close to each other. These close results indicate COV values which are less than 10%. EI results recorded from S_ECC mixture were higher than those of sound F_ECC specimens. It can be stated from EI results of sound specimens at 28 days that ECC_S have denser structure according to the ECC_F. This case is attributed to the higher reactivity and higher specific surface area of slag. Thus slag leads to reduced overall porosity and pore size, which can significantly decrease the transportation rate of ions.

Obvious increments for both two specimens with initial pre-loading can be seen from Table 3. However, increments for ECC_S were much higher than those for ECC_F. For example, the increment rate of the average EI values of F_ECC specimens with pre-loading was 28% while the same value was 101% for the S_ECC. This behavior could be attributed to the crack characteristics exhibited by different ECC mixtures. S_ECC specimens resulted in a smaller number of cracks but higher average crack widths which is caused by increased chemical bonding between fiber and matrix and fracture toughness values [23]. However, although similar microcracking damage was introduced to the specimens, EI testing was performed after removal of pre-loading. This caused complete closure of some of the small microcracks, especially in F_ECCs, since these specimens exhibited tighter crack widths compared to S_ECCs, as seen in Table 3. Thus, it is worth noting that EI results have affected by crack widths rather than number of cracks [24].

As can be seen in Table 3, rate of EI results increase with further curing is much remarkable for both sound and pre-loaded F_ECC specimens. EI results exhibit that, self-healing performance of F_ECC specimens is better than performance of S_ECC specimens. Results may seem contradictory in comparison with other studies in the literature [16, 25]. However, these contradictory results may be explained by the different formation mechanisms of final self-healing products and their probable effects on electrical measurements. Many papers indicate that the self-healing products of pre-loaded F_ECC and S_ECC mixtures in moist environments are generally C–S–H gels and calcium carbonate. Although C–S–H gels

Table 3 Electrical impedance results at certain days and crack characteristics

			Electrical impedance values (kΩ) at certain days							Average crack widths (μm)	Average number of cracks
			28	28 + 15	28 + 30	28 + 45	28 + 60	28 + 75	28 + 90		
F_ECC	Sound	1	7.41	50.1	76.2	112	131	141	148	–	–
		2	6.77	52.8	76.9	111	133	143	144	–	–
		3	8.19	61.8	93.2	138	168	168	190	–	–
		4	7.63	59.8	94.3	128	162	175	185	–	–
	Pre-loaded	1	8.56	80	110	167	204	216	235	48	2
		2	10.8	92.3	137	203	242	260	288	37	3
		3	9.89	83.3	125	183	226	235	253	42	3
		4	9.16	86.8	129	192	233	243	265	60	2
S_ECC	Sound	1	10.4	26	33.3	48.6	51.6	55.2	67.7	–	–
		2	12.2	27.7	37.4	52	58.2	62.7	77.8	–	–
		3	11.7	25.1	35.3	52.1	56	57.5	67.4	–	–
		4	11.8	27.2	33.4	52.6	55.5	58.7	68.9	–	–
	Pre-loaded	1	23.8	62.8	99	110	112	116	140	72	2
		2	22.3	61.9	91.5	112	122	128	172	65	2
		3	22.7	62	95	107	117	120	154	55	3
		4	23.7	62.3	95	114	126	138	156	102	1

in S_ECC and calcium carbonate in F_ECC are also available at lower quantities [9, 24]. These papers mentioned that due to lower amounts of SiO_2 and reduced pozzolanic capability of S_ECC specimens compared to F_ECC specimens, higher concentrations of portlandite are more likely to be available in the cementitious systems of S_ECC specimens, leading to the presence of pore solution with higher pH values. High pH of pore solution leads to the formation of carbonic acid as a result of reaction between H_2O and CO_2. Carbonic acid (H_2CO_3) may dissolve bicarbonate and carbonate ions and these ions react with Ca^{+2} ions leached away from C–S–H gels and portlandite to form stable calcium carbonate crystals in the cracks. Presence of these carbonates in pore fluid can be substantially influential on the electrical properties of specimen, given the fact that individual ionic conductivities of bicarbonate and carbonate ions (44.5 and 72 cm^2 $equiv^{-1}$ Ω^{-1}) [26] are relatively high, being almost equal to Na^+ and K^+ ions. Thus, reduced EI results, which refer to lower healing rates in S_ECC specimens may be attributed to the higher conductivity of pore fluid caused by the higher ionic concentrations of bicarbonate and carbonate ions in case of higher pH values.

3.2   Rapid Chloride Permeability Test (RCPT) Results

Rapid chloride permeability test results are presented in Table 4. Results of sound specimens clearly show that S_ECC specimens are prone to conduct less chloride ions rather than F_ECC specimens. This may be attributed to the fact that slag particles (425 m^2/kg) are finer than Class-F fly ash particles (269 m^2/kg) and have higher cementing capability than pozzolanic behavior, which can increase results by contributing to better particle distribution and compact microstructure of cementitious matrices. Additionally, RCPT is an electrochemical testing method and is affected by pore solution of specimens which have different alkali contents (Table 1). However, almost all specimens have RCPT values lower than 1000 C which is considered very low according to ASTM C 1202 [15]. As pre-loading was applied to the specimens, additional paths were formed for ions to travel through the pore solution. After the initial pre-loading, RCPT results were raised 137% and 182% for F_ECC and S_ECC specimens, respectively. This behavior of S_ECC specimens was attributed to the stronger chemical bonding between PVA fibers and cementitious matrices, which increase the possibility for fiber rupture instead of pull-out, resulting in a lower number of cracks with increased widths.

  As can be seen in Table 4, further curing introduce decrements in RCPT results irrespective of mixture type. Decrements in RCPT values are due to the improving matrix properties with further curing. Rate of decrements from both mixtures was closer to each other at later ages. However, sound F_ECC specimens exhibited better performance than S_ECC specimens according to RCPT results and this case can be attributed to very slow hydration of fly ash particles. Although sound S_ECC specimens have lower results at the end of the initial 28 days, it appears that F_ECC

Table 4 Rapid chloride permeability results at certain days and crack characteristics

			Rapid chloride permeability values (C) at certain days							Average crack widths (μm)	Average number of cracks
			28	28 + 15	28 + 30	28 + 45	28 + 60	28 + 75	28 + 90		
F_ECC	Sound	1	863	203	105	75	64	62	44	–	–
		2	789	193	100	75	59	55	43	–	–
		3	1006	222	108	78	65	60	41	–	–
		4	981	201	108	76	61	61	39	–	–
	Pre-loaded	1	2058	739	517	413	322	353	342	28	4
		2	2512	734	624	503	426	423	421	34	3
		3	1924	629	423	383	373	367	270	52	2
		4	1970	670	429	343	322	296	293	45	2
S_ECC	Sound	1	596	316	226	155	153	137	117	–	–
		2	594	330	241	171	155	138	120	–	–
		3	645	346	233	179	170	142	124	–	–
		4	607	300	219	155	146	124	115	–	–
	Pre-loaded	1	1858	948	732	630	552	510	361	49	3
		2	1357	729	503	311	253	238	231	73	2
		3	1499	776	755	443	331	296	233	77	2
		4	2169	1361	894	851	780	720	617	64	2

specimens were more affected by additional curing, indicating the importance of further curing on pozzolanic capability.

RCPT results of pre-loaded specimens exhibited remarkable decrements after the curing period of 90 days. After the period of 15 days, RCPT results of almost all ECC specimens changed from "moderate" to "very low," according to ASTM C 1202. So it can be said that, curing period of 15 days in a moist environment is enough for almost-failed ECC specimens to be regarded as harmless in terms of RCPT results.

3.3   Resonant Frequency (RF) Results

Resonant frequency values are shown in Table 5 and it is clearly seen that the values of sound specimens are very close to each other. For instance, F_ECC specimens have an average value of 17.8 kHz after the first 28 days while S_ECC specimens have an average value of 18.9 kHz. Although the differences are relatively small when comparing the values after 28 days, the higher RF results of S_ECC specimens can be correlated with the superior performance of slag particles favoring the attainment of denser microstructure and better paste properties.

After the initial pre-loading, RF results of sound specimens fell independently from the mixture type. According to results, RF results of sound F_ECC and S_ECC specimens to decrease by 45% and 63%, resulting in average RF values of 9.8 and 7.0 kHz in the pre-loaded state, respectively. Significantly reduced RF results with pre-loading were expected, considering that the initial microcracking almost caused complete failure of specimens and is detrimental to overall integrity. It appears that sound S_ECCs were more significantly influenced by initial pre-loading due to increased matrix toughness, fiber-to-matrix chemical bonding and lower ductility compared to F_ECCs.

As further curing applied, results recorded from RF measurements of sound and pre-loaded specimens were inconsistent, regardless of mixture type due to the nature of RF testing and factors affecting it. Although results exhibit variation when compared among themselves, average RF measurements seem to be less variant. Average RF results of both sound and pre-loaded specimens from F_ECC and S_ECC mixtures were stable and show slight increments in values with prolonged curing. Based on past experience, this is due to the combined effects of continuous hydration of anhydrous cementitious particles and precipitation of stable calcium carbonate, which plug the cracks, significantly favoring the unity of specimens [24, 27].

Table 5 Resonant frequency results at certain days and crack characteristics

			Resonant frequency values (kHz) at certain days							Average crack widths (µm)	Average number of cracks
			28	28 + 15	28 + 30	28 + 45	28 + 60	28 + 75	28 + 90		
F_ECC	Sound	1	18.0	18.0	18.0	18.1	16.5	18.4	18.3	–	–
		2	17.7	18.0	18.6	18.1	16.4	12.2	18.5	–	–
		3	17.9	18.0	18.3	18.0	18.4	18.3	18.3	–	–
		4	17.5	17.7	17.8	17.9	18.1	18.2	18.0	–	–
	Pre-loaded	1	10.1	11.0	10.7	11.2	10.9	10.8	10.6	48	2
		2	9.2	10.0	11.0	9.5	11.3	11.4	10.5	37	3
		3	8.9	9.6	9.3	9.3	9.1	9.3	9.1	42	3
		4	11.1	10.6	10.8	10.8	11.2	11.5	10.9	60	2
S_ECC	Sound	1	18.7	18.9	16.4	11.4	11.3	18.8	18.9	–	–
		2	18.7	17.6	18.9	19.0	11.4	19.1	16.3	–	–
		3	18.5	18.5	18.6	18.9	16.4	19.0	11.6	–	–
		4	19.0	19.0	8.7	11.3	11.1	18.9	11.3	–	–
	Pre-loaded	1	7.0	7.8	7.0	8.0	7.0	7.8	7.4	72	2
		2	7.3	7.3	8.0	7.5	8.0	7.1	7.5	65	2
		3	6.3	6.8	7.0	7.2	6.5	7.0	7.0	55	3
		4	7.5	8.3	7.9	8.4	8.1	8.0	8.2	102	1

4   Conclusions

In this study, autogenous self-healing capabilities of ECC specimens with Class-F fly ash and ground granulated blast furnace slag content were studied. Self-healing performance was assessed through non-destructive test (NDT) methods: electrical impedance (EI), rapid chloride permeability test (RCPT) and resonant frequency (RF). The presented study reached the following conclusions:

- Pre-loading introduced remarkable increments in EI measurements, independently from mixture type, although increase rates of S_ECC specimens after initial pre-loading were more significant than increase rates of F_ECC specimens. Further curing increased EI results, however these increments were more pronounced for F_ECC specimens.
- Increased RCPT results after the pre-loading compared to sound specimens decreased with the further curing. RCPT reduction was more pronounced for sound F_ECC specimens rather than sound S_ECC specimens. Besides, pre-loaded ECC specimens have also same trend indicating a certain level of self-healing, although percentage changes in RCPT results with time were comparable for different mixtures, especially at later ages.
- RF results were affected by initial pre-loading; average results of sound specimens dropped by 45% and 63% for F_ECC and S_ECC mixtures, respectively. In general, values from both sound and pre-loaded specimens were stable and showed slight increments with further curing, which may suggest self-healing occurrence.

EI testing seems to be easy to conduct autogenous self-healing assessments. Another advantageous point is that RCPT seemed to be in a decreasing trend while EI results are constantly increasing. Accordingly, results recorded from RCPT and EI methods can be compared and validated. Although these test methods support each other, they should also be examined in terms of subjects such as test setup to be selected, type of current to be used (AC or DC), position of the electrodes etc. This study is considered as an initial work for further related studies to be published.

References

1. Alexander, M.G., Stanish, K.: Durability Design and Specification of Reinforced Concrete Structures Using a Multi-factored Approach, p. 10. CONMAT'05 (2005)
2. Mehta, P.K., Burrows, R.W.: Building durable structures in the 21st century. Concr Int **23**, 57–63 (2001)

3. Li, V.C.: ECC-tailored composites through micromechanical modeling. In: Banthia, N. (ed.) Proceeding Fiber Reinforced Concrete: Present and the Future Conference, pp. 64–97. CSCE Press, Montreal (1998)
4. Şahmaran, M., Li, V.C.: Engineered cementitious composites: can they be accepted as a crack-free concrete. Transp Res Rec **39**, 1033–1043 (2010)
5. Yang, Y., Lepech, M.D., Yang, E.H., Li, V.C.: Autogenous healing of engineered cementi-tious composites under wet–dry cycles. Cem Concr Res **39**, 382–390 (2009)
6. Lepech, M., Li, V.C.: Water permeability of cracked cementitious composites. In: Eleventh International Conference on Fracture, pp. 20–25. Turin, Italy; (2005)
7. Şahmaran, M., Li, V.C.: Durability of mechanically loaded engineered cementitious composites under highly alkaline environments. Cem Concr Compos **30**, 72–81 (2008)
8. Li, M., Şahmaran, M., Li, V.C.: Effect of cracking and healing on durability of engineered cementitious composites under marine environment. High Performance Fiber Reinforced Cement Composites (HPFRCC-5), pp. 313–322. Stuttgart, Germany (2007)
9. Alyousif, A., Lachemi, M., Yildirim, G., Şahmaran, M.: Effect of self-healing on the different transport properties of cementitious composites. J Adv Concr Technol **13**, 112–123 (2015)
10. Şahmaran, M., Yildirim, G., Ozbay, E., Ahmed, K., Lachemi, M.: Self-healing ability of cementitious composites: effect of addition of pre-soaked expanded perlite. Mag Concr Res **66**, 409–419 (2014)
11. Tang, W., Kardani, O., Cui, H.: Robust evaluation of self-healing efficiency in cementitious materials—a review. Const. Build Mater. **81**, 233–247 (2015)
12. Spragg, R., Bu, Y., Snyder, K., Bentz, D., Weiss, J.: Electrical testing of cement-based materials: role of testing techniques, sample conditioning, and accelerated curing. West Lafayette, Indiana: Joint Transportation Research Program, Indiana Department of Transportation and Purdue University; https://doi.org/10.5703/1288284315230 Publication FHWA/IN/JTRP-2013/28
13. Hou, T.C.: Wireless and Electromechanical Approaches for Strain Sensing and Crack Detection in FRC materials, Ph.D. Dissertation. Civil and Environmental Engineering, University of Michigan, Ann Arbor, MI (2008)
14. ASTM C 215: Test Method for Fundamental Transverse, Longitudinal, and Torsional Frequencies of Concrete Specimens. ASTM International, West Conshohocken, Pennsylvania (1997)
15. ASTM C 1202: Standard Test Method for Electrical Indication of Concrete's Ability to Resist Chloride Ion Penetration. ASTM International, West Conshohocken, Pennsylvania (2012)
16. Şahmaran, M., Yildirim, G., Erdem, T.K.: Self-healing capability of cementitious composites incorporating different supplementary cementitious materials. Cem. Concr. Compos. **35**, 89–101 (2013)
17. Özbay, E., Şahmaran, M., Lachemi, M., Yücel, H.E.: Self-healing of microcracks in high-volume fly-ash-incorporated engineered cementitious composites. ACI Mater. J. **110**(1), 32–42 (2013)
18. Zhang, Z.G., Qian, S.Z., Ma, H.: Investigating mechanical properties and self-healing behavior of micro-cracked ECC with different volume of fly ash. Const. Build Mater. **52**, 17–23 (2014)
19. Wu, M.Y., Hu, X.M., Zhang, Q., Xue, D., Zhao, Y.Y.: Growth environment optimization for inducing bacterial mineralization and its application in concrete healing. Const. Build Mater. **209**, 631–643 (2019)
20. Ozyildirim, H.C.: Laboratory Investigation of Lightweight Concrete Properties. Virginia Center for Transportation Innovation and Research, Charlottesville, VA; FHWA A/VCTIR 11-R17 (2011)
21. Ramezanianpour, A.A., Pilvar, A., Mahdikhani, M., Moodi, F.: Practical evaluation of relationship between concrete resistivity, water penetration, rapid chloride penetration and compressive strength. Const. Build. Mater. **25**, 2472–2479 (2011)

22. Rupnow, T.D., Icenogle, P.: Evaluation of Surface Resistivity Measurements as an Alternative to the Rapid Chloride Permeability Test for Quality Assurance and Acceptance. Louisiana Department of Transportation, Baton Rouge, LA; FHWA/LA.11/479 (2011)
23. Şahmaran, M., Yildirim, G., Noori, R., Ozbay, E., Lachemi, M.: Repeatability and pervasiveness of self-healing in engineered cementitious composites. ACI Mater J **112**, 513–522 (2015)
24. Ranade, R., Zhang, J., Lynch, J.P., Li, V.C.: Influence of micro-cracking on the composite resistivity of engineered cementitious composites. Cem. Concr. Res. **58**, 1–12 (2014)
25. Van Tittelboom, K., Gruyaert, E., Rahier, H., De Belie, N.: Influence of mix composition on the extent of autogenous crack healing by continued hydration or calcium carbonate formation. Const. Build. Mater. **37**, 349–359 (2012)
26. Adamson, A.W.: Physical Chemistry, 2nd edn. Academic Press, Orlando (1973)
27. Yildirim, G., Şahmaran, M., Ahmed, H.U.: Influence of hydrated lime addition on the self-healing capability of high-volume fly ash incorporated cementitious composites. J. Mater. Civ. Eng. **04014187**, 1–11 (2014)

Autogenous Self-healing Assessment of 1-Year-Old Cementitious Composites

Gürkan Yıldırım[ID]**, Hüseyin Ulugöl**[ID]**, Oğuzhan Öztürk**[ID]**, and Mustafa Şahmaran**[ID]

Abstract Traditional concrete materials are prone to cracking and as cracks form, durability issues arise which reduce the expected service life of the materials followed by structures incorporating them. This, in many occasions, may lead to repetitive repair and maintenance or even re-construction of certain structural/non-structural sections and structures. Thus, it is highly desirable to reduce the chance and/or further development of cracking. Engineered Cementitious Composites (ECC) are feasible materials to suppress cracking formation and progression through their strain-hardening response under uniaxial tensile loading conditions. Even at the stage of failure, these materials exhibit micron-size cracks which significantly improve the capability to resist against detrimental durability issues. Moreover, these microcracks are constantly reported to be closed through autogenous healing mechanisms with no external interference from outside which significantly improve the mechanical and durability performance and service life of these materials and structures incorporating them. However, the performance of autogenous self-healing in ECC is called into question, especially for late-age specimens since reactions which produce products to plug the micro-size cracks stabilize as the specimens get more and more mature. To clarify this subject, in this study, 1-year-old specimens produced from ECC mixtures incorporated with different mineral admixtures (i.e. Class-F fly ash and ground granulated blast furnace slag) were tested for their self-healing performance. For self-healing evaluation, specimens which were severely preloaded for creating microcracks, were subjected to four different curing conditions which included "Water", "Air", "CO_2-water" and "CO_2-air" for 90 additional days beyond initial 1 year. Tests used for self-healing

G. Yıldırım
Kırıkkale University, Kırıkkale, Turkey

H. Ulugöl (✉) · M. Şahmaran
Hacettepe University, Ankara, Turkey

O. Öztürk
Konya Technical University, Konya, Turkey

assessments were electrical impedance (EI) and rapid chloride permeability (RCP). Results indicate that water is a must-have component for enhanced autogenous self-healing efficiency. "CO_2-Water" curing results in the most effective self-healing performance regardless of the composition of ECC mixtures. By properly adjusting mixture proportions and curing conditions, microcracks as large as nearly half a millimeter (458 µm) can be healed in only 30 days of further curing. Overall, results clearly suggest that late-age autogenous self-healing capability of ECC can be made as effective as the early-age with proper further environmental conditioning and mixture design.

Keywords Autogenous self-healing · Engineered cementitious composites (ECC) · Mineral admixtures

1 Introduction

Engineered Cementitious Composites (ECC) are special branch of High Performance Fiber-Reinforced Cementitious Composites (HPFRCCs) with unique properties. The most important feature of ECC is the capability of suppressing crack formation and even preventing the growth of existing cracks [1–3]. This is related to the pseudo strain-hardening behavior of the material which is realized through the formation of many multiple micro-size cracks when strained [4]. The mixture design of ECC clearly plays a vital role in achieving abovementioned features. Conventionally, ECC mixtures incorporate cement, fine sand, mineral admixtures, water, superplasticizer and short/randomly-dispersed fibers. To achieve uniform fiber distribution and reduce matrix fracture toughness for increased ductility, maximum grain size of sand is restricted in ECC which increases the amount of cementitious materials (cement and mineral admixtures) in the mixture compositions. When the higher amounts of cementitious materials and intrinsic multiple microcracking behavior of ECC materials come together, possibility of autogenous self-healing of microcracks mostly triggered via ongoing hydration reactions and calcium carbonate precipitation arises. Autogenous self-healing in ECC has been of topic to many studies in the literature [5–10]. However, the effectiveness of this mechanism to plug the microcracks has been repeatedly called into question for late-age specimens, given the fact that the amount of unhydrated cementitious materials which will be used in self-healing reactions would decrease substantially at later ages. In order to address this issue, in this study, autogenous self-healing capability of 1-year-old ECC mixtures was assessed.

2 Experimental Program

2.1 Materials and ECC Mixture Proportioning and Specimens

In this study, fine silica sand (d_{max} = 0.4 mm) with a specific gravity of 2.6 and CEM I 42.5R Portland cement (PC) were used. Polyvinyl alcohol (PVA) fibers were used at 2% of mixture volume (26 kg/m^3) and their diameter, length, nominal tensile strength, modulus of elasticity, maximum elongation and specific gravity were 39 μm, 8 mm, 1610 MPa, 42.8 GPa, 6% and 1.3, respectively. A polycarboxylic ether-based superplasticizer (SP) was used for desirable fresh properties. There were two different types of ECC mixtures produced with Class F fly ash (FA) (ECC-FA) and ground granulated blast furnace slag (S) (ECC-S). Physical properties and oxide compositions of PC, FA and S were shown in Table 1. All mixtures were designed to have constant water to cementitious materials ratio (W/CM) of 0.27. Proportion of cementitious materials was such that mineral admixture to Portland cement ratio was constant at 1.2. ECC mixture designs were shown in Table 2.

To be used in for self-healing evaluation of ECC mixtures, cylindrical specimens with dimensions of Ø100 × 200 mm were produced and they were taken out of their molds right after 24 h curing at 50 ± 5% RH, 23 ± 2 °C. Then they were

Table 1 Physical properties and oxide compositions of FA, S and PC

Oxide composition	FA	S	PC
CaO	3.5	35.1	61.4
SiO$_2$	60.8	37.6	20.8
Al$_2$O$_3$	21.7	10.6	5.6
Fe$_2$O$_3$	5.5	0.28	3.4
MgO	1.7	7.9	2.5
SO$_3$	0.34	3.0	2.5
K$_2$O	2.0	1.1	0.77
Na$_2$O	0.74	0.24	0.19
Loss on ignition	1.6	2.8	2.2
Physical properties			
Specific gravity	2.1	2.8	3.1
Blaine fineness (m^2/kg)	269	425	325

Table 2 ECC mixture designs per kg/m^3

Mixture ID	PC	FA	S	Water	PVA	Sand	SP
ECC-FA	566	680	–	331	26	453	5.1
ECC-S	593	–	712	347	26	474	6.0

kept in the plastic bags for 1 year at $95 \pm 5\%$ RH, 23 ± 2 °C. After 1 year of curing, cylindrical specimens were cut to disc specimens with the height of 50 mm on which all tests were performed.

2.2 Pre-loading, Further Curing and Self-healing Assessment

Before applying pre-loading for the creation of microcracks, ultimate splitting tensile deformation capacities of all mixtures were determined. Considering that the ultimate deformation capacities of different ECC mixtures were similar, it was decided to pre-load all specimens from different mixtures up to 70% of the ultimate splitting tensile deformation capacity. In addition to pre-loaded specimens, sound specimens were also separated for comparison purposes.

For the assessment of self-healing, four different types of further environmental conditions were chosen. These were applied in two different curing cabinets. In one of the cabinets, sound and pre-loaded specimens were subjected to an environmental conditioning of 50 ± 5 °C and $50 \pm 5\%$ RH in water (Water) and air (Air), while they were subjected to 50 ± 5 °C, $50 \pm 5\%$ RH and 3% CO_2 in water (CO_2-water) and air (CO_2-air) in the second cabinet. Further conditioning was carried out for 90 days after 1 year of initial curing and proposed tests were performed after each 15 days of further curing in addition to the reference measurements recorded right after 1 year of initial curing.

As abovementioned, all tests were performed using Ø100 × 50 mm cut-off cylindrical specimens. For self-healing evaluation, rapid chloride permeability (RCP) and electrical impedance (EI) tests were utilized. Moreover, changes in the widths and number of microcracks were followed using a video microscope. Details of these test methods can be found in [6, 11].

3 Results

3.1 Self-healing Assessment According to Video Microscopy

Right after the initial preloading, all microcracks were examined by microscope, their number and widths were determined. As can be seen from Table 3, fly ash containing ECC mixtures have lower average crack widths however larger number of cracks than slag containing mixtures. Larger widths and smaller number of cracks clearly indicate that ECCs with slag have a stronger and more mature matrix than ECCs with fly ash. This behavior is caused by the more cementitious (rather than pozzolanic) nature of slag which increases fiber-to-matrix chemical bonding and possibility of fiber damage/rupture resulting in microcracks larger in width and lower in number.

Table 3 Microcrack characteristics after 90 days of further curing

Mixture ID	Curing condition	Total # of cracks from all tested specimens	Average of initial CW (μm)	Max. CW (μm)	Max. CW closed after 90d. (μm)
ECC-FA	CO_2-air	40	112	348	119
	CO_2-water	35	138	458	458
	Air	26	109	302	121
	Water	34	102	463	99
ECC-S	CO_2-air	37	152	332	–
	CO_2-water	28	166	453	386
	Air	37	136	396	39
	Water	29	174	471	397

CW Crack width

In the literature, maximum allowable crack widths that can be closed by autogenous self-healing were reported to widely range from 10 to 300 μm [12–15]. In this regard, self-healing performances of ECC mixtures under different curing conditions were evaluated taking different crack widths and curing conditions into consideration and shown in Fig. 1. Results exhibit that all specimens from different mixtures exhibit self-healing of microcracks. Considering different curing conditions, the self-healing rates of specimens cured in water are much better than the performance of ones cured in the air. Clearly better performance of specimens cured in CO_2-rich environments (especially CO_2-water) was obtained. As can be seen from Fig. 1, better performance of CO_2-water curing was much more evident for specimens having microcracks with larger widths (>200 μm) and was attributed to more pronounced calcium carbonate precipitation under this curing condition. Figure 2 shows the healing process of an ECC-FA specimen with CO_2-water curing.

3.2 Self-healing Assessment According to Electrical Resistivity

One of the assessment parameters of self-healing is electrical impedance (EI) values of sound and pre-loaded specimens. EI testing is affected by the porosity, pore solution chemistry, pore network tortuosity and moisture state [12]. As can be seen in Fig. 3, although EI values of the samples on the 180th day were very close, after the pre-loading, some EI values increased signally. Maximum EI increment after pre-loading was seen at ECC-S specimens (see Fig. 3c). This case is attributed decisiveness of crack width values on individual EI results rather than crack numbers.
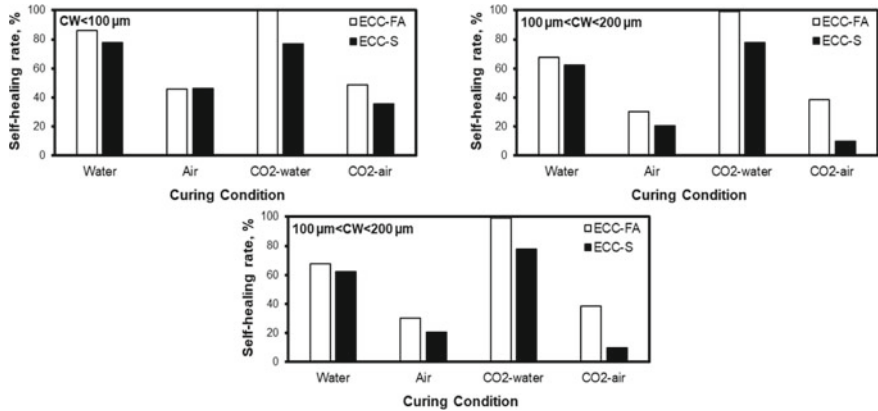
Fig. 1 Self-healing rates of microcracks with different ranges of width after 90 days of additional curing (CW: Crack width)
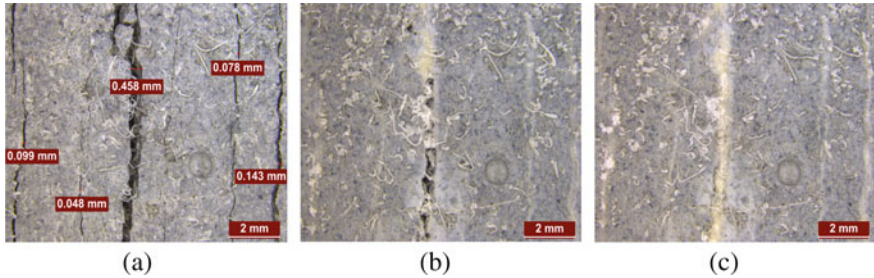
Fig. 2 Video microscopy photos of microcracks of a representative ECC-FA specimen **a** after initial pre-loading on 365 days, **b** after 15 days of further CO_2-water curing, **c** after 30 days of further CO_2-water curing

Another point is that EI values of specimens cured at water, which have water content in their pores, do not change much. However, sound specimens have a trend to give higher EI results as conditioning in air with or without CO_2 continues. This situation comes from densification of paste, which further decreased amount of pore solution transporting conductive ions and the number of least-resistive paths. For sound specimens, ECC-FA specimens have the highest EI results at the end of the conditioning period. For example, while EI results of sound specimens further cured for 90 days under CO_2-air conditioning increased by 1210% (60–792 kΩ), the same increment rate was 810% (45–409 kΩ) for ECC-S mixtures. This increments of further air-cured sound specimens were attributed to the ionic states of specimens when specimens were tested. As it is observed, chemical content of pore solution of cementitious materials affects EI results, especially at late ages.

Figure 3 exhibits that EI results of ECC-S specimens cured at air with additional CO_2 content were higher than other mixtures, while EI results of ECC-S specimens
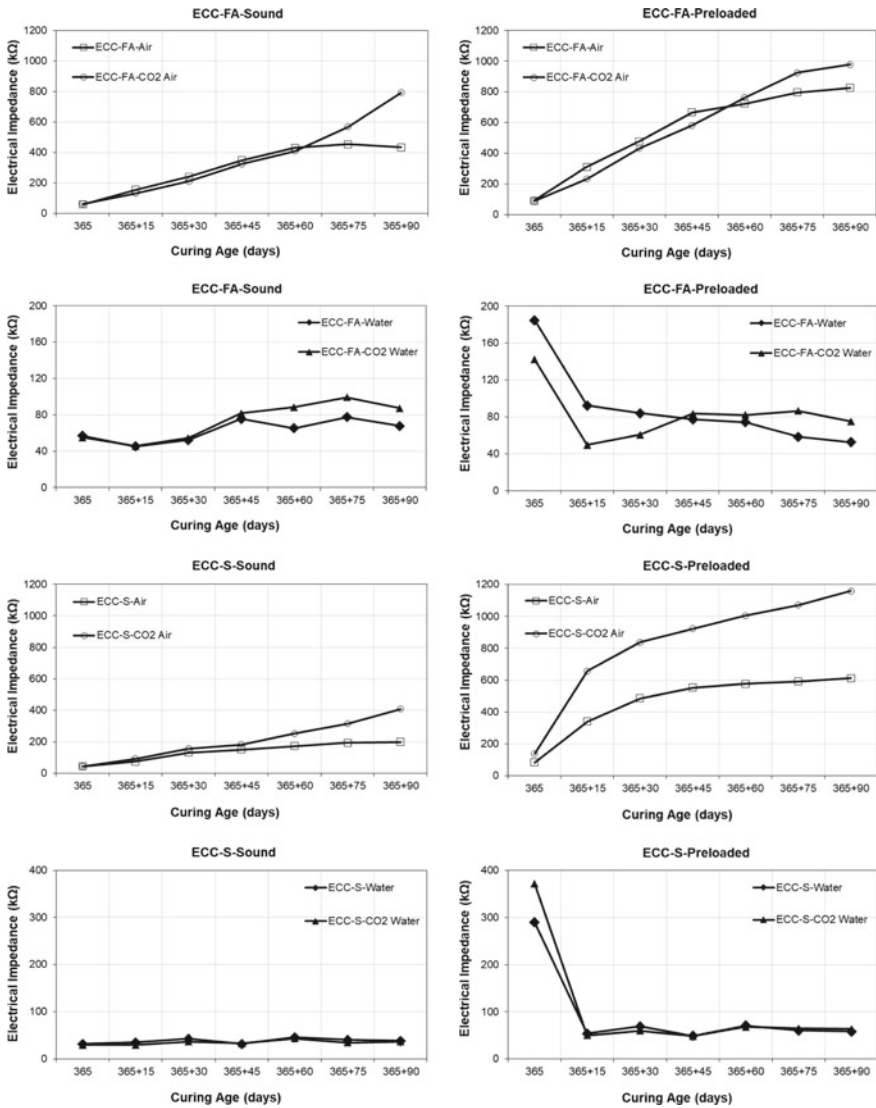
Fig. 3 EI results of sound and pre-loaded ECC-FA and ECC-S

cured at air without additional CO_2 were lower. As it is known carbonation begins at the surface of the specimens, and is then governed by CO_2 diffusion through the surface. The largest crack widths of ECC-S specimens, which are caused by higher maturity of paste, had a higher surface area and increased diffusion depths. Therefore, carbonation reactions were more effective in these specimens in case of there were additional CO_2 content in the air.

3.3 Self-healing Assessment According to Rapid Chloride Permeability Test

Figure 4a,b show the RCP testing results of sound and pre-loaded specimens of fly ash, and blast furnace slag content respectively. At the end of the period of 365 days, these specimens gave 150 C and 186 C current values in order. These low values were attributed to the maturity of specimens.

Fly ash with amount of 30–40% delays hydration because of the reduce in the amount of $Ca(OH)_2$ which reacts with fly ash [13]. Although RCP test is an electrochemical test method, pore solution chemistry affects results. However, EI testing is affected by the ionic composition of pore solution and porosity and pore tortuosity [14]. Average RCP testing results of sound specimens increased from 127 C to 514 C for ECC-FA and from 177 C to 594 C for ECC-S. Although RCP results increased after pre-loading, results were still in the very low range (less than 1000 C) according to ASTM C1202 standard.

Average of RCP testing results of pre-loaded specimens decreased as conditioning continue independently from type of conditioning environment. However, rate of decrement in RCP testing results at first period of 15 days is higher than following periods. For example, average RCP testing results of pre-loaded specimens of ECC-FA and ECC-S subjected to 15 days of further CO_2-water curing improved by 79% (from 527 C to 111 C) and 63% (from 530 C to 196 C) respectively.
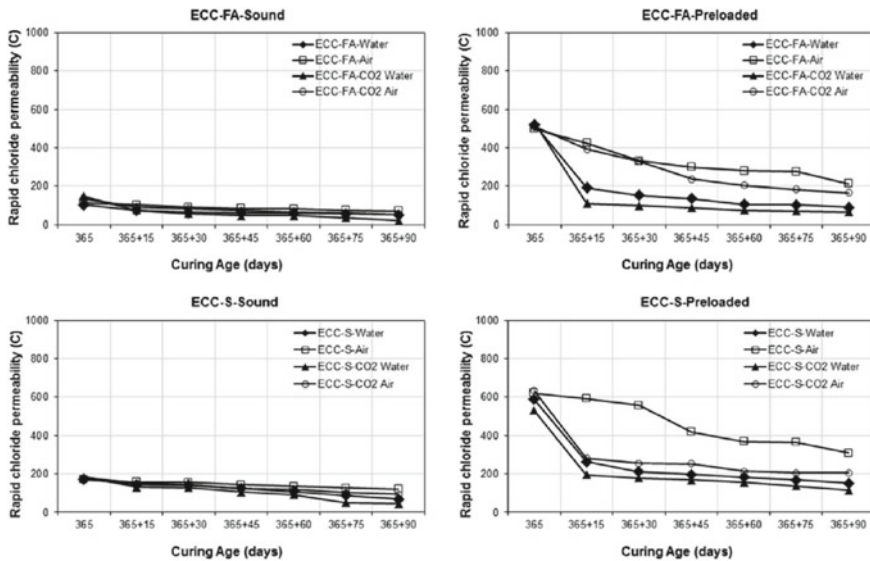
Fig. 4 RCP results of sound and pre-loaded **a** ECC-FA and **b** ECC-S

Self-healing performances according to the decrements in RCP testing results of different ECC mixtures were so close to each other. However, decrement rates were slightly more pronounced for ECC-FA, especially with water-based further curing. According to Andrade [15], OH^- ions in pore fluid act as supporting electrolytes and are responsible for the movement of substantial amounts of charge during RCP testing, given their higher conductivity (198 cm^2 $equiv^{-1}$ Ω^{-1}) compared to other ions present in the pore fluid (Na^+, K^+, Ca^{+2}, and Cl^-). The higher decrement rates in RCP test results of ECC-FA specimens could therefore be related to OH^- ion depletion caused by diminished portlandite with further pozzolanic capability. These results indicate that RCP test results are more influenced by matrix properties than the ionic state of pore solution.

4   Conclusions

This study concentrated on autogenous self-healing capability of 1-year-old ECC specimens with fly ash and ground granulated blast furnace slag content. Autogenous self-healing assessments of these specimens were made by electrical impedance and rapid chloride permeability results. CO_2-water curing gave the best self-healing performance for all type of specimens and second best performance was water curing. According to these results, it can be said that water is clearly needed for autogenous self-healing. Additionally, a well-designed mixture proportion is required to close cracks completely. In this study, 458 µm crack of 1-year-old specimen could be healed in a conditioning period of 30 days. However, a complete healing process of a crack lasts 90 days.

EI results of sound specimens for all specimens increased significantly after the pre-loading, indicating that crack widths, rather than crack numbers, have an important role in increasing EI results upon pre-loading. Depending on mixture type, further conditioning and subsequent drying of specimens for EI testing, EI results similar to those of sound specimens can be obtained from severely damaged specimens, especially ECC-FA. However, EI testing is quite sensitive to changes in pore solution chemistry and moisture state of specimens at the time of testing. RCP testing is less dependent on the ionic states of specimens. One-year RCP test results of most of ECC specimens (sound and pre-loaded) are either very low (less than 1000 C) or negligible (less than 100 C), in accordance with ASTM C1202. Micro-cracking caused marked escalations in RCP test results due to the creation of new paths for free movement of chloride ions. However, even after micro-cracking, which caused severe damage, average chloride ion penetrability results of specimens from different mixtures stayed at very low levels. 15 days of further water-based curing (especially CO_2-water) was enough for most pre-loaded specimens to achieve nearly the same RCP test results as sound specimens, suggesting self-healing occurrence.

References

1. Li, V.C.: Advances in ECC research. ACI Spec. Publ. **206**, 373–400 (2002)
2. Li, V.C.: On engineered cementitious composites (ECC)—a review of the material and its applications. J. Adv. Concr. Technol. **1**, 215–230 (2003)
3. Li, V.C.: Engineered cementitious composites (ECC)—material, structural, and durability performance. In: Nawy, E. (ed.) Concrete Construction Engineering Handbook, pp. 1–46. CRC Press, Boca Raton (2008)
4. Yıldırım, G., Alyousif, A., Şahmaran, M., Lachemi, M.: Assessing the self-healing capability of cementitious composites under increasing sustained loading. Adv. Cem. Res. **27**, 581–592 (2015)
5. Şahmaran, M., Li, V.C.: Durability properties of micro-cracked ECC containing high volumes fly ash. Cem. Concr. Res. **39**, 1033–1043 (2009)
6. Jacobsen, S., Marchand, J., Hornain, H.: SEM observations of the microstructure of frost deteriorated and self-healed concretes. Cem. Concr. Res. **25**, 1781–1790 (1995)
7. Liu, S., Zuo, M.: Influence of slag and fly ash on the self-healing ability of concrete. Adv. Mater. Res. **306**, 1020–1023 (2011)
8. Şahmaran, M., Yaman, İÖ.: Influence of transverse crack width on reinforcement corrosion initiation and propagation in mortar beams. Can. J. Civil Eng. **35**, 236–245 (2008)
9. Reinhardt, H.W., Jooss, M.: Permeability and self-healing of cracked concrete as a function of temperature and crack width. Cem. Concr. Res. **33**, 981–985 (2003)
10. Edvardsen, C.: Water permeability and autogenous healing of cracks in concrete. ACI Mater. J. **96**, 448–455 (1999)
11. Clear, C.A.: The Effects of Autogenous Healing Upon the Leakage of Water Through Cracks in Concrete, p. 28. Cement and Concrete Association, Wexham Springs (1985)
12. Shi, C.: Effect of mixing proportions of concrete on its electrical conductivity and the rapid chloride permeability test (ASTM C1202 or ASSHTO T277) results. Cem. Concr. Res. **34**, 537–545 (2004)
13. Song, G., van Zijl, G.P.A.G.: Tailoring ECC for commercial application. In: 6th RILEM Symposium on Fiber-Reinforced Concretes (FRC)—BEFIB, pp. 1391–1400, Varenna, Italy (2004)
14. Yıldırım, G., Aras, G.H., Banyhussan, Q.S., Şahmaran, M., Lachemi, M.: Estimating the self-healing capability of cementitious composites through nondestructive electrical-based monitoring. Ndt & E Int. **76**, 26–37 (2015)
15. Andrade, C.: Calculation of chloride diffusion coefficients in concrete from ionic migration measurements. Cem. Concr. Res. **23**, 724–742 (1993)

Impact of Super Absorbent Polymers on Early Age Behavior of High Performance Concrete Walls

J. Kheir, L. De Meyst, J. R. Tenòrio Filho, T. A. Hammer, A. Klausen, B. Hilloulin, A. Loukili, and N. De Belie

Abstract The prediction of the early age behavior of cementitious materials is a difficult task, because many of the material properties are very sensitive to curing conditions as it is the case for High Performance Concrete (HPC), which usually has a very low water to cement ratio ($0.2 < $ w/c $ \leq 0.3$). Early age cracking, a common problem for HPC, is caused by Autogenous Shrinkage (AS) and self-desiccation during the cement hydration reactions when the deformation is restrained. However, to avoid the crack development initiated by AS, several solutions can be adopted; one example is the addition of a promising material considered as an internal curing agent, the Super Absorbent Polymers (SAP) which

J. Kheir (✉) · L. De Meyst · J. R. Tenòrio Filho · N. De Belie
Magnel-Vandepitte Laboratory for Structural Engineering and Building Materials,
Ghent University, Technologiepark Zwijnaarde 60, 9052 Ghent, Belgium
e-mail: judy.kheir@ec-nantes.fr; judy.kheir@ugent.be

L. De Meyst
e-mail: laurence.demeyst@ugent.be

J. R. Tenòrio Filho
e-mail: roberto.tenorio@ugent.be

N. De Belie
e-mail: nele.debelie@ugent.be

J. Kheir · B. Hilloulin · A. Loukili
Institut de Recherche en Génie Civil et Mécanique (GeM), UMR-CNRS 6183,
Ecole Centrale de Nantes, 1 rue de la Noë, 44321 Nantes, France
e-mail: benoit.hilloulin@ec-nantes.fr

A. Loukili
e-mail: ahmed.loukili@ec-nantes.fr

T. A. Hammer
Architecture, Materials and Structures, SINTEF Building and Infrastructure,
7465 Trondheim, Norway
e-mail: torarne.hammer@sintef.no

A. Klausen
The Norwegian University of Science and Technology-NTNU, 7491 Trondheim, Norway
e-mail: anja.klausen@ntnu.no

limits the capillary depressions that enhance the formation of the crack. In this study the main goal is to mitigate the shrinkage using SAPs in infrastructure under severe conditions. Therefore, a demonstrator wall was built simulating a typical case with high risk of cracking. With the help of fiber optic SOFO sensors embedded in the wall, real-time deformations are recorded and compared with the demountable mechanical strain gauges (DEMEC) measurements to further investigate the behavior of SAPs in real scale infrastructure. The amount of extra water (in SAP) needed to mitigate shrinkage was determined by performing chemical shrinkage tests on different cement paste combinations. Tests of autogenous shrinkage were performed on mortars using corrugated tubes and showed that SAPs reduce to some extent the AS. Under restrained conditions via ring tests, SAP specimens did not crack. Therefore, SAPs were found promising towards mitigating the shrinkage and enhancing the early age behavior of concrete for a better durability.

1 Introduction

Early-age behavior prediction of cementitious materials is not an easy task, because many properties of the material are sensitive to curing conditions, as it is the case for High Performance Concrete (HPC), which has a low water to cement ratio ($0.2 <$ w/c ≤ 0.35), small aggregate size and supplementary cementitious materials (silica fume, fly ash …) with admixtures [1, 2]. Due to their exceptional mechanical properties and durability, HPCs are highly demanded these days especially for structures placed under severe conditions. Early-age cracking is their challenge, since high performance concrete goes through a lot of autogenous shrinkage which develops fast within the first days of age due to cement hydration reactions. Because of the low water to cement ratio, there's an insufficient amount of water for maximum hydration with low water to cement ratios but these ratios are kept low to enhance the durability by reducing porosity [3]. The lack of enough water for a full hydration and the reduced porosity in the concrete matrix result in a drastic decrease of the relative humidity (RH) in the pore structure, and an increase of the pressure within the pore structure which in turn causes the appearance of autogenous shrinkage [4, 5]. The tensile stresses inside pores arising from high autogenous shrinkage at early age cause macroscopic cracks due to the low tensile strength of the matrix at that age, especially in restrained conditions [6, 7]. The formation of cracks in these structures threatens their service life span and their functionality since numerous chemical agents can penetrate through these cracks, along with water and gases that induce carbonation, steel corrosion, chloride intrusion, frost and chemical attacks. Thus, it is very important to follow the evolution of AS deformations in order to effectively limit the early-age cracking risk. In order to enhance the life span of the reinforced infrastructures, early age

properties must be studied. In order to reduce or mitigate the shrinkage an internal curing agent must be added. The idea behind this method is the release of water in the concrete matrix during hydration when the RH decreases and initiates self-desiccation. Considered as an effective method, internal curing mitigates self-desiccation of HPCs by maintaining high RH [8–10]. Super Absorbent Polymers (SAPs) are the agents commonly used for providing internal curing [11]. SAPs are introduced as dry materials in the mix, when mixed with water, these polymers take up water from the mix and swell. In this way, an internal reservoir is created by the curing agent inside the concrete mix, that will further release its absorbed water gradually during matrix hardening to maintain high RH and continue the hydration process [11, 12]. Thus, to decide on the design for a reference HPC wall without SAP an early age crack assessment was done which would show early age cracking. This wall would then be compared to a SAP wall in order to see the effect of SAPs towards mitigate shrinkage cracks, thus different shrinkage tests were performed on concrete. In addition, to measure the real time deformation behavior of walls, fiber optic (SOFO) sensors were embedded inside the walls to record AS over a period of 4 months to monitor full shrinkage of the walls. Results obtained were then compared with demountable mechanical strain gauges DEMEC using points that were glued on the wall after demolding at the same position of SOFOs and recorded manually. Restrained shrinkage tests were also performed on the mix using the ring method, to further study the behavior of SAPs towards mitigating shrinkage under restrained condition since the walls are restrained at the bottom (attached to a slab). Chemical shrinkage tests were used in order to calculate the amount of SAPs and extra water needed to be added to the mix.

2 Materials and Methods

2.1 Super Absorbent Polymers

Commercial SAPs based on poly (acrylamide-co-acrylic acid) were used in the restrained and autogenous shrinkage tests for the wall. These SAPs have an average dry particle size of 100 μm and an absorption capacity in cement slurry equal to 27 g per g of SAP.

2.2 Parameter Determination for Simulation of the HPC Wall

A set of parameters is needed in order to simulate the strains in an HPC wall (cast on a non-deforming slab). These parameters result from specific experiments performed on the examined concrete mix which can be found in Table 1.

Table 1 Mix design of HPC concrete walls

Materials	REF (kg/m^3)	SAP (kg/m^3)
Cement CEM III/A 52.5 R–Dyckerhoff Variodur 40	778	778
Silica fume–Elkem Microsilica D940	154	154
Free water	186	186
Filler–Betofill VK50	185	185
Sand–Årdal taksteinsand (0–4 mm)	402	402
Aggregates–Steinskogen Basalt (4–8 mm)	649	649
Superplasticizer–SIKA UHPC 2	8.6[a]	9.33[b]
SAP	–	2.33[c]
Extra water for SAP	–	63

[a]1.1 m% by weight of CEM III/A 52.5 R for REF
[b]1.1 m% by weight of CEM III/A 52.5 R + 0.1 m% extra for BASF
[c]0.3 m% SAPs by weight of CEM III/A 52.5 R

The parameters are the following according to the developed procedure by Klausen [13]: hydration heat development (measured), autogenous shrinkage (measured), compressive and uniaxial tensile strength development (measured), coefficient of thermal expansion—CTE (measured), creep (measured) and activation energy (assumed based on experience).

In addition, one test was performed in the Temperature-Stress Testing Machine (TSTM at NTNU, Trondheim, Norway) (Fig. 1), simulating the heat of hydration in a 50 mm thick wall (under realistic condition for temperature). It is built to measure the stress generation of a sealed concrete specimen during the phase of hardening under a chosen degree of restraint (R = 30%).

It was decided to build a wall of 2 m × 1.5 m × 0.05 m on a mature slab based on the simulation results (Fig. 2). A fast temperature rise was predicted followed by a fast temperature drop after peak temperature, and an even faster drop after removal of the formwork at 18 h of age. After about 20 h a stress/strength ratio >1 would be reached.

Fig. 1 TSTM system
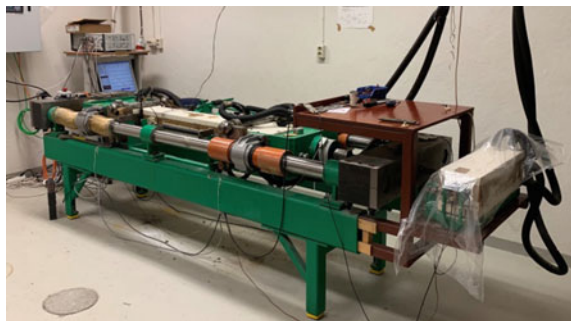
Fig. 2 Reference wall (left),
SAP wall (right)
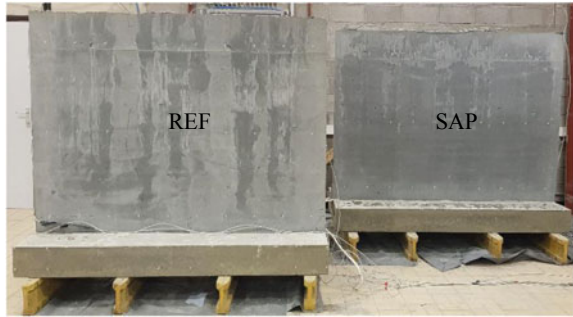
2.3 Chemical Shrinkage

According to ASTM C1608, chemical shrinkage tests were performed on pastes to choose the amount and the extra water needed for SAPs to mitigate shrinkage. After setting, chemical shrinkage is measured while water is being sucked into the sample refilling the emptied pores. Tests are followed for 28 days to ensure that pastes have undergone enough hydration. Measurements are undertaken on saturated specimens with limited sample size (thickness less than 3 mm) to avoid the emptying of water filled pores inaccessible by the top water added gently on top of the paste.

2.4 Autogenous Shrinkage

HPC concrete specimens were performed according to the standard ASTM C1698. Concrete is poured in sealed corrugated tubes that are placed over supports provided with spring-loaded LVDTs (linear variable differential transformers) at each end for measuring length changes, under isothermal conditions (see Fig. 3a). These LVDTs have a measuring range of 5 mm and an accuracy of 2.5 µm. Measurements (the change in length) were recorded every ten minutes for 20 days. The setup was placed in a climate controlled room where the temperature is 20 °C ± 2 °C and relative humidity is 60% ± 5%. Mass of the tubes were recorded at the beginning and end of the test to make sure there was no evaporation or absorption during the test.

To monitor the real time deformations in the concrete structures, AS measurements were recorded through fiber optic SOFO sensors embedded inside the HPC walls for a period of 120 days. Five SOFOs were installed in the cast wall: 3 long sensors of a 1 m length for the top (T) at 130 cm above the connection with the plate, the middle (M) at 70.5 cm and the bottom (B) at 13 cm and 2 short ones with a length of 25 cm for the bottom edges as seen in Fig. 3b.

Deformations on the outside of the wall were manually measured by demountable strain gauges. DEMEC points were glued on the walls at the same
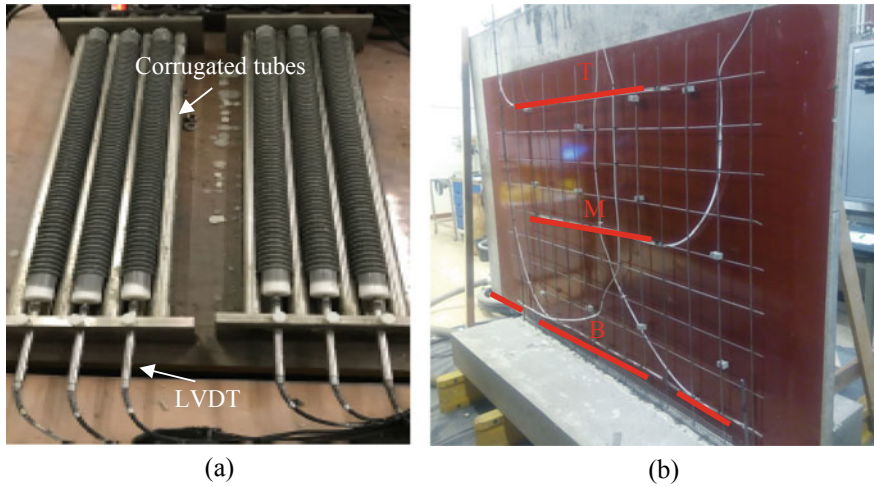
Fig. 3 **a** Representation of ASTM C 1698 setup and **b** position of fiber optic SOFO sensors embedded inside the HPC walls

positions of the SOFO sensors and recorded daily for 20 days. Measurements were recorded to 120 days at irregular intervals.

2.5 *Restrained Shrinkage*

The standard method ASTM C1581-04 known as the ring test was performed on concrete specimens. Fresh mixed concrete is poured around a steel ring equipped with strain gauges that measure its deformation. For the reference and the SAP mixes one ring was cast and kept in a climate controlled where temperature is 20 °C ± 2 °C and relative humidity is 60% ± 5%. After 24 h, the shrinkage in outer steel ring was removed and the specimen was covered with plastic foil to avoid drying shrinkage in order to only observe the effect of SAPs against autogenous restrained condition.

3 Results and Discussion

The amount of extra curing water (divided by the total mass of binder) that should be used in the mix for the SAPs to mitigate shrinkage was determined based on the chemical shrinkage tests performed on different binder paste compositions and is equal to w/b_sap = 0.078. In order to determine the amount of SAPs needed, an amount of 0.3% over the cement mass was considered based on the water absorption of SAP in cement slurry and RILEM recommendation [14].

3.1 Autogenous Shrinkage

A representation for the autogenous shrinkage results measured using corrugated tubes can be found in Fig. 4. The starting point for theses curves i.e. t_0 is equal to the final setting time recorded from penetrometer tests performed on concrete. For reference mixture $t_0 = 5.5$ h of age and for SAP $t_0 = 9$ h. Three tubes were measured for each mixture, the reference curves (curves lying in the negative range) show a shrinkage in the range of 500–600 µm/m, which means that the reference mixture undergoes a lot of autogenous shrinkage. Whereas curves of the SAP mixture lie in the positive range indicating a slight expansion counteracting the shrinkage behavior. These results show the effectiveness of SAPs towards reducing autogenous shrinkage.

3.2 Restrained Shrinkage

For the restrained shrinkage in the ring test, a sudden peak in the results is an indication of a crack. The reference concrete cracked at the age of 2 days, while no cracks were recorded for the SAP specimens that were followed for 20 days in the ring tests as seen in Fig. 5. The curves represent the results taken from the sensors recording the steel ring deformations. There were three sensors for each ring and one ring for each mix. For the reference curves, only two were shown because one sensor was not working properly. The values obtained shows the effectiveness of SAP towards reducing shrinkage under restrained conditions as it is the case of the walls that are restrained at the bottom since they are connected to a slab.

Fig. 4 Representation of autogenous shrinkage results for reference concrete mixture (negative curves) and SAP mixture (positive curves)
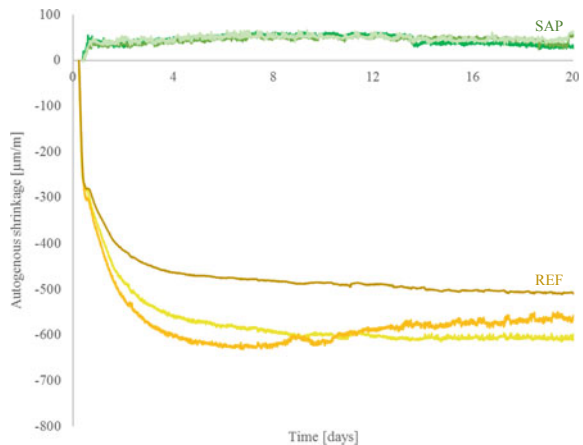
Fig. 5 Result of restrained shrinkage using ring test method for the reference (REF) and SAP concrete mixtures for 20 days
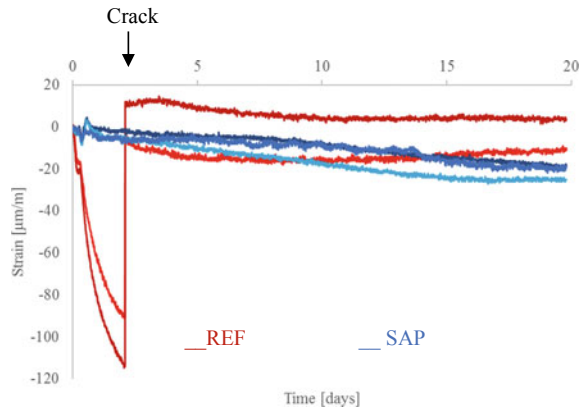
3.3 Deformations in a Restrained HPC Wall

Real time deformation results recorded from fiber optic sensors embedded inside the walls are represented in Fig. 6. Measurements were plotted from the final setting time of the mixtures recorded by penetrometer tests and equal to 5.5 h of age for the reference concrete and 9 h for SAP mix. Over the period of 120 days, shrinkage strain increases in time, for the reference wall shrinkage is way higher than SAP wall shrinkage. The order of the shrinkage, even though it is not so relevant for the SAP wall, is the same for both walls in such a way that he top shrinks more than the middle that shrinks more than the bottom part. An expected result since the walls are restrained at the bottom and therefore cannot freely shrink unlike the top part.

Shrinkage curves obtained from DEMEC measurements were also in accordance with the results found from SOFO sensors. The curves overlap for the first 30 days and then continue with the same behavior for the whole measurement period at each position: bottom (a), middle (b) and top (c) for the reference wall. Same behavior

Fig. 6 Representation of autogenous results recorded from fiber optic SOFO sensors embedded inside the walls with t_0 = 5.5 h of age for reference mixture (REF) and t_0 = 9 h for SAP mixture (SAP) at different positions: top (T), middle (M) and bottom (B2)
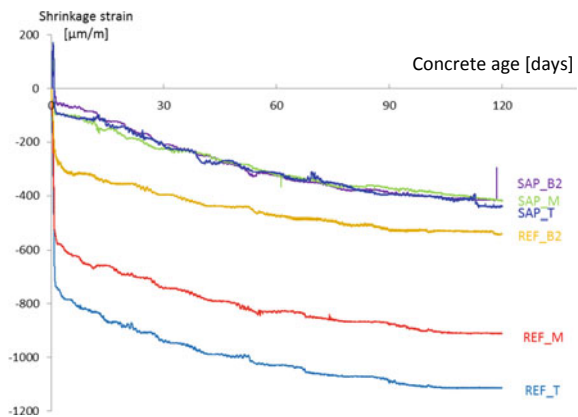
was also seen for the SAP wall. DEMEC measurements for the SAP wall show lower values that coincide with the SOFO ones and therefore prove that SAPs reduce the autogenous shrinkage.

4   Conclusion

The behaviour of SAPs towards mitigating shrinkage in large scale wall specimens was investigated in this study, and the conclusions can be summarized as follows.

Autogenous shrinkage results for the SAP mix showed how the addition of these polymers in concrete reduces the AS over the testing period of 4 months. This type of shrinkage was investigated using corrugated tubes.

Two HPC walls were cast: a REF and one with SAP, cracks were shown on the reference wall at early age after 20 h. The biggest crack runs up to half of the height of the wall and is 180 μm wide at the bottom. On the other hand, no cracks occurred for the SAP wall. Real-time deformations were recorded using fibre optic SOFO sensors embedded in the walls which were also compared to measurements taken from mechanical strain gauges that were placed on the wall. The early release of water from the SAPs into the mix reduces the shrinkage over the whole service life of a structure. Restrained shrinkage was also performed on concrete using ring tests to further understand the behaviour of SAP toward restrained conditions. This measurement was essential for the walls, because they were restrained at the bottom, it reflects the behaviour of real structures constructed with HPC. The specimens for the reference mixtures cracked after only 2 days, whereas SAP specimens didn't crack.

References

1. Bentz, D.P., Jensen, O.M., Hansen, K.K., Olesen, J.F., Stang, H., Haecker, C.: Influence of Cement Particle-Size Distribution on Early Age Autogenous Strains and Stresses in Cement-Based Materials, vol. 35, no. 188803, pp. 129–135 (2001)
2. Baroghel Bouny, V., Mounanga, P.: Autogenous Deformations of Cement Pastes: Part II. W/C Effects, Micro–Macro Correlations, and Threshold Values (2006)
3. Darquennes, A., Staquet, S., Espion, B.: Determination of Time-Zero and Its Effect on Autogenous Deformation Evolution, December 2014, pp. 37–41 (2011)
4. Craeye, B., Geirnaert, M., Schutter, G.D.: Super absorbing polymers as an internal curing agent for mitigation of early-age cracking of high-performance concrete bridge decks. Constr. Build. Mater. **25**, 1–13 (2011)
5. Chen, H., Wyrzzykowski, M., Scrivener, K., Lura, P.: Prediction of self-desiccation in low water-to-cement ratio pastes based on pore structure evolution. Cem. Concr. Res. **49**, 38–47 (2013)
6. Lura, P., Jensen, O.M., van Breugel, K.: Autogenous shrinkage in high-performance cement paste: an evaluation of basic mechanisms. Cem. Concr. Res. **33**, 223–232 (2003)

7. Lura, P., van Breugel, K., Maruyama, I.: Effect of curing temperature and type of cement on early-age shrinkage of high-performance concrete. Cem. Concr. Res. **31**, 1867–1872 (2001)
8. Jensen, O.M., Hansen, P.F.: Water-entrained cement-based materials: I. Principles and theoretical background. Cem. Concr. Res. **31**, 647–654 (2001)
9. Lura, P.: Autogenous Deformation and Internal Curing of Concrete. Delft University of Technology, TU Delft (2003)
10. Zhutovsky, S., Kovler, K., Bentur, A.: Assessment of Distance of Water Migration in Internal Curing of High-Strength Concrete, ACI SP-220 'Autogenous Deformation of Concrete', pp. 181–197. Farmington Hills, Michigan (2004)
11. Jensen, O.M.: Use of superabsorbent polymers in concrete. Concr. Int. **35**, 48–52 (2013)
12. Shen, D., Wang, X., Cheng, D., Zhang, J.: Effect of internal curing with super absorbent polymers on autogenous shrinkage of concrete at early age. Constr. Build. Mater. **106**, 512–522 (2016)
13. Klausen, A.B.E.: Early Age Crack Assessment of Concrete Structures Experimental Investigation of Decisive (2016)
14. Wyrzykowski, M., Mechterine, V., Lura, P., Igarashi, S.-I.: Recommendation of RILEM TC 260-RSC : using superabsorbent polymers (SAP) to mitigate autogenous shrinkage. In: Materials and Structures, vol. 51, no. 5, pp. 1–7. Springer, Netherlands (2018)

Influence of Crack Geometry and Crack Width on Carbonation of High-Volume Fly Ash (HVFA) Mortar

Tim Van Mullem, Laurence De Meyst, Jessica P. Handoyo, Robby Caspeele, Nele De Belie, and Philip Van den Heede

Abstract Carbonation of concrete results in a drop of the pH which can induce steel corrosion. This is costly to repair and therefore an accurate assessment of the carbonation resistance is required. Carbonation of uncracked concrete has been well-studied. However, in reality many of the concrete structures exhibit cracks, but only limited data is available on the influence of cracks on the carbonation process. Two types of cracks in cylindrical High-Volume Fly Ash mortar specimens were investigated: (1) an artificial crack created by pulling out a cast-in metal plate with a thickness of 100, 200 or 300 µm, and (2) a realistic crack created by splitting cylinders and reattaching them with silicon spacers (with a thickness of 100, 200 or 300 µm). After crack creation the specimens were stored in a carbonation chamber for different durations and the carbonation front was visualised using phenolphthalein. This paper reports on the influence of the crack width and the crack geometry on the CO_2 ingress. Artificial cracks with different crack widths did not show a difference in carbonation front. On the other hand, a significant difference could be observed for realistic cracks with different crack widths; realistic cracks with a nominal crack width of 100 µm induced a substantially lower carbonation depth. This demonstrates the influence of crack tortuosity on carbonation; the smaller the crack width, the larger the influence of the tortuosity. Comparing artificial cracks to realistic cracks, it could be concluded that the carbonation depth is lower for realistic cracks. Due to the wall effect near artificial cracks, more pores can be found in the crack area which makes them more susceptible to CO_2 ingress.

Keywords Carbonation · Crack width · Crack geometry · Crack tortuosity

T. Van Mullem · L. De Meyst · J. P. Handoyo · R. Caspeele · N. De Belie (✉) ·
P. Van den Heede
Magnel-Vandepitte Laboratory, Department of Structural Engineering and Building
Materials, Faculty of Engineering and Architecture, Ghent University, Technologiepark
Zwijnaarde 60, 9052 Gent, Belgium
e-mail: Nele.DeBelie@UGent.be

1   Introduction

Carbonation of cementitious materials is a phenomenon in which CO_2 in the air enters the cementitious matrix and reacts with the calcium hydroxide present in the pore solution, the calcium-silicate-hydrates and other calcium bearing phases. The consumption of hydroxyl ions associated with calcium hydroxide carbonation results in a drop of the pH which can induce steel corrosion if the carbonation front reaches the reinforcement. This is very costly to repair. In reality many concrete structures and elements exhibit cracks. Cracks pose a significant risk for the durability of concrete, as they allow CO_2 to quickly enter in the concrete bulk and reach the reinforcement.

Self-healing concrete has the ability to close its own cracks [1]. Unfortunately, the influence of cracks on the carbonation process is not very well documented in literature. Alahmad et al. [2] already reported that an interlocking phenomenon exists which limits the carbonation in small cracks. Yet, to propose test procedures for self-healing concrete more information about both the influence of the crack width, as well as the crack geometry is required. When studying the efficiency of self-healing concrete cracks can be created by pulling out thin metal plates [3]. This approach results in a low variation of the crack width, which is an important parameter for self-healing concrete [4]. This makes it a fast an easy applicable method. On the other hand, this creates cracks without the crack tortuosity that is existing in realistic cracks.

To study the influence of the crack geometry, two sets of specimens were made. One had realistic cracks, and one had artificial cracks. Each set had specimens with different nominal crack widths (100, 200, 300 μm), to study the influence of the crack width on carbonation.

2   Materials and Methods

2.1   Mortar Composition

All samples which are described in this paper were made from the same batch of mortar. The mortar was made with a sand to binder ratio of 3. The sand had a grading 0/4. In order to allow for a fast development of the carbonation front, half of the cement (CEM I 52.5 N) was replaced with fly ash (class F). Additionally, a water to binder ratio of 0.55 was used.

2.2 Artificial Cracks

Cylindrical moulds with a diameter of 100 mm and a height of 75 mm were pre-pared with a thin brass plate in the middle of the circular casting surface, so that the brass plate was inserted in the concrete over a width of 60 mm and a depth of 30 mm. The mould was filled in two layers and was compacted using a vibrating needle and a vibrating table. The day after casting, the specimens were demoulded. At the same day an artificial crack was created in the specimens by pulling out the copper plates. The crack width varied depending on the nominal thickness of the used copper plates which was either 100, 200, or 300 μm. Both after casting and after demoulding samples were stored in a curing room (20 °C, 95% RH).

2.3 Realistic Cracks

Cylindrical moulds with a diameter of 100 mm and a height of 50 mm were filled with mortar and compacted, similar as in Sect. 2.2. The day after casting the specimens were demoulded, and they were stored in a curing room (20 °C, 95% RH). Before the samples were cracked, the side surface was covered with aluminium tape. At an age of 40 days the specimens were completely cracked in a Brazilian splitting test. Subsequently, the two halves of the specimens were fitted back together with silicon strips (width of 15 mm) placed at the outer edge of the cracked plane, similar as in [5]. Two metal straps were used to tie each specimen together. The obtained crack width was dependent on the thickness of the silicon strips, which had a nominal value of 100, 200, or 300 μm respectively.

2.4 Carbonation Test

At an age of 51 days the samples with artificial cracks, as well as the samples with realistic cracks, were placed in a carbonation chamber with a CO_2 concentration of 1%, relative humidity of 60% and temperature of 20 °C. Prior to placing them in the carbonation chamber, the specimens were completely coated with an epoxy (even if the side was already covered with aluminium tape, in order to protect small ruptures in the tape), except for the exposure surface. At different exposure times, specimens were removed from the carbonation chamber. The specimens with artificial cracks were split perpendicular to their crack, and the specimens with realistic crack were sawn perpendicular to their crack. The carbonation front was visualised on both halves of the specimens using a 1% phenolphthalein solution.

3   Results and Discussion

3.1   Mortar Characterisation

Immediately after mixing the workability of the mortar was determined. The mortar obtained a slump of 21 cm measured according to EN 12350–2 [6] and a flow table value of 62–63 cm according to EN 12350–5 [7]. This high workability can be explained by the relatively high water to binder ratio. The fresh density amounted to 2165 kg/m^3.

The compressive strength was measured on cubes with a side of 150 mm. For mortar the compressive strength is usually measured on the two halves of the prisms $(40 \times 40 \times 160$ mm$^3)$ obtained from the 3-point bending test to determine the bending tensile strength (EN 196–1 [8]). It is possible to calculate the strength which would be obtained on specimens with a surface of 40×40 mm^2 from the results of the cubes, using form factors given by NBN B 15–220 [9]. This equivalent strength is given in Table 1. After 28 days there is still a significant increase in the compressive strength as a result of the pozzolanic action of the fly ash [10].

3.2   Artificial Cracks

The depth of the CO_2 ingress measured on the split surface of the specimens with an artificial crack is shown in Fig. 1. Specimens were stored in a carbonation chamber for 14, 24, 31, 42, 56, or 63 days. At a duration of 14, 24 and 56 days only one specimen was removed from the carbonation chamber; therefore, these graphs do not show any error bars. Looking at the data from all 6 durations, there is no influence of the crack width on the carbonation depth. The specimens which were removed from the carbonation chamber after 24 days seem to be an exception to this statement; the carbonation depth is lower for specimen with a nominal crack width of 100 μm. However, it is noted that only one specimen of each nominal crack width was taken out at the duration of 24 days, which could explain the deviation from the general observation. For specimens taken out at 42 and 56 days

Table 1 Mean compressive strength which would be obtained with a loading surface of 40×40 mm^2 calculated from strength results obtained on cubes $150 \times 150 \times 150$ mm^3 (according to NBN B15-220)

Age	Original mean compressive strength on cubes 150 mm (MPa)	Mean compressive strength if loading surface would be 40×40 mm^2 (MPa)
14 days	21.1	24.8
28 days	26.3	30.8
56 days	31.7	37.2
84 days	34.7	40.7

Fig. 1 Carbonation depth (mm) with respect to distance away from the crack (mm) for artificial cracks with a nominal width of 100, 200, and 300 μm after 14, 24, 31, 42, 56, and 63 days storage in a carbonation chamber. Errors bars represent the standard deviation

the CO_2 ingress away from the crack appears to be slightly bigger for the 300 μm cracks; yet, the CO_2 ingress at the location of the crack is equal.

A statistical analysis (using SPSS Statistics 26) was performed on the carbonation depth at the location of the crack at 31, 42 and 63 days to check whether there was indeed no influence of the crack width on the results. During the analysis the threshold of the significance level α was set to 5%. For both 31 and 63 days the ANOVA test showed no significant differences (for 31 days also a Welch and a Brown-Forsythe test was executed since no equal variances could be assumed based on the mean). For 42 days of exposure the ANOVA test resulted in a significance level α of 1.8%. A subsequent Tamhane's T2 test indicated a significant difference between the carbonation depth of specimens with a nominal crack width of 100 and 200 μm ($\alpha = 2.6\%$) but not a significant difference between the carbonation depth of specimens with a nominal crack width of 100 and 300 μm ($\alpha = 9.8\%$). This can be explained by the fact that the mean carbonation depth of specimens with a nominal crack width of 200 and 300 μm was equal, but the variance was lower for the specimens with a width of 200 μm. Taking into account that the difference between the mean carbonation depths is smaller than 1.5 mm, it can be assumed that there is no practical difference in CO_2 ingress depending on the crack width of an artificial crack.

The observation that the crack width of an artificial crack does not influence the CO_2 ingress for the studied range of crack widths is in accordance with literature [2]. It can be explained by the fact that there is a lack of tortuosity. Indeed, realistic cracks are arbitrary and somewhat capricious, while the artificial cracks which were created in these specimens by pulling out metal plates are perfectly straight and constant in width over the height of the specimen.

3.3 Realistic Cracks

The depth of the CO_2 ingress measured on the sawn surface of the specimens with a realistic crack is shown in Fig. 2. Specimens were stored in a carbonation chamber for 14, 24 or 31 days. Irrespective of the nominal crack width, CO_2 ingressed much faster inside the crack and immediately adjacent to the crack (the crack zone), than further away from the crack (the uncracked zone). In contrast to the results of the artificial cracks, it is clear that for realistic cracks there is an influence of the crack width on the CO_2 ingress. This influence also extends beyond the position of the crack towards the crack zone. This is especially clear when comparing the results of a nominal crack width of 100 µm with those of 300 µm. Comparing the results of 14 days of storage in a carbonation chamber with those of 31 days, the difference in carbonation depth inside cracks of 100 µm versus 300 µm also increases with time.

To confirm the influence of the crack width on the CO_2 ingress, a statistical analysis (similar as for the artificial cracks, using SPSS Statistics 26) was performed on the carbonation depth at the location of the crack at 14, 24 and 31 days. For all test durations ANOVA tests gave significant results ($\alpha < 0.1\%$). Subsequent Tukey post-hoc tests showed a significant difference ($\alpha < 1.5\%$) between the specimens with a nominal crack width of 100 µm compared to those with a nominal crack width of 200 and 300 µm. For a test duration of 31 days even a significant difference ($\alpha = 2.9\%$) between specimens with a nominal crack width of 200 µm and 300 µm was obtained. A Student–Newman–Keuls test (with a significance level threshold of 5%) also showed a difference between 200 and 300 µm already at a test duration of 24 days, despite a Tukey test not indicating a significant difference.

Based on the visual observations and the subsequent statistical analysis, it can be concluded that there is an influence of the crack width on the CO_2 ingress. This difference is most evident when comparing small nominal crack widths of 100 µm to large crack widths of 300 µm. With time the difference becomes more distinct, so that the difference with intermediate cracks with a width of 200 µm also becomes more noticeable. The influence of the crack width can be attributed to the crack tortuosity or in other words the rough internal crack geometry. This tortuosity partly
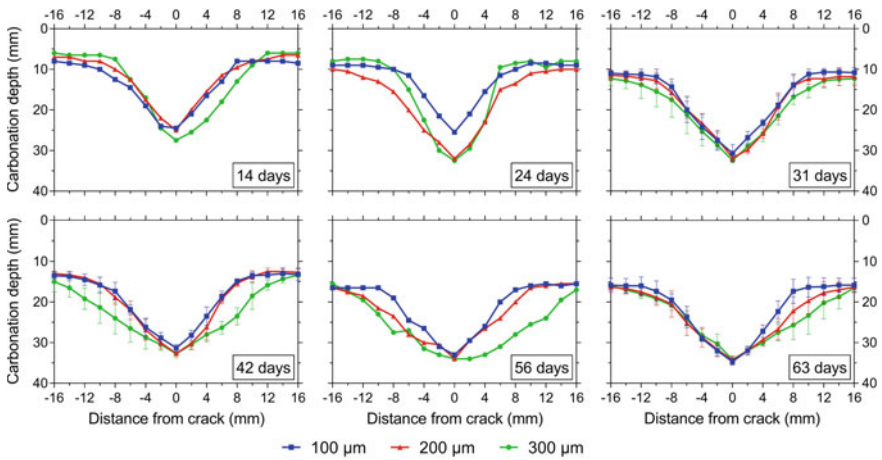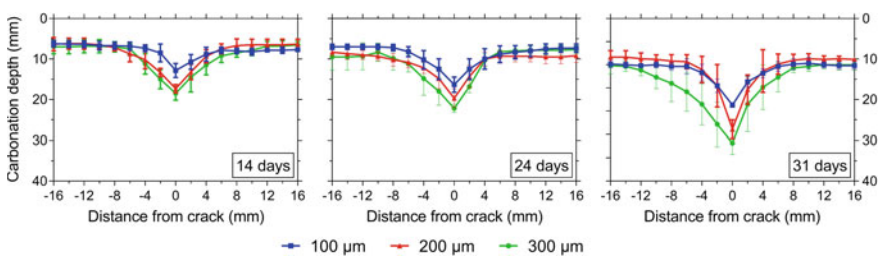

Fig. 2 Carbonation depth (mm) with respect to distance away from the crack (mm) for realistic cracks with a nominal width of 100, 200, and 300 µm after 14, 24, and 31 days storage in a carbonation chamber. Errors bars represent the standard deviation

obstructs the inflow of CO_2. So as the width of a crack in concrete decreases, the crack walls come closer together and consequently the relative influence of the rough crack walls becomes more pronounced, resulting in a reduced inflow of CO_2. Alahmad et al. [2] also studied the influence of cracks on the carbonation ingress in plain mortar. They termed this effect the interlocking phenomenon. They stated that for cracks with a width lower than 41 µm the CO_2 ingress perpendicular to the crack drops. The results in Fig. 2 indicate that this boundary might be higher.

3.4 Comparison of Artificial and Realistic Cracks

In Fig. 3 the carbonation depth in realistic cracks is compared to the carbonation depth in artificial cracks for 31 days of storage in a carbonation chamber. The carbonation depth in the uncracked zone is the same in both samples with a realistic crack and samples with an artificial crack. This was expected since the specimens had the same mix composition and were placed in a carbonation chamber at the same age.

The influence of the crack width on the CO_2 ingress is clear for the realistic cracks, while there seems to be no influence for the artificial cracks, as already discussed in Sects. 3.2 and 3.3.

It is important to highlight that there is a difference in crack depth between the specimens with realistic cracks and the specimens with artificial cracks. For the specimens with realistic cracks the crack runs over the entire height of the specimen, as a result of the Brazilian splitting. For the specimens with artificial cracks the crack is the result of a metal plate which was pulled out, so the crack is only as deep as the height over which the metal plate was inserted in the mortar (30 mm). After 31 days of storage in a carbonation chamber the CO_2 has ingressed beyond the tip of the artificial cracks.
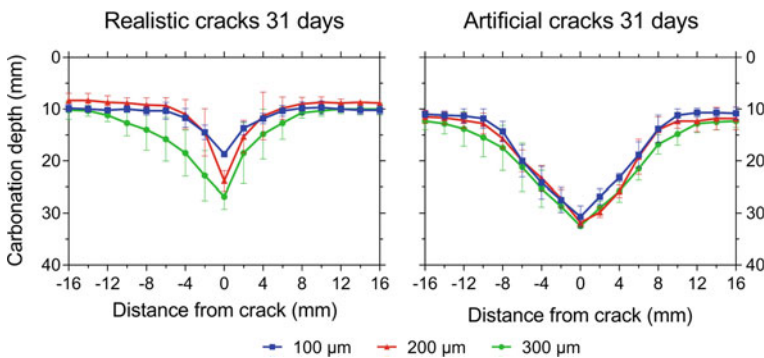
Fig. 3 Comparison of carbonation depth (mm) of realistic and artificial cracks with different nominal width (100, 200, and 300 µm) after 31 days storage in a carbonation chamber

The CO_2 has ingressed deeper into the artificial cracks then into the realistic cracks, even for cracks with a nominal width of 300 μm for which the influence of the tortuosity is the lowest (an independent samples t-test comparing the 300 μm cracks resulted in a significance level lower than 0.2%). The artificial cracks were created much sooner than the realistic cracks, see Sect. 2, yet this could have had only a limited influence since the specimens were stored for most of the time in a very humid curing environment. Aside from the lower carbonation depth inside the crack, a narrower carbonated area around the crack is observed in the samples with realistic cracks. During casting, the crack wall of artificial cracks is a mould surface where the distribution of the aggregates around this area is not the same as the distribution in the bulk of the sample. This phenomenon is called the wall effect. Due to this effect in artificial cracks, more cement paste is found in the crack area. On the one hand this delays the development of the carbonation front as there is more material that can carbonate. On the other hand the development of the carbonation front will increase as more pores exist around the crack. This last effect seems to be dominant, causing a faster CO_2 ingress and a higher carbonation depth perpendicular to the crack wall. Additionally, realistic cracks also benefit from their crack tortuosity, which for smaller cracks partly obstructs the inflow of CO_2.

4   Conclusions

This study investigated the influence of the crack width and the crack geometry on the carbonation of HVFA mortar. The results indicate that for artificial cracks there is no influence of the crack width on the carbonation as a result of the lack of crack tortuosity. Realistic cracks, on the other hand, do have cracks with tortuosity. For these cracks it is clear that there is an influence of the crack width on the CO_2 ingress, especially when comparing specimens with a nominal crack width of 100 μm to specimens with a nominal crack width of 300 μm. Comparing artificial cracks to realistic cracks, indicates a higher carbonation depth and a wider carbonated zone for artificial cracks. This is a result of a lack of crack tortuosity in combination with the wall effect present in artificial cracks which results in a higher degree of pores.

References

1. De Belie, N., Gruyaert, E., Al-Tabbaa, A., Antonaci, P., Baera, C., Bajare, D., Darquennes, A., Davies, R., Ferrara, L., Jefferson, T.: A review of self-healing concrete for damage management of structures. Adv. Mater. Interfaces **5**(17), 1800074 (2018)
2. Alahmad, S., Toumi, A., Verdier, J., François, R.: Effect of crack opening on carbon dioxide penetration in cracked mortar samples. Mater. Struct. **42**(5), 559–566 (2009)
3. Van den Heede, P., Van Belleghem, B., Araújo, M.A., Feiteira, J., De Belie, N.: Screening encapsulated polymeric healing agents for carbonation-exposed self-healing concrete, service life extension, and environmental benefit. In: International Congress on Polymers in Concrete, pp. 83–89. Springer (2018)
4. Ferrara, L., Van Mullem, T., Alonso, M.C., Antonaci, P., Borg, R.P., Cuenca, E., Jefferson, A., Ng, P.-L., Peled, A., Roig-Flores, M., Sanchez, M., Schroefl, C., Serna, P., Snoeck, D., Tulliani, J.M., De Belie, N.: Experimental characterization of the self-healing capacity of cement based materials and its effects on the material performance: A state of the art report by COST Action SARCOS WG2. Constr. Build. Mater. **167**, 115–142 (2018)
5. Shin, K.J., Bae, W., Choi, S.-W., Son, M.W., Lee, K.M.: Parameters influencing water permeability coefficient of cracked concrete specimens. Constr. Build. Mater. **151**, 907–915 (2017). https://doi.org/10.1016/j.conbuildmat.2017.06.093
6. CEN (2019) EN 12350-2:2019 Testing Fresh Concrete—Part 2: Slump Test
7. CEN (2019) EN 12350-5:2019 Testing Fresh Concrete—Part 5: Flow Table Test
8. CEN (2016) EN 196-1: 2016 Methods of Testing Cement—Part 1: Determination of Strength
9. BIN (1973) NBN B 15-220 Proeven op beton - Drukproef - Invloed van de afmetingen en vormen van het proefstuk op de druksterkte van het beton
10. Siddique, R.: Performance characteristics of high-volume Class F fly ash concrete. Cem. Concr. Res. **34**(3), 487–493 (2004). https://doi.org/10.1016/j.cemconres.2003.09.002

Effect of Curing Temperature on the Alkali Activation of German Brown Coal Fly Ash

David W. Law, Patrick Sturm, Gregor J. G. Gluth, and Chamila Gunasekara

Abstract Due to environmental concerns regarding the use of Portland cement as the principal binder material in concrete and mortar it is imperative to identify alternative materials that could reduce the carbon footprint of the construction industry. One alternative to address these issues is the use of alkali activated materials, in particular, when based on waste streams that currently have no or only limited industrial application. This paper reports a preliminary study into the synthesis of geopolymer mortar utilizing Brown Coal Fly Ash. The ash had a CaO content of $\sim 39\%$, indicating that synthesis at ambient or low temperature may be feasible. The paper reports initial trials on the effect of curing temperature, ambient to 120 °C, on the mechanical properties of the mortars produced. The results showed that ambient cured mortar achieved a compressive strength of 6.5 MPa at 3 days. A curing temperature of 60 °C gave the optimum results with a compressive strength of almost 20 MPa and a flexural strength of 3.5 MPa obtained.

1 Introduction

The production of Portland Cement (PC) releases significant quantities of greenhouse gases into the atmosphere with global cement production responsible for 5–8% of anthropogenic CO_2 emissions. This accounts for around 2.2 billion tons of CO_2 emission per year [1–3], corresponding to approx, 3.4% of the world's

D. W. Law (✉) · C. Gunasekara
Civil and Infrastructure Engineering, School of Engineering, RMIT University, Melbourne, VIC 3000, Australia
e-mail: david.law@rmit.edu.au

P. Sturm · G. J. G. Gluth
Division 7.4 Technology of Construction Materials, Bundesanstalt für Materialforschung und-prüfung (BAM), Unter den Eichen 87, 12205 Berlin, Germany

69

greenhouse gases being generated by the production of PC [4]. The replacement of PC with supplementary cementitious materials is an established methodology to reduce both energy consumption and the production of greenhouse gases. One of the most common supplementary materials used is Fly Ash (FA) from coal fired power stations, with the levels of substitution ranging from 20 to 30% as specified for a supplementary cementitious material [5, 6], and up to 80% in High Volume Fly Ash concretes [7, 8]. More recently the alkali activation of fly ash with close to 100% replacement has been achieved in geopolymer concretes [9–12].

Class F FA is produced from burning anthracite and bituminous coals and Class C fly ash from lignite and sub-bituminous coals, ASTM C618 [13]. Class F is the most widely used, both as a replacement for PC and in the production of geopolymers, due to the higher aluminosilicate content and lower CaO and sulphur content compared to class C. Brown coal fly ash (BC FA) is characterized as Class C FA. However, some types of BC FA may not be categorized as either class F nor class C due to the high sulphur content [14, 15]. The annual production of brown coal ash in 2008 was estimated to be 938 million tons compared to 5762 million tons of black coal fly ash. The largest producers of brown coal are Germany, Russia, the USA and Australia. In Australia, lignite coal is referred to as brown coal, whereas in Europe, both sub-bituminous coal and lignite coal can be defined as brown coal [16]. Presently brown coal fly ash is not used as a binder in structural concrete, and almost all the fly ash produced is stored disposed of in landfill or in storage ponds [17, 18].

To date there has been little study on the alkali activation of BC FA. Dirgantara et al. [19] investigated the suitability of BC FA for production of geopolymers and reported that compressive strengths in excess of 55 MPa could be achieved for mortar specimens and that elevated curing of 120 °C for 24 h was required to achieve structural integrity and to optimize the strength development. Tennakoon et al. [20] developed blended brown coal fly ash geopolymers with low calcium fly ash and blast furnace slag. The study shows that brown coal fly ash with higher aluminium content improved the rate of reaction of the geopolymer.

This paper reports a study into the production of geopolymer mortar utilizing Brown Coal Fly Ash from Germany. The ash has a high CaO content suggesting that synthesis at ambient or temperatures lower than the 120 °C recommended for brown coal fly ash in previous studies may be feasible. The paper reports initial trials on the effect of curing temperature, ambient to 120 °C on the compressive strength of the mortars produced.

2 Methodology

The brown coal fly ash used in this study was obtained from a German supplier, where the ash is treated with water (to slake the free lime contained in the original ash), homogenized and ground before being distributed. The chemical composition of the ash was determined by inductively coupled plasma optical emission

Table 1 Chemical composition of the fly ash

	SiO$_2$	Al$_2$O$_3$	Fe$_2$O$_3$	CaO	K$_2$O	TiO$_2$	P$_2$O$_5$	MgO	Na$_2$O	SO$_3$	LOI
Mass (%)	29.0	12.2	8.2	38.6	0.3	0.5	0.1	2.7	0.3	6.6	2.0

Table 2 Particle size distribution of fly ash

Sieve size	10 μm	20 μm	30 μm	45 μm	50 μm	75 μm	100 μm
% Passing	45.59	71.90	85.70	96.51	98.51	99.97	100

Table 3 Estimated amorphous and crystalline content and specific surface area of the fly ash

	Phase (%)		Surface area
	Crystalline	Amorphous	BET surface area (m^2/kg)
Ash	69.8	30.2	3635

spectrometry (ICP-OES) after total digestion in a microwave oven, Table 1. The particle size distribution, as determined by laser granulometry after wet dispersion in propan-2-ol, is given in Table 2. The phase assemblage was determined using a Bruker AXS D8 ADVANCE X-Ray Diffraction (XRD) instrument with a copper anode, operating at 40 kV and 35 mA. The crystalline phases and amorphous content was determined using the Bruker EVA-4 software and Rietveld analysis with the Bruker TOPAS-5 software [21]. The fly ash surface area was determined using Brunauer–Emmett–Teller (BET) method by N$_2$ adsorption, Table 3. The density of the BC FA was determined to be 2.81 g/cm^3 by helium pycnometry.

A Malvern Zetasizer was utilized to determine the zeta potential of both the sieved raw source material and the powdered geopolymer matrices. Each material was dispersed into a capsule of deionised water at a concentration of 1/100th by mass. All computations and analysis are performed on the Zetasizer software (v. 7.11).

The activator was a blend of commercially available sodium silicate with 15.0 ± 0.4% Na$_2$O and 27.2 ± 0.6% SiO$_2$ (i.e. a modulus of 1.87) and 15 M NaOH solution, prepared by dissolving NaOH pellets in deionized water, and additional water. The sand used for mortar production was CEN standard sand according to EN 196-1 (quartz; nominal particle size range 0.08–2 mm).

A 15% dosage (defined as Na$_2$O/fly ash ratio by weight), an alkaline modulus (AM), of 1.0, defined as the total molar SiO$_2$/Na$_2$O ratio of the activator solution and a water/solids ratio (w/s) of 0.91 were selected based on previous research [22], Table 4. Mixing was done using a mortar mixer conforming to EN 196-1. The activator solutions (sodium silicate solution, NaOH solution together with the water) were pre-mixed, by hand, 15 min prior to adding to the solids. Following pre-mixing of the activator the BC FA and sand were mixed for 5 min at low speed. The activator solution was then added to the solids and mixed by hand for 2 min. The mix was then stirred at low speed and high speed for 4 and 2 min respectively.

Table 4 Mix designs of the BC FA geopolymer mortars

Mix design	AM	Dosage	Mass ratio of materials per m^3 (kg)						
			FA	Sand	Activator solution			Water/ solid
					Water	Water–glass	15 M NaOH	
AM1.00	1.00	15.0	400	1100	230	205	91	0.91

The mortar mix was placed in $40 \times 40 \times 160$ mm rectangular moulds, compacted with two-layer placing and tamping and vibrated for 20 s for each layer on a vibrating table. The moulds were kept sealed in plastic bags at ambient conditions (21 ± 2 °C, $55 \pm 10\%$ RH) for one day. Elevated cured specimens then were sealed with plastic to prevent evaporation and placed in an oven at the designated temperature for a further 24 h. The temperature curing range was ambient, 40, 50, 60, 70 and 120 °C, selected based on previous research by Dirgantara et al. which had shown that the optimum curing temperature for BC FA was 120 °C [22]. At the conclusion of the elevated curing period the moulds were removed from the oven and left at room temperature to cool before placing in a controlled environment at 23 °C and 50% RH. Ambient cured specimens were transferred to the controlled environment after one day under ambient conditions (i.e. with no heat curing).The specimens were then demoulded and tested at 3 days post casting The compressive and flexural strength testing was carried out in compliance with the EN 196-1. The specimens were tested until failure. The flexural strengths are an average of three tests and the compressive strength, an average of six tests, are reported.

3   Results

The strength vs time data for the compressive and flexural strength of the mortars are shown in Figs. 1 and 2. The data show an increase in both compressive and flexural strength with increasing curing temperature up to 60 °C, followed by a decrease in strength at higher temperatures. The optimum strength achieved at 3 days for the 60 °C specimens were a compressive strength of 19.71 MPa and a flexural strength of 3.59 MPa. Ambient curing achieved a compressive strength of 6.31 MPa, the lowest of all the curing temperatures applied. However, the flexural strength, 1.21 MPa is greater than that achieved by the mortar cured at 120 °C, 0.92 MPa. The data clearly highlights the optimum temperature of 60 °C. Both sets of strength data demonstrate a high level of consistency. The highest variability for the compressive strength was exhibited the mortar cured at 50 °C, which has a standard deviation of 2.14 MPa (approx. 15%). There is a greater variation in the flexural strength, though other than the 120 °C sample (approx. 22%), which has the lowest flexural strength, all the other specimens have values less than 12.5%.
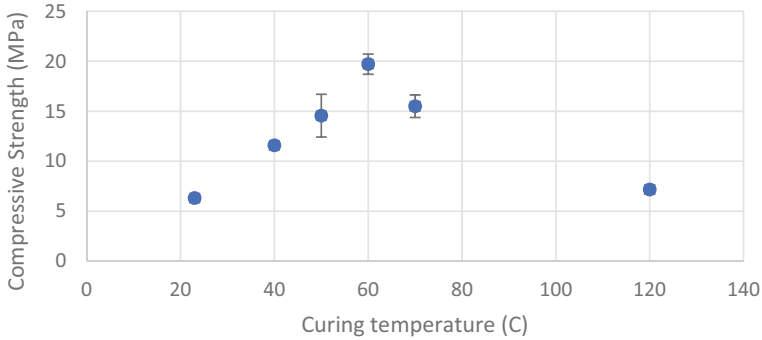
Fig. 1 Compressive strength versus curing temperature
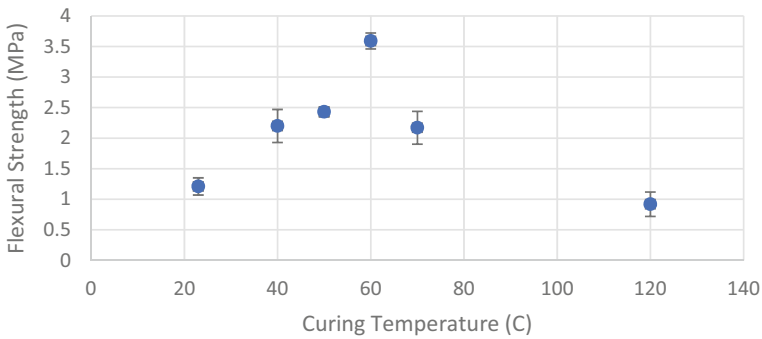
Fig. 2 Flexural strength versus curing temperature

At curing temperatures at 70 °C and above, cracks were observed in the mortar specimens following the heat curing. In addition, a distinct variation in colour was observed in the mortar. In the ambient cured specimens, the specimens had a uniform light grey colour, however, in the heat cured specimens all the samples displayed a striated appearance with a lighter and darker section, as illustrated in Fig. 3.

4 Discussion

The chemical composition, amorphous content, zeta potential and fineness have been identified as key parameters influencing geopolymer performance [22–25]. The employed raw ash had a very high Ca content, 38.9%, compared to Class F FA, though similar to other BC FA and to alkali activated slags [22, 26]. This high Ca

Ambient   **40 °C**
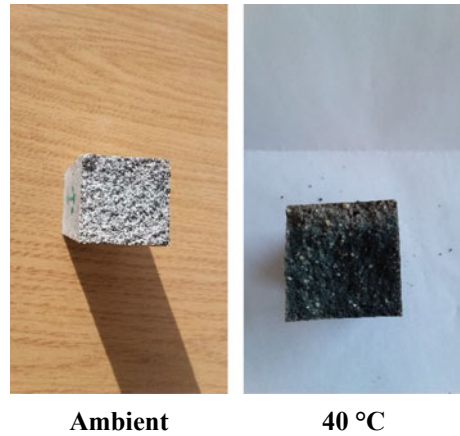
content is hypothesized as a primary factor contributing to the polymerization at ambient temperatures. Previous studies on Australian BC FA have reported that structural integrity is not achieved with ambient curing, and a curing temperature of 120 °C is required for optimal performance. Similarly heat curing is required for Class F FA to optimize performance, while slag based alkali activated materials, containing high Ca, generally employ ambient curing [10].

An increase in finesses has been reported as contributing to an increase in compressive strength, with the percentage passing at 45 µm and the percentage less than 20 µm both reported as influencing the performance of the ash. This employed ash had approx. 70% of particles below 20 µm and over 85% passing at 45 µm, with a total BET surface area of 3635 m^2/kg, Tables 2 and 3. These are both comparable or higher than values generally reported for Class F and Class C FA previously, indicating that the fineness of the material would not be expected to adversely affect compressive strength and the higher fineness may also contribute to activation under ambient curing [20, 27, 28].

The zeta potential relates to the ease of deprotonation of the raw FA and is related to the rate of dissolution of the metallic ions from the surface of the ash particles. A more negative zeta potential indicates that the ash will deprotonate easily and that the calcium and aluminosilicate present will readily be dissolved [29]. The zeta potential of the employed raw BC FA was determined to be +4.12. This would indicate that despite the relatively high fineness observed in the BC FA the ash does not deprotonate readily. This would in turn inhibit the reactivity of the ash and could account for the relatively low compressive strengths observed.

The zeta potential of the mortar was determined at 7 days. The zeta potential of the mortar relates to the ease of agglomeration, which in turn affects the rate of polymerisation. The less negative the potential the more likely agglomeration. The ambient cured mortar had a zeta potential of −23.4 mV, while the zeta potential of the 60 °C cured mortar was −29.2. While the slightly less negative value for the ambient cured mortar would suggest that agglomeration would occur at a higher

rate under this curing regime than at 60 °C both would be classified as in the fairly stable range for agglomeration. The reported zeta potential is also slightly less negative than those reported for Class F FA geopolymers [11], suggesting that polymerisation would be more likely to occur in the Class F FA mortars, although the compressive strengths observed are generally lower than those observed for Class F FA mortars. As such, it is concluded that the low strengths observed are more readily attributed to the small positive zeta potential of the ash which would inhibit dissolution.

Figure 4 displays the XRD pattern of the raw ash and the ambient cured and 60 °C cured mortars at 7 and 28 days. The principal phases in the raw ash were identified as quartz ($\sim$45%), gehlenite (17–20%) and anhydrite (27–30%). Small quantities of lime ($\sim$4.5%) and portlandite ($\sim$3%) were also identified together with minor amounts of brownmillerite, yeelimite, cristobalite, calcite and belite/larnite. The amorphous content was estimated to be 30.2% corresponding to the broad peak between 20° and 40°. This is comparable with other reported Class C and BC FA but low compared with Class F FA used in the production of geopolymer concrete which are generally in the range 65–80% amorphous fraction [11, 22, 27]. It has been established that the higher the amorphous content in the fly ash, the higher the reactivity of the ash. Hence, the relatively low amorphous content would also be expected to limit the quantity of aluminosilicate material available for the dissolution and geopolymerisation.

The main phases identified in both the mortars, ambient and 60 °C cured, were quartz ($\sim$90%) gehlenite (2–4%) and belite/larnite ($\sim$4%) together with thenardite ($\sim$2–3%) as the principle crystalline reaction product; in addition, some portlandite (<1%) was observed in the 60 °C cured specimens at 7 days, At 28 days calcite (1–4%) was present in both mortars.
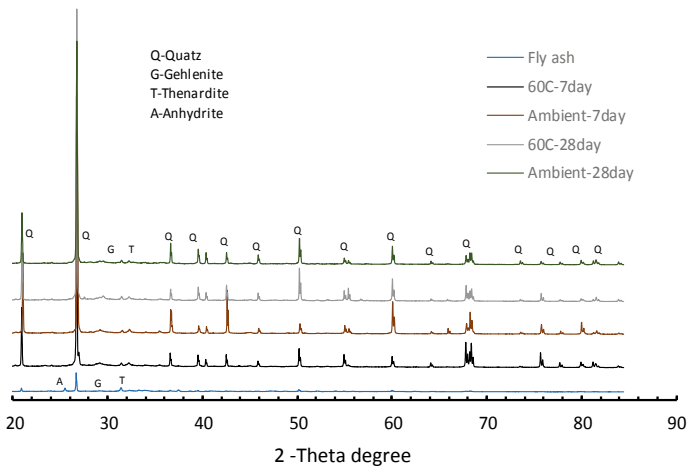
Fig. 4 XRD Analysis, Raw ash, Ambient and 60 °C heat cured mortar

Given the relatively low curing temperatures and the strength achieved at 3 days the results suggest that the German BC FA may be a suitable material to be used as an alkali activated material. Further research is required to optimize the activator composition and to assess the long term performance. Based on this data it may be possible to develop an ambient cured concrete to reduce the environmental impacts due to cement production in the construction industry.

5   Conclusion

The main findings from the study can be summarised as;

- The optimum compressive strength, 19.71 MPa, and flexural strength, 3.59 MPa, at 3 days were achieved at a curing temperature of 60 °C. A significant drop in performance was observed at higher curing temperatures, while a compressive strength of 6.31 MPa was achieved with ambient curing.
- The raw ash had a zeta potential of +4.12, indicative a low tendency to deprotonate, while the mortars have zeta potentials in the range −20 to −30, classified as the fairly stable range for agglomeration. The raw ash had an amorphous content of $\sim 30\%$, a surface area of 3635 m^2/kg and a CaO content of almost 40%.
- The relatively low curing temperature required compared to other BC FA and to Class F FA is attributed to the high Ca content and the high surface area, coupled with the tendency for agglomeration, although the ash has a zeta potential that would inhibit deprotonation and the polymerization reaction.

References

1. He, Z., et al.: Comparison of CO2 emissions from OPC and recycled cement production. Constr. Build. Mater. **211**, 965–973 (2019)
2. Rodgers, L.: BBC News-Climate Change: The Massive CO_2 Emitter You May Not Know About (2018)
3. Stajanča, M., Eštoková, A.: Environmental Impacts of Cement Production (2012)
4. Inti, S., Sharma, M., Tandon, V.: Ground granulated blast furnace slag (GGBS) and rice husk ash (RHA) uses in the production of geopolymer concrete. In: Geo-Chicago 2016, pp. 621–632 (2016)
5. AS3972, (ed.): Portland and Blended Cements, 2nd edn. Australian Standard (2010)

6. 197-1:2011, B.E.: Cement: Composition, Specifications and Conformity Criteria for Common Cements, BSI (2011)
7. Shaikh, F.U.A., Supit, S.W.M.: Mechanical and durability properties of high volume fly ash (HVFA) concrete containing calcium carbonate (CaCO3) nanoparticles. Constr. Build. Mater. **70**, 309–321 (2014)
8. Roychand, R., et al.: Micro and nano engineered high volume ultrafine fly ash cement composite with and without additives. Int. J. Concr. Struct. Mater. **10**(1), 113–124 (2016)
9. Rickard, W.D.A., Gluth, G.J.G., Pistol, K.: In-situ thermo-mechanical testing of fly ash geopolymer concretes made with quartz and expanded clay aggregates. Cem. Concr. Res. **80**, 33–43 (2016)
10. Provis, J.L., Palomo, A., Shi, C.J.: Advances in understanding alkali-activated materials. Cem. Concr. Res. **78**, 110–125 (2015)
11. Gunasekara, C., et al.: Zeta potential, gel formation and compressive strength of low calciumfly ash geopolymers. Constr. Build. Mater. **95**, 592–599 (2015)
12. Fernandez-Jimenez, A., Palomo, A., Criado, M.: Microstructure development of alkali-activated fly ash cement: a descriptive model. Cem. Concr. Res. **35**(6), 1204–1209 (2005)
13. C618-17a, A., Standard Specification for Coal Fly Ash and Raw or Calcined Natural Pozzolan for Use in Concrete. ASTM International, West Conshohocken, PA (2017)
14. Dirgantara, R., Law, D.W., Molyneaux, T.C.K.: Compressive strength variability of brown coal fly ash geopolymer concrete. Int. J. Res. Eng. Technol. **3**(13), 165–169 (2014)
15. Macphee, D.E., Black, C.J., Taylor, A.H.: Cements incorporating brown coal fly-ash from the Latrobe valley region of Victoria Australia. Cem. Concr. Res. **23**(3), 507–517 (1993)
16. Britt, A., et al.: Australia's Identified Mineral Resources 2014, p. 4. Geoscience Australia, Canberra (2015)
17. Macphee, D.E., Black, C.J., Taylor, A.H.: Cements incorporating brown coal fly ash from the Latrobe Valley region of Victoria, Australia. Cem. Concr. Res. **23**(3), 507–517 (1993)
18. CIA: Recommended Practice Geopolymer Concrete. Concrete Institute of Australia, Sydney (2011)
19. Dirgantara, R., et al.: Suitability of brown coal fly ash for geopolymer production. J. Mater. Civ. Eng. **29**(12), 04017247 (2017)
20. Tennakoon, C., et al.: Characteristics of Australian brown coal fly ash blended geopolymers. Constr. Build. Mater. **101**, 396–409 (2015)
21. Whitfield, P.S., Mitchell, L.D.: Quantitative Rietveld analysis of the amorphous content in cements and clinkers. J. Mater. Sci. **38**(21), 4415–4421 (2003)
22. Dirgantara, R., et al.: Suitability of brown coal fly ash for geopolymer production. J. Mater. Civil Eng. **29**(12) (2017)
23. van Jaarsveld, J.G.S., van Deventer, J.S.J., Lukey, G.C.: The characterisation of source materials in fly ash-based geopolymers. Mater. Lett. **57**(7), 1272–1280 (2003)
24. Hardjito, D., Rangan, B.V.: Development and Properties of Low-Calcium Fly Ash-Based Geopolymer Concrete. Curtin University (2005)
25. Fernandez-Jimenez, A., et al.: Quantitative determination of phases in the alkali activation of fly ash Part I. Potential ash reactivity. Fuel **85**(5–6), 625–634 (2006)
26. Provis, J.L., Bernal, S.A.: Geopolymers and related alkali-activated materials. Annu. Rev. Mater. Res. **44**(44), 299–327 (2014)
27. Alvarez-Ayuso, E., et al.: Environmental, physical and structural characterisation of geopolymer matrixes synthesised from coal (co-)combustion fly ashes. J. Hazard. Mater. **154**(1–3), 175–183 (2008)
28. Diaz, E.I., Allouche, E.N., Eklund, S.: Factors affecting the suitability of fly ash as source material for geopolymers. Fuel **89**(5), 992–996 (2010)
29. Kukier, U., et al.: Composition and element solubility of magnetic and non-magnetic fly ash fractions. Environ. Pollut. **123**(2), 255–266 (2003)

Use of Microwave-Accelerated Curing Under Low-Pressure in the Production of Ultra-Durability Portland Type I-Portland Cement Pastes

Natt Makul

Abstract Globally, the pressure mounts towards attaining low carbon emissions in the energy sector, which has propelled the G8 Summit to advocate for radical high technology approaches for cement production. Among the modern technologies recommended, which also offers the techno-economic advantages is the microwave-based curing. Low pressure accelerated microwave heating, also called accelerated dewatering, is an innovative technique that enhances the properties of HSCP. This study has analyzed the effect of this improvement including the impact of the pressure on feed direction, MW cavity, and the different HSPC samples for every MW treatment batch. The initial state of this treatment established the following. First, to evade internal structure cracks, the delay time should precede the setting time (averagely 30 min after mixing). Secondly, the moisture and temperature increase differences within the MW cavity should be minimal. By following low-pressure microwave treatment will significantly improve properties of HSCP by increasing the resistance to drying shrinkage and water permeability.

Keywords Microwave-accelerated curing · Low-pressure · Ultra-durability · Cement pastes

1 Introduction

For the past four decades, microwave heating has had considerable effect on the concrete industry. This improvisation can apply in a variety of contexts categorized into three groups [1–4].

Group I. The first application of microwave heating deals with the analysis and prediction of properties of the concrete-based element. For example, elements and characteristics of Portland concrete, as well as its chloride presence, can be studied

N. Makul (✉)
Department of Building Technology, Faculty of Industrial Technology, Phranakhon Rajabhat University, 9 Changwattana Road, Bangkhen Bangkok 10220, Thailand
e-mail: natt@pnru.ac.th

after exposure to microwave heating [5]. It can also forecast the CS of conventional concrete [6], evaluate the water-cement ratio of the concrete setting [7], and "reflecting the near-field measurement to nondestructively test the concrete" [8]. Furthermore, microwave heating can also examine the water permeability capacity of the concrete roof [9].

Group II. The second application focuses on the enhancement of concrete-based properties. Microwave heating serves as one of the improvisation methods that is preferred over conventional treatments due to low carob emissions, its efficiency, and the high durability cement produced. It helps in improvisation of the mechanical constituents of concrete including "the accelerated curing of mortar dewatering of the fresh concrete incorporated using the MW-vacuum technique to enhance the compressive strength of concrete in the low-pressure state and with concrete mixed with slag powder" [10–24].

Group III. For this third application, microwave heating can serve as an agent for the recycling of supplementary concrete wastes or destruction of the concrete material. This approach can decommission the cement polluted reinforced concrete slab" [25], restore or destroy cement and supplementary elements, which specifically serves in the metakaolin treatment [26]. It can as well enhance the high-reactivsity rice husk ash that can act as a partial alternative of cement-based element [19] and transform the carbon black-asphalt HSPC [27]. Besides, it can improvise the performance, characteristics of recycled concrete HSPC [28], generate better performing, and durable aggregate from wasted cement materials [29], renovate the in situ HSPC [30], transform destroyed mortar [27, 31, 32].

This study utilized the microwave cavity pressure of 30 and 50 kPa. "The feed direction of the microwave energy (symmetrically or asymmetrically perpendicular directions of the HSPC specimen placement) and the number of HSPC specimens per batch of MW curing (12 and 24 specimens with dimensions of 5 cm × 5 cm × 10 cm in length × width × thickness) concerning the temperature increase and moisture content (in term of remaining w/c)" [33].

2   Methodology and Materials

2.1   Materials

The HSPC were made by mixing tap water (pH ≈ 7.5) with Portland cement Type 1 (OPC). Their constituents are as shown in Table 1. OPC's main constituent element is CaO ($68.02 \pm 1.06\%$). Its subsidiary elements are as shown in Table 1.

Table 1 Chemical composition and physical properties of the OPC

Chemical composition (% by mass)	OPC (mean + standard deviation)
SiO_2	19.84 ± 0.52
Al_2O_3	4.21 ± 0.28
Fe_2O_3	3.19 ± 0.09
MgO	1.25 ± 0.02
CaO	68.02 ± 1.06
Na_2O	0.18 ± 0.03
K_2O	0.33 ± 0.06
SO_3	1.59 ± 0.17
Loss on ignition	0.92 ± 0.04
Physical properties	OPC (mean + Standard deviation)
Particle size at 50% cumulative passing (μm)	13.50 ± 0.39
Specific gravity	3.15 ± 0.02
Specific surface area (m^2/kg)	1325 ± 14.02

2.2 MW System

The role of a multi-mode double-feed MW device is to dehydrate the HSPC. It has a vacuum pump suited for this functionality. The physical dimension of the tool is as observed in Fig. 1. The MW model comprises a cylinder-based cavity manufactured from steel. For its horizontal direction, it has 72 cm length with a diameter of 24 cm. Its estimated volume is 1.30×10^5 cm^3. The polypropylene (PP) lining measurements comprise a length of 50 cm and a diameter of 22 cm. It has an estimated volume of 0.76×10^5 cm^3. Besides, there is the installation of air-cooled magnetrons within the side and roof of the MW cavity. Thus, the magnetron for the roof is known as magnetron 1. This symmetrical magnetron is vertically placed. On the other hand, the side magnetron, which is asymmetric, is known as magnetron 2. Approximate MW power produced by each of these magnetrons is 800 W. The third section of the MW deals with regulation of feeding of the two magnetrons alongside the temperature. The last section is a 1.0 hp vacuum pump that reduces and ejects the internal air from 50 and 30 kPa.

2.3 HSPC Sample Preparation, Water Treatment, and Testing Methods

Based on the experiment by Makul, "the HSPC was prepared by controlling the water content regulated with the specific w/c of 0.25, 0.35, and 0.45." [33] The study presumed air volume to be 1.0% in the HSPC. This is as exhibited in Table 2. Under a 1.0 m^3 air volume regulation, "the increase in water-cement ratio leads to a

Fig. 1 HSPC specimens after applying the low-pressure MW curing

rise in water content and a reduction in the content of OPC. The compressive strength of the aggregate samples at days 1 (not water curing), 3, 7 and 28 complies with ASTM C39/C39M-18" [34].

2.4 Low-Pressure MW Treatment Procedures to Dehydrate HSPC

To generate the HSPC, the experiment by American Society for Testing and Materials used "the sets of 192-HSCP specimens in dimensions of 5 cm × 5 cm × 10 cm of length × width × thickness were cast. After 30 min of mixing, before application of MW treatment," the concrete samples for each batch of the treatment (12 and 24 samples) were continuously improvised in four steps that involved

Table 2 Mixture proportions per cubic meter of HSPC

Water-cement ratio (w/c) (by mass)	OPC (kg)	Water (kg)	Water reducing admixture Type A (% of cement content)	Assumed air content (% by volume)
0.25	1745	436	0.5	1.0
0.35	1483	519	0.5	1.0
0.45	1290	581	0.5	1.0

Table 3 Case studies of HSPC under MW curing

Case	w/c	Pressure within cavity (kPa)	Magnetron	Number of HSPC specimens	Time of application (Min)
1	0.25	30	1	12	100
2	0.25	50	1	12	100
3	0.35	30	1	12	50
4	0.35	50	1	12	40
5	0.45	30	1	12	50
6	0.45	50	1	12	40

arrangement of samples, pumping air into the cavity to reduce internal pressure, measuring temperature increase after treatment, and lastly, demolding the treated samples [34]. This is as shown in Table 3.

3 Results and Discussion

3.1 Temperature Increase and Moisture Content During Applying MW Energy

Figure 2 shows "the temperature increase in the HSCP specimens under pressures of 30 and 50 kPa for 12 specimens per batch of MW curing with control initial w/c values of 0.25 (experiment 1 and 2), 0.35 (experiment 3 and 4) and 0.45 (experiment 5 and 6). In an experiment (30 kPa) and 2 (50 kPa), during the initial stage (averagely the first 30 min) of MW treatment, the temperature of the aggregate samples persistently rose." This increase was from "0.72 °C/min for 30 kPa and 0.70 °C/min for 50 kPa); from 30 to 100 min, the rate of temperature increases lowed (0.64 °C/min for 30 kPa and 0.40 °C/min for 50 kPa)" [33]. These actions remained constant with the concrete properties such that the dormant period had a 30 min delay time. It was at this time that the rate of hydration was the least due to the occurrence of ettringite "$(Ca_6Al_2(SO_4)_3(OH)_{12} \cdot 26H_2O)$" [33]. After exposure to the concrete to heat, the dormant period significantly declined. On the other hand, the rate of hydration starts at a high pace as seen from the mount in temperature to 60 min up from the initial 30 min. At the end of the 100 min of improvisation, the temperature rose due to the heat resulting from the hydration process and the MW. During the end of the treatment, the rise in temperature is the same for the first two experiments ($\sim$71 °C). This was specifically during the 100 min of application time. The declining dormant period may eventually encourage the production of secondary delayed ettringite. These lead to concrete cracks. Therefore, the maximum temperature should not go beyond 70 °C.
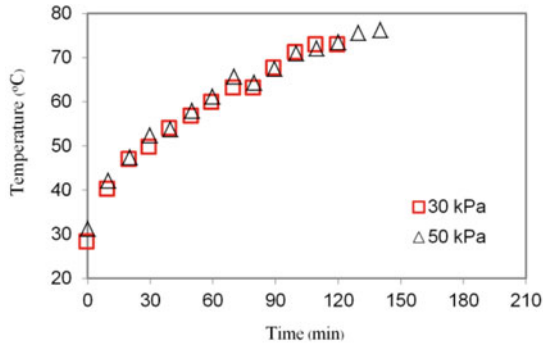
(a) 12 specimens, w/c of 0.25, pressures of 30 and 50 kPa, magnetron 1 (vertical magnetron)
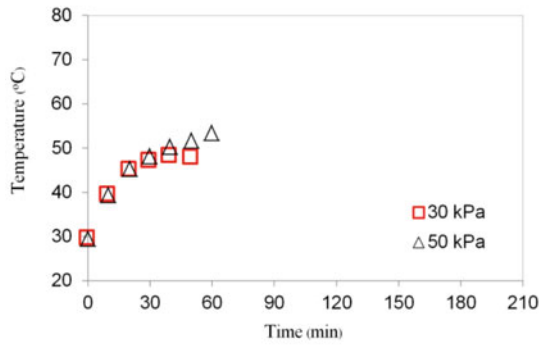
(b) 12 specimens, w/c of 0.35, pressures of 30 and 50 kPa, magnetron 1 (vertical magnetron)
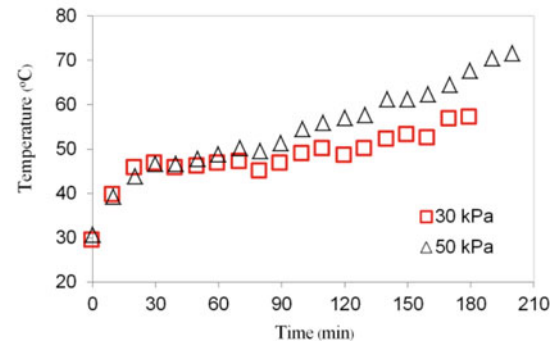
(c) 12 specimens, w/c of 0.45, pressures of 30 and 50 kPa, magnetron 1 (vertical magnetron)

Fig. 2 Magnetron 1 time and temperature increase under 30 and 50 kPa that has regulated w/c of **a** 0.25, **b** 0.35 and **c** 0.45

As observed in Fig. 2b, for experiments 4 and 3, the initial water-cement ratio increased from 0.25 to 0.35. Case 4 had a 40 min application of MW curing while case 3 had 50 min of application. "The rates of temperature increase in the first

30 min of low-pressure MW curing are 0.59 °C/min for 30 kPa and 0.62 °C/min for 50 kPa." For these experiments, as opposed to case 2 and 1, the increase in the water content had an effect on the level of heat produced by MW, the quantity "absorbed and the low rate of the hydration reaction 'the high water content causes the low formation rate of calcium-silicate-hydrate(C-S–H)." During the end of MW improvisation, temperature differences were recorded among the aggregate samples "between pressures of 30 and 50 kPa (difference at 100 min = 3.90 °C) compared to cases 1 and 2 (difference at 100 min = 0.10 °C)." This implies that the water-cement ratio affects samples' temperature. When the water to cement level increases, the temperature difference will as well increase.

What is observed in Fig. 2c is experiments 6 and 5 for HSCP prepared by regulating the water to cement rate by 0.45 with a corresponding duration of 40 and 50 min. The change in temperature increase correlates to those observed in experiments 4 and 3. For the first 30 min, when exposed to 30 kPa, the mount in temperature was 0.59 °C/min. When exposed to 50 kPa, this rate declined to 0.54 °C/min. These changes can be illustrated as "compensating effects from the heat generation," that is huge volumes of heat can be produced from optimum water content since it contains a high dielectric constant [20]. Conversely, there is a low hydration reaction due to the low formation rate of C-S-H. Thus, there will be a similar optimum temperature increases when improvisation subsides for experiment 6 ($\sim$46.8 °C) and 5 ($\sim$47.6 °C).

Dehydration of the sample HSCP "correlates with the temperature increase from low-pressure MW curing (heating up) and heat from the hydration reaction with outward moisture transfer. Figure 3 shows the moisture content (in terms of the remaining w/c) and time at pressures of 30 and 50 kPa with magnetron 1 (vertical) for 12 specimens at controlled initial water-cement ratio of 0.25, 0.35 and 0.45." The residual water-cement ratio of sample HSCP continued to decline with more MW treatment time.The standard rate of water to cement remaining until 100 min for experiment 1 (1.07×10^{-3} per min) correlates to that of experiment 2 (1.00×10^{-3} per min). This implies that the aggregate's small w/c for experiment 1 (30 kPa pressure) hardly influences the temperature mount when matched with experiment 2 at 50 kPa with limited water level from the aggregate samples. When the water-cement ratio rises to 0.35 (Fig. 3b), the ratio that remains in both experiments of 30 and 50 kPa is less in experiment 4 (1.33×10^{-3} per minute) than in experiment 3 (1.61×10^{-3} per minute).

The difference in water ratio implies that "at lower pressure, the internal water of the aggregate specimens" undergo rapid translocation and evaporation. The reason is that there is a more vapor pressure difference in the samples compared with the pressure in the cavity. This behavior correlates with experiment 5 (1.69×10^{-3} per min) and 6 (1.43×10^{-3} per min) with 0.45 w/c. This is observed in Fig. 3c.
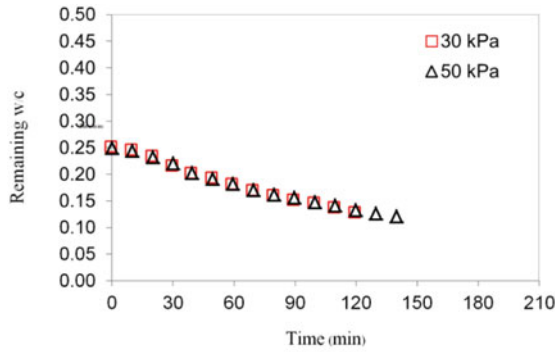
(a) 12 specimens, w/c of 0.25, pressures of 30 and 50 kPa, magnetron 1 (vertical magnetron)
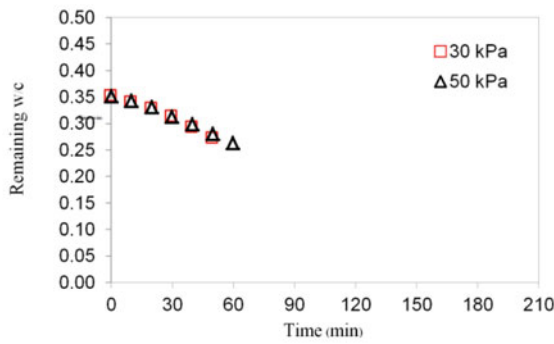
(b) 12 specimens, w/c of 0.35, pressures of 30 and 50 kPa, magnetron 1 (vertical magnetron)
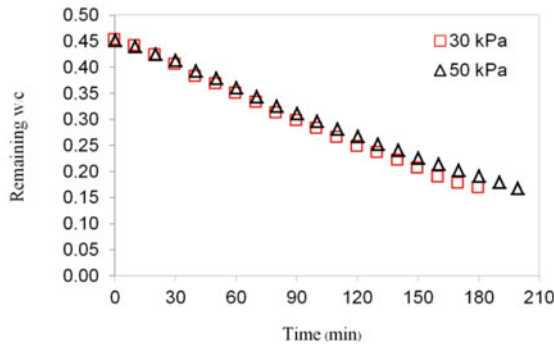
(c) 12 specimens, w/c of 0.45, pressures of 30 and 50 kPa, magnetron 1 (vertical magnetron)

Fig. 3 Moisture content and time of HSCP under the pressures of 30 and 50 kPa and magnetron 1 (vertical magnetron) for 12 specimens with a controlled w/c of **a** 0.25, **b** 0.35 and **c** 0.45

3.2 Resistance to Drying Shrinkage (DS) and Water Pemeability (WP)

As shown in Fig. 4a, the resistance to drying shrinkage compared to control HSCP of exposed to MW treatment will be based on the amount of water (residual w/c) and temperature increase. A comparison of the water-cement ratio among the HSCP have different DS. For instance, the HSCP samples in experiment 1 (50 kPa pressure) and in experiment 2 (50 kPa pressure) have a higher CS compared with HSCP under the water treatment. For instance, as for the 0.35 water-cement ratio, the long-term DS at day 720 of HSCP in the two pressures are averagely 24.16 and 25.57% compared with that of the water-treated HSCP, correspondingly. The possible justification is that the MW treatment of HSCP samples in the dormant
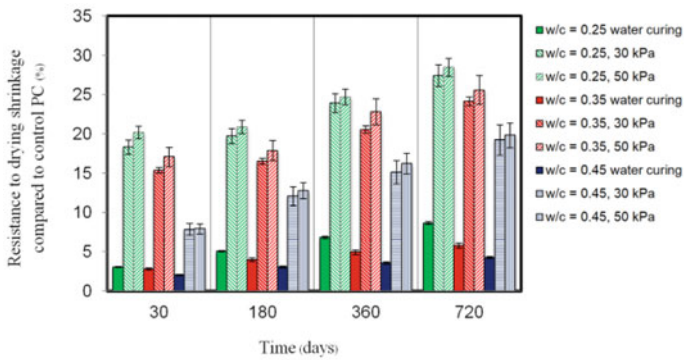
(a) Drying shrinkage and elapsed time in percent compared to of HSPC at 1 day with w/c values of 0.25, 0.35 and 0.45 at the pressure level of 30 kPa, magnetron 1 and 12 specimens.
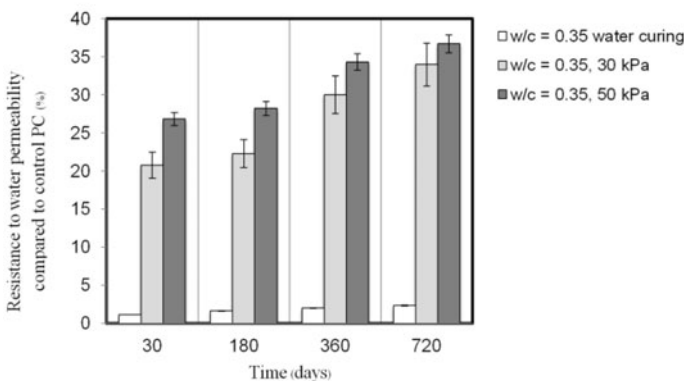
(b) Water permeability and elapsed time of HSPC at 1 day with an initial w/c of 0.35 at the pressure level of 50 kPa, magnetron 1 and 24 specimens.

Fig. 4 **a** Drying shrinkage and **b** water permeability of HSCP

period lessens the duration while at the same time amplifying the rate of hydration. Hence, C-S-H becomes more and generates a lower DS. The same DS for HSCP specimens with less pressure of 30 and 50 kPa is the same when placed under MW treatment.

Figure 4b shows the resistance to water permeability (WP) compared to control HSPC. During the first 30 day of MW improvement, HSCP specimens with the controlling initial water-cement ratio of 0.35 can induce a lower DS compared with the water-treated specimens, although with a ratio that does not exceed 0.25-w/c admixture. The reason for this less ratio is that the 0.35-w/c specimen contains high water content compared with the 0.25-w/c specimen. This indicates that with more pores, there is a less internal structure density and a correspondingly low rate of hydration. This occurrence is the same when the ratio rises to 0.45 w/c. Additionally, after the first day of MW improvement from the 180, 360, and 720 days, the treated HSCP improved more compared with the water-treated paste, yet the WP enhanced is less than that of the first 30 days. Therefore, the low-pressure cavity of treatment can address the issue of low-WP improvement by keeping the optimum temperature at not more than 70 °C [20].

4   Conclusion

This study has analyzed the effect of this improvement including the impact of the pressure on feed direction, MW cavity, and the different HSCP samples for every MW treatment batch. The initial state of this treatment established the following. First, to evade internal structure cracks, the delay time should precede the setting time (averagely 30 min after mixing). Secondly, the water-cement ratio and temperature should not go beyond 0.45 and 70 °C respectively. Thirdly, the moisture and temperature increase differences within the MW cavity should be minimal. This should be the case for both pressure levels within the MW cavity (30 and 50 kPa). Lastly, the feed direction of the low-pressure MW treatment should have a direct impact on moisture level and temperature increase. By following each of these procedures, low-pressure microwave treatment will significantly improve properties of HSCP by increasing the resistance to drying shrinkage and water permeability.

References

1. Makul, N., Rattanadecho, P., Agrawal, D.K.: Applications of microwave energy in cement and concrete—a review. Renew. Sust. Energ. Rev. **37**, 715–733 (2014). https://doi.org/10.1016/j.rser.2014.05.054
2. Buttress, A., Jones, D., Dodds, C., Dimitrakis, G., Campbell, C., Dawson, A., Kingman, S.: Understanding the scabbling of concrete using microwave energy. Cem. Concr. Res. **75**, 75–90 (2015). https://doi.org/10.1016/j.cemconres.2015.04.009
3. Buttress, A., Jones, A., Kingman, S.: Microwave processing of cement and concrete materials—towards an industrial reality? Cem. Concr. Res. **68**, 112–123 (2015). https://doi.org/10.1016/j.cemconres.2014.11.002
4. Vizi, G., Vandenbosch, G.: Building materials and electromagnetic radiation: the role of material and shape. J. Build. Eng. **5**, 96–103 (2016). https://doi.org/10.1016/j.jobe.2015.11.010
5. Haddad, R., Al-Qadi, I.: Characterization of portland cement concrete using electromagnetic waves over the microwave frequencies. Cem. Concr. Res. **28**(10), 1379–1391 (1998). https://doi.org/10.1016/s0008-8846(98)00076-3
6. Pheeraphan, T., Cayliani, L., Dumangas, M., Nimityongskul, P.: Prediction of later-age compressive strength of normal concrete based on the accelerated strength of concrete cured with microwave energy. Cem. Concr. Res. **32**(4), 521–527 (2002). https://doi.org/10.1016/s0008-8846(01)00715-3
7. Bescher, E., Sambol, M., Rice, E., Mackenzie, J.: Determination of water-to-cement ratio in freshly mixed rapid-setting calcium sulfoaluminate concrete using 2.45 GHz microwave radiation. Cem. Concr. Res. **34**(5), 807–812 (2004). https://doi.org/10.1016/j.cemconres.2003.09.023
8. Castro, A., Valcuende, M., Vidal, B.: Using microwave near-field reflection measurements as a non-destructive test to determine water penetration depth of concrete. NDT & E Int. **75**, 26–32 (2015). https://doi.org/10.1016/j.ndteint.2015.06.003
9. Kot, P., Ali, A., Shaw, A., Riley, M., Alias, A.: The application of electromagnetic waves in monitoring water infiltration on concrete flat roof: the case of Malaysia. Constr. Build. Mater. **122**, 435–445 (2016). https://doi.org/10.1016/j.conbuildmat.2016.06.092
10. Hutchison, R., Chang, J., Jennings, H., Brodwin, M.: Thermal acceleration of Portland cement mortars with microwave energy. Cem. Concr. Res. **21**(5), 795–799 (1991). https://doi.org/10.1016/0008-8846(91)90174-g
11. Naik, T., Ramme, B.: Determination of the water content of concrete by the microwave method. Cem. Concr. Res. **17**(6), 927–938 (1987). https://doi.org/10.1016/0008-8846(87)90081-0
12. Xuequan, W., Jianbgo, D., Mingshu, T.: Microwave curing technique in concrete manufacture. Cem. Concr. Res. **17**(2), 205–210 (1987). https://doi.org/10.1016/0008-8846(87)90103-7
13. Dongxu, L., Xuequan, W.: A study on the application of vacuum microwave composite dewatering technique in concrete engineering. Cem. Concr. Res. **24**(1), 159–164 (1994). https://doi.org/10.1016/0008-8846(94)90097-3
14. Leung, C., Pheeraphan, T.: Microwave curing of Portland cement concrete: experimental results and feasibility for practical applications. Constr. Build. Mater. **9**(2), 67–73 (1995). https://doi.org/10.1016/0950-0618(94)00001-i
15. Leung, C., Pheeraphan, T.: Very high early strength of microwave cured concrete. Cem. Concr. Res. **25**(1), 136–146 (1995). https://doi.org/10.1016/0008-8846(94)00121-e
16. Leung, C., Pheeraphan, T.: Determination of optimal process for microwave curing of concrete. Cem. Concr. Res. **27**(3), 463–472 (1997). https://doi.org/10.1016/s0008-8846(97)00015-x

17. Pheeraphan, T., Leung, C.: Freeze-thaw durability of microwave cured air-entrained concrete. Cem. Concr. Res. **27**(3), 427–435 (1997). https://doi.org/10.1016/s0008-8846(97)00014-8

18. Rattanadecho, P., Suwannapum, N., Chatveera, B., Atong, D., Makul, N.: Development of compressive strength of cement PC under accelerated curing by using a continuous microwave thermal processor. Mater. Sci. Eng. **472**(1–2), 299–307 (2008). https://doi.org/10.1016/j.msea.2007.03.035

19. Makul, N., Agrawal, D.K.: Microwave (2.45 GHz)-assisted rapid sintering of SiO_2-rich rice husk ash. Mater. Lett. **64**(3), 367–370 (2010). https://doi.org/10.1016/j.matlet.2009.11.018

20. Makul, N., Rattanadecho, P., Agrawal, D.K.: Microwave curing at an operating frequency of 2.45 GHz of Portland cement PC at early-stage using a multi-mode cavity: experimental and numerical analysis on heat transfer characteristics. Int. Commun. Heat Mass **37**(10), 1487–1495 (2010). https://doi.org/10.1016/j.icheatmasstransfer.2010.09.001

21. Makul, N., Rattanadecho, P., Pichaicherd, A.: Accelerated microwave curing of concrete: a design and performance-related experiments. Cement Concr. Compos. **83**, 415–426 (2017). https://doi.org/10.1016/j.cemconcomp.2017.08.007

22. Kong, Y., Wang, P., Liu, S., Gao, Z.: Hydration and microstructure of cement-based materials under microwave curing. Constr. Build. Mater. **114**, 831–838 (2016). https://doi.org/10.1016/j.conbuildmat.2016.03.202

23. Makul, N.: Innovative hybrid curing method for accelerating the strength of high-performance cement PC using microwave heating coupling with low-pressure processing. Constr. Build. Mater. **105**, 245–252 (2016). https://doi.org/10.1016/j.conbuildmat.2015.12.084

24. Makul, N., Vongpradubchai, S., Rattanadecho, P.: An experimental study of microwave drying under low pressure to accelerate the curing of Portland cement PC using a combined unsymmetrical double-fed microwave and vacuum system. Int. J. Heat Mass Transfer **127**, 179–192 (2018). https://doi.org/10.1016/j.ijheatmasstransfer.2018.06.119

25. Lagos, L., Li, W., Ebadian, M., White, T., Grubb, R., Foster, D.: Heat transfer within a concrete slab with a finite microwave heating source. Int. J. Heat Mass Transfer **38**(5), 887–897 (1995). https://doi.org/10.1016/0017-9310(94)00200-f

26. Oriol, M., Pera, J.: Pozzolanic activity of metakaolin under microwave treatment. Cem. Concr. Res. **25**(2), 265–270 (1995). https://doi.org/10.1016/0008-8846(95)00007-0

27. Jahanbakhsh, H., Karimi, M., Jahangiri, B., Nejad, F.: Induction heating and healing of carbon black modified asphalt concrete under microwave radiation. Constr. Build. Mater. **174**, 656–666 (2018). https://doi.org/10.1016/j.conbuildmat.2018.04.002

28. Akbarnezhad, A., Ong, K., Zhang, M., Tam, C., Foo, T.: Microwave-assisted beneficiation of recycled concrete PC. Constr. Build Mater **25**(8), 3469–3479 (2011). https://doi.org/10.1016/j.conbuildmat.2011.03.038

29. Bru, K., Touzé, S., Bourgeois, F., Lippiatt, N., Ménard, Y.: Assessment of a microwave-assisted recycling process for the recovery of high-quality PC from concrete waste. Int. J. Miner. Process **126**, 90–98 (2014). https://doi.org/10.1016/j.minpro.2013.11.009

30. Mangat, P., Grigoriadis, K., Abubakri, S.: Microwave curing parameters of in-situ concrete repairs. Constr. Build. Mater. **112**, 856–866 (2016). https://doi.org/10.1016/j.conbuildmat.2016.03.007

31. Borinaga-Treviño, R., Orbe, A., Norambuena-Contreras, J., Canales, J.: Effect of microwave heating damage on the electrical, thermal and mechanical properties of fibre-reinforced cement mortars. Constr. Build. Mater. **186**, 31–41 (2018). https://doi.org/10.1016/j.conbuildmat.2018.07.108

32. Makul, N., Keangin, P., Rattanadecho, P., Chatveera, B., Agrawal, D.: Microwave-assisted heating of cementitious materials: relative dielectric properties, mechanical property, and experimental and numerical heat transfer characteristics. Int. Commun. Heat Mass **37**(8), 1096–1105 (2010). https://doi.org/10.1016/j.icheatmasstransfer.2010.06.029

33. Makul, N.: Production of high-early-compressive-strength Portland cement paste using low-pressure microwave-accelerated heating and curing: processing characteristics and factors affected. Heliyon **5**(7), e02098 (2019). https://doi.org/10.1016/j.heliyon.2019.e02098
34. American Society for Testing and Materials, ASTM D4491/D4491M-17 Standard Test Methods for Water Permeability of Geotextiles by Permittivity. Annual Book of ASTM Standard, vol. 4.02, Philadelphia, PA (2016). https://global.ihs.com/doc_detail.cfm?document_name=ASTM%20D4491%2FD4491M&item_s_key=00656358

Performance Requirements, Challenges and Existing Solutions of PCM in Massive Concrete for Temperature Control

Mohammad Kheradmand, Romeu Vicente, Miguel Azenha, and José Luís Barroso de Aguiar

Abstract The development of new solutions and techniques targeted towards better control of the temperature rise in massive concrete at early ages aiming at the reduction of thermal cracking risk, is of paramount importance, namely in respect to durability. To mitigate this issue, one of the most researched solutions that has attracted most interest is the incorporation of Phase Change Materials (PCMs) into massive concrete. PCMs have the capacity to store and release energy in the form of heat within a specific temperature range. The application of PCM in massive concrete, with a melting temperature point/range in between the casting temperature of concrete and the expectable peak temperature (had PCM not been added in the mixture), has the potential to reduce the internal temperature rise, and associated temperature gradients. Therefore, the internal thermal stresses are reduced, and consequently the inherent thermal cracking risk. This paper carries out a critical review on requirements and challenges of different applications of PCMs into massive concrete structures.

Keywords Phase change materials (PCMs) · Massive concrete · Heat of hydration · Cracking

M. Kheradmand (✉) · R. Vicente
RISCO, Department of Civil Engineering, University of Aveiro, Aveiro, Portugal
e-mail: romvic@ua.pt

M. Azenha
ISISE, Department of Civil Engineering, University of Minho, Braga, Portugal
e-mail: miguel.azenha@civil.uminho.pt

J. L. B. de Aguiar
CTAC, Department of Civil Engineering, University of Minho, Braga, Portugal
e-mail: aguiar@civil.uminho.pt

1 Introduction

According to ACI 116R [1], massive concrete is defined as "*any volume of concrete with dimensions large enough to require that measures be taken to cope with generation of heat from hydration of the cement and attendant volume change, to minimize cracking*". In concrete structures such as dams, a very high/huge quantity of hydration heat is generated in the concrete curing process, inherently to the large volumes of concrete involved. Existing data shows that that massive volumes of concrete are very susceptible/vulnerable to early age cracking during the construction period, therefore there is the need for attention towards the issue of temperature control [2]. This subject has been attracting the attention of both researchers and practitioners for several years. The 1988 report of International Commission on Large Dams (ICOLD) [3] for dam work status displayed that the vast majority of concrete dams which have been built in the world, may suffer temperature cracking phenomena. Indeed, 30 out of the 243 dams mentioned in the report, have suffered thermal cracking. According to Ke et al. [4], concrete thermal cracking can greatly reduce the durability and even the safety of the structure. Therefore, active measures need to be taken to reduce thermal cracking risks. Amongst such measures, temperature control techniques are frequently the chosen strategy, as they mitigate the cause of thermal cracking at its origin [5].

Traditionally, temperature control has been addressed through several strategies, such as: (i) reducing the heat generation potential of the concrete mixture by combining cement with supplementary cementitious materials, and therefore reducing cement content [6]; (ii) use of low heat of hydration cement (cements with decreased amount of Portland clinker e.g. CEM II/CEM V) while, bearing in mind, that the development of the mechanical properties of such concrete is slower in compare with Portland cement CEM I [7]; (iii) lowering initial temperature of concrete upon placement by using cooler aggregates/water, using ice chips in the mixture, or even liquid nitrogen for cooling [8]; (iv) using active cooling measures for concrete after placement through embedded cooling pipes [9]; (v) construction management (phasing), including scheduling of construction stages and procedures to achieve lower temperatures [10]. Another possibility for the mitigation of thermal cracks in hardening concrete has been proposed in recent years, by incorporating phase change materials (PCMs), which are able to store latent heat, as additives in concrete [11]. The principle of operation of PCMs in the scope of massive concrete can be explained through the following example in the context of the construction of a structure. In a recently cast concrete element, when the increasing core temperature of massive concrete (heat released due to cement hydration heat) reaches the melting point of the embedded PCM, it induces the corresponding phase change and inherent heat absorption/storage (endothermic process), thus reducing the internal temperature rise of concrete, as compared to the on expectable if PCM had not been embedded. As temperature rises are smaller, so are temperature gradients (both temporal and spatial), therefore the thermal cracking risk is comparatively reduced. The aim of this paper is to focus on the overall following fundamental

questions: (1) what are the methods and typical quantity of incorporation of PCM (in weight or volume) in massive concrete? (2) What is the typical global energy that the PCMs in massive concrete are being able to store? Giving some insight on the above mentioned questions, may pave the ground for the feasibility of future conduction of experimental and numerical studies based on the lessons learnt from the review on past literature.

2 Phase Change Materials in Massive Concrete Application

2.1 Classification of PCMs

The most typical classification of PCMs are organic, inorganic and eutectic [12]. Table 1 presents a list of the advantages and disadvantages of the three types of PCMs.

Table 1 Classification, advantages and drawbacks of PCMs adapted from [12]

Classification	Advantages	Disadvantages
Organic PCMs	• Available in a large melting temperature range (from 12 to +135 °C) • High latent heat capacity (between 80 to 260 kJ/kg) • No supercooling • Chemically stable • Recyclable • Good compatibility with host materials • Relatively cheap • No corrosive to metal	• Low thermal conductivity (around 0.2 W/m K) • Relatively large volume change (e.g. 10% in paraffin PCMs) • Flammability
Inorganic PCMs	• High latent heat capacity • High thermal conductivity (around 0.5 W/m K) • Low volume change • Low cost	• Corrosive to metal
Eutectics	• Sharp melting temperature • Properties can be tailored to match specific requirements • High volumetric thermal storage	• Limited data on thermo-physical properties for many combinations • High cost

2.2 Strategies for Incorporation of PCMs into Massive Concrete

In principle, it would be desirable to add PCMs into massive concrete for effective temperature control, without impairing any other performance requirement. The typical incorporation methods that have been used are direct incorporation, impregnation of lightweight aggregates, and encapsulation (micro and macro) [13]. For the purpose of clarity, different incorporation methods of PCM are illustrated schematically in Fig. 1. From temperature control point of view in the concrete, use of PCM impregnated LWAs can provide better distribution of PCM in the concrete and therefore, PCM can homogenously transfer the heat through the matrix when compared with embedded pipes. Microencapsulation or macro encapsulation are techniques in which PCMs are enclosed in a micro/macro capsule, which can be incorporated into the concrete in different manners [14]. A key drawback of this form of capsuled PCM is the cost of production associated to the encapsulation process [15].
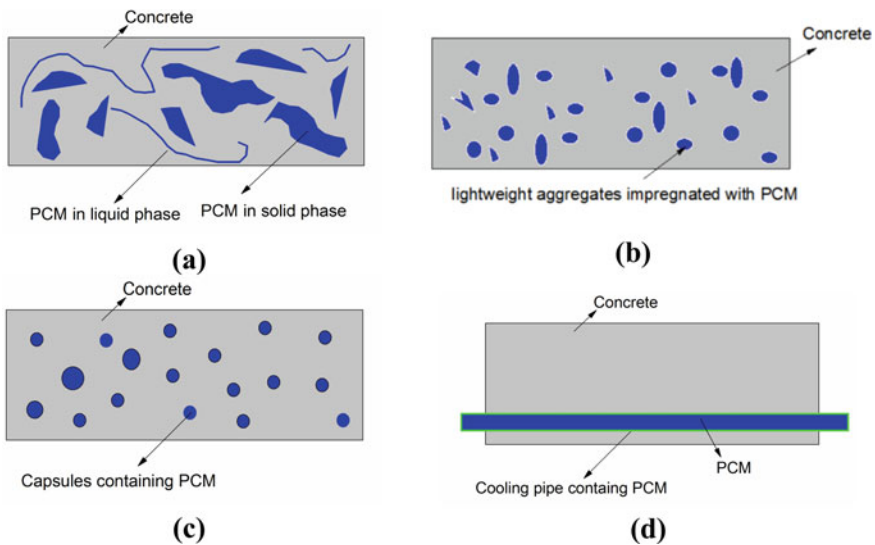
Fig. 1 Schematic illustration of four methods to incorporate PCM into massive concrete: **a** direct incorporation of PCM; **b** impregnating PCM into light weight aggregates; **c** encapsulation (micro or macro) containing PCM; and **d** cooling pipe with PCM

3   PCM for Temperature Control of Massive Concrete

Massive concrete has high cracking probability due to the temperature differences between exterior surface and the core of the concrete structure by heat of hydration after pouring and casting of a large amount of concrete. Core temperature of the fresh concrete increases due to the chemical reactions during hydration of cement [16]. The development of tensile strain rises due to the temperate differentials within a concrete section, exceeding the actual tensile strain capacity of the concrete this could cause early age cracking. Therefore, temperature control is essential in attaining the structural integrity, serviceability and durability of massive concrete structures, as to avoid the inherent damage. As mentioned above, one of the possibilities to reduce thermal cracking in hardening concrete through temperature control involves the use of PCMs embedded into concrete. The principle of operation of incorporated PCM for control of temperature in mass concrete is schematically illustrated in Fig. 2.

As can be seen, when the temperature increases, the PCM absorbs heat by melting. Thus, the peak temperature of the concrete is attenuated/decreased and the delay of maximum temperature is notorious (Fig. 2a). This has implications on the stress development of the concrete. First when the temperature increases results in occurrence of compressive stresses. The magnitude of these stresses decreased with the incorporation of the PCM (Fig. 2b). Several research works have been carried out on methods of incorporating PCM into massive concrete structures at both laboratory scale and real scale levels. All previous research work reports that refer to different forms of incorporating PCM into concrete identify distinct procedures of incorporation [17–20]: (i) replacement with sand; (ii) replacement/addition ratio of the amount of cement; (iii) addition of a % of the total weight of concrete; and (iv) addition of total volume of concrete; (v) impregnation of PCM into lightweight aggregates (then coated or without coating) used in concrete. Different quantities of
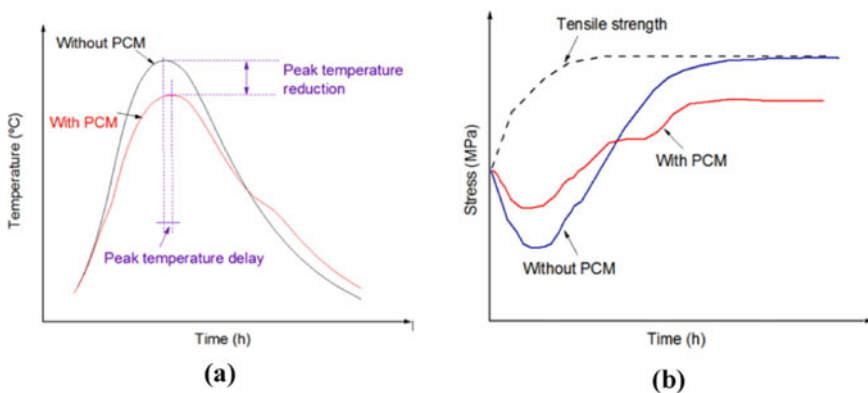
Fig. 2 Function of PCM in concrete: **a** on the temperature variation; and **b** on the stress performance

PCM into the concrete have been attempted in the literature as: 0.78 kg/m^3 [21], 23.3–113.7 kg/m^3 [18], 40 kg/m^3 [20], 50–120 kg/m^3 [22], 150 kg/m^3 [19] and 180 kg/m^3 [23].

When designing a massive concrete structural component, this action requires the control of the heat of hydration, therefore it is important to know the performance requirements for heat storage of PCM's in massive concrete, in a quantitative manner. Hence, is necessary to frame the typical energy involved on behalf of the cement present in a given concrete mixture. Cement content (here understood as the weight of cement per unit volume of concrete, and expressed in kg/m^3) has a large influence on the strength of concrete and the amount of heat generated in the concrete. The average hydration heat of normal cements is about 292 kJ/kg, whereas for low heat cements, the average hydration heat is of 205 kJ/kg [24]. Therefore, one criteria for the selection of the PCM should be based on the amount of hydration of the cement used in the proposed concrete as to be able to successfully mitigate thermal stress in massive concrete components.

4 PCM Use for Massive Concrete

A large number of PCMs are known to melt with a latent heat capacity in any required range compatible with the main purpose of temperature control of massive concrete applications (e.g. a range between 30 and 50 °C that is likely attained in most concrete massive structures). However, for their incorporation as latent heat storage materials they should exhibit desirable thermodynamic, kinetic and chemical properties. Furthermore, economic considerations and availability in the markets has to be taken in to account. It is important to show relationships between properties of PCMs in order to provide insights for the designers and engineers when PCM is worthy for application in massive concrete structures. Figure 3a shows, the relationship between melting temperatures and the latent heat capacity of different types of commercially available pristine PCM solutions (as announced by manufacturers) which will allow to understand better different options in the range of interest. Organic PCMs have relatively higher latent heat capacity when compared with inorganic and eutectic PCMs.

To evaluate and rank different PCMs can be very complicated as there are a number of factors that can be accounted for. Indeed, PCMs with melting peak temperatures in the range of 30–50 °C is of main interest. Figure 3b plotted the relationships between the logarithmic thermal conductivity (W/m K) and the melting temperatures (°C) for different PCMs. Thermal conductivity of the concrete is normally in the range of 1.7–2.53 W/m K according to ACI standard [31], therefore, in the case of using PCM, since all the considered PCMs have lower values of thermal conductivity (below the value of concrete), can affect the thermal conductivity of the final product and cause effects on temperature development.

The latent heat capacity, melting temperature and thermal conductivity of the studied PCMs are shown in Table 2. Commercial organic PCM number 7, from
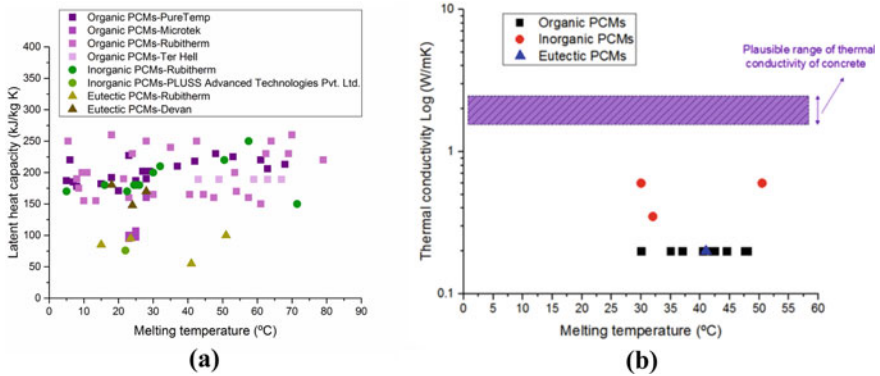
Fig. 3 a Latent heat capacity versus melting temperature for different types of studied PCMs; **b** thermal conductivity values (solid phase) versus melting temperatures for different types of studied PCMs [25–30]

RUBITHERM manufacturer (it will be referred to as "Manufacturer A") with melting temperature of 42.5 °C, latent heat capacity of 250 J/g, thermal conductivity of 0.2 W/m K has the highest enthalpy value among others, which, indicate higher capacity potential for absorption of heat (due to the cement hydration in concrete).

Table 2 Latent heat capacity and thermal conductivity scores of the considered PCMs

No.	Type	Melting temperature (°C)	Latent heat capacity (J/g)	Thermal conductivity (W/m K)	References
1	Organic	37	210	0.2	[25]
2	Organic	42	218	0.2	[25]
3	Organic	48	230	0.2	[25]
4	Organic	30	165	0.2	[27]
5	Organic	35	240	0.2	[27]
6	Organic	40.5	165	0.2	[27]
7	Organic	42.5	250	0.2	[27]
8	Organic	44.5	165	0.2	[27]
9	Organic	47.5	160	0.2	[27]
10	Organic	43	189	–	[28]
11	Organic	49	189	–	[28]
12	Inorganic	30	200	0.6	[27]
13	Inorganic	32	210	0.35	[27]
14	Inorganic	50	220	0.6	[27]
15	Eutectic	41	55	0.2	[30]

– Such values were not available

For the purpose of comparison, Fig. 4 shows the logarithmic average cost values (€/kg) versus melting temperature (°C) for the different types of PCMs. The market price of the PCMs was given by the producers based on direct quotations sourced from the suppliers from November 2018 to December 2018 for 100 kg of pristine PCM. Both types of organic and inorganic PCMs from "Manufacturer A" have the same price range (8 and 10 €/kg). However, the price of a commercially available organic microencapsulated PCM is roughly 10 times more expensive than the pristine PCM. This is due to the microencapsulation technique and many functionally additives for improving of their effectiveness.

Figure 5 illustrates logarithmic cost (€/kg) versus latent heat capacity (kJ/kg) of the studied PCMs. It can be stated that, lower cost with higher latent heat capacity can be considered as a favourable PCM choice. For example, PCMs from "Manufacturer A". Both organic and inorganic solutions clearly show the lowest cost and highest latent heat capacities, when compared with other types of the PCMs. It is interesting to note that, the cost of the PCM does not normally vary with melting temperatures of the PCM when ordered from the same producer. In fact, the quantity of the ordered PCM is also a very important factor to take into account as it may change the price of PCMs as well as shipping costs and packaging costs. It is also important to mention that, in the cases of some companies there is a minimum batch quantity for ordering PCMs.

Regarding the application of the PCM into the massive concrete, it is interesting to give an example of one cubic meter of ordinary ready-mix concrete in Portugal
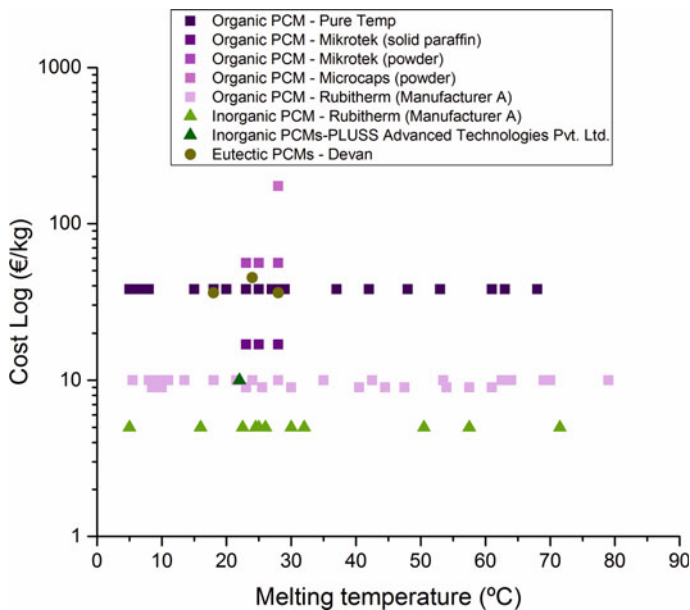
Fig. 4 Cost values versus melting temperatures for different types of PCMs [25–30]
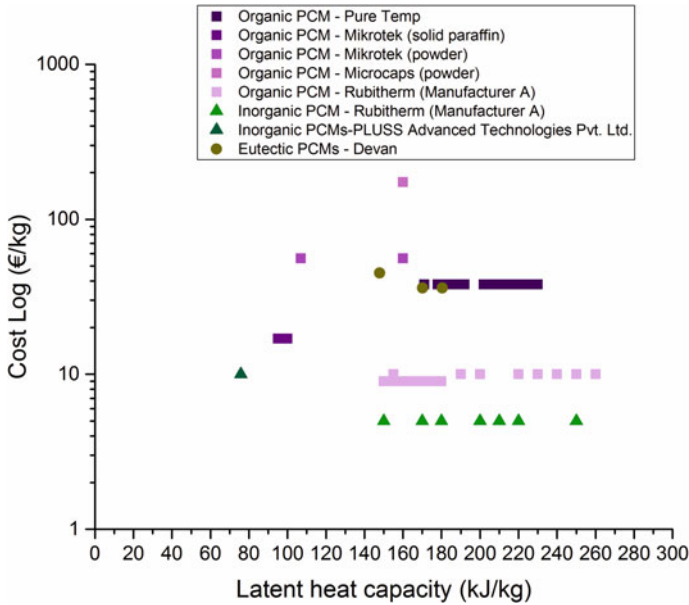
Fig. 5 Log cost values versus latent heat capacity for different types of PCMs [25–30]

costs about 50 euros. Let's consider an example of one cubic meter of the concrete and the possibility of incorporation 90 kg of PCM per cubic metre of concrete would be required [32]. This amount of PCM will be able to reduce the peak temperature rise of the concrete around 10 °C [32]. With a cost of 10 Euro/kg, it will cost in total 900 euros (concrete only would represent 6% of the total cost of 1 m^3), which is of course, not reasonable from a practical point of view at today's prices. Foreseeing that PCMs in other industrial fields becomes more generalized (e.g. in thermal comfort of buildings), the scale effect in production can make drop the price that can make the use of PCM more competitive for applications of temperature control of massive concrete structures during early ages.

5   Concluding Remarks and Outlook

Generally, when designing a latent heat capacity system based on PCMs, the following processes that need to be considered are: (i) Choice of the PCM type for the operational temperature range (depending on the ambient temperature) and identification of a suitable PCM with high latent heat capacity for the heat exchange with the concrete matrix; (ii) Best possible cost-effectiveness of the PCM chosen; and (iii) Definition of the adequate method for the PCMs incorporation.

A simple ranking method based on the phase change enthalpy was considered to identify the optimal solution among the studied PCM regarding thermal performance of PCM. It was concluded that the inorganic PCM from with melting temperature of 42.5 °C with latent heat capacity of 250 J/g and thermal conductivity of 0.2 W/m K was the best ranked PCM from the group under study.

Selected incorporation strategy of PCM into the concrete should be considered as a way of raising the latent heat capacity of the concrete, thereby reducing the temperature evolution generated from cement hydration within concrete structure in early ages. Direct incorporation technique of PCMs in massive concrete structures, reveals to be the most practical and easy way of PCM incorporation, retaining all the traditional processes of mixing and casting of the concrete industry (i.e. lowest impact on people and processes).

As a final note, even though, PCMs that are available on the market, they are still costly, technology is likely to bring down the prices, specifically for higher capacity of latent heat solutions or for better performance requirements. Another crucial issue is the strategy of incorporating PCM into the concrete, that should besides being cost efficient, have the ability to induce temperature control in mass concrete in an evenly manner with good PCM dispersion. Future research works on concrete containing PCMs are still needed, in respect to many features, such as the methods of preparation, clear mitigation of the strength reduction, as well as durability issues. The production of concrete incorporating PCM should be driven by sustainable, eco-efficient and cost-benefit advantages.

References

1. ACI Committee 116, Cement and Concrete Terminology (ACI 116R-00), vol. 73. American Concrete Institute, Farmington Hills, Mich (2000)
2. Azenha, M., Sfikas, I.P., Wyrzykowski, M., Kuperman, S., Knoppik, A.: Temperature Control, RILEM State-of-the-Art Reports, pp. 153–179 (2019)
3. The International Commission on Large Dams, Report of the International Commission on Large Dams (ICOLD), Non-Governmental International Organization in Dam Engineering, Paris, France (1988)
4. Ke, J., Hui, P., Chen, W., Fan, W., Shaofei, Y.: Simulation Analysis on Mass Concrete Temperature Field of Navigation Lock in Changsha Integrated Hub (2016)
5. Ouyang, J., Chen, X., Huangfu, Z., Lu, C., Huang, D., Li, Y.: Application of distributed temperature sensing for cracking control of mass concrete. Constr. Build. Mater. **197**, 778–791 (2019)
6. Zhao, Z., Wang, K., Lange, D.A., Zhou, H., Wang, W., Zhu, D.: Creep and thermal cracking of ultra-high volume fly ash mass concrete at early age. Cement Concr. Compos. **99**, 191–202 (2019)
7. C.P.C. EN 197-1.: Specifications and Conformity Criteria for Common Cements (2011)
8. Ha, J.-H., Jung, Y.S., Cho, Y.-G.: Thermal crack control in mass concrete structure using an automated curing system. Autom. Constr. **45**, 16–24 (2014)
9. Roush, K., O'Leary, J.J.C.I.: Cooling Concrete with Embedded Pipes, vol. 27, issue 5, pp. 30–32 (2005)

10. Fairbairn, E.M., Silvoso, M.M., Toledo Filho, R.D., Alves, J.L., Ebecken, N.F.J.C.: Structures, Optimization of Mass Concrete Construction Using Genetic Algorithms, vol. 82, issue 2–3, pp. 281–299 (2004)
11. Bentz, D.P., Turpin, R.: Potential applications of phase change materials in concrete technology. Cement Concr. Compos. 29(7), 527–532 (2007)
12. Zhou, D., Zhao, C.-Y., Tian, Y.: Review on thermal energy storage with phase change materials (PCMs) in building applications. Appl. Energy 92, 593–605 (2012)
13. Zhou, D., Zhao, C., Tian, Y.: Review on thermal energy storage with phase change materials (PCMs) in building applications. Appl. Energy 92, 593–605 (2012)
14. Luisa, C.C., Cabeza, F., Nogués, M., Medrano, M., Leppers, R., Zubillaga, O.: Use of microencapsulated PCM in concrete walls for energy savings. Energy Build. 39(2) 113–119 (2007)
15. Regin, A.F., Solanki, S., Saini, J.: Heat transfer characteristics of thermal energy storage system using PCM capsules: a review. Renew. Sustain. Energy Rev. 12(9), 2438–2458 (2008)
16. De Schutter, G.: Finite element simulation of thermal cracking in massive hardening concrete elements using degree of hydration based material laws. Comput. Struct. 80(27), 2035–2042 (2002)
17. Kim, Y.-R., Khil, B.-S., Jang, S.-J., Choi, W.-C., Yun, H.-D.: Effect of barium-based phase change material (PCM) to control the heat of hydration on the mechanical properties of mass concrete. Thermochim. Acta 613, 100–107 (2015)
18. Hunger, M., Entrop, A., Mandilaras, I., Brouwers, H., Founti, M.: The behavior of self-compacting concrete containing micro-encapsulated phase change materials. Cement Concr. Compos. 31(10), 731–743 (2009)
19. Farnam, M.K.Y., Liston, L., Washington, T., Erk, K., Tao, B., et al.: Evaluating the use of phase change materials in concrete pavement to melt ice and snow. J. Mater. Civ. Eng. (2015)
20. Kim, G., Lee, E., Kim, Y., Khil, B.: Hydration heat and autogenous shrinkage of high-strength mass concrete containing phase change material. J. Asian Architect. Build. Eng. 9(2), 455–462 (2010)
21. Fenollera, M., Míguez, J.L., Goicoechea, I., Lorenzo, J., Ángel Álvarez, M.: The influence of phase change materials on the properties of self-compacting concrete. Materials 6(8), 3530–3546 (2013)
22. Sakulich, D.P.B.A.R.: Incorporation of phase change materials in cementitious systems via fine lightweight aggregate. Constr. Build. Mater. 35, 483–490 (2012)
23. Thiele, A.M., Sant, G., Pilon, L.J.E.C.: Management, Diurnal Thermal Analysis of Microencapsulated PCM-Concrete Composite Walls, vol. 93, pp. 215–227 (2015)
24. Awal, A.S.M.A., Shehu, I.A.: Evaluation of heat of hydration of concrete containing high volume palm oil fuel ash. Fuel 105, 728–731 (2013)
25. PureTemp 29 Technical Data Sheet. http://www.puretemp.com/stories/puretemp-29-tds. Retrieved 16 Feb 2017 (2017)
26. Microtek, Microtek Leads the Way for Microencapsulation Technologies. http://www.microteklabs.com/index.html (2017)
27. RUBITHERM®, Technologies GmbH PCM Technology and Development. https://www.rubitherm.eu/en/about-us.html (2017)
28. Ter Hell.: Manufacturer of technical grade Paraffins: Ter Hell Paraffin Hamburg FRG. http://www.terchemicals.com/ (2017)
29. Pluss Advanced Technologies Pvt. Ltd. (PLUSS®).: R&D and Manufacturing of Specialized Polymers, Stuttgart, Germany (2018)
30. DEVAN Chemicals.: The Thermic® Thermoregulating Technology Microencapsulated Phase Change Materials (PCMs). http://www.devan.net/ (2017)
31. M.C.A.M.O.C.P. ACI Committee 207, Part 1, 207.1, pp. 21–23 (1994)
32. Šavija, B., Schlangen, E.: Use of phase change materials (PCMs) to mitigate early age thermal cracking in concrete: theoretical considerations. Constr. Build. Mater. 126, 332–344 (2016)

Microencapsulation of Isophorone Diisocyanate with Silica Shell

Ahsanollah Beglarigale, Doğa Eyice, Yoldaş Seki, and Halit Yazıcı

Abstract In several studies, Isophorone diisocyanate (IPDI), a monomeric aliphatic diisocyanate, has been microencapsulated with various polymeric shells for self-healing purposes in polymer-based materials. In this study, for the first time, isophorone diisocyanate was microencapsulated with silica shell via interfacial polycondensation of a silica precursor (TEOS). The shell materials of the IPDI-loaded microcapsules reported in the literature are polymeric (organic). It is known from the literature that silica shell can chemically and physically bonded to cementitious matrices, allowing the microcapsules to remain stable for years without deterioration. Essential parameters such as the amounts of core material (IPDI), shell-forming material, and surfactant as well as the stirring speeds were investigated through yield, optical microscopy, SEM, TGA, and FTIR analyses. Promising results were obtained in the process of microencapsulation of isophorone diisocyanate with silica shell. The optimum core material/shell-forming material, oil phase/aqueous phase, and surfactant/oil ratios were found to be 1.0, 0.18, and 0.08, respectively.

Keywords Microcapsules · Isophorone diisocyanate · Self-healing · Silica shell

1 Introduction

Isophorone diisocyanate (IPDI), a monomeric aliphatic diisocyanate, has been used as a catalyst free healing agent in a few studies since 2008. IPDI was microencapsulated for the first time via interfacial polymerization of polyurethane in a

A. Beglarigale (✉)
Department of Civil Engineering, Istanbul Okan University, İstanbul, Turkey
e-mail: ahsan.beglari@okan.edu.tr

D. Eyice · H. Yazıcı
Department of Civil Engineering, Dokuz Eylül University, İzmir, Turkey

Y. Seki
Department of Chemistry, Dokuz Eylül University, İzmir, Turkey

stabilized aqueous emulsion by Yang et al. [1]. Yang et al. [1] have emphasized that "diisocyanates are reactive with water, introducing the possibility of one-part, catalyst-free self-healing system that is functional in an aqueous or moisture-laden environment" (p. 9650). The microcapsules were synthesized by interfacial polymerization of a toluene diisocyanate (polyurethane prepolymer) in an oil-in-water emulsion. They have successfully synthesized high yields ($\sim 70\%$) of a free-flowing powder of microcapsules which contain a liquid core (IPDI) content of 70 wt% [1]. Kardar [2] has also produced similar IPDI-loaded polyurethane microcapsules using different polyol monomers. In addition, these kinds of microcapsules have been synthesized with different prepolymers [3–6].

Yi et al. [7] have proposed IPDI-loaded multilayer microcapsules synthesized using Pickering emulsion templates. Lignin nanoparticles were used to prepare the oil-in-water Pickering emulsion template. In other words, lignin nanoparticles were used as an emulsion stabilizer instead of classical surfactants. The oil phase was a mixture of diphenyl methane diisocyanate (MDI) and IPDI (core material). Because of the higher reactivity of MDI as compared to IPDI, isocyanate groups of MDI can preemptively react with hydroxyls of lignin or water at the interface of emulsion droplets and form thin polyurethane membrane [7]. Therefore, the IPDI remained as the only liquid core material. At the end of process, the emulsion was added to the polyvinyl alcohol (PVA) solution that contains melamine formaldehyde prepolymer (pre-MF). Microcapsules were formed by firstly interfacial polymerization of isocyanate groups and pre-MF (forming tightly cross-linked polyuria), and then in situ polymerization of pre-MF on the surface of microcapsules (forming melamine-formaldehyde polymer). In addition, Wang et al. [8] have prepared a novel IPDI-loaded poly(urea-formaldehyde) (PUF) microcapsule. Micromechanical behavior of the shell of microcapsules was enhanced by embedding oxygen plasma treated carbon nanotubes (OPCNTs).

In this study, microcapsules based on IPDI core (healing agent) and silica shell were synthesized via the interfacial polycondensation of a silica precursor (TEOS). Yang et al. [9] have encapsulated methylmethacrylate monomer and triethylborane as the healing agent with silica based shell through an interfacial self-assembly process. They have stated that the silica based shell of microcapsules form a stronger bond with the cementitious matrix. The shell can chemically and physically bonded to the matrix, allowing the microcapsule to remain stable for years without deterioration. Therefore, this study has dealt with the idea of possible microencapsulation of IPDI as a self-healing agent with silica-based shell for the first time in the literature.

Zhang et al. [10] have microencapsulated the n-octadecane (a phase change material) with silica-based shell through interfacial polycondensation. However, in this study, it was aimed to encapsulate a reactive monomeric aliphatic diisocyanate (IPDI) with the silica shell. Although the principle was similar, but the parameters were highly different.

2 Experimental Program

2.1 Materials

Isophorone diisocyanate (IPDI), core material (catalyst-free healing agent), was purchased from Sigma-Aldrich. Shell-forming material (silica precursor), tetraethyl orthosilicate (TEOS), were also obtained from Sigma-Aldrich. Tween 80 (Fluka chemika) was used as non-ionic surfactant (emulsifier). Hydrochloric acid (HCl) purchased from Sigma-Aldrich were used as the pH reducer material. Deionized water was the continuous phase of the emulsion.

2.2 Microencapsulation Method

As mentioned earlier, IPDI was microencapsulated via the interfacial polycondensation of a silica precursor (TEOS). This method has two main steps as follows: (1) dispersion of the oil phase (IPDI + TEOS) in water phase, (2) reducing the pH of emulsion to desired value to initiate the condensation of silica hydrolysates. Similar procedures have also carried out by Zhang et al. [10] for encapsulation of n-octadecane (a phase change material) with inorganic silica. They have described the process as follows: an oil mixture of TEOS and core material is dispersed in the aqueous solution containing surfactant to obtain an oil/water emulsion. Then, the HCl aqueous solution, the catalyst, should be added into the emulsion. The water molecules/acidic catalyst can access to the surface of oil droplets (TEOS/core material) by penetration into the micelles. In the catalysis of acid, hydrolysis and condensation of the TEOS molecules on the surface of oil droplets begins [10]. They have emphasized that the polycondensation of the silica oligomers occurs with increasing the pH value. Finally, a silica shell of microcapsules can be formed on the oil droplets by gradually increasing of deposition of SiO_2 gels derived from silica polycondensation.

In typical process, the synthesis of microcapsules was performed in a 100 mL beaker by using a digital hotplate stirrer (DAIHAN-MSH-20D) and a magnetic oval stirrer bar (30 mm). It must be noted that many preliminary tests were carried out to find out the material ratios, pH values, and stirring speeds. Two solutions were prepared in the synthesis process as follows: (1) S1 is a solution of surfactant, Tween 80, in 50 mL of deionized water. Various amounts (0.3, 0.5, 0.6, 0.8, 0.9, 1.0, and 1.2 g) of Tween 80 were examined, (2) S2 is a solution of 4.5 g of shell-forming (TEOS) and 4.5 g of core material (IPDI). In addition, the optimization of pH control times were carried out in 250 mL beaker (doubled materials) by using a magnetic oval stirrer bar with 40 mm length.

In a typical microencapsulation procedure, S2 was emulsified in S1 solution at a speed of 800 rpm (various stirrer speeds were analyzed) for 20–30 min. After dispersion and stabilization of TEOS/IPDI micro droplets in the water phase, the

stirring speed were reduced to 500 rpm and then, pH was adjusted to the desired value by adding (dropwise) of the HCl aqueous solution with various concentrations. WTW Inolab pH 7110 Set 2 was used for the pH measurements. The emulsion was continuously stirred at 40 °C for 24 h to complete the interfacial polycondensation of silica precursor. It must be noted that, adjusting the pH value continuously to desired value for at least 30 min after raising temperature to 40 °C has remarkably positive effect on microencapsulation.

The microcapsules were vacuum filtered, and then washed ethanol/water for removing of surfactant residue and non-encapsulated materials. The microcapsules were transferred to watch glasses and dried at room temperature for 48 h or in oven at 40 °C, and then weighed for yield calculation.

2.3   Characterization of Microcapsules

FTIR-ATR analyses of the samples were made by using Fourier transform infrared spectrometer (Perkin Elmer Spectrum BX) in the range 4.000–650 cm^{-1}.

Thermal stability of microcapsules was analyzed by TGA using a DTG-60/60 Simultaneous Thermogravimetry/Differential Thermal Analyzer (Shimadzu). The analyses were carried out at a heating rate of 10 °C/min from room temperature to 800 °C under nitrogen atmosphere.

Scanning electron microscopy (SEM) observation of the microcapsules was made by a Carl Zeiss 300 V (Germany) scanning electron microscope, operated at 3 kV. Prior to SEM imaging, gold sputtering was performed on the samples.

The digital photomicrographs were captured by a digital microscope (DM). The microcapsules were dispersed in water, and then few droplets of the suspension were analyzed by the optical microscope.

3   Results and Discussion

3.1   Preliminary Tests

Parameters such as the amounts of core material (IPDI), shell-forming material (TEOS), and surfactant (Tween 80) as well as the stirring speed for emulsification (SS-E) and the stirring speed for polycondensation (SS-P) were examined. Adjusting pH continuously to desired value after raising temperature to 40 °C had remarkably positive effect on microencapsulation. However, this finding was obtained in the next section. Therefore, it was not applied in the preliminary tests. The parameters that were examined in this section are presented in Table 1. It can be seen from Table 1 that the P-EP1, P-EP2, and P-EP2 experiments were failed. Many similar tests with various amounts of IPDI and TEOS were also carried out. However, most of them were failed due to the low amount of surfactant or inappropriate oil/water ratios.

Table 1 The parameters examined in the preliminary tests

Experiment	IPDI (g)	TEOS (g)	T80 (g)	SS-E (rpm)	SS-P (rpm)	pH	Description, yield (%)
P-EP1	2	2	0.3	800	500	2.8	Failed
P-EP2	2	1	0.3	800	500	2.8	Failed
P-EP3	4.5	4.5	0.3	800	500	2.8	Failed
P-EP4	4.5	4.5	0.5	500	300	2.8	59.2%
P-EP5	4.5	4.5	0.8	500	300	2.8	61.1%
P-EP6	4.5	4.5	0.9	500	300	2.8	59.0%
P-EP7	4.5	4.5	1.2	500	300	2.8	58.5%
P-EP8	4	3	0.8	500	300	2.8	55.0%

As can be seen the yield value of P-EP4 synthesis was 59.2%. However, the SEM and DM analyses revealed that the obtained powder does not contain considerable microcapsules. For example, Fig. 1 shows SEM micrographs and EDS spectra of the P-EP4 sample. Irregular-shaped particles with mainly consist of C element can be seen in the micrographs. However, few microcapsules were also detected in this sample. As can be seen from the EDS spectra, one of those microcapsules consists of Si (indicates silica shell), C (indicates core material, IPDI monomer), and O elements. Therefore, it revealed the existence of silica (shell material) and IPDI (core material).

Increasing the Tween 80 weight from 0.5 to 0.8 g affected positively the synthesis process. Figure 2a shows the DM photomicrograph and SEM micrograph of the P-EP5 sample. As can be seen from the images the number of microcapsules remarkably increased in this synthesis.

To avoid damaging the scanning electron microscope during the vacuuming operation, immediately after the microcapsules are poured onto the carbon tape, the sample stub should be hit to anywhere several times to make sure that the unbonded particles are removed. This necessary application leads to a significant loss of spherical capsules from the stub. On the other hand, the irregular smaller particles, which have more contact point and surface area with the carbon tape, were stronger bonded. Therefore, the SEM micrographs were not as realistic as the photomicrographs. The average diameters of microcapsules were obtained by measuring of at least 50 microcapsules on photomicrographs. The average diameter of microcapsules was 160 μm. Figure 2b shows EDS spectra of a microcapsule synthesized in the P-EP5 experiment. The microcapsule consists of Si (indicates silica shell), C (indicates core material, IPDI monomer), and O elements. Therefore, it revealed the existence of silica shell and IPDI. It should be noted that the maximum yield value was obtained in the in the P-EP5 experiment.
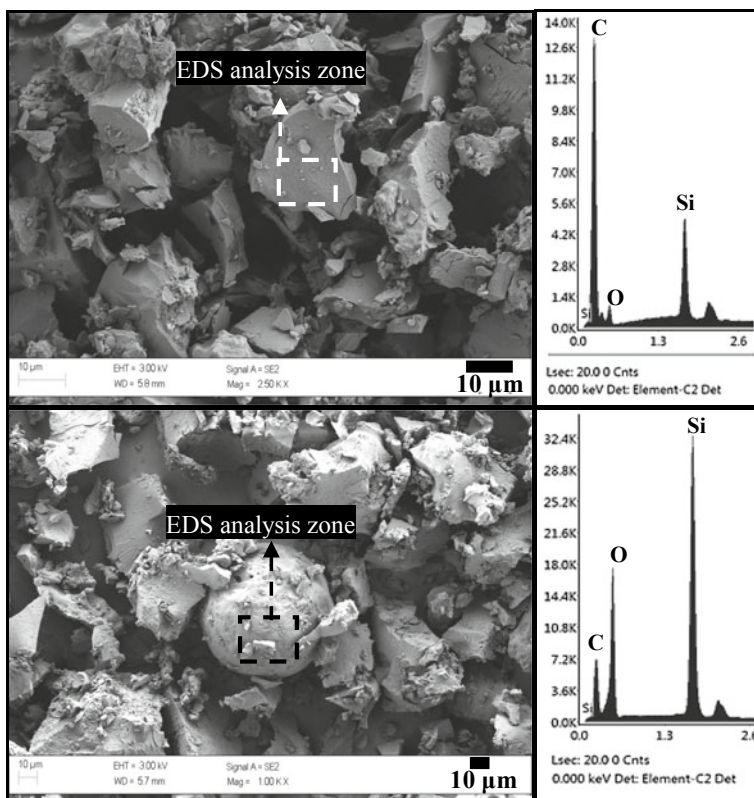
Fig. 1 SEM micrograph and EDS spectra of the particles (possible microcapsules) synthesized via the P-EP4 experiment

The other samples (P-EP6, P-EP7, and P-EP8) were not better than the P-EP5 samples. Therefore, the P-EP5 was tried to be systematically optimized in the continuation of this sections.

3.2 Optimization

Based on the preliminary tests the following parameters were kept constant in the optimization process; (a) The stirring speed for polycondensation: 500 rpm. (b) Emulsion temperature: 40 °C. (c) Polycondensation time: 24 h. (d) The ratio (by weight) of core material (IPDI) to shell-forming material (TEOS): 1.0. (e) The ratio (by weight) of oil phase (IPDI + TEOS) to aqueous phase (water, continuous phase): 0.18.
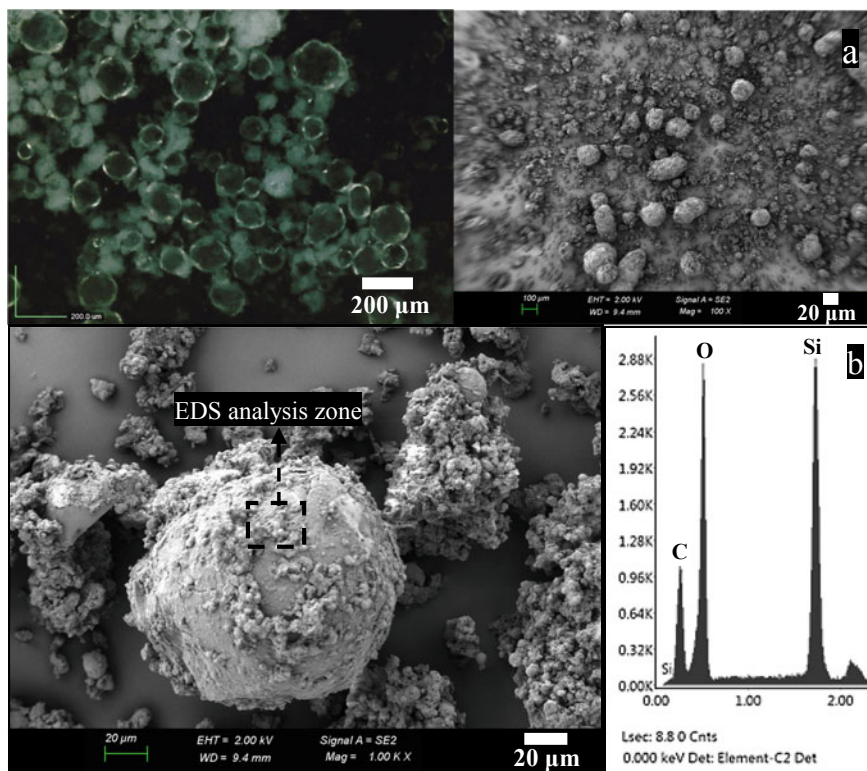
Fig. 2 a DM photomicrograph and SEM micrograph of the microcapsules synthesized via the P-EP5 experiment. **b** SEM micrograph and EDS spectra of a microcapsule synthesized via the P-EP5 experiment

The effects of Tween 80 (surfactant) weight ratio and stirring speed for emulsification (SS-E) were determined through the yield, microscopy, TGA, and FTIR analysis.

The Effect of Tween 80 Weight Ratio on Properties of Microcapsules. In this section, the effects of Tween 80 (surfactant) on IPDI/Silica microcapsules were examined. Firstly, the control samples should be described. Based on the preliminary tests the following procedure was carried out in synthesis of control sample; Two solutions were prepared in the synthesis process as follows: (1) S1 is a solution of surfactant, Tween 80 (0.8 g), in 50 mL of deionized water. (2) S2 is a solution of 4.5 g of shell-forming (TEOS) and 4.5 g of core material (IPDI). S2 was emulsified in S1 solution at a speed of 800 rpm for 20–30 min. After dispersion and stabilization of TEOS/IPDI micro droplets in the water phase, the pH value of emulsion was adjusted to 2.8. The emulsion was continuously stirred (500 rpm) at 40 °C for 24 h to complete the interfacial polycondensation of silica precursor. As mentioned earlier, adjusting the pH value continuously to desired value for at least 30 min after

raising temperature to 40 °C has remarkably positive effect on microencapsulation. Therefore, this finding was applied in the syntheses process.

In order to examine the effect of Tween 80 weight ratio on microcapsules, two different samples were synthesized. As can be seen from Table 2, the Tween 80 weight was increased to 1.0 g in sample M-TW1.0. In other words, the ratio of surfactant (Tween 80) to oil phase (IPDI + TEOS) was increased from 0.088 to 0.110. On the other hand, the Tween 80 weight was decreased to 0.6 g in M-TW0.6 sample. In other words, the ratio of surfactant to oil phase was decreased from 0.088 to 0.66.

After vacuum filtration, sufficient washing, and oven drying, free-flowing white powders were obtained. The control sample was more free-flowing than the M-TW1.0 and M-TW1.0 samples.

Microencapsulation yields (%) MY were calculated by the following equation:

$$MY(\%) = \frac{W_M}{W_{TWEEN80} + W_{IPDI} + W_{TEOS}} \tag{1}$$

where W_M, $W_{TWEEN80}$, W_{IPDI}, and W_{TEOS} are the weights of dried microcapsules powder, Tween 80 (surfactant), core material (IPDI), and shell-forming material (TEOS), respectively. As can be seen from Table 2 there is not significant differences between yield values of the samples.

Based on many DM and SEM analyses, the most well-shaped microcapsules were obtained in the control sample. The average diameter of microcapsules was 153 μm. Figure 3a shows a DM photomicrograph of control sample. Figure 3b shows SEM micrograph and EDS spectra of a control microcapsule. It can be seen from the EDS spectra that the microcapsule consists of Si (indicates silica shell), C (indicates core material, IPDI monomer), and O elements. Therefore, it revealed the existence of silica shell and IPDI.

TG data obtained from TGA curve are summarized in Table 3. Furthermore, the effect of Tween 80 weight ratio on TGA curves of the samples is shown in Fig. 4. The temperatures at 5% mass loss value decreased with increasing mass of Tween 80. The highest residual mass was obtained with higher mass of Tween 80. There are three basic mass loss values in thermogram of samples. Mass loss below 150 °C is due to moisture content. Encapsulated IPDI evaporation takes place in the temperature range 200–300 °C. The maximum degradation rates for Control, M-TW1.0, and M-TW0.6 were obtained to be 293, 296, and 291 °C, respectively. The mass loss in the temperature range 300–500 °C may be attributed to thermal

Table 2 Sample codes, varieties, and yield values (effect of Tween 80)

Sample code	Tween 80 (g)	Stirring speed (rpm)	pH	Yield (%)
Control	0.8	500	2.8	62.3
M-TW1.0	1.0	500	2.8	65.0
M-TW0.6	0.6	500	2.8	60.4
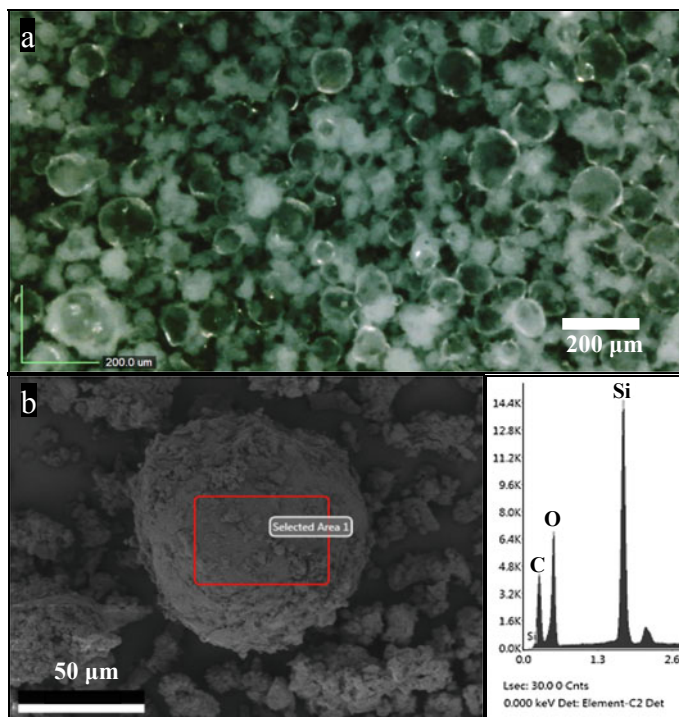
Fig. 3 a Photomicrographs of the control microcapsules. **b** SEM micrograph and EDS spectra of a microcapsule in control sample

degradation of silica shell materials. As can be seen from Table 3, maximum degradation temperatures for Control, M-TW1.0, and M-TW0.6 were obtained to be 352, 344, and 348 °C, respectively. It is probable that SiO_2 shells make a physical protective barrier on the surface of IPDI.

Figure 5 shows the FTIR spectra of Control, M-TW1.0, and M-TW0.6 samples. Si–O–Si asymmetric stretching vibration shows a broad band between 1200–1000 cm^{-1}, which confirms the formation of SiO_2. The absorption band around 1630 cm^{-1} may be ascribed to bending vibration of adsorbed water, probably available in the pores of SiO_2 [11]. C=O stretching vibration peaks of IPDI can be

Table 3 The effect of Tween 80 weight ratio on TGA data

Sample	Mass loss (up to 110 °C)	Temperature at 5% mass loss (°C)	Max degradation temperature	Residual mass (up to 800 °C) %
Control	1	205	352	12
M-TW1.0	4	178	344	17
M-TW0.6	4	220	348	19
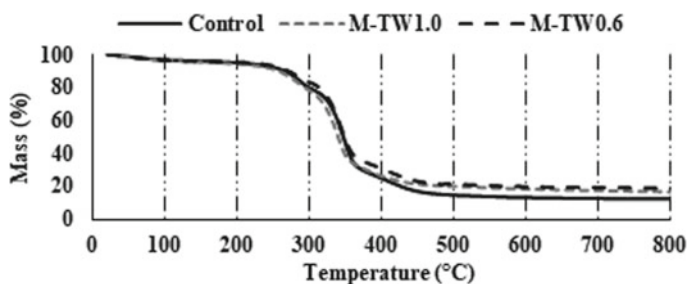
Fig. 4 TGA curves for the samples (effect of Tween 80)

seen at 1696, 1699, and 1699 cm^{-1} for Control, M-TW1.0, and M-TW0.6, respectively. Figure shows a weak peak in the range 2200–2230 cm^{-1} due to N=C=O group, which shows a little unreacted isocyanate group is in the micro-capsule core [12]. However the peak belonging to N=C=O group is more apparent for M-TW0.6.

Effect of Stirring Speed for Emulsification on Properties of Microcapsules. In order to examine the effect of stirring speed for emulsification (SS-E) on the microcapsules, two different samples were synthesized. As can be seen from Table 4, the SS-E was increased to 800 and 1100 rpm in M-SE800 and M-SE100 samples, respectively. It is well known that the diameter of droplets in emulsion and
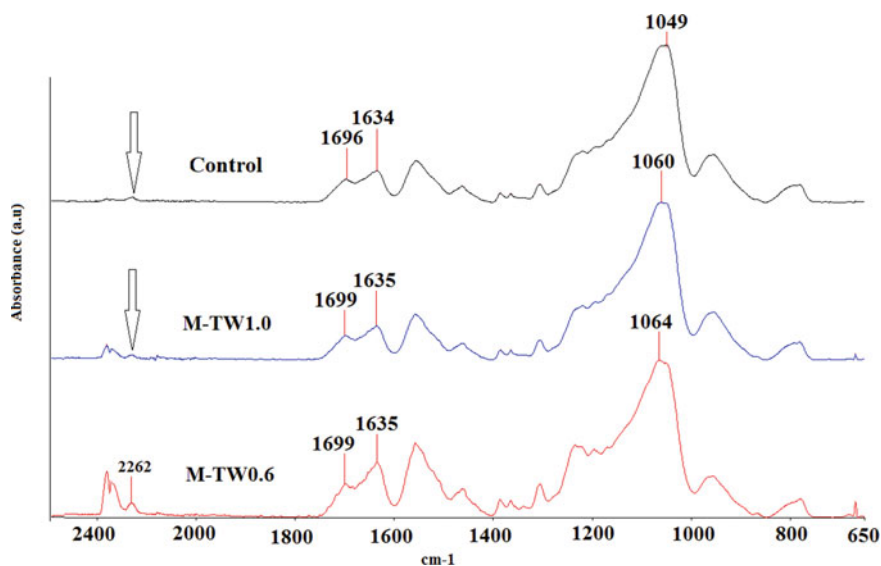
Fig. 5 FTIR spectra for the samples (effect of Tween 80)

as result the diameter of microcapsules can be changed by modifying the SS-E. In addition, the morphology of microcapsules can highly be affected by the SS-E.

After vacuum filtration, sufficient washing, and oven drying, a free-flowing white powder was obtained. The M-SE800 sample was the most free-flowing powder in this section, even better than the control sample. As can be seen from Table 4 the yield values have not been highly affected by modifying the SS-E.

Figure 6 shows EDS spectra of the M-SE800 sample. As can be seen from the figure, the EDS spectra were not highly changed as compared to Control microcapsules. As discussed earlier, the SEM micrographs were not as realistic as the DM photomicrographs. The photomicrographs of the M-SE800 and control samples are presented in Fig. 7. As can be seen, the M-SE800 microcapsules were much smaller but more uniform as compared to the control microcapsules. It can be explained by the fact that increasing the SS-E leads to reduce the diameter of droplets in emulsion and increase in stability of emulsion.

The average diameter of M-SE800 microcapsules was 42 μm. In other words, increasing the SS-E from 500 to 800 rpm reduced the average diameter of IPDI/silica microcapsules from 153 to 42 μm. SEM and DM analyses revealed that the M-SE1100 was the worst sample. It seems that excessive increasing of SSE affects negatively the emulsification process.

Table 4 Sample codes, varieties, and yield values (effect of SS-E)

Sample code	Tween 80 (g)	Stirring speed (rpm)	pH	Yield (%)
Control	0.8	500	2.8	62.3
M-SE800	0.8	800	2.8	64.6
M-SE1100	0.8	1100	2.8	61.4
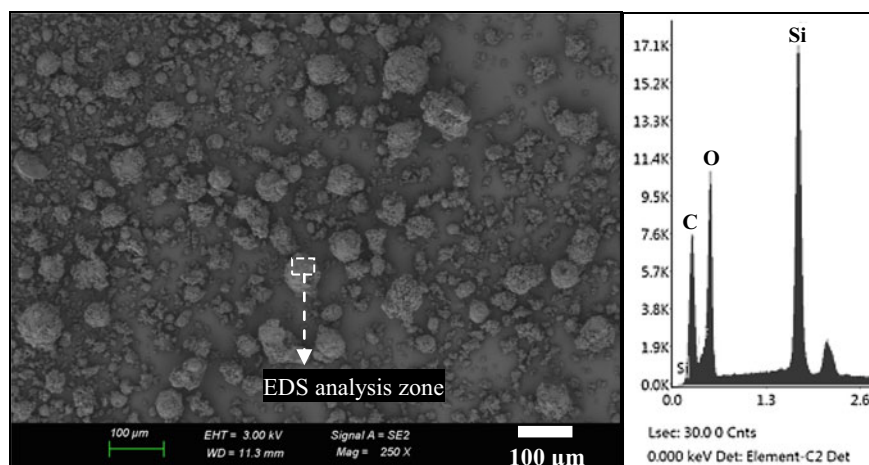
Fig. 6 SEM micrograph and EDS spectra of the M-SE800 microcapsules
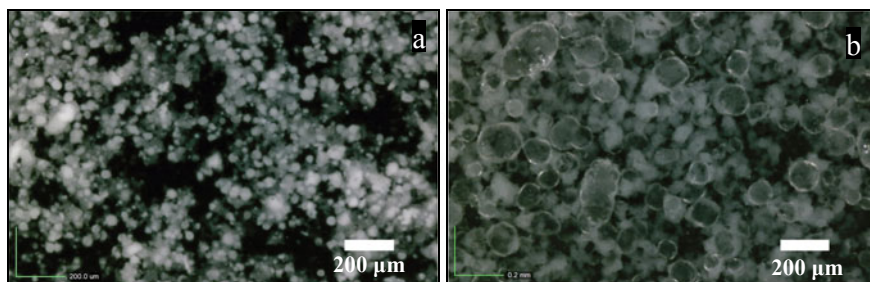
Fig. 7 Photomicrographs of **a** M-SE800 and **b** Control microcapsules

TGA data are summarized in Table 5. The stirring speed has not affected the maximum degradation temperatures of the samples. However, temperature at 5% mass loss increased as stirring speed increases from 500 to 1100 rpm. The highest residual mass was obtained at 800 rpm.

Table 5 The effect of SS-E on TGA data

Sample	Mass loss (up to 110 °C)	Temperature at 5% mass loss (°C)	Max degradation temperature	Residual mass (up to 800 °C) %
Control	1	205	352	12
M-SE800	3	218	352	18
M-SE1100	2	229	352	15
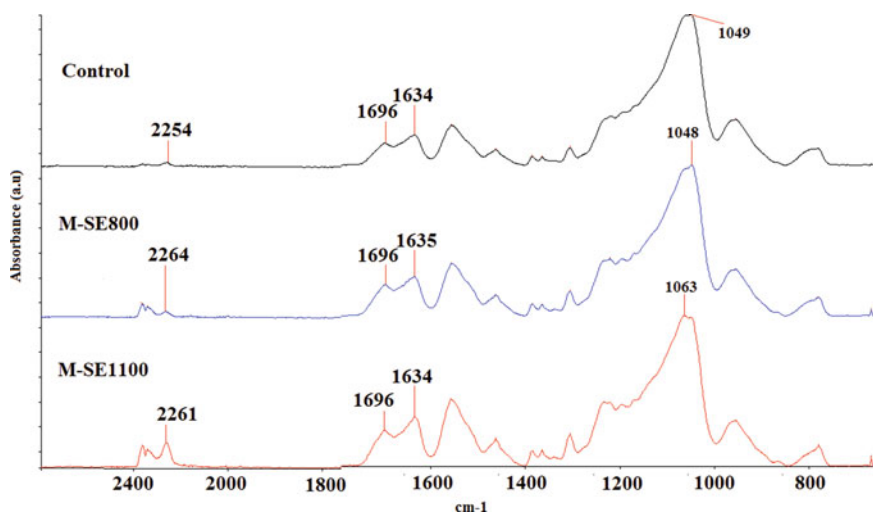
Fig. 8 FTIR spectra for the samples (effect of SS-E)

The effect of SS-E on chemical structure of the samples is given in Fig. 8. The peaks at 2254, 2264, and 2261 cm^{-1} for Control, M-SE800, and M-SE1100 correspond to N=C=O group. Unreacted isocyanate group in the microcapsule core is more apparent for the sample M-SE1100.

4 Conclusions

This study has dealt with the idea of possible microencapsulation of isophorone diisocyanate as a self-healing agent with silica-based shell for the first time in the literature. Microcapsules based on IPDI core (healing agent) and silica shell was synthesized via the interfacial polycondensation of a silica precursor.

The optimum core material/shell-forming material, oil phase/aqueous phase, and surfactant/oil ratios were 1.0, 0.18, and 0.08, respectively. The most effective stirring speed for emulsification was found to be 800 rpm. In addition, it was observed that adjusting pH continuously to desired value after raising temperature of the emulsion has remarkably positive effect on the microencapsulation process. It must be noted that this study is an undergoing project; therefore, further optimization must be carried out on these microcapsules.

References

1. Yang, J.L., Keller, M.W., Moore, J.S., White, S.R., Sottos, N.R.: Microencapsulation of Isocyanates for self-healing polymers. Macromolecules **41**(24), 9650–9655 (2008)
2. Kardar, P.: Preparation of polyurethane microcapsules with different polyols component for encapsulation of isophorone diisocyanate healing agent. Prog. Org. Coat. **89**, 271–276 (2015)
3. Alizadegan, F., Pazokifard, S., Mirabedini, S.M., Danaei, M., Farnood, R.: Polyurethane-based microcapsules containing reactive isocyanate compounds: Study on preparation procedure and solvent replacement. Colloid Surface A **529**, 750–759 (2017)
4. Di Credico, B., Levi, M., Turni, S.: An efficient method for the output of new self-repairing materials through a reactive isocyanate encapsulation. Eur. Polym. J. **49**(9), 2467–2476 (2013)
5. Haghayegh, M., Mirabedini, S.M., Yeganeh, H.: Microcapsules containing multi-functional reactive isocyanate-terminated polyurethane prepolymer as a healing agent. Part 1: synthesis and optimization of reaction conditions. J. Mater. Sci. **51**(6), 3056–3068 (2016)
6. Haghayegh, M., Mirabedini, S.M., Yeganeh, H.: Preparation of microcapsules containing multi-functional reactive isocyanate-terminated-polyurethane-prepolymer as healing agent, part II: corrosion performance and mechanical properties of a self healing coating. Rsc. Adv. **6**(56), 50874–50886 (2016)
7. Yi, H., Yang, Y., Gu, X.Y., Huang, J., Wang, C.Y.: Multilayer composite microcapsules synthesized by Pickering emulsion templates and their application in self-healing coating. J. Mater. Chem. A **3**(26), 13749–13757 (2015)

8. Wang, W., Xu, L.K., Liu, F., Li, X.B., Xing, L.K.: Synthesis of isocyanate microcapsules and micromechanical behavior improvement of microcapsule shells by oxygen plasma treated carbon nanotubes. J. Mater. Chem. A **1**(3), 776–782 (2013)

9. Yang, Z.X., Hollar, J., He, X.D., Shi, X.M.: A self-healing cementitious composite using oil core/silica gel shell microcapsules. Cement Concrete. Comp. **33**(4), 506–512 (2011)

10. Zhang, H.Z., Sun, S.Y., Wang, X.D., Wu, D.Z.: Fabrication of microencapsulated phase change materials based on n-octadecane core and silica shell through interfacial polycondensation. Colloid Surface A **389**(1–3), 104–117 (2011)

11. Li, B.X., Liu, T.X., Hu, L.Y., Wang, Y.F., Gao, L.N.: Fabrication and Properties of Microencapsulated Paraffin@SiO2 Phase Change Composite for Thermal Energy Storage. Acs. Sustain. Chem. Eng. **1**(3), 374–380 (2013)

12. Zhan, S.P., Chen, S.H., Chen, L., Hou, W.M.: Preparation and characterization of polyurea microencapsulated phase change material by interfacial polycondensation method. Powder Technol. **292**, 217–222 (2016)

The Response of Synthetic Alkali-Silica Reaction Products to Carbonation

Satyanarayana R. Narneni and Daman K. Panesar

Abstract Alkali-silica reaction (ASR) is one of the most studied deterioration mechanisms of concrete. However, the ASR mechanism in the presence of external environments such as carbonation is yet to be understood. The present study simplifies this research gap by subjecting the synthetic ASR gels to carbonation and evaluating the changes in the gels through microanalytical studies. Synthetic ASR gels are prepared and subjected to 3 days of carbonation at 3% CO_2 concentration. Thermogravimetric analysis indicated the uptake of CO_2 in the form of calcite validating the interaction of ASR and carbonation. Nanoindentation demonstrated the improvement in mechanical properties of the synthetic gel due to carbonation. Electron microscopy coupled with energy dispersive spectroscopy revealed the compositional changes of the gel caused by its interaction with CO_2 that led to the improvement in their mechanical properties. These results suggest a possible increase in the deterioration of concrete due to the interaction of ASR and carbonation.

Keywords Synthetic ASR product · Carbonation · Thermogravimetric analysis · SEM–EDS · Nanoindentation

1 Introduction

Concrete structures made with reactive aggregates are vulnerable to damage by alkali-silica reaction (ASR). Reactive silicates from the aggregates, alkali from the hardened cement paste (HCP), and water from the external sources will generate expanding ASR products inside the concrete elements. These products exert internal stresses in concrete thus developing map cracking. These cracks will further act as pathways for water and other harmful ions, eventually leading to the loss of structural soundness of the concrete. Avoiding the reactive aggregates, limiting

S. R. Narneni (✉) · D. K. Panesar
Department of Civil and Mineral Engineering, University of Toronto, Toronto, Canada
e-mail: satyanarayana.narneni@mail.utoronto.ca

the moisture and available alkali in the concrete are used to halt the deterioration of concrete elements [11]. Standards such as ASTM C1293 [2], ASTM C1260 [1], etc. are developed to qualitatively assess the reactivity of the aggregates. However, owing to their laboratory nature, these standard tests are performed without the influence of the external environmental conditions such as carbonation. As the ASR progresses in the concrete elements, the network of ASR cracks will enable the faster ingress of harmful contaminants into concrete elements. These harmful contaminants will react with the concrete phases and with the ASR products existing inside the cracks. One of such harmful ingression mechanisms is the carbonation. While carbonation of cement phases is well studied, carbonation effect on the ASR product inside the cracks is unknown. Standard test methods for ASR employ 100% RH environment or immersion for the acceleration of expansions (ASTM C1293 and ASTM C1260 respectively). However, such high moistures will hinder the carbonation reactions in the laboratory as the pores are saturated. Thus, the laboratory studies eliminate the interactions of carbonation and ASR from their testing schemes deviating from the reaction mechanisms in field concrete elements. In the present study, synthetic ASR product is prepared and used to understand the effect of carbonation on ASR products. The effect of carbonation is examined through microscopic methods to understand what chemical and morphological changes can occur in ASR product due to the presence of carbonation. The results help in explaining the mortar and concrete expansion in the presence of both ASR and carbonation.

2 Background

Alkali (Na and K) from the pore solution, reactive silica from aggregates and water from internal or external sources react to form ASR product. As the reaction product interacts with the portlandite ($Ca(OH)_2$) at the aggregate-paste interface, the alkali in the ASR product will be replaced by Ca. This process releases the alkali back into the pore solution to generate new ASR products [11]. Previous studies investigated the role of the chemical composition of the ASR gels on their expansion capabilities in laboratory synthetic gels [4, 14]. Replacing alkali with Ca will also change the ASR product structure from viscous paste to brittle material. Even in the absence of Ca, decreasing the alkali/silica ratio in the ASR product composition also results in the transformation of ASR product from viscous paste to brittle structure [6]. These morphological changes can influence the crack development in concrete.

ASR products with low viscosity will transport across the concrete matrix. However, low viscosity ASR product will exert lesser stress on the concrete pore walls compared to the high viscosity ASR product. Thus, early stages of ASR product will play a primary role in transport across aggregate and HCP matrix while later stages of ASR product play a primary role in applying the stresses on the concrete. In addition, ASR products in field concrete are found to be in amorphous
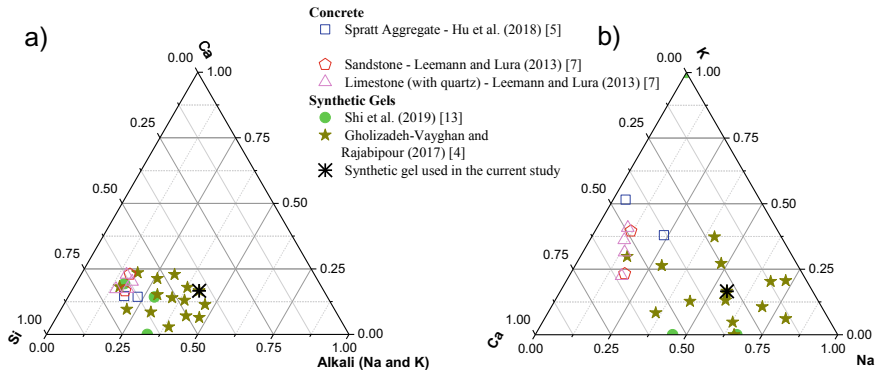
Fig. 1 Ternary plots of Ca–Alkali–Si (**a**) and K–Na–Ca (**b**) of typical compositions of ASR in concrete and synthetic ASR gels reported in the literature

gel structures in early stages, while later-stage ASR products (from 100-year-old structures) are found to be ordered crystalline products [9] with similar chemical composition to calcium silicate hydrate [8], the primary binding material of the concrete. Typical ASR products from laboratory concrete specimens made from different aggregates and synthetic ASR products are plotted in Fig. 1 as ternary plots of Ca–Alkali–Si (Fig. 1a) and K–Na–Ca (Fig. 1b).

3 Materials and Methods

The ability to produce large quantities and lack of interference from the aggregates and cement paste makes the synthetic gels suitable for testing the intrinsic properties of ASR. Methods of preparation of the ASR gel include; (1) sol–gel method, (2) mixing of reactive aggregate with alkali, (3) mixing at low water content, and (4) mixing at high water content. The following subsections briefly describe the synthetic ASR gel preparation in these methods.

3.1 Sol–Gel Method

Sodium silicate solutions are passed through an ion-exchange column to make silicic acid sol. The silicic acid sol is doped with NaOH solution and further condensed. Later the sol is mixed with NaOH and Ca(OH)$_2$, to achieve the required chemical composition. The sol–gel method widely used in making silicate gels. However, obtaining a low water content (with low Na, and high Ca) levels are difficult through sol–gel method [4].

3.2   Mixing Reactive Aggregate with Alkali

This method involves the generation of ASR gel by mixing small grains of aggregates with an alkaline solution. To achieve faster reaction, higher temperatures (80 °C) are generally used [10].

3.3   Mixing at a High-Water Content

In this method used by Shi et al. [13], the authors mixed the amorphous silica and CaO (burnt from $CaCO_3$), NaOH, and KOH pellets with water. The water to solid ratio is in the range of 4.89 to 17.3. Such high-water contents alleviated the problem of water evaporation due to the dissolution of alkali. A curing period of 80 days at 80 °C was applied to get a uniform chemical composition of the samples.

3.4   Mixing at a Low-Water Content (Approach Adapted in This Study)

In this method used in Gholizadeh-Vayghan and Rajabipour [4], dry amorphous silica and $Ca(OH)_2$ were mixed with an alkaline solution with water to solid ratio of around 0.67 (including the water from alkali and $Ca(OH)_2$). To avoid evaporation of water, due to the dissolution of alkali, constituents are cooled prior to the mixing. A curing period of 60 days at 25 °C is used to achieve the uniform chemical composition of the ASR gel. Low-water content mix allowed the authors to cast the gel in moulds to create specimens for expansion and mass change measurements.

ASR gel composition in the concrete cracks changes over time. Although initial ASR gels do not have Ca, the alkali in the gel will be replaced by Ca. The alkali will be released back into the pore solution of concrete for more ASR to occur. Accommodating this behaviour, synthetic ASR gel studies use a range of mix proportions that represent various gel compositions present in the concrete over time (Fig. 1a, b).

In the present study, synthetic gels are made from mixing at a low water content of constituents (subsection 3.4). Mixed samples are kept at 23 °C for the ASR product formation. The mix design and the mixing method for the samples are obtained from a previous study which assessed free expansion, mass changes across various synthetic gels with a spectrum of different compositions. The sample of interest was labelled as $C^{IH}N^{IH}K^{IH}$ in the previous study [4]. The mix compositions of the ASR products are shown in Table 1.

After curing, the sample was divided into two parts (non-carbonated and carbonated). The non-carbonated sample is kept in sealed chambers while the

Table 1 Composition of the synthetic ASR product used in the study

ASR constituent	NaOH (g)	KOH (g)	Ca(OH)$_2$ (g)	Micro silica SiO$_2$ (g)	Water (ml)
Quantity	159.8	67.3	151.9	304.7	316.3

Table 2 Timeline of the synthetic ASR product

Sample name	Time frame			
Non-carbonated sample	6 days of sealed curing		6 months of sealed conditioning at 23 °C	Drying and microstructural analysis
Carbonated sample	3 days of sealed curing	3 days in 3% of CO$_2$ concentration, 23 °C, and 50% RH		

carbonated sample is kept in a carbonation chamber at (3% of CO$_2$ concentration, 23 °C, and 50% RH) for 3 days. The timeline of the samples is shown in Table 2.

After curing and conditioning, samples were dried with immersion in the isopropyl alcohol for a week and later vacuum dried till constant mass. For TGA, the samples were then crushed to pass through 45-micron sieve, while for SEM and nanoindentation, samples were impregnated with epoxy and made into thin sections of 50-micron adhered to glass plates.

4   Results

4.1   TGA

Thermo-gravimetric analysis (TGA) was performed on the gels to understand the compositional changes in the synthetic gel as a result of carbonation. TGA will identify the weight changes of the phases with increasing temperature of the sample. These weight changes are associated with the various reactions (dehydration, oxidation, etc.) that take place inside the TGA chamber as the temperature of the system is rising [12]. In cementitious compounds, TGA is extensively used to identify portlandite and calcite contents which will be affected by hydration and carbonation of the HCP. A similar method is employed in quantifying the portlandite and calcite contents in the ASR gels. In HCP, portlandite will undergo dehydration at a temperature range of 400 to 500 °C while calcite will decarbonate at a temperature above 600 °C [12].

Figure 2 shows the influence of early age carbonation (at 3 days age) on the synthetic gel after prolonged conditioning (6 months). The composition of the gel will be modified after exposure to the carbonation. In Fig. 2, the carbonated gel has a mass loss of 2.14% associated with calcium hydroxide (loss of water) and a mass
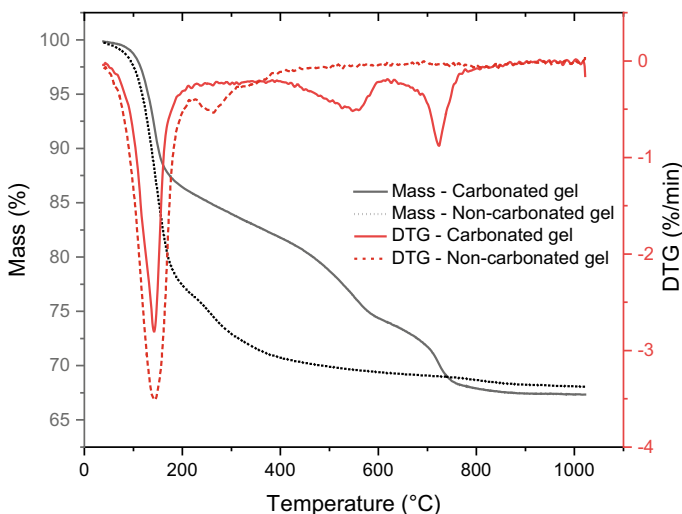
Fig. 2 TGA and DTG curves of non-carbonated and carbonated synthetic ASR gels

loss of 2.72% associated with calcium carbonate (loss of carbon dioxide). However, the non-carbonated gel does not have mass losses related to calcium hydroxide or calcium carbonate, suggesting the presence of the calcium in the oxide form inside the gel.

From Table 1, mix designs of both carbonated and non-carbonated gels contain 11.50% CaO (by weight). In carbonated gel, with 3% of CO_2 concentration exposure for 3 days, out of 11.50% CaO added, 3.46% CaO was held in the form of $CaCO_3$ (corresponding to 2.72% mass loss of CO_2 in TGA) and 6.66% CaO was held in the form of $Ca(OH)_2$ (Corresponding to 2.14% of mass loss of water in TGA). In non-carbonated gel, the CaO exists as part of the gel structure. These differences suggest the uptake of CO_2 by the synthetic gel and changes in the chemical composition of the gel due to exposure to CO_2. Subsequently, such changes result in modification of mechanical properties of the gel which can be understood from nanoindentation.

4.2   Nanoindentation

Indentation techniques reveal the mechanical properties of the material at nano and micro levels. Micro and nanomechanical properties will be useful in identifying the contribution of individual phases to the mechanical properties of the heterogeneous material. In ASR, indentation techniques are used to understand the mechanical properties of the in-situ and laboratory ASR products, in order to understand their capacity to exert stresses on the concrete pore walls. These indentation results allow

the authors to correlate the mechanical properties of the ASR product to their chemical composition [5]. In nanoindentation, combined modulus (or reduced modulus) E_r of the specimen—indenter combination is given by "Eq. (1)".

$$\frac{1}{E_r} = \frac{\left(1 - v_s^2\right)}{E_s} + \frac{\left(1 - v_i^2\right)}{E_i} \tag{1}$$

Where E_s and E_i are the indentation moduli of the specimen and indenter and v_s and v_i are the Poisson's ratios of the specimen and the indenter respectively. These moduli values are different from Young's moduli of the respective materials [3]. From the indentation test, the combined modulus is calculated from "Eq. (2)".

$$E_r = \frac{\sqrt{\pi}}{2\sqrt{A}} \frac{dP}{dh} \tag{2}$$

Indentation hardness (H) of the specimen is calculated from "Eq. (3)"

$$H = \frac{P_{max}}{A} \tag{3}$$

where A is the projected area of the indentation and P_{max} is the maximum load and $\frac{dP}{dh}$ is the slope of the unloading curve in indentation.

In the current study, Berkovich indenter tip was used to test the hardness of the polished carbonated and non-carbonated synthetic gel samples. Target load of 2 mN with a loading and unloading rates of 4 mN/min was applied for both gel specimens on the thin sections. The loading cycle and the typical load depth plot of nanoindentation from the current study are shown in Fig. 3. The hardness and the reduced modulus of elasticity were calculated for both specimens and shown in Table 3.

The indentation test results were fit into Gaussian mixture model which showed that the non-carbonated sample indentation test data has two phases (phase 1 and 2 as shown in Table 3) which have different moduli and hardness values. Furthermore, the indented locations were analyzed to see the chemical
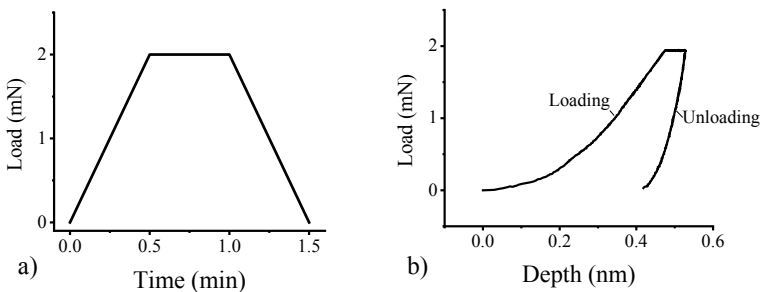

Fig. 3 Indentation load cycle **a** and a typical load depth curve **b** from the current study

Table 3 Indentation results of non-carbonated and carbonated synthetic ASR gels

Sample name	No of tests	Phases	Combined modulus GPa			Hardness GPa		
			Quantity (%)	Avg	Std dev	Quantity (%)	Avg	Std dev
Non-carbonated gel	39	Phase 1	70	9.37	0.81	72	0.41	0.05
		Phase 2	30	14.53	1.43	28	0.80	0.10
Carbonated gel	78	–	100	22.32	6.06	100	1.56	0.57

compositional changes of these two phases in non-carbonated samples. In carbonated gel test results, 100% of the data was fit into a single normal probabilistic curve.

Statistical hypothesis testing with 99.95% confidence interval and one-tail student t-distribution revealed that the carbonated gel combined modulus and hardness values are statistically significantly greater than the non-carbonated gel values for both phases 1 and 2. These observations from nano-mechanical properties suggest that carbonation also increases the mechanical properties of the gel significantly. This effect is similar to replacement of alkali with Ca in the early age ASR gel or reducing the alkali to silica ratio of the gel, processes that result in the increase of mechanical properties of the gel. These improved mechanical properties help the ASR gel exert higher stresses on the concrete, leading to an increase in damage.

4.3 SEM–EDS

Electron microscopic techniques are instrumental in understanding microstructural features in materials. Scanning electron microscopy (SEM) coupled with energy dispersive spectroscopy (EDS) will enable the investigation of the morphology coupled with chemical composition of the sample. Non-carbonated and carbonated synthetic gel samples were observed under the electron microscope to understand the correlation between the gel composition and their nanoindentation results. The SEM images of indentation locations of both gels were shown in Fig. 4. In Fig. 4a non-carbonated gel, both phases 1 and 2 are shown. The weight compositions of the elements that are representative of indented locations are shown in Table 4.

In addition, upon investigating the other locations of the non-carbonated gel, phase 2 is observed to be only a local occurrence where Ca/Si is greater than one. This caused an increase in indentation properties from phase 1 to phase 2. However, very low Si content in non-carbonated gel phase 2 resulted in lower indentation properties compared to carbonated gel.
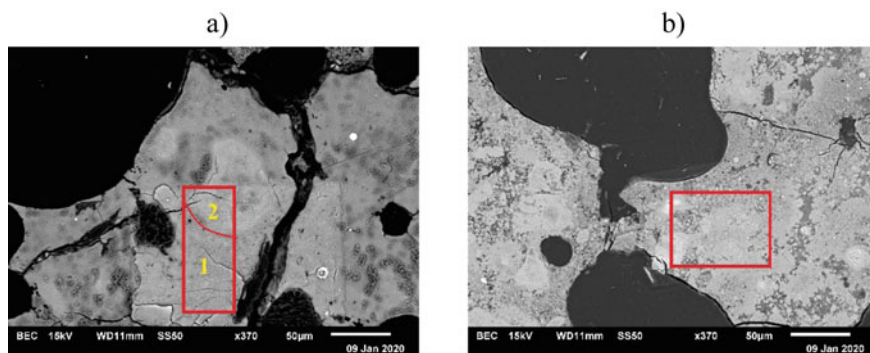
Fig. 4 SEM images of non-carbonated (**a**) and carbonated (**b**) synthetic ASR gels with indentation locations shown in rectangular outlines

Table 4 Alkali, Ca, and Si composition (atomic %) of indented locations of gels obtained from EDS

Element	Phases	Na		K		Ca		Si	
		Avg	Std	Avg	Std dev	Avg	Std dev	Avg	Std dev
Non carbonated gel	1	6.80	2.57	2.41	0.50	7.18	0.51	18.47	1.36
	2	5.79	2.44	1.43	0.19	15.83	0.98	11.89	0.64
Carbonated gel	–	5.30	1.74	3.12	0.97	11.52	3.96	14.62	4.87

Comparing the non-carbonated gel phase 1 to the carbonated gel, an increase in Ca content (atomic %) from 7.18% to 11.52% can be seen in Table 4. This increase of Ca resulted in the increased indentation properties (modulus and hardness) of the material. However, carbonated gel also has large quantities of highly porous structure which is difficult to indent due to its porous structure. This structure of the carbonated gel is shown in Fig. 5. It is worth noting that this porous structure has very low quantities of Ca in it. The partial composition (alkali, Si, and Ca) of the porous portion of the carbonated gel is given in Table 5.

It is interesting to note that the highly porous structure (indicated by spectrums 2, 3, 4, and 5 in Fig. 5) has very low Ca content (1.22% to 2.84% shown in Table 5), while, solid structure (indicated by spectrum 1 in Fig. 5) has very high Ca content (11.57% shown in Table 5). A general conclusion can be drawn that Ca is deposited at a location in the form of calcite or portlandite in carbonated gels.

Fig. 5 Highly porous
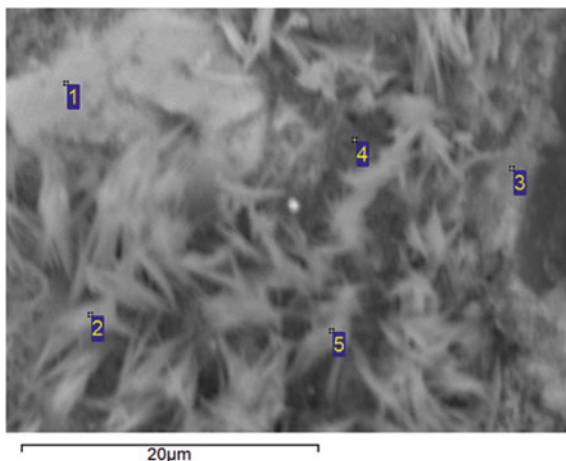structure of carbonated gel
with point spectrum locations

Table 5 Alkali, Si, and Ca
composition (atomic %) of
porous carbonated gel

Point spectrum	Na	Si	K	Ca
1	7.85	9.02	4.34	11.57
2	19.72	9.66	4.29	1.48
3	20.33	17.68	6.43	1.22
4	5.19	26.62	7.88	2.84
5	19.74	8.93	5.36	1.46

5   Discussion

From the results of TGA, carbonated gel has higher quantities of portlandite, and
calcite compared to non-carbonated gel. From this behaviour, interaction of carbon
dioxide with the synthetic gel is warranted. The presence of calcite can be explained
by interaction of CaO in the gel with the carbon dioxide and adequate moisture. As
the calcite formation occurs in the gel, CaO released from the gel may have also
deposited as portlandite in locations with limited carbon dioxide exposure or sat-
urated conditions. However, this hypothesis can be confirmed by observing pH
changes in the gel during carbonation.

Nanoindentation results combined with EDS indicate the improvement in the
combined modulus and hardness from non-carbonated gel (phase 1) to carbonated
gel which can be attributed to the increase in the Ca content in the indented location
of the carbonated gel. This increase in Ca content can be attributed to carbonation.
However, additional microscopic investigation is needed to understand if the Ca
from carbonated gel is contributing to the increased indentation properties in
crystalline form (calcite or portlandite) or amorphous gel form. From the SEM
analysis of carbonated gel, deposits of Ca can be seen adjacent to a highly porous
structure (Fig. 5). This can be explained by the leaching of Ca from the gel to form

calcite or portlandite. This phenomenon leaves behind highly porous structures with low Ca content and solid deposits with high Ca content.

From the discussion, it can be concluded that introducing carbonation to the synthetic ASR gels can result in modifying the chemical composition, mechanical properties, porosity, and structure of the gels. These learnings can be applied to ASR products in mortars and concrete to predict their behaviour.

6   Conclusion

Synthetic ASR gels were prepared and subjected to carbonation to understand the effect of carbonation on ASR. TGA of the synthetic gels confirmed the uptake of carbon dioxide by the presence of calcite in carbonated gels. Nanoindentation was used to understand the mechanical properties of non-carbonated and carbonated gels. These indentation results are combined with EDS to understand the implication of elemental compositional changes due to carbonation on the mechanical properties. Carbonation of the synthetic ASR gels resulted in increased indentation properties (combined modulus and hardness) of the gel and made the gel highly porous.

Future work is underway to examine if similar changes in ASR products material properties due to carbonation can create additional stresses in mortars and concrete elements resulting in cracks.

References

1. ASTM International.: ASTM C1260–14 Standard Test Method for Potential Alkali Reactivity of Aggregates (Mortar-Bar Method) (2014)
2. ASTM International.: ASTM C1293–18a Standard Test Method for Determination of Length Change of Concrete Due to Alkali-Silica Reaction (2018)
3. Fischer-Cripps, A.C.: Nanoindentation, 3rd ed. Springer (2011)
4. Gholizadeh-Vayghan, A., Rajabipour, F.: The influence of alkali–silica reaction (ASR) gel composition on its hydrophilic properties and free swelling in contact with water vapor. Cem. Concr. Res. **94**, 49–58 (2017)
5. Hu, C., Gautam, B., Panesar, D.: Nano-mechanical properties of alkali-silica reaction (ASR) products in concrete measured by nano-indentation. Constr. Build. Mater. **158**, 75–83 (2018)
6. Kawamura, M., Arano, N., Terashima, T.: Composition of ASR gels and expansion of mortars, materials science of concrete: the Sidney diamond symposium, Special Volume, American Ceramic Society, Westerville, OH, pp. 261–276 (1998)
7. Leemann, A., Lura, P.: E-modulus of the alkali–silica-reaction product determined by micro-indentation. Constr. Build. Mater. **44**, 221–227 (2013)

8. Leemann, A., Le Saout, G., Winnefeld, F., Rentsch, D., Lothenbach, B (2010) Alkali-silica reaction: the influence of calcium on silica dissolution and the formation of reaction products. J. Am. Cer. Soc. **94**(4), 1243–1249

9. Peterson, K., Gress, D., Van Dam, T., Sutter, L.: Crystallized alkali-silica gel in concrete from the late 1890s. Cem. Concr. Res. **36**(8), 1523–1532 (2006)

10. Prado, R.J., Tiecher, F., Hasparyk, N.P., Molin, D.C.C.D.: Structural characterization of alkali-silica reaction gel: an x-ray absorption fine structure study. Cem. Concr. Res. **123**, 105774 (2019)

11. Rajabipour, F., Giannini, E., Dunant, C., Ideker, J., Thomas, M.: Alkali–silica reaction: current understanding of the reaction mechanisms and the knowledge gaps. Cem. Concr. Res. **76**, 130–146 (2015)

12. Scrivener, K., Snellings R., Lothenbach, B.: Practical guide to microstructural analysis of cementitious materials, 1st ed., CRC Press (2017)

13. Shi, Z., Geng, G., Leemann, A., Lothenbach, B.: Synthesis, characterization, and water uptake property of alkali-silica reaction products. Cem. Concr. Res. **121**, 58–71 (2019)

14. Struble, L., Diamond, S.: Swelling properties of synthetic alkali silica gels. J. Am. Ceram. Soc. **64**(11), 652–655 (1981)

Salt-Scaling Resistance of SAP-Modified Concrete Under Freeze–Thaw Cycles

José Roberto Tenório Filho [ID]**, Els Mannekens, Didier Snoeck** [ID]**, and Nele De Belie** [ID]

Abstract Concrete structures can be subjected to a range of deteriorating processes due to environmental exposure. When subjected to freeze–thaw cycles, the concrete can experience scaling of the surface layer and internal damage that can further lead to cracking and open the path to other deleterious agents. During winter times, the use of de-icing salts is a very common practice to aid in the cleaning and clearance of roads, bridges and tunnels which increases the effects of scaling. Lately, a lot of research has been developed on the use of superabsorbent polymers (SAPs) to increase the durability of concrete structures by means of internal curing, self-sealing and self-healing. The SAP-modified concrete presents a higher resistance to salt-scaling when compared to concrete mixtures without SAPs. In this paper, the scaling resistance of four concrete compositions with and without superabsorbent polymers is studied. One commercial SAP applied to mitigate the autogenous shrinkage and two "in-house" developed SAPs are used. Cylindrical specimens were exposed to 28 freeze–thaw cycles with a 3% NaCl solution. Two of the SAP containing-mixtures showed a reduction of 49% (commercial SAP) and 54% ("in-house" SAP) in salt-scaling in comparison with the reference mixture. On the other hand, another "in-house" developed SAP induced an increase in scaling. The water kinetics of the SAPs was found to play a major role in the performance of the mixtures regarding the scaling resistance.

Keywords Superabsorbent polymers · Freeze–thaw · Salt-scaling resistance

J. R. Tenório Filho · D. Snoeck · N. De Belie (✉)
Magnel-Vandepitte Laboratory, Department of Structural Engineering and Building Materials, Faculty of Engineering and Architecture, Ghent University, Tech Lane Ghent Science Park, Campus A, Technologiepark Zwijnaarde 60, B-9052 Ghent, Belgium
e-mail: nele.debelie@ugent.be

J. R. Tenório Filho
SIM vzw, Technologiepark 48, Zwijnaarde, B-9052 Ghent, Belgium

E. Mannekens
Chemstream bv, Drie Eikenstraat 661, 2650 Edegem, Belgium

131

1   Introduction

Concrete structures are subjected to a range of deteriorating processes due to environmental exposure. Next to carbonation, chloride ingress and sulphate attack, concrete structures are subjected to freezing and thawing. In this last mechanism, the concrete is subjected to scaling of the surface layer and internal damage that can further lead to cracking and this opens the path to other deleterious agents.

During winter times, especially in northern countries, the use of de-icing salts is a very common practice to aid in the cleaning and clearance of roads (including bridges and tunnels) which increases the effects of scaling. In Belgium, for example, approximately 40% of the roads are made of concrete [1], and in Flanders 350 million euros is used for maintenance of roads and bridges every year [2].

Lately, a lot of research has been developed on the use of superabsorbent polymers (SAPs) to increase the durability of concrete structures by means of internal curing, self-sealing and self-healing.

Superabsorbent polymers (or hydrogels) consist of a natural or synthetic water-insoluble 3D network of polymeric chains cross-linked by chemical or physical bonding. They possess the ability to take up a significant amount of liquids from the environment (in amounts up to 500 times their own weight) [3]. Once in contact with the mixing water of the fresh cementitious material, SAPs absorb and retain a certain amount of the water (depending on their absorption capacity), later on acting as water reservoirs for the system, keeping its level of internal relative humidity high for a considerable time frame.

After internal curing, the SAPs leave behind macro-pores which are beneficial for freeze–thaw resistance [2, 4–7] as their macro-porosity resembles an air-entrained system [8]. However, the use of SAPs gives a more stable mixture and better mechanical properties when compared to air-entraining admixtures [6].

The addition of SAPs in the range of 0.10–0.34% in relation to the mass of cement has been reported to promote a reduction of at least 50% in the scaling after more than 25 freeze–thaw cycles in both cement mortars and concrete mixtures [9, 10]. Not only the amount of SAPs but also their particle size, and production process might have an impact on the scaling resistance. In mixtures with the same amount of additional water, smaller SAP particles lead to a higher viscosity of the mixture, lower bleeding and consequent higher scaling resistance [9].

In this paper, three SAP-containing concrete mixtures and a reference mixture without SAPs were investigated. The SAPs used were previously studied to mitigate autogenous shrinkage by means of internal curing and to promote sealing of cracks in concrete mixtures and now their influence on the scaling resistance of the concrete under freeze–thaw cycles will be discussed.

2 Experimental Program

2.1 Materials and Mixing Compositions

All tests were performed on concrete mixtures produced with cement type CEM III-B 42.5 N—LH/SR (CBR, Belgium); a polycarboxylate superplasticizer (Tixo, 25% conc., BASF, Belgium, at a constant dosage of 1.8% in relation to the cement mass); sea sand 0/4 (absorption of 0.4% in mass); sea sand 0/3 (absorption of 0.3% in mass); limestone 2/20 (absorption of 0.5% in mass). One commercial SAP, hereby identified as SAP1 and two "in-house" developed SAP, named SAP2 and SAP3 were used.

SAP1, made by BASF (Germany) is a copolymer of acrylamide and sodium acrylate produced by bulk polymerization. It has a mean particle size (d50) of 40 μm and absorption capacity of 24 g of water per g of SAP in concrete. This SAP has been previously studied as internal curing agent and self-sealing/healing promoter for mortar mixtures [11, 12]. SAP2, produced by ChemStream bvba (Belgium) mainly consists of the co-monomers NaAMPS (2-acrylamido-2-methyl-1-propanesulfonic acid sodium salt) and SVS (sodium vinyl sulfonate), diluted with a non-charged or neutral monomer ACMO (acryloyl morpholino acrylate) (50% mol). It has a mean particle size (D_{50}) of 100 μm and absorption capacity of 49 g of water per g of SAP in concrete. SAP3 mainly consists of the monomer NaAMPS (2-acrylamido-2-methyl-1-propanesulfonic acid sodium salt). It has a mean particle size (D_{50}) of 100 μm and absorption capacity of 12 g of water per g of SAP in concrete.

The amounts of SAP1 and SAP2 were determined to mitigate autogenous shrinkage. On the other hand, SAP3 was originally used to promote the sealing of cracks, which is why different amounts were used. Detailed information on the composition of the concretes is shown in Table 1.

Table 1 Information of the studied concrete mixtures, values in kg/m^3

Mixture	REF	C_SAP1	C_SAP2	C_SAP3
Cement (kg/m^3)	356	339	324	340
Sand 0/3 (kg/m^3)	421	405	386	406
Sand 0/4 (kg/m^3)	343	330	315	331
Limestone 2/20 (kg/m^3)	1086	1043	996	1046
SAP (kg/m^3)	0	1.70	1.62	3.40
Superplasticizer (kg/m^3)	6.35	6.10	5.83	6.12
Additional water (kg/m^3)	0	40.68	84.15	37.42
w/c$_{(total)}$ [–]	0.46	0.58	0.72	0.57
Slump [mm]	160	165	140	150
Compressive strength at 28 days [MPa] (n = 3)	54.9 ± 2.0	42.7 ± 2.4	32.0 ± 0.7	45.8 ± 1.8

All concrete mixtures were produced in a mixer with a capacity of 12 L, in batches of 10 L. In the mixing procedure the dry materials were first mixed for 1 min (including SAPs, when present), then the mixing water and superplasticizer were added and mixed for an additional 2 min. When SAPs were present, the additional entrained water was added during the third minute and the mixing proceeded for an additional 2 min. The total mixing time was 3 min for the reference mixture and 5 min for the SAP-containing mixtures.

Since additional water was used in the mixtures with SAPs, the final volume of concrete produced tends to be higher in comparison to the reference without SAPs. For that reason, and to keep all materials proportioned for 1 m^3 of concrete, the total water-to-cement ratio is presented taking into account the additional water for the SAPs, but it should be highlighted that this additional water absorbed by the SAPs is used for internal curing and not part of the water contributing to the effective water-to-cement ratio of the mixtures, which is 0.46 for all of the mixtures.

2.2 Testing the Scaling Resistance

The scaling test followed the recommendations of the standard EN 12390–9 with the temperature cycle as shown in Fig. 1. The freezing medium used was a 3% NaCl solution (prepared with demineralized water), corresponding to a thin layer of 3 mm poured on the top surface of the specimens (25 ml of solution for each specimen, in this case).

For each concrete mixture a cylinder with a diameter of 10 cm and a height of 20 cm was cast. After 25 days, each cylinder was cut in three smaller cylinders with a diameter of 10 cm and a height of 5 cm. They were then placed into a PVC tube
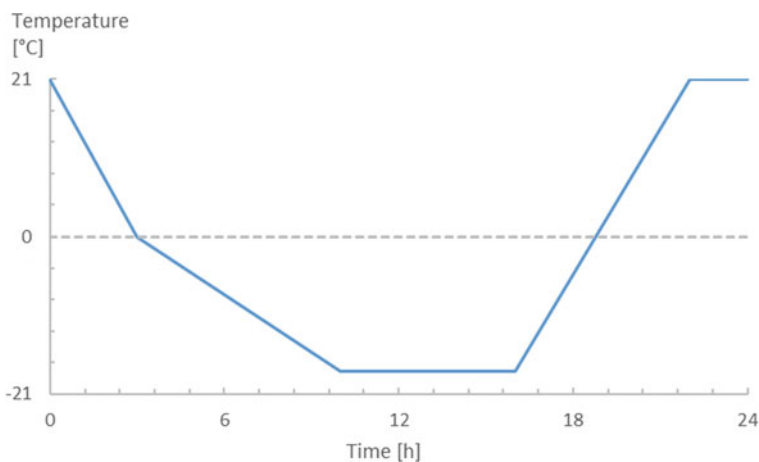

Fig. 1 Temperature cycle

with an inner diameter of 10 cm and a height of 7 cm. A thin layer of epoxy was applied at the sides to prevent any leakage of the freezing fluid from the top of the surface. From the 26th till the 28th day, a thin layer of 3 mm of demineralized water was poured on the top surface of the specimens to verify the absence of any leakage. On the 28th day, the specimens were placed inside an insulating recipient (see Fig. 2), the freezing medium was poured on them and the specimens were put inside the freeze–thaw chamber.

The scaled material was measured after 7, 14, 21 and 28 cycles.

2.3   Air Void Analysis

The air void distribution and the spacing factor were studied according to EN-480, using polished concrete specimens of 100 mm × 100 mm × 20 mm. An automated air void analyzer was used (see Fig. 3). Prior to the test the specimens were painted with black ink, dried for 24 h in an oven at 35 °C, then a layer of white barium sulphate powder was applied to fill in the voids on the surface.

3   Results and Discussion

As it can be observed in Fig. 4, SAP1 and SAP3 promoted a considerable reduction in the amount of scaled material over the 28 cycles in comparison with the reference mixture. After 28 cycles the reduction was around 49% and 55% for SAP1 and SAP3, respectively. The results are in compliance with the findings of [6, 9].

In literature, some failure thresholds are usually mentioned regarding the amount of scaled material. In [6] and [13] a value of 1.5 kg/m^2 is cited, while the Belgian standard for concrete paving flags [14] mentions a limit of 1.0 kg/m^2, both after

Fig. 2 Specimen ready to be tested

Fig. 3 RapidAir used to perform air void distribution analysis
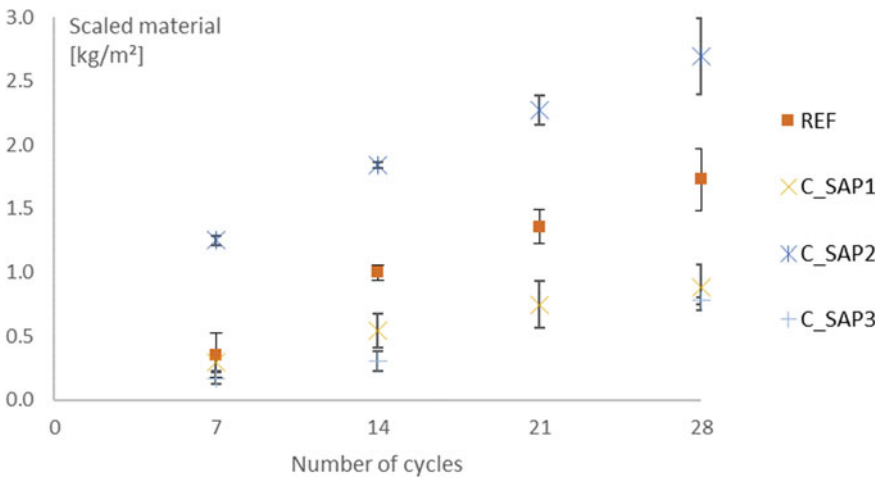

Fig. 4 Accumulated scaled material over the freeze-thawing cycles

conducting 28 freeze–thaw cycles. Both SAP1 and SAP3 enabled the production of a concrete mixture in compliance with both the thresholds cited up to 28 freeze–thaw cycles. On the other hand, the reference mixture presented a scaling higher than 1.0 kg/m^2 after 14 cycles and a value higher than 1.5 between the 21st and 28th cycle.

In contrast to SAP1 and SAP3, SAP2 was not only unable to improve the scaling resistance, but the mixture C_SAP2 showed a higher scaling during the whole testing period in comparison to all the other mixtures (55% higher than the reference after 28 cycles). In the air void analysis, the spacing factors found were 0.45 ± 0.01 mm for the REF mixture, 0.29 ± 0.01 mm for C_SAP1, 0.40 ± 0.06 mm for C_SAP2 and 0.36 ± 0.02 mm for C_SAP3.

Figure 5 depicts the relation between the amount of scaled material after 28 cycles and the spacing factor of each concrete mixture.

For all cases, the inclusion of SAPs promoted the reduction in the spacing factor in comparison to the reference. However, no linear behavior was found between the scaling and the spacing factor of the concrete mixtures.

By not considering the spacing factor of the mixture C_SAP2, a linear relation is found amongst the other mixtures. This means that, for the mixture C_SAP2 in particular some other factor might be playing an important role in the development of the scaling. In fact, previously the authors found an indication that the water was being released at once by SAP2. Considering the high amount of additional water in this mixture, the fact that it could be released to the concrete at once and also the impact it has on the compressive strength of the mixture (see Table 1), it is reasonable to state that the kinetics of water release of that SAP is the main factor influencing its inferior performance under freeze–thaw cycles.
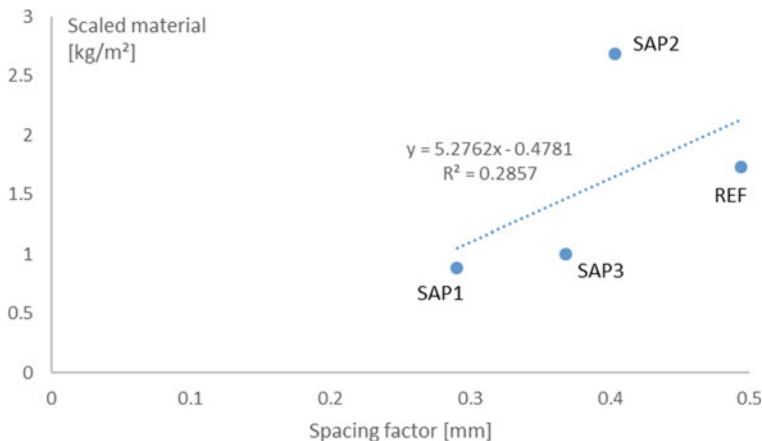

Fig. 5 Accumulated scaled material as a function of the spacing factor for the studied concrete mixtures

4   Conclusions

Both SAP1 and SAP3 (at a dosage of 0.5% and 1.0% over the weight of cement, respectively) proved to increase the scaling resistance of the concrete when submitted to freeze–thaw cycles with de-icing salts, which is an interesting feature when considering structures exposed to freezing conditions.

SAP2, on the other hand, showed a very negative impact on scaling resistance of the concrete in comparison to the reference and the other SAPs, which might be closely related to its kinetics of water release.

Considering a broad scenario for the application of the SAPs, where a smart concrete mixture is desired (meaning here, a mixture with the features of mitigation of autogenous shrinkage and/or self-sealing of cracks), SAP2 should not be used for structures subjected to freeze-thawing.

References

1. Apers, J., Broucke, A., Vandewalle, L.: Betontechnologie. 4e herziene druk Brussel: Belgische betongroepering (2006)
2. Craeye, B., Cockaerts, G., Kara De Maeijer, P.: Improving freeze–thaw resistance of concrete road infrastructure by means of superabsorbent polymers. Infrastructures **3**(1), 4 (2018)
3. Mechtcherine, V., Reinhardt, H.W.: Application of Super Absorbent Polymers (SAP) in Concrete Construction, in State-of-the-Art Report Prepared by Technical Committee 225-SAP. RILEM, p. 165 (2012)
4. Laustsen, S., Hasholt, M.T., Jensen, O.M.: Void structure of concrete with superabsorbent polymers and its relation to frost resistance of concrete. Mater. Struct. **48**(1–2), 357–368 (2015)
5. Li, F.P., et al.: Durability of concrete modified with superabsorbent polymers. Mater. Performance **57**(3), 54–58 (2018)
6. Mechtcherine, V., et al.: Effect of superabsorbent polymers (SAP) on the freeze-thaw resistance of concrete: results of a RILEM interlaboratory study. Mater. Struct. **50**(1) (2017)
7. Wyrzykowski, M., Terrasi, G., Lura, P.: Expansive high-performance concrete for chemical-prestress applications. Cem. Concr. Res. **107**, 275–283 (2018)
8. Riyazi, S., Kevern, J.T., Mulheron, M.: Super absorbent polymers (SAPs) as physical air entrainment in cement mortars. Constr. Build. Mater. **147**, 669–676 (2017)
9. Kusayama, S., Kuwabara, H., Igarashi, S.: Comparison of salt scaling resistance of concretes with different types of superabsorbent polymers. In: Application of Superabsorbent Polymers and Other New Admixtures in Concrete Construction. RILEM Publications S.A.R.L (2014)
10. Tan, Y.W., et al.: Performances of cement mortar incorporating superabsorbent polymer (SAP) using different dosing methods. Materials **12**(10) (2019)

11. Snoeck, D.: Self-Healing and Microstructure of Cementitious Materials with Microfibres and Superabsorbent Polymers, in Faculty of Architecture and Engineering. Ghent University, Ghent, Belgium (2015)
12. Tenório Filho, J.R., D. Snoeck, De Belie, N.: The effect of superabsorbent polymers on the cracking behavior due to autogenous shrinkage of cement-based materials. In: 60th Brazilian Concrete Conference. Foz do Iguacu, Brazilian Concrete Institute, Brazil (2018)
13. Romero, H.L., et al.: Study of the damage evolution of concrete under freeze-thaw cycles using traditional and non-traditional techniques. In: Xlll International Conference on Cement Chemistry. Madrid (2011)
14. Standardisation, N.-B.F.: NBN EN 1339—Concrete paving flags—Requirements and test methods (2003)

Pore-Scale Numerical Modeling Tools for Improving Efficiency of Direct Carbon Capture in Compacts

Ravi A. Patel and Nikolaos I. Prasianakis

Abstract Carbonate bonded materials are considered to be a viable alternative to reduce carbon emission from cement industry. Such materials are carbon emission negative since they sequestrate CO_2 through carbonation reaction and present potential of making commercial profit. However, carbonation reaction depends on several factors such as pore structure, particle size distribution, relative humidity, temperature, CO_2 gas pressure, etc. The design of carbonate bonded materials requires a fine tuning of these parameters which is preliminary done through extensive experimental campaigns. Here we present an alternative approach of in-silico based design of carbon bonded material, where microstructure modeling plays a central role in the design process. Finally, a newly developed microstructure modeling framework is presented. This framework utilizes the discrete element method to generate the initial compact structure, the lattice Boltzmann method to compute the equilibrium distribution of liquid and gas phase, and as a last step a cellular automation-based model for evolution of microstructure due to the carbonation reaction. The model qualitatively reproduces the experimental observations thus providing confidence in our modeling approach. Quantitive comparison with experiments available in the literature and further refinement of the model is ongoing. The developed microstructure modeling framework is foreseen as a valuable tool for designing carbon bonded materials.

Keywords Carbon bonded materials · Carbonation · Microstructure modeling · Model aided material design

R. A. Patel (✉) · N. I. Prasianakis
Laboratory of Waste Management (LES), Paul Scherrer Institute, Villigen, Switzerland
e-mail: ravi-ajitbhai.patel@psi.ch

1   Introduction

The carbon emission originating from the cement industry amounts to around 8% of the global emissions. In order to achieve the goal of Paris agreement on climate change cement industry would have to bring these emissions down by at least 16% by 2030 [1]. Sequestration of CO_2 to create construction materials is considered as one of the alternatives for reducing emission and upon commercialization this can lead to viable alternatives to ordinary Portland based concrete. In such "carbonate bonded materials" the binding matrix consists of carbonates (calcium carbonate or magnesium carbonate) as a product of the reaction of binders or industrial waste such as steel slags with CO_2. The strength is achieved by formation of carbonates which leads to lower porosity and finer microstructures. Recently, such materials have also been commercially introduced by different startups [2, 3].

The design of carbon bonded materials requires the fine tuning of different parameters affecting carbonation process such as initial pore structure, particle size distribution, relative humidity, temperature, CO_2 gas pressure, etc. Most of the studies have been experimental and in particular focusing on the effect of these factors on carbonation efficiency and on carbonation rates. However, limited information exists on microstructure and strength evolution [4]. Furthermore, the strength evolution would depend on the size and shape of the specimens. Therefore, laboratory studies alone, cannot help to directly optimize the material and create a product of industrial scale. In addition, at present there is no existing computational framework to model microstructure evolution of carbonate bonded materials. This is the motivation for the development of the microstructure modeling framework.

In Sect. 2, a vision on the role of microstructure model as tool to optimize carbonate bonded materials is discussed. This is followed by detailed description of newly developed microstructure modeling framework for carbonate bonded materials in Sect. 3. Finally, conclusions and outlook are presented in Sect. 4.

2   Microstructure Model Driven Engineering of Carbonate Bonded Materials

The concept that "*material microstructure governs its properties*" has been understood since early dawn of material science of cement-based materials and the quest to understand microstructures has resulted into several microstructure models (for details see [5]). Such microstructure models take basic inputs such as initial clinker composition, w/c ratio, particle size distribution, etc. as input and can provide three-dimensional microstructure representation of cement paste. Using these microstructure models material properties such as elasticity, diffusivity, permeability, etc. can be computed [6–9]. However, such models have hardly been used for material discovery and optimization which still remains largely
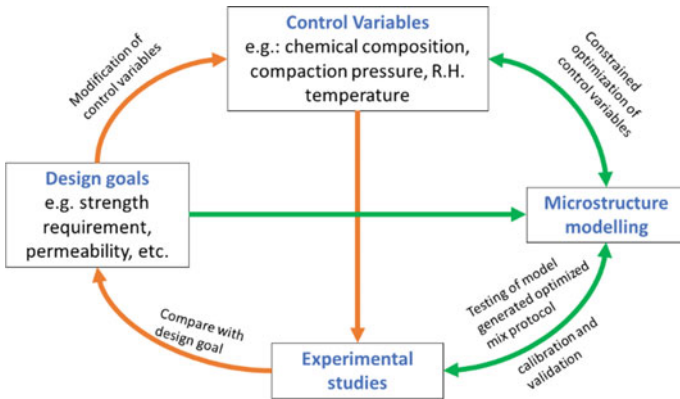
Fig. 1 Current workflow (in orange) and proposed microstructure modelling driven workflow (in green) for engineering carbonate bonded materials

experimentally driven. This is also the case for design of carbonate bonded materials as shown in Fig. 1 (orange arrows). However, for carbonate bonded materials there are several parameters that can be controlled. Their combination can lead to very extensive and long experimental campaigns. Therefore, a new methodology is proposed for the design cycle of carbonate bonded materials with microstructure modeling as a key component of this framework, aiming to significantly reduce the time to solution. Within this new material design framework, it is proposed to identify an optimized range of control parameters which can be easily varied e.g. relative humidity, temperature, etc. using microstructure model. Once, this optimized range of control parameters have been obtained a more focused experimental campaign can be carried out to find the protocol which matches with the design goals. The data obtained from the experimental campaign can be used to further calibrate and validate the model thus improving its robustness on-fly. Thus, the role of the microstructure model is not just to develop or improve predictive models but is envisioned to be an integral part of the design process with a specific role to reduce the number of needed experiments and subsequently the overall experimental costs. The microstructure modeling framework is proposed in the next section with aim to fulfil this role.

3 Microstructure Modelling of Carbonate Bonded Materials

The overview of workflow developed for microstructure modeling of carbonate bonded material is shown in Fig. 2. The workflow utilizes combines different numerical techniques and consists of two main steps: (a) the generation of initial
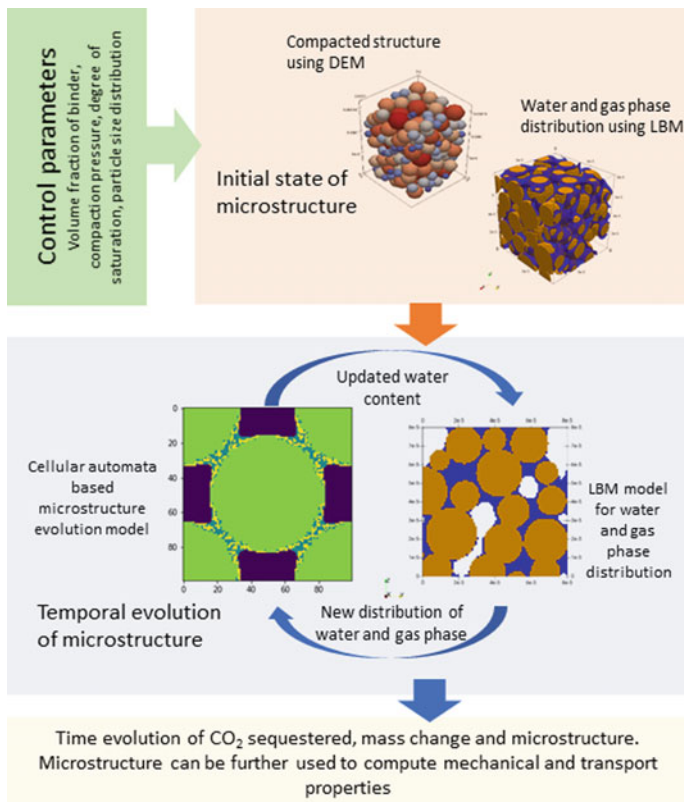
Fig. 2 Workflow for microstructure modelling of carbonate bonded materials

microstructure and, (b) the water distribution and temporal modeling of microstructure evolution due to carbonation. The details of the modeling framework are presented in the sections below.

3.1 Initial Microstructure Generation of Compacts

In order to generate initial microstructure of compacts discrete the element method (DEM) [10] has been utilized. Discrete element method captures particle motion by time integration of Newton's second law. Interaction between particle is assumed through linear elastic contact forces and coulomb friction. For this study the open-source DEM modeling tool YADE [11, 12] has been utilized. The generation of initial microstructure consist of three phases as shown in Fig. 3. At first the required number of particles with a given particle size distribution (PSD) are randomly distributed in a volume larger than the final volume as shown in Fig. 3a. This

Fig. 3 Different stages of simulation for initial microstructure generation of packing **a** Random distribution of particles in large domain **b** raining stage **c** final packing at a sustained pressure of 10 kg/cm^2

followed by raining stage where particles are allowed to settle under constant gravitational acceleration. The simulation stage at 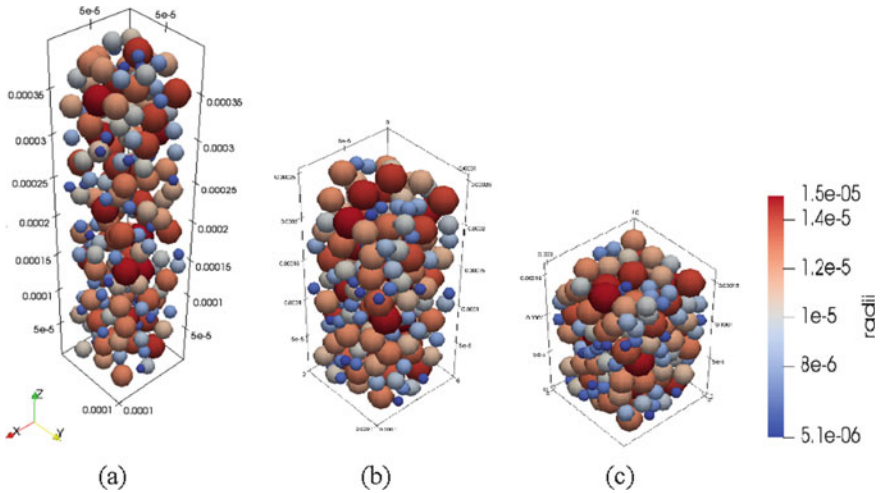the end of raining stage is shown in Fig. 3b. At the end of raining stage, a loading plate is introduced on the top and a constant strain rate is applied. The direction of strain rate is adjusted based on loading/unloading to achieve the final pressure required. The microstructure of compact for 10 kg/cm^2 pressure is shown in Fig. 3c.

3.2 Modeling of Water Distribution in Microstructure

The equilibrium distribution of water and gas phase in the initial microstructure and during the microstructure evolution is computed using lattice Boltzmann method (LBM). LBM are highly efficient for pore-scale simulation compared to conventional numerical scheme and has the advantage of handling boundary conditions in complex geometries. For multiphase (gas, water and solid system) we have used Shan-Chen single component two phase LBM [13, 14]. This model has been implemented in open-source LBM code *Yantra* [15]. Figure 4 shows the water and gas phase distribution for 40% saturation as computed using LBM. For this simulation we have cropped the compact microstructure generated in Fig. 3c to have domain size of 80 μm^3 and assumption is made that solid phase is perfectly wetting.
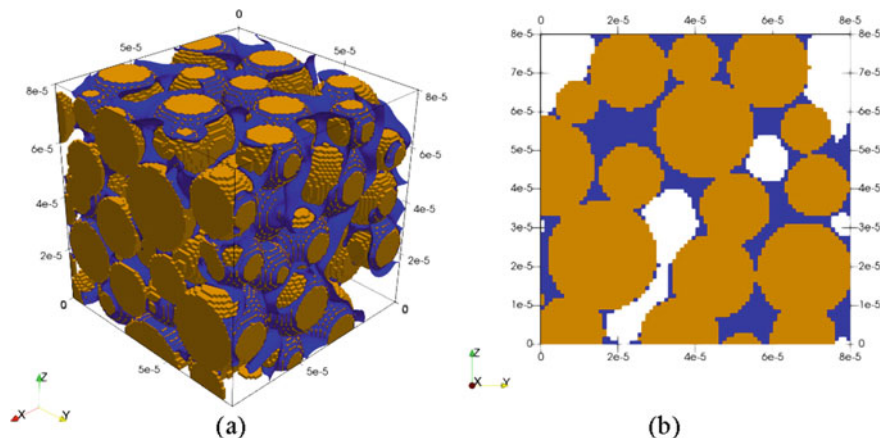
Fig. 4 **a** Water and gas phase distribution in initial compacted microstructure (cropped to achieve 80 μm^3 domain) **b** cross-section plane normal to direction at the center of domain. Solids in orange, water in blue and gas phase is the empty space in domain

3.3 Modeling of Microstructure Evolution of Carbonate Compacts

The microstructure evolution model is based on cellular automata (CA) and inspired from the hydration model CEMHYD3D [16] which is based on cellular automata. The cellular automata model heuristically mimics reaction diffusion process of carbonation reaction rather than explicitly modeling it. Alternatively, pore-scale lattice Boltzmann method based reactive transport model can be used to simulate carbonation reaction [17–19]. However, such models are computationally intensive. This poses a severe restriction for their use for optimization of control parameters which would require large number of simulations under different conditions. This justifies the choice of developing CA based model for carbonate bonded materials.

In the developed model within a given simulation cycle, three sub-steps are performed. First sub step is CO_2 dissolution step wherein the liquid phase voxels at liquid–gas interface are marked as voxel containing dissolved CO_2 with certain reaction probability. This sub-step is followed by dissolved CO_2 transport step in which CO_2 dissolved is transported within the aqueous phase using random walk method. The CO_2 voxel interacts with reactive solid to form a dissolved carbonate phase with certain probability. This sub-step is finished when the dissolved CO_2 cannot further interact with reactive solid phase. In the final sub-step, the dissolved carbonate phase is transported using random walk method. The carbonate phase is allowed to precipitate both through heterogenous and homogenous nucleation. For heterogenous nucleation, certain interface voxels of reactive solid and liquid phase are randomly marked. The homogenous nucleation occurs under certain

pre-specified probability which can be controlled to have more homogenous or heterogenous nucleation. After each simulation step if the water content of the sample is changing the LBM solver can be invoked to find new equilibrium distribution of gas and liquid phase in the microstructure.

For demonstration of model we have chosen initial reactive solid configuration as shown in Fig. 5. Initial saturation state is considered to be 20% and distribution of liquid and gas phase is shown in Fig. 5. It is further assumed that carbonation reaction does not change the saturation state and the volume ratio of precipitating carbonate and reactive solid is one. Figure 5 shows that the model is able to predict precipitation of carbonate leading cementation of the reactive phase which is also observed in SEM images [20]. Figure 6 shows the plot of percentage of reacted
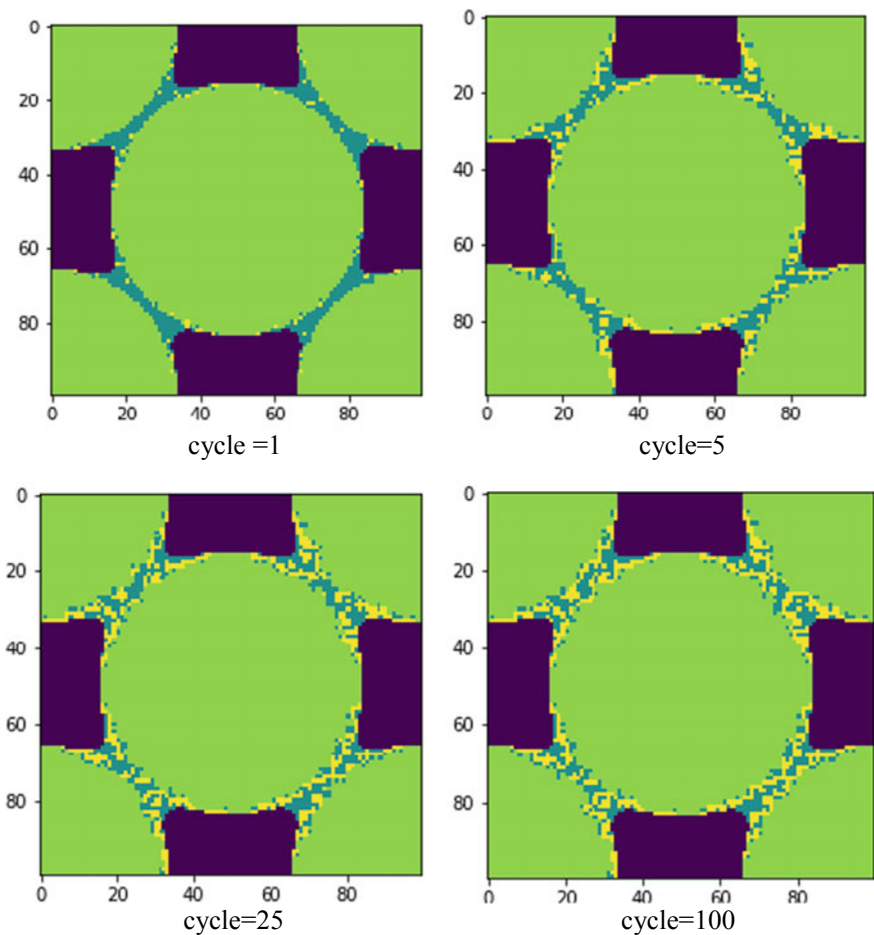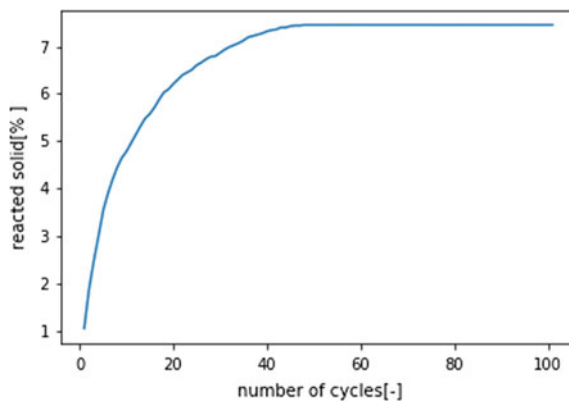

Fig. 5 Time evolution of microstructure due to carbonation reaction. Green = reactive solid, yellow = carbonate phase, light blue = water, dark blue = gas

Fig. 6 Plot of percentage of reacted solid as function of number of simulation steps

solid for this simulation as function of number of simulation cycles. This curve can be considered to be equivalent to the amount of CO_2 sequestered versus time which is commonly measured in experiments [20]. The shape of the curve qualitatively follows the same trend as measured in experiments. Note that the model is able to predict the stoppage of carbonation reaction due to blockage of transport pathway and surface of reactive solid and does not require any calibration to achieve such a behavior. From the model maximum amount of reacted solid and in turn maximum amount of CO_2 sequestered is a direct output. In order to convert number of simulation cycles to physical time a conversion factor is needed which can be calibrated from the experimental data.

4 Concluding Remarks and Future Work

A vision for modelling aided design of carbon bonded materials has been laid. In this vision the microstructure modeling plays a central role. It is seen as a tool which can help to obtain optimized range of control parameters and thus help in reducing the extent of the experimental campaign. Finally, a newly developed microstructure modeling framework for carbon bonded materials has been presented. This framework utilizes different numerical techniques to generate initial microstructure and time evolution of the microstructure. The developed model agrees well with qualitative experimental observations thus giving confidence in developed model. Quantitive comparison with experiments available in literature and further refinement of the model is ongoing. The developed microstructure modeling framework is foreseen as a valuable tool for computer aided design of carbon bonded materials.

References

1. BBC News: Climate change—The massive CO_2 emitter you may not know about. https://www.bbc.com/news/science-environment-46455844 (n.d.). Accessed 30 Oct 2019
2. Solidia®: Making Sustainability Business As Usual SM. https://www.solidiatech.com/. (n.d.). Accessed 31 Jan 2020
3. Carbonation|Orbix: https://www.orbix.be/en/technologies/carbonation. (n.d.). Accessed 31 Jan 2020.
4. Nielsen, P., Baciocchi, R., Costa, G., Quaghebeur, M., Snellings, R.: Carbonate-bonded construction materials from alkaline residues. RILEM Tech. Lett. **2**, 53–58 (2017)
5. Thomas, J., Biernacki, J., Bullard, J.: Modeling and simulation of cement hydration kinetics and microstructure development. Cem. Concr. Res. **41**, 1257–1278 (2011)
6. Patel, R.A., Perko, J., Jacques, D., De Schutter, G., Ye, G., Van Bruegel, K.: Effective diffusivity of cement pastes from virtual microstructures: role of gel porosity and capillary pore percolation. Constr. Build. Mater. **165**, 833–845 (2018)
7. Zhang, M., Ye, G., Van Breugel, K.: Microstructure-based modeling of permeability of cementitious materials using multiple-relaxation-time lattice Boltzmann method. Comput. Mater. Sci. **68**, 142–151 (2013)
8. Zalzale, M., McDonald, P.J., Scrivener, K.L.: A 3D lattice Boltzmann effective media study: understanding the role of C-S-H and water saturation on the permeability of cement paste. Model. Simul. Mater. Sci. Eng. **21**, 085016 (2013)
9. Smilauer, V., Bittnar, Z.K.: Microstructure-based micromechanical prediction of elastic properties in hydrating cement paste. Cem. Concr. Res. **36**, 1708–1718 (2006)
10. Cundall, P.A., Strack, O.D.L.: A discrete numerical model for granular assemblies. Géotechnique **29**, 47–65 (1979)
11. Kozicki, J: YADE-OPEN DEM : An Open—Source Software Using a Discrete Element Method to Simulate Granular Material pp. 1–19 (2008)
12. Overview—Yade 2020–01–29.git-186b0e6 documentation. https://yade-dem.org/doc/. (n.d.). Accessed 31 Jan 2020
13. Shan, X., Chen, H.: Simulation of nonideal gases and liquid-gas phase transitions by the lattice Boltzmann equation. Phys. Rev. E. **49**, 2941–2948 (1994)
14. Martys, N.S., Chen, H.: Simulation of multicomponent fluids in complex three-dimensional geometries by the lattice Boltzmann method. Phys. Rev. E. Stat. Physics, Plasmas, Fluids, Relat. Interdiscip. Top. **53**, 743–750 (1996). https://doi.org/10.1103/PhysRevE.53.743
15. Patel, R.A.: https://bitbucket.org/yantralbm/yantra (2016)
16. Bentz, D.P., Coveney, P.V., Garboczi, E.J., Kleyn, M.F., Stutzman, P.E.: Cellular automaton simulations of cement hydration and microstructure development. Model. Simul. Mater. Sci. Eng. **2**, 783 (1994)
17. Patel, R.A., Churakov, S.V., Prasianakis, N.I.: A multi-level pore scale reactive transport model for the investigation of combined leaching and carbonation of cement paste. Cem. Concr. Compos. (under rev 2020)
18. Patel, R.A., Prasianakis, N.I.: Development of pore-scale model for ingress of CO_2 brine through cement paste. In: SynerCrete'18 International Conference of Interdisciplinary Approaches for Cement based Materials and Structural Concrete, Funchal, Maderia, Portugal (2018)
19. 19. Chen, L., Kang, Q., Tang, Q., Robinson, B.A., He, Y.-L., Tao, W.-Q.: Pore-scale simulation of multicomponent multiphase reactive transport with dissolution and precipitation. Int. J. Heat Mass Trans. **85**, 935–949 (2014)
20. Quaghebeur, M., Nielsen, P., Horckmans, L., Van Mechelen, D.: Accelerated carbonation of steel slag compacts: development of high-strength construction materials. Front. Energy Res. **3** (2015)

Assessing the Alkali-Sensitivity of the Mechanical Behavior of Jute Fibers to Evaluate Their Durability in Cementitious Composites Applications

C. B. de Carvalho Bello, A. Cecchi, and L. Ferrara

Abstract Jute fibers have been studied for their numerous properties and, recently, much attention has been paid to the possibility of using them as reinforcing material in cement based matrices for structural engineering applications. In the context of structural reinforcement methods, the use of composite materials reinforced with synthetic fibers is now quite common, due to their light weight, versatility and adaptability. However, in recent years, the scientific community has been interested on the use of natural composite materials, with the goal of finding innovative solutions with renewable, recyclable, sustainable and biodegradable products for the construction industry. This research investigates the use of jute fibers to assess their suitability as reinforcing materials in cementitious composites for historic/ existing masonry structures retrofitting. As a matter of fact, these applications have to consider the possible low durability of jute, like all other cellulose-based fibers, especially into alkaline environments. This work reports the ongoing experimental investigation to set the mechanical performance of jute fibers. The experimental program considers jute yarns in their natural condition and evaluates how the alkaline matrices would affect the fiber mechanical properties. The paper summarizes the first results obtained from durability tests on jute yarns as a first step towards the assessment of the long-term performance of Natural Fiber Reinforced Cementitious Composites.

C. B. de Carvalho Bello (✉) · A. Cecchi
Università IUAV Di Venezia, Venice, Italy
e-mail: decarvalho@iuav.it

L. Ferrara
Politecnico Di Milano, Milan, Italy

1 Introduction

Jute fibers can be combined with polymers or mortar-based matrices to obtain several composites. In the civil engineering field, they represent an alternative to replace synthetic fibers, to obtain low cost, renewable and biodegradable composites [1, 2].

Jute fiber composites have several potentials and applications for structural purpose, being used as an eco-sustainable alternative to:

– Structural reinforcements used into the NFRC (Natural Fibers Reinforced Cementitious), FRCM (Fiber Reinforced Contentious Mortars), TRM (Textile Reinforced Mortars), FRP (Fiber Reinforced Polymers);
– Bio-concrete, an innovative concrete reinforced with natural fibers, in alternative to reinforcements with asbestos fibers;
– Fiber reinforced self-healing mortar, due to self-healing stimulating capacity of vegetal fibers [3];
– Pultruded structural elements.

Furthermore, jute fiber composites in the civil engineering has several advantages, including, e.g.:

– Carbon footprint reduction, with low emission of CO_2 in atmosphere and low energy consumption during their processing.
– Compatibility with existing masonry structures, when combined with cementitious mortar;
– Improved sustainability, toughness, ductility, flexural capacity and crack resistance of cementitious composites in which jute fibers are used as reinforcement [4–6].
– Lower hazard manufacturing processes, since they are non-abrasive to the equipment and do not cause irritations to human beings.

Despite all the aforementioned advantages, natural fiber composite materials present many limitations and the use of cement-based composites reinforced with jute and others vegetal fibers as a construction material is limited mainly due to the long-term durability of fibers in the alkaline environment. Previous studies indicate that mechanical proprieties of vegetal fibers are strongly reduced in alkaline conditions [7–9]. Considering the material alkali sensitivity, many researchers are investigating strategies to improve durability of plant fibers in cement-based matrices [10, 11], also proposing different treatments to this purpose [12].

In this paper the first results are presented of experimental tests on the mechanical properties of jute yarns immersed in three different alkaline environments and evaluated at progressive time steps: 7, 15, 30, 60 days. The evolution of the mechanical behavior of the jute fibers is meant as the basis to define their durability properties as well as those of cement-based matrices in which they are employed as reinforcement.

2   Materials and Methods

2.1   Specimens

Corchorus is a genus of about 100 species that grows in wet and warm climates (Bangladesh, India, China, Nepal, Uzbekistan, South Sudan, Zimbabwe, Egypt, Brazil and Vetnam). Tossa Jute (Corchorus Olitorius) is one of the mains jute types [13].

Tossa is softer, silkier and stronger than white jute (Corchorus Capsularis). This study considers jute yarns of Tossa fibers from Brazil (Fig. 1), formed with several twisted filaments with linear density about 920 Tex, used as samples 1000 mm long. Physical characterization on each specimen, as mass determination and measurements, was performed.

2.2   Conditioning Solutions

Three different solutions, that simulates the alkaline conditions of most used cement based matrices were considered:

- Carbonated concrete, that contains only calcium hydroxides with pH 10.0, called *Environment 1*;
- Lime mortar, that contains only calcium hydroxides with pH 12.5, called *Environment 2*;

Fig. 1 Jute yarn

Table 1 Environments chemical composition

Environment	Ca(OH)$_2$ (%)	KOH (%)	NaOH (%)	pH
1 Carbonated concrete	0.003	0	0	10
2 Lime mortar	0.16	0	0	12.5
3 Concrete	0.16	1.4	1	13

– Concrete environment, that contains calcium, sodium and potassium hydroxides with pH 13.0, called *Environment 3*;

Table 1 shows the environments chemical composition.

2.3 Mechanical Tests

Mechanical tests were performed on both dry (unconditioned) and conditioned yarns (Fig. 2); tests were carried out at room temperature using a universal testing machine, with a load cell of 1 KN and with displacement control at a rate of 0.5 mm/sec, in accordance with the ISO 2062:2009 standard [14].

Fig. 2 Test set-up

Tensile strength of jute yarn is measured at their natural condition and at progressive time steps: 7, 15, 30, 60 days exposure in the aforementioned conditioning environments.

3   Results and Discussions

The yarns failure mode results in accordance with yarns morphology and geometry. A progressive rupture of each yarn characterizes the fibers failure mode. The following Figs. 3, 4 and 5 and Tables 2, 3 and 4 show the tensile test results for the three environments considered and refers to the average rupture force obtained in the experimental tests, with the respective standard deviation.

In Environment 1 (carbonated concrete) Jute yarns lose about 15% of their initial rupture force after 7 days of immersion and 20% after 15 days.
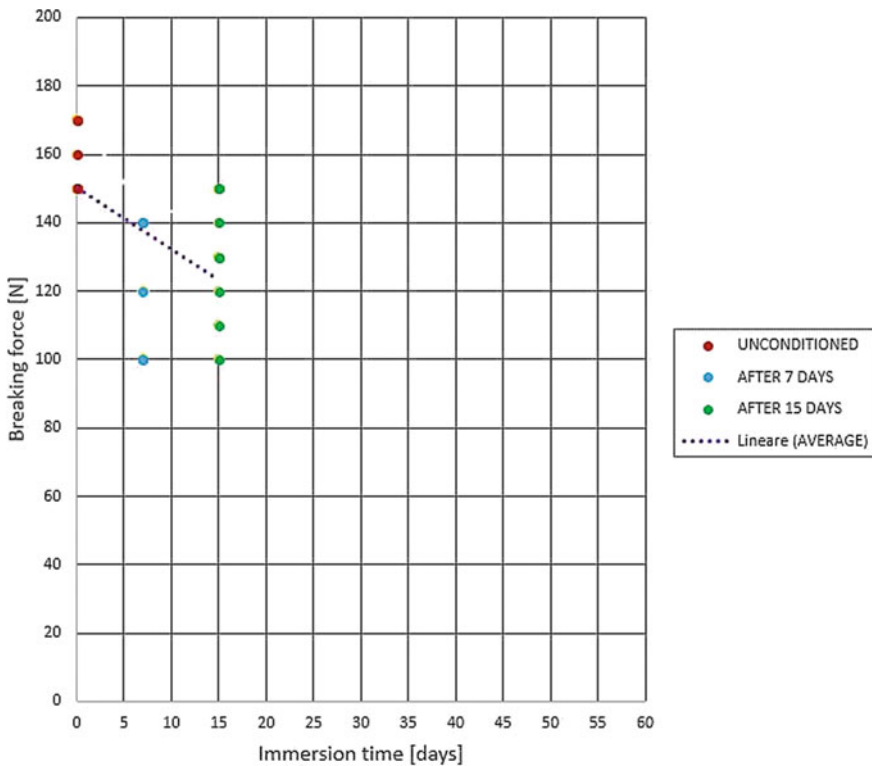

Fig. 3 Environment 1: tensile test results
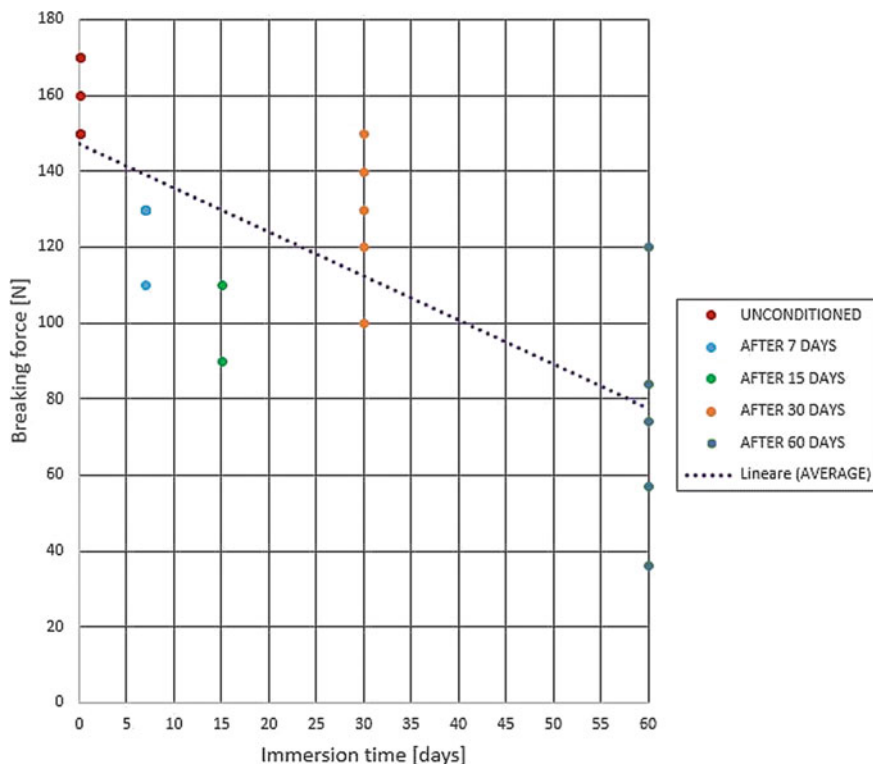
Fig. 4 Environment 2: tensile test results

In Environment 2 (lime solution) Jute yarns lose about 21% of their initial rupture force after 7 days of immersion and 37% after 15 days, 20% after 30 days and almost 54% after 60 days.

In environment 3 (concrete) Jute yarns lose about 30% of their initial breaking force after 7 days of immersion and 37% after 15 days (Fig. 5).

The results of environment 1 show that the carbonated solution is the least aggressive condition and environment 3, the "concrete solution", is the most aggressive one for the tested jute fibers.

With reference to environment 2 (lime mortar), tests performed up to 60 days have revealed a peculiar trend: the mechanical properties decreased during the first 15 days, then featured a moderate recovery up to one month, to undergo a further and more important decay in the longer term. This behaviour is related to the sodium hydroxide concentration in the tested solution, which may likely have produced the observed behaviour. As a matter of fact it is known that plant fibres immersed in a low concentrated sodium hydroxide solution (4 to 8%) can in the short period undergo some increase in the fibre mechanical properties. This procedures, also known as mercerization, has been investigated by several authors, in
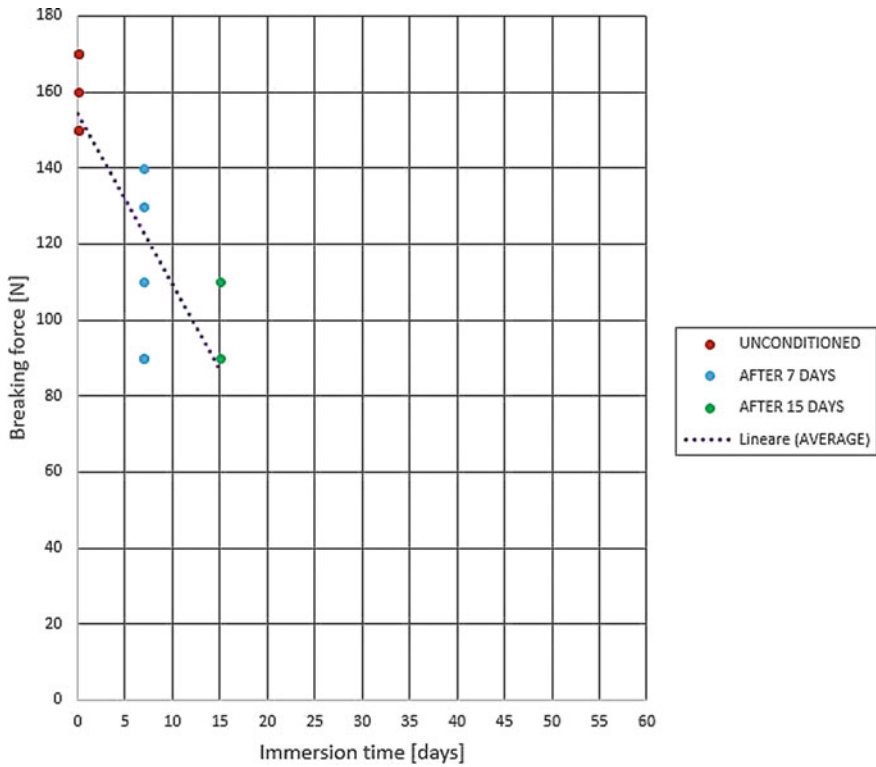
Fig. 5 Environment 3: tensile test results

Table 2 Jute yarns into environment 1

Time	Breaking force (N)	Residual strength (%)
Unconditioned	160 [±7.89]	100
7 days	120 [±21.28]	75
15 days	129 [±16.46]	80

Table 3 Jute yarns into environmental 2

Time	Breaking force [N]	Residual strength (%)
Unconditioned	160 [±7.89]	100
7 days	126 [±7.87]	79
15 days	100 [±16.57]	63
30 days	128 [±19.61]	80
60 days	74 [±31.64]	46

Table 4 Jute yarns into environmental 3

Time	Breaking force (N)	Residual strength (%)
Unconditioned	160 [±7.89]	100
7 days	112 [±21.04]	70
15 days	100 [±16.65]	63
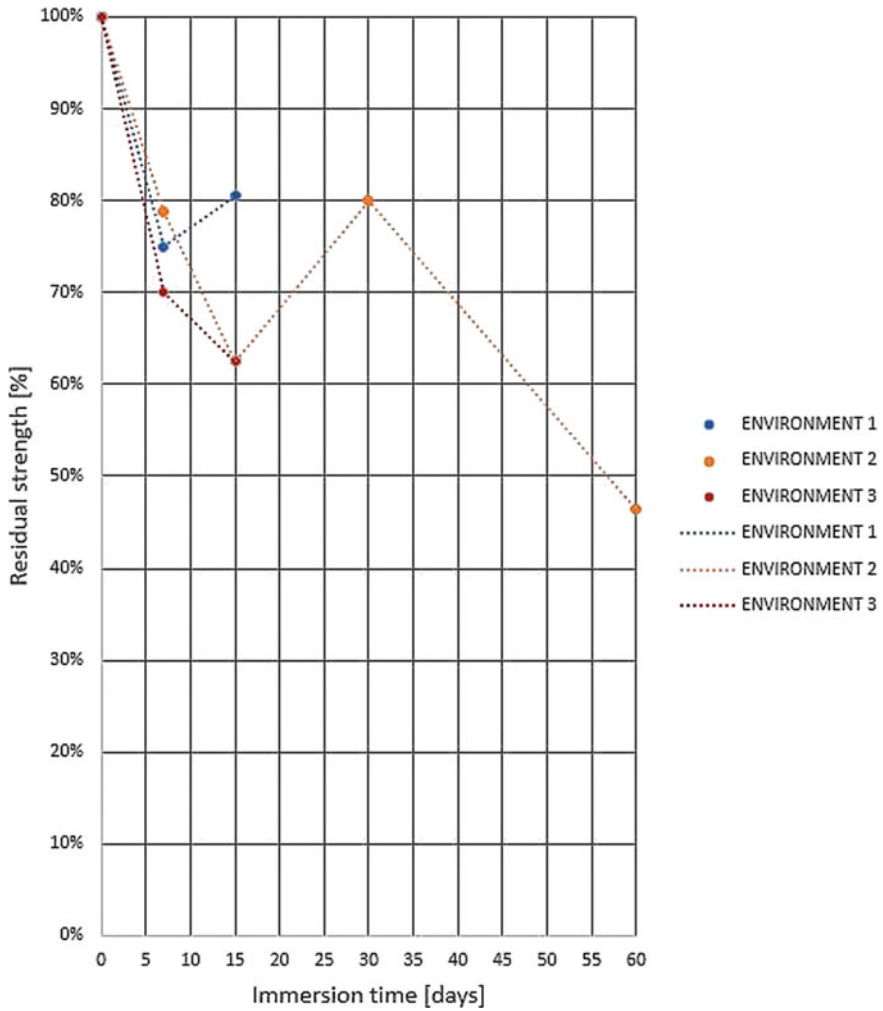
Fig. 6 Average values of jute yarns durability tests

search of the appropriate exposure time and alkali concentration to treat the fibers [15]. Jute loses 20% of its strength in the first 7 days but, considering further loss up to 15 days and recovery up to 1 month, it can be said that up to 1 month the performance yields constant.

The results presented constitute the first step of a work in progress and further experimentation is needed. For their application in civil engineering filed special attention should be given when combined with cement-based matrix.

References

1. Ticoalu A., Aravinthan T., Cardona F.: A review of current development in natural fiber composites for structural and infrastructure applications. In: Southern Region Engineering Conference (SREC 2010), pp. 10–12. Australia (2010)
2. Begum, K., Islam, M.A.: Natural fiber as a substitute to synthetic fiber in polymer composites: a review. Res J Eng Sci **2**(3), 46–53 (2013)
3. Ferrara, L., Ferreira, A.R., Krelani, V., Silva, F., Toledo Filho, R.D.: Effect of natural fibres on the self healing capacity of high performance fibre reinforced cementitious composites, In: Proceedings of shcc Rilem 3rd International RILEM Conference on Strain Hardening Cementitious Composites, pp. 9–16. RILEM Publications S.A.R.L., Netherlands (2014)
4. Toledo Filho R. D., Ghavami K., England G. L: Scrivener K. Development of vegetable fibre-mortar composites of improved durability. Cem. Concr. Compos. **25**, 185–96 (2003).
5. Ardanuy, M., Claramunt, J., García-Hortal, J.A., Barra, M.: Fiber-matrix interactions in cement mortar composites reinforced with cellulosic fibers. Cellulose **18**, 281–289 (2011)
6. Toledo Filho, R.D., Scrivener, K., England, G.L.: Ghavami Kbility of alkali sensitive sisal and coconut fibres in cement mortar composites. Cem. Concr. Compos. **22** (2000)
7. de Carvalho Bello, C.B., Cecchi, A.: Experiments on natural fibers: durability and mechanical properties. Adv Mater Process Technol **3**(4), 632–639 (2017)
8. Roma, L.C., Martello, L.S., Savastano, H.: Evaluation of mechanical, physical and thermal performance of cement-based tiles reinforced with vegetable fibers. Constr. Build Mater. **22**, 668–674 (2008)
9. Bergstrom, S.G., Gram, H.E.: Durability of alkali-sensitive fibres in concrete. Int. J. Cement Compos. Lightweight Concr. **6**(2), 75–80 (1984)
10. Hashim, M.Y., Roslan, M.N., Amin, A.M., Zaidi, A.M.A., Ariffin, S.: Mercerization treatment parameter effect on natural fiber reinforced polymer matrix composite: A brief review. World Acad. Sci. Eng. Technol. **6**, 1382–1388 (2012)
11. Santosa, S.F., Tonolib, G.H.D., Mejiac, J.E.B., Fiorellic, J., Savastano, H.: Non-conventional cement-based composites reinforced with vegetal fibers: A review of strategies to improve durability. Materiales de Construccion **65**(317) (2015)
12. Fidelis, M.A., Silva, F.A., Toledo Filho, R.D.: The influence of fiber treatment on the mechanical behavior of Jute textile reinforced concrete. Key Eng. Mater. **600**, 469–474 (2014)

13. Misnon, M.I., Islam, M.M., Epaarachchi, G.A.., Lau, K.T.: Potentiality of utilising natural textile materials for engineering composites applications. Mater Design **59**, 359–368 (2014)
14. ISO 2062:2009: Textiles—Yarns from Packages—Determination of Singleeneakig Force and Elongation at Break ung constt Rate Extension (CRE) tester (2009)
15. Kalia, S., Kaith, B.S., Kaur, I.: Pretreatments of natural fibers and their application as reinforcing material in polymer composites: A review. Polymer Eng. Sci. **49**, 1253–1272 (2009)

Long-Term Capillary Imbibition of Mortars with Slag and Fly Ash

Natalia Alderete [ID], **Yury A. Villagrán-Zaccardi** [ID], and **Nele De Belie** [ID]

Abstract Short-term capillary imbibition (or absorption) tests are practical and provide useful information about the performance of cementitious materials. Most of these tests are performed for a short period (<1 week), however, if the test continues for a longer period there is still liquid ingress. This further ingress of liquid is believed to be related to moisture diffusion inside the sample during long-term measurements. Such process occurs at a much slower rate than the short-term capillary imbibition. This paper describes the effect of supplementary cementitious materials (SCMs) on long-term capillary imbibition tests and presents the application of an earlier developed approach that relates the water uptake to $t^{0.25}$ for long-term measurements. To assess the whole capillary imbibition phenomenon, long-term measurements were performed for 10 weeks in mortar mixes with and without SCMs. Cement was partially replaced by ground granulated blast-furnace slag (SB) and fly ash (FA). The advance of the capillary rise was restricted much more in mixes with FA or SB than in the OPC mix. As these samples were tested at 360 days, this led to a more refined microstructure in the SB and FA mixes in comparison with the OPC mix. The decrease of water uptake with time occurred in all mixes and it can be explained by the changing hydraulic diffusivity in cementitious materials due to their hygroscopic behaviour. Long-term measurements reveal primary and secondary periods of capillary imbibition that are well described by a bi-linear relationship with the fourth root of time.

Keywords Capillary imbibition · Sorptivity · Mortar mixes · Supplementary cementitious materiales

N. Alderete (✉) · Y. A. Villagrán-Zaccardi · N. De Belie
Ghent University, Technologiepark Zwijnaarde 60, Campus Ardoyen, B-9052 Gent, Belgium
e-mail: nataliamariel.alderete@ugent.be

Y. A. Villagrán-Zaccardi
LEMIT—CONICET, 52 Entre 121 y 122 S/n, 1900 La Plata, Argentina

1   Introduction

One common transport mechanism to describe the durability of cementitious materials is by means of capillary water ingress. The rate of water uptake, sorptivity, can be useful to describe the pore connectivity of cementitious materials. This parameter is obtained from standardised experiments and has been used to predict the performance of concrete when exposed to potentially aggressive environments. Still, the analysis of results of laboratory tests is not always accurate and complete.

Laboratory experiments are typically performed by short-term assessments of water uptake of preconditioned samples. This preconditioning normally consists of drying and waterproofing the lateral faces of the samples. Then, the bottom flat face is put in contact with water, barely immersed over (3 ± 1) mm. The amount of water uptake is calculated as the weight gain per unit surface area and it is related to the time elapsed from the start of the contact with water. In cementitious materials, the common relation with the square root of time faces the significant difficulty of the lack of linearity of the relationship between water uptake and $t^{0.5}$. This is known in the literature as the anomalous behaviour of cementitious materials [1–4].

The anomalous behaviour during short term experiments and the traditional analysis method in function of the square root of time has been extensively discussed in [3]. Villagrán et al. [3] developed a new approach and validated it with literature and own experimental data. Capillary imbibition in cementitious materials is described in the short term with the fourth root of time, considering swelling of the C–S–H gel as main cause for the anomalous behaviour. The hygroscopic nature of the C–S–H causes it to swell during water uptake and this leads to deformations under internal restriction in the whole sample. Furthermore, physical evidence of swelling in connection with imbibition was presented in [5], where the volumetric stability of mortar and concrete samples was registered using strain gauges. Based on the general sub-diffusion model, as presented by Su [6], a process connected with a variable hydraulic diffusivity of the material in relation to moisture content, was found to be the most appropriate explanation to describe the deviation from the $t^{0.5}$ law in the short term. The registered deformations measured by Alderete et al. [5] during capillary imbibition were dependent on the moisture content as it advanced in height. Such findings give support to the fourth root approach for short-term imbibition, since the consideration of a varying tortuosity affecting the transport process means considering a hydraulic diffusivity varying with moisture content. As mentioned in [5], the affinity of the C–S–H with water results in swelling and gives origin to the designation of 'imbibition' as the process causing water uptake due to capillary potential in unsaturated cementitious materials. The implication of swelling seems more inherent to this description than if the term absorption is applied.

The new question that arises is what happens in long-term measurements. Prolonged exposure of samples has shown that water uptake further continues at a very low rate even after the capillary rise has covered the total height of the

samples. Then, the water ingress into the cementitious matrix can be divided in two periods: one initial or primary imbibition period ruled by capillary forces, and a secondary period in which diffusion could be the driving phenomenon. Most of the literature focuses on the primary period of capillary imbibition. However, additional water uptake occurring after the water front has covered the total height of samples, has been documented by several researchers [7–11]. This process progresses at a much slower rate than the short-term capillary imbibition, and it may be related to a secondary process that involves the finest range of pores. Hall [12] indicated an unavoidable need of experimental data for long term imbibition in order to validate newly constructed transport models. A deep analysis of the long-term capillary imbibition in cementitious materials was done in [13], however, the particular effect of supplementary cementitious materials (SCMs) on the secondary imbibition deserves more examination. The influence of SCMs is particularly interesting as they produce additional C–S–H during the pozzolanic action, and this may intensify the effect of swelling during the imbibition. Moreover, additional volume of gel pores are formed, with some potential contribution to the transport by diffusion during long term experiments.

To contribute to the description of the effect of the SCMs, long-term capillary imbibition experiments were performed. For that purpose, capillary imbibition tests were conducted for 10 weeks on mortar mixes with and without SCMS. Two SCMs, ground granulated blast-furnace slag (SB) and fly ash (FA), were used at different replacement levels. The impact of the cement replacement by the SCMs on the primary and secondary imbibition period is discussed.

2 Materials and Methods

2.1 Characterization of the Studied SCMs

Table 1 displays the chemical composition, density and size parameters of the OPC (type CEM I 42.5 N), SB, and FA used. Laser diffractometry was used to determine the particle size parameters (dv10, dv 50 and dv90). The optimal optical parameters considered in the analysis were chosen as suggested in [14].

The reactivity of the SCMs used was evaluated by means of the modified Chapelle test, isothermal calorimetry in pastes and compressive strength in mortars. Compressive strength was measured on prismatic samples of 40 mm × 40 mm 160 mm (NBN EN 196–1, 2016). A minimum of three samples were tested for each mix. Tests were performed at 28 and 90 days. The relative compressive strength of the mortar mixes was calculated considering the result of the OPC mortar at 28 days as reference. The compressive strength of OPC mortar was 52 MPa and 55 MPa at 28 and 90 days, respectively. The modified version of the Chappelle test was conducted according to French standard NF P18-513:2012. The hydration heat of the SCMs was monitored by isothermal calorimetry in pastes.

Table 1 Chemical composition, density and size parameters of OPC, SB, and FA

Properties	OPC				SB				FA			
Chemical composition (%)	CaO	64.67	S	nd	CaO	38.34	S	1.4	CaO	3.02	S	nd
	SiO$_2$	20.74	Fe$_2$O$_3$	1.52	SiO$_2$	33.7	Fe$_2$O$_3$	0.43	SiO$_2$	54.19	Fe$_2$O$_3$	7.92
	MgO	0.95	K$_2$O	0.77	MgO	8.18	K$_2$O	0.34	MgO	1.92	K$_2$O	3.38
	Al$_2$O$_3$	4.91	MnO	nd	Al$_2$O$_3$	11.36	MnO	8.18	Al$_2$O$_3$	23.5	MnO	nd
	Na$_2$O	0.27	Cl$^-$	0.07	Na$_2$O	0.35	Cl$^-$	0.01	Na$_2$O	0.39	Cl$^-$	<0.01
	SO$_3$	2.96	LOI	nd	SO$_3$	0.03	LOI	0.16	SO$_3$	0.94	LOI	1.84
Density (g/cm^3)	3.11				2.88				2.14			
Particle size dv10/50/90 (μm)	4.9/20.1/58.5				1.8/13.9/35.0				0.4/10/61.7			

nd not determined, *LOI* loss on ignition

These pastes were produced with the same amount of replacement (20, 40 and 60% wt.) of cement by SCMs to compare the results.

2.2 Mortar Mixes and Samples for the Long-Term Capillary Imbibition Tests

Seven mortar mixes were prepared: a mortar mix with only OPC, and another six mixes with 3 cement replacement ratios for each studied SCM: 20, 40, and 60% for SB, and 20, 30 and 40% for FA. The nomenclature of the mixes with SCM includes the abbreviation of the SCM used followed by the weight percentage of cement replacement. The tested mortar mixes had a water-to-binder ratio (w/b) of 0.45 and a sand-to-binder ratio (s/b) of 3. Normalized siliceous sand and tap water were used in all mixes.

Samples for sorptivity tests were cured in a conditioned room at 20 °C $\pm$ 2 °C and 95% $\pm$ 5% RH for 90 days and then they were cut. Next, they were taken back to the same conditioned room until 360 days of age and conditioned for testing. The tested samples consisted in cylinders of 50 mm in diameter and height, with the testing face being sawed for convenient avoidance of skin and mould effects.

At least three samples for each mix were tested. Samples were laterally covered with aluminum-butyl tape to ensure one dimensional flow. The preconditioning procedure consisted in 72 h immersion in water and then drying in an oven at 50 °C until mass decrease was lower than a mass fraction of 0.1% within 24 h. The capillary imbibition test consisted in putting the samples in contact with water, with an immersion depth of their bottom face of (3 $\pm$ 1) mm. Water evaporation was avoided by putting a lid on top of the water container (Fig. 1). The water level was checked regularly and the immersion depth was kept at (3 $\pm$ 1) mm during the whole testing period.

Long-term capillary imbibition tests were performed for 10 weeks. Measurements were performed after exposure periods of 0.5, 1, 2, 3, 4, 5, 6, and 24 h and after that every 24 h during the first week, and then once a week.
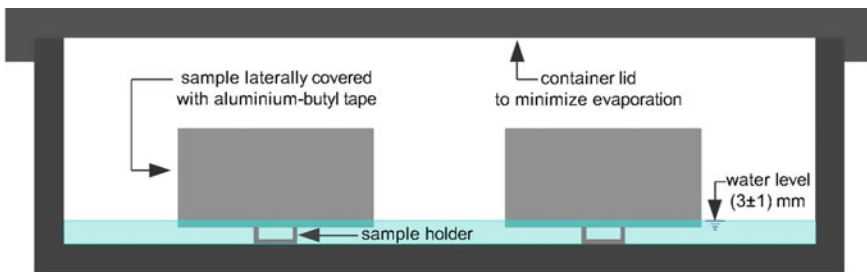

Fig. 1 Capillary imbibition set-up

3   Results and Discussions

3.1   *Reactivity of the Studied SCMs*

From the modified Chapelle test, portlandite consumption values of 1000 and 1800 (mg Ca(OH)$_2$/g SCM) were found for SB and FA, respectively. As SB is latent hydraulic, it does not consume calcium hydroxide to the same extent as FA, however, this does not mean that SB is not as reactive. In the latent hydraulic reaction, calcium hydroxide rather functions as an activator. The (modified) Chapelle test provides information about the calcium hydroxide consumption, which is most valuable for pozzolans such as FA, rather than slags.

Figure 2 shows the heat production during the first week of hydration of the tested pastes expressed per gram of binder. The same amount of SCM was replaced in each case to be able to compare the results. The curve of the OPC paste is shown in both graphs as reference. All curves reflect that increasing SCM content in the paste composition leads to a heat reduction (per gram of binder). This decrease is more pronounced in the case of FA than SB, which indicates that SB is more hydraulically reactive than FA.

The compressive strength was evaluated in the same mortar mixes used for the capillary imbibition test (SB20, SB40, SB60, FA20, FA30 and FA40). Figure 3 shows the relative compressive strength of all mixes at 28 and 90 days. Results indicate that SB40 and SB60 had the same or even better performance than the OPC mortar, only the SB20 mix had a slightly lower compressive strength at 28 days. However, at 90 days, all mixes with SB had a higher compressive strength than the OPC mix at 90 days. In the case of FA mixes, the dilution effect seems to be dominant at 28 days. Similar results, i.e. compressive strength decrease with an increase in the replacement of fly ash, have been found by Chindaprasirt et al. [15] with 20 and 40% of cement replacement by fly ash. At 90 days, when the hydration
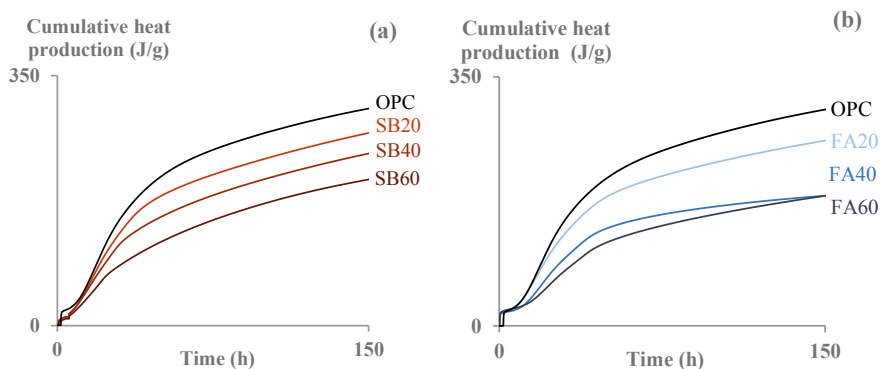

Fig. 2 Cumulative heat evolution of pastes (in J/g binder) with different amount of SB (**a**), and FA (**b**). The evolution of the paste without SCMs (OPC) is shown in both cases as reference

of FA particles has more time to develop, the mortar with 20% of FA had a similar performance to the OPC mortar. However, mixes with 30 and 40% of FA had lower compressive strength than the OPC mortar. Thus, based on the different experiments performed, it seems that SB is more reactive than FA, as seen in the calorimetry, and therefore higher compressive strength results are expected.

3.2 Long-Term Capillary Imbibition in Mortars

The evolution of the long-term capillary imbibition from the primary to the secondary period is shown in Figs. 4, 5 and 6. There are two marked stages that can be related to the change in the main driving force, from capillarity to diffusion. The graphs display the capillary imbibition capacity (CIC) in mg/mm^2 on the vertical axis and the fourth root of time in s$^{0.25}$ on the horizontal axis. Error bars represent the standard deviation (n = 3). The slope of the fitting equations until 96 h represent the primary capillary imbibition rate (CIR$_{t96}$), then a 'shift' or crossover in the slope is observed after 96 h, followed by the secondary imbibition at reduced rate (sCIR$_{t96}$). The primary imbibition period (until the top face starts to show visible moisture content) takes place within the first 96 h. A transition period (highlighted in the graphs) is connecting the primary and secondary stages, during which the top face evolves from partially wet to totally wet state. The start of the secondary capillary imbibition period varies for some mixes. The corresponding coefficients of determination are shown in the graphs and they indicate an excellent agreement (values > 0.98) with the fourth root of time approach for both primary and secondary periods.

Figure 4 shows the results of the OPC mortar mix. The 'shift' between the primary and the secondary period is marked for OPC samples when the samples showed presence of water on the top of the samples at 96 h. This conversion has been also found during the deformation measurements in [5]. After that shift, there is a decrease in the slope during the secondary period.
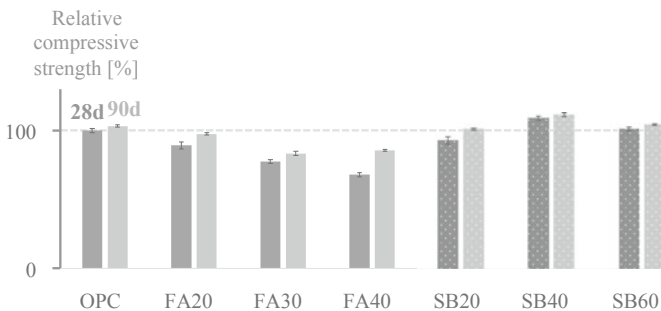

Fig. 3 Results at 28 and 90 days of the compressive strength of FA and SB mortars in relation to OPC mortar
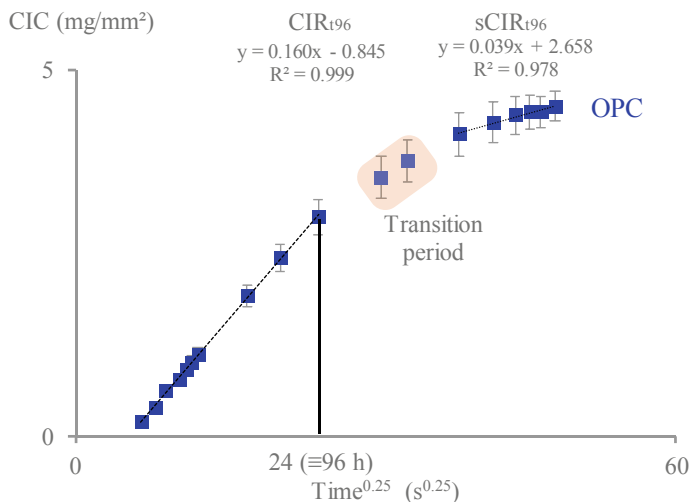
Fig. 4 Long-term capillary imbibition results of OPC mortar samples

Figures 5 and 6 display the results of the SB and FA mortar mixes, respectively. Samples from mortar mixes with SCMs, with a more complex pore structure, slow down the flow, and this is translated into a smaller CIR_{t96} and $sCIR_{t96}$ and a more gradual transition period. In the case of SB mixes, the change in the slope after 96 h ($\equiv 24$ $s^{0.25}$) is clearly less pronounced than for OPC mortars at all replacement levels. For FA mortar mixes, the change in the slope is also less pronounced than for OPC mortars, however with higher CIR values than SB mixes. This difference is related to the higher reactivity that SB has in comparison to FA, as described before.

In all cases, samples from mortar mixes with SCMs took longer time to have the top face totally wet. Hence, the secondary imbibition period started later in SB and FA mixes in comparison to OPC mixes. SCMs are known to increase the tortuosity of cementitious materials, which is translated into a longer 'effective' distance. Accordingly, results from OPC mortar indicate a higher value of the CIR_{t96} than the rest of the mixes, and the water flow can reach the top of the samples faster. As these samples were tested at 360 days, enough time was allowed to SCMs for reacting and developing the secondary reaction products, which lead to a more refined and tortuous microstructure in the SB and FA mixes in comparison with the OPC mix. In this sense, the primary coefficient seems to be more affected by the reactivity of each SCM than the secondary coefficient. Whereas the inclusion of SCMs reduced the CIR_{t96} (from 0.16 mg/mm^2/s$^{0.25}$ for OPC mortar to values between 0.099 to 0.077 and between 0.112 to 0.09 mg/mm^2/s$^{0.25}$ for SB and FA, respectively), it increased the $sCIR_{t96}$ (from 0.039 mg/mm^2/s$^{0.25}$ for OPC mortar to values between 0.058 to 0.051 and between 0.061 to 0.047 mg/mm^2/s$^{0.25}$ for SB and FA, respectively). The pozzolanic action that affects the capillary porosity does

Fig. 4 (continued)
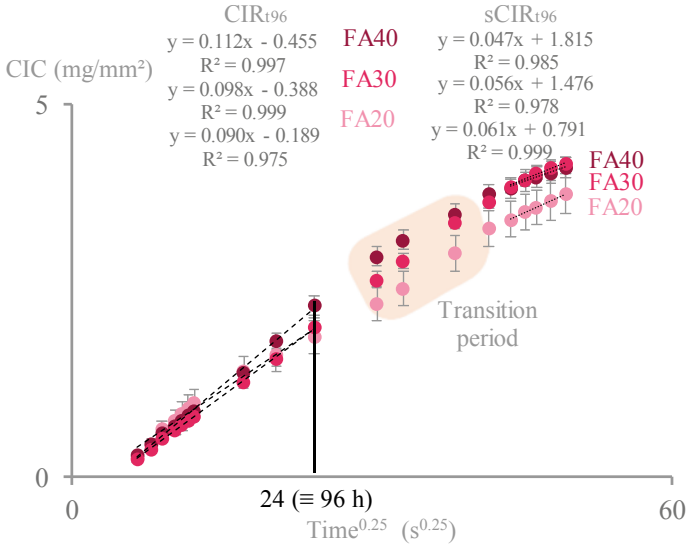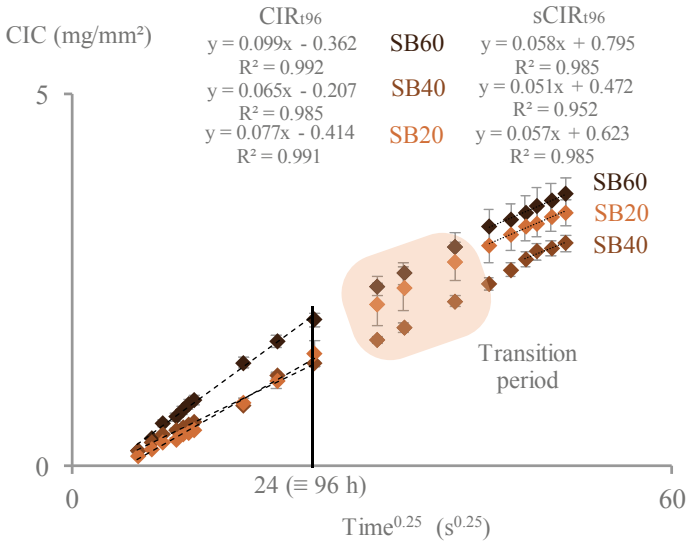

Fig. 5 Long-term capillary imbibition results of SB mortar samples

not have such a great impact on the smaller pore range size. Constrictions and tortuous paths hinder the advance of the capillary rise to a much higher extent in mixes with SB or FA than in the OPC mix, but this does not seem to influence the secondary imbibition period in the same manner. On the contrary, the secondary
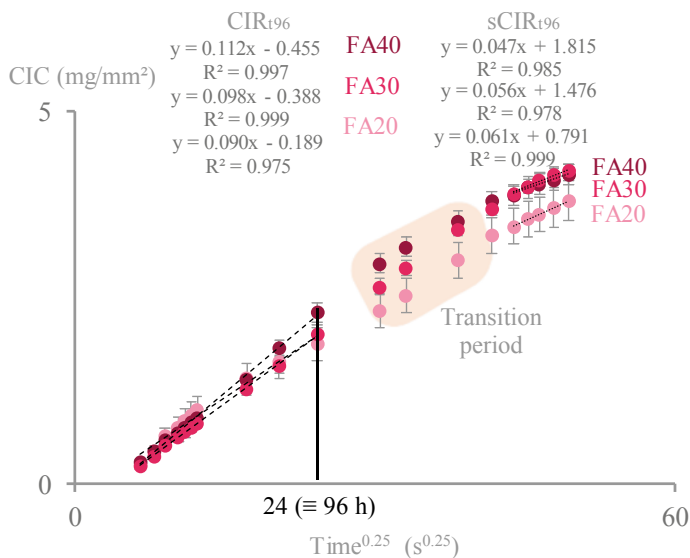
Fig. 6 Long-term capillary imbibition results of FA mortar samples

imbibition rate seems to increase. One-dimensional diffusion in the secondary stage can be considered the main explanation for delayed transport evolving with $t^{0.25}$. This secondary period is a process that happens at a much slower rate than the short-term capillary imbibition. This is probably related to the C–S–H content and not to the capillary porosity.

4   Conclusions

Data from long-term experiments of capillary imbibition applied on cementitious materials with and without SCMs showed two marked periods during water uptake. The trends observed from the results presented give support to the description of the long-term capillary imbibition phenomenon as a two-phase transport process.

Long-term capillary imbibition tests in mortar mixes revealed the existence of primary and secondary periods. Both periods display increasing water uptake proportional to $t^{0.25}$. Furthermore, mixes with SCMs had a more marked transition period and lower imbibition rate, which indicates a lower flow rate due to their increased tortuosity. The shape of the capillary imbibition curve further evidenced this.

Whereas replacing OPC by SCMs reduced the primary imbibition rate, it increased the secondary imbibition rate. Therefore, the reaction of SCMs seems to affect sorptivity by increasing the tortuosity of the pore structure and reducing the connectivity of capillary pores, but in the long term it increases the volume of fine pores (such as gel pores) through which single path transport takes place.

The long-term exposure of unsaturated samples involves additional water uptake after the capillary rise has covered the total height of samples. This is a process that occurs at a much slower rate than the short-term capillary imbibition, and it can be related to a secondary transport through the finest range of pores. The extensive empirical evidence makes the fourth root of time model very convenient for describing anomalous water absorption in cementitious materials.

References

1. Lockington, D.A., Parlange, J.-Y.: Anomalous water absorption in porous materials. J. Phys. D. Appl. Phys. **36**, 760–767 (2003)
2. Küntz, M., Lavallée, P.: Experimental evidence and theoretical analysis of anomalous diffusion during water infiltration in porous building materials. J. Phys. D. Appl. Phys. **34**, 2547–2554 (2001)
3. Villagrán Zaccardi, Y.A., Alderete, N.M., De Belie, N.: Improved model for capillary absorption in cementitious materials: Progress over the fourth root of time. Cem. Concr. Res. **100**, 153–165 (2017). https://doi.org/10.1016/j.cemconres.2017.07.003
4. Hall, C.: Anomalous diffusion in unsaturated flow: Fact or fiction? Cem. Concr. Res. **37**, 378–385 (2007). https://doi.org/10.1016/j.cemconres.2006.10.004
5. Alderete, N.M., Villagrán Zaccardi, Y.A., De Belie, N.: Physical evidence of swelling as the cause of anomalous capillary water uptake by cementitious materials. Cem. Concr. Res. **120**, 256–266 (2019). https://doi.org/10.1016/j.cemconres.2019.04.001
6. Su, N.: Equations of anomalous absorption onto swelling porous media. Mater. Lett. **63**, 2483–2485 (2009). https://doi.org/10.1016/j.matlet.2009.08.039
7. Kaufmann, J., Studer, W.: One-dimensional water transport in covercrete—application of non-destructive methods. Mater. Struct. **28**, 115–124 (1995)
8. Hall, C., Hoff, W.: Water transport in brick, stone and concrete, 2nd edn. CRC Press, Taylor and Francis Group, London, USA (2009). https://doi.org/10.1520/CCA10518J
9. Bentz, D.P., Ehlen, M.A, Ferraris, C.F., Garboczi, E.J.: Sorptivity-based service life predictions for concrete pavements. In: 7th International Conference of Concrete Pavements–Orlando, Florida, USA, Sept. 1, pp. 9–13 (2001)
10. Castro, J., Bentz, D., Weiss, J.: Effect of sample conditioning on the water absorption of concrete. Cem. Concr. Compos. **33**, 805–813 (2011). https://doi.org/10.1016/j.cemconcomp.2011.05.007
11. Spragg, R.P., Castro, J., Li, W., Pour-Ghaz, M., Huang, P.-T., Weiss, J.: Wetting and drying of concrete using aqueous solutions containing deicing salts. Cem. Concr. Compos. **33**, 535–542 (2011). https://doi.org/10.1016/J.CEMCONCOMP.2011.02.009
12. Hall, C.: Capillary imbibition in cement-based materials with time-dependent permeability. Cem. Concr. Res. **124** (2019). https://doi.org/10.1016/j.cemconres.2019.105835
13. Alderete, N.M., Villagrán Zaccardi, Y.A., De Belie, N.: Mechanism of long-term capillary water uptake in cementitious materials. Cem. Concr. Compos (2019). https://doi.org/10.1016/J.CEMCONCOMP.2019.103448
14. Alderete, N.M., Villagrán Zaccardi, Y.A., Dos santos Coelho, G.S., De Belie, N.: Particle size distribution and specific surface area of SCMs compared through experimental techniques. In: International RILEM Conference of Materials System and Structures of Civil Engineering, pp. 61–72 (2016)
15. Chindaprasirt, P., Jaturapitakkul, C., Sinsiri, T.: Effect of fly ash fineness on compressive strength and pore size of blended cement paste. Cem. Concr. Compos. **27**, 425–428 (2005). https://doi.org/10.1016/J.CEMCONCOMP.2004.07.003

Geopolymer Concrete Structures: Bond with Deformed Steel Bars

V. Romanazzi, M. Leone, M. Aiello, and M. R. Pecce

Abstract The promising performances showed by geopolymer concrete led several researchers to investigate about possibilities of using this material in reinforced structural elements. Since geopolymer binder has a different microstructure from Ordinary Portland Cement (OPC) it is necessary to investigate, also, on its bonding behavior with steel bar that as well-known influences the service and ultimate conditions. For this reason, in the last decades both direct pull-out and beam-end tests were carried out with this material. Generally, it has been observed that Geopolymer Concrete (GPC) has higher bond strength than OPC concrete due to the higher compression strength and the dense and compact microstructure of GPC. This means that the existing design equation for bond strength prediction of ordinary concrete can be conservatively used also for GPC. In this paper the bond-slip behavior between GPC and steel reinforcing bar with two different diameters has been investigated.

Keywords Bond strength · Geopolymer concrete · Steel bar

1 Introduction

The Ordinary Portland Cement (OPC) has been used for years as binding agent in concrete production process. Nowadays, it is estimated that more than 4 billion tonnes of cement are produced each year. Due to its chemical and thermal combustion processes, cement industry is responsible for the production of about 8% of the global carbon dioxide (CO_2) emissions [1]. In order to meet the need to control the global warming and reduce the CO_2 emissions to the environment, in the last years several research activities have been focused on finding new alternative

V. Romanazzi (✉) · M. Leone · M. Aiello
University of Salento, 73100 Lecce, LE, Italy
e-mail: vincenzo.romanazzi@unisalento.it

M. R. Pecce
University of Sannio, 82100 Benevento, BN, Italy

materials that can be used as binder in concrete production. Among the alternatives, geopolymer binder showed good bonding properties and allow to enhance the mechanical properties of concrete.

The production of Geopolymer Concrete (GPC) requires an aluminosilicate material that can be natural (e.g. kaolin or calcined clay) or derived from industrial waste (e.g. fly ash, ground granulated blast furnace slag (GGBFS) and silica fume). These materials provide a source of silicon and aluminum that are dissolved in an alkaline activating solution to polymerize into molecular chain and network and create the binder [2]. Compared to OPC production, the CO_2 emissions are reduced up to 80% since the activation process of geopolymer cement requires no heat. According to current research, GPC has considerable potential to be used in reinforced structural elements in place of OPC concrete [3–6].

One of the main parameters in reinforced concrete members design is the bond between steel bar and concrete matrix. Since geopolymer binder has a different microstructure from OPC, it is necessary to assess the bond behavior between GPC and deformed steel bar. For this reason, several direct pull-out tests and beam-end test has been carried out in order to study the bond-slip curve of reinforcing steel bar in GPC. Generally, it has been observed that GPC has higher bond strength than OPC concrete [7, 8]. Several authors observed also that during the direct pull-out test, the significant increase of the bond strength led to the yielding of the steel bar followed by concrete splitting failure [9, 10]. In particular, in most cases the splitting type failure of GPC resulted to be explosive and sudden denoting the brittle nature of the material [11–13].

In this paper, geopolymer concrete bond with deformed steel bars is analyzed through the standard RILEM direct pull-out test [14]. This test allows to define the bond-slip behavior for geopolymer concrete. The geopolymer binder used in this work is composed of only industrial by-products: silica fume and GGBFS. Direct pull-out tests were performed with two different steel bar diameters in order to analyze how this parameter affects the bond strength of GPC. At last, a direct comparison between experimental results and fib Model Code bond strength prevision [15] has been done. From this comparison it comes out that the fib Model Code equation for OPC concrete bond with ribbed steel bar can be conservatively used also for GPC. Moreover, analyzing the results it was observed that the bar diameter didn't affect significatively the bond strength.

2 Material

2.1 Mix Design

The GPC mix used in this work (Table 1) has been designed within a project that aims to develop sustainable and cost-efficient solutions for materials and encourage the use of recycled materials in construction industry. For this reason, the authors

Table 1 Geopolymer concrete recipe

Components	Quantity (kg/m^3)
GGBFS	224
Limestone and gypsum	128
Silica Fume	48
Ingessil (Activator solution)	170
Water	140
Additive (Plasticizer)	8
Sand	1092
Gravel	

reserve the right to omit all the mix design detail and focus only on the bond strength of this GPC mixture. The result of the mix design consists of a binder composed by: GGBFS (by-product of iron and steel-making); silica fume (by-product of the silicon and ferrosilicon alloy production) and filler powder with limestone and gypsum.

2.2 *Mechanical Properties*

The mechanical characterization carried on this GPC mixture included tests on compression (at different curing age), tensile and flexural strength, modulus of elasticity and the analysis of the constitutive behavior through compressive tests. The results are not here discussed while the main data are addressed according to the following.

The compression strength, evaluated according to UNI EN 12,390–3 [16] after 28 days of curing, resulted to be around 60 MPa, while the elastic modulus, estimated according to UNI EN 12,390–13 [17] was equal to 29,096 MPa. Since it was found a significant increase in compression strength after 28 days of curing, therefore it was necessary to assess the compression strength also at the same time of pull-out strength. Due to laboratory needs, the pull-out tests were performed 100 days after GPC casting and the cubic compression strength resulted to be equal to 77 MPa.

3 Direct Pull-Out Test

3.1 *Bond Strength Prevision*

According to the fib Model Code, the bond strength between OPC concrete and ribbed steel bar can be estimated from the average compressive strength of concrete as indicated in Eq. (1)

$$\tau_{b,\max} = 2.5 \cdot \sqrt{f_{cm}} \qquad\qquad (1)$$

in which $\tau_{b,\max}$ is the bond strength and f_{cm} is the average compressive strength. In order to compare this prevision with the experimental results of this work, in Table 2 is reported the ultimate bond strength value calculated according to Eq. (1) by using the average compressive strength of GPC obtained in the mechanical characterization.

Besides the indication of fib Model Code, Dahou et al. [18] proposed two new empirical models for GPC bond strength with ribbed steel bar, defined in Eqs. (2) and (3).

$$\tau_{U,GPC} = 3.83 \cdot \sqrt{f_c} \qquad\qquad (2)$$

$$\tau_{U,GPC} = 0.54 \cdot f_c \qquad\qquad (3)$$

According to [18], the model in Eq. (2) resulted to be more accurate and offered the advantage to be similar to fib model in Eq. (1). In particular, the constant parameter for GPC model is 53% greater than the fib model for OPC concrete, denoting that bond strength is higher in GPC than in OPC concrete. For these reasons, the results of bond strength prevision for the GPC mix used in this work according only Eq. (2) are reported in Table 2.

3.2 Test Setup

Direct pull-out tests were performed according to RILEM recommendations [14] in order to analyze the bond-slip behavior between GPC and reinforcing steel bar and

Table 2 Pull-out tests results

Steel bar diameter (mm)	Sample	Failure mode	$\tau_{b,\max}$ (MPa)	$\tau_{b,\max,av}$ (MPa)	fib MC 2010 (MPa)	Dahou et al. [18] (MPa)
φ12	GPC_P_12_1*	–	–	25.5 (3%)	21	30
	GPC_P_12_2	P	26.2			
	GPC_P_12_3	S	24.9			
	GPC_P_12_4	S	25.4			
φ16	GPC_P_16_1*	–	–	24.2 (3%)	21	30
	GPC_P_16_2	S	23.0			
	GPC_P_16_3	S	24.7			
	GPC_P_16_4	S	24.1			
	GPC_P_16_5	S	24.9			

P = bar Pull-out from concrete, S = concrete Splitting, Coefficient of variation (CoV) is indicated in brackets near average values
*These samples have not been considered since their behavior resulted to be largely out of range

the influence of the bar diameter on bond strength, taking into account also the bond strength prevision.

A total of 9 pull-out samples were casted with the GPC mixture described before: four with ϕ 12 mm embedded steel bar and five with ϕ 16 mm steel bar. The GPC specimens were cubic with side equal to 10ϕ and the bar was centered in order to have a concrete cover equal to 4, 5ϕ. In each sample a plastic sheet was applied so that the bonded zone in resulted equal to 5ϕ as indicated in [14]. Both ϕ12 mm and ϕ16 mm reinforcing bar were about 550 mm length and made of a grade B450C steel, largely used for structural elements in Italy. The direct pull-out tests setup is showed in Fig. 1.

The relative slip between the deformed steel bar and the GPC cube was measured by means of a LVDT (Linear Variable Displacement Transducer) anchored to the unloaded side of the steel bar. Other two LVDTs and a strain gauge have been positioned on the loaded side of the steel bar, as showed in Fig. 1. Therefore, the applied force and the deformation of the steel bar in the unbonded zone were recorded. The bond stress, τ_b, was estimated through the Eq. (4) under the hypothesis that the bond stress remains uniform within the bond length.

$$\tau_b = \frac{F}{\pi \cdot \phi \cdot L_b} \tag{4}$$
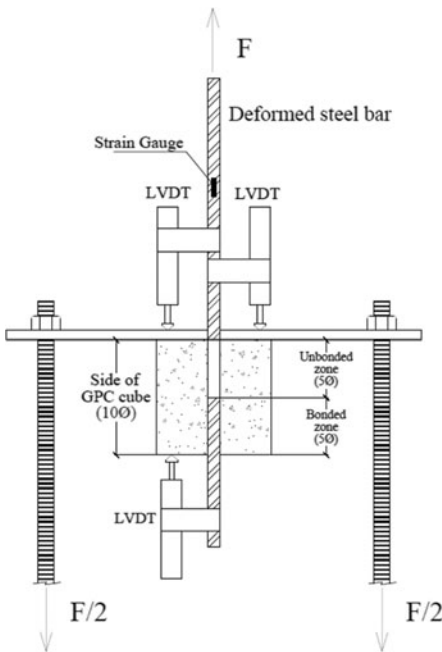
where L_b is the bonded length.

Fig. 1 Direct Pull-out test setup

3.3   Results

Bond-slip behavior of GPC with ϕ12 mm embedded steel bar is showed in Fig. 2 and the related ultimate bond strength values are reported in Table 2. In particular, the graphs of Fig. 2 has been obtained by using the relative slip between GPC and the steel bar measured with the LVDT positioned on the unloaded side of the bar. The average value of bond strength achieved by specimens with ϕ12 mm bar diameter resulted to be equal to 25.5 MPa with a low CoV value that underlines the effectiveness of the tests. In bond stress versus slip curves of both specimens GPC_P_12_2 and GPC_P_12_4 (Fig. 2) can be also distinguished the hardening stage of the steel bar after its yielding.

All the pull-out specimens with ϕ12 mm embedded steel bar exhibited a concrete splitting failure (Fig. 3a), except the sample GPC_P_12_2 whose steel bar was pulled out from the concrete matrix (Fig. 3b). Seen the brittle and sudden failure of samples GPC_P_12_2 and GPC_P_12_4, the descendant branch of their curves (dashed part of graphs in Fig. 2) has to be considered only from a qualitative point of view.

On the other hand, the bond-slip curves of GPC with ϕ16 mm embedded steel bar are showed in Fig. 4 and the related bond strength values in Table 2. In this case, the average bond strength of the four specimens is slightly lower, equal to 24.2 MPa (again CoV = 3%). As previously explain, the bond-slip curves in Fig. 4 have been obtained by using the relative slip measured from the LVDT positioned on the unloaded side of the bar, while the descendant branch (dashed part of curves), after concrete splitting failure, must be considered only qualitatively. In fact, all tested pull-out specimens with ϕ16 mm embedded steel bar showed off a concrete sudden and explosive splitting failure: the samples broke into two pieces
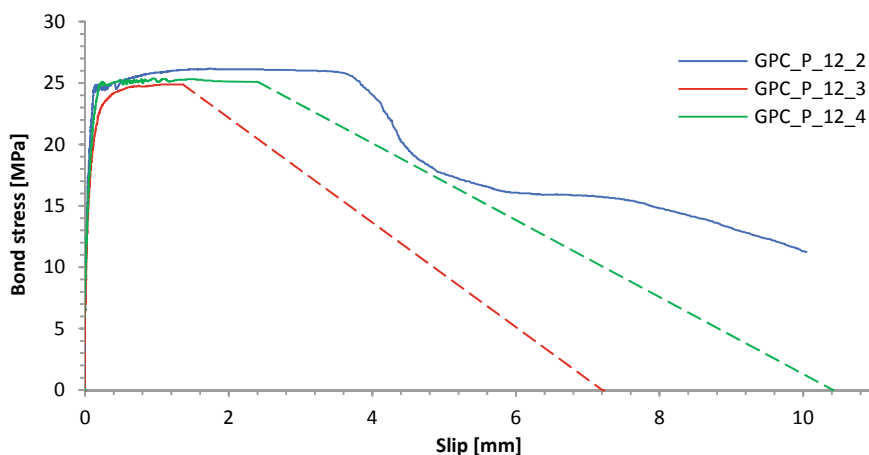
Fig. 2 Bond-slip behavior between GPC and 12 mm deformed steel bar
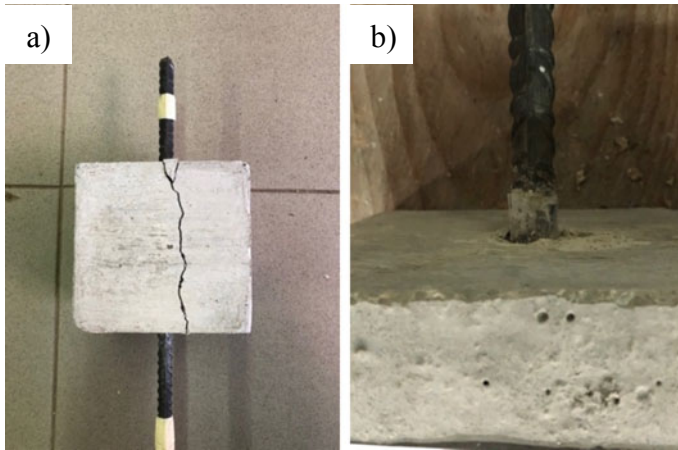
Fig. 3 **a** Concrete splitting failure and **b** pull-out failure after test
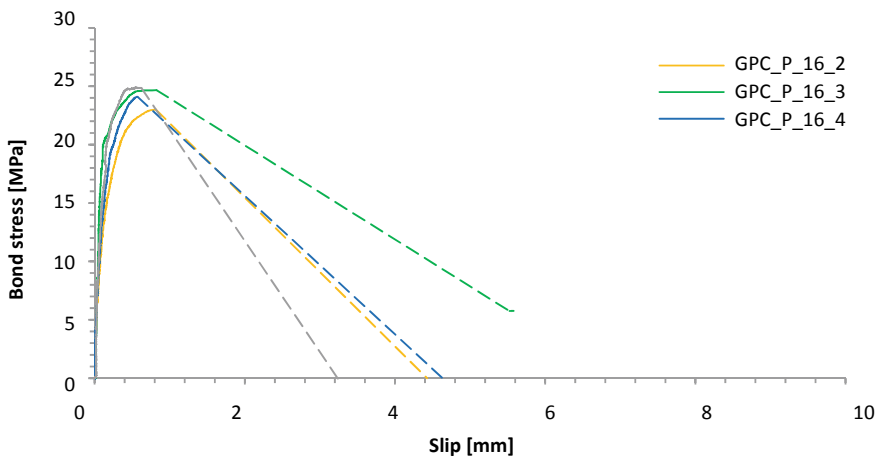
Fig. 4 Bond-slip behavior between GPC and 16 mm deformed steel bar

along the middle of a cube side falling off the test frame (Fig. 5). These observations confirm the brittle nature of GPC, as also observed in [11–13].

In the Fig. 6 the comparison between the specimens with different diameter is reported in terms of bond stress versus slip curves. The figures show as the bar diameter didn't affect the bond behavior: in fact, the curves are almost similar in the ascendant branch while no further consideration can be done in relation to the descendant part due to the brittle failure of the specimens. This observation is also confirmed also by the average bond strength reported in the Table 2.
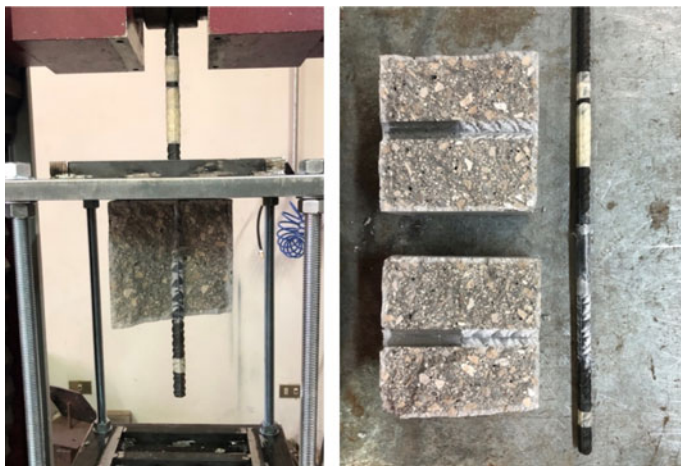
Fig. 5 Pull-out samples after concrete splitting failure of the sample GPC_P_16_2
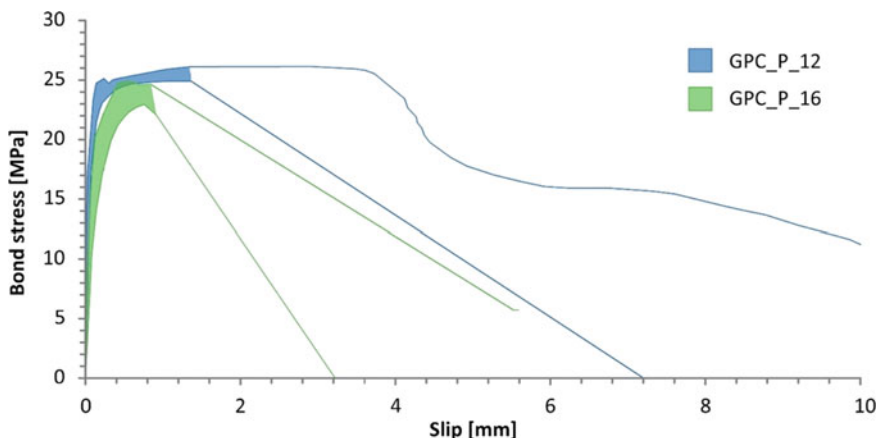
Fig. 6 Comparison between ϕ12 and ϕ16 mm steel bar

From a direct comparison between the experimental results and the bond strength prevision given by the fib Model Code (Eq. (1)) [15] reported in Table 2, it can be seen that the values obtained in this work are higher than those indicated by the standard. This means that the fib Model Code equation for OPC concrete bond with ribbed steel bar can be conservatively used also for GPC. Despite this, the experimental values obtained in this work are slightly lower in respect to the estimation given by Dahou et al. [18]. In particular, the difference between the two values resulted to be between 17 and 23%.

4 Conclusion

This paper analyzed the bond-slip behavior between GPC and deformed steel bar with two different diameters. In particular, this GPC mixture has been obtained by using GGBFS (by-product of iron and steel-making) and silica fume (by-product of the silicon and ferrosilicon alloy production). A total of 9 direct pull-out test were performed in order to assess the bond strength of GPC: four with ϕ12 mm embedded steel bar and five with ϕ16 mm embedded steel bar. The experimental results showed in this work led to the following conclusions:

- The variations observed between the two steel bar diameters in terms of bond stress versus slip behavior are negligible. Moreover, the bond strength between GPC and ϕ12 mm embedded steel bar resulted to be slightly higher than the bond strength of GPC with ϕ16 mm steel bar.
- According to the obtained results the bond strength prevision given by the fib Model Code can be conservatively used also for GPC. Moreover, the results showed in this work are lower than the value suggested by Dahou et al. for bond strength between GPC and steel bar.

References

1. Lehne, J., Preston, F.: Making concrete change innovation in low-carbon cement and concrete. Chatham House Rep. 1–122 (2018) https://doi.org/10.1088/1742-6596/1015/3/032163
2. Abdul Aleem, M.I., Arumairaj, P.D.: Geopolymer concrete—a review. Int. J. Eng. Sci. Emerg. Technol. **1**(2), 118–122 (2012) https://doi.org/10.7323/ijeset/v1
3. Singh, B., Ishwarya, G., Gupta, M., Bhattacharyya, S.K.: Geopolymer concrete: a review of some recent developments. Constr. Build. Mater. **85**, 78–90 (2015). https://doi.org/10.1016/j.conbuildmat.2015.03.036
4. Mo, K.H., Alengaram, U.J., Jumaat, M.Z.: Structural performance of reinforced geopolymer concrete members: a review. Constr. Build. Mater. **120**, 251–264 (2016). https://doi.org/10.1016/j.conbuildmat.2016.05.088
5. Ding, Y., Dai, J.G., Shi, C.J.: Mechanical properties of alkali-activated concrete: a state-of-the-art review. Constr. Build. Mater. **127**, 68–79 (2016). https://doi.org/10.1016/j.conbuildmat.2016.09.121
6. Ma, C.K., Awang, A.Z., Omar, W.: Structural and material performance of geopolymer concrete: a review. Constr. Build. Mater. **186**, 90–102 (2018). https://doi.org/10.1016/j.conbuildmat.2018.07.111
7. Sarker, P.: Bond strengths of geopolymer and cement concretes. Adv. Sci. Technol. **69**, 143–151 (2010). https://doi.org/10.4028/www.scientific.net/ast.69.143
8. Tekle, B.H., Khennane, A., Kayali, O.: Bond properties of glass fibre reinforced polymer bars with fly-ash based geopolymer concrete. In: 10th International Conference of Composite Science and Technology, October, pp. 1–8 (2015)
9. Fernández-Jiménez, A., Palomo, A.: Engineering properties of compacted fly ash. Aci Mater. J. (March 2006)

10. Castel, A., Foster, S.J.: Bond strength between blended slag and class F fly ash geopolymer concrete with steel reinforcement. Cem. Concr. Res. **72**, 48–53 (2015). https://doi.org/10.1016/j.cemconres.2015.02.016

11. Sofi, M., Van Deventer, J.S.J., Mendis, P.A., Lukey, G.C.: Bond performance of reinforcing bars in inorganic polymer concrete (IPC). J. Mater. Sci. **42**(9), 3107–3116 (2007). https://doi.org/10.1007/s10853-006-0534-5

12. Topark-Ngarm, P., Chindaprasirt, P., Sata, V.: Setting time, strength, and bond of high-calcium fly ash geopolymer concrete. J. Mater. Civ. Eng. **27**(7), 1–7 (2015). https://doi.org/10.1061/(ASCE)MT.1943-5533.0001157

13. Al-Azzawi, M., Yu, T., Hadi, M.N.S.: Factors affecting the bond strength between the fly ash-based geopolymer concrete and steel reinforcement. Structures **14**(January), 262–272 (2018). https://doi.org/10.1016/j.istruc.2018.03.010

14. RILEM TC: RC 6 Bond Test for Reinforcement Steel. 2. Pull-Out Test (1983)

15. CEB-FIP: Fib Model Code for Concrete Structures (2010)

16. UNI EN 12390–3: Testing Hardened Concrete—Part 3: Compressive Strength of Test Specimens, pp. 4–10 (2001)

17. UNI EN 12390–13: Testing Hardened Concrete—Part 13: Determination of Secant Modulus of Elasticity in compression (2013)

18. Dahou, Z., Castel, A., Noushini, A.: Prediction of the steel-concrete bond strength from the compressive strength of Portland cement and geopolymer concretes. Constr. Build. Mater. **119**, 329–342 (2016). https://doi.org/10.1016/j.conbuildmat.2016.05.002

10 Years of Research on Sugar Cane Bagasse Ash as Supplementary Cementitious Material

Guilherme C. Cordeiro, Romildo D. Toledo Filho, Eduardo M. R. Fairbairn, and Luis M. Tavares

Abstract We present a survey of 10 years of researches carried out by the Federal University of Rio de Janeiro (COPPE/UFRJ) and the State University of Northern Rio de Janeiro (UENF) on the use of sugar cane bagasse ash (SCBA) as supplementary cementitious material (SCM). The main findings of such comprehensive studies are here summarized: the use of SCBA for producing concrete; the role of grinding and calcination; the physical and chemical effects; the use of SCBA in industrial scale; blending of SCBA and rice husk ash (RHA); and long-term compressive behavior.

Keywords Supplementary cementitious materials · Pozzolans · Sugar cane bagasse ash · CO_2 emissions · Numerical modeling

1 Introduction

In the cement production, greenhouse gas (GHG) emissions come from both industrial process and fuel combustion. During the industrial process CO_2 is emitted due to the heating of limestone ($CaCO_3 \rightarrow CaO + CO_2$) to obtain calcium oxide (CaO), which is the main oxide in the OPC. To reduce emissions, several recommendations can be followed in the cement industry. Concerning the industrial process an alternative is the replacement of clinker by mineral additions that can also act as cementitious materials such as blast furnace slag and pozzolans.

G. C. Cordeiro
Universidade Estadual Norte Fluminense, Campos, Brazil
e-mail: gcc@uenf.br

R. D. Toledo Filho · E. M. R. Fairbairn (✉) · L. M. Tavares
Universidade Federal do Rio de Janeiro, Rio de Janeiro, Brazil
e-mail: eduardo@coc.ufrj.br

R. D. Toledo Filho
e-mail: toledo@coc.ufrj.br

L. M. Tavares
e-mail: tavares@metalmat.ufrj.br

The main pozzolans currently used in cement industry are fly ash, a by-product of coal-fired power plants, and silica fume, a by-product of metallurgical processes. Other pozzolans have also been used in a reduced scale, such as natural pozzolans and metakaolin. More recently, agro-industrial ashes such as rice husk and sugar cane bagasse ashes have been studied as potential replacement as cement.

Sugar cane bagasse ash (SCBA) is a by-product generated by burning bagasse in boilers of sugar and ethanol plants and consists mainly of silica (SiO_2). This characteristic can indicate the potential of SCBA for use as a mineral admixture in paste, mortar, and concrete because the silica is presented in a no crystalline or partially crystalline state. Since the late 90's studies had been carried out showing that SCBA presents adequate behaviour in blended-based cementitious materials [1–4].

Since the year of 2006 [5], a comprehensive study has been developed within the framework of joint research programs that involves researchers of the Federal University of Rio de Janeiro (COPPE/UFRJ) and the State University of Northern Rio de Janeiro (UENF). This study encompasses several aspects of the use of the SCBA produced in Brazil as substitute for clinker aiming to reduce GHG emissions. In this paper we present a survey of the main findings of this research campaign which includes experiments and numerical simulations.

2 Use of SCBA as Cement Replacement in Conventional and High-Performance Concretes

Until 2008, few papers had been published reporting the use of SCBA as cement replacement for application in concrete (see, for instance, [6]). In a paper of 2008 [7] we studied two types of concretes (conventional and high-performance) made with 0, 10, 15 and 20% of a residual sugar cane bagasse ash (SCBA) as cement replacement (in mass). In an early research [8], it had been stressed the importance of grinding the ash to improve its homogeneity and reactivity in mortars. Therefore, we used ultra-fine SCBA to produce the concretes.

The SCBA was collected during the boiler cleaning operation of a sugar and alcohol factory situated in the State of Rio de Janeiro, Brazil. In the factory, the bagasse was burnt in boilers at temperatures varying from 700 to 900 °C. The ashes were submitted to open circuit dry grinding using a vibratory mill for 120 min. Portland cement without mineral addition (similar to ASTM type I) was used in the experimental program. The chemical composition of SCBA and cement are shown in Table 1 and the concrete mixture proportions are shown in Table 2.

Table 1 Chemical composition (%) of SCBA and Portland cement (PC)

Material	SiO_2	Al_2O_3	Fe_2O_3	CaO	Na_2O	K_2O	MnO	TiO_2	MgO	P_2O_5	LOI*
SCBA	78.34	8.55	3.61	2.15	0.12	3.46	0.13	0.50	1.65	1.07	0.42
PC	20.85	4.23	5.25	63.49	0.16	0.40	–	–	–	–	1.05

*LOI, loss on ignition

Table 2 Mixture proportions (kg/m^3) of concretes

w/cm	Mixture	PC	SCBA	Fine agg.	Coarse agg.	Water	Superpl.
0.6	CC-Ref	365.9	–	724.7	1001.0	220.3	–
0.6	CC-SCBA-10	329.3	36.6	724.7	1001.0	220.3	–
0.6	CC-SCBA-15	311.0	54.9	724.7	1001.0	220.3	–
0.6	CC-SCBA-20	292.7	73.2	724.7	1001.0	220.3	–
0.35	HPC-Ref	478.0	–	860.0	905.3	167.4	1.43
0.35	HPC-SCBA-10	430.2	47.8	860.0	905.3	167.4	1.43
0.35	HPC-SCBA-15	406.3	71.7	860.0	905.3	167.4	1.43
0.35	HPC-SCBA-20	382.4	95.6	860.4	905.8	167.4	1.20

Figure 1 displays the evolution of compressive strength with time (7, 28, 90 and 180 days), together with typical stress–strain curves in compression at 28 days. For conventional concretes, the results at 7 and 28 days indicated that the SCBA mixtures presented compressive strength slightly lower than that of the CC-R. At 90 and 180 days of curing, the average compressive strength values of CC-SCBA-20 and CC-R did not present statistical differences. The CC-SCBA-10 and CC-SCBA-15 mixtures showed slightly lower compressive strengths than the CC-R; however, no differences were observed amongst them. The high-performance concretes showed a similar behaviour. In this case, there was no significant differences between the strength values of HPC-SCBA-10 and HPC-R, which are statistically equal after 7 days of curing. The other mixtures (HPC-SCBA-15 and HPC-SCBA-20) presented slightly lower values (about to 10%) of compressive strengths. For the curing time of 28, 90, and 180 days, the use of SCBA had no significant influence on the compressive strength of high-performance concretes. The values of Young's modulus presented only small changes when cement is replaced by SCBA. Its average value was 24.5 GPa for conventional concretes and 33.4 GPa for high-performance concretes. Slight variations have also been reported for the tensile strength that varied from 2.99 to 3.26 MPa for conventional concretes and from 4.99 to 5.57 MPa for high-performance concretes.
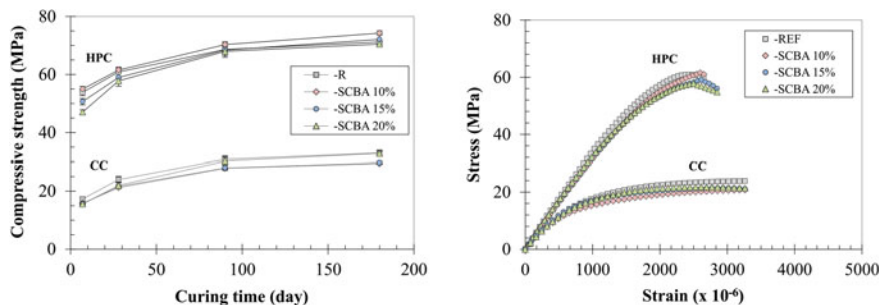

Fig. 1 Compressive strength (7, 28, 90 and 180 days) and stress–strain curves at 28 days

The main rheological characteristics of the concretes are displayed in Table 3. It can be observed that the plastic viscosity increased marginally due to incorporation of SCBA in concrete. However, the yield stresses always decreased when the SCBA is used, which suggests a positive effect of the ash in the concrete rheology.

In the rapid chloride permeability test, according to ASTM C1202-05 standard, the concrete containing SCBA presented best performance (see Fig. 2). The conventional concretes with SCBA presented "high" permeability, which was slightly lower than that of the reference concrete. The mineral admixture reduced the penetrability of high-performance concrete from "low" to "very low" classification.

The research reported in paper [8] indicated a great potential for the use of SCBA as partial replacement of cement. As Brazil is the world's largest producer of sugar cane, this mineral addition is particularly interesting for the reduction of GHG emissions due to the manufacture of cement.

3   The Role of Grinding and Calcination for Using Sugar Cane Bagasse Ash as Pozzolan

Grinding has a beneficial effect on grains that have pozzolanic potential, because of the controlled reduction in particle size and increase in specific surface area. Such increase in specific surface area is directly responsible for the kinetics of their pozzolanic reactions, which can be limited in the case of poorly reactive pozzolans. The use of pozzolans in the fine and ultrafine size ranges along with Portland cement can also allow reaching greater packing density of the mortar or cement mixture, due to the so-called microfiller effect [9]. The other physical effect that becomes potentially important with the reduction in particle size is the heterogeneous nucleation. In this case, pozzolan fine particles settle in between the clinker crystals, allowing a nucleation of hydrates on foreign fine particles by reducing the energy barrier [10].

In a paper published in 2009 [11], we studied the benefits that grinding can bring for the use of SCBA as cement replacement. The same ash whose chemical composition is described in Table 1 was grinded in several ways and the main characteristics of the produced particles were studied. Grinding tests were carried out in either open circuit or closed circuit, using tumbling mills with balls or short cylinders, a vibratory mill and a hammer mill, all operating in dry mode. In Fig. 3 we show the evolution of the particle size distribution for grinding ties varying from 8 to 240 min in a vibratory mill, as well as the relationship between D_{80} and pozzolanic activity index for the SCBAs, where the dotted line represents the minimum value that characterizes a material as pozzolanic according to the Brazilian standards.

Table 3 Rheological properties

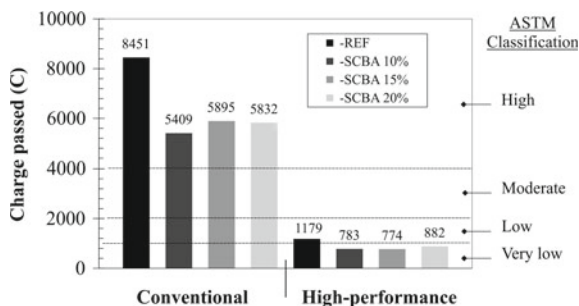|	CC-R	CC-SCBA-10	CC-SCBA-15	CC-SCBA-20	HPC-R	HPC-SCBA-10	HPC-SCBA-15	HPC-SCBA-20
Slump (mm)	140	160	160	170	130	150	170	170
Yield stress (Pa)	901	612	615	731	693	362	196	211
Plastic viscosity (Pa.s)	54	82	71	67	306	353	363	380

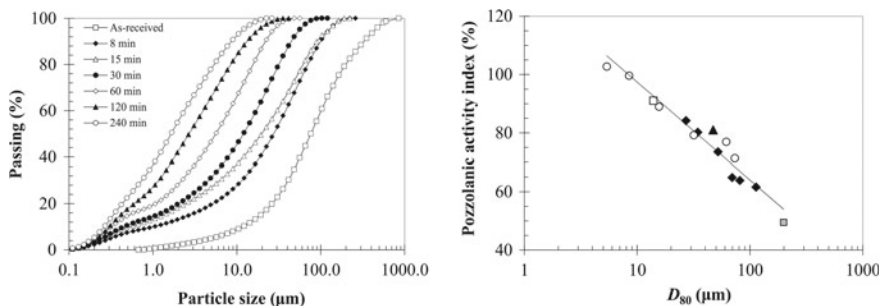**Fig. 2** Chloride-ion permeability of different concretes

Fig. 3 Particle size distribution (left) and pozzolanic activity index (right) for several grinding times

The investigation reported in reference [11] stressed that, although different size distributions were produced by the different mills and milling configurations, the pozzolanic activity of the ground ash was directly correlated to its fineness, characterized by D_{80} or Blaine fineness. From a low pozzolanic activity of less than 50% of the as-received ash, values above 100% could be reached after prolonged grinding times.

In what concerns calcination, bagasse samples were burnt in an aired electric oven at different temperatures ranging from 400 to 800 °C. For all calcination temperatures the pozzolanic activity, structural state of silica and loss on ignition of the ashes were determined. Moreover, the SCBA with greater pozzolanicity was characterized by using chemical analysis, scanning electron microscopy, density, specific surface area and chemical reactivity. The results indicated that the temperature of calcination is an important parameter to produce SCBA with pozzolanic activity. Furthermore, the SCBA produced with air calcination at 600 °C presented

amorphous silica, low carbon content and high specific surface area. The sample produced with these characteristics presented considerable pozzolanic activity according to both mechanical and chemical methods of evaluation. Details of the heating programs can be seen in reference [12].

4   Does SCBA Act as Pozzolan or as Filler?

Although the advantages of using SCBA as cement replacement had already been demonstrated by earlier researches, the actual mechanisms that are responsible for these were not yet well understood. It was not clear if the advantageous use of SCBA was due to physical or chemical effects. This difficulty is partially due to that both effects are coupled to influence the results from most used evaluation methods. In this way, a study had been carried out to evaluate the chemical and physical effects of a residual SCBA on the properties of cement mortars [13]. For this aim, we compared the performance of mortars containing SCBA and crushed quartz (CQ)—considered as an insoluble or low-reactivity material. We grinded both materials until they have similar physical characteristics, such as particle size distribution (Fig. 4), Blaine fineness and virtual packing density. Figure 4 shows also the morphology of the particles obtained by SEM.

Table 4 shows the main physical and pozzolanic characteristics of the particles. These results demonstrated that the pozzolanic activity of SCBA was established from the comparison with an insoluble material having similar particle size distribution and at the same packing density.

5   The Use of SCBA in Industrial Scale

The efficiency of SCBA to reduce CO_2 emissions in industrial scale was demonstrated in a paper [14] that used the methodology established by the United Nations Framework Convention on Climate Change (UNFCC). A simulation was carried out to estimate the potential of CO_2 emission reductions. The State of São Paulo
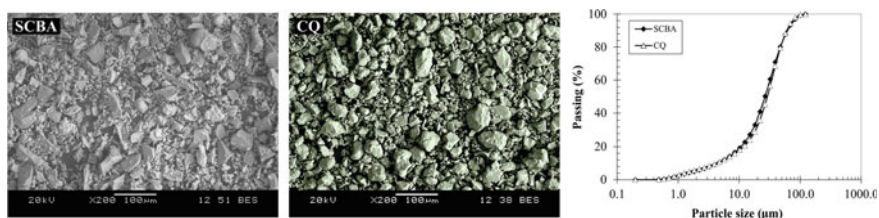

Fig. 4 SEM images and particle size distribution of SCBA-T and CQ-T

Table 4 Physical and pozzolanic characteristics of SCBA-T and CQ-T

Material	D_{50} (μm)	Virtual packing density	Blaine specific surface (m²/kg)	Pozzolanic index with cement (%)	Pozzolanic index with lime (MPa)	Chapelle activity (mg CaO/g)
SCBA-T	26.6	0.66	295	81	5.20	173
CQ-T	29.1	0.66	210	62	0.14	32

(Brazil) (area of 248,000 km²) and its border areas was chosen for this case study because it concentrates about 60% of the national sugar cane and ash production together with an important concentration of cement factories. Since one of the key variables to estimate the CO_2 emissions is the average distance between sugar cane/ethanol factories and the cement plants (see Fig. 5), a genetic algorithm was developed to solve the optimization problem of finding the best connection between the producers and consumers of SCBA.

The increasing of blend in cement production using SCBA, for the simulation carried out in this study, was of 519.3 kilotonnes of CO_2 per year. The use of UNFCC methodology shown that SCBA can partially replace clinker in cement reducing CO_2 emissions into the atmosphere and contributing to mitigation of climate changes.

6 Blending of SCBA and Rice Husk Ash (RHA): Application to Dam Construction

The early researches concerning the optimal sharing of SCBA indicated that percentages of SCBA (alone) greater than 20% were not efficient. Therefore, we investigated SCBA/RHA blended mixture presenting 60% of ordinary Portland cement (OPC), 20% of SCBA and 20% of RHA in comparison with a reference concrete containing 100% of cement. The main characteristics of the reference and SCBA/RHA concretes are given in Table 5. The adiabatic temperature rise and specific creep for an age of loading of 7 days are given in Fig. 6. The simulation of the construction of the spillway of a hypothetical hydropower plant was carried using a finite element method thermo-chemo-mechanical model [15]. Since the SCBA/RHA concrete had lower heat hydration, lower Young´s modulus and greater tensile strength, the simulation indicated that the blended concrete is much more efficient regarding thermal cracking of massive concrete at the early ages.

Figure 7 shows the evolution of the Df_2 fields, a variable that stands for the cracking intensity. It shows that the stress levels developed by SCBA/RHA concrete are always lower than the reference concrete. Furthermore, it is indicated that the reference concrete cracks in a broad area at the top of the pile while the SCBA/RHA concrete remains essentially uncracked.
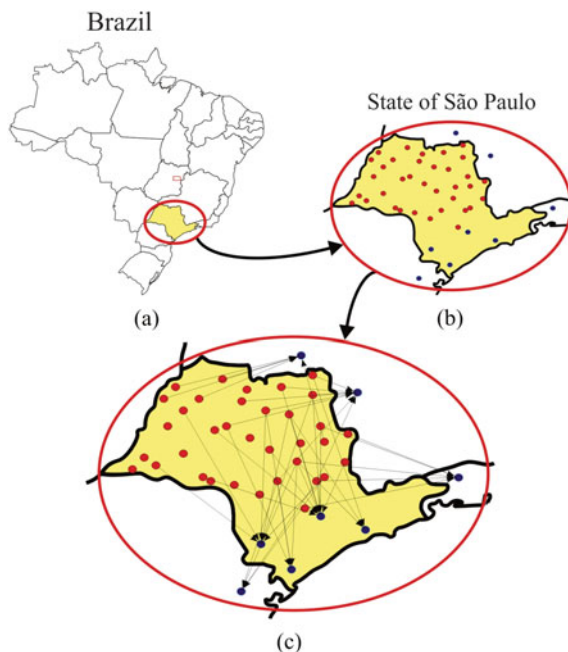
Fig. 5 Project area: **a** State of São Paulo. **b** Localization of the sugar cane/ethanol plants (red circles) and cement factories (blue circles). **c** Result of the optimization procedure used to determine the average distance

Table 5 Mixture proportions (kg/m^3) and mechanical properties (MPa)

	OPC	SCBA	RHA	Fine agg.	Coarse agg.	W	E	f_c	f_t
Reference	366	–	–	725	1001	220	27,500	34.8	3.33
SCBA/RHA	220	73	73	725	1001	220	26,800	39.5	3.77

7 Long-Term Compressive Behavior of Concretes with SCBA

In a recent paper [16] we presented results of compressive tests performed on concretes made of cement blended with SCBA for ages up to 10 years. In this way, samples of the concretes described in Sect. 2 of the present paper, were tested and have strength and Young's modulus measured. Some results for compressive strength are presented in Fig. 8. We can conclude that the results of compressive strength and modulus of elasticity after 10 years of curing of conventional and high-strength concretes confirmed the assessment of this kind of SCBA, with high quartz contamination and low carbon content, to be used as an SCM.
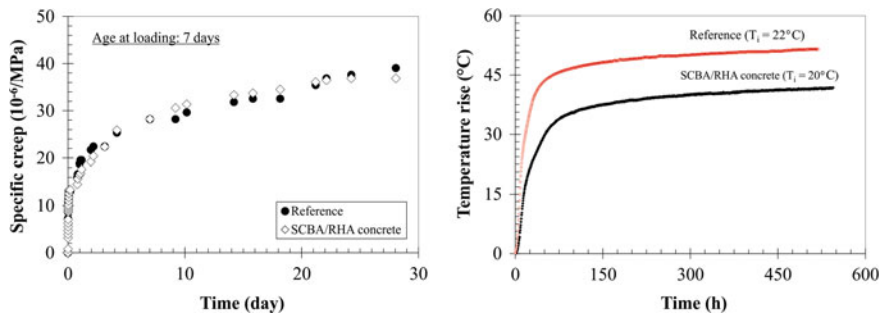
Fig. 6 Creep (left) and adiabatic temperature rise (right) for reference and SCBA/RHA concretes
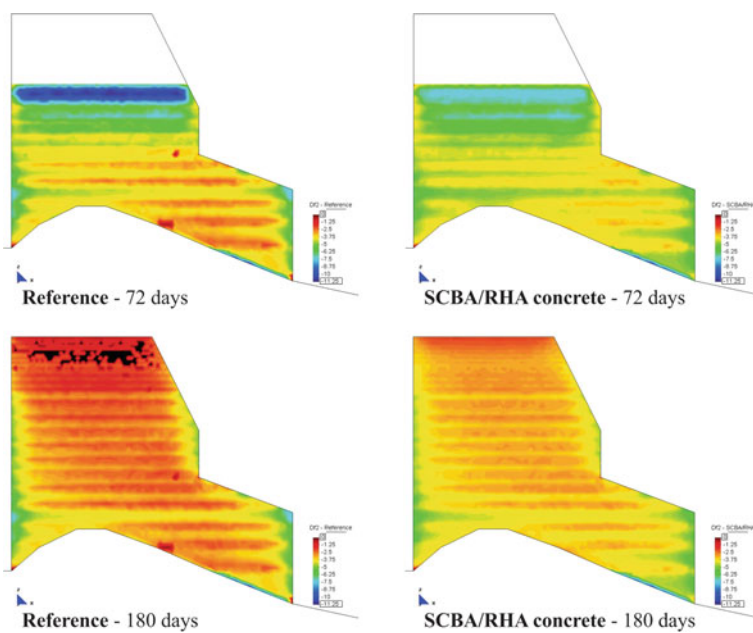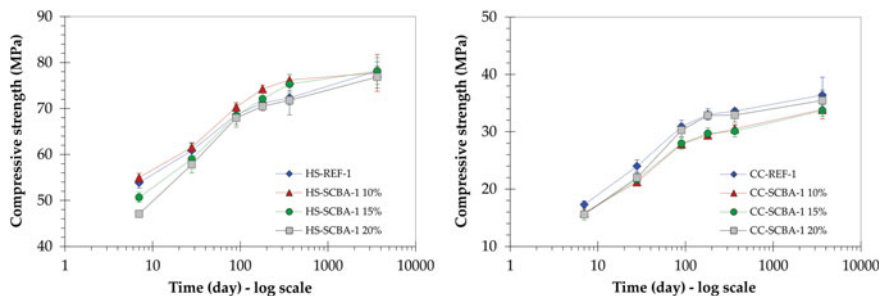

Fig. 7 Fields of cracking intensity variable Df$_2$

Fig. 8 Long-term compressive strengths for high-performance (left) and conventional (right) concretes

References

1. Martirena Hernández, J.F., Middendorf, B., Gehrke, M., Budelmann, H.: Use of wastes of the sugar industry as pozzolana in lime-pozzolana binders: study of the reaction . Cement Concr. Res. **28**, 1525–1536 (1998)
2. Singh, N.B., Singh, V.D., Sarita, R.: Hydration of bagasse ash-blended Portland cement. Cement Concr. Res. **30**, 1485–1488 (2000)
3. Morales, E.V., Villar-Cociña, E., Frías, M., Santos, S.F., Savastano, H., Jr.: Effects of calcining conditions on the microstructure of sugar cane waste ashes (SCWA): Influence in the pozzolanic activation. Cement Concr. Compos. **31**, 22–28 (2009)
4. Ganesan, K., Rajagopal, K., Thangavel, K.: Evaluation of bagasse ash as supplementary cementitious material. Cement Concr. Compos. **29**, 515–524 (2007)
5. Cordeiro, G.C.: Use of sugar cane bagasse ash and rice husk ashes as mineral admixture in concrete. Ph.D. Thesis, COPPE, The Federal University of Rio de Janeiro. Available at http://www.coc.ufrj.br (2006). Last assessed 29 Nov 2019
6. Vulcano-Greullet, N., Sarret, E., Wintzerith, F.: Study of bagasse ashes behaviour in hydraulics mixtures. In: Bruno, D. et al. (eds.) Proceedings of International Composites in Construction, Cosenza, Italy, September, pp. 235–238 (2003)
7. Cordeiro, G.C., Toledo Filho, R.D., Fairbairn, E.M.R.: Use of ultra-fine sugar cane bagasse ash as mineral admixture for concrete. ACI Mater. J. **105**, 487–493 (2008)
8. Cordeiro, G.C., Toledo Filho, R.D., Fairbairn, E.M.R., Tavares, L. M.: Influence of mechanical grinding on the pozzolanic activity of residual sugarcane bagasse ash. In: Vazquez, E., et al. (eds.) Proceedings of the International RILEM Conference on Use of Recycled Materials in Buildings and Structures, Barcelona, Spain, pp. 731–740 (2004)
9. Goldman, A., Bentur, A.: The influence of microfillers on enhancement of concrete strength. Cement Concr. Res. **23**(4), 962–972 (1993)
10. Lawrence, P., Cyr, M., Ringot, R.: Mineral admixtures in mortars—effect of inert materials on short-term hydration. Cement Concr. Res. **33**(12), 1939–1947 (2003)
11. Cordeiro, G.C., Toledo Filho, R.D., Fairbairn, E.M.R., Tavares, L.M.: Ultrafine grinding of sugar cane bagasse ash for application as pozzolanic admixture in concrete. Cement Concr. Res. **39**, 110–115 (2009)

12. Cordeiro, G.C., Toledo Filho, R.D., Fairbairn, E.M.R.: Effect of calcination temperature on the pozzolanic activity of sugar cane bagasse ash. Constr. Build. Mater. **23**, 3301–3303 (2009)
13. Cordeiro, G.C., Toledo Filho, R.D., Tavares, L.M., Fairbairn, E.M.R.: Pozzolanic activity and filler effect of sugar cane bagasse ash in Portland cement and lime mortars. Cement Concr. Compos. **30**, 410–418 (2008)
14. Fairbairn, E.M.R., Americano, B.B., Cordeiro, G.C., Paula, T.P., Toledo Filho, R.D., Silvoso, M.M.: Cement replacement by sugar cane bagasse ash: CO_2 emissions reduction and potential for carbon credits. J. Environ. Manage. **91**, 1864–1871 (2010)
15. Fairbairn, E.M.R., Ferreira, I.A., Cordeiro, G.C., Silvoso, M.M., Toledo Filho, R.D., Ribeiro, F.L.B.: Numerical simulation of dam construction using low-CO_2-emission concrete. Mater. Struct. **43**, 1061–1074 (2010)
16. Cordeiro, G.C., Paiva, O.A., Toledo Filho, R.D., Fairbairn, E.M.R., and Tavares, L.M.: Long-term compressive behavior of concretes with sugarcane bagasse ash as a supplementary cementitious material. J. Test. Eval. **46**(2), 564–573 (2018)

Thermal Performance of Steel and Fibre Reinforced Concrete Composite Floor

**Talita L. Silva, Isabel B. Valente, Joaquim Barros,
Maria José Roupar, Sandra M. Silva, and Ricardo Mateus**

Abstract In general, steel and concrete composite floors tend to present a reduced functional performance (considering thermal and acoustic conditions), due to their low mass and to the high conductivity of the steel elements. By including components with high thermal insulation capacity in these structural systems, it is possible to maintain the structure lightness and not compromise the thermal performance. Within this work, the analysis is dedicated to a composite floor in which a fibre reinforced concrete (FRC) slab is associated with a concrete filled "U" type steel profile. The fibre reinforcement avoids the use of conventional reinforcement, with significant savings in term of fabrication time. Filler blocks are inserted, composed by thermal insulation material (EPS), between the "U" shaped steel profiles, which act as formwork during the casting phase and, after the concrete hardening, contributing to improve the system´s thermal performance. This system was evaluated through numerical assessment. The analysis enabled to determine the thermal transmittance (U-value) and to identify the critical zones in terms of thermal insulation efficiency. The performance of the proposed solution was also compared to other flooring solutions. According to the results obtained, the proposed composite floor presents a better thermal behaviour than other more traditional flooring systems.

Keywords Steel and concrete composite floor · Fibre reinforced concrete · Thermal performance · Numerical analysis

1 Introduction

The performance of flooring solutions should be evaluated considering their mechanical and functional behaviour, in order to guarantee thermal comfort and structural safety to the users. Structural elements, as slabs, are in many cases in

T. L. Silva · I. B. Valente (✉) · J. Barros · M. J. Roupar · S. M. Silva · R. Mateus
University of Minho, Braga, Portugal
e-mail: isabelv@civil.uminho.pt

direct and constant contact with the outside environment, and due to their large size, they play a very important role in the heat transfer processes that occur. Despite columns and beams being smaller when compared to slabs, they also create thermal bridges. This is due to the assembly of construction elements that are composed by different materials and due to structural elements that are commonly composed by higher conductivity materials (concrete and steel), in comparison to the surrounding construction elements (e.g. walls).

Thermal bridges not only provide heat transfer/loss, but can also promote moisture problems. Excess moisture without adequate ventilation can lead to the appearance of bacteria and mold, compromising the users' health [1].

To characterize the thermal behaviour of a building element, it is necessary to determinate its thermal transmittance (U-value) and its thermal resistance (R).

Thermal transmittance is inversely proportional to the construction element thermal resistance and the interior and exterior surface thermal resistances. Thermal resistance of a material or construction element can be determined through the relation between its thickness and its thermal conductivity. Thermal conductivity represents the amount of heat transfer through a layer of a thermally homogeneous material when there is a temperature difference between two flat and parallel surfaces. Interior and exterior surface thermal resistances are influenced by the air speed, the surface emissivity and the heat flux direction, which can be in horizontal or vertical direction [2, 3]. Smaller thermal transmittance, or higher thermal resistance, leads to better thermal performance of a construction element. These properties can be quantified considering analytical and numerical approaches and must be validated by experimental testing.

Over the years, building structures have become increasingly light and slim. As a result, it has been possible to reduce the overall construction weight, and to create wider and more flexible spaces for various applications. These advantages go beyond architectonic aspects. In fact, lighter structures tend to result in more sustainable constructions. Steel and concrete composite floors are an example of a lighter and optimized structural system. However, compared to some conventional floors, the thermal performance of steel and concrete composite floors is generally less efficient, due to the reduced mass and the high conductivity of their constituent materials.

This work aims to evaluate the thermal performance of a new steel and concrete composite floor. The proposed solution, named PreSlabTec, was developed to provide the users with a good thermal performance, as well as the overall structural safety. When the thermal behaviour improves, the costs associated with heating or cooling equipment can decrease, which makes the solution more energy-efficient and, consequently, more sustainable.

PreSlabTec is a steel and concrete composite floor, where "U" shaped steel profiles are associated with fibre reinforced concrete (FRC) slab. Filler blocks in insulation material, such as expanded polystyrene (EPS), are inserted between the steel profiles, and act as formwork at the casting phase. When the concrete hardening is complete, the filler blocks contribute to improve the system's thermal performance. In this work, thermal performance is evaluated through numerical

assessment. Some analyses are performed to examine the proposed solution thermal performance and to compare it with some traditionally flooring systems.

2 Geometry and Materials Definition

The proposed system is composed by "U" shaped steel profiles, with alveolar openings, which are associated with a FRC concrete slab. The steel profiles are fabricated with steel SJ235, and a thermal conductivity value of (λ) 50.0 W/(m °C) is considered for these elements. During the casting phase, these profiles are filled with FRC and the alveolar openings allow some FRC transfer to the outside of the profile. Fibre reinforced concrete is used to avoid the use of conventional reinforcement. It was considered that FRC thermal conductivity (λ) is equal to 2.0 W/(m °C), which corresponds to reinforced concrete with a percentage of reinforcement that is below 1% (by volume). This property will be updated after the experimental testing. The filler blocks are compose by EPS with a thermal conductivity (λ) of 0.036 W/(m °C). Two transversal tubular joists cross the alveolar openings in the "U" steel profile in the ends of the slab. These cross-section profiles have the same thermal conductivity as the "U" profiles. The geometry of the PreSlabTec is shown in Fig. 1.

3 Numerical Assessment

The thermal study was carried out considering 2D numerical modelling, with the aid of Therm 7 software [4], which is based on the finite element method (FEM).

The performance of all construction elements must be in accordance with the requirements of the legislation of its implementation place. The Portuguese
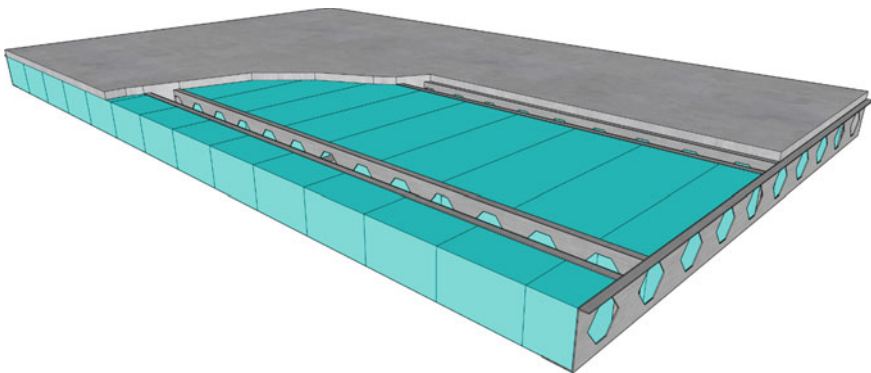

Fig. 1 Proposed steel and concrete composited floor: 3D view

legislation imposes requirements for building envelopes that must be fulfilled [5], as those between outside and inside spaces. The worst possible situation is considered, i.e., the slab acts as the horizontal separation between outside and inside spaces, where there is a significant temperature difference between the PreSlabTec surfaces.

3.1 Models

Four numerical models were created to evaluate the PreSlabTec cross section. The first model, MN_A, corresponds to the cross section with alveolar openings in the "U" steel profiles (see Fig. 2a). Model MN_B corresponds to the cross section without alveolar openings in the "U" steel profile (see Fig. 2b). The third model, MN_C, correspond to the position where a transversal tubular joist crosses the alveolar openings in the "U" steel profile (see Fig. 2c) and model MN_D corresponds to the same cross section that was chosen for model MN_C, but in the exact position of the tubular joist wall (see Fig. 2d).

The thermal properties of the materials were described in Sect. 2. According to [3], when the air spaces are unventilated, the air conductivity changes under the heat flux direction.
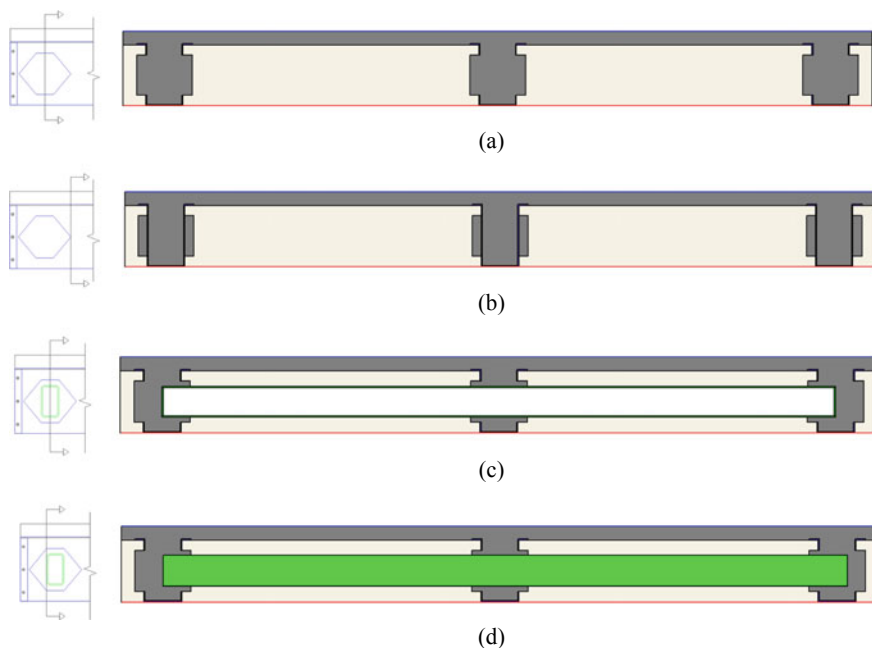

Fig. 2 Cross sections of the numerical models: **a** MN_A; **b** MN_B; **c** MN_C; **d** MN_D

A thermal conductivity value of 0.513 W/(m °C) was attributed to the air inside the cross section profiles, when the heat flux is ascendant and a thermal conductivity value of 0.372 W/(m °C) was set when the heat flux is descendant.

The models were analysed considering winter and summer seasons, in which occur the highest temperature variability between inside and outside surfaces. According to [6], when temperature inside the building is lower than 18 °C in winter and higher than 25 °C in summer, it is necessary to heat or cool the building. Exterior temperatures were set so that there would be a difference of at least 10 °C between the interior and the exterior.

Adiabatic conditions were attributed to the lateral surfaces of the model, which means that there are no thermal exchanges with the building envelopes (see Fig. 3). This enables the characterization of the PreSlabTec thermal performance without considering the influence of other surrounding construction components.

The surface resistances were applied in accordance with those indicated in [3]. The boundary conditions according to the seasons of the year and heat flux direction are described in Table 1.

3.2 Results

The numerical model MN_A presents the smaller thermal transmittance and the higher thermal resistance. This result was expected due to the larger area of insulating material (EPS). In contrast, model MN_D obtains the higher thermal transmittance in consequence of the larger quantity of steel, which is a conductive material. All the results obtained with the numerical models are collected in Table 2.

Although the boundary conditions are the same for all models and the thermal transmittance values obtained in the analysis are close to each other, it can be seen that in models with better thermal performance, the heat flux acting on the building
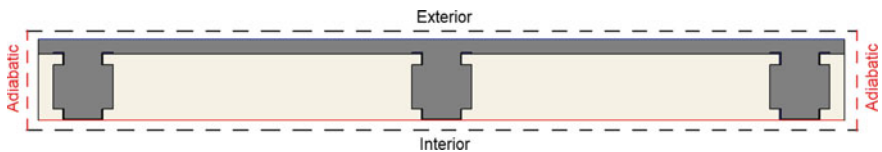

Fig. 3 Boundary conditions

Table 1 Boundary conditions according to the heat flux direction

	Ascending heat flux (↑)		Descending heat flux (↓)	
Surface	Interior	Exterior	Interior	Exterior
Temperature (°C)	18	8	25	35
$R_{surface}$ [(m^2 °C)/W]	0.10 (↑)	0.04 (↑)	0.17 (↓)	0.04 (↓)

Table 2 Numerical results

Model	Heat flux direction	U [W/(m² °C)]	R [m² °C)/W]	Heat flux (W/m²)
MN_A	↑	1.01	0.99	10.35
	↓	0.82	1.23	8.16
MN_B	↑	1.16	0.87	11.79
	↓	0.90	1.11	8.98
MN_C	↑	1.12	0.89	11.43
	↓	0.91	1.10	9.12
MN_D	↑	1.32	0.76	13.48
	↓	1.07	0.93	10.71
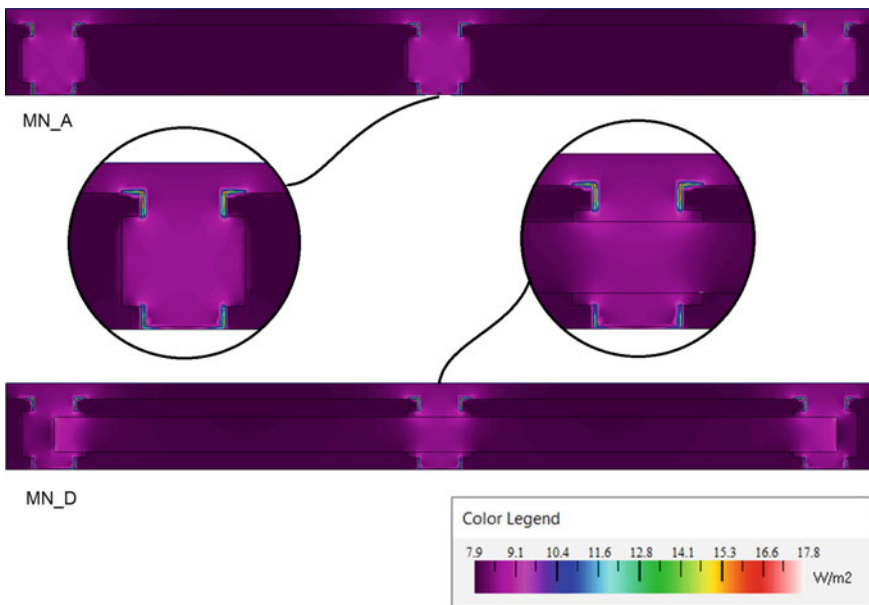
Fig. 4 Heat flux magnitude for an ascending heat flux

element is lower (see Table 2). This results from the higher thermal resistance of the corresponding solution.

It is possible to analyse the heat flux intensity in the models through the heat flux magnitude, which is higher according to the highest conductibility of the materials. In the MN_A model there is a heat flux difference of approximately 2 W/m² between the area with EPS and the part of the cross section that is inside of the steel profile (FRC beam + "U" steel profile). However, between some areas of the steel profile and the other elements of the model there is a more significant difference, of approximately 10 W/m² (see Fig. 4).

An ascending heat flux of 10.35 W/m^2 was obtained in the MN_A model. In Fig. 4 it can be seen that in the majority of the model, the heat flux is approximately 7.9 W/m^2, which means that the area corresponding to the "U" steel profile has a considerable influence on the global result, although its area is significantly smaller.

The heat flux magnitude is higher in model MN_D, when the cross-section steel profile is directly next to the "U" steel profile and involved by FRC. When it is involved by EPS, the heat flux magnitude, for this area, is the same as the one obtained in MN_A model (Fig. 4).

The global thermal transmittance (U_T) of the proposed solution can be averaged, by accounting the area of each part of the cross section, $A_{MN,n}$, and its thermal transmittance, $U_{MN,n}$ (see Eq. 1). The construction solution presents a global thermal transmittance of 1.12 W/(m^2 °C) for winter, ascending heat flux, and 0.89 W/(m^2 °C) for summer, descending heat flux.

$$U_T = [\Sigma(U_{MN\_n} \times A_{MN\_n})]/\Sigma A_{MN\_n} \tag{1}$$

4 Comparative Analysis

For comparison purposes, it was decided to analyze other common flooring solutions.

Considering this, some additional numerical models were created, corresponding to pre-selected flooring solutions, in order to assess their thermal performance.

To carry out this comparative study, three constructive solutions were selected: a reinforced concrete slab, a steel and concrete composite floor and a precast floor. These solutions were designed considering the same actions, the same span (3.2 m) and the same cross-section width (2.21 m). The cross sections geometries are described in Fig. 5.

A thermal conductivity value of 2.5 W/(m °C) was attributed to reinforced concrete. For the steel and concrete composite floor, the value of thermal conductivity of concrete was considered equal to 2.0 W/(m °C) (less reinforcement) and the value of 50.0 W/(m °C) was attributed to the trapezoidal sheeting. For the precast floor, a thermal conductivity of 2.0 W/(m °C) was attributed to concrete and the value of 0.34 W/(m °C) was considered in the ceramic filler blocks. The boundary conditions considered in the PreSlabTec model were also applied to these models. The results on thermal transmittance obtained from the developed models are presented in Fig. 5.

The proposed solution, PreSlabTec, has a better overall performance than all the other solutions because of the large amount of insulation material that is disposed in its composition. In relation to the solutions analysed, the results were also consistent with the expected ones, as reinforced concrete floor and steel and concrete composite floor presented a higher thermal transmittance. Table 3 describes the average U-value (U_m) obtained for ascending and descending heat flux, considering all floors analyzed.
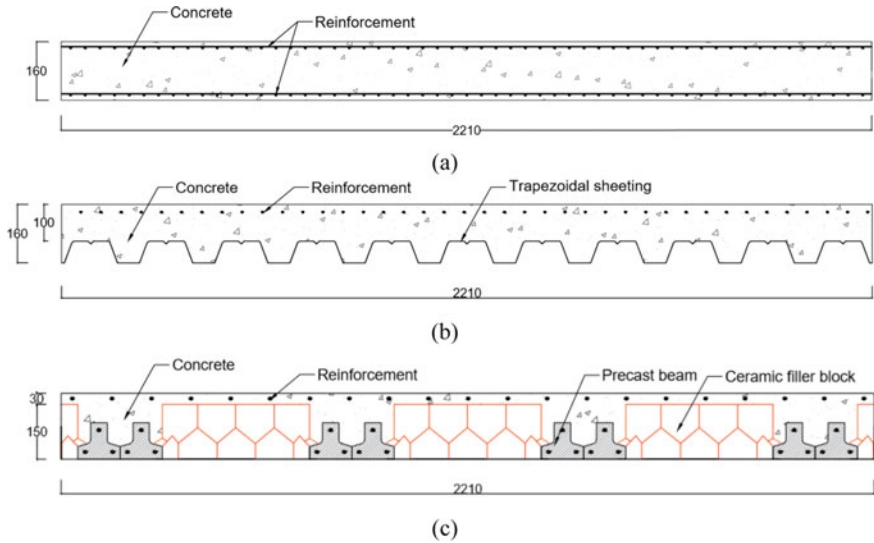
Fig. 5 Cross sections of the floor used in the comparative analysis: **a** concrete floor; **b** steel and concrete composite floor; **c** precast floor. Unit: millimeter

Table 3 Comparative results

Construction solution	U_m[W/ (m^2 °C)]	R [(m^2 °C)/W]	Heat flux (W/m^2)
PreSlabTec	1.00	1.01	10.16
Concrete slab (Fig. 5a)	4.28	0.24	43.24
Composite slab (Fig. 5b)	4.28	0.27	52.79
Prefabricated slab (Fig. 5c)	2.76	0.37	27.94

The benefits are not only related to the thermal behaviour of the solution. According to [5] the U_{max} for horizontal building envelopes varies between 0.40 and 0.30 W/(m^2 °C) depending on the climate zone of Portugal. As previously mentioned, these requirements are defined for building envelopes, as those that are in contact with the exterior. Considering this, all the solutions analysed would need additional insulation to fulfill the thermal transmittance demanded in [5], but in this case, the PreSlabTec solution would need a smaller amount of insulation material (e.g. EPS applied continuously on one of the slab surfaces, exterior or interior) to achieve the same thermal transmittance level as the other slab solutions analysed. In consequence, there is a cost reduction and a space gain that results from its lower thickness.

5 Future Study—Experimental Tests

Laboratory tests will be performed to evaluate the experimental thermal performance of the proposed flooring system. The tests will be carried out according to [7] and the collected data will be used to determine its thermal transmittance (U) and its thermal resistance (R).

Due to the different materials used in the cross section and the geometrical variations imposed, different specimens will be created to allow the characterization of the different parts of the slab.

The experimental test should be conducted under stable thermal conditions. When the test is performed in a laboratory environment, it is possible to control the temperature that is acting on the building element to promote temperature differences between the opposite surfaces of the specimen and to avoid unstable results.

These conditions can be achieved by implementing a hot box. The hot box is composed by two chambers, metering chamber and climatic chamber, whose walls are formed by insulating material. The metering chamber contains a heating equipment and the resulting air temperature is controlled. The climatic chamber is used to control the air temperature on the opposite side of the metering chamber [8]. Masked hot box will be used since it allows to involve the whole building element. The hot box walls will be composed by 200 mm extruded polystyrene (XPS), $\lambda = 0.038$ W/(m °C), and 50 mm of mineral wool, $\lambda = 0.037$ W/(m °C) (see Fig. 6).
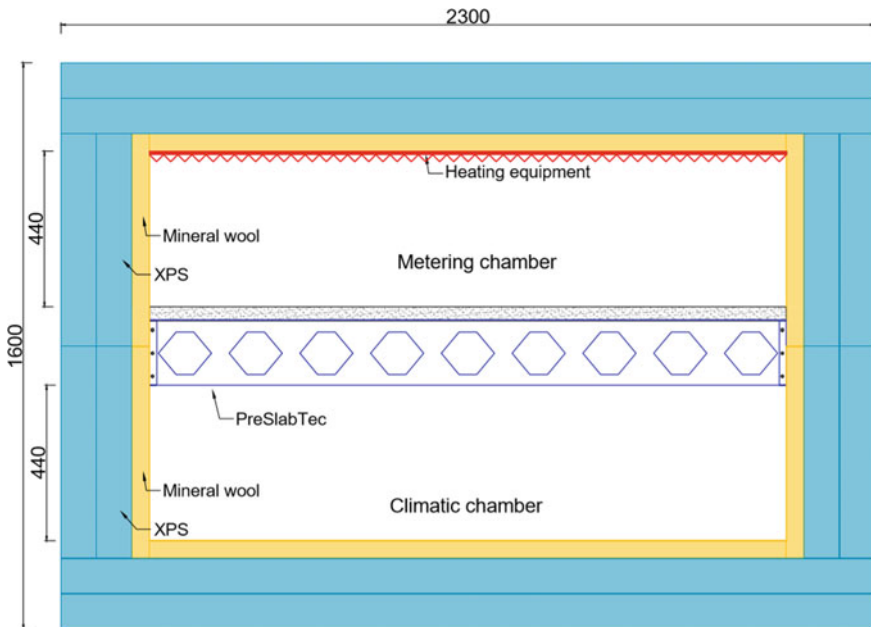

Fig. 6 Masked hot box. Unit: millimeter

During the experimental tests, the thermal conductivity of the fibre reinforced concrete (FRC) will also be characterised in order to calibrate and validate the numerical models.

6   Conclusions

This work presents a new structural flooring system designed to provide a good thermal performance in addition to its optimized structural behaviour.

The study was developed considering a numerical approach. The proposed solution presented a good performance, given the boundary conditions applied. However, there are some critical areas: the ones located next to the steel profile, where additional insulation is needed to avoid thermal bridges.

A complementary analysis was developed to evaluate the thermal behaviour of the proposed system in comparison to some traditional floors. It showed a thermal performance that is better than all the other traditional flooring systems analyzed.

In addition to this study, experimental tests will be carried out to validate the results obtained and to characterize the thermal performance of FRC.

References

1. Teni, M., Krstić, H., Kosiński, P.: Review and comparison of current experimental approaches for in-situ measurements of building walls thermal transmittance. Energy Buildings (203), 109417 (2019)
2. RCCTE: Regulamento das Características do Comportamento Térmico dos Edifícios. Decreto-Lei nº 80/2006, de 4 de abril (2006)
3. LNEC. ITE50: Térmica, Coeficientes de Transmissão Térmica de Elementos da Envolvente dos Edifícios. Lisboa (2006)
4. Finlayson, E., Mitchell, R., Dariush, A., Huizenga, C., Curcija, D.: Therm 2.0: Program Description—A PC Program for Analyzing the Two-Dimensional Heat Transfer Through Building Products. Ernest Orlando Lawrence Berkeley National Laboratory (1998)
5. Portaria n.º379-A/2015 de 22 de outubro. Diário da República nº 207/2015, 2º Suplemento, Série I. Min. do Ambiente, Ord. do Território e Energia. Lisboa
6. REH: Regulamento de Desempenho Energético dos Edifícios de Habitação. Decreto-Lei n.º 118/2013 (2013)
7. ISO 9869-1:2014: Thermal insulation—building elements. In-situ measurement of thermal resistance and thermal transmittance—Part 1: Heat flow meter method (2014)
8. ASTM C1363-11: Standard Test Method for Thermal Performance of Building Materials and Envelope Assemblies by Means of a Hot Box Apparatus

Interface Evaluation of Carbon Textile Reinforced Composites

Rebecca M. C. Silva, Ana C. C. Trindade, and Flávio A. Silva

Abstract Cement production is responsible for high CO_2 emissions. Focusing on environmental sustainability, there is nowadays a desire to make thinner concrete elements, thereby reducing the amount of cement used. Textile reinforced concrete (TRC) is a cementitious matrix composite reinforced with one or multiple layers of 2D or 3D fabrics that present elevated mechanical performance aligned with high load-bearing capacity. The textiles can be constituted by several types of fibres. Carbon fibres are an attractive option due to their superior mechanical and durability properties. However, they present a low bond with the cementitious matrix. The bond between the textile reinforcement and the matrix is the weakest region of the composite, therefore governing the element behaviour up to its failure. Polymeric coatings can be used to enhance the interaction between the carbon fabric and the cementitious matrix. Nevertheless, these materials present a decomposition temperature extremely lower than the one of the carbon fabrics, limiting their use in case of elevated temperature conditions. An alternative to improve the bond and, consequently, the composite mechanical performance is matrix modification and use of inorganic high-tech ceramics, such as geopolymers, as coatings. This paper aims to present a comparison of the interface behaviour of carbon textile reinforced composites embedded in distinct matrices. For this, pull-out tests will be performed in carbon yarns impregnated with SBR. A cementitious and a geopolymer matrix will be evaluated. Furthermore, the influence of an additional geopolymer coating will also be analyzed.

Keywords Textile reinforced composites · Carbon fabric · Bond · Interface · Pull-out tests

R. M. C. Silva (✉) · A. C. C. Trindade · F. A. Silva
Department of Civil and Environmental Engineering, Pontifícia Universidade Católica do Rio de Janeiro (PUC-Rio), Rio de Janeiro, Brazil
e-mail: rebecca.mansur@aluno.puc-rio.br

1 Introduction

Between 1970 and 2005, global cement production almost quadrupled [1]. The cementitious industry is responsible for approximately 5% of the global CO_2 emissions [2], ranging from 0.73 to 0.99 (in mass) per kg [2]. Approximately 45% of these emissions come from the burning of fossil fuels used in the kilns for clinker manufacturing. The clinker manufacturing itself is responsible for approximately 50% of the CO_2 emissions, since the calcination of limestone results in, besides calcium oxide, CO_2. The last 5% is released indirectly by transportation and other processes [1–3]. With the growing demand for more sustainable structures, there is currently a desire to build thinner concrete elements, thereby reducing the required cement consumption.

Textile reinforced concrete (TRC) is a cementitious matrix composite reinforced with one or multiple layers of 2D or 3D fabrics [4]. These materials present elevated mechanical performance aligned with high load-bearing capacity [4–6], and, therefore, can be used for the strengthening of existing structures [7–15], and the construction of new structural elements, such as slabs [16–18], self-supporting sandwich elements [19–24], and shell structures [25–28].

The characteristics of TRC are directly related to the properties, amount, and arrangement of the fibers used in the fabrics. Carbon fabrics are becoming extremely attractive as textile reinforcement in cementitious matrices due to their elevated mechanical and durability properties [29–31]. Moreover, due to the modern fabrication technology, it is possible to economically produce carbon fabrics with reproducible and predictable properties. The main disadvantage in using this type of fabric is related to its bond with the cementitious matrix. Carbon fibers are hydrophobic, and due to their inadequate wettability and chemical inertness, they present a low bond with water-based materials, such as the cementitious matrices. The load-bearing capacity of composite materials is governed by the weakest phase, which is, in general, the interface between the matrix and the reinforcement. Due to the low bond of the carbon with the cementitious matrix, even with the high mechanical properties of the carbon, TRC elements generally show insufficient mechanical performances.

Nevertheless, previous studies [32–36] presented methods that can improve the fabric-matrix interaction, resulting in an enhancement in the mechanical behavior of the composite. One method is to use organic coatings, as polymers. The coating fills the spaces and binds all filaments within a yarn, forming a single unit. Thus, the load is efficiently carried by all filaments. Donnini et al. [34], Dvorkin and Peled [33], and Xu et al. [32] demonstrated an improvement between the carbon fabric and a cementitious matrix through the enhancement of the composite mechanical capacity by adding a coating of flexible epoxy resin. Donnini et al. [34] and Silva and Silva [37] showed that a sand layer over the resin can further increase the composite mechanical behavior. However, in case of extreme temperature exposures, the polymeric coating may reduce the mechanical performance of the

composite, since it decomposes in a temperature range bellow the decomposition characteristic limits of usual carbon fabrics [38].

A technique to improve the bond between the carbon fabric and the cementitious matrix in such exposures to high temperatures and fire occurrence is through impregnation with mineral fillers. Schneider et al. [36] demonstrated a comparison with carbon yarns impregnated with epoxy resin and styrene butadiene rubber (SBR), recording a significant improvement on the bond of carbon yarns with concrete matrices at temperatures of 100 and 200 °C by using mineral impregnation. The mineral particles penetrated inside the yarn, and due to their silica content, produced a pozzolanic reaction with the cement matrix, enhancing the interaction between the reinforcement and the matrix [33]. The size of the particles influenced the efficacy of this treatment. Peled et al. [35] showed that silica fume with micro size particles can provide an enhancement in the bond between the carbon yarn and the cementitious matrix, while when using nano silica as coating, the bond strength was considerably reduced. In contrast, Lu et al. [39] impregnated carbon fibers with nano silica and observed an enhancement on the interfacial strength.

An additional method to enhance the fabric adhesion could be trough matrix modification. Geopolymers are ceramic materials produced through the combination of sodium or potassium-based alkali solutions with an aluminosilicate source, such as metakaolin or fly ashes [40–42]. This material presents elevated content of reacted nano-silica in its composition [42], generally resulting in high thermal resistance [41, 43]. The combination of these characteristics makes the geopolymer an interesting alternative in the replacement of cementitious matrices in textile reinforced composites. It also presents an adequacy for coating processes in carbon fabrics, in order to improve the bond of the textile reinforcement and the cementitious matrix.

This paper aims to present a comparison of the interface behavior of carbon textile reinforced composites. For this, pull-out tests will be performed in carbon yarns coated with styrene-butadiene resin (SBR). Two different ceramic matrices (cementitious and geopolymer) will be evaluated. Furthermore, the influence of an additional coating of a geopolymer on their bond behavior will also be analyzed.

2 Experimental Program

2.1 Materials

For the cementitious matrix, a fine-grained concrete was used. A mix proportion of 1:1:0.3 (sand: cementitious material: water by weight), as presented in Table 1, was used. Portland cement CP-II F-32, defined by the Brazilian standard [44], and river sand with a maximum diameter of 1.18 mm were used.

The geopolymer matrix and coating were produced from the combination of metakaolin (MK), provided from *Metacaulim do Brasil*, as the main aluminosilicate

Table 1 Cementitious matrix composition

Composition	
Sand (1.18 mm) (kg/m^3)	947
Cement CP-II F-32 (kg/m^3)	632
Water (kg/m^3)	279.7
Fly ash (kg/m^3)	265
Silica fume (kg/m^3)	50.5
Superplasticizer (Glenium 51) (kg/m^3)	6.31

Table 2 Geopolymer matrix composition

Composition	
WG/MK ratio	1.712
WG (kg/m^3)	1195.3
MK (kg/m^3)	698.1
Sand (1.18 mm) (kg/m^3)	349.0

source, with a sodium-based solution according to the formulation *Na$_2$O. Al$_2$O$_3$. 4SiO$_2$. 11H$_2$O*. The alkali solution was obtained through the dissolution of sodium hydroxide from Sigma-Aldrich® in water, followed by the addition of fumed silica CAB-O-SIL® M-5 from Cabot. The solution was mixed for 24 h in a magnetic stirrer, resulting in a stable water–glass (WG). River sand with a maximum diameter of 1.18 mm was incorporated into the geopolymer matrix as fine aggregate. Table 2 presents the geopolymer matrix composition.

The average compressive strength and Young's modulus at 28 days of both matrices are shown in Table 3.

The carbon yarns used were extracted from the carbon fabric SITgrid17KB from V. Fraas GmbH. Table 4 shows the properties of the carbon fabric according to the supplier. The yarn presents a cross-sectional area of 3.34 ± 0.12 mm^2. Figure 1 shows an image obtained on a stereoscopic microscope Nikon model SMZ800N that was used to obtain the cross-sectional area through image analysis with the software ImageJ.

In the case of the carbon yarns coated with the geopolymer, the coating was applied directly to the carbon yarns. This process was performed at least 48 h before the composite manufacturing to guarantee the completion of the geopolymer cure regime.

Table 3 Cementitious [37] and geopolymer matrices mechanical properties

	Cementitious matrix	Geopolymer matrix
Compressive strength (MPa)	70.7	52.0
Young's modulus (GPa)	27.6	10.5

Table 4 Properties of the carbon fabric

	Carbon fabric
Supplier	V. Fraas—SITgrid17KB
Coating	Styrene butadiene resin (SBR)
Tensile strength (MPa)	1700
Young's modulus (GPa)	250

Fig. 1 Cross-sectional area of the carbon yarn
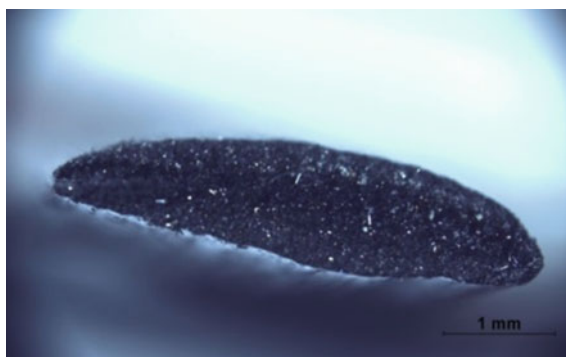
2.2 Composite Manufacturing

Both matrices were produced using a planetary mixer with a maximum capacity of 5 L and a maximum rotation of 281 rpm. For the cementitious matrix, the cementitious materials and sand were dry mixed for 60 s. The water was added, and the mix was homogenized for 4 min. Then, the superplasticizer was incorporated, and the mix was blended for an additional 5 min. For the geopolymer matrix, the metakaolin and the sodium-based water–glass were mixed for approximately 3 min, until it became a homogeneous mixture. The sand was then added, and the mix was once more homogenized.

For the pull-out tests, cylinders with 25 mm diameter and 20 mm height were cast in PVC molds supported on an acrylic plate, as shown in Fig. 2. The matrix was put on the molds, and one yarn of the carbon fabric was positioned in the center of the cylinders. The embedded length of the yarns was 20 mm. The cementitious matrix specimens were removed from the molds after 24 h and stored in a wet chamber with 100% humidity and temperature of 21 ± 2 °C until testing. The geopolymer matrix specimens were sealed just after casting and maintained in ambient temperature for 48 h to avoid dehydration processes in early ages. After this period, the specimens were removed from the molds and stored in plastic bags until testing.

Fig. 2 Fabrication of the
specimens for pull-out tests
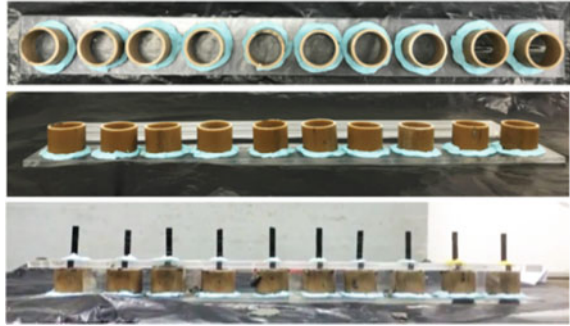
2.3   Pull-Out Tests

The pull-out tests were performed in a MTS 810 universal testing machine with
load capacity of 250 kN. A load cell with 2.5 kN capacity was used for an enhanced
data acquisition. The tests were controlled by a displacement rate of 1.5 mm/min.
Figure 3 shows the setup for the pull-out tests. The specimens were attached to the
machine through claws, in a fixed boundary condition system. The yarn slip was
obtained directly from the machine displacement. The specimens were tested after
14 days of casting.

The average interfacial shear stress (τ) was obtained through the equation

$$\tau = \frac{P_{max}}{2\pi r l} \tag{1}$$

where P_{max} is the maximum pull-out load, l is the embedded length (20 mm) and r
is the equivalent radius of the yarn, assuming a circular section.

3   Discussion and Analysis

Figure 4 shows the pull-out load versus slip curves obtained from the tests and
Table 5 presents the average results and the standard deviation for the maximum
pull-out load (P_{max}), the average interfacial shear stress (τ), and the slip at maxi-
mum pull-out load (δ_{max}).

Previous to the matrix cracking, the dominant mechanism of stress-transfer is an
elastic one. After the first crack on the matrix occurs, there is the start of the yarn
debonding. When the debonding process is complete, the yarn tends to slip within
the matrix, and the transfer mechanism is mainly controlled by the frictional slip. In
this phase, there is a sudden drop in the pull-out load versus slip curve, and the load
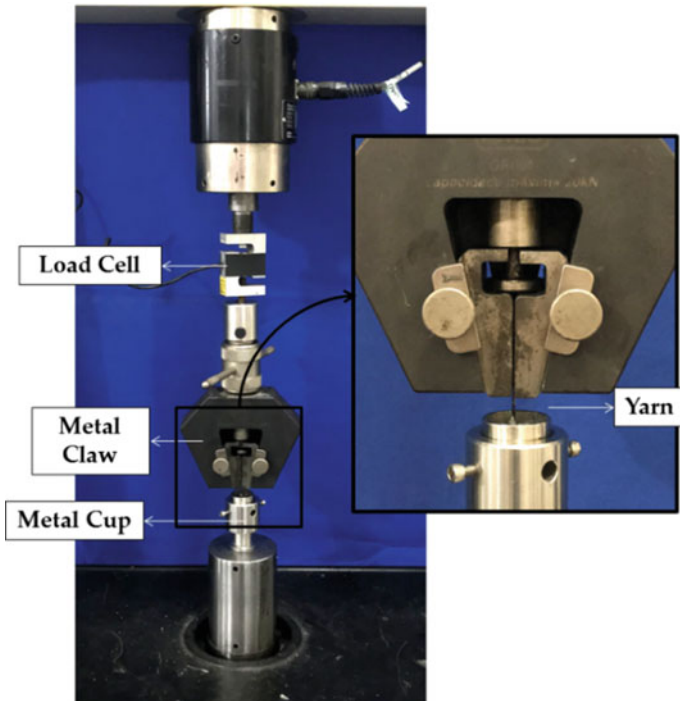distribution is then adjusted due to each fiber-matrix interface [45].

Fig. 3 Setup for the pull-out tests

From Fig. 4a, b, it is possible to observe that the pull-out behaviors of the composites made with cementitious and geopolymer matrices are quite similar. Nevertheless, until the complete fiber debonding, the geopolymer matrix composites (GM + C) reached slightly higher pull-out loads than the cementitious composites (CM + C). This could indicate an improved bond of the SBR carbon yarn within the geopolymer matrix. This improvement may be related to the intrinsic geopolymer rheological properties in its fresh state, which could enhance the adhesion of the carbon yarn to the matrix.

In the frictional slip phase, the cementitious matrix composites reached slightly higher loads than the geopolymer matrix ones, indicating that the yarn found more resistance to slip within the cementitious matrix. Minor variations in the geometry and position of the yarn inside the matrix during the molding process could have caused this difference. However, the grain size and homogeneity of the two different matrices may also play an important role in such modifications. Metakaolin, used in the geopolymer matrix, generally has a particle size in the range of 1 μm [46], while cement grains vary in range approximately from 10 to 75 μm [47].

Figure 4c shows the pull-out load *versus* slip of the composites with the cementitious matrix and the carbon yarns coated with the geopolymer material (CM + GPC). The geopolymer coating negatively influenced the pull-out behavior,
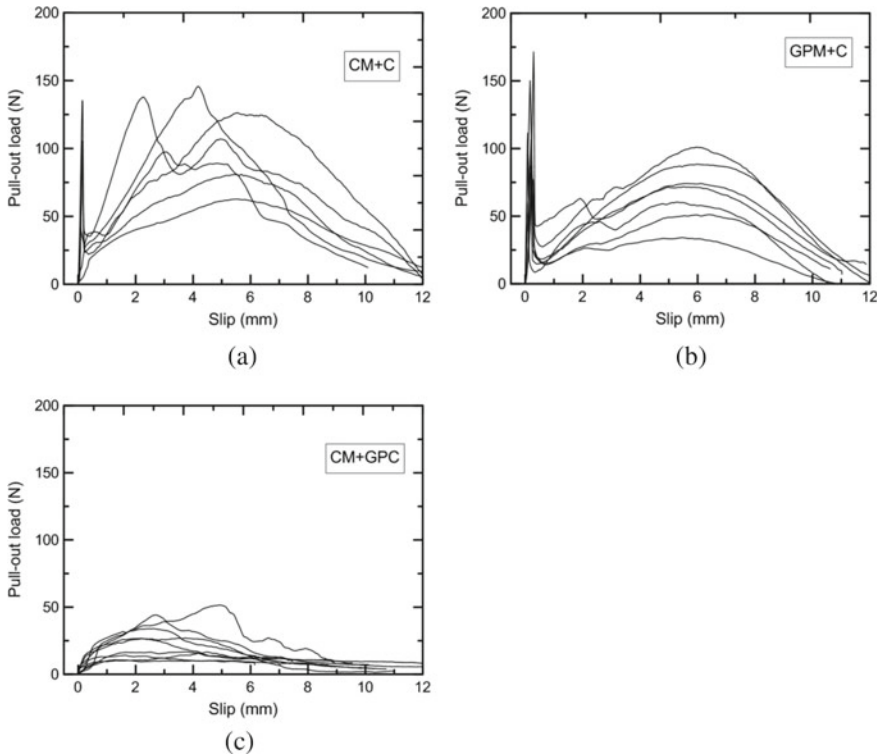
Fig. 4 Pull-out load versus slip curves for the composites with **a** cementitious matrix and carbon yarn (CM + C); **b** geopolymer matrix and carbon yarn (GPM + C); **c** cementitious matrix and carbon yarn with geopolymer coating

Table 5 Average results and standard deviation obtained from the pull-out tests

	P_{max} (N)	τ (MPa)	δ_{max} (mm)
CM + C	112.8 (27.9)	0.870 (0.215)	3.45 (1.91)
GPM + C	124.5 (32.1)	0.961 (0.248)	0.183 (0.065)
CM + GPC	26.8 (13.4)	0.207 (0.103)	3.44 (1.16)

since it could not penetrate within the carbon yarn and did not present significant adhesion with the cementitious matrix. It is also evident its inability to adhere to the SBR coating present within the carbon fabric. Therefore, instead of enhancing the bond, it facilitated the yarn pull-out. The authors believe that in order for this modification to be used properly, the geopolymer coating should be applied to the native carbon yarn, without any polymeric coating clearly acting as a barrier,

showing little to no adhesion to the geopolymer matrix. Further studies are being performed to analyze the efficiency of the geopolymer as the main coating to improve the bond between carbon yarns and cementitious matrices.

4   Conclusions

The geopolymer matrix showed an improved bond with the SBR carbon yarn than the cementitious matrix one. This may be related to the geopolymer intrinsic rheological characteristics. On the other hand, during the frictional slip stress-transfer mechanisms, the cementitious matrix offered greater resistance to the yarn slip. Minor variations in the geometry and position of the yarn during casting can be the reason for this difference. Nevertheless, it may also be related to the distinct grain sizes of the materials used and homogeneity of the two matrices.

Differently from what was expected, the geopolymer coating applied to the SBR carbon yarn negatively influenced the bond of the carbon yarn with the cementitious matrix. This additional coating facilitated the yarn pull-out. The authors believe that, for the nano-silica present in the geopolymer to improve the bond between carbon yarns and cementitious matrices, this coating must be applied directly to the native carbon, i.e., without any polymer coating acting as a barrier. Studies in this area are being conducted.

References

1. Taylor, M., Tam, C., Gielen, D.: Energy efficiency and CO_2 emissions from the global cement industry. In: Energy Efficiency and CO_2 Emission Reduction Potentials and Policies in the Cement Industry, pp. 61–67. Paris (2006)
2. Mahasenan, N., Smith, S., Humphreys, K.: The cement industry and global climate change: current and potential future cement industry CO_2 emissions. In: Greenhouse Gas Control Technologies, Volume II—6th International Conference, pp. 995–1000, Elsevier, Kyoto (2003)
3. Worrell, E., Price, L., Martin, N., Hendriks, C., Meida, L.O.: Carbon dioxide emissions from the global cement industry. Annu. Rev. Energy Env. **26**(1), 303–329 (2001)
4. Brameshuber, W.: Report 36: textile reinforced concrete-state-of-the-art report of RILEM TC 201-TRC. RILEM Publications (2006)
5. Dvorkin, D., Poursaee, A., Peled, A., Weiss, W.J.: Influence of bundle coating on the tensile behavior, bonding, cracking and fluid transport of fabric cement-based composites. Cement Concr. Compos. **42**, 9–19 (2013)
6. Schuetze, E., Lorenz, E., Curbach, M.: Static and dynamic fatigue strength of textile reinforced concrete. In: IABSE Symposium Report, pp. 1–8. International Association for Bridge and Structural Engineering, Nara (2015)
7. Brückner, A., Ortlepp, R., Curbach, M.: Textile reinforced concrete for strengthening in bending and shear. Mater. Struct. **39**(8), 741–748 (2006)
8. Ambrisi, A.D., Focacci, F.: Flexural strengthening of RC beams with cement-based composites. J. Compos. Constr. **15**(5), 707–720 (2011)

9. Ombres, L.: Flexural analysis of reinforced concrete beams strengthened with a cement based high strength composite material. Compos. Struct. **94**(1), 143–155 (2011)
10. Al-Salloum, Y.A., Elsanadadey, H.M., Alsayed, S.H., Iqbal, R.A.: Experimental and numerical study for the shear strengthening of reinforced concrete beams using textile-reinforced mortar. J. Compos. Constr. **16**(1), 74–90 (2012)
11. Schladitz, F., Frenzel, M., Ehlig, D., Curbach, M.: Bending load capacity of reinforced concrete slabs strengthened with textile reinforced concrete. Eng. Struct. **40**, 317–326 (2012)
12. Loreto, G., Leardini, L., Arboleda, D., Nanni, A.: Performance of RC slab-type elements strengthened with fabric-reinforced cementitious-matrix composites. J. Compos. Constr. **18**(3), A4013003 (2013)
13. Babaeidarabad, S., De Caso, F., Nanni, A.: URM walls strengthened with fabric-reinforced cementitious matrix composite subjected to diagonal compression. J. Compos. Constr. **18**(2), 04013045 (2013)
14. Babaeidarabad, S., Loreto, G., Nanni, A.: Flexural strengthening of RC beams with an externally bonded fabric-reinforced cementitious matrix. J. Compos. Constr. **18**(5), 04014009 (2014)
15. Azam, R., Soudki, K.: FRCM strengthening of shear-critical RC beams. J. Compos. Constr. **18**(5), 04014012 (2014)
16. Schumann, A., Michler, H., Schladitz, F., Curbach, M.: Parking slabs made of carbon reinforced concrete. Struct. Concr. **19**, 647–655 (2018)
17. May, S., Steinbock, O., Michler, H., Curbach, M.: Precast slab structures made of carbon reinforced concrete. Structures **18**, 20–27 (2018)
18. May, S., Michler, H., Schladitz, F., Curbach, M.: Lightweight ceiling system made of carbon reinforced concrete. Struct. Concr. **19**(6), 1862–1872 (2018)
19. Salmon, D.C., Einea, A., Tadros, M.K., Culp, T.D.: Full scale testing of precast concrete sandwich panels. ACI Struct. J. **94**, 239–247 (1997)
20. Hegger, J., Zell, M., Horstmann, M.: Textile reinforced concrete–realization in applications. In: International FIB Symposium Tailor Made Concrete Structures: New Solutions For Our Society, pp. 357–362. CRC Press, Amsterdam (2008)
21. Hegger, J., Schneider, H., Sherif, A., Molter, M., Voss, S.: Exterior Cladding Panels as an Application of Textile Reinforced Concrete. Special Publication **224**, 55–70 (2004)
22. Colombo, I.G., Colombo, M., Di Prisco, M.: Bending behaviour of Textile Reinforced Concrete sandwich beams. Constr. Build. Mater. **95**, 675–685 (2015)
23. Anh Nguyen, V., Jesse, F., Curbach, M.: Experiments to establish the loadbearing behaviour of lightweight sandwich beams using textile-reinforced and expanded polystyrene concrete. Struct. Concr. **5**(17), 760–767 (2016)
24. Junes, A., Si Larbi, A.: An experimental and theoretical study of sandwich panels with TRC facings: use of metallic connectors and TRC stiffeners. Eng. Struct. **113**, 174–185 (2016)
25. Scholzen, A., Chudoba, R., Hegger, J.: Thin-walled shell structures made of textile-reinforced concrete: Part I: Structural design and construction. Struct. Concr. **16**(1), 106–114 (2015)
26. Scholzen, A., Chudoba, R., Hegger, J.: Thin-walled shell structures made of textile-reinforced concrete: Part II: Experimental characterization, ultimate limit state assessment and numerical simulation. Struct. Concr. **16**(1), 115–124 (2015)
27. Sharei, E., Scholzen, A., Hegger, J., Chudoba, R.: Structural behavior of a lightweight, textile-reinforced concrete barrel vault shell. Compos. Struct. **171**, 505–514 (2017)
28. Hegger, J., Curbach, M., Stark, A., Wilhelm, S., Farwig, K.: Innovative design concepts: application of textile reinforced concrete to shell structures. Struct. Concr. **19**(3), 637–646 (2018)
29. Chand, S.: Review—carbon fibers for composites. J. Mater. Sci. **35**(6), 1303–1313 (2000)
30. Sauder, C., Lamon, J., Pailler, R.: The tensile behavior of carbon fibers at high temperatures up to 2400 °C. Carbon **42**(4), 715–725 (2004)
31. Arboleda, D., Babaeidarabad, S., Nanni, A.: Durability of fabric reinforced cementitious matrix (FRCM) composites. In: 7th International Conference of FRP Composites in Civil Engineering, pp. 384. International Institute for FRP in Construction, Vancouver (2014)

32. Xu, S., Krüger, M., Reinhardt, H.-W., Ožbolt, J.: Bond characteristics of carbon, alkali resistant glass, and aramid textiles in mortar. J. Mater. Civ. Eng. **16**(4), 356–364 (2004)
33. Dvorkin, D., Peled, A.: Effect of reinforcement with carbon fabrics impregnated with nanoparticles on the tensile behavior of cement-based composites. Cem. Concr. Res. **85**, 28–38 (2016)
34. Donnini, J., Corinaldesi, V., Nanni, A.: Mechanical properties of FRCM using carbon fabrics with different coating treatments. Compos. B Eng. **88**, 220–228 (2016)
35. Peled, A., Mechtcherine, V., Nicke, D., Hempel, S.: Modifying carbon roving-cement matrix bond by inorganic coating. In: High Performance Fiber Reinforced Cement Composites (HPFRCC7), pp. 61–67. RILEM, Stuttgart (2015)
36. Schneider, K., et al.: Mineral-impregnated carbon fibre reinforcement for high temperature resistance of thin-walled concrete structures. Cement Concr. Compos. **97**, 68–77 (2019)
37. Silva, R.M.C., Silva, F.A.: Mechanical and bond behavior of carbon textile reinforced concretes under tensile loading. In: 4th Brazilian Conference on Composite Materials, pp. 289–297. Rio de Janeiro (2018)
38. Silva, F.A., Butler, M., Hempel, S., Toledo Filho, R.D., Mechtcherine, V.: Effects of elevated temperatures on the interface properties of carbon textile-reinforced concrete. Cement Concr. Compos. **48**, 26–34 (2014)
39. Lu, M., et al.: Improved interfacial strength of SiO_2 coated carbon fiber in cement matrix. Cement Concr. Compos. **91**, 21–28 (2018)
40. Duxson, P., et al.: Geopolymer technology: the current state of the art. J. Mater. Sci. **42**(9), 2917–2933 (2007)
41. Trindade, A.C.C., Alcamand, H.A., Borges, P.H.R., Silva, F.A.: Influence of elevated temperatures on the mechanical behavior of jute-textile-reinforced geopolymers. J. Ceram. Sci. Technol. **8**(3), 389–398 (2017)
42. Trindade, A.C.C., Borges, P.H.R., Silva, F.A.: Evaluation of fiber-matrix bond in the mechanical behavior of geopolymer composites reinforced with natural fibers. Adv. Civ. Eng. Mater. **8**(3), 361–375 (2019)
43. Trindade, A.C.C., de Silva, F.A., Alcamand, H.A., Borges, P.H.R.: On the mechanical behavior of metakaolin based geopolymers under elevated temperatures. Mater. Res. **20**, 265–272 (2017)
44. Brazilian Standard NBR 11578.: Cimento Portland composto. Associação Brasileira de Normas Técnicas (ABNT) (1991)
45. Bentur, A., Mindess, S.: Fiber reinforced cementitious composites. In: Civil Engineering. CRC Press (2006)
46. Trindade, A.C.C., Liebscher, M., Curosu, I., Mechtcherine, V., Silva, F.A.: Effect of aggregate incorporation on the mechanical performance of K- and Na-based strain-hardening geopolymer composites (SHGC) reinforced with PVA fibers. Constr. Build. Mater (submitted online in 2019)
47. Mehta, P.K., Monteiro, P.J.M.: Concrete: Microstructure, Properties and Materials. McGraw-Hill (2006)

Calorimetry Study of the Influence of Portland Cement Content, Slag/Fly Ash Ratio, and Activator Type on the Early Hydration of Hybrid Cements

Gregor J. G. Gluth and Solen Garel

Abstract Hybrid cements (cements composed of Portland clinker, supplementary cementitious materials and an alkaline activator) potentially combine advantages of conventional cements with those of alternative binders, such as low heat of hydration and improved durability in some environments. While fly ash-based hybrid cements have been studied in considerable detail, slag-dominated hybrid cements appear to have received less attention. Here, the latter materials have been studied by isothermal calorimetry, X-ray diffraction and strength testing. The heat of hydration of these cements was as low as $\sim 50\%$ of that of an ordinary Portland cement, while their strength after 28-day curing was in the range 31–61 MPa. The phase assemblages after 28-day curing depended on the activator, with Na_2SO_4 leading to ettringite and Na_2CO_3 leading to hemicarbonate formation, respectively, besides C–A–S–H, portlandite and hydrotalcite. The U phase was identified when a high Na_2SO_4 dose and/or fly ash was employed. Na_2SO_4 accelerated the early reaction of the Portland clinker, while Na_2CO_3 appeared to decrease the extent of reaction of the clinker and led to a shift of the second hydration peak (likely related to slag reaction) to later hydration times, as did substitution of slag by fly ash. Increasing Na_2SO_4 dose from 4 to 6% did not lead to further acceleration of hydration or improved strength.

Keywords Hybrid cements · Portland-alkaline cements · Alkali-activated materials · Calorimetry · Heat of hydration

G. J. G. Gluth (✉) · S. Garel
Bundesanstalt für Materialforschung und -prüfung (BAM), 12205 Berlin, Germany
e-mail: gregor.gluth@bam.de

1 Introduction

Hybrid cements is a term used to denote binders composed of Portland cement (OPC) or Portland clinker, a high proportion of a supplementary cementitious materials (SCM) such as hard coal fly ash or ground granulated blast furnace slag, and an alkaline activator, usually in solid form. The activator can be, for example, Na_2SO_4, Na_2CO_3, NaOH, sodium silicate, or a mixture of two or more of these salts. During the last few years, these cements have received increasing attention [1–5], and recently parallels have been drawn between these materials and ancient Roman concretes, implying an excellent durability of concretes based on hybrid cements in salt-rich environments such as seawater [6]. Further potential advantages of these binders include a low heat of hydration, high final strength and a lowered CO_2 footprint compared to conventional Portland and blended cements, while retaining a comparatively rapid strength evolution due to the use of an activator.

While detailed early-hydration (calorimetry) studies have been published for fly ash-based hybrid cements [1, 2, 4], calorimetry data for slag-based hybrid cements is scarcer and less well understood [5]. To contribute to these issues and extend the data base concerning early hydration, phase assemblage and strength of hybrid cements, the present study investigated blends with varying proportions of OPC, slag and fly ash, activated with Na_2SO_4 or Na_2CO_3, by isothermal calorimetry, compressive strength testing and X-ray diffraction (XRD).

2 Materials and Methods

2.1 Starting Materials, Hybrid Cements and Curing

Starting materials for the hybrid cements were an OPC (CEM I 42.5 R), a ground granulated blast furnace slag and a hard coal fly ash. Their chemical compositions, determined by ICP-OES after total microwave digestion, are shown in Table 1. The slag was almost completely amorphous, containing only very minor amounts of gehlenite and calcite as impurities. The fly ash contained a high fraction of amorphous phase (estimated ~ 65–70 wt%) as well as mullite, quartz, hematite, lime, anhydrite and ferrite spinel (phase assemblages determined by XRD, see Sect. 2.2). The solid activators Na_2SO_4 and Na_2CO_3 were of analytical grade.

Table 1 Chemical compositions of the starting materials (in wt%)

Oxide/LOI	SiO_2	Al_2O_3	Fe_2O_3	CaO	MgO	Na_2O	K_2O	SO_3	LOI
OPC	19.5	4.7	2.8	62.9	2.0	0.3	1.0	3.4	2.7
Slag	33.4	12.0	0.3	43.8	4.9	0.3	0.8	1.8	1.2
Fly ash	57.4	17.5	7.0	7.4	0.6	0.5	1.0	0.3	4.1

Table 2 Compositions of the pastes, given on a 100 g of (OPC + slag + fly ash) basis. Solids in the water/solids ratios (w/s) include the activator

	OPC (g)	Slag (g)	Fly ash (g)	Na_2SO_4 (g)	Na_2CO_3 (g)	Water (g)	w/s
OPC	100	–	–	–	–	40.0	0.40
S70-4s	30	70	–	4	–	41.5	0.40
S80-4s	20	80	–	4	–	41.5	0.40
S80-4c	20	80	–	–	4	41.5	0.40
S85-4s	15	85	–	4	–	41.5	0.40
S85-6s	15	85	–	6	–	42.5	0.40
S40F40-s	20	40	40	4	–	41.7	0.40
S20F60-s	20	20	60	6	–	42.3	0.40

From these starting materials, seven different hybrid cements with varying proportions of OPC, slag and fly ash were designed, and the activator type or dose varied for some of these; a neat OPC was studied for comparative purposes. All binders were mixed with deionized water at a water/solids ratio of 0.40 to produce pastes; their compositions are shown in Table 2.

The pastes were mixed in a beaker with an "IKA-WERK" mechanical mixer at a speed of 300–350 rpm for 30–60 s, and then ∼15 g of the paste immediately poured into two plastic ampoules and these inserted in the calorimeter (Sect. 2.2). The remainder of the paste was cast into 20 mm × 20 mm × 20 mm silicone molds. These were stored for two days in a covered sink over an open water surface at 21 °C, the specimens then removed from the molds, wrapped in Parafilm and cured for additional 26 days at 21 °C.

At the age of 28 days, the compressive strengths of the pastes were determined on at least four individual cube specimens per mix-design (loading rate 240 N/s), and subsequently randomly taken fracture pieces were ground with mortar and pestle (agate) to a powder. These powders were stored for approx. two weeks over saturated K_2CO_3 solution (RH = 43%) in an argon-flushed desiccator until start of the XRD measurements (Sect. 2.2).

2.2 Calorimetry and X-ray Diffraction Measurements

Calorimetry was conducted in a "TAM Air" isothermal calorimeter according to EN 196-11:2018 up to the age of 7 days; the temperature was set at 20 °C. The time between addition of water to the cements and the start of the measurements was recorded and the obtained calorimetry data adjusted accordingly. All measurements were conducted in duplicate; as the repeatability was very good, only one calorimetry curve per paste is shown below. Results will be expressed in J/g or mW/g, where the unit mass refers to the sum of all solids in the paste, viz. OPC, slag, fly ash plus the activator.

XRD patterns were obtained on a "Rigaku Ultima IV" diffractometer in Bragg-Brentano geometry. Sample holders were filled by top loading and the experimental conditions were: Cu$K\alpha$ radiation (λ = 1.54187 Å); tube operating at 40 kV, 40 mA; sampling interval: 0.02° 2θ; scan rate: 0.5° 2θ min^{-1}; scanning range: 5–65° 2θ; divergence slit: in-plane 0.5°, axial 10 mm; strip detector D/teX Ultra with 5° Soller slits. The sample holders were spun at 15 rpm during the measurements.

3   Results and Discussion

3.1   Early Hydration

Figure 1 shows the cumulative heat release of the cement pastes up to 7 days of reaction. As expected, the released heat was highest for the neat OPC paste, and there was a tendency of lower heat release with decreasing OPC fraction in the hybrid cements. The standard values of the heats of hydration (average of two measurements after 7 days of hydration as specified in EN 196-11:2018; heat release during the first 30 min after the addition of water ignored to minimize the influence of heat introduced due to external mixing [7]) were OPC: 318 J/g; S70-4s: 218 J/g; S80-4s: 180 J/g; S80-4c: 154 J/g; S85-4s: 157 J/g; S85-6s: 173 J/g; S40F40-4s: 179 J/g; and S20F60-6s: 182 J/g. The uncorrected values, i.e. the heats of hydration including the first 30 min of reaction, were 18–26 J/g higher.
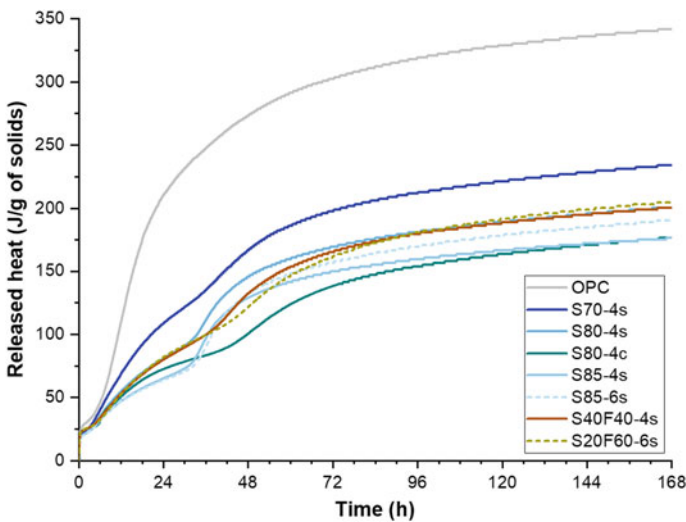

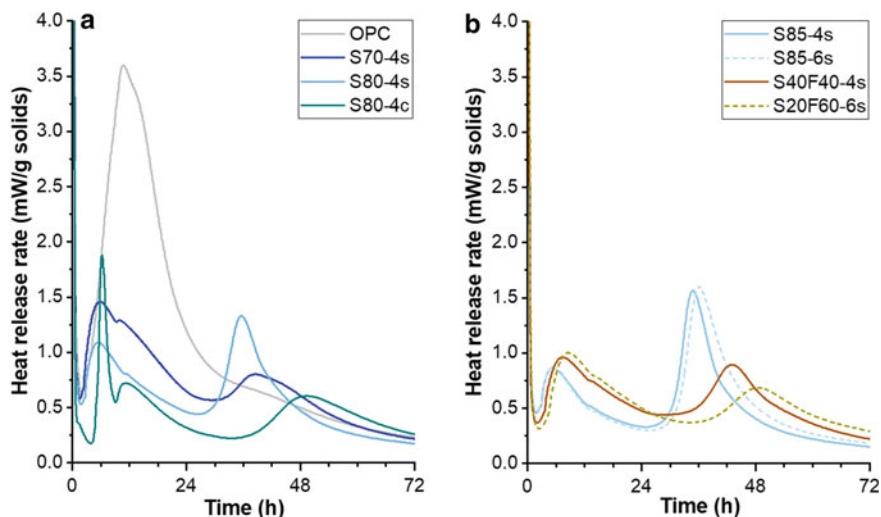**Fig. 1** Heat release of the cement pastes up to 7 days

Fig. 2 Heat release rate of the cement pastes up to 3 days

A more detailed discussion and a tentative interpretation of the characteristics of the hydration of the pastes is facilitated by their heat flow curves, shown in Fig. 2. The heat flow curve of OPC paste exhibited the typical heat release rate evolution, with the main hydration (mostly formation of C–S–H and portlandite) peak at ~ 11 h and a shoulder at ~ 13–14 h, which is related to the dissolution of C_3A and resumption of ettringite formation ("sulfate depletion peak") [7–9]. In addition, a shoulder can be discerned at ~ 40 h, which has been assigned to the conversion of ettringite to AFm phase [8].

In the heat flow curves of all hybrid cements, a peak with a similar (slightly earlier) position and similar shape, but lower intensity, as the main hydration peak of the OPC paste was present. Its integrated intensity decreased with a decreasing proportion of OPC in the hybrid cements and, thus, the peak is assigned to the reaction of the Portland clinker in the blends.

In the Na_2SO_4-activated hybrid cements, the onset of this main hydration peak, the acceleration period and the maximum of the main hydration peak was shifted to earlier hydration times, compared to the neat OPC paste. This can be attributed to the accelerating effect of Na_2SO_4 on the early hydration of alite and Portland clinker [10, 11] as well the "filler effect" of the slag or the slag/fly ash blend on the reaction of the Portland clinker at this stage of reaction [12].

In the hybrid cements, the "sulfate depletion peak" was somewhat better resolved from the main peak, i.e. enhanced, compared to the OPC paste (similar to what has previously been observed for OPC-filler blends [12] and fly ash-based hybrid cements [1]). This was particularly pronounced in the Na_2CO_3-activated paste S80-4c, where the two peaks were well separated, the reason for which cannot be deduced from the present results. It also remains unclear whether the "sulfate

depletion peak" in the hybrid cements is caused solely by the same reactions as in OPC pastes.

In addition, it can be noted that the total heat of hydration after 7 days was lower by ~ 25 J/g for S80-4c than for the other hybrid cements with 20% OPC, partly due to less heat of reaction from the Portland clinker up to ~ 30 h (Figs. 1 and 2).

The second major peak in the heat flow curves of the hybrid cements, with its maximum at ~ 35–50 h, can be tentatively assigned to the reaction of the SCM (slag or slag/fly ash blend) in these cements, inter alia based on the similarity of its position with the maxima of the heat flow curves of Na_2SO_4- and Na_2CO_3-activated slags with $\sim 6\%$ MgO presented in refs. [13, 14].

The peak occurred at ~ 39 h for S70-4s; at ~ 36 h for S80-4s, S85-4s and S85-6s; at ~ 43 h for S40F40-4s; and at ~ 49–50 h for S20F60-6s and S80-4c. Thus, a general trend was that substitution of slag by fly ash as well as use of Na_2CO_3 instead of Na_2SO_4 led to a later reaction of the SCM in the hybrid cements. The higher Na_2SO_4 dose in S85-6s than in S85-4s did not shift the position of this peak to earlier hydration times. Similarly, the higher activator dose in S20F60-s than in S40F40-4s could not fully compensate for the higher proportion of fly ash in this hybrid cement.

3.2 28-Day Phase Assemblage and Compressive Strength

Figure 3 shows the XRD patterns of the cement pastes after 28-day curing. The OPC paste exhibited the expected hydration products, viz. portlandite, ettringite, monosulfate and hemicarbonate (or a mixture of hemicarbonate and monocarbonate) as well as unreacted belite, ferrite and some calcite.

The phase assemblages of the hydrated hybrid cements can be subdivided into three groups. The hybrid cement pastes with only slag (no fly ash), activated with Na_2SO_4, contained portlandite, C–A–S–H (with reflections like C–S–H(I) [15]), ettringite, hydrotalcite and calcite. In addition, the U phase (a sodium-containing AFm phase) [16] was identified through its reflections at 10.00 Å ($8.84° 2\theta$) and 3.53 Å ($25.23° 2\theta$) in paste S85-6s with the highest Na_2SO_4 dose.

Paste S80-4c contained portlandite, C–A–S–H, hemicarbonate, hydrotalcite and calcite. As the activator for this paste was Na_2CO_3, the absence of ettringite and the presence of hemicarbonate were expected. The prominent reflections at 2.78 Å ($32.20° 2\theta$) and 2.74 Å ($32.68° 2\theta$) in the XRD patterns of this paste indicate a higher amount of unreacted belite in this paste than in the Na_2SO_4-activated pastes, in line with the calorimetry results.

The hybrid cements with slag and fly ash contained portlandite, ettringite, hemicarbonate, hydrotalcite, calcite and the U phase (again evidenced by reflections at 10.00 Å and 3.53 Å) as well as unreacted mullite and quartz from the fly ash. The presence of C–A–S–H could not be unambiguously identified in these pastes; thus, it is possible that a more N-A-S-H-like gel formed in the pastes, in line with their lower total Ca content.
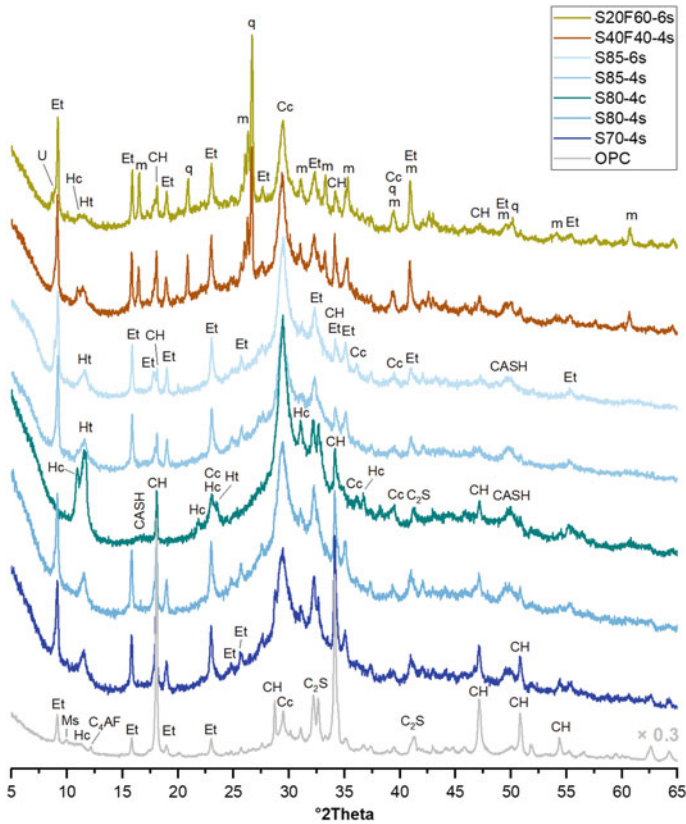
Fig. 3 XRD patterns of the cement pastes after 28-day curing. Selected major reflections are labeled: CASH, C–A–S–H; Cc, calcite; CH, portlandite; C_2S, belite; C_4AF, ferrite; Et, ettringite; Hc, hemicarbonate; Ht, hydrotalcite; m, mullite; Ms, monosulfate; q, quartz; U, U phase

Calcite in all of these pastes formed likely, at least in part, by carbonation of the specimens during curing and storage. It is noted that no vaterite or aragonite was identified, contrary to what is often observed for alkali-activated slags.

The compressive strengths of the hydrated pastes after 28 days of curing are shown in Fig. 4. For the hybrid cements with slag (no fly ash), the strengths were generally in line with their OPC content, i.e. strength decreased with decreasing OPC fraction. The only exception was S80-4c, which exhibited a lower strength than the corresponding Na_2SO_4-activated paste S80-4s as well as S85-4s and S85-6s, in line with the calorimetry and XRD results that indicate a lower degree of reaction of the OPC in S80-4c, but possibly also influenced by the subsequent reaction of the slag.

The hybrid cements with slag and fly ash exhibited a lower strength than S80-4s with the same OPC fraction and the same activator (Na_2SO_4) but only slag as SCM. These differences in strength evolution are likely related to different hydration
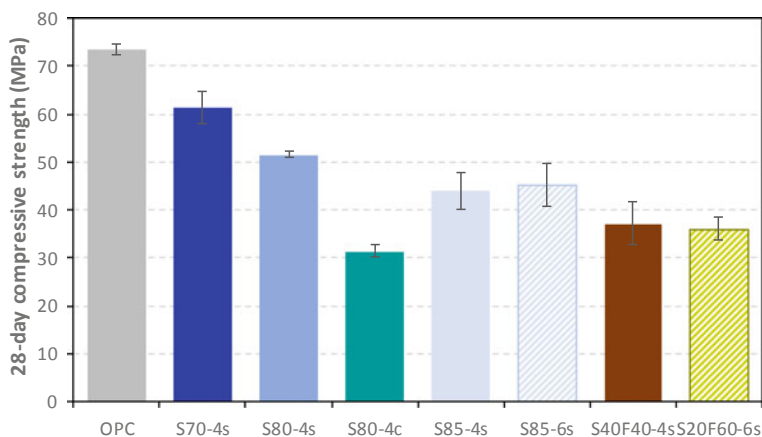
Fig. 4 Compressive strength of the cement pastes after 28-day curing

products in these pastes (no C–A–S–H was identified in S40F0-4s and S20F60-6s, in accord with their lower Ca content).

The higher Na_2SO_4 dose and/or the higher fly ash proportion in S20F60-6s than in S40F40-4s led to a slightly higher heat of hydration (Fig. 1), but not to a higher compressive strength. Finally, it is noted that also in S85-6s the higher activator dose than in S85-4s caused a higher heat of hydration (Fig. 1), but not a significantly higher compressive strength.

4 Conclusions

In the present study, hybrid cements based on slag or slag/fly ash blends exhibited a heat of hydration (determined according to EN 196-11:2018) that was only 48–69% of neat OPC (CEM I 42.5 R), which is a major advantage for the construction of large concrete elements, while at the same time retaining a fast early hydration and acceptable 28-day compressive strengths in the range 31–61 MPa.

The first main peak in the heat flow curves of the hybrid cements was tentatively assigned to the hydration of the Portland clinker, and the second main peak to the hydration of the slag or the slag/fly ash blend. Use of Na_2SO_4 as activator accelerated the reaction of the clinker, compared to the neat OPC paste. An increase of the Na_2SO_4 dose from 4 to 6% generally caused a higher heat of hydration but did not lead to a faster reaction or higher compressive strength. Use of Na_2CO_3 instead of Na_2SO_4 as well as partial substitution of slag by fly ash led to a shift of the second main peak to later hydration times, likely related to a lower efficiency of the Na_2CO_3 in activating the slag and the generally slower reaction of fly ash than of slag, respectively. In addition, use of Na_2CO_3 appeared to decrease the degree of

reaction of the clinker. The tentative conclusions regarding the early hydration drawn here need to be confirmed via hydration stoppage and subsequent microstructural characterization at the appropriate times as indicated by the heat flow curves of the cements (Fig. 2).

The phase assemblages of the hybrid cements with slag (no fly ash) after 28 days of curing where much in line with expectations, yielding portlandite, C–A–S–H [C–S–H(I)-like] and hydrotalcite in all of them, ettringite in the Na_2SO_4-activated cements, and hemicarbonate in the Na_2CO_3-activated cements. In the fly ash-containing cements, ettringite and portlandite appeared to be the major reaction products, while the presence of C–A–S–H could not be unequivocally verified by XRD. The latter is likely related to the lower Ca content of these cements, which could lead either to a different structure of the precipitating C–(N-)A–S–H gel or a more N–A–S–H gel-like reaction product. A peculiar feature was the occurrence of the U phase in the hybrid cements with high Na_2SO_4 dose and/or fly ash-for-slag substitution. The consequences of its presence, e.g. for durability, need to be elucidated in future work. In addition, the influence of the slag composition (particularly MgO and Al_2O_3 contents), which is of major importance for the reactions of Na_2SO_4- and Na_2CO_3-activated slags [13, 14, 17], on the reactions and properties of hybrid cements should be a focus of future work.

References

1. Donatello, S., Fernández-Jimenez, A., Palomo, A.: Very high volume fly ash cements. Early age hydration study using Na_2SO_4 as an activator. J. Am. Ceram. Soc. **96**, 900–906 (2013)
2. Garcia-Lodeiro, I., Fernandez-Jimenez, A., Palomo, A.: Hydration kinetics in hybrid binders: early reaction stages. Cement Concr. Compos. **39**, 82–92 (2013)
3. García-Lodeiro, I., Fernández-Jiménez, A., Palomo, A.: Variation in hybrid cements over time. Alkaline activation of fly ash–portland cement blends. Cem. Concr. Res. **52**, 112–122 (2013)
4. Alahrache, S., Winnefeld, F., Champenois, J.-B., Hesselbarth, F., Lothenbach, B.: Chemical activation of hybrid binders based on siliceous fly ash and Portland cement. Cement Concr. Compos. **66**, 10–23 (2016)
5. Mota, B., Matschei, T., Scrivener, K.: Impact of sodium gluconate on white cement-slag systems with Na_2SO_4. Cem. Concr. Res. **122**, 59–71 (2019)
6. Palomo, A., Monteiro, P., Martauz, P., Bilek, V., Fernandez-Jimenez, A.: Hybrid binders: a journey from the past to a sustainable future (*opus caementicium futurum*). Cem. Concr. Res. **124**, 105829 (2019)
7. Wadsö, L., Winnefeld, F., Riding, K., Sandberg, P.: Calorimetry. In: Scrivener, K., Snellings, R., Lothenbach, B. (eds.) A Practical Guide to Microstructural Analysis of Cementitious Materials, pp. 37–74. CRC Press, Boca Raton (2016)
8. Taylor, H.F.W.: Cement Chemistry, 2nd edn. Thomas Telford, London (1997)
9. Jansen, D., Goetz-Neunhoeffer, F., Lothenbach, B., Neubauer, J.: The early hydration of ordinary Portland cement (OPC): an approach comparing measured heat flow with calculated heat flow from QXRD. Cem. Concr. Res. **42**, 134–138 (2012)
10. Mota, B., Matschei, T., Scrivener, K.: The influence of sodium salts and gypsum on alite hydration. Cem. Concr. Res. **75**, 53–65 (2015)

11. Mota, B., Matschei, T., Scrivener, K.: Impact of NaOH and Na_2SO_4 on the kinetics and microstructural development of white cement hydration. Cem. Concr. Res. **108**, 172–185 (2018)
12. Berodier, E., Scrivener, K.: Understanding the filler effect on the nucleation and growth of C–S–H. J. Am. Ceram. Soc. **97**, 3764–3773 (2014)
13. Bernal, S. A., Ke, X., Provis, J. L.: Rational design of alkali activated slag materials. In: 15th International Congress on the Chemistry of Cement, article No. 457. Research Institute of Binding Materials Prague, Prague (2019)
14. Bernal, S.A.: Advances in near-neutral salts activation of blast furnace slags. RILEM Tech. Lett. **1**, 39–44 (2016)
15. Richardson, I.G.: Model structures for C–(A)–S–H(I). Acta Crystallogr. B **70**, 903–923 (2014)
16. Li, G., Le Bescop, P., Moranville, M.: The U phase formation in cement-based systems containing high amounts of Na_2SO_4. Cem. Concr. Res. **26**, 27–33 (1996)
17. Myers, R.J., Bernal, S.A., Provis, J.L.: Phase diagrams for alkali-activated slag binders. Cem. Concr. Res. **95**, 30–38 (2017)

Chloride Ion Penetration into Cracked UHPFRC During Wetting-drying Cycles

Ana Mafalda Matos, **Sandra Nunes**, **Stefan Chaves Figueiredo**,
Erik Schlangen, and **José L. Barroso Aguiar**

Abstract The subject of this paper is the extent to which, during wetting–drying cycles, chloride ions can penetrate Ultra-high-Performance Fibre Reinforced Cementitious Composites (UHPFRC) specimens subjected to combined mechanical and environmental load. Pre-cracking was obtained by subjecting prismatic specimens ($40 \times 40 \times 60mm^3$) to four-point bending until a predefined crack opening displacement (COD) is reached, using a dedicated test setup. Three target CODs were studied: 300, 350 and 400 μm. Exposure to a concentrated chloride solution (3.5% NaCl) was used as an environmental load. Specimens we subjected to wetting–drying cycles for one year. After this exposure period, the chloride penetration was characterised both qualitatively (by colourimetric analysis with silver nitrate) and quantitatively (by determining the chloride profile). The effect of damage level on chloride penetration and its impact on structures durability is discussed in the current paper.

Keywords Ultra-high-performance fibre reinforced cementitious composites (UHPFRC) · Cracking · Chloride exposure · Durability

A. M. Matos · S. Nunes (✉)
CONSTRUCT-LABEST, Faculty of Engineering (FEUP), University of Porto, Porto,
Portugal
e-mail: snunes@fe.up.pt

S. C. Figueiredo · E. Schlangen
MICROLAB, Faculty of Civil Engineering and Geosciences, Delft University of Technology,
Delft, The Netherlands

J. L. B. Aguiar
School of Engineering, University of Minho, Guimarães, Portugal

227

1 Research Scope

The design of UHPFRC aims at a densely compacted cementitious matrix (herein referred as UHPC) using a high content of reactive powders, a minimal amount of water, a high-range water reducer and an adequate fine aggregate gradation, in order to produce high flowability and improved mechanical and durability properties [1]. This superior mechanical and durability performance of UHPFRC makes it particularly suitable for use in rehabilitation and strengthening of reinforced concrete structures. This concept relies on the casting of thin layers/jackets of UHPFRC to strengthening and waterproofing a specific structural concrete element [2].

UHPFRC is being utilized in several applications around the world [3, 4], but it still faces some challenges for broader implementation. In this context, a PhD research programme was developed at the Faculty of Engineering, Porto University, Portugal (FEUP), addressing some of those issues, namely:

- Developing a new UHPC mixture for rehabilitation/strengthening applications employing local available raw materials (including waste materials) and on-site fabrication under regular casting and curing conditions [5]
- To mitigate autogenous shrinkage of UHPC employing internal curing, in order to minimise the early ages cracking risk [5]
- To investigate several critical durability aspects of the new UHPC mixture and compare its performance to other UHPCs reported in the literature
- Studying the influence of cracking on key durability parameters, such as water transport by capillary suction [6] and chloride ion penetration.

Whereas most common commercially-available UHPCs involve high contents of silica fume and thermal curing, the UHPC under study does not. Another distinctive characteristic is that it incorporates a waste generated from oil refinery industry (ECat), acting as an internal curing agent [5].

The current paper focuses on the influence of cracking on chloride ion penetration, in view of the rehabilitation/strengthening applications. UHPFRC small beams, with a typical fibre content of 3.0%, were pre-cracked using a four-point bending test. Different crack patterns were obtained on the specimen's tensile face. Then specimens were subjected to wetting–drying cycles, using a concentrated chloride solution (3.5% NaCl), during one year. After this exposure period, the chloride penetration was characterised both qualitatively (by colourimetric analysis with silver nitrate) and quantitatively (by determining the chloride profile).

2 Experimental Programme

2.1 UHPFRC Mix Proportions, Specimens Manufacturing and Curing

The new UHPFRC recently developed [5] is constituted by CEM I 42.5R Portland cement complying with EN 197-1; silica fume (specific surface area of 19632 m^2/kg; SiO_2 content >90%) fulfilling the requirements of EN 13263-1; limestone filler (specific surface of 550 m^2/kg; $CaCO_3$ > 98%), complying with the requirements of EN 12620; siliceous natural sand (0–1 mm) and ECat (a spent equilibrium catalyst, generated by Sines Refinery, Portugal). A polycarboxylate type superplasticiser with a specific gravity of 1080 kg/m^3 and 40% solid content and potable water were included. As reinforcement, 3.0% by volume of smooth short steel fibres (13 mm length and 0.21 mm diameter) and 2750 MPa of tensile strength were used. Table 1 presents the mixture proportions of the new UHPFRC. More details concerning the origin and properties of raw materials can be found elsewhere [5].

UHPFRC mixtures were produced using a mixer as specified in with NP EN 196-1 following the mixing procedure described in [5]. Several prismatic specimens (40 × 40 × 160 mm^3) were moulded in one lift without any mechanical vibration due to the self-compacting ability of the mixtures. The number of specimens produced for each condition is detailed in Table 2. The specimens were then covered with a plastic sheet and demoulded after one day, and then kept underwater in a chamber at 20 ± 2 °C until the testing age.

The referencing of specimens considered the fibre content, the target COD and the specimen replicate number. For example, "3.0%-350-1", corresponds to a specimen number one, incorporating 3.0% steel fibres and a target COD_{load} of 350 μm. Specimens used for assessment of flexural strength at 28 days are referenced as "3.0%-W28-i".

Table 1 Mixture proportions of the new UHPFRC [5]

Material	(kg/m³)
Cement	690.2
Silica fume	33.6
Limestone filler	250.6
ECat	155.5
Siliceous sand	775.0
Superplasticizer	19.5
Steel fibres	235.0
Mixing water	160.9
ECat's absorption water	46.6

Table 2 Testing plan

References	Conditioning before cracking	Target COD_{load}	Chloride exposure condition	Testing age	Outcomes
3.0%-W28-i	Immersion in water at 20ºC up to 28 days	Test conducted up to failure	none	28 days	Load-displacement curves
3.0%-0-i		0 µm	Unloaded	379 days	Chlorides content profile and penetration depth
3.0%-300-i		300 µm	Loaded	379 days	
3.0%-350-i		350 µm	Unloaded	379 days	
3.0%-400-i		400 µm	Unloaded		

2.2 Cracking Method and Loading Strategy

After 28 days of water curing, prismatic specimens were cracked by imposing different crack open displacements (COD), namely, 300, 350 and 400 µm, through four-point bending loading, according to the procedure described in EN 12390-5 (Fig. 1). The test was carried out employing an Instron 300 kN Instron testing machine, under displacement control with a displacement rate of 0.003 mm/s. Two linear variable differential transducers (LVDT) were fixed on each side of the specimen, perpendicular to the loading direction, to monitor the COD (Fig. 1). When the target COD was achieved (COD_{load}), the specimens "3.0%-350-i" and "3.0%-400-i" were unloaded, and the residual COD was recorded (COD_{res}).

In the specific case of "3.0%-300-i" specimens, when the predefined COD_{load} = 300 µm was achieved, the specimens were unloaded and taken out from

Fig. 1 Four-point bending test cracking method
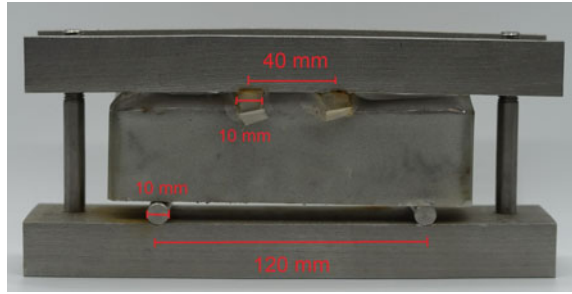
the testing machine. Then, these were immediately allocated on a stainless-steel frame, as shown in Fig. 2, while keeping the LVDTs on the specimens. Subsequently, the specimens were re-loaded up to the predefined COD_{load} of 300 µm using threaded rods tightened by a torque wrench. Afterwards, LVDTs were removed carefully, and the wetting–drying chlorides cycles were carried out for these specimens in a loaded state.

Before initiating the wetting–drying cycles, the side and compression surfaces of all prisms were sealed using waterproof tape to ensure the chloride penetration only through the cracked surface. Is must be noted that it was not possible to protect the loaded surfaces of specimens kept in the stainless-steel frame (3.0%-300-i).

2.3 Characterisation of the Crack Pattern Produced by Bending

After cracking, a mesh was drawn in the zone of maximum tension strain (in between the two applied forces) (Fig. 3a) in all specimens except those from 3.0%-300-i series. The widths of cracks observed in the tension face of each specimen were measured using a Microscope Multizoom Nikon AZ100 in the unloaded state. Measurements were taken from cracks crossing the three lines A, B and C, as shown in Fig. 3a. A typical photo of a crack with measurements is shown in Fig. 3b.

2.4 Wetting–Drying Chloride Cycles

For the long term chloride experiment the "3.0%-0-i" (non-cracked), "3.0%-300-i" (loaded, kept inside the stainless steel frame), "3.0%-350-i" and "3.0%-400-i" (unloaded, with residual COD) specimens were tested, as described in Table 2. Specimens were subjected to weekly wetting–drying cycles consisting of 48 h
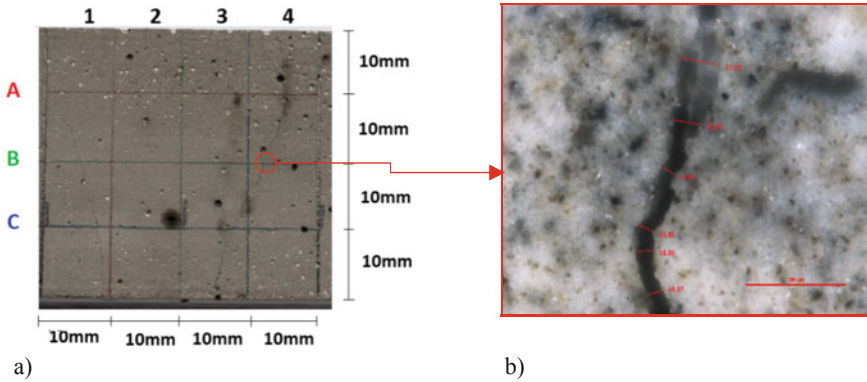
Fig. 3 a Scheme for measuring of the crack number and widths; **b** Typical photo with measurements of crack width

partial immersion in a 3.5% NaCl water solution, followed by five days of drying at 20ºC and 50%RH, for 1 year.

2.5   Chloride Penetration Analysis

After the exposure to chlorides, the chloride penetration depth was measured on dry cut specimens surface, using the colourimetric method. A silver nitrate solution was sprayed on the specimen's surface, the chloride depth was measured from the visible white silver chloride precipitation. The other half of the specimen was used for chemical analysis to determine the chloride content following the procedure described in EN 196-2. The samples were taken from the central part of the specimen (in between the two load points) in the direction of chloride penetration close to a macro-crack (when visible), and following the "dry drilling method" procedure according to RILEM Recommendation TC 178-TMC [7], in steps of approximately 5 mm. The steel fibres were removed from the powder sample using a magnet. The chloride content profile was also determined on a water-cured specimen not exposed to external chlorides (C_0).

3   Results and Discussion

3.1   COD Recovery After Unloading (COD_{load} and COD_{res})

Figure 4a shows the load–displacement curves obtained while establishing target COD_{load}, as well as, the curves of specimens tested under four-point bending up to
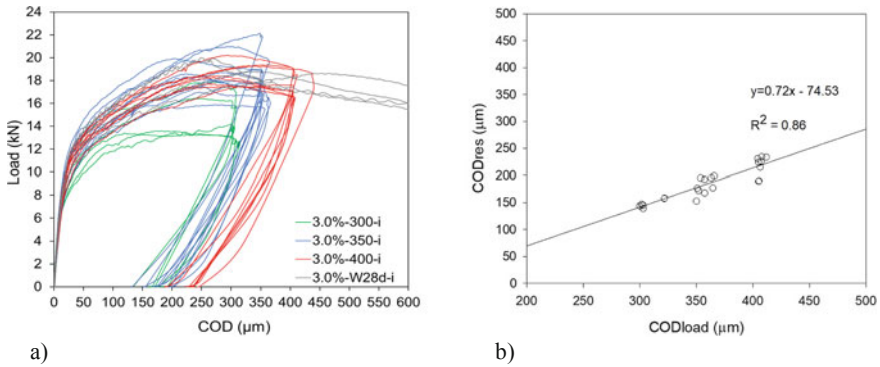
a)   b)

Fig. 4 **a** Load-displacement curves obtained at 28 days while establishing target COD_{load} of 300, 350 and 400 μm; and **b** relation between COD_{load} and COD_{resn}

the beginning of softening region, at 28 days (grey lines in Fig. 4a). Results of COD_{res} obtained after unloading as a function of COD_{load} are represented in Fig. 4b, displaying a good linear relation between COD_{res} and COD_{load}. This trend is in agreement with studies of Ma et al. [8] and also with previous studies carried out by the authors [6].

3.2 Crack Pattern Produced by Bending

The average number of cracks observed over a length of 40 mm remained below 9 (see Fig. 5a) while the median of crack width results is under 32 μm (see Fig. 5b, black marks). These results agree with previous findings of the authors [6]. The maximum crack width (see Fig. 5b, red marks) results seem to increase with the increase of COD_{res}.

3.3 Chloride Penetration

After one year of wetting–drying chlorides cycles, all specimens were in excellent condition with no evidence of surface scaling or additional cracking. Nevertheless, as expected, the corrosion of fibres closer to the surface was observed.

For cracked specimens, 3.0%-350-i and 3.0%-400-i, two zones can be distinguished: the zone close to the macro-crack (D_{crack}) and the remaining zones in between the loading points (D_m) with only fine micro-cracks as depicted in Fig. 6. The powder sample for chloride content determination was always extracted near the macro-crack zone. In the cracked specimens (3.0%-350-i and 3.0%-400-i), a localised and significant chloride penetration (between 10 and 17 mm) was
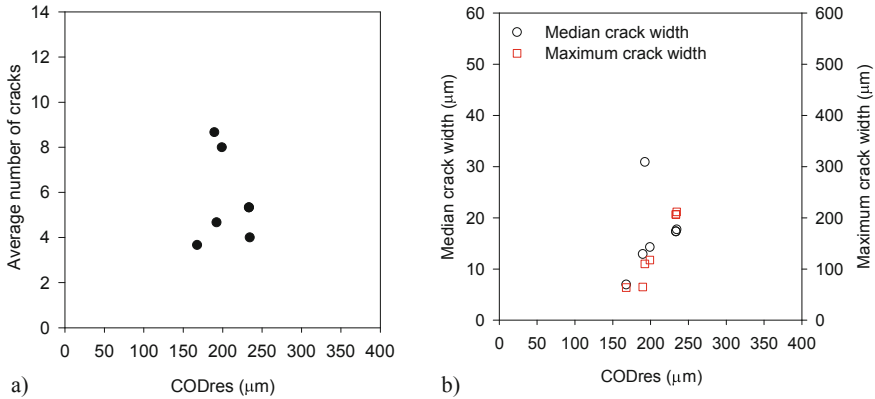
Fig. 5 **a** Average number of cracks and **b** relationship between COD_{res} and median/maximum crack width
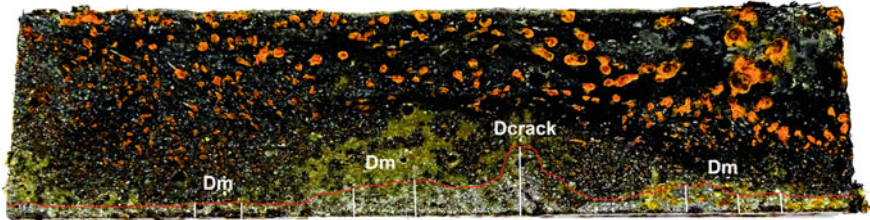

Fig. 6 Chloride penetration on a specimen with a macro-crack formation (3.0%-350-i)

observed close to the macro-crack. On the other hand, in reference specimens or uncracked areas of specimens (similar to D_m), more uniform penetration occurred (roughly 2–3 mm).

Concerning loaded-cracked specimens, 3.0%-300-i, a different chloride penetration pattern was observed, since these specimens present only micro-cracks. These micro-cracks promoted suction of aqueous chloride solution, giving rise to a maximum chloride penetration depth of 18–19 mm.

The average chloride content profiles are presented in Fig. 7. The chloride content is expressed as the percentage of chloride ions by the mass of the sample (UHPFRC without steel fibres). The non-cracked specimens (3.0%-0-i, Fig. 7) showed a high chloride concentration close to the specimen's surface with a decreasing tendency towards the inner part of the specimen. These results are in agreement with the colourimetric analysis with silver nitrate. The maximum chloride content varied between 0.47 and 0.79% at a depth ranging from 0 to 5 mm, then, between 5 and 10 mm depth, the chloride content drastically decreased (around 50%) for values between 0.26 and 0.41%. Afterwards, chloride content kept decreasing with an asymptotic shape converging to 0.20%.

Fig. 7 Chloride profiles
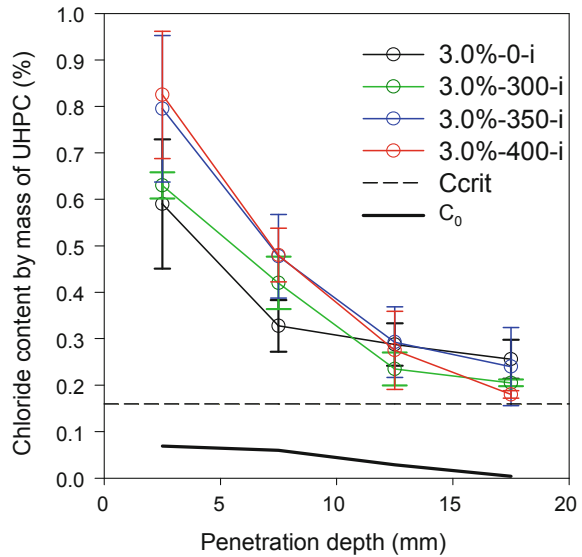
On cracked-unloaded specimens, 3.0%-350-i and 3.0%-400-i, samples were taken near a macro-crack, and it seems that the chloride profiles are similar despite the different COD_{load} applied. Maximum chloride content takes place close to the surface and then decreases as the penetration depth increases. The maximum chloride content, near the surface, varied between 0.61–0.98% and 0.62–0.90% for 3.0%-350-i and 3.0%-400-i specimens, respectively. It is common practice to discard the first mm of a chloride profile and take the next increment, around the 10 mm depth, as a constant initial, pseudo surface concentration [9]. Thus, Fig. 8 illustrates the results of chloride content at 5–10 mm depth as a function of maximum crack width. The chloride content seems not to change significantly with the maximum crack width. However, more data would be necessary to find a clear tendency.

On cracked-loaded specimens, 3.0%-300-i, the maximum chloride content in the cracked area was 0.61–0.65%. The 3.0%-300-i specimens presented also improved behaviour in terms of resistance to ingress of chlorides, compared to the remaining cracked specimens, which might be explained by the occurrence of self-healing. After the first wetting–drying cycles the fine micro-cracks sealed, which slowed the chlorides ingress.

European standard EN 206-1 restricts the chloride content to 0.40% by mass of binder for reinforced concrete structures. The critical chloride content (Ccrit) suggested in EN 206-1 is depicted in Fig. 8 (black dash line), which corresponds to a Ccrit = 0.16% by mass of UHPC. Non-cracked specimens (Fig. 7, black line) presented significant content of chlorides, higher than Ccrit = 0.16% up to 20 mm depth. Besides, the chloride content assessed on the main (and visible) crack of specimens 3.0%-300-i, 3.0%-350-i and 3.0%-400-i revealed that up to a depth of

Fig. 8 Relationship between chloride content (5–10 mm depth) with maximum crack width
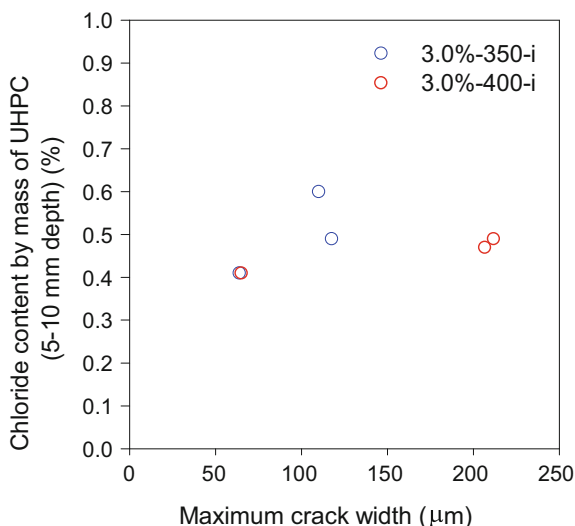
20 mm, the chloride content was above 0.16%. Though, it shows a decreasing tendency for higher depths.

Based on the results from this experimental campaign only, one can conclude that a minimum of 20 mm cover to reinforcement might be necessary to avoid rebar corrosion. This would be feasible considering the typical thickness of new UHPFRC reinforcement layers, of 40–80 mm [10].

Nevertheless, it should be pointed that: (i) this Ccrit value suggested in EN 206-1 is not a proper chloride threshold value, but rather a practical limit value for the production of fresh concrete [11]; (ii) wetting–drying cycles in laboratory environment can be more severe than "in-situ" exposure to normal ambient conditions (temperature, humidity, carbonation, seawater composition) and the influence scale factors must also be considered. Field experiments are crucial for calibration purposes of laboratory tests or modelling, but very time-consuming and not compatible with the typical duration of a PhD project.

4 Conclusions

After 1-year chlorides exposure, UHPFRC specimens were in excellent condition. However, through the colourimetric test, a penetration depth of approximately 10–19 mm was found on the main crack surrounding area. On the other hand, in non-cracked regions, the penetration depth was of about 2–3 mm, which was similar to the penetration over non-cracked specimens (3.0%-0-i).

EN 206-1 standard suggests a Ccrit equal to 0.40% by mass of binder (cement plus type II additions), which is equivalent to 0.16% by mass of UHPC under study.

Chloride contents observed in this experimental campaign were superior to Ccrit = 0.16% by mass of UHPC up to 20 mm, particularly, near a macro-crack of specimens 3.0%-350-i" and "3.0%-400-i".

Based on this campaign results only, a UHPFRC cover of at least 20 mm would be recommended. However, it should be considered that accelerated testing in the laboratory can be more severe than the exposure of real structures to natural ambient conditions. Thus, real field tests would be necessary to calibrate laboratory results.

References

1. Wang, D., Shi, C., Wu, Z., Xiao, J., Huang, Z., Fang, Z.: A review on ultra high performance concrete: Part II. hydration, microstructure and properties. Constr. Build. Mater. **96**, 368–377, Oct (2015)
2. Azmee, N.M., Shafiq, N.: Ultra-high performance concrete: from fundamental to applications. Case Stud. Constr. Mater. **9**, e00197, Dec (2018)
3. Bruhwiler, E., Denarie, E.: Rehabilitation and strengthening of concrete structures using ultra-high performance fibre reinforced concrete. Struct. Eng. Int. **23**(4), 450–457, Nov (2013)
4. Fehling, E., Schmidt, M., Walraven, J., Leutbecher, T., Frohlich, S.: Ultra-high performance concrete UHPC: fundamentals, design, examples. Ernst & Sohn, Wiley, Berlin, Germany (2014)
5. Matos, A.M., Nunes, S., Costa, C., Barroso-Aguiar, J.L.: Spent equilibrium catalyst as internal curing agent in UHPFRC. Cem. Concr. Compos. **104**, 103362, Nov (2019)
6. Matos, A.M., Nunes, S., Aguiar, J.L.B.: Capillary transport of water in cracked and non-cracked UHPFRC specimens. J. Adv. Concr. Technol. **17**(5), 244–259, May (2019)
7. Vennesland, Ø., Climent, M.A., Andrade, C.: Recommendation of RILEM TC 178-TM. Testing and modelling chloride penetration in concrete. Methods for obtaining dust samples by means of grinding concrete in order to determine the chloride concentration profile. Mater. Struct. Constr. **46**(3), 337–344 (2013)
8. Ma, Z., Zhao, T., Yao, X.: Influence of applied loads on the permeability behavior of ultra high-performance concrete with steel fibers. J. Adv. Concr. Technol. **14**(12), 770–781 (2016)
9. Broomfield, J.P.: Corrosion of steel in concrete. Understanding, investigation and repair, 2nd ed. Taylor & Francis (1997)

10. Wassmann, K., Brühwiler, E., Lunk, P.: Strengthening of RC slabs using UHPFRC—concepts and applications. In: 4th International Symposium on Ultra-High Performance Concrete and High-Performance Materials (2016)
11. Angst, U., Elsener, B., Larsen, C.K., Vennesland, Ø.: Critical chloride content in reinforced concrete—a review. Cem. Concr. Res. **39**(12), 1122–1138, Dec (2009)

Cracking Potential of Alkali-Activated Concrete Induced by Autogenous Shrinkage

Zhenming Li, Shizhe Zhang, Xuhui Liang, Albina Kostiuchenko, and Guang Ye

Abstract Alkali activated concrete (AAC) has not received broader industry acceptance, one reason of which lies in the uncertainties in the durability against shrinkage and potential cracking. Many studies reported that AAC exhibit larger autogenous shrinkage than OPC concrete. However, it is unable to deduce that AAC should show higher cracking potential than OPC concrete only based on the higher autogenous shrinkage of AAC. The cracking potential of concrete is determined by multiple factors including autogenous shrinkage, creep/relaxation, elastic modulus, and tensile properties of the concrete. However, very few studies have considered these parameters. Furthermore, the influence of precursors (e.g. slag or fly ash) on the cracking potential of AAC induced by autogenous shrinkage is also rarely studied. The aim of this study, therefore, is to investigate the autogenous shrinkage-induced cracking potential of slag and fly ash-based AAC. The free autogenous shrinkage of the specimens is measured by Autogenous Deformation Testing Machine (ADTM). The autogenous shrinkage-induced stress and cracking of the concrete under restraint condition is tracked by Thermal Stress Testing Machine (TSTM). Additionally, the influence of precursors on the autogenous shrinkage induced cracking potential is discussed.

Keywords Cracking · Alkali-activated materials · Concrete · Shrinkage · Slag · Fly ash

Z. Li (✉) · S. Zhang · X. Liang · A. Kostiuchenko · G. Ye
Delft University of Technology, Delft, The Netherlands
e-mail: z.li-2@tudelft.nl

G. Ye
Ghent University, Ghent, Belgium

1 Introduction

In recent decades, alkali activated concrete (AAC) made from industrial by-products such as slag and fly ash, has emerged as a promising alternative to ordinary Portland cement (OPC) concrete. Along with its higher strength, good durability and fire resistance [1–3], AAC also shows environmental advantages such as lower CO_2 emission and energy consumption when used as building materials compared with conventional OPC concrete [4, 5].

Autogenous shrinkage is an important property since it can induce internal tensile stress and consequent micro- or macro- cracking of the concrete. While the cracking potential of OPC concrete induced by autogenous shrinkage has been widely studied, the related performance of AAC is poorly understood.

The aim of this paper is to study the autogenous shrinkage-induced cracking potential of alkali-activated slag and alkali-activated slag and fly ash concrete. The free autogenous shrinkage of the specimens is measured by Autogenous Deformation Testing Machine (ADTM). The autogenous shrinkage-induced stress of the concrete under restraint condition is measured by Thermal Stress Testing Machine (TSTM). The cracking of the concrete is monitored.

2 Materials and Methods

2.1 Materials and Mixture Proportions

The precursors used were granulated blast-furnace slag (hereinafter termed slag as an abbreviation) supplied by Ecocem Benelux BV and fly ash from Vliegasunie BV. The chemical compositions of slag and fly ash were determined by X-ray fluorescence (XRF) (as shown in Table 1). The fly ash complies with Class F (EN 450, ASTM C618) since it has low CaO content (<10% reactive CaO) and content of "$SiO_2 + Al_2O_3 + Fe_2O_3$" higher than 70%. The particle size of slag, as determined by laser diffraction analyzer, ranges from 0.1 to 50 μm, with a d50 of 18.3 μm. The particle size of fly ash is between 0.14 and 138 μm, with a d50 of 48.1 μm. The alkaline activator was prepared by mixing anhydrous pellets of sodium hydroxide with deionized water and commercial sodium silicate solution. For 1000 g of precursor, an activator containing 384 g of water, 1.146 mol of SiO_2 and 0.76 mol of Na_2O was applied.

Table 1 Chemical compositions of slag and fly ash measured by XRF

Precursor	Oxide (mass %)									
	SiO_2	Al_2O_3	CaO	MgO	Fe_2O_3	SO_3	K_2O	TiO_2	Other	LOI
Slag	31.77	13.25	40.50	9.27	0.52	1.49	0.34	0.97	0.21	1.31
FA	56.8	23.8	4.8	1.5	7.2	0.3	1.6	1.2	1.6	1.2

Table 2 Mixture proportions of AAS concrete and AASF concrete (kg/m³)

Mixtures	AAS	AASF
Slag	400	200
Fly ash	0	200
Activator	200	200
Aggregate (0–4 mm)	789	789
Aggregate (4–8 mm)	440	440
Aggregate (8–16 mm)	525	525

LOI Loss on ignition

The mixture design of AAC is shown in Table 2. Alkali-activated slag concrete and alkali-activated slag-fly ash blended concrete are studied. For the slag and fly ash blended systems, one slag to fly ash weight ratio, 50%–50%, is focused in this study. Other ratios like 30%–70% and 70%–30% do not have substantial differences on the microstructure and shrinkage behaviors of the paste [6], so these ratios are not concerned in this research. Pure fly ash based system does not show considerable stiffness and strength at ambient condition, and is therefore not studied in this paper.

2.2 Experimental Methods

Compressive strength and splitting strength of AAC were measured according to NEN-EN 12,390 [7]. The measurements were conducted at the age of 1, 3, 7, 28 days and on the day when the AAC beam specimen in TSTM cracked.

The autogenous shrinkage of AAC was measured by an Autogenous Deformation Testing Machine (ADTM) [8]. The concrete was cast in a prismatic mould, $1000 \times 150 \times 100$ mm³, made with thin steel plates provided with an external insulating material. The moulds could be cooled or heated by a series of tubes located between the plates and the insulating material. The tubes were connected with cryostats and the temperature of the circulating water was controlled by computer.

The TSTM is based on a horizontal steel frame in which the concrete specimen can be loaded in compression or in tension under various temperatures. The specimen has a prismatic shape ($1500 \times 150 \times 100$ mm³) with dovetailed heads at the ends. The middle part of the specimen is in a temperature-controlled mould, similar to the ADTM mould described in the previous section. Two rigid steel claws hold the specimen. One of the claws is fixed to the frame and the other lies on roller-bearings and can be moved with the hydraulic actuator to exert a tensile or compressive force. Attached to the claws is a short formwork that forms a smooth (curved) transition between the straight insulated mould and the slanting inner sides of the claws. The load is recorded with a load-cell with a loading capacity of 100 kN and a resolution of 0.049 kN.

3   Results and Discussion

The strength development of the concrete is shown in Fig. 1. It can be seen that AAS concrete showed high compressive and splitting strength, which is consistent with the findings in the literature [6, 9, 10]. AASF concrete showed relatively lower compressive and splitting strength.

The free autogenous shrinkage of AAC is shown in Fig. 2. The autogenous shrinkage of AAC was higher than the common autogenous shrinkage of normal OPC based concrete [11]. AASF concrete showed lower autogenous shrinkage than AAS concrete. These findings are in line with the autogenous shrinkage results on pastes [12].

In Fig. 2, it can also be observed that AASF concrete experienced slight expansion at the very early age. Considering the relatively low stiffness of AASF concrete at the early age, the thermal effect due to the reaction heat and the pushing force of LVDT to the measure bars probably accounted for the early-age expansion of AASF concrete [14]. These effects were supposed to exist also during the test of

Fig. 1 Compressive (**a**) and splitting tensile strength (**b**) of AAS and AASF concrete
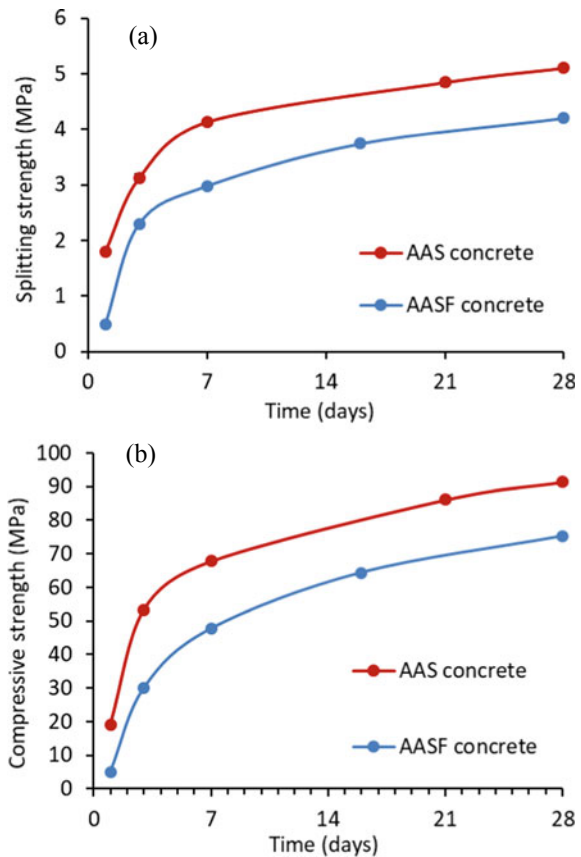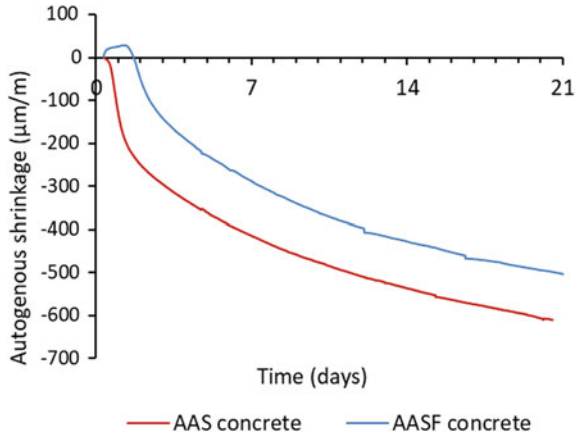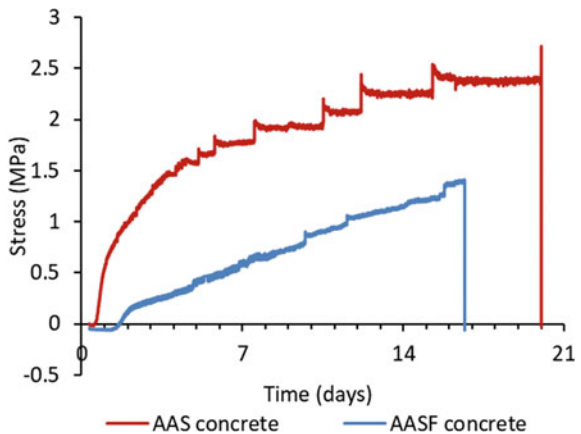
Fig. 2 Autogenous shrinkage of AAS and AASF concrete

AAS concrete, but the expansion of AAS concrete was probably compensated by the rapidly developed autogenous shrinkage. As a result, AAS concrete did not show bulk expansion at the early age, as shown in Fig. 2.

Figure 3 shows the stress development in AAS and AASF concrete. The sudden drop in the stress to around zero indicates the occurrence of cracking of the concrete. AAS concrete showed a rapid development of stress due to the high autogenous shrinkage. On the other hand, AASF concrete was subject to slight compressive stress in the first 1.5 days due to the restrained expansion. In addition, the tensile stress generated in AASF concrete was substantially lower than in AAS concrete, but the tensile strength (1.4 MPa) of AASF concrete was also lower than that of AAS concrete (2.7 MPa). As a result, AASF concrete cracked even earlier than AAS concrete. Therefore, the replacement of slag to fly ash does not necessarily decrease the cracking potential of the concrete.

Fig. 3 Autogenous shrinkage-induced stress in AAS and AASF concrete

Compared to the results of OPC concrete with similar compressive strength [13, 14], AAS and AASF concrete show lower cracking potential, although their autogenous shrinkage is higher. The mechanism behind might lie in the pronounced relaxation of AAC, which reduced the stress in the concrete.

4 Concluding Remarks

In this study, the free autogenous shrinkage, the cracking potential of two AAC, namely AAS and AASF concrete, subjected to restrained autogenous shrinkage are studied. AASF concrete shows lower autogenous shrinkage and lower self-induced stress compared to that of AAS concrete. However, AASF concrete cracked earlier than AAS concrete due to the lower tensile strength of AASF concrete. Therefore, the cracking potential of AAC does not necessarily reduce by only reducing the slag con-tent in the binder material. Furthermore, the autogenous shrinkage of AAS and AASF concrete is larger than the common autogenous shrinkage of OPC concrete. Nonetheless, the cracking time of AAC is later than those of OPC concrete according to results in the literature.

References

1. Provis, J.L., van Deventer, J.S.J.: Geopolymers: Structures, Processing, Properties and Industrial Applications. Woodhead, Cambridge, UK (2009)
2. Juenger, M.C.G., Winnefeld, F., Provis, J.L., Ideker, J.H.: Advances in alternative cementitious binders. Cem. Concr. Res. **41**, 1232–1243 (2011). https://doi.org/10.1016/j.cemconres.2010.11.012
3. Arbi, K., Nedeljković, M., Zuo, Y., Ye, G.: A review on the durability of alkali-activated fly ash/slag systems: advances, issues, and perspectives. Ind. Eng. Chem. Res. **55**, 5439–5453 (2016). https://doi.org/10.1021/acs.iecr.6b00559
4. Thomas, S.R.J., Ye, H., Radlinska, A., Peethamparan, S.: Alkali-activated slag cement concrete. Concr. Int. **38**, 33–38 (2016)
5. Duxson, P., Provis, J.L., Lukey, G.C., van Deventer, J.S.J.: The role of inorganic polymer technology in the development of "green concrete." Cem. Concr. Res. **37**, 1590–1597 (2007). https://doi.org/10.1016/j.cemconres.2007.08.018
6. Nedeljković, M.: Carbonation mechanism of alkali-activated fly ash and slag materials: In view of long-term performance predictions, Delft University of Technology (2019)
7. NEN-EN 12390-3, Testing hardened concrete—Part 3: Compressive strength of test specimens (2009)
8. Lokhorst, S.J.: Deformational behaviour of concrete influenced by hydration related changes of the microstructure, Delft University of Technology (2001)
9. Fernández-Jiménez, A., Palomo, J.G., Puertas, F.: Alkali-activated slag mortars: mechanical strength behaviour. Cem. Concr. Res. **29**, 1313–1321 (1999)
10. Wang, S.-D., Scrivener, K.L., Pratt, P.L.: Factors affecting the strength of alkali-activated slag. Cem. Concr. Res. **24**, 1033–1043 (1994)

11. Darquennes, A., Staquet, S., Delplancke-Ogletree, M.P., Espion, B.: Effect of autogenous deformation on the cracking risk of slag cement concretes. Cem. Concr. Compos. **33**, 368–379 (2011). https://doi.org/10.1016/j.cemconcomp.2010.12.003
12. Li, Z., Lu, T., Liang, X., Dong, H., Granja, J., Azenha, M., Ye, G.: Mechanisms of autogenous shrinkage of alkali-activated slag and fly ash pastes. Cem. Concr. Res. **135**, 106107 (2020)
13. Igarashi, S.I., Bentur, A., Kovler, K.: Autogenous shrinkage and induced restraining stresses in high-strength concretes. Cem. Concr. Res. **30**, 1701–1707 (2000). https://doi.org/10.1016/S0008-8846(00)00399-9
14. Lura, P., Van Breugel, K., Maruyama, I.: Effect of curing temperature and type of cement on early-age shrinkage of high-performance concrete. Cem. Concr. Res. **31**, 1867–1872 (2001). https://doi.org/10.1016/S0008-8846(01)00601-9

Influence of Nanofibrillated Cellulose (NFC) on the Mechanics of Cement Pastes

Letícia O. de Souza, Lourdes M. S. Souza, and Flávio A. Silva

Abstract The use of nanomaterials in several fields has been growing in the past few years due to their unique physical and mechanical properties. Nevertheless, the use of these materials in civil engineering is fairly new and still requires extensive research to completely understand their potential. The search and development of new cementitious materials that are less harmful to the environment are significantly important. In this scenario, the nanocellulose comes as an interesting option of reinforcement for cementitious elements. One of the constraints of the more intensive employment of nanomaterials is the formation of agglomerates that act as defects and stress concentrators in the elements. In this way, the development of efficient dispersion techniques is essential for the total exploitation of the mechanical properties of the nanomaterials, including the nanocellulose. In the present research, nanofibrillated cellulose (NFC) obtained from Eucalyptus pulp fiber was added into cement pastes thin elements in several contents. The mechanical behavior was assessed by means of four-point bending tests. The percentage of NFC varied between 0 and 1% of the mass of cement. In an attempt to explore most of the properties of NFC and then enhance the mechanical properties of the composites, dispersion strategies were applied as a step on the mixture procedure. Chemical dispersion methods were combined with mechanical stirring in order to produce a homogenous solution of water and NFC. Results showed expressive improvements regarding mechanical properties upon the addition of NFC on the cement pastes. The flexural strength enhanced by more than 400%, and the flexural modulus more than 13 times. Results also indicated that the dispersion methods applied were able to influence positively the flexural strength, and this improvement is sensible to the content of NFC.

L. O. de Souza (✉) · F. A. Silva
Department of Civil and Environmental Engineering, Pontifícia Universidade Católica
Do Rio de Janeiro (PUC-Rio), Rio de Janeiro, Brazil

L. M. S. Souza
Tecgraf Instute, Pontifícia Universidade Católica Do Rio de Janeiro (PUC-Rio),
Rio de Janeiro, Brazil

247

1 Introduction

The component responsible for the strength of plants is cellulose. Due to cellulose hierarchical structure, nanoparticles can be extracted from them by mechanical and/ or chemical means, resulting in a nanomaterial with remarkable properties [1, 2]. Their characteristics such as fibrils length and crystallinity depend on the type of the source plant [1, 3, 4]. Besides the mechanical properties, they present a high specific area, high water absorption capacity and, are expected to be more stable towards durability than their source plant. These materials are also desirable due to their environmentally friendly characteristic and their availability [1, 3, 4].

Due to the aforementioned characteristics, the impact of nanocellulose on the properties of cementitious materials is worthy of being investigated. Research papers about the different types of nanocellulose inclusions had shown their influence on the properties of cementitious materials [5–19]. Modified properties cover the hardened, such in the case of compressive and flexural response, and fresh states. The mechanical enhances are commonly related to the hydration improvement that nanocellulose promotes [5, 13, 20]. The interaction between the cement particles and the nanocellulose, mainly the free hydroxyls groups, is also a reason for the changes of cementitious materials behavior [6, 13, 21].

Despite the benefits, the dispersion of nanomaterials is one of the primary issues in the successful use of this type of material. When nanocellulose is added into the matrix, due to the existence of interaction forces between the particles, they tend to form agglomerates that may act as defects or stress concentrators [1, 19, 22]. These interactions usually limit the potential of mechanical reinforcement and tend to magnify when the size of the particle decreases [1, 4]. There are strategies of dispersion of nanomaterials to overcome agglomeration issues. One may apply each strategy as a pre-step of the mixture or even as a pre-treatment of the nanofibers, with the functionalization of selected groups on the surface of the particles. The use of superplasticizer is quite common since it is advantageous for both the dispersion and workability matters [5, 12, 23]. Studies have indicated the existence of an optimal amount of nanocellulose that leads to the best mechanical response; beyond this value, agglomerations are formed and the performance decreases [5, 12, 13, 23, 24].

One of the forms in which nanocellulose is presented is as nanofibrillated cellulose (NFC). NFC is composed of fibrillar units with both cellulose crystals and amorphous parts. It presents a high aspect ratio and, usually form agglomerated networks [25–27]. Even a low content of NFC, less than 0.4%, is capable of significantly improving the mechanical performance of cementitious materials [5, 6]. Onuaguluchi et al. [5] evaluated flexural mechanical properties of different proportions of NFC inclusions: 0.05, 0.1, 0.2 and 0.4% of cement weight. It was observed that the addition of NFC enhanced both flexural strength and energy

absorption, with an optimal volume fraction of 0.1%. The drawback observed in the tests was the brittle failure mode due to the high bond and non-homogeneous dispersion of the nanofibers. Effects of the addition of NFC pre-treated by 2,2,6,6-tetramethylpiperidine-1-oxyl (TEMPO)-mediated oxidation on compressive strength in cementitious composites were investigated by Mejdoub et al. [6]. Compressive strength increased with the NFC addition, presenting the highest increase of 43% for 0.3% of fiber inclusion. Negative effects were observed for specimens with 0.5% of fiber addition due to poor dispersion [6]. Jiao et al. [14] studied the influence of NFC on compressive and flexural strengths of cement pastes of different ages. Although there was no significant change of the mechanical properties for 3 and 7 days-aged specimens, the 28-day aged ones presented flexural and compressive strengths increased by 15% and 20%, respectively. These enhancements occurred at an optimal content of 0.15% of NFC.

In this research, the nanofibrillated cellulose (NFC) obtained from Eucalyptus was used to reinforce cement paste laminates in different contents, 0, 0.5, and 1%. In order to investigate the optimal percentage of the nanomaterial regarding mechanical properties, four-point bending tests were performed. Different dispersion approaches were applied with the aim of increasing the mechanical properties. The use of superplasticizer and the use of non-ionic surfactant combined with mechanical stirring were studied. Specimens reinforced with NFC without dispersion techniques applied were also evaluated for comparison, as well as non-reinforced ones.

2 Materials and Methods

2.1 Materials and the Fabrication of the Composites

In the present research, nanofibrillated cellulose obtained from defibrillation method of Eucalyptus bleached pulp was used to reinforce cement pastes. The NFC was kindly provided by the Forestry Sciences Department at Federal University of Lavras (UFLA—Universidade Federal de Lavras) and was produced according to the following procedure. The pulp was dispersed in water at fiber content of around 2.0 wt% for 48 h. The mixture was submitted to mechanical stirring to facilitate the defibrillation process. The solution was then processed for 30 cycles through the mechanical defibrillator, SuperMasscolloider grinder, Massuko-Sangyo, model MKCA6-2, using 1500 rpm grindstone rotation, with a gap of 0.01 mm between the rotating grindstones. The resulting NFC consisted of a gel with around 2% of nanofibers. The defibrillation process aims to remove the defects and the parts not as strong as cellulose from natural fibers. To facilitate the addition of NFC into the cement paste, the gel was filtered until reaches 10% of NFC concentration.

In order to produce the cement pastes, cement Portland was the Brazilian Type V, with composition in accordance with ABNT NBR 5733:1991 was

employed. The water/cement (w/c) ratio was of 0.45 and tap water was used. In order to maintain the w/c ratio constant, the water present on the gel was discounted from the mixing water. The employed superplasticizer was a polycarboxylic ether-based additive, Glenium 51 MS, with a solid content of 32%, from BASF. The used surfactant was the non-ionic Pluronic F-127, purchased from Sigma-Aldrich.

For the reinforced cement paste preparation, the following procedure was carried: the mixing water and the NFC (solution in the case of dispersed NFC) were mixed for thirty seconds on a mixer at 136 rpm; half of the cement was added and mixed for another thirty seconds at 136 rpm; the remaining cement was added and mixed for 2 min at 281 rpm. The cement paste was poured on steel molds of $250 \times 60 \times 10 \text{ mm}^3$ (length $\times$ width $\times$ thickness). The specimens were demolded after 24 h and stored for 27 days in water.

2.2 Methods

The four-point bending tests were carried on a servo-hydraulic MTS testing machine with a load capacity of 100 kN. They were performed with a displacement rate of 0.05 mm/min. Two 25 mm displacement transducers were added to the system for axial displacement acquisition. An additional load-cell of 2.5 kN was included in the system for more accurate load acquisition. At least three specimens for each variation were tested. Figure 1 shows the test configuration.

The methods of dispersion explored in the present study are explained as follows:

(i) Superplasticizer combined with mechanical stirring: addition of superplasticizer to the NFC gel with the mixing water. The solution was mixed in a mechanical stirrer revolving at around 900 rpm for 30 min. The added amount was of 1% in weight of cement.

(ii) Pluronic addition: addition of the non-ionic surfactant to the mixing water and the NFC gel. The solution was mixed in a mechanical stirrer revolving at around 900 rpm for 30 min. The amount of surfactant addition was of 20% in weight of NFC nanofibrils.

The dispersion methods were applied to 0.5 and 1% of NFC. For comparison purposes, the nanocellulose was also added into the cement paste without dispersion techniques on the same content. The reference specimens are the ones with no addition of NFC (0%). The content of NFC is in relation to the mass of cement and it is concerned with the NFC solid content, not the gel.

Fig. 1 Four-point bending
test configuration
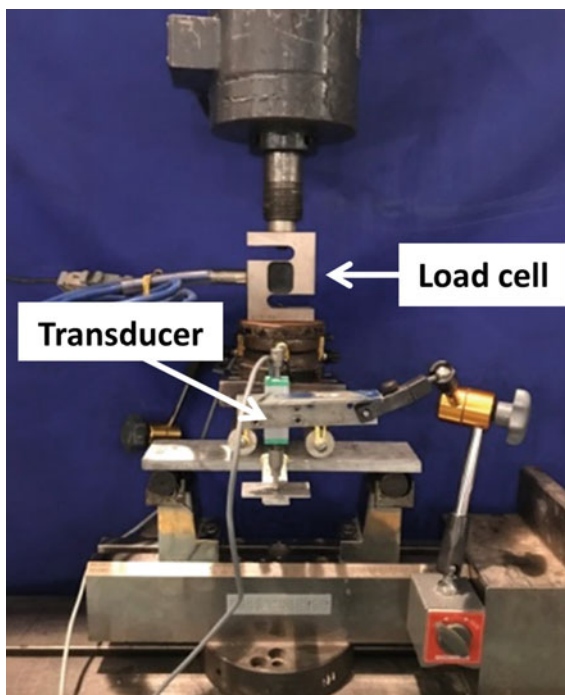
3 Results and Discussion

Figure 2 presents one curve of each type of the specimen submitted to the four-point bending test. Figure 2a shows the stress versus displacement of the plates reinforced with 0.5% of NFC: without dispersion method (WD), with addition of superplasticizer (Super), and with addition of Pluronic (Surfac). The reference specimen is also presented for comparison. Figure 2b shows the curves of the plates reinforced with 1% of NFC, submitted to the same dispersion methods of the 0.5% ones: WD, Super, and Surfac. Table 1 brings the mean values of the mechanical properties, namely flexural strength, modulus and deflection, for each case. The ratio σ/σ_{ref} and E/E_{ref} represents the increase of the flexural strength and modulus, respectively, with respect to the specimens without nanocellulose (Ref).

From Table 1 it is possible to notice that the addition of any amount of NFC with dispersed or non-dispersed promoted the increase of the flexural strength and modulus and significantly reduced the deflection capacity. This behavior was already observed in other cementitious composites reinforced with micro and nanofibers [28, 29] and is usually attributed to the strong bond between the cellulosic inclusion and cement particles. The strong bond is due to the existence of hydroxyl groups on the surface of nanocellulose and the van der Waals forces involved.
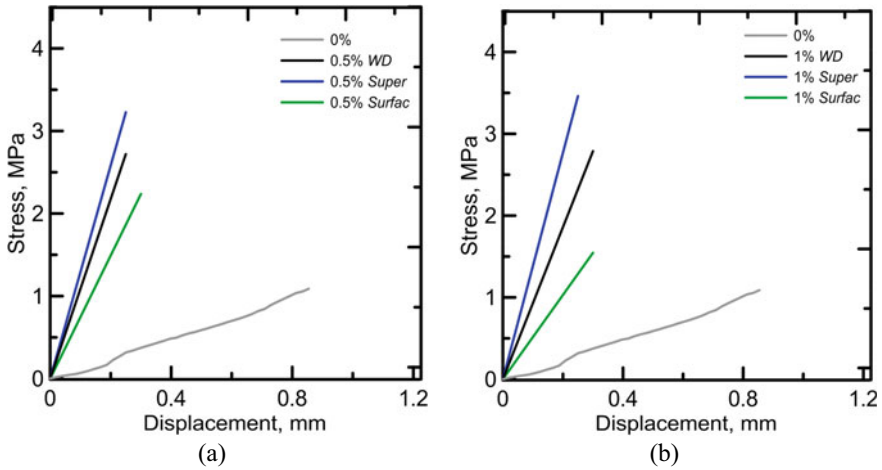
Fig. 2 Stress versus displacement curves of **a** 0.5% NFC reinforced plates and; **b** 1% NFC reinforced plates. The reference curve (0%) is shown for comparison

Table 1 Mean values of flexural strength, modulus and deflection of the specimens reinforced with 0.5% and 1% of NFC, for each dispersion technique addressed and for specimens without dispersion applied (WD) and the reference (0%)

NFC content (%)	Dispersion technique	Strength (MPa)	σ/σ_{ref}	Modulus (GPa)	E/E_{ref}	Deflection (mm)
0	–	1.1 ± 0.1	1.0	0.7 ± 0.2	1.0	0.92 ± 0.28
0.5	WD	2.4 ± 0.4	2.2	9.5 ± 1.1	13.6	0.24 ± 0.03
	Super	4.4 ± 0.5	4.1	12.9 ± 0.8	18.4	0.34 ± 0.06
	Surfac	2.3 ± 0.2	2.2	7.2 ± 0.2	10.3	0.30 ± 0.04
1	WD	3.3 ± 0.3	3.0	8.3 ± 0.5	11.8	0.38 ± 0.03
	Super	3.5 ± 0.2	3.3	11.3 ± 1.9	16.1	0.32 ± 0.05
	Surfac	1.7 ± 0.1	1.6	5.5 ± 0.8	7.9	0.31 ± 0.03

If no dispersion method is applied (WD), the optimal content may vary with the analyzed property. Considering the flexural strength the optimal content is 1%, with 300% of enhancement. Considering the flexural modulus, the 0.5% of NFC is the optimal content, with more than thirteen times of improvement. In fact, the flexural modulus is the mechanical property that increased the most in any case of NFC reinforcement. Even with the simple addition of NFC, without dispersion methods the mechanical properties enhanced expressively.

Although the different ratios, the dispersion methods similarly affected the mechanical properties. For both NFC contents, the use of superplasticizer enables the enhancement of the mechanical behavior if compared with the non-dispersed specimens. While for the use of surfactant, there was no benefit under the mechanical properties investigated. Thus, the method that employs the

superplasticizer was able to enhance the strength and modulus of both contents. With the superplasticizer method of dispersion applied, the flexural strength and modulus enhanced if compared with the 0.5% NFC WD, indicating that this methodology acted as an efficient dispersion technique. In fact, applying this method as a pre-step on the mixing procedure promoted for the 0.5%-reinforcement better mechanical properties than the ones presented by 1% of NFC (see Table 1). Therefore, the superplasticizer with mechanical stirring applied to the 0.5% of NFC resulted in a composite with better mechanical response than the 1% of NFC submitted to the same condition. The 1% of NCF probably exceeds the capacity to separate the particles for the amount of superplasticizer employed.

4   Conclusions

In the present paper, nanofibrillated cellulose (NFC) produced from Eucalyptus was used as reinforcement of cement pastes. Two dispersion methods were investigated with the purpose of improving mechanical properties. From the experimental data analyzed and the results and discussion aforementioned, it is possible to draw the following conclusions:

- The NFC is capable of reinforcing cement pastes, resulting in expressive gains regarding flexural mechanical properties. The exception is the loss of the deflection capacity upon the reinforcement.
- Without dispersion methods, the optimal content differs for each property analyzed. Regarding flexural strength, the addition of 1% of NFC resulted in an enhancement of three times. While for the flexural modulus, the reinforcement of 0.5% of NFC promoted an improvement of more than three times. These values are in comparison with non-reinforced cement pastes.
- The use of surfactant, Pluronic, combined with mechanical stirring as dispersion method did not result in any positive effect in the mechanical properties if comparing with the non-dispersed reinforced composites.
- The dispersion of NFC in water with the addition of superplasticizer submitted to mechanical stirring for 30 min was the most effective dispersion method. The application of this methodology promoted significant improvement for both contents of NFC reinforcement, 0.5% and 1.0% of NFC.
- The 0.5% of NFC submitted to the dispersion with superplasticizer was the most promising option with an improvement of 4.1 and 18.4 times of flexural strength and modulus, respectively. These values are in comparison with non-reinforced cement pastes.

References

1. Dufresne, A.: Nanocellulose: a new ageless bionanomaterial. Mater. Today **16**, 220–227 (2013)
2. Abitbol, T., Rivkin, A., Cao, Y., Nevo, Y., Abraham, E., Ben-Shalom, T., Lapidot, S., Shoseyov, O.: Nanocellulose, a tiny fiber with huge applications. Curr. Opin. Biotechnol. **39**, 76–88 (2016)
3. Abdul Khalil, S., Davoudpour, Y., Islam, N., Mustapha, A., Sudesh, K., Dungani, R., Jawaid, M.: Production and modification of nanofibrillated cellulose using various mechanical processes: a review. Carbohyd. Polym. **99**, 649–665 (2014)
4. Eichhorn, J., Dufresne, A., Aranguren, M., Marcovich, E., Capadona, R., Rowan, J., Weder, C., Thielemans, W., Roman, M., Renneckar, S., Gindl, W., Veigel, S., Keckes, J., Yano, H., Abe, K., Nogi, M., Nakagaito, N., Mangalam, A., Simonsen, J., Benight, S., Bismarck, A., Berglund, A., Peijs, T.: Review: current international research into cellulose nanofibres and nanocomposites. J. Mater. Sci. **45**, 1–33 (2010)
5. Onuaguluchi, O., Panesar, K., Sain, M.: Properties of nanofibre reinforced cement composites. Constr. Build. Mater. **63**, 119–124 (2014)
6. Mejdoub, R.: Nanofibrillated cellulose as nanoreinforcement in Portland cement: Thermal, mechanical and microstructural properties. J. Compos. Mater. **51**, 2491–2503 (2017)
7. Stephenson, K.M.: Characterizing the behavior and properties of nanocellulose reinforced ultra high performance concrete, Maine (2011)
8. Ardanuy, M., Claramunt, J., Arévalo, R., Parés, F., Aracri, E., Vidal, T.: Nanofibrillated cellulose (Nfc) as a potential reinforcement for high performance cement mortar composites. BioResources **7**(3), 3883–3894 (2012)
9. Jiao, L., Su, M., Chen, L., Wang, Y., Zhu, H., Dai, H.: Natural cellulose nanofibers as sustainable enhancers in construction cement. PLoS ONE **11**, 1–13 (2016)
10. Claramunt, J., Ardanuy, M., Arevalo, R., Pares, F.: Mechanical performance of ductile cement mortar composites reinforced with nanofibrillated cellulose. Strain Hardening Cement Composites, pp. 131–138 (2011)
11. Ferrara, L., Ferreira, S., Della Torre, M., Krelani, V., Silva, F., Dias, R., Filho, T.: Effect of cellulose nanopulp on autogenous and drying shrinkage of cement based composites. Nanotechnology in Construction, p. 325 (2015)
12. Cao, Y., Zavaterri, P., Youngblood, J., Moon, R., Weiss, J.: The influence of cellulose nanocrystal additions on the performance of cement paste. Cem. Concr. Compos. **56**, 73–83 (2015)
13. Cao, Y., Tian, N., Bahr, D., Zavattieri, P., Youngblood, J., Moon, R., Weiss, J.: The influence of cellulose nanocrystals on the microstructure of cement paste. Cem. Concr. Compos. **74**, 164–173 (2016)
14. Cao, Y., Zavattieri, P., Youngblood, J., Moon, R., Weiss, J.: The relationship between cellulose nanocrystal dispersion and strength. Constr. Build. Mater. **119**, 71–79 (2016)
15. Cao, Y., Weiss, W.J., Youngblood, J., Moon, R., Zavattieri, P.: Performance-enhanced cementitious materials by cellulose nanocrystal additions. Prod. Appl. Cellul. Nanomater. (2013)
16. Cao, Y., Verian, K.: A VEDA simulation on cement paste: using dynamic atomic force microscopy to characterize cellulose nanocrystal distribution. MRS Commun. **7**, 672–676 (2017)
17. Mazlan, D., Md Din, M.F., Tokoro, C., Ibrahim, I.: Cellulose nanocrystals addition effects on cement mortar matrix properties. Int. J. Adv. Mech. Civil Eng. **3**, 44–48 (2016)
18. Fu, T., Montes, F., Suraneni, P., Youngblood, J., Weiss, J.: The influence of cellulose nanocrystals on the hydration and flexural strength of Portland cement pastes. Polymers **9** (2017)

19. Sun, X., Wu, Q., Zhang, J., Qing, Y., Wu, Y., Lee, S.: Rheology, curing temperature and mechanical performance of oil well cement: combined effect of cellulose nanofibers and graphene nano-platelets. Mater. Des. **114**, 92–101 (2017)
20. Mohamed, M.A.S., Ghorbel, E., Wardeh, G.: Valorization of micro-cellulose fibers in self-compacting concrete. Constr. Build. Mater. **24**, 2473–2480 (2010)
21. Correia, V., Santos, S.F., Soares Teixeira, R., Savastano Junior, H.: Nanofibrillated cellulose and cellulosic pulp for reinforcement of the extruded cement based materials. Constr. Build. Mater. **160**, 376–384 (2018)
22. Mondal, S.: Preparation, properties and applications of nanocellulosic materials. Carbohyd. Polym. **163**, 301–316 (2017)
23. Peters, S., Rushing, T., Landis, E., Cummins, T.: Nanocellulose and microcellulose fibers for concrete. Transp. Res. Rec. J. Transp. Res. Board **2142**, 25–28 (2010)
24. Mejdoub, R., Hammi, H., Suñol, J., Khitouni, M., M'nif, A., Boufi, S.: Nanofibrillated cellulose as nanoreinforcement in Portland cement: thermal, mechanical and microstructural properties. J. Compos. Mater. **51**, 2491–2503 (2017)
25. Tonoli, G., Holtman, K., Glenn, G., Fonseca, A., Wood, D., Williams, T., Sa, V., Torres, L., Klamczynski, A., Orts, W.: Properties of cellulose micro/nanofibers obtained from eucalyptus pulp fiber treated with anaerobic digestate and high shear mixing. Cellulose **23**, 1239–1256 (2016)
26. Bufalino, L., Neto, A., Tonoli, G., Fonseca, A., Costa, T., Marconcini, J., Colodette, J., Labory, C., Mendes, L.: How the chemical nature of Brazilian hardwoods affects nanofibrillation of cellulose fibers and film optical quality. Cellulose **22**, 3657–3672 (2015)
27. Netravali, A., Chabba, S.: Composites get greener. Mater. Today, 22–29 (2003)
28. Silva, L., Parveen, S., Filho, A., Zottis, A., Rana, S., Vanderlei, R., Fangueiro, R.: A facile approach of developing micro crystalline cellulose reinforced cementitious composites with improved microstructure and mechanical performance. Powder Technol. **338**, 654–663 (2018)
29. Ardanuy, M., Claramunt, J., Dias, R., Filho, T.: Cellulosic fiber reinforced cement-based composites: a review of recent research. Constr Build Mater **79**, 115–128 (2015)

Rheological Behaviour and Flow Properties of Alkali-Activated Materials

Mohammed Fouad Alnahhal, Taehwan Kim, and Ailar Hajimohammadi

Abstract Great efforts are being made by researchers concerning the development of cement-less concrete to reduce both greenhouse gas emissions and energy use. Alkali-activated materials (AAMs) are one of the viable alternatives which are attracting increasing attention in practice and research due to their lower CO_2 emissions. In this paper, the rheological behaviour of binary blended alkali-activated fly ash/slag pastes is investigated. Various rheological measurements were conducted such as paste fluidity, viscosity, yield stress and thinning index. The effect of different parameters was assessed including the slag content, SiO_2/Na_2O ratio as well as the solution/binder ratio. The experimental results revealed that increasing the slag content increases the viscosity and yield stress and reduced the overall paste fluidity at elapsed times. The viscosity of AAM pastes was in the range of 0.77–7.55 Pa.s. The AAM pastes behaved like a shear-thinning fluid, where the apparent viscosity decreased by increasing the shear rate. The SiO_2/Na_2O ratio in the activator had no significant effect on shear thinning parameters and fluidity. The thinning index, which is the ratio between viscosity at low and high shear rates, of AAM pastes was found to be in the range of 1.92–4.01. The volumetric solution-to-binder ratio was shown to effectively influence the thinning index. The findings of this study confirm that the fluidity and thinning index are independent of the chemical composition of the used activator but depend upon the changes done in the volume of both slag and activation solutions.

Keywords Rheology · Alkali activated materials · Paste fluidity · Thinning index

M. F. Alnahhal · T. Kim (✉) · A. Hajimohammadi
School of Civil and Environmental Engineering, University of New South Wales,
Sydney, NSW 2052, Australia
e-mail: taehwan.kim@unsw.edu.au

1 Introduction

In today's fast-growing urbanization, environmental sustainability is a significant factor that cannot be ignored by architects, engineers, researchers and, above all, by the construction industry; one of the means to achieve the balance in construction industry is through the development of alternative binders that entirely replace Portland cement. The annual worldwide production of Portland cement for concrete manufacturing approached 4.10 billion tonnes in 2017 [1] and the demand for cement will continue to globally increase due to the increase in the population and the economic growth in the developing countries [2]. One of the promising alternative binder systems is alkali-activated materials (AAMs) and significant efforts are being made by researchers concerning the development and applications of AAM concrete [3]. AAMs, including those classified as "geopolymers", could be obtained from aluminosilicate sources such as metakaolin, blast furnace slag or fly ash. Along with lower CO_2 emissions, the use of AAMs provides several benefits due to their superior performance when compared to Portland cement concrete. These benefits include: (a) better resistance against aggressive chemicals [4], (b) less expansion due to alkali-silica reaction [5], and (c) good fire resistance at elevated temperatures [6].

Engineers and scientists have expended significant efforts to understand and control the rheological properties of concrete because it affects not only the quality of fresh and hardened concrete but also shape stability and scalability of the innovative 3D printable materials. Although AAMs have been studied by many authors as an alternative "green" concrete, very limited studies have dealt with its rheological behaviour and flow properties [7–10]. In this research, the rheological behaviour (including viscosity, yield stress, and thinning index) and the paste fluidity of AAMs were investigated. The effect of different parameters was assessed including the GGBFS content as well as the SiO_2/Na_2O ratio and the volume of the alkaline activator.

2 Experimental Program

2.1 Materials

In this investigation, two types of industrial by-products were utilized as aluminosilicate sources, namely, fly ash (FA) from Eraring power station in New South Wales, Australia and Ground Granulated Blast Furnace Slag (GGBFS) supplied by Blue Circle Southern Cement, Australia. The chemical composition of FA and GGBFS is shown in Table 1. The specific gravities of FA and GGBFS are 2.1 and 2.8, respectively.

The alkaline activator was a mixture of sodium hydroxide (NaOH) and sodium silicate solutions. The commercial sodium silicate solution, supplied by PQ

Table 1 Chemical Composition of fly ash and GGBFS

Chemical compositions (%)	Fly ash	GGBFS
SiO_2	66.56	31.52
Al_2O_3	22.47	12.22
CaO	1.64	44.53
Fe_2O_3	3.54	1.14
MgO	0.65	4.62
MnO	0.06	0.36
Na_2O	0.58	0.21
K_2O	1.75	0.33
P_2O_5	0.11	0.02
TiO_2	0.88	1.03
SO_3	0.1	3.24
LOI	1.66	0.79

Australia under the commercial name of Vistrol D-A53, had the following composition: 14.7% of Na_2O, 29.4% of SiO_2, 55.9% of water (by weight). The NaOH solution with 30% concentration (Molarity $\approx$ 10 M) was prepared by dissolving 400 g of NaOH pellets per litre of solution.

2.2 Mixture Design

The FA, GGBFS and chemical activators were added in the mixes with different dosages to maintain prescribed alkali dosages (M+) and alkali moduli (Ms) as shown in Tables 2 and 3. M+ is the mass ratio of Na_2O in the activating solution (i.e. Na_2O from NaOH solution + Na_2O from sodium silicate solution) to the binder dry mass. Ms is the mass ratio SiO_2/Na_2O in the alkali activator.

In the first stage, the FA was replaced by GGBFS at levels of 10, 20, 30 and 40% by volume, while the solution/binder (by volume) ratio and Ms were kept constant at 0.9 and 1.0, respectively, to study the effect of GGBFS on the flow properties and rheological behaviour, as shown in Table 2. The volumetric solution/binder ratio was shown to most strongly influence the rheological parameters of the paste [11]. Therefore, the GGBFS replacement was done in volume basis to maintain the solution/binder at 0.9.

In the second stage, the volumetric solution/binder ratios of 1.0 and 1.1 were tested for the mix containing 20% GGBFS and Ms of 1.0, as shown in Table 3.

In the third stage, the effect of SiO_2/Na_2O was examined by using Ms of 1.1, 1.2, 1.3 and 1.5, while keeping the solution/binder and GGBFS content constant at 0.9 and 20%, respectively, as shown in Table 3.

Table 2 Mixture proportions for stage I

Mixture (kg/m^3)	Stage I			
	S10	S20	S30	S40
Replacement level (volume) (%)	10	20	30	40
GGBFS	147	295	442	589
Fly ash	994	884	773	663
NaOH 10 M	180	180	180	180
Sodium silicate	299	299	299	299
Additional water	137	137	137	137
Solution/binder (volume)	0.9	0.9	0.9	0.9
Solution/binder (weight)	0.54	0.52	0.51	0.49
w/s (weight)	0.32	0.31	0.31	0.3
SiO$_2$ (kg/m^3)	87	87	87	87
Na$_2$O (kg/m^3)	87	87	87	87
Ms, SiO$_2$/Na$_2$O	1	1	1	1
M+, Na$_2$O/binder (%weight)	7.7	7.5	7.2	7.0

Table 3 Mixture proportions for Stage II and Stage III

Mixture (kg/m^3)	Stage II			Stage III			
	SB0.9	SB1.0	SB1.1	Ms1.1	Ms1.2	Ms1.3	Ms1.5
Replacement level (volume) (%)	20	20	20	20	20	20	20
GGBFS	295	280	267	295	295	295	295
Fly ash	883	840	800	884	884	884	884
NaOH 10 M	180	173	165	165	145	127	93
Sodium silicate	299	281	270	324	356	386	442
Additional water	137	180	218	132	127	121	110
Solution/binder (volume)	0.9	1	1.1	0.9	0.9	0.9	0.9
Solution/binder (weight)	0.52	0.57	0.61	0.53	0.53	0.54	0.55
w/s (weight)	0.32	0.36	0.39	0.31	0.31	0.31	0.31
SiO$_2$ (kg/m^3)	87	83	79	95	105	114	130
Na$_2$O (kg/m^3)	87	83	79	87	87	87	87
Ms, SiO$_2$/Na$_2$O	1	1	1	1.1	1.2	1.3	1.5
M +, Na$_2$O/binder (% weight)	0.75	0.75	0.75	7.5	7.5	7.5	7.5

2.3   Mixing and Testing Procedures

Mixing procedure: The mixing protocol, mixture proportions, and mixture composition are important factors that affect the rheology of cementitious pastes [12]. For a given mixture, all FA and GGBFS were first pre-blended for 1 min. Liquid activators were prepared prior to mixing with the binders and allowed to cool down to ambient temperature, and they were used on the same day as prepared, to avoid precipitation of solid sodium metasilicate hydrates [13]. The activator and the binders were then mixed under vacuum at 140 rpm for 30 s, followed by 280 rpm for 60 s. immediately after mixing, the homogeneously mixed paste was used for the paste fluidity and rheological measurements.

Paste fluidity: The flow table test was used to determine the effect of different parameters on the fluidity of the AAM pastes. A cone-geometry was used for the test with 70 mm top diameter, 100 mm bottom diameter and 50 mm height. The test on the fresh paste was carried out at different elapsed times after mixing in order to study the change in the spread diameter due to hardening. At different intervals, the paste was poured into the cone, and then the cone was lifted as slowly as possible to minimize inertial effects [13]. Due to the high fluidity, the pastes were allowed to spread on the flow table without dropping, and the average diameter of the spread was measured after 1 min.

Viscosity and yield stress: Discovery Hybrid Rheometer (DHR-2) was used to perform the flow sweep to determine the viscosity and yield stress of the AAM pastes. A sandblasted concentric cylinder geometry was used with the inner and outer diameters of 28 mm and 30.33 mm, respectively, making the gap width as 1.16 mm. For each batch to be tested using the rheometer, the dry fly ash and GGBFS were blended for 1 min prior to mixing with the activating solution. The precursors were then mixed with the activator using a vacuum mixer at 140 rpm for 30 s, followed by 60 s at 280 rpm. The homogeneously mixed paste was immediately used for testing. The testing procedure consists of pre-shearing the paste at 100 s^{-1} for 60 s followed by 60 s resting time. After that, logarithmic flow sweep was performed (using 10 points per decade) by ramping up the shear rate from 0.1 s^{-1} to 100 s^{-1}, and then ramping down from 100 s^{-1} to 0.1 s^{-1} in a stepwise, as shown in Fig. 1. At each step (i.e. at each shear rate), the instrument was set to make an equilibrium time of 5 s as well as an averaging time of 5 s to calculate the viscosity and shear stress at each step. All measurements were made at 25 °C.

Thinning index: As shown in Eq. (1), this index represents the ratio between the apparent viscosity at a low shear rate (0.1 s^{-1}) and the viscosity at a shear rate ten times higher (1 s^{-1}) in accordance with ASTM D2196 [14].

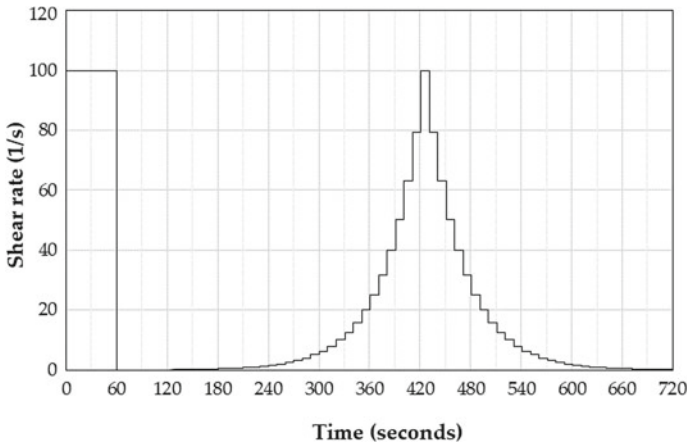$$\text{Thinning index (TI)} = \eta_{0.1}/\eta_1 \tag{1}$$

Fig. 1 Flow sweep testing procedure

With this test method, the extent of shear thinning is indicated by the drop in viscosity with increasing shear rate. consequently, the degree of thixotropy can be obtained by comparison of viscosities at increasing and decreasing shear rates (i.e. viscosity recovery). The high-shear treatment approximates shearing during pastes casting. The viscosity behaviour measured after high shear is indicative of the characteristics of the paste soon after casting.

3   Results and Discussion

3.1   Paste Fluidity

The influence of mix design parameters on the fluidity of AAM pastes was examined. Immediately after mixing, all pastes showed a spread diameter of 240 mm which indicates the high fluidity of the mixtures, as shown in Fig. 2. This diameter was gradually decreased to 120 mm over time, as shown in Fig. 3, which indicates zero fluidity and a stiff paste. However, the hardening time was varied among the pastes, depending on the GGBFS content, solution/binder ratio and Ms ratio. According to Fig. 2a, the fluidity was decreased sharply over time when the GGBFS content was increased from 10 to 40%. Oderji et al. [15] stated that the presence of more CaO in the mixture, due to larger amounts of FA was replaced with GGBFS, leads to higher loss of fluidity over time. This could be attributed to the higher rate of gel formation at an early age for pastes containing higher amounts of GGBFS. The fluidity varied slightly by changing the chemical composition and the volume of the activator, as shown in Fig. 2b, c. For instance, the spread diameter of the paste made of Ms 1.5 was slightly lower than the other mixtures but there was no distinct trend observed in terms of the effect of the SiO_2 concentration on fluidity in this study.
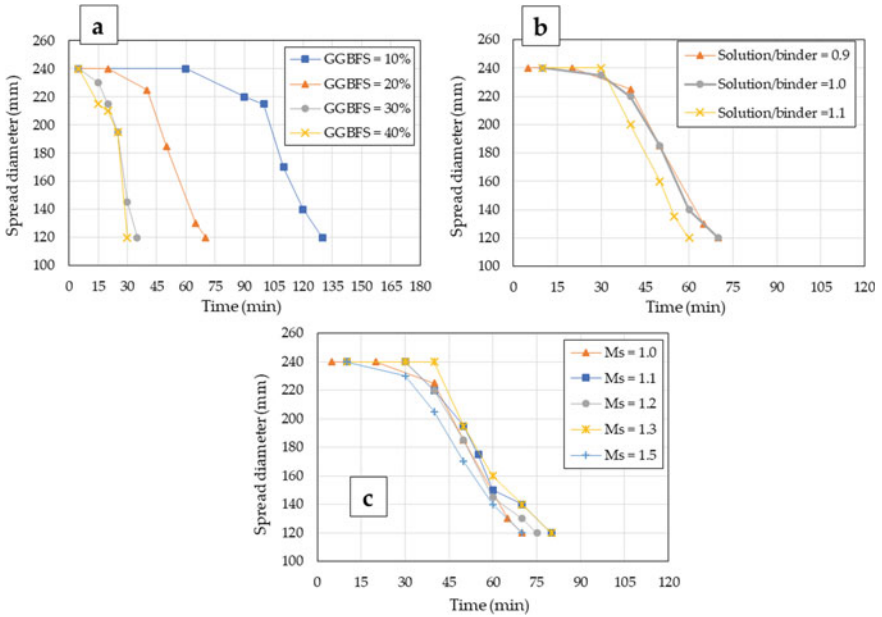
Fig. 2 Spread diameter of the pastes at different intervals after mixing. **a** GGBFS 10–40%, **b** solution/binder 0.9–1.1 and **c** Ms 1.00–1.5
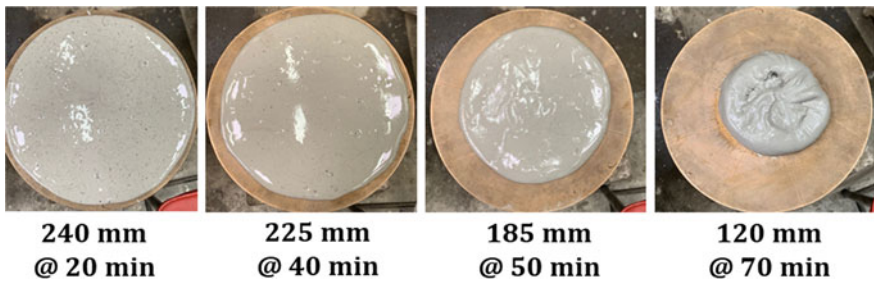

Fig. 3 The change in spread diameter at different elapsed times for S20 mix with 20% GGBFS

3.2 Viscosity and Yield Stress

The AAM paste behaves like a non-Newtonian fluid and its shear stress curve fit well with some models such as Bingham model (Eq. 2) and Herschel–Bulkley model (Eq. 3).

$$\tau = \tau_o + \eta\dot\gamma \qquad (2)$$

$$\tau = \tau_o + k\dot\gamma^n \qquad (3)$$

where η, τ, τ_o, $\dot\gamma$, k and n are the plastic viscosity (Pa.s), shear stress (Pa), yield stress (Pa), shear rate (s^{-1}), consistency coefficient (Pa.s) and dimensionless fluidity index, respectively. To determine the viscosity and yield stress of the pastes, the descending shear rate-shear stress profile was chosen for analysis. Previous research showed that AAM pastes are well fitted to the Herschel-Bulkley model, while the cement paste fitted Bingham model [16, 17].

Effect of GGBFS: Flow sweep curves for pastes containing 10–40% GGBFS under the hysteresis cycles are shown in Fig. 4. Viscosities and yield stresses for paste mixtures were calculated by fitting the descending shear rate-shear stress curve to the Herschel–Bulkley model. Table 4 shows the yield stress and the viscosity value for each mixture. The results showed an increase in the yield stress from 0.81 Pa to 4.93 Pa when the GGBFS content was increased from 10 to 40%. At 40% GGBFS content, a more increase in yield stress (4.93 Pa) was recorded. A similar trend was also observed for the viscosity. It should be noted that all other parameters except for the binder contents were kept constant. Therefore, this behaviour could be attributed to the role of particle geometry, including the particle shape and size distribution, in determining the rheological properties of suspensions [18, 19]. Fly ash is well-known to have spherical particles compared to irregular particle shape for GGBFS. As a result, increasing the GGBFS content tends to increase the interparticle surface friction of angular GGBFS, which in turn reflects the yield stress and viscosity.
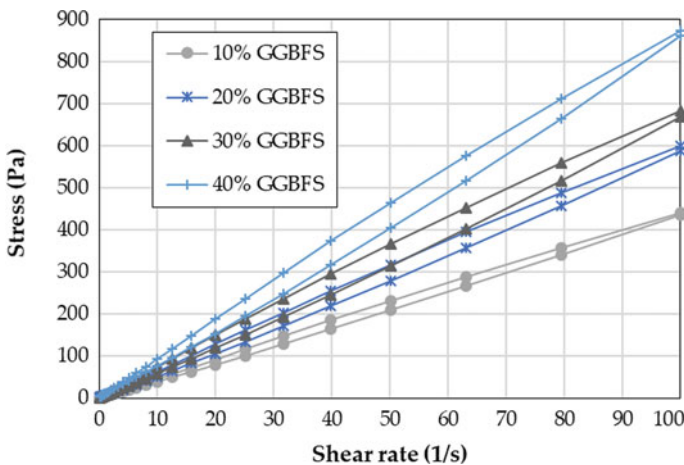

Fig. 4 Flow sweep curve for pastes containing 10–40% GGBFS

Table 4 Yield stress and viscosity of all mixtures

Mix	S10	S20	S30	S40	SB1.0	SB1.1	Ms1.1	Ms1.2	Ms1.3	Ms1.5
Yield stress (Pa)	0.81	1.56	2.50	4.93	0.99	0.69	1.31	1.58	1.34	1.11
Viscosity (Pa.s)	3.30	4.12	4.48	5.66	1.63	0.77	4.25	5.43	5.42	7.55

Effect of solution/binder ratio: As can be seen from Table 4, the increase of the solution/binder ratio from 0.9 to 1.1 resulted in a decrease in the yield stress and viscosity. For instance, the yield stress of the mix S20 with solution/binder = 0.9 was 1.56 Pa compared to 0.99 Pa and 0.69 Pa for mixes SB1.0 and SB 1.1, respectively. The GGBFS content, SiO_2/Na_2O and Na_2O/binder were kept constant for all these mixtures (20%, 1.0 and 7.5%, respectively) and only water content was adjusted to achieve the predesignated ratios of solution to binder. Therefore, the influence of particles friction and suspending alkaline silicate solution can be ignored in comparative evaluations. On the other hand, the particle spacing will differ across these suspensions due to the increase in the solution volume, and thus the influence of Van Der Waals forces is likely dominating. Therefore, the increased solution volume increases the potential of particle separation, which in turn decreases the yield stress and viscosity of the suspensions [11] (Fig. 5).

Effect of alkali modulus (Ms). In this part, the effect of SiO_2 concentration on the rheological parameters was examined, and the results are shown in Table 4 and Fig. 6. It can be seen from the results that the yield stress of pastes made with Ms of 1.0–1.5 varied in a narrow range between 1.56 Pa and 1.11 Pa, which indicates the negligible effect of silicate concentration on the yield stress. The yield stress is
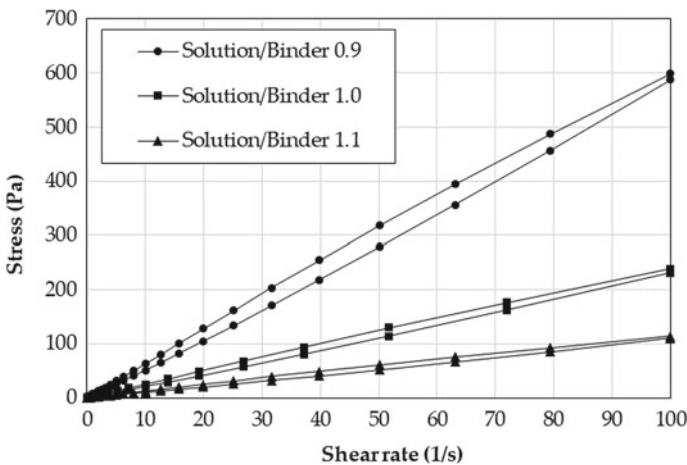

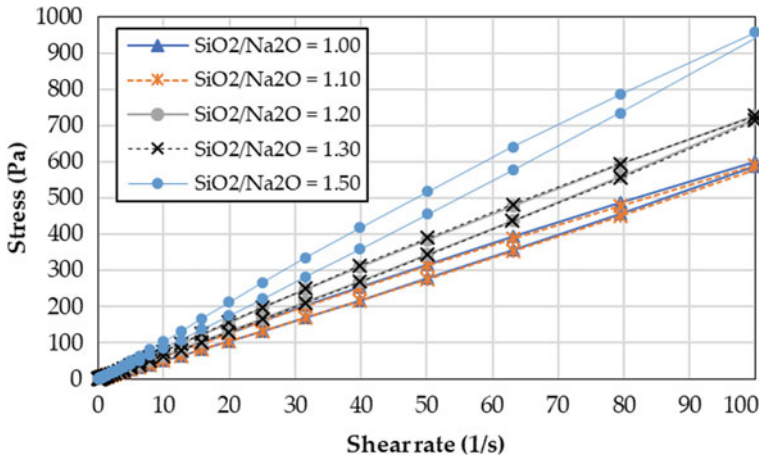**Fig. 5** Flow sweep curve for pastes at different solution/binder ratio

Fig. 6 Flow sweep curve for pastes at different Ms ratio

known to be affected by the inter-floc interaction and the formation of early age reaction products, which mainly controlled by the hydroxyl [OH⁻] ions. The concentration of OH^- ions is more or less identical in the pastes made with Ms of 1.0–1.5 due to the fixed amount of Na_2O. As a result, at a very early age, the binder dissolution and subsequent gel formation would be similar for these mixes. Puertas et al. [9] found that the SiO_2/Na_2O ratio had no significant effect on yield stress at early ages (7 min). However, a significant effect of this ratio can be observed at higher reaction times.

On the other hand, a significant increase was observed in the viscosity from 4.12 Pa.s to 7.55 Pa.s when the Ms was increased from 1.0 to 1.5. This can be explained by the high concentration of SiO_2 ions in the activator with higher Ms. The silicate solution could be considered as a purely viscous fluid compared to other fluids such as water. Consequently, the increased volume of the sodium silicate solution, that is required to maintain the Ms at high levels, contributes to the increase of the overall viscosity of the paste. Furthermore, AAM pastes can be considered as suspensions of precursors in a suspending alkaline activator Newtonian solution [20]. Therefore, the viscosity of the paste is controlled by the viscosity of the activator and the packing properties of the grains. Nevertheless, the influence of the precursors is neglected due to the fixed amount of GGBFS and FA in these mixtures.

3.3   Thinning Index

Figure 7 illustrates the shear thinning behaviour of all pastes indicated by the drop in viscosity with increasing shear rate from $0.1 \, s^{-1}$ to $1 \, s^{-1}$. In addition, the
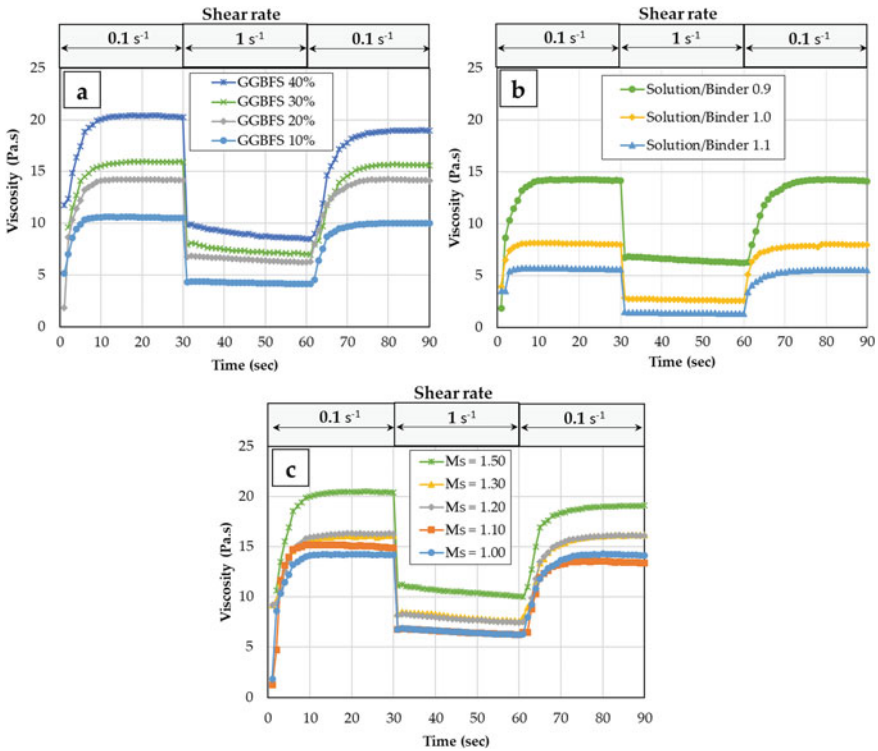
Fig. 7 Viscosity of AAM pastes at different shear rates. **a** GGBFS 10–40%, **b** solution/binder 0.9–1.1 and **c** Ms 1.00–1.5

Table 5 Thinning index of AAM pastes

Shear rate (s^{-1})	Viscosity (Pa.s)									
	S10	S20	S30	S40	SB1.0	SB1.1	Ms1.1	Ms1.2	Ms1.3	Ms1.5
0.1	10.6	14.1	15.7	20.2	8.1	5.7	15.0	16.0	15.8	20.2
1.0	4.3	6.5	7.4	9.0	2.7	1.4	6.5	7.8	8.0	10.5
TI	2.47	2.17	2.12	2.24	3.01	4.01	2.31	2.05	1.98	1.92

thinning index (TI) values of all pastes at different GGBFS content, solution/binder ratio and Ms ratio are shown in Table 5. As seen, the TI of AAM pastes is in the range of 1.92–4.01. Moreover, the results reveal that the TI is independent on the GGBFS content or Ms ratio, where the values varied in a narrow range under these parameters. These findings are in line with those obtained by Mehdizadeh and Kani [16] for alkali activated phosphorous slag. However, it is noteworthy to mention that the TI at 1.1 solution/binder ratio was almost two times higher compared to TI at 0.9 solution/binder ratio. These results show a strong dependency of the TI on the activation solution volume in the mixture.

4   Conclusions

In this study, the effect of GGBFS content, as well as volume and chemical composition of alkali activator on the rheological behaviour and flow properties of AAM pastes, was investigated. Based on the results, the following conclusions can be drawn:

- All pastes showed high fluidity immediately after mixing with a spread diameter of 240 mm. However, the fluidity of pastes was decreased sharply over time for the pastes made of higher amounts of GGBFS because a CaO-rich source leads to more early age gel formation in these pastes.
- All pastes showed a shear thinning behaviour with the curve fitting well with the Herschel–Bulkley model.
- The yield stress and viscosity values of AAM pastes were increased with the increase in the GGBFS content, and the chemical composition of the activator had no significant effect on fluidity and yield stress.
- The findings showed that the thinning index is independent on the GGBFS content or Ms ratio but strongly dependent on the volumetric solution-to-binder ratio.

References

1. USGS, Cement—Mineral Commodity Summaries, Cement statistics and Information—Annual Publications. U.S. Department of the Interior, U.S. Geological Survey (2018)
2. Biernacki, J.J., Bullard, J.W., Sant, G., Brown, K., Glasser, F.P., Jones, S., Ley, T., Livingston, R., Nicoleau, L., Olek, J.: Cements in the 21st century: challenges, perspectives, and opportunities. J. Am. Ceram. Soc. **100**(7), 2746–2773 (2017)
3. Provis, J.L., Palomo, A., Shi, C.: Advances in understanding alkali-activated materials. Cem. Concr. Res. **78**, 110–125 (2015)
4. Khan, H.A., Khan, M.S., Castel, A., Sunarho, J.: Deterioration of alkali-activated mortars exposed to natural aggressive sewer environment. Constr. Build. Mater. **186**, 577–597 (2018)
5. Li, Z., Thomas, R.J., Peethamparan, S.: Alkali-silica reactivity of alkali-activated concrete subjected to ASTM C 1293 and 1567 alkali-silica reactivity tests. Cem. Concr. Res. **123**, 105796 (2019)
6. Singh, B., Ishwarya, G., Gupta, M., Bhattacharyya, S.K.: Geopolymer concrete: a review of some recent developments. Constr. Build. Mater. **85**, 78–90 (2015)
7. Alonso, M., Gismera, S., Blanco, M., Lanzón, M., Puertas, F.: Alkali-activated mortars: workability and rheological behaviour. Constr. Build. Mater. **145**, 576–587 (2017)
8. Montes, C., Zang, D., Allouche, E.N.: Rheological behavior of fly ash-based geopolymers with the addition of superplasticizers. J. Sustain. Cem. Based Mater. **1**(4), 179–185 (2012)
9. Puertas, F., Varga, C., Alonso, M.: Rheology of alkali-activated slag pastes. Effect of the nature and concentration of the activating solution. Cem. Concr. Compos. **53**, 279–288 (2014)
10. Rifaai, Y., Yahia, A., Mostafa, A., Aggoun, S., Kadri, E.-H.: Rheology of fly ash-based geopolymer: effect of NaOH concentration. Constr. Build. Mater. **223**, 583–594 (2019)

11. Vance, K., Dakhane, A., Sant, G., Neithalath, N.: Observations on the rheological response of alkali activated fly ash suspensions: the role of activator type and concentration. Rheol. Acta **53**(10–11), 843–855 (2014)
12. Kim, J.H., Yim, H.J., Ferron, R.D.: In situ measurement of the rheological properties and agglomeration on cementitious pastes. J. Rheol. **60**(4), 695–704 (2016)
13. Tan, Z., Bernal, S.A., Provis, J.L.: Reproducible mini-slump test procedure for measuring the yield stress of cementitious pastes. Mater. Struct. **50**(6), 235 (2017)
14. ASTM D2196–05, Standard Test Methods for Rheological Properties of Non-Newtonian Materials by Rotational (Brookfield type) Viscometer. ASTM International, West Conshohocken, PA (2005)
15. Oderji, S.Y., Chen, B., Ahmad, M.R., Shah, S.F.A.: Fresh and hardened properties of one-part fly ash-based geopolymer binders cured at room temperature: effect of slag and alkali activators. J. Clean. Prod. **225**, 1–10 (2019)
16. Mehdizadeh, H., Kani, E.N.: Rheology and apparent activation energy of alkali activated phosphorous slag. Constr. Build. Mater. **171**, 197–204 (2018)
17. Palacios, M., Banfill, P.F., Puertas, F.: Rheology and setting of alkali-activated slag pastes and mortars: effect of organic admixture. ACI Mater. J. **105**(2), 140 (2008)
18. Yang, T., Zhu, H., Zhang, Z., Gao, X., Zhang, C., Wu, Q.: Effect of fly ash microsphere on the rheology and microstructure of alkali-activated fly ash/slag pastes. Cem. Concr. Res. **109**, 198–207 (2018)
19. Bentz, D.P., Ferraris, C.F., Galler, M.A., Hansen, A.S., Guynn, J.M.: Influence of particle size distributions on yield stress and viscosity of cement–fly ash pastes. Cem. Concr. Res. **42**(2), 404–409 (2012)
20. Favier, A., Hot, J., Habert, G., Roussel, N., de Lacaillerie, J.-B.d.E.: Flow properties of MK-based geopolymer pastes. A comparative study with standard Portland cement pastes. Soft Matter **10**(8), 1134–1141 (2014)

Material Characterization of Geopolymer Concrete for Its Beneficial Use in Composite Construction

Joachim Juhart, Christopher Gößler, Cyrill Grengg, Florian Mittermayr, Andrew McIntosh, and Bernhard Freytag

Abstract Geopolymer concrete (GPC) is an inorganic, mineral-based construction material with high resistance to chemical attack and further excellent properties such as rapid strength development and relatively low CO_2 emissions in comparison to ordinary Portland cement based normal concrete (PCC). However, production technologies, corresponding to the workability and time-dependent properties during the hardening of GPC are not known in detail. The aim of an ongoing research project is to combine GPC with PCC to form composite structures for applications in chemically aggressive environments such as sewers. This paper deals with material properties of GPC, which have significant impact on the composite action. GPC formulations with different workability (soft and stiff-plastic consistencies) were developed and investigated with regard to their compressive and tensile strength development over time, as well as shrinkage during hardening under different ambient conditions (autogenous shrinkage, drying shrinkage, early shrinkage). The GPCs investigated show significant autogenous shrinkage and drying shrinkage. Under dry conditions, additionally very high early shrinkage occurs immediately after the beginning of hardening, which was tested using the image correlation method. The extent of this early shrinkage depends strongly on the thickness of the specimen. As another result of this experimental study, equations for the prediction of the strength development over time are given in this paper.

J. Juhart (✉) · F. Mittermayr
Institution of Technology and Testing of Construction Materials, Graz University
of Technology, Graz, Austria
e-mail: joachim.juhart@tugraz.at

C. Gößler · B. Freytag
Laboratory for Structural Engineering, Graz University of Technology, Graz, Austria

C. Grengg
Institute of Applied Geosciences, Graz University of Technology, Graz, Austria

A. McIntosh
Banah UK Ltd, Coleraine, Northern Ireland

271

1 Introduction

The deterioration of concrete structures due to the interaction with chemically aggressive solutions and gases is a major concern of the construction industry. It is frequently observed that in waste and wastewater infrastructure ordinary Portland cement-based concrete (PCC) decomposes with high rates (~ 1 cm/year under highly aggressive conditions). The reason for this fast deterioration is the exposure to acidic solutions [1, 2]. Thus, alternative solutions have to be found. In this context, geopolymer concrete (GPC) shows great potential [3]. Compared to existing PCC construction materials which matrix is formed by the cement hydration reactions (calcium hydroxide and calcium silicate hydrates), the GPC matrix is produced by polycondensation of alumino-silicates [1]. Thereby, alumina silicate powder materials (calcined clays, volcanic rocks, blast furnace slag (BFS), fly ash (FA)) are mixed with alkaline reagent solutions (either sodium or potassium soluble silicate) and water. This binder paste is further mixed with aggregates in order to form a material with similar mechanical properties as PCC [4]. GPC technology avoids the formation of Ca-rich acid-dissolvable hydration products, present in PC-based materials. The absence of these phases is mainly responsible for the high acid resistance of GPC [5, 6].

Economic considerations and the use of GPC for repair measures of existing concrete infrastructure lead to the idea of GPC–PCC composite structures. This composite technology appears to have a considerable market potential. The PCC— i.e. standardized normal concrete—provides the main part of the structural settings and the geopolymer acts as both, a structural part and a barrier against chemically aggressive attack. The materials have to be strongly bonded to each other at their interface. To develop such a new composite technology, material parameters of both, PCC and GPC have to be well understood. Whereas the relevant material parameters for PCC have been extensively studied, there is little corresponding literature for GPC. Depending on the type of raw material used for GPC synthesis and on the mix design, a wide range of material properties can be expected [3, 4].

In general, composite constructions are built by bringing the fluid or pasty adhesive (GPC) into close and continuous contact to the solid adherent (PCC). The final mechanical strength of the adhesive interface depends mainly on (i) material properties of both adhesive and adherent (as tensile strength, shear strength, thermal and hygric deformation coefficients etc.) and (ii) properties and pre-treatment of the adherent's surface (roughness, open porosity, wettability etc.) [7]. The development of a strong bond highly depends on the (tensile) strength development of the adhesive over time $f_{ct}(t)$. This is because internal stresses occur during the hardening process of an adhesive due to constraints by the solid adherent. Driving forces are changes in temperature (if the thermal expansion of the bonding materials

differs from each other), or shrinkage/expansion of the adhesive during the hardening process. Shrinkage/expansion can occur due to autogenous deformation during the chemical hardening process or hygric/thermal deformations driven by external climatic conditions (temperature differences and wetting/drying cycles). These stresses can either cause cracks or induce delamination starting at the edge of a cover layer in the interface, see Fig. 1 and [8].

This study focuses on material properties of metakaolin based GPC in terms of strength development and shrinkage. The latter is the loss in volume of a porous building material that occurs without the influence of external load by changing the water balance [9]. The water balance changes can be due to varying ambient conditions (reversible adsorption and desorption of water)—so-called drying shrinkage (DS)—or come from chemical reactions during hardening (irreversible). Under sealed conditions the latter is combined with self-extraction ("inner drying") [10], which in sum is called autogenous shrinkage (AS). DS depends strongly on temperature and relative humidity and the proportion of drying surface to the total volume. Very early shrinkage (ES) occurs in fresh, still workable concrete and is mainly due to capillary forces between the particles that increase with drying out. It is also known as "plastic shrinkage" or "solidification shrinkage" [11]. It occurs on the surface and can cause cracks in the fresh concrete in the first few hours. Cracks in all cases occur, when stress induced by hindered shrinkage exceeds the concrete's tensile strength. However, cracks do not occur before setting, as no stresses can be transferred into the matrix [11]. Setting means that fresh concrete is no longer plastically deformable.
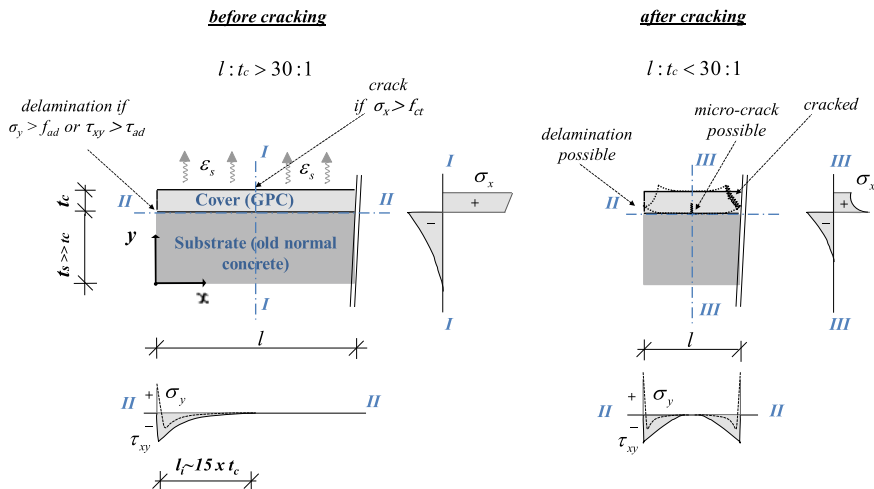

Fig. 1 Stress distribution of enforcements σ_x, σ_y, τ_{xy} due to constrained hygric shrinkage ε_s depending on ratio l: t_c (extent: cover layer-thickness) of a GPC-PCC composite body. With: f_{ct}… tensile strength, f_{ad}…tensile adhesion strength, τ_{ad}…shear adhesion strength of cover, l_i… initiation length, modified after [8]

2 Materials and Methods

2.1 GPC Production

The binder for the present GPC consists of a metakaolin-rich calcined clay and ground granulated blast furnace slag (GGBFS), mixed with a potassium based fluid activator [12]. Silicate sand 0/4 mm was used as aggregate. Two mixes with different consistencies (B_012/soft consistency for wet cast applications and B_013/ stiff-plastic for dry cast) were developed by varying the volumetric ratio of paste to aggregate, see Table 1.

Mix-volumes of 1.0—1.2 L were prepared using a 4.5 l (total volume) Hobart mixer with three speed transmissions. For preparing larger batches (>5 L) i.e. to fill shrinkage trays the 10 l RV10 Eirich-mixer was used. First, the activator and additional water were put into the mixer then the powder precursor was added during continuously mixing at the lowest speed for 3 min. Subsequently the aggregates were added and mixed for another 2.5 min at the same speed. Finally, the mix was homogenized for 0.5 min at maximum speed.

2.2 Consistency Test of GPC

To test the consistency of the GPC according to EN 1015–3:2007, the GPC mix was poured into a Hägermann cone with a 100 mm base diameter on a dry glass plate of a compaction table. The cone was lifted to allow a free flow of the concrete. No jolts were applied for two minutes. At this time two perpendicular diameters of the concrete were measured. Subsequently, 15 jolts of the table were applied and the diameters were measured again. For results see Table 1.

2.3 Compressive and Tensile Strength Development Over Time

Prisms of 40/40/160 mm were manufactured of each GPC mix and tested for compressive strength (n = 3) according to EN 196–1:2016 and for splitting tensile strength (n = 4) according to ONR 23,303 (corresponding to EN 12,390–6:2010)

Table 1 Composition and consistency of GPC

	unit	mix B_012	mix B_013
Water glass	kg/m^3	270	232
Banahcem		400	344
Water		121	104
Crushed sand 0/4		1504	1663
Paste volume	l/m^3	430	370
Water/solid-ratio	–	0.37	0.37
Flow-table spread (without jolts/with jolts)	mm	132/165	100/115

after 24 h, 7 days and 28 days. The prisms were prepared and stored as follows: (i) compaction of the fresh GPC in plastic-moulds by a vibration table for about 1 min; (ii) covering using a plastic lid and (iii) storing it in >90% relative humidity (r.h.) until demoulding, which was carried out after 3–5 h of hardening and then again storing it in >90% r.h. until testing. Then strength tests were carried out after 3–5 h, 24 h, 7 d, 28 d.

2.4 Shrinkage During Hardening Under Different Conditions

In order to characterize the shrinkage behaviour comprehensively, several test methods were applied. They aimed to test (i) the autogenous shrinkage of the GPC, (ii) the hygric shrinkage or drying shrinkage of the GPC under varying ambient humidity, and (iii) the very early shrinkage with rapid drying.

(i) **Autogenous shrinkage**. Autogenous shrinkage (AS) was measured using stainless steel shrinkage troughs (Schleibinger shrinkage drain) with the dimensions 40/60/1000 mm. Each trough was prepared with a 2 mm thick rubber sheet and a plastic foil working as a flexible interlayer to ensure, that the sample can move freely in the trough. The fresh GPC was poured into the trough immediately after mixing. The deformation measurement started at the plastic state of GPC and before the maximum temperature of the reaction. The free concrete surface was covered with a plastic foil. An inductive measuring sensor (resolution of 0.3 μm and an accuracy better than 1 μm) was installed at one end of the trough. This sensor is activated before setting and before the maximum temperature of reaction. It continuously records the change of length of the GPC specimen. A temperature sensor embedded in the middle of each specimen recorded the GPC temperature.
The troughs were placed in a room with defined room climate conditions (23 °C ± 2 °C, 50% r.h. ±5 %). The influence of temperature change is not taken into account (about ±10 μm/°Km). In a first series, AS was determined as the mean of 2 specimens for each mix (B_012a and B_013). The test of the soft-consistency mix was repeated (B_012b, 1 specimen) with double sealing.

(ii) **Drying shrinkage**. The drying shrinkage (DS) was measured in this study in 2 different ways. Firstly, the shrinkage trough measurements described above were continued after removal of the cover on the 7th day. Consequently, the GPC could dry out under ambient conditions (23 °C, 50% r.h.). Secondly, the length change of prisms 40/40/160 mm was determined according to ONR 23,303 (corresponding to EN 12,617–4:2002). Therefore, the prisms were manufactured as described above, with steel-markings embedded in concrete at both ends. Prisms were demoulded after 3 h. At this time, the initial length measurements were carried out. Afterwards the samples (n = 6)

were stored at high humidity of >90% r.h. which is similar to sealed spec-
imen in the shrinkage trough of V1 for a fist period of 7 days. The shrinkage
deformations were determined from the difference between the initial length
after 3 h and the length measurements after 6 h, 24 h, 48 h etc. After this
period, the samples were stored under ambient conditions of 23 °C and 50%
r.h. (n = 3) and 20 °C and 65% r.h. (n = 3) and were measured continuously
for a further week. Finally, all specimens were stored again at 20 °C
and >90% r.h till the end of measurement.

(iii) **Very early shrinkage**. The amount of early shrinkage (ES) depends on the
thickness of the GPC body. This is the reason why the test setup involves
specimens of varying thickness. The specimens were discs with four different
thicknesses (t = 5, 10, 20 and 40 mm) and same diameter
(d = 105 ± 1 mm) made from both GPCs (soft consistency, B_012 and
stiff-plastic B_013). The discs were produced by pouring the GPC into
plastic rings of the respective heights. The rings were placed on a 2 mm thick
rubber sheet to ensure free moving of the GPC layers. The bottom and the
inner parts of the rings were waxed to avoid friction and to prevent the
circumference sides of GPC from drying. Continuous vibration during
casting ensured compaction. After casting, gauge marks were placed on the
surface and the samples were stored at 23 °C and 50% r.h. Deformations of
the samples were measured by using the image correlation method (optical
measuring equipment from Sobriety using the Mercury RT software). Two
cameras take photographs from the samples and its gauge marks at the same
time. The measuring software calculates the relative movements of the gauge
marks. These are recalculated into the shrinkage strains due to ES. The
measurements were started at the setting time of the GPC and ran for 7 days.
Figure 2 shows the ES test set-up.

a)   b)
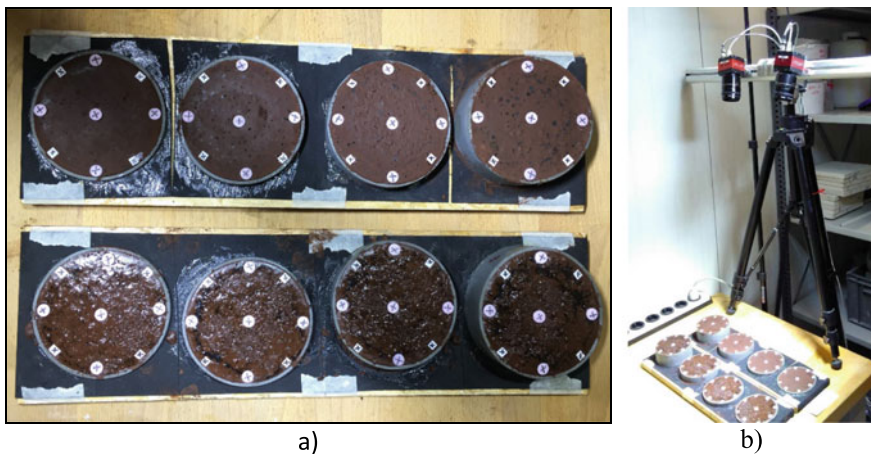
Fig. 2 Very early shrinkage test: **a** discs of mix B_012 above, B_013 below, **b** camera set up

3   Results

All presented properties are time-dependent. We consider the time of mixing in the fluid activator into the powder as starting point of the chemical reaction and therefore as "zero time" of the time axis in the presented plots. In the first minutes to hours, the mix is a highly viscous suspension and plastically deformable. From setting time t_s on, a continuous solid body is formed during hardening [11]. t_s of the fresh mix is decisive for stress-inducing deformations, because tensile stress can be transferred in the matrix only after this time. According to [11] t_s was determined as the point of the maximum deformation rate during AS shrinkage at 2.25 h after "zero time" for both mixes B_012 and B_013. It is known from high-strength concretes, that t_s occurs slightly after the end of setting determined with the VICAT device (in accordance to EN 196–3:2017) [11].

3.1   Compressive and Tensile Strength Development Over Time

Figure 3 shows the development of the compressive strength f_{cm} and the splitting tensile strength f_{tm} of the GPC mixes B_012 and B_013 over time. f_{cm} runs asymptotically against ~ 60 N/mm^2 and the splitting tensile strength f_{tm} against ~ 5 N/mm^2 after 28 d. A fitting function for $f_{cm}(t)$ and $f_{tm}(t)$ was found by a regression analysis on the basis of the equations given in model code 2010 for PCC [12] by re-calculating their coefficients. It should be noted that a factor of 0.9 was applied to the ratio of tensile strength to splitting tensile strength. Since the mean values of the different mixes are very close, only one function is fitted for each type
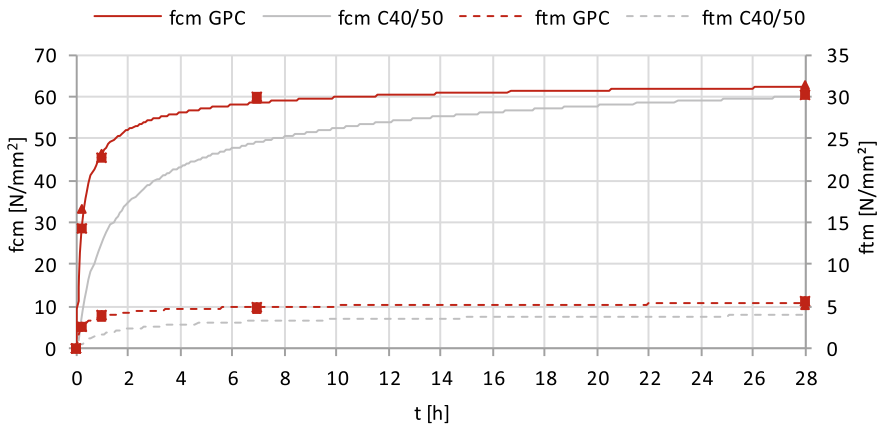
Fig. 3 Compressive and tensile splitting strength development of GPC versus normal concrete

of strength. Thus, the strength developments of our GPC can be specified as follows:

$$f_{cm}(t) = 62.2 * exp\{0.049 * [1 - (28/t)^{\wedge}0.58]\} \tag{1}$$

$$f_{tm}(t) = 5.32 * exp\{0.097 * [1 - (28/t)^{\wedge}0.45]\} \tag{2}$$

Note that in Eqs. (1) and (2) f_{cm} and f_{tm} are given in [N/mm^2] and time t in [d].

Results in Fig. 3 are presented compared to data of PCC from the model code 2010 [13] (class 40/50 with f_{cm} = 60 N/mm^2, f_{tm} = 3.9 N/mm^2). The f_{tm}/f_{cm} ratio (=0.081) of GPC at an age of 28 d is larger by 25% than that of PCC according to model code (=0.065).

3.2   Shrinkage During Hardening Under Different Conditions

AS and DS measured with the shrinkage trough. Figure 4 shows the shrinkage strains of the two GPC mixes (B_012a, B_012b with soft consistency and B_013 with stiff consistency) as measured with the shrinkage trough from time of setting on (t_s = 2.25 h). First, the AS is measured under sealed conditions in the period from 0 to 7 d. After initially very rapid shrinkage within the first 24 h, the samples reach nearly equal values of 0.25‰ (B_012b) and 0.28‰ (B012a and B_013) after 7 d.

Only after the removal of the sealant, larger differences in the shrinkage behaviour of the two mixtures become apparent, namely that B_012 (with higher paste volume) shrinks more than B_013. This DS progresses very rapidly in the first 24 h
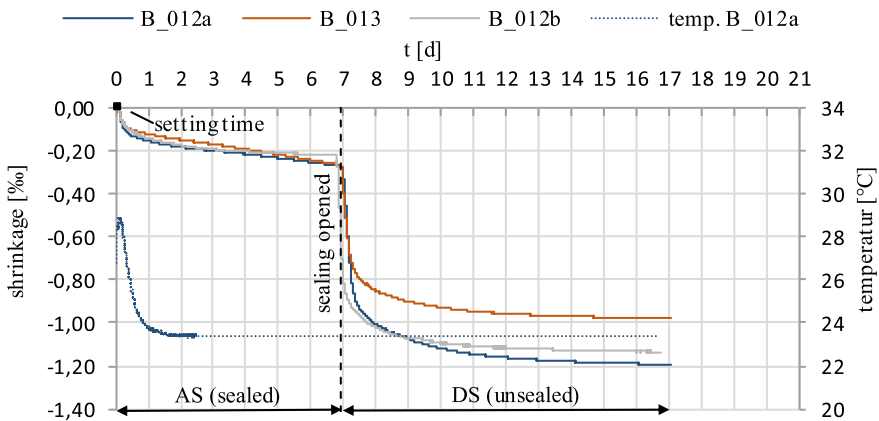
Fig. 4 AS and DS measured with the shrinkage trough
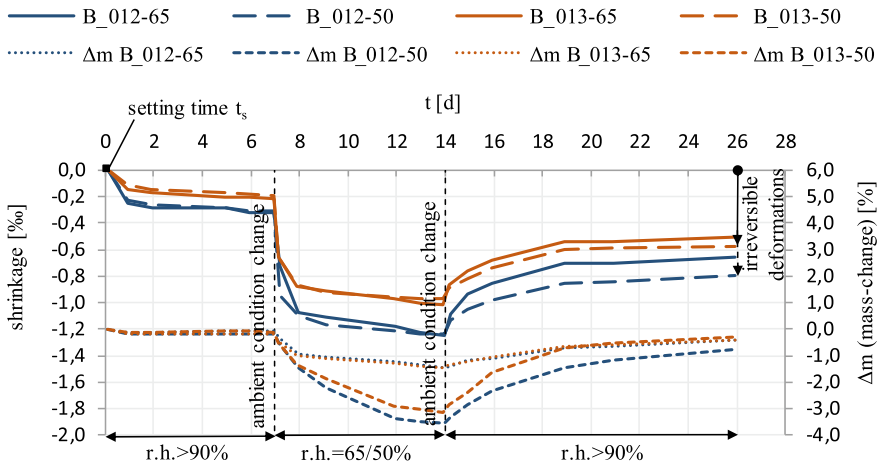
Fig. 5 Hygric shrinkage during hardening under changing ambient conditions

after the removal of the sealant and asymptotically tends towards a maximum with time, which was not quite reached in the measuring period.

Total shrinkage (AS and DS) measured on prisms during changing ambient conditions. Very similar results to the shrinkage trough measurements were obtained by measuring hardened prisms 40/40/160 mm, although the measurement started shortly after t_s, namely at ~ 3 h after demoulding, Fig. 5. In the first period samples were stored at 20 °C and r.h. of >90% for 7 d. The 6 samples of B_012 achieved an average shrinkage of about 0.3‰ and those of B_013 about 0.2‰. In the following period of another 7 d, 3 samples of each mixture were stored at 23 °C and 50% r.h. and 3 samples at 20 °C and 65% r.h. The total shrinkage after 14 d was about 1.2‰ (B_012) and about 1‰ (B_013), regardless of whether shrinking took place at 50% or 65%. The mass loss due to drying, however, was significantly larger for samples stored at low humidity (50% r.h.) compared to the ones stored at higher humidity (65% r.h.) (see Fig. 5). In a further period, the samples were all stored at r.h. >90%, which led to a reduction in shrinkage deformations. However, this decrease was less than the initial shrinkage, leaving an irreversible deformation after the cycle of desiccation and reabsorption of moisture. In the samples dried under lower r.h. (23 °C, 50% r.h.), larger deformations were left behind compared to the ones under higher r.h. (20 °C, 65% r.h.), see Fig. 5.
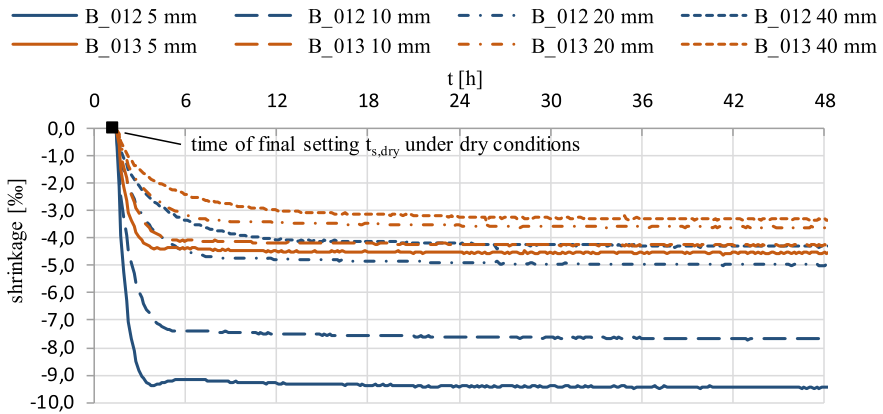
Fig. 6 Shrinkage strains due to very early drying of freely moveable layers with different thickness of the soft (B_012) and stiff mix (B_013)

3.3   Early Shrinkage and Drying with Different Layer Thickness

With the experimental setup for ES described above, the effect of very early drying was studied, which may occur in practice in the absence of curing. Figure 6 shows the shrinkage strain curves of the samples with different thicknesses at constant diameter as a result of drying at 23 °C and 50% r.h from "zero time" on. From 1.4 h after zero time on, deformation was measured. This approximately corresponds to the time of final setting $t_{s,dry}$ = 70 min, measured acc. to VICAT, EN 196–3:2017, under dry conditions. It shows that the deformation is directly related to the superficial desiccation. Thin slices reduce their diameter considerably more and faster compared to thick slices. Mixture B_012 with larger paste volume shrinks more than B_013 with smaller paste volume. It is noteworthy that the shrinkage strains of the thinnest layer at very early drying after 24 h with about 9 ‰ of B_012 and 4.5 ‰ of B_013 are four times the shrinkage strains of the sealed samples in the shrinkage troughs, the prisms tested in >90% r.h. respectively. No significant further increase during the following time was recorded.

4   Discussion

The effects of consistency and paste volume of two GPC mixes on their strength development and shrinkage behavior under different curing conditions was evaluated. Main findings are discussed within this section.

4.1 Compressive and Tensile Strength Development Over Time

Modified fitting functions adopted from the model code 2010 [13] were found, to be able to predict the strength development $f_{cm}(t)$ and $f_{tm}(t)$ of produced GPC. Despite the varied paste volume used, the compressive and splitting tensile strength of the two mixes did not differ significantly. Strength of GPC develops much faster compared to PCC. After about 3 h, GPC already reached 50% of its 28 d values which allows earlier demolding in practical applications. After 24 h 77% and after 7 d 95% of the 28 d values were reached. These results are in agreement with existing data in the literature [4, 5]. In comparison, a typical PCC concrete of class C45/50 exhibits much lower strength at the early age of 3 h. Even after 28 d, its final strength is not fully reached. The f_{tm}/f_{cm} ratio of GPC (=0.081) is slightly larger compared to the PCC (=0.065) from the model code 2010.

4.2 Shrinkage During Hardening Under Different Conditions

AS was very pronounced in the tested GPC over a time of several days (roughly up to 4 d (0.25–0.28‰)). This values are higher than that of PCC and are in the range of ultra high strength concrete (UHPC), which is known for its high AS [8]. The DS, which was measured in two measuring arrangements (shrinkage trough and prisms) by changing the ambient conditions, is also found to be very pronounced and to be higher for the mix with higher volume of paste B_012 compared to the lower paste volume mix B_013. It is noteworthy, that different ambient conditions of 50% r.h. and 65% r.h. resulted in similar shrinkage strains, but different mass change values. This means that drying of the GPC leads to shrinkage deformations of the GPC only up to a critical moisture content. Any further reduction of the moisture does not lead to any more volume changes. Independent of the test setup and even of the ambient conditions, B_012 shrinks by about 0.9‰ and B_013 by about 0.7‰ within 7 days due to drying. The final shrinkage value is not yet reached. The DS process was not fully reversible after cycles of desiccation and reabsorption of moisture, see the irreversible deformation in Fig. 5. In the specimens under drier condition (23 °C, 50% r.h.), larger strains were left behind compared to the less dried ones (20 °C, 65% r.h.). Initial drying is assumed to lead to a structural change at the microstructural level during the formation of the polymeric geopolymer network.

The tests of early drying shrinkage on samples of different thicknesses revealed, that thin layers shrink more and faster than thick layers. However, no crack formation was observed in thin layers (5 and 10 mm). Thick layers (20 and especially 40 mm) showed very small superficial cracks, which were induced by hindered deformation due to surface drying. Thick layers shrink more slowly than thin layers,

obviously more moisture is transported from the inside of thick layers than from thinner layers.

5   Conclusion

Two GPC mixes with different consistencies were investigated with respect to their strength development and shrinkage under different curing conditions. The same fitted function was found for both mixes for the development of the compressive and splitting tensile strength over time, which corresponds to the approach for normal concrete (PCC) in the model code 2010 with coefficients adapted for GPC. The strengths of GPC develops much faster in the first few hours compared to those of PCC and the strength development seems to have essentially reached its final value after 28 d in contrary to PCC.

It is shown that the investigated GPC exhibits both significant AS and DS. Larger shrinkage deformations occur in the mixture with a larger volume of paste and softer consistency (B_012) Autogenous shrinkage is very pronounced in the first 4–7 d, different from that known from PCC (and UHPC) [8, 10]. The drying shrinkage, which was measured in two measuring arrangements immediately after the AS on the same specimens by changing the ambient conditions after 7 d was also very pronounced and DS was not fully reversible. In addition, depending on the climatic conditions (T, r.h.), very high early shrinkage (capillary shrinkage) can occur immediately after the setting, the extent of which also depends strongly on the thickness of the coating.

References

1. Grengg, C., Mittermayr, F., Ukrainzcyk, N., et al.: Advances in mineral based construction materials for sewer systems affected by microbiological induced concrete corrosion: a review. Water Res **134**, 341–352 (2018)
2. Druga, B., Weise, K., Ukrainzcyk, N., et al.: Interaction of wastewater microorganisms with geopolymer and cementitious materials. Microorg. Mater. Interact. RILEM, 163–172 (2018)
3. Pacheco-Torgal, F., Labrincha, J., Leonelli, C., et al.: Handbook of Alkali- Activated Cements, Mortars and Concretes, 1st Edition. Woodhead Publishing (2014)
4. Davidovits, J.: Geopolymer Chemistry and Applications, 4th ed. Springer (2013)
5. Provis, J.L., van Deventer, J.S.J.: Geopolymers. Structures, Processing, Properties and Industrial Applications. CRC Press, Woodhead Publishing, Great Abington, Cambridge, UK (2009)

6. Pacheco-Torgal, F., Abdollahnejad, Z., Miraldo, S., et al.: An overview on the potential of geopolymers for concrete infrastructure rehabilitation. Constr. Build. Mater. **36**, 1053–1058 (2012)
7. Juhart, J., Freytag, B., Santner, G., Baumgartner, E.: Adhesion of fine-grained HPC and UHPC to Steel and Glass. In: Ultra-High Performance Concrete and Nanotechnology in Construction, Proceedings, Schriftenreihe Baustoffe und Massivbau, Vol. 19, pp. 717–724. Kassel University Press, Kassel (2012)
8. Juhart J.: Adhäsion von UHPC an Stahl und Glas. Ein Beitrag zu Adhäsion und Haftfestigkeit von Hochleistungs- und Ultra-Hochleistungs-Feinkornbeton an Stahl und Glas unterschiedlicher Rauheit. Dissertation, Graz University of Technology (2011). https://graz.pure.elsevier.com/en/publications/adhesion-of-uhpc-to-steel-and-glass
9. Grube H.: Ursachen des Schwindens von Beton und Auswirkungen auf Betonbauteile: Heft 52: Beton-Verlag GmbH, Düsseldorf (Schriftenreihe der Zementindustrie) (1991)
10. Ma, J., Dehn, F., König, G.: Autogenes Schwinden von selbstverdichtendem UHPC. In: Yuan, Y., Shah, S. P., Lü, H. (Hg.) (eds.) Proceedings, International Conference on Advances in Concrete and Structures (ICACS). Xuzhou, Jiangsu/China (2003)
11. Fontana P.: Einfluss der Mischungszusammensetzung auf die frühen autogenen Verformungen der Bindemittelmatrix von Hochleistungsbetonen. TU Braunschweig (2007) [Zugriffsdatum: 2010–10–26]
12. Kwasny, J., Soutsos, M., McIntosh, J.A., Cleland, D.J.: banahCEM—comparison of properties of a laterite-based geopolymer with conventional concrete. In: M.R. Jones et al. (eds.) Proceedings of 9th International Concrete Conference 2016: Environment, Efficiency and Economic Challenges for Concrete, pp. 383–394. University of Dundee (2016)
13. fib (International Federation for Structural Concrete).: fib Model Code for Concrete Structures 2010. Wilhelm Ernst & Sohn, Berlin (2013)

Long-Term Performance of Cement Composites with Wood Biomass Ash

Ivana Carević, Nina Štirmer, Jelena Šantek Bajto,
and Karmen Kostanić Jurić

Abstract Positive trend of using wood biomass as renewable energy source (RES) results in generating large amounts of wood biomass ash (WBA). WBA is mostly landfilled as a waste. WBA could be used as secondary raw material in another industry reducing the environmental and social problems related to its disposal. In order to ensure enough cement for construction needs and while reducing fuel and raw material requirements and subsequent emissions during cement production, the use of new waste materials in the cement and construction industry is necessary. Therefore, one possible option is WBA utilization in the construction sector as a new raw material. The chemical and physical properties of WBA are different from coal fly ash (FA) and currently do not meet the existing requirements for concrete application. Application of novel materials in the construction composites highlights the need for generic, quantitative relations between chemical and physical properties and its behavior and effect on the cement composites. This research investigated the long-term durability performance of cement composites where WBA is used as partial cement replacement. Gas permeability and capillary absorption were investigated on mortars where fly WBAs, originating from different combustor technologies, were used as replacement of cement CEM I 42.5R.

Keywords Fly wood biomass ash · Cement mortar · Gas permeability · Capillary absorption

I. Carević (✉) · N. Štirmer · J. Š. Bajto
Faculty of Civil Engineering, University of Zagreb, Zagreb, Croatia
e-mail: ivana.carevic@grad.unizg.hr

K. K. Jurić
Tomting 2010 Ltd., Zagreb, Croatia

1 Introduction

The increase in the number of wood biomass energy plants has resulted in an increase of ash amount generated by incineration of biomass. Wood biomass ash (WBA) has been declared as a waste. According to the Waste Directive (2008/98/EC) [1] and new Directive (EU) 2018/851 [2], the key concepts of waste management is waste prevention, then re-use and recycling, and finally its disposal. While significant progress has been made in the combustion technology and in the reduction of CO_2 emissions, the problem of WBA management is still a topic of scientific, technical and economic debate. Traditional WBA can be used in agriculture and in forestry as a fertilizer [3–6]. But the pH value and heavy-metal content should be considered [4, 5, 7], which significantly limit such application. Also the recovery of WBAs in the agronomy cannot be considered as a long-term sustainable solution [8]. Research data also show potential of WBA use in the cement and concrete industry [9–11]. The variable composition and the large number of factors that affect WBA properties slow down the progress in the characterization of this material. Due to this problem, currently valid standards limit the use of WBAs in the concrete production (ASTM C618 [12] and EN 450–1 [13]), while only a few countries, such as Austria, Germany and Denmark regulates the agricultural recovery of WBAs by guidelines [7]. In order to overcome the barrier to the commercial use of WBAs, a detailed analysis and characterization of the material should be made, and the influence of its application demonstrated. Proving the properties of construction products with WBAs opens the door to commercial products, and thus a simple and secure recovery system. Previous studies have shown that up to 20% of binders in concrete mixtures can be replaced by WBA with retention of the usual mechanical and durability properties [14, 15].

Establishing cooperation between the energy sector and the concrete industry would solve the problem of waste and reduce CO_2 emissions as one of the leading problems in the cement production. In addition to the mutual environmental benefits, establishing such cooperation would mean minimizing the economic burden of both sectors.

This research investigates the long-term durability performance of cement composites where WBA is used as cement replacement. The main objective is to examine the influence of WBA on the durability properties of cement composites, particularly on gas permeability and capillary absorption after 1 year of specimens' age. For this study, fly WBAs were collected from different energy power plants in Croatia where different combustor technology is used. Fly WBAs were used to partially replace cement CEM I 42.5R.

2 Materials and Methods

In this study, wood biomass fly ashes (WBA) collected from 3 different power plants in Croatia were used as collected. Characterization of used WBAs (chemical composition, particle-size distribution, particle morphology, heavy-metal content and mineralogical composition) are in detail discussed by Carević et al. [16]. Summary of chemical and physical properties of WBAs and cement used are presented in Table 1.

Mortars with 5, 10 and 15% of fly WBA as cement replacement were prepared according to EN 196–1 [17] standard where the mass ratio of CEN standard sand, cement and water components is 3:1:0.5 with water cement ratio of 0.5. All mixtures were produced with cement CEM I 42.5 R and potable water temperature 20 ± 2 °C. Fresh mortars properties were obtained immediately after mixing. After casting, the specimens were kept covered at laboratory conditions for 24 h until demolding, to prevent water evaporation. Specimens for durability testing (capillary absorption, gas permeability) were demoulded and cured at 20 °C with relative humidity >95%, until testing. For the gas permeability testing the samples were preconditioned at 40 °C until a constant sample weight (approximately 7 days).

Table 1 Chemical and physical properties of WBAs and cement

	CEM	WBA1	WBA2	WBA3
Technology used in power plant		Grate combustor	Pulverized fuel combustor	Bubbling fluidized bed combustor
P_2O_5	0.22	1.84	1.82	4.03
Na_2O	0.846	0.545	0.646	0.63
K_2O	1.25	9.2	6.05	6.21
CaO	59.8	51.9	46.75	47.35
MgO	2.01	3.75	8.26	4.71
AL_2O_3	4.94	2.28	6.16	3.56
TiO_2	0.23	0.15	0.34	0.25
Fe_2O_3	3.15	1.47	2.85	1.69
SiO_2	21.88	9.28	19.8	14.45
SO_3	3.33	3.58	2.73	3.95
Free CaO	2.5	13.5	7.3	8.8
Free MgO	0.75	3.8	3.3	4.5
LOI	3.6	13.8	3.8	12.7

Table 2 Test methods for fresh and hardened mortar properties

Method	Standard
Consistence of fresh mortar	EN 1015–3
Bulk density of fresh mortar	EN 1015–6
Air content of fresh mortar	EN 1015–7
Capillary absorption	EN 13,057
Gas permeability	EN 993–4

After that, the specimens were coated with a two-component epoxy resin at a minimum thickness of 1 cm per edge to achieve uniaxial capillary absorption. Coefficient of capillary absorption is calculated from the initial linear portion in the graph water absorption per unit area by the square root of the immersion time (hours). The percentage of water absorption was determined as the difference in mass at the initial and last readings. The examined properties in fresh and hardened state of mortars are shown in Table 2. All results were compared to the reference mixture M0.

3   Results and Discussion

Fresh state properties are given in Fig. 1. Results of testing fresh mortars properties show that different amounts of WBA per mass of cement does not have any significant influence on the density and temperature of the mixtures. On the other hand, replacement of cement with WBA influenced on the consistence of mortars: the workability of the mixtures decreased from 3.3% (M3-5 and M3-10) to 20% for M1-15. The same impact was noticed by other researches [18, 19, 20]. This can be explained by irregularly shaped and high porosity particles of WBA, together with high carbon and free CaO content [19, 20] that could increase water demand of the mixtures. Also, it was noticed that by increasing the WBA share per mass of cement, air content is decreased.

Capillary absorption is defined as transport of fluids due to surface tension that appears in capillary pores. Tests results for coefficient of the capillary absorption and absorption depending on WBA type and share used in mortars are shown in Fig. 2. After age of 28 days, it can be observed that the values of capillary absorption are generally lower than reference one (from 1.1% to 14.85%), except for mixtures M3-10 and M2-15. According to [21], the capillary water absorption after 28 days does not change for a specimens with 5% of WBA, but for 10%, water absorption increases. Same findings were observed by [22] where capillary absorption increased by 1.76% when using 30% of the WBA. Same trend was visible only in the specimens M1 prepared with WBA. After 1 year, due to the process of hydration and filling of the cement matrix structure, decrease in the values of coefficient of capillary absorption for all mixtures can be seen. With aging
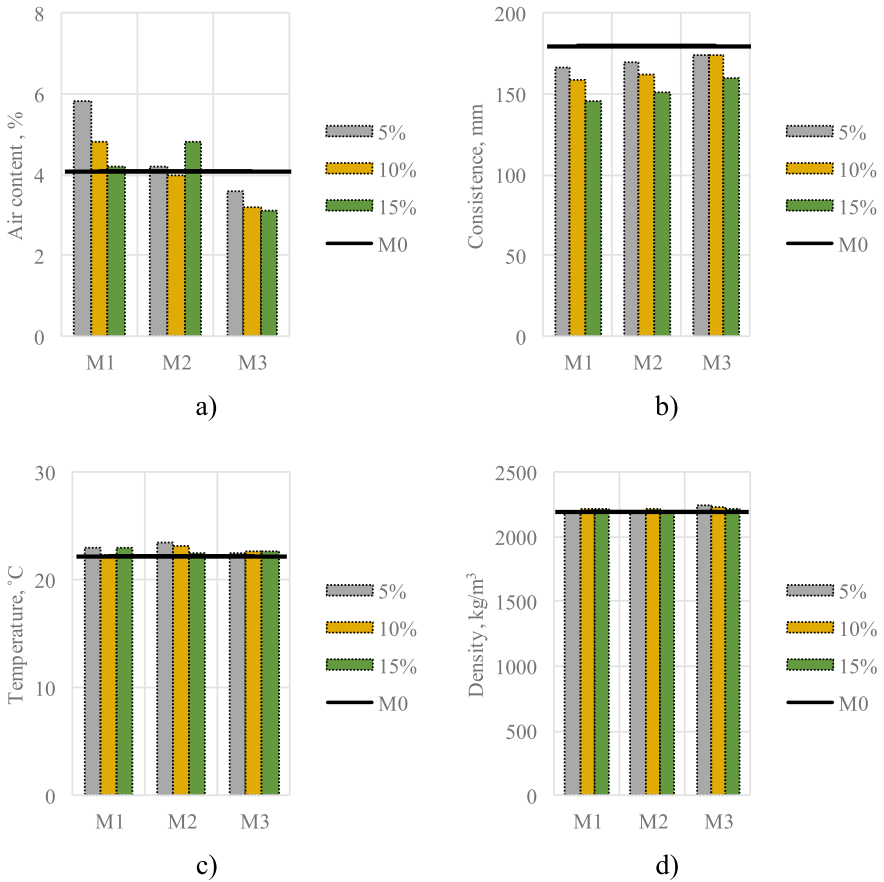
Fig. 1 Fresh state results: **a** Air content; **b** Consistence; **c** Temperature; **d** Density

of cement mixtures and hydration process, capillary porosity and consequently the ability to absorb water decreases [23], which is, also, evident in this case. But while comparing mixtures with WBA to the reference mixture, results show different trend at the age of 28 days: all values are quite higher from the reference once: from 3.89% for M2-5 to 223% for M1-10. One of the possible explanation for higher capillary absorption is the change in the pore structure with ageing due to partially replacement of cement with WBA: higher volume of capillary pores and lower mean pore size could lead to an increase in capillary absorption of the specimens, as concluded by the authors [24]. Even though, based on quality criteria classification given by [23], it can be said that new mortars show good performance in terms of capillary water uptake, proving that incorporation of WBA does not lower mortar quality. The authors [25] propose the use of coal fly ash (FA) together with WBA in order to reduce the capillary absorption coefficient. The authors state that the
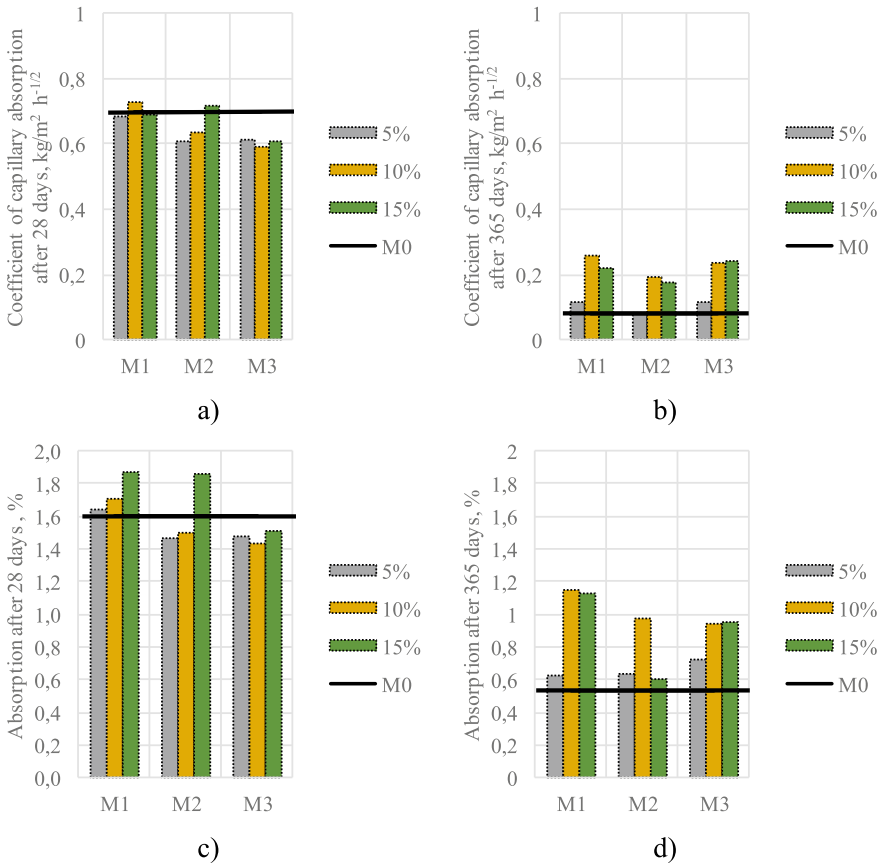
Fig. 2 a Capillary absorption of mortars after 28 days; b Capillary absorption of mortars after 365 days; c Absorption of mortars after 28 days; d Absorption of mortars after 365 days

synergistic action of WBA and FA results in a decrease in the porosity by the pozzolanic reaction.

Figure 3 shows the gas permeability coefficient of mortars with WBA compared to the reference mixture after 28 and 365 days. With further hydration and ageing of the specimens, decreasing of the coefficient can be observed which is in line with the results of capillary absorption testing. Compared to the reference mixture after 28 days, gas permeability coefficient was 0.56% and 68% higher for M2-15 and M1-15 respectively, while 17% lower for M3-15. But after 365 days, all mixtures with 15% WBA had higher values of gas permeability coefficient from 101% (M1-15) to 346% (M3-15) in comparison with the reference mixture.
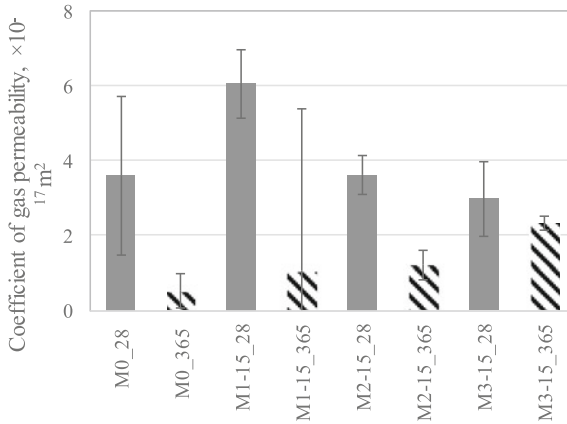
Fig. 3 Gas permeability of reference specimens and specimens with 15% of WBA after 28 and 365 days

4 Conclusions

Using WBA as a new raw material in the concrete industry offers an interesting alternative to today's materials but gives the range of variables that affect the chemical and physical composition of WBAs, so additional research of its potential has to be done.

Preliminary results of long-term durability properties of cement composites made with WBA in different amounts per cement mass are shown in the paper. From obtained results, the following conclusions can be derived:

- Replacement of cement with WBA reduced consistency of mortar, especially with WBA content higher than 5%.
- The preliminary results show a positive contribution of WBA on the capillary absorption when cement is replaced with 5% and 10% of WBA by mass for samples at the age of 28 days. But after 1 year, incorporation of WBA raises capillary suction in comparison with reference mixture indicating a change in the pore structure in the cement matrix.
- With ageing, partial substitution of cement with 15% WBA by mass of cement negatively effect on gas permeability. Irrespective of the incineration technology, the same trend was observed in all prepared specimens with WBA.

In order to develop cement materials containing WBA, it is necessary to understand their long-term durability and interaction with the environment. Therefore, as a next step closer to WBA use, additional research in a term of microstructure of hydrated cement composites is suggested.

References

1. European Parliament and Council: Directive 2008/98/EC of the European Parliament and of the Council of 19 November 2008 on waste and repealing certain directives. Off. J. Eur. Union, L 312/3, 30 (2008)
2. European Parliament and the Council of the European Union: Directive (EU) 2018/851 of the European Parliament and of the Council of 30 May 2018 amending Directive 2008/98/EC on waste. Off. J. Eur. Union, L150/109, 31 (2018)
3. Pesonen, J., Kuokkanen, T., Rautio, P., Lassi, U.: Bioavailability of nutrients and harmful elements in ash fertilizers: effect of granulation. Biomass Bioenergy **100**, 92–97 (2017)
4. Steenari, B.M., Lindqvist, O.: Stabilisation of biofuel ashes for recycling to forest soil. Biomass Bioenergy **13**, 39–50 (1997)
5. Pitman, R.M.: Wood ash use in forestry—a review of the environmental impacts. Forestry **5** (79), 563–588 (2006)
6. Mellbo, P., Sarenbo, S., Stålnacke, O., Claesson, T.: Leaching of wood ash products aimed for spreading in forest floors—Influence of method and L/S ratio. Waste Manag. **11**(28), 2235–2244 (2008)
7. Lanzerstorfer, C.: Characterization of fly ashes from biomass combustion with focus on their utilization. University of Natural Resources and Life Sciences (2016)
8. Maresca, A., Hansen, M., Ingerslev, M., Astrup, T.F.: Column leaching from a Danish forest soil amended with wood ashes: fate of major and trace elements. Biomass Bioenergy **109**, 91–99 (2018)
9. Xu, G., Shi, X.: Characteristics and applications of fly ash as a sustainable construction material: a state-of-the-art review. Resour. Conserv. Recycl. **136**, 95–109 (2018)
10. Siddique, R.: Utilization of wood ash in concrete manufacturing. Resour. Conserv. Recycl. **67**, 27–33 (2012)
11. Doudart de la Grée, G.C.H., Florea, M.V.A., Keulen, A., Brouwers, H.J.H.: Contaminated biomass fly ashes—characterization and treatment optimization for reuse as building materials. Waste Manag., **49**, 96–109 (2016)
12. ASTM International: ASTM C 618 Standard Specification for Coal Fly Ash and Raw or Calcined Natural Pozzolan for Use (2010)
13. CEN European Committee for Standardization: Fly ash for concrete—Part 1: Definition, specifications and conformity criteria (EN 450–1:2012) (2012)
14. Tosti, L., van Zomeren, A., Pels, J.R., Comans, R.N.J.: Technical and environmental performance of lower carbon footprint cement mortars containing biomass fly ash as a secondary cementitious material. Resour. Conserv. Recycl. **134**, 25–33 (2018)
15. Rajamma, R., Ball, R.J., Tarelho, L.A.C., Allen, G.C., Labrincha, J.A., Ferreira, V.M.: Characterization and use of biomass fly ash in cement-based materials. J. Hazard. Mater. **172**, 1049–1060 (2009)
16. Carević, I., Serdar, M., Štirmer, N., Ukrainczyk, N.: Preliminary screening of wood biomass ashes for partial resources replacements in cementitious materials. J. Clean. Prod. **229**, 1045–1064 (2019)
17. CEN The European Committee for Standardization: Methods of testing cement—Part 1: Determination of strength (EN 196–1:2016) (2016)
18. Ukrainczyk, N., Vrbos, N., Koenders, E.A.B.: Reuse of woody biomass ash waste in cementitious materials. Chem. Biochem. Eng. Q. **30**, 137–148 (2016)

19. Cheah, C.B., Ramli, M.: The implementation of wood waste ash as a partial cement replacement material in the production of structural grade concrete and mortar: an overview. Resour. Conserv. Recycl. **55**, 669–685 (2011)
20. Wang, S., Miller, A., Llamazos, E., Fonseca, F., Baxter, L.: Biomass fly ash in concrete: mixture proportioning and mechanical properties. Fuel **87**, 365–371 (2008)
21. Rissanen, J., Ohenoja, K., Kinnunen, P., Romagnoli, M., Illikainen, M.: Milling of peat-wood fly ash: effect on water demand of mortar and rheology of cement paste. Constr. Build. Mater. **180**, 143–153 (2018)
22. Garcia, M.D.L., Sousa-Coutinho, J.: Strength and durability of cement with forest waste bottom ash. Constr. Build. Mater. **41**, 897–910 (2013)
23. Sashidhar, C., Sudarsana Rao, H.: Durability studies on concrete with wood ash additive. In: 35th Conference on Our World in Concrete & Structures, Singapore (2010)
24. State-of-the-Art Report RILEM TC 230-PSC. In: Beushausen, H., Luco, L.F. (eds.) Performance—Based Specifications and Control of Concrete Durability. Springer (2015)
25. Medina, J.M., Sáez del Bosque, I.F., Frías, M., Sánchez de Rojas, M.I., Medina, C.: . Constr. Build. Mater. **225**, 429–440 (2019)

Steel Reinforcement in Slag Containing Binders and Its Susceptibility to Chloride-Induced Corrosion

Shishir Mundra and **John L. Provis**

Abstract The construction industry has moved from using plain Portland cement (PC) to binders with high proportions of supplementary cementitious materials such as blast furnace slags such as CEM II, CEM III A/B, and is increasingly targeting alkali-activated slags (AAS). The reducing nature of the blast furnace is retained by the slag, which contains $\sim$1–3 wt.% sulfur (expressed as SO_3), mostly in a reduced state and available to dissolve when mixed with water or an alkaline solution. The pore solution chemistry of many modern 'alternative' construction materials can be characterised as being rich in reduced sulfur species, and highly alkaline. There remain many open questions about the influence of such alkaline-sulfide solutions on the passive film formed on common mild steel reinforcement, and thus the susceptibility of this steel to chloride-induced corrosion. This study focusses on the influence of reduced sulfur species on mechanisms of passivation of steel and the phenomena of localised corrosion due to chlorides in highly alkaline electrolyte solutions with containing varying concentrations of reduced sulfur species, via electrochemical and spectroscopic techniques. The presence of HS^- in alkaline electrolytes alters not only the passivation behaviour of mild steel, but also the mechanism of chloride-induced corrosion. In alkaline solutions containing sulfide, the competitive adsorption of $[OH^-]$ and $[HS^-]$ inhibits and retards the formation of a passive film, conventionally a Fe (III) oxide, and instead forms a surface film on the reinforcement composed of an assemblage of $Fe(OH)_2$ and Fe-S complexes. In alkaline-sulfide solutions, the critical chloride concentration to induce corrosion was found to be dependent on the concentration of sulfide (i.e. the reducing capability of the electrolyte), and on the time that steel specimens were exposed to the electrolyte, consistent with the progressive formation of a sulfidic layer on the steel. Additionally, it has been shown that in the presence of high concentrations of

S. Mundra (✉) · J. L. Provis
Department of Materials Science and Engineering, The University of Sheffield,
Mappin Street, Sheffield S1 3JD, UK
e-mail: shishir.mundra@bam.de

S. Mundra
Bundesanstalt für Materialforschung und -prüfung (BAM), Unter den Eichen 87,
12205 Berlin, Germany

HS^-, the onset of chloride induced corrosion cannot be easily detected by conventional electrochemical measurements of OCP, R_p or i_{corr}, as these tend to be highly influenced by the chemistry of the pore solution. Therefore, interpretation of electrochemical data obtained for aqueous systems containing HS^- based on standard guidelines that assume Fe to be the sole redox-active species would result in misleading conclusions regarding whether the steel is in the passive or the active state.

Keywords Sulfide · Mild steel · Corrosion · High alkalinity · Cement

1   Introduction

Modern cements used in the construction industry rely heavily on the replacement of Portland cement (PC) with supplementary cementitious materials such as ground-granulated blast furnace slags (GGBS), to reduce emissions from the cement and construction industry. However, the usage of GGBS substituted cements is not new and has been in practice since the beginning of the twentieth century been standardised in several countries around the world. An alternative to PC based binders is alkali-activated slags (AAS), that have garnered significant attention within industry and academia due to their potential to be produced with lower emissions, and in some cases better mechanical properties when compared to PC, for certain infrastructure applications. AAS are the products of the reaction between GGBS and an activator, generally an alkali-hydroxide or -silicate solution and sometimes near neutral salts such as alkali-carbonate/sulfate solutions. Significant research has been targeted on understanding the underlying reaction mechanisms, the resistance to chloride ingress and other aggressive species, to understand the long-term durability of these alternative binders. However, when such binders are used in reinforced concrete applications, it is important that we also understand how the steel reinforcement interacts with the chemistry of these binders and assess the susceptibility of the steel-reinforcement to corrosion [1]. There do not yet exist many studies that highlight this.

The phase assemblage, pore solution chemistry and the pore structure of AAS are significantly different from PC-based binders. The hydrate phase assemblage is dominated by an aluminium substituted calcium silicate hydrate (C-A-S-H) gel, and depending on the MgO content in the precursor, also hydrotalcite-like phases, AFm-group layered hydrous calcium aluminates, and zeolites such as gismondine and garronite, are sometimes also detected as secondary reaction products. Additionally, the type of activator used also changes the chemistry of AAS. In AAS, the concentration of soluble alkalis was also found to be >1 M [2–5], and the concentrations of Ca, Al and Si generally between 0.01 and 10 mM [2–5]. The pore solutions of AAMs, in general, have higher concentrations of soluble alkalis when compared to that of PC, primarily due to the nature of the activator and hydration mechanisms. With concentrations of counter-ion species such as

aluminate and silicate being low, it can be inferred that the electro-neutrality of the pore solution is preserved by the presence of hydroxyl ions, therefore providing the pore solution with significant alkalinity to maintain the passivity of the reinforcement [5].

One of the major differences between the pore solution chemistries of plain PC binders and AAS is the presence of reduced sulfur species. GGBS retains the reducing nature of the blast furnace and contains approximately 1–3 wt.% SO_3, which dissolves readily as HS^-. Given the high susceptibility of HS^- to oxidise, minor quantities of oxidised sulfur species may also exist in the pore solutions of AAS.

The importance of HS^- in defining the passivation of the steel reinforcement in highly alkaline environments, and its importance in determining the susceptibility of steel to chloride induced corrosion, was first highlighted for AAS by Holloway and Sykes [6]. This study is focussed on gaining fundamental insights into the mechanisms of passivation and depassivation in highly alkaline sulfide-containing environments, though a solution approach, by employing electrochemical and spectroscopic techniques.

2 Materials and Methods

2.1 Materials

Mild steel reinforcement (class B500 according to ISO/DIS 6935–2 [7]) of diameter 12 mm, with a chemical composition: 97.91 wt.% Fe, 0.21 wt.% C, 0.13 wt.% Cr, 0.20 wt.% Ni, 0.47 wt.% Cu, 0.23 wt.% Si, 0.76 wt.% Mn, 0.03 wt.% S, 0.02 wt.% Mo, and 0.04 wt.% P, were acquired through a local supplier in Sheffield. The steel reinforcement was sectioned into small pellets of thickness between 5.5–6.5 mm, and polished using SiC abrasive papers with 240 to 600 grit sizes and degreased using acetone, prior to electrochemical testing. Pore solution of AAS were simulated using reagent grade NaOH (Sigma Aldrich) and $Na_2S \cdot 9H_2O$ (Alfa Aesar). Chloride was introduced into the simulated pore solutions using commercial grade NaCl (EMD Chemicals). Table 1 shows the chemistry of various solutions studied.

Table 1 Molar quantities of NaOH and $Na_2S.9H_2O$ used to simulate pore solutions of AAS. NaCl was added in simulated pore solutions to investigate the chloride threshold value for depassivation of the steel reinforcement

NaOH (M)	$Na_2S.9H_2O$ (M)	NaCl (M)
0.80	0	0 to 2.8
0.80	0.001	0 to 2.8
0.80	0.01	0 to 2.8
0.80	0.09	0 to 2.8
0.80	0.45	0 to 2.8

All electrochemical tests were conducted in a 400 mL corrosion cell (at 22 ± 2 °C) using a potentiostat/galvanostat PGSTAT 204 obtained from Metrohm Autolab B.V., as described in more detail in [8, 9]. A three electrode setup (electrolyte volume 250 mL), comprising a stainless-steel counter electrode, an Ag/AgCl (saturated 3 M KCl) reference electrode, and the mild steel surface (surface area: 0.287 cm^2) acting as the working electrode [8, 9], was used. The reference electrode was positioned near the surface of the working electrode using a Luggin capillary. Further details can be found in [8, 9].

2.2 Electrochemical Tests

Open circuit potential

Mild steel specimens were exposed to alkaline solutions (0.80 M OH$^-$) with varying concentrations of sulfide (0 M, 0.01 M and 0.45 M) for 0, 5, 12 and 28 days in tightly sealed (parafilm) plastic vials in a vacuum desiccator. To understand passivation of the steel reinforcement in sulfide containing alkaline solutions, specimens were immediately transferred to the corrosion cell after respective exposure regimes, with the electrolyte being of the same composition used during exposure. Each specimen was allowed to stabilise for 15 min in the electrolyte, and the open circuit potential was monitored for 30 min unless the change in potential as a function of time (dV/dt) reached ≤ 1 μV/s before 30 min. The open circuit potential is then taken as the mean potential recorded during the last 60 s of the test.

Anodic polarization

Mild steel specimens were exposed to alkaline solutions (0.80 M OH$^-$) with varying concentrations of sulfide (0.001 M, 0.01 M, 0.09 M and 0.45 M) for 0, 5, 12 and 28 days in tightly sealed (Parafilm) plastic vials in a vacuum desiccator. After each of the exposure regimes, steel specimens were removed from the vials and transferred to the corrosion cell for anodic polarisation in fresh electrolytes prepared with a chemical composition matching the respective exposure solution. Additionally, NaCl (0 to 2.8 M) was added to the fresh electrolytes to determine the chloride threshold value for assessing the depassivation of the steel reinforcement. The steel specimens were polarized to +1 V versus the open circuit potential, at a scan rate of 0.167 mV/s and step potential 0.244 mV. For each given concentration of chlorides in the solution, if anodic polarisation curves exhibited a sudden rise in the current, this concentration was considered as the chloride threshold value.

2.3 X-ray Photoelectron Spectroscopy

Steel specimens were exposed to 0.80 M OH$^-$ solutions with 0.45 M HS$^-$ in Parafilm-sealed plastic vials within a vacuum desiccator, for 28 days. After 28 days, the steel specimens were dried in nitrogen, then wrapped in Parafilm and transferred to an airtight container for transport to the X-ray photoelectron spectroscopy (XPS) facility. The specimens were then unwrapped, mounted onto the sample holder using double sided sticky conducting tape, and loaded into the Kratos AXIS Supra spectrometer for the measurements to be carried out under ultra-high vacuum. The exact parameters used in the experiments and curve fitting can be found in [9].

3 Results and Discussion

Figure 1 shows the measured open circuit potential (vs. Ag/AgCl) of steel specimens immersed in solutions with compositions 0.80 M NaOH, 0.80 M NaOH + 0.01 M HS$^-$ and 0.80 M NaOH + 0.45 HS$^-$, as a function of time. The open circuit potential of the steel reinforcement in all three solutions (0.80 M NaOH, 0.80 M NaOH + 0.01 M HS$^-$ and 0.80 M NaOH + 0.45 HS$^-$) exhibits a constant value after 12 days of immersion, and is around −0.1 V, −0.45 V and −0.7 V versus Ag/AgCl, respectively. The results indicate a clear decrease in the open circuit potential with an increase in the sulfide content in the electrolyte, suggesting a reduction in the amount of dissolved oxygen (or other oxidising agents) within the electrolyte upon an increase in the sulfide concentration [10]. As seen in Fig. 1, the open circuit potentials in simulated pore solutions of AAS (0.80 M OH$^-$ + 0.45 M HS$^-$) are much lower than those observed for PC-based binders. Similar values of open circuit potential have been reported for AAS mortars and concretes in the literature [6, 11]. Generally, the steel reinforcement in alkaline solutions representative of PC-based binders forms a passive film, a few nanometers in thickness, almost instantaneously and the open circuit potential varies between −0.1 V and 0.1 V [10, 12]. This passive film is generally an iron oxide or a hydrated iron oxide film that protects the steel reinforcement from the action of aggressive species such as chlorides. Given that the open circuit potentials in alkaline solutions with 0.45 M HS$^-$ is close to −0.7 V versus Ag/AgCl, it would be highly improbable to form a conventional iron oxide film, which makes it critical that we understand the surface film formed on the mild-steel reinforcement.

Figure 2A and B show the S 2p and Fe 2$p_{3/2}$ X-ray photoelectron spectroscopy (XPS) spectra obtained for steel specimens exposed to 0.80 M OH$^-$ + 0.45 M HS$^-$ for 28 days, respectively. In Fig. 2A, the deconvolution of the S 2p spectra shows the presence of two peaks centered at 160.98 eV and 162 eV, that could be attributed to the presence of Fe^{2+}S and Fe^{2+}S/Fe^{3+}S, respectively, on the surface of the steel. Due to the broad nature of the Fe 2$p_{3/2}$ peak and the large background
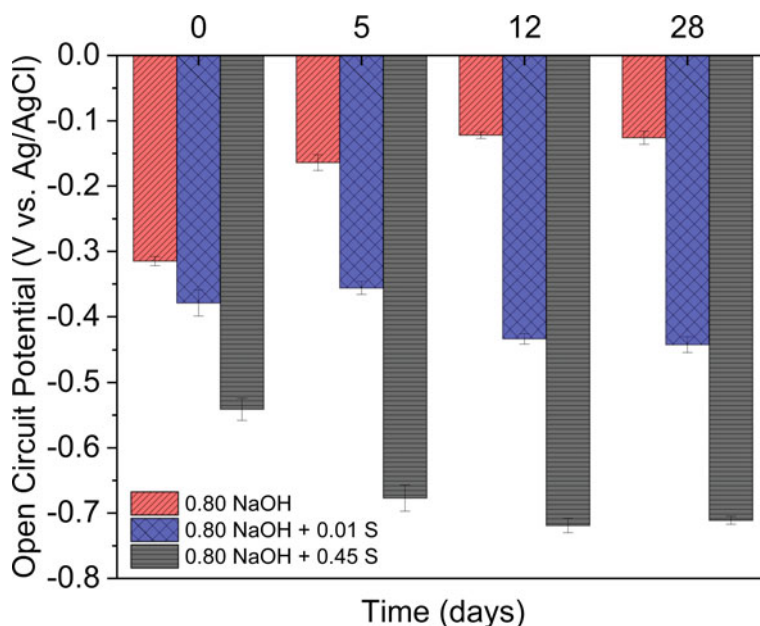
Fig. 1 The evolution of open circuit potential (vs. Ag/AgCl) of steel specimens exposed to 0.80 M OH⁻, 0.80 M OH⁻ + 0.01 M HS⁻ and 0.80 M OH⁻ + 0.45 M HS⁻

associated with the signal in this energy range, deconvolution of the Fe $2p_{3/2}$ spectra (Fig. 2B) was more complex. However, based on the open circuit potential values shown in Fig. 1, it can be asserted that the surface of the reinforcement is rich in Fe-S complexes. Given that the open circuit potentials measured for steel in simulated pore solutions of AAS remain around −0.7 V versus Ag/AgCl, it would be highly unlikely a FeOOH film is formed on the surface of the steel reinforcement. The peak associated with the FeOOH is probably due to exposure of samples to air during experimentation/sample preparation. Additionally, it could also be due to the oxidation of an inner surface film of Fe(OH)$_2$ [9].

Based on the observations of such low open circuit potentials and the absence of a conventional iron oxide film, one may be tempted to suggest that the susceptibility of steel to chloride induced corrosion is higher when exposed to alkaline sulfide containing solutions than sulfide-free solutions [13–15]. To assess the susceptibility of steel to undergo chloride-induced corrosion in alkaline solutions as a function of the concentration of sulfide and time, anodic polarization tests were conducted in electrolytes with varying chloride contents. Table 2 shows the critical chloride content (shown as the molar ratio [Cl⁻]/[OH⁻]) for steel exposed to solutions containing 0.80 M OH⁻, and varying sulfide concentrations (0.001 M, 0.01 M, 0.09 M and 0.45 M HS⁻). Surprisingly, no chloride-induced corrosion or pitting corrosion was observed in simulated pore solution of AAS (0.80 M OH⁻ + 0.45 M HS⁻), even up to the highest chloride concentrations tested (saturation with respect
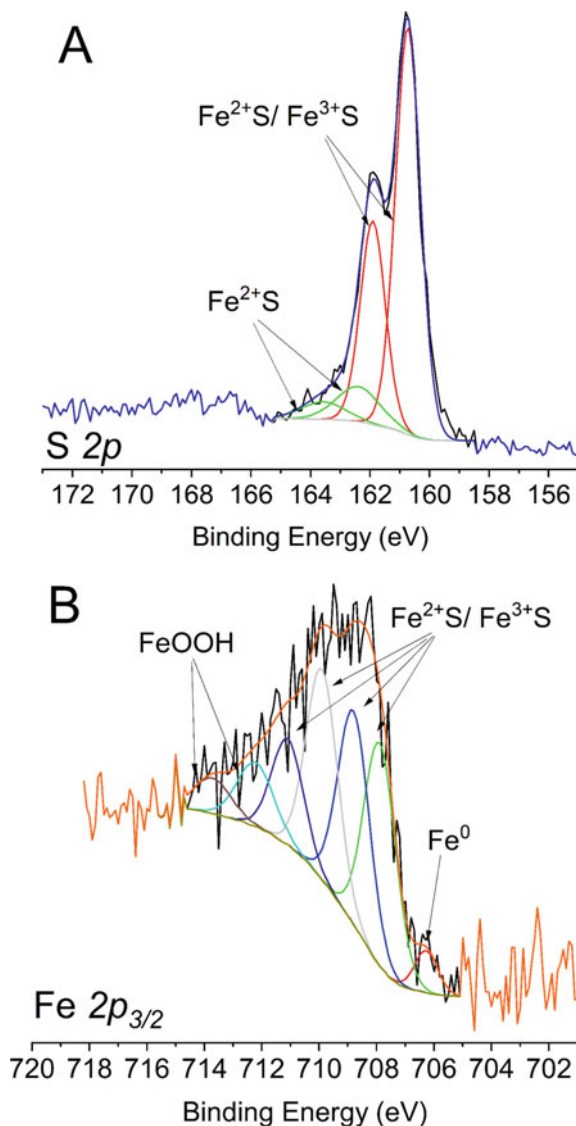
to NaCl). Additionally, in solutions containing 0.01 M and 0.09 M HS$^-$, the critical
chloride concentration varied as a function of time.

Similar results of no chloride-induced corrosion in AAS mortars have been
reported by various authors [6, 11]. Such observations of open circuit potentials in
the range of −0.7 V and no pitting corrosion for cases when the chloride concen-
tration is as high as 2.8 M, question the usefulness of some of the guidelines/
recommendations formulated for PC based binders [13–15] in the case of AAS or
PC-GGBS blends with high amounts of GGBS.

Table 2 Influence of [HS$^-$] and exposure time on the 'chloride threshold' value of mild steel, represented as the molar ratio [Cl$^-$]/[OH$^-$] which induces pitting corrosion, as determined using anodic polarisation. Cases where chloride-induced corrosion was not observed for electrolytes with [Cl$^-$]/[OH$^-$] = 3.5 have been classified as 'No Pitting'

Exposure time	0.80 M OH$^-$ + 0.001 M HS$^-$	0.80 M OH$^-$ + 0.01 M HS$^-$	0.80 M OH$^-$ + 0.09 M HS$^-$	0.80 M OH$^-$ + 0.45 M HS$^-$
0 days	0.7	2.5	3.1	No Pitting
5 days	No Pitting	3	3	No Pitting
12 days	No Pitting	2.8	3	No Pitting
28 days	No Pitting	2	3.2	No Pitting

4   Conclusion

The results of this study show that in alkaline sulfide containing solutions the nature of the surface film and the electrochemical properties of the steel-solution interface are significantly different from those observed in alkaline sulfide-free solutions. With increasing sulfide concentration, the open circuit potential of the steel reinforcement decreases. The surface film formed under these conditions is an Fe-S complex, rather than a conventional iron (III) oxide passive film. In addition to the pH and the chloride concentration, the critical chloride content was found to be dependent on the duration of exposure, and the sulfide content.

No signs of pitting corrosion were observed on the steel surface in solutions that represented the pore solution of AAS for concentrations of chloride up to 2.8 M. One possible explanation for such an observation is that in the presence of high concentrations sulfide in the pore solutions of AAS, the formation of macro-cell is highly unlikely. The concentration of dissolved oxygen at the solution-steel interface becomes the primary factor that controls the susceptibility of steel to chloride induced corrosion. In addition to the redox couple Fe/Fe^{2+}, the HS$^-$ at the steel-solution interface can also be oxidised and therefore, polarization techniques used to estimate the resistance to polarization and corrosion current density become highly unreliable.

Further research needs to be conducted on AAS mortars, concretes and pore solutions to elucidate the mechanisms of passivation and depassivation of the steel-reinforcement.

References

1. Mundra, S., Bernal, S.A., Criado, M., Hlaváček, P., Ebell, G., Reinemann, S., Gluth, G.J.G., Provis, J.L.: Steel corrosion in reinforced alkali—activated materials. RILEM Tech. Lett. **2**, 33–39 (2017)
2. Puertas, F., Fernández-Jiménez, A., Blanco-Varela, M.: Pore solution in alkali-activated slag cement pastes. Relation to the composition and structure of calcium silicate hydrate. Cem. Concr. Res. **34**, 139–148 (2004)
3. Song, S., Jennings, H.: Pore solution chemistry of alkali-activated ground granulated blast-furnace slag. Cem. Concr. Res. **29**, 159–170 (1999)
4. Gruskovnjak, A., Lothenbach, B., Holzer, L., Figi, R., Winnefeld, F.: Hydration of alkali-activated slag: comparison with ordinary Portland cement. Adv. Cem. Res. **18**, 119–128 (2006)
5. Lloyd, R.R., Provis, J.L., van Deventer, J.S.J.: Pore solution composition and alkali diffusion in inorganic polymer cement. Cem. Concr. Res. **40**, 1386–1392 (2010)
6. Holloway, M., Sykes, J.M.: Studies of the corrosion of mild steel in alkali-activated slag cement mortars with sodium chloride admixtures by a galvanostatic pulse method. Corros. Sci. **47**, 3097–3110 (2005)
7. ISO/DIS 6935–2, Steel for the reinforcement of concrete—part 2: ribbed bars. International Organization for Standardization (2015)
8. Mundra, S., Criado, M., Bernal, S.A., Provis, J.L.: Chloride-induced corrosion of steel rebars in simulated pore solutions of alkali-activated concretes. Cem. Concr. Res. **100**, 385–397 (2017)
9. Mundra, S.: Corrosion of steel in alkali-activated materials. PhD Thesis, The University of Sheffield (2018)
10. Scott, A., Alexander, M.G.: Effect of supplementary cementitious materials (binder type) on the pore solution chemistry and the corrosion of steel in alkaline environments. Cem. Concr. Res. **89**, 45–55 (2016)
11. Criado, M., Provis, J.L.: Alkali activated slag mortars provide high resistance to chloride-induced corrosion of steel. Front. Mater. **5**, #34 (2018)
12. Volpi, E., Olietti, A., Stefanoni, M., Trasatti, S.P.: Electrochemical characterization of mild steel in alkaline solutions simulating concrete environment. J. Electroanal. Chem. **736**, 38–46 (2015)
13. Andrade, C., González, J.A.: Quantitative measurements of corrosion rate of reinforcing steels embedded in concrete using polarization resistance measurements. Mater. Corros. **29**, 515–519 (1978)
14. Andrade, C., Alonso, M.C., González, J.A.: An initial effort to use the corrosion rate measurements for estimating rebar durability. In: Berke, N., Chaker, V., Whiting, D. (eds.) Corros. Rates Steel Concr., STP25013S ed., ASTM International, West Conshohocken, PA, pp. 29–37 (1990)
15. ASTM C876–15, Standard test method for corrosion potentials of uncoated reinforcing steel in concrete, ASTM International (2015)

Using Waste Materials in Durable Environmentally Friendly Concrete

Rana Morsy and Sohair Ghoniem

Abstract Solid waste management is one of the major environmental concern all over the world. Big amounts of waste tires are generated each year and utilization of this waste is a big issue from the aspects of disposal of this amount of this waste, and health hazards. One of the recommended methods to utilize of this waste to be used as an ingredient of Portland cement concrete that could be used in concrete block paving, pedestrian blocks, highway sound walls, residential driveways, and garage floors. In this study, an experimental investigation has been performed using a waste rubber tires and bentonite in the concrete mix design. Rubber waste is used to replace fine aggregate in the concrete with different percentages (5, 20, 25, 30, 40%). Slump test are conducted to evaluate the workability of fresh concrete. Compressive strength of cubes at 7 days and 28 days are studied and compared with conventional concrete. The research work addresses the effect of using waste rubber tires and bentonite on durability of concrete. For this purpose, specimens were submerged in solution containing 50 g/l of NaOH and H_2SO_4, and according to the results it can be stated, that rubberized concrete can be used in to improve concrete durability. Based on the test results, the ideal percentage of mix which shows maximum compressive strength is identified. The optimal mix from the laboratory experimental investigation contained 20% waste rubber tires and 5% Bentonite replacement that exhibited a compressive strength of 33 MPa at 28 days.

Keywords Waste rubber · Bentonite · Compression strength · Durability

R. Morsy (✉)
Civil Engineering Department, Housing and Building Research Center, Giza, Egypt
e-mail: rana.morsy@buc.edu.eg

S. Ghoniem
Chemical Engineering Department, Badr University in Cairo, Cairo, Egypt

1   Introduction

The use of waste rubber tires in civil engineering applications are stimulated more environmental awareness. During the last years, much research has been carried out to recycle the waste tires by grinding them into small particles (rubber crumb) and use in asphalt, sealants, rubber sheets and concrete [1]. The current applications of recycling waste tires in civil engineering practices are mainly: used as modifiers to asphalt paving mixtures; used as an additive to concrete mixtures; used as light weight fillers [2].

The size of waste tires used in concrete ranges from rubber chips (25–50 mm) to crumb rubber powders (4.75–0.075 mm) to be used in concrete as a replace part of coarse or fine aggregates. The addition of waste tire rubber into concrete mixtures significantly changes the properties of the concrete. Because of the hydrophobic nature of rubber, the bond between the rubber and hydrated cement is considered to be weak, that leads to a significant reduction of compressive and tensile strength of concrete mixed with waste rubber tires [3]. However, concrete becomes more ductile, as illustrated by the limited viscoelasticity and higher post failure toughness [4]. Eldin and Senouci [5] investigated the strength and toughness of concrete with partial replacement of coarse aggregates by waste tire chips. The investigation showed that the compressive strength and splitting tensile strength both were reduced, in the mean while the results highlighted an enhancement in its toughness and ability to absorb fracture energy. Another research has found that the replacement of 15% of coarse aggregate with rubber chips results in a 45% reduction of compressive strength and 25% reduction in splitting tensile strength [6]. The results conducted by the using of waste tires in concrete showed a significant a reduction in the strength of concrete.

In addition to environmental benefits, the most significant advantage of waste rubber tires in concrete is the light weight. Rubber has much lower specific gravity than aggregates, so the replacement of aggregates with rubber consequently reduces the overall specific gravity of the waste rubber tires concrete (rubberized concrete) [7]. Another benefit of rubberized concrete is their high ability of energy absorbing characteristics. Many researchers have found that rubberized concrete can effectively increase the ductility and prevent the occurrence of brittle failures [6, 8] that promote the using of rubberized concrete in structural components subjected to dynamic load and impact load such as bridge slabs and airport runways. However, the significant reduction of strength has prohibited these applications.

The reduction of concrete strength can be related to two main factors: the hydrophobic nature of rubber, that creates a weak bond between the rubber chips and mortar; and the low stiffness of rubber that leads the researchers to work on the properties of rubber improvement so that it can widen the applications of the rubberized concrete. Two approaches have been performed to enhance the rubberized concrete behavior and reduce the loss of strength. The first approach is by grinding waste rubber into small particles. Since rubber chips produce flaws in concrete mass. However, only if the rubber particles can be reduced to the

dimension that is comparable to cement particles (around 20 ηm) have a significant improvement in both compressive and tensile strength [9]. The second approach to improve the performance of rubberized concrete is by treating the surface of rubber particles [10]. Sodium hydroxide (NaOH) solution showed the best result that tested to enhance the hydrophilicity of the rubber surface [11].

The main objective of this study is to investigate the potential of using solid waste which is the rubber waste tire to produce an environmentally friendly concrete. An experimental investigation has been adopted using a waste rubber tire in the concrete mix design as a partially replaced of fine aggregates with the size of 20 μm. The experimental investigations performed on several concrete mixtures and testing includes slump test, compressive strength; durability test. The results showed a potential to produce a durable environmentally friendly concrete applicable for various civil engineering applications.

2 Materials

The main objective was to produce for a concrete mix that can achieve a compressive strength of 30 MPa.

2.1 Waste Rubber Tires

The size of crumb rubber that used in the experimental investigation is chipped tire with the size of 20 μm is generated by mechanical grinding at ambient temperature. The reduction of rubber size to about 20 μm comparable to sand particles as shown in Fig. 1. Crumb rubber is added to the concrete mixtures as a waste disposal with different percentages 5, 20, 25, 30, 40% from the fine aggregate.

Fig. 1 Crumb rubber used for the concrete mixtures

Fig. 2 Bentonite used for the concrete mixtures
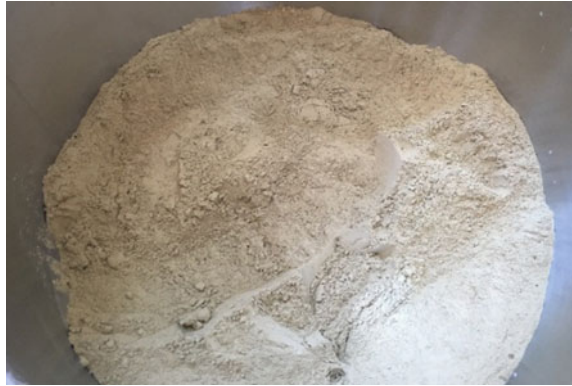
2.2 Bentonite

Bentonite is an absorbent aluminum phyllosilicate, impure clay consisting mostly of montmorillonite generated from the alteration of volcanic ash. Bentonite is available in powder and solution form contains different minerals in addition to montmorillonite, these minerals may include quartz, calcite, feldspar and gypsum. It presents strong colloidal properties when comes in contact with water, its volume also increases several times, creating gelatinous and viscous fluid. Bentonite has special properties like hydration swelling, water absorption, viscosity and thixotropy which make it a valuable material for wide range of uses and applications (Fig. 2).

2.3 Cement

The Ordinary Portland Cement was used in this study with specific gravity equals to 3.15 (g/cm^3).

2.4 Aggregates

The coarse and fine aggregates were used in the concrete mix. The selected stone size for the coarse aggregate was 5, 10 and 20 mm.

3 Mix Design

In this study, 4 series concrete was produced by adding waste rubber tires in concrete mix with various contents: 5, 20, 25, 30 and 40% of the total cement volume. The produced concrete series are coded according to the ratio of rubber in the concrete mix as:

Table 1 The design mix ratios of the concrete types for 1 m^3

Materials	Weight (Kg)					
	WRC	WRC-5	WRC-20	WRC-25	WRC-30	WRC-40
Cement	440	431	420	397	375	352
Water	220	220	220	220	220	220
Rubber	0	15	61	76	91	121
Sand	660	627	528	495	462	396
Gravel (20 mm)	440	440	440	440	440	440
Gravel (10 mm)	290	290	290	290	290	290
Gravel (5 mm)	440	440	440	440	440	440
Bentonite	0	6.7	16.8	33.5	50.3	67

- WRC = Control concrete without rubber.
- WRC-5 = Concrete with rubber of 5%.
- WRC-20 = Concrete with rubber of 20%.
- WRC-25 = Concrete with rubber of 25%.
- WRC-30 = Concrete with rubber of 25%.
- WRC-40 = Concrete with rubber of 25% (Table 1).

4 Experimental Investigation

4.1 Specimen Preparation

Concrete mixing was done in a laboratory pan mixer and in accordance with ASTM C192/192 M-06 [12]. The mixes were then prepared and cured according to ASTM C192/192 M-06 [12]. 150 × 150 × 150 mm moulds were used for casting the concrete cubes. Three specimens were tested per mix and compacted on a vibrating compactor and the curing method described in the standard was made.

4.2 Workability

Slump tests, showed in Fig. 3, were performed on the mixes to measure consistency as described in ASTM C1611 / C1611M [13]. Flow values of slumps are reported in Table 3 that evidences a noticeable decrease of the slump value from reference mix WRC because of the amount of bentonite. Increasing the amount of rubber with its smooth surface allows a better mix workability at the same bentonite amount.

Fig. 3 Slump test

4.3 Compressive Strength Test

Compressive strength tests were conducted according to BS EN 12,390–3:2019 [14] as shown in Fig. 4. The concrete cubes were tested at 7, and 28 days and the results tabled in Table 3. Each test batch was prepared for a specific age Table 2.

4.4 Durability Test

The durability of the concrete mixtures is tested, through sulfate attach and alkali attach by submerging specimens in solution containing 50 g/l of H_2SO_4 and NaOH separately for 10 days after 28-days curing of the specimen. The compressive strength is determined for the tested specimen and the results indicate that the mixtures containing bentonite performed better than control mix. The cubes were tested, and the results has been recorded in Table 3.

5   Results

The target strength for the concrete was 40 MPa, the compressive strengths of the different mixes are shown in the Fig. 5 below at 7, and 28 days. The reference mix WRC without additional rubber and bentonite demonstrates the highest compressive strength value. Mix WRC-05 with partial replacing the content of sand with waste rubber, a reduction in the compressive strength reaches to 4% reduction at 7-days, and 2% increase at 28-days. WRC-20 mix the tested compressive strength reached 20 MPa at 7-days and 36 MPa at 28-days which is a reduction of 20% at 7-days and 12% at 28-days. The tested results for WRC-25 mix showed a

Fig. 4 Durability test

Table 2 Compressive strength of the designed mixes

Mix	Slump (mm)	Compressive strength (N/mm^2)	
		7 days	28 days
WRC	80	24	40
WRC-5	71	23	41
WRC-20	60	20	36
WRC-25	47	18	33
WRC-30	45	16	29
WRC-40	40	12	23

Table 3 Compressive strength and weight of the mixtures subjected by sulfate and alkali attach

Mix	Weight (Kg)	After submerging in solution of H$_2$SO$_4$		After submerging in solution of NaOH	
		Compressive strength (N/mm^2)	Weight (Kg)	Compressive strength (N/mm^2)	Weight (Kg)
WRC	7.94	25.6	7.14	35	6.98
WRC-20	7.61	34.8	7.08	35	6.85
WRC-25	7.45	36.0	6.93	32	6.78

compressive strength at 7-days 18 MPa which represent a 32% reduction and a compressive strength at 28-days 33 MPa which represent a 21% reduction.

The tested results for WRC-30 mix showed a compressive strength at 7-days 16 MPa which represent a 50% reduction and a compressive strength at 28-days 29 MPa which represent a 38% reduction. The tested results for WRC-40 mix showed a reduction in the compressive strength reaches to 12 MPa at 7-days, and 23 MPa at 28-days. Although these mixes had comparable compressive strengths,
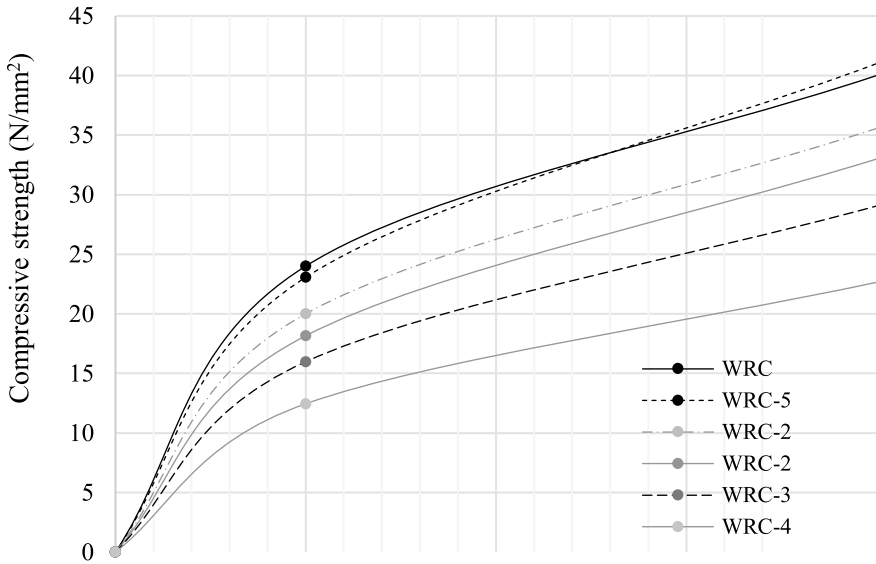
Fig. 5 Compressive strength results at age 7 and 28 days
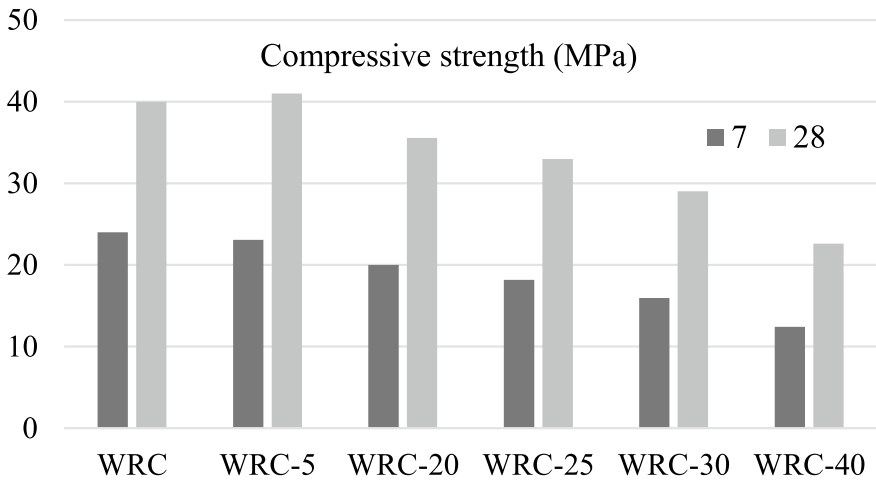
Fig. 6 Compressive strength decrease percentage

they also had low workability as demonstrated by the respective low slump values in Table 3. And this decrease in the slump value related to addition of Bentonite to the concrete mix that have a hygroscopic nature (Fig. 6).

6 Conclusion

The main objective of this study is to investigate the potential use of solid waste for producing concrete materials with a big cost saving. A laboratory investigation is performed to produce a concrete mix with the highest possible amount of sand which also met the strength requirement of 30 MPa for various civil engineering applications. From the laboratory investigation it can be seen that in order to produce an optimal concrete mix which achieves the required strength, it is recommended that WRC-25 mix from this investigation be used. WRC-10 mix achieved a compressive strength of 30 MPa at 28 days and contains additional waste rubber tires content of 25% resulting in a concrete mix and better performance against acidic and alkalic attach compared to conventional concrete.

References

1. Maupin, G.W.: Final report evaluation of asphalt rubber stress absorbing membranes, VTRC98-R11. Virginia Transportation Research Council (1997)
2. Balaha, M., Badawy, A., Hashish, M.: Effect of using ground waste tire rubber as fine aggregate on the behavior of concrete mixes. Indian J. Eng. Mater. Sci. **14**, 427–435 (2007)
3. Topçu, I., Demir, A.: Durability of rubberized mortar and concrete. J. Mater. Civil Eng. **19**, 173–178 (2007)
4. Ling, T., Nor, H., Lim, S.: Using recycled waste tires in concrete paving blocks. Proc. Inst. Civil Eng. Waste Resour. Manage. **163**, 37–45 (2010)
5. Eldin, N.N., Senouci, A.B.: Measurement and prediction of the strength of rubberized concrete. Cement Concr. Compos. **16**(4), 287–298 (1994)
6. Kim, S., Yi, N., Kim, H., Kim, J., Song, Y.: Material and structural performance evaluation of recycled PET fiber reinforced concrete. Cem. Concr. Compos. **32**, 232–240 (2010)
7. Turatsinze, A., Garros, M.: On the modulus of elasticity and strain capacity of self-compacting concrete incorporating rubber aggregates. Resour. Conserv. Recycl. J. **52** (10), 1209–1215 (2008)
8. Khaloo, A., Dehestani, M., Rahmatabadi, P.: Mechanical properties of concrete containing a high volume of tire-rubber particles. Waste Manag. J. **28**, 2472–2482 (2008)
9. Chou, L., Lin, C., Lu, C., Lee, C., Lee, M.: Improving rubber concrete by waste organic sulfur compounds. Waste Manag. J. **28**, 29–35 (2010)
10. Oiknomou, N., Stefanidou, M., Mavridou, S.: Improvement of the bonding between rubber tire particles and cement paste in cement products. In: 15th Conference of the Technical Chamber of Greece, Alexandroupoli, Greece, pp. 234–42 (2006)
11. Segre, N., Joekes, I.: Use of tire rubber particles as addition to cement paste. Cem. Concr. Res. J. **30**, 1421–1425 (2000)
12. ASTM C192/192M-16.: Standard Practice for Making and Curing Concrete Test Specimens in the Laboratory. ASTM International, West Conshohocken, PA, (2016)
13. ASTM C1611 / C1611M-18.: Standard Test Method for Slump Flow of Self-Consolidating Concrete. ASTM International, West Conshohocken, PA (2018)
14. BS EN 12390–3:2019.: Standard Test Method for Compressive Strength. British Standards Institution, London (2019).

Magnesium-Phosphate Cement Pastes to Encapsulate Industrial Waste Powders

Matthieu De Campos[iD]**, Catherine A. Davy**[iD]**, Murielle Rivenet**[iD]**, and Justo Garcia**

Abstract Although Ordinary Portland Cement (OPC) is the main cement considered in relation to industrial and radioactive waste management (as being the most widely used in the world), several waste types are incompatible with OPC. In particular, magnesium potassium phosphate cements (MKPC) are more suited to some waste types. They are promising durable alternatives to OPC cements, owing to their fast and adjustable setting time and to a high compressive strength on the short term. However, in stoichiometric proportions (Mg/P = 1), MKPC pastes swell significantly. Swelling decreases with increasing (Mg/P), i.e. with increasing content in over-stoichiometric MgO. In the context of hazardous waste management, our idea is to incorporate as much of powdered waste as possible, in replacement to over-stoichiometric MgO. The adequate granulometry and nature of powders, suitable with MKPC, need to be determined. Therefore, in this research, in MKPC pastes, over-stœchiometric MgO is replaced by fillers of varying nature and granulometry (fineness). First results explain the phenomena and phase formation, responsible for MKPC swelling, and how this is avoided when adding adequate powders. The most adapted filler, which removes swelling and allows sufficient spread, is described, as well as the threshold mass ratio of fines/cement (F/C), above which swelling of stœchiometric MKPC cement is eliminated.

Keywords Magnesium phosphate cement · Formulation · Dimensional stability · Encapsulation · Filler

M. De Campos (✉) · C. A. Davy · M. Rivenet
Univ. Lille, CNRS, Centrale Lille, ENSCL, Univ. Artois, UMR 8181—UCCS—Unité de Catalyse Et Chimie du Solide, 59000 Lille, France
e-mail: matthieu.de-campos@univ-lille.fr

J. Garcia
Orano, R&D, 125, Avenue de Paris, 92320 Châtillon, France

1 Introduction

Current environmental issues require a reduction in greenhouse gas emissions. In this context, the building materials industry is turning to alternative binders that emit less CO_2 during their manufacture [1]. Magnesium potassium phosphate cements (MKPC) address these concerns. Indeed, the production of raw materials requires less energy than OPC, and they have many advantages. MKPC display fast setting time, high compressive strength at early age and good chemical stability [2]. These characteristics make it a material of choice for road repairs and for solidification/stabilization of hazardous materials, e.g. radioactive industrial waste [3].

MKPC are inorganic materials made of phosphate bonds. Their formation is due to an acid–base reaction between MgO and an acid phosphate source, leading to the formation of K-struvite of formula $MgKPO_4 \cdot 6H_2O$. Different reaction mechanisms, leading to K-struvite, have been proposed in the literature [1, 5, 6]. The latest works suggest a mechanism based on dissolution and precipitation phenomena. According to Qiao [4], the formation of K-struvite is obtained after the successive precipitation and dissolution of intermediate species, namely phosphorrösslerite of formula $MgHPO_4 \cdot 7H_2O$ and a magnesium phosphate hydrate of formula Mg_2KH $(PO4)_2 \cdot 15H_2O$, depending on the paste pH (Table 1). Complementarily, the work of Le Rouzic et al. [7] shows the formation of newberyite $MgHPO_4 \cdot 3H_2O$ as another intermediate phase towards the formation of K-Struvite, at a pH lower than 6. On the whole, the formation of different hydrated phases prior to K-struvite depends on the paste pH, on water availability and also on the (Mg/P) MgO-to-KH_2PO_4 molar ratio [8, 9]. The mechanism, described by Qiao [4], and leading to the formation of K-struvite may be described in five successive stages (Table 1).

The whole process is summarized by the following *global* chemical reaction:

$$MgO + KH_2PO_4 + 5H_2O \rightarrow MgKPO_4 \cdot 6H_2O \tag{1}$$

This reaction is characterized by a magnesium to phosphate (Mg/P) molar ratio of 1, and a water-to-cement mass ratio W/C of 0.51 (where cement C corresponds to both MgO and KH_2PO_4). However, these proportions are not respected in most of the literature. The magnesium phosphate matrix formulated at stoichiometry displays significant swelling after setting. According to the works of Ma et al. [10] and Xu et al. [9], it is compulsory to select over-stoichiometric proportions, so that the optimal (Mg/P), avoiding swelling and providing maximal mechanical performance, is of 6. Le Rouzic et al. [11] show that the disappearance of swelling occurs for (Mg/P) >3. In [10], non-swelling MKPC pastes display a compressive strength on the order of 70 MPa at 28 days (for a W/C of 0.2).

For hazardous waste management, the idea is to add granular materials (powders) in MKPC cements, instead of over-stoichiometric MgO, following the work of Cau-Dit-Coumes et al. [12]. The introduced powders are assumed to play the same role in limiting swelling, as over-stoichiometric MgO. To our knowledge, there is currently no systematic study on the effect of powders on a stoichiometric MKPC

Table 1 Reaction mechanism leading to the formation of K-struvite in a diluted MKPC system with a water-to-cement mass ratio W/C = 10 and a molar Mg/P = 4, 6, 8 and 10, from [4]

Stage	Phenomenon occurring	Chemical reaction	pH range
I	Dissolution of KH_2PO_4	$KH_2PO_4 \rightarrow K^+ + H_2PO_4^-$	<6.3
II	Formation of phosphorrösslerite $MgHPO_4 \cdot 7H_2O$	$MgO + H_2PO_4^- + 7H_2O$ $\rightarrow MgHPO_4 \cdot 7H_2O + HO^-$	6.3–7.4
III	Transformation of phosphorrösslerite to $Mg_2KH(PO_4)_2 \cdot 15H_2O$	$2MgHPO_4 \cdot 7H_2O + K^+ + HO^-$ $\rightarrow Mg_2KH(PO_4)_2 \cdot 15H_2O$	7.4–7.3
IV	Formation of $Mg_2KH(PO_4)_2 \cdot 15H_2O$	$2HPO_4^{2-} + 2MgO + K^+ + 16H_2O$ $\rightarrow Mg_2KH(PO_4)_2 \cdot 15H_2O + 3HO^-$	7.3–9.4
V	Transformation of $Mg_2KH(PO_4)_2 \cdot 15H_2O$ to K-struvite	$Mg_2KH(PO_4)_2 \cdot 15H_2O + K^+ + HO^-$ $\rightarrow 2KMgPO_4 \cdot 6H_2O + 4H_2O$	9.4–8.5

matrix. This contribution proposes to study different MKPC pastes, with varying powder nature, content and granulometry, in the fresh state (spread) and in the hardened state (presence or not of swelling, nature of phases formed). The chosen powders are either silica fume or class F fly ash, but these may be extended to other powders, e.g. bigger silica sand grains, or industrial waste (radioactive or not).

2 Experimental Procedures

2.1 Physical Characterization

The raw powder materials used in this study (KH_2PO_4, MgO, fly ash and silica fume) have undergone various physical characterizations. Their particle size distribution is determined using a digital optical microscope, the MORPHOLOGI G3. Powder dispersion is carried out using the SDU (sample dispersion unit). This is used with a powder amount of 1 mm^3, a dispersion pressure of 300 kPa, and a deposition time of 1 min. This allows to digitize each studied particle, and to study their morphological characteristics (particle size and shape).

Figure 1 shows that the granulometry of MgO is similar to that of fly ash, although it contains a greater amount of the smallest particles (on the order of 1–7 microns). Comparatively, silica fume is significantly finer (with a d_{50} smaller than one micron).
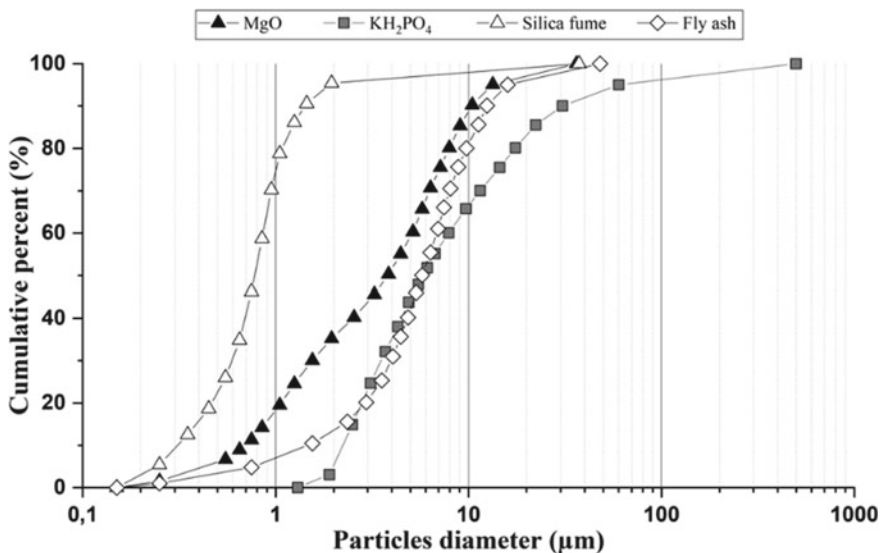
Fig. 1 Comparison of raw material granulometry (cumulative percentages are surface area proportions, i.e. they are similar to volume proportions)

2.2 Chemical Characterization

The powders are characterized by X-Ray Fluorescence (XRF). The device used is a Bruker© S2 Ranger, equipped with a palladium tube.

Thermogravimetric analysis is performed from room temperature to a target temperature of 700 °C, at a slow heating rate of 5 °C per minute, under an argon atmosphere. The device used is a SETARAM© differential thermal analyzer coupled to ThermoGravimetry Analysis (TGA).

The MKPC paste samples are also characterized qualitatively by X-ray diffraction. The apparatus used is a BRUKER© D8 advance, with a 2theta angle between 5° and 60°, at a step of 0.02° and with an analysis time of 1 s. Sample analysis is performed at 7 days after mixing.

2.3 Preparation of Cement Pastes

MKPC pastes are prepared using hardburnt MgO (Magchem 10 CR from M.A.F. Magnesite BV, purity 98.3%), potassium dihydrogen phosphate KH_2PO_4 (purity 99% from Acros Organics) and deionized water. The mineral additions used in replacement to over-stoichiometric MgO are class F fly ash (FA) from a local thermal power station (Harnes, France), and commercial silica fume (SF). Chemical composition and absolute density of the powders are described in Table 2. Their physical characterization has been provided previously (Fig. 1).

In order to prevent the MKPC paste from setting too quickly, for all formulations, boric acid H_3BO_3 is added at 3%wt (% of the total cement mass), as in [13].

The mixing protocol is derived from the EN 196–1 standard. Preliminarily, boric acid is mixed with water. Then, cement ($MgO + KH_2PO_4$) and water are mixed for 30 s at low speed; for the subsequent 30 s, fines are incorporated at low speed; mixing is stopped and the MKPC paste is let to rest for 1 min and 15 s; a final mixing is performed at high speed for 1 min. The MKPC pastes are then cast in tubes of 2.5 cm diameter and 6 cm height, and sealed for 7 or 28 days. Four cement paste formulations are investigated (Table 3).

Table 2 Chemical composition of the powders, obtained by XRF

	Chemical composition (%weight)									Absolute density (g.cm^{-3})
	SiO$_2$	Al$_2$O$_3$	Fe$_2$O$_3$	K$_2$O	CaO	MgO	TiO$_2$	SO$_3$	P$_2$O$_5$	
Magnesium oxide MgO	–	–	0.15	–	1.26	97.79	–	–	0.74	3.58
KH$_2$PO$_4$	–	–	–	55.12	–	–	–	–	44.81	2.34
Silica fume (SF)	94.86	0.44	0.18	1.48	1.17	0.30	-	0.90	–	2.24
Fly ash (FA)	43.25	20.37	14.58	7.86	6.58	2.90	2.04	1.02	–	1.76

Table 3 Formulations used

Name	Fines used	Molar ratio Mg/P*	Mass ratio W/C**	Mass ratio W/Powder***	Mass ratio F/C	%wt H_3BO_3/ Cement
M1W51Mg	–	1	0.51	0.51	–	3
M1W51FA	FA	1	0.51	0.42–0.21	0.2–1.4	3
M1W51F1	FA	1	0.51	0.255	1	3
M1W51SF	SF	1	0.51	0.49–0.25	0.05–1	3

*Mg/P = Mg to phosphate (P) molar ratio; **C = Cement (MgO + KH_2PO_4); ***P = Powder (meaning cement + additional powder)

2.4 Volume Change Measurement and Swelling Analysis

This experiment aims at quantifying MKPC swelling, by quantifying the paste volume change after a given setting time. As described above, the paste is placed in a 2.5 cm diameter tube. The paste initial paste height H_0 (at the time of its synthesis) is measured, then the tube is sealed for 7 or 28 days.

At 7 days curing, samples **M1W51Mg** and **M1W51F1** are analyzed by thermogravimetry, and **M1W51Mg** is analyzed by XRD.

After 28 days curing, sample height H_{28} is measured. H_0 and H_{28} values allow to define ΔH, which is the ratio of sample heights H_{28} to H_0 (Fig. 2). If there is a volume change in the sample, this affects its height only. The values of ΔH allow to define three cases. If ΔH is less than 1, the sample has shrinked, whereas if ΔH is greater than 1, the sample has swollen. Finally, if ΔH is 1, the sample displays dimensional stability (Fig. 2).

3 Results and Discussions

3.1 Swelling Analysis of the Stoichiometric Matrix (M1W51Mg)

The stoichiometric MKPC matrix displays an immediate bleeding after mixing, which prevents any measurement of paste rheology (Fig. 3). In addition, once
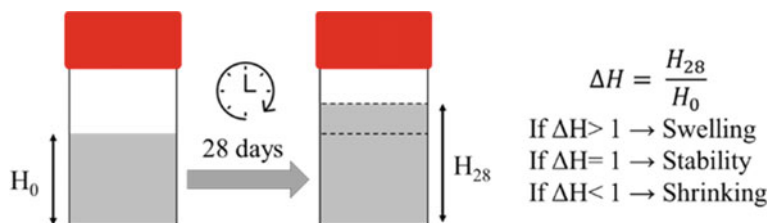
Fig. 2 Schematic representation of volume change measurements
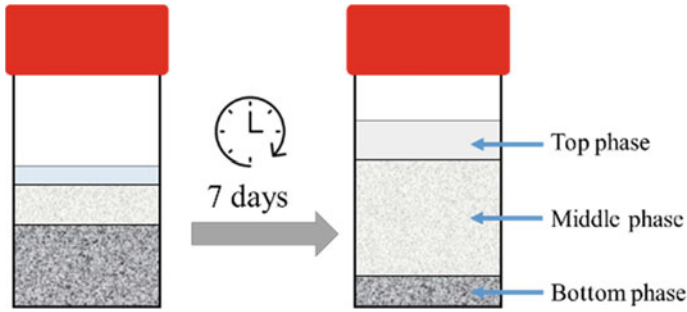
Fig. 3 Schematic evolution of the **M1W51Mg** stoichiometric cement matrix, without fine addition, from one day to seven days after casting

placed in a mold, phase segregation appears and develops over time. Water is also present at the surface, but it is no longer measurable after 7 days curing. After a few minutes curing and up to 7 days, visual observation shows the presence of three distinct solid layers, one at the bottom (probably large white particles of KH_2PO_4), one in the middle, and one at the top (attributed to MgO particles). This is analyzed in more detail by XRD and TGA, by carefully taking off parts of each of the three solid layers.

With TGA, the decomposition temperatures are determined by deriving the mass signal over time (Table 4). These correspond to heatflow data (TDA), and reveal a significant difference in phase composition.

The top part of the sample has a single endothermic peak at 104 °C. According to the literature [14, 15], this corresponds to the decomposition of K-struvite with the release of water.

Table 4 Summary of phase identification by TGA of cement pastes **M1W51-Mg** (3 phases) and **M1W51F1** after 7 days curing

Name	Solid location in the sample	Decomposition temperature (°C)	Phase	References
M1W51-Mg	Top part	104 °C	K-Struvite: $MgKPO_4 \cdot 6H_2O$	[14, 15]
	Middle part	86 °C	$Mg_2KH(PO_4)_2 \cdot 15H_2O$	[16]
		118 °C	$MgHPO_4 \cdot 7H_2O$	
	Bottom part	73 °C	$Mg_2KH(PO_4)_2 \cdot 15H_2O$	[17]
		226 °C	KH_2PO_4	
M1W51F1	Sampling in the middle (good homogeneity)	69 °C	$Mg_2KH(PO_4)_2 \cdot 15H_2O$	[16]
		103 °C	$MgKPO_4 \cdot 6H_2O$	[14, 15]

The intermediate part has two endothermic peaks at 86 and 118 °C. According to the literature [16], the first peak corresponds to the decomposition of a hydrated phase of formula $Mg_2KH(PO_4)_2 \cdot 15H_2O$ and the second to the decomposition of Phosphorrösslerite $MgHPO_4 \cdot 7H_2O$.

The lower part of the sample is characterized by the presence of 2 endothermic peaks, a first one at 73 °C and a second at 226 °C. The first peak is attributed to the magnesium phosphate hydrate of formula $Mg_2KH(PO_4)_2 \cdot 15H_2O$, also present in the middle part of the sample. Moreover, preliminary thermal analysis of KH_2PO_4 alone allows the peak at 226 °C to be assigned to a phase change of KH_2PO_4 [17]. The presence of KH_2PO_4 at the sample bottom is explained by its limited solubility in water 250 g/l [18] compared to its amount involved to make the MKPC (initially set at 1528 g/l of water).

X-Ray diffraction analysis allows a more accurate analysis of the species present. At the sample surface, the presence of two crystalline phases, namely K-Struvite ($MgKPO_4 \cdot 6H_2O$) and magnesium oxide MgO is confirmed. No characteristic diffraction peaks of KH_2PO_4 are detected.

In the middle part of the sample, a total of 6 phases is revealed, 5 of which are known from the literature. These are K-Struvite ($MgKPO_4 \cdot 6H_2O$), Phosphorrösslerite $MgHPO_4 \cdot 7H_2O$, Newberyite $MgHPO_4 \cdot 3H_2O$, $Mg_2KH(PO_4)_2 \cdot 15H_2O$, KH_2PO_4 and an unidentified phase. This same phase is also present in the analysis of the lower phase. It is not identified precisely by TGA, because its decomposition peaks are probably superimposed to those already identified.

The lower part displays three main phases (Table 5), including KH_2PO_4. The latter has higher diffraction peaks than the two others, which are also present in the middle part.

Table 5 Summary of the phase identification X-ray diffractogram of the 3 phases of the stoichiometric matrix M1W51-Mg. Label X corresponds to the presence of the phase and (*) to a minor phase

Phases	Cell volume ($Å^3$) (crystal system; space group)	Top phase	Middle phase	Bottom phase
MgO (ICSD 158103)	74.69 (cubic; F m −3 m)	X		(*)
KH_2PO_4 (ICSD 201374)	387.33 (tetragonal; I −4 2 d)		X	X
$MgHPO_4.7H_2O$ (ICSD 107677)	1879.52 (monoclinic; C 1 2/c 1)	(*)	(*)	(*)
$Mg_2KH(PO_4)_2.15H_2O$ (ICSD 32527)	503.67 (triclinic; P −1)		X	X
$Mg_3(PO_4)_2.22H_2O$ (ICSD 100365)	666.57 (triclinic; P −1)		X	X
$MgKPO_4.6H_2O$ (ICSD 5289)	473.36 (orthorhombic; P m n 21)	X		
$MgHPO_4.3H_2O$ (ICSD 8228)	1091.11 (orthorhombic; P b c a)		(*)	(*)
Unidentified species	–		X	X

Interpretation. Initially, for the stoichiometric matrix (**M1W51Mg**), the water volume is significantly bigger than the powders volume. Moreover, for both KH_2PO_4 and MgO powders, their amount is greater than their solubility in water at 25 °C (250 g/l for KH_2PO_4 and 0.62 mg/l for MgO). This explains that, just after mixing, although KH_2PO_4 and MgO dissolve, they remain in significant amount as powders in the liquid.

Right after mixing, the dissolved reactants are uniformly distributed in the paste. They form phosphorrösslerite all over the sample volume, at the surface of undissolved MgO particles, at a pH around 6–7 (Stage II in Table 1). Despite that, the initial volume of powder solids is too small to avoid water bleeding, i.e. an observable amount of water above the mix (Fig. 4a).

A few moments after mixing, while phosphorrösslerite progressively forms in the liquids, the undissolved particles of KH_2PO_4 and MgO sediment. The larger undissolved particles of KH_2PO_4 settle faster than the smaller ones made of MgO (Fig. 4b). This is consistent with previous X-ray diffraction results, where MgO is mainly present in the top part of the sample, and KH_2PO_4 is rather in the middle and bottom (Table 5).

The larger amount of KH_2PO_4 at the sample bottom leads to a pH gradient (with a lower pH at the sample bottom), so that progressively, depending on the height considered in the sample, a threshold is reached, allowing the transformation of phosphorrösslerite into $Mg_2KH(PO4)_2 \cdot 15H_2O$. This hydrate has a cell volume significantly smaller than phosphorrösslerite (Table 5), meaning that a contraction of the solids occurs where it is formed. This is observed in the middle part of the sample (Fig. 4c).

All over the solidification process, while the pH remains below 7.4, phosphorrösslerite forms, and because its cell volume is significantly bigger than
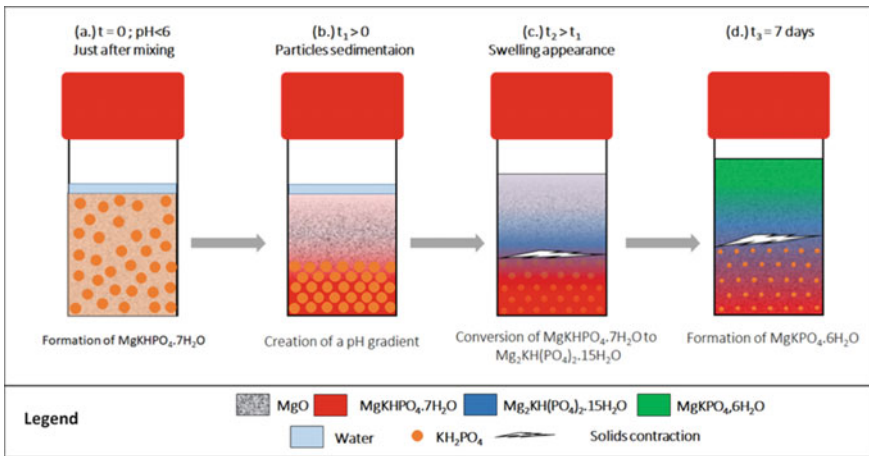
Fig. 4 Schematic mechanism of swelling development in the stoichiometric matrix (**M1W51-Mg**)

the other hydrates, the sample volume becomes bigger than its initial value (in the liquid state).

Further, as soon as $Mg_2KH(PO_4)_2 \cdot 15H_2O$ forms, and when the pH is of at least 7.3 (Table 1), K-struvite $MgKPO_4 \cdot 6H_2O$ starts to solidify. Because of the differential sedimentation between KH_2PO_4 and MgO, this pH range is only reached in the top part of the sample, so that K-struvite is solely observed there (Table 5 and Fig. 4d).

In this context, the use of over-stoichiometric MgO provides phase homogeneity and avoids sedimentation of all particles.

3.2   Swelling Inhibition of the Stoichiometric Matrix with Fine Addition

When using over-stoichiometric MgO, swelling is eliminated, but is this effect mainly physical or chemical?

This role of over-stoichiometric MgO (as a reactive or unreactive powder) is studied by analyzing the influence of mineral additions (fly ash or silica fume) on the dimensional stability of the stoichiometric MKPC. The latter is mixed with an increasing amount of mineral addition, either fly ash or silica fume (Table 3). Visual inspection is performed after 7 days curing (Fig. 5 on the example of silica fume).

Results show that swelling decreases when increasing the fine-to-cement F/C mass ratio, until disappearing for F/C around 1 and bigger.

Dimensional variations values ΔH (after 28 days curing) are presented in Fig. 6. The elimination of swelling is obtained at a minimal (F/C) of 0.6 for silica fume, and 0.8 for fly ash. For greater (F/C) than these values, no swelling is quantified, and the remaining effect of the additional powders is solely on paste rheology (not shown). With silica fume, rheology is not sufficient (no spread is achieved for reasonable W/C values), contrarily to fly ash.
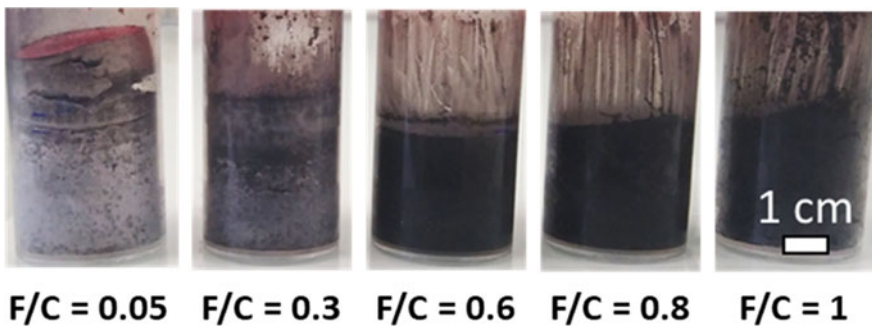
Fig. 5 Macro-photographs of different stoichiometric samples with different fine-to-cement F/C mass ratios (i.e. MKPC added with silica fume, named **M1W5SF**), after 28 days curing in a sealed tube
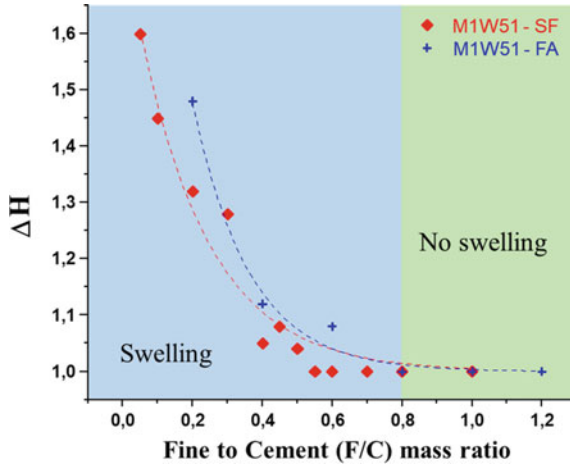
Fig. 6 Dimensional changes ΔH depending on the fine-to-cement (F/C) mass ratio

Finally, a (F/C) mass ratio of 1 (associated to the stoichiometric MKPC paste) is chosen for further mechanical characterization (not shown). With this value, the paste spread is suitable for the industrial application of stabilisation and solidification of nuclear wastes.

Understanding of swelling disappearance. The addition of fly ash avoids phase segregation and also powder sedimentation. This allows a homogeneity of all the constituents of the MKPC paste. Therefore, KH_2PO_4 particles are better distributed inside the material after the mixing step, preventing the formation of a pH
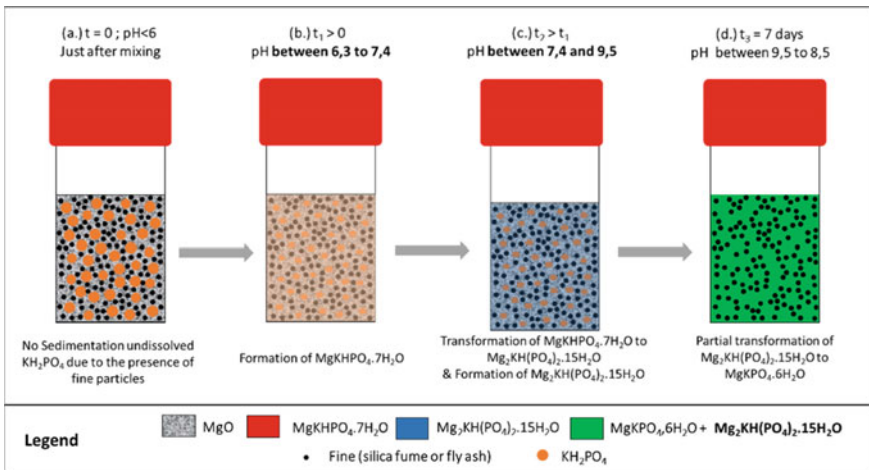
Fig. 7 Schematic setting mechanism of stoichiometric matrix with fine addition (**M1W51F1**)

gradient (Fig. 7). K-struvite can then be generated according to the mechanism described in Table 1.

In order to check for reaction progress rate, TGA-TDA (Table 4) is performed on the stoichiometric matrix with fly ash addition (**M1W51F1**). Results at 7 days show the presence of two compounds, namely the magnesium phosphate hydrate Mg_2KH $(PO_4)_2 \cdot 15H_2O$ (as a minor phase) and K-Struvite (as the major phase).

4   Conclusion

This work highlights the feasibility of formulating a stoichiometric MKPC paste, with the addition of mineral additives, such as fly ash. Indeed, this addition avoids phase segregation/sedimentation and bleeding of the fresh cement paste, and consequently, a pH gradient due to the liquid over-saturation in KH_2PO_4.

An optimal proportion of fly ash is obtained for a (F/C) mass ratio of 1, in relation to an adequate spread of the fresh paste (contrarily to MKPC pastes formulated with silica fume).

This preliminary work opens up the possibility of incorporating other industrial waste (e.g. hazardous waste) in a powdered form. The most important parameters for the formulation of these new cement matrices will then be the physico-chemical properties of the waste (chemical reactivity with MKPC), and the (F/C) mass ratio to be used to allow sufficient spread and mechanical performance. Future work will focus on the incorporation of these wastes, and the study of their interactions and effects on the mechanical and leaching properties when incorporated in the MKPC matrix.

References

1. Walling, S.A., Provis, J.L.: Magnesia-based cements: a journey of 150 years, and cements for the future? Chem. Rev. **116**(7), 4170–4204 (2016)
2. Chau, C.K., Qiao, F., Li, Z.: Microstructure of magnesium potassium phosphate cement. Constr. Build. Mater. **25**(6), 2911–2917 (2011)
3. Wagh, A.S., Jeong, S.Y., Singh, D.: High strength phosphate cement using industrial byproduct ashes. High Strength Concr. Proc. 542–553 (1999)
4. Qiao, F.: Reaction Mechanisms of Magnesium Potassium Phosphate Cement and its Application (2010)
5. Soudee, E.: Liants phsophomagnésiens : mécanisme de prise et durabilité (1999)

6. Wagh, A.S.: Chemically Bonded Phosphate Ceramics: Twenty-First Century Materials with Diverse Applications, 2nd edn (2016)

7. Le Rouzic, M., Chaussadent, T., Platret, G., Stefan, L.: Mechanisms of k-struvite formation in magnesium phosphate cements. Cem. Concr. Res. **91**, 117–122 (2017)

8. Chau, C.K., Qiao, F., Zongjin, L.: Potentiometric study of the formation of magnesium potassium phosphate hexahydrate. J. Mater. Civ. Eng. 586–591 (2012)

9. Xu, B., Lothenbach, B., Leemann, A., Winnefeld, F.: Reaction mechanism of magnesium potassium phosphate cement with high magnesium-to-phosphate ratio. Cem. Concr. Res. **108**, 140–151 (2018)

10. Ma, H., Xu, B., Liu, J., Pei, H., Li, Z.: Effects of water content, magnesia-to-phosphate molar ratio and age on pore structure, strength and permeability of magnesium potassium phosphate cement paste. Mater. Des. **64**, 497–502 (2014)

11. Le Rouzic, M., Chaussadent, T., Stefan, L., Saillio, M.: On the influence of Mg/P ratio on the properties and durability of magnesium potassium phosphate cement pastes. Cem. Concr. Res. **96**, 27–41 (2017)

12. Cau Dit Coumes, C., Lambertin, D., Lahalle, H., Antonucci, P., Cannes, C., Delpech, S.: Selection of a mineral binder with potentialities for the stabilization/solidification of aluminum metal. J. Nucl. Mater. J. **453**(1–3), 31–40 (2014)

13. Hall, D.A., Stevens, R., El-Jazairi, B.: The effect of retarders on the microstructure and mechanical properties of magnesia-phosphate cement mortar. Cem. Concr. Res. **31**(3), 455–465 (2001)

14. Xu, B., Winnefeld, F., Kaufmann, J., Lothenbach, B.: Influence of magnesium-to-phosphate ratio and water-to-cement ratio on hydration and properties of magnesium potassium phosphate cements. Cem. Concr. Res. **123**(June), 105781 (2019)

15. Lahalle, H., et al.: Influence of the w/c ratio on the hydration process of a magnesium phosphate cement and on its retardation by boric acid. Cem. Concr. Res. **109**(July 2017), 159–174 (2018)

16. Lahalle, H.: Conditionnement de l'aluminium métallique dans les ciments phospho-magnésiens. Université de Bourgogne Franche-Comté (2016)

17. Vyazovkin, S., Ferrin, T.L.: Thermomechanical study of the high temperature phase transition in $KH_2 PO_4$. Solid State Commun. **113**, 627–631 (2000)

18. Lide, D.R.: Handbook of Chemistry and Physics 84th edition (2003)

Microstructural Evaluation of Fibre-Reinforced Slag-Based Foams

M. Češnovar, K. Traven, and V. Ducman

Abstract Alkali-activated foam materials were produced using electric arc furnace steel slag and ladle furnace basic slag as precursors, sodium water glass (Na_2SiO_3) and sodium hydroxide (NaOH) as alkali activators, and hydrogen peroxide (H_2O_2) as a foaming agent. The anionic surfactant sodium dodecyl sulfate (SDS) was used for the stabilization of pores in the matrix. In order to improve the mechanical properties (fracture resistance expressed as bending strength), seven types of fibres (polypropylene (PP), polyvinyl alcohol (PVA), basalt (B), cellulose (C), steel fibre (S), mineral wool (M) and wood fibres (W)) were added to selected mixtures and embedded into the AAF matrix. The bending and compressive strength measurements show that the addition of fibres, especially PP, improved bending strength. Microstructural analysis gives an insight into the interfacial zones between the fibres and the AA matrix. Where a non-uniform distribution of fibres and/ or a weak contact between fibres and the matrix was detected, there was negligible or no impact on the mechanical properties. In the cases where the fibres were uniformly distributed and a good adhesion between fibres and the matrix was established, the bending strength increased.

Keywords Alkali activated foams · Chemical foaming · Stabilizing agent · Fibres · Microstructure

M. Češnovar (✉) · K. Traven · V. Ducman
Slovenian National Building and Civil Engineering Institute (ZAG), Dimičeva 12, 1000 Ljubljana, Slovenia
e-mail: mark.cesnovar@zag.si

M. Češnovar
International Postgraduate School Jožef Stefan, Jamova 39, 1000 Ljubljana, Slovenia

1 Introduction

Foam made out of alkali-activated materials based on different aluminosilicate-based sources is a lightweight product intended to be used in the building sector as thermal and acoustic insulation [1]. Given their low density, good thermal properties, fire stability and applicable mechanical properties, alkali-activated foam (AAF) materials offer an environmentally friendly alternative to ordinary insulation materials such as aerated cement concrete, mineral wool or EPS [2]. The main result of the process of foaming is that stabile voids remain in the matrix of the alkali-activated material. There are a few well introduced techniques such as mechanical [3] or chemical [4] foaming, which make the material porous. Surface agents are also important additives to minimize the surface tension and create the right size distribution of pores [5]. Reaching very low densities results in low thermal conductivity but also decreases mechanical strength. Bai et al. [6] studied porosity, insulative and mechanical properties of AA foams and showed results of low density (0.37 g.cm^{-3}), low thermal conductivity (0.11 W.m^{-1} K^{-1}) and an acceptable compressive strength of 0.3 MPa. Papa et al. [7] studied a correlation between microstructure and the porosity of alkali bonded perlite. Densities of produced samples were around 0.46 g.cm^{-3}, compressive strength 1.6 MPa, and thermal conductivity 0.084 W.m^{-1} K^{-1}. Poor mechanical properties of AA foams result from brittleness which causes material to be more fragile in comparison to a non-porous AAM. Besides the type of precursor, alkaline activators (dosage, type), curing (setting) program and shrinkage play a major role. The alkali activated pastes suffer from autogenous and drying shrinkage [8], as in the ordinary Portland cement system. Studies of autogenous shrinkage show that the appearance of cracks in the early stage of curing is problematic because they develop quickly at the time when the strain of the AA binder is low [9]. Furthermore, expansion of the AAM could appear at certain stages of curing, especially when samples are cured in controlled humidity conditions, so such expansion cannot be the result of autogenous deformation according to the desiccation theory for OPC [10]. This could therefore be attributed to chemical shrinkage or expansion meaning that the absolute volume change of material occurs as a result of chemical reactions [11]. The mechanism of chemical expansion is used in the process of foaming so the deformation associated with the cracking of AA foams could have a strong impact on the mechanical properties of porous AA materials. One promising solution to minimize the deformation and cracking in alkali-activated foams is the use of fibres [12]. Many authors report that it is favourable to use locally found fibres from natural bio resources such as bamboo [13], hemp [14], cotton [15], wood [16], and sisal [17], etc. because they are recyclable, renewable and consequently environmentally friendly. Fibres used in alkali-activated materials must also remain stable in a highly alkaline environment and sustainable when exposed to different environments, including high temperatures [18]. Natural cellulose-based bio fibres usually decompose at temperatures around 360 °C [13]. Therefore some studies of reinforced alkali-activated materials have used basalt [12], steel [19] or glass fibres

[20], all of which should survive elevated temperatures. Puertas et.al. reported that drying shrinkage of alkali-activated fly ash was reduced by 20% when reinforced with alkali-resistant glass fibre and the AAM exhibited a 50% recovery of mechanical strength after exposure to high temperature (1200 °C) [20]. Synthetic fibres such as polypropylene (PP) [21], polyvinyl alcohol (PVA) [22], or a combination of both steel and PP [23] are also being used because of their good performance.

Despite numerous studies in the field of fibre-reinforced alkali-activated materials, very few have been carried out using lightweight foams. Therefore this study investigates the influence of bio (wood fibres, cellulose), synthetic (PP, PVA), mineral (basalt, grinded waste mineral wool) and steel fibres on mechanical strength and assesses the microstructural incorporation of these fibres into a foamed alkali-activated matrix made from Slovenian ladle and electric arc furnace slags.

2   Materials and Methods

2.1   Raw Materials

The reinforcement test started by using the optimal mixture AR 0.5 (1:1 Ladle to EAF Slag) previously made in a study of the effects of curing on (ladle and electric arc furnace) slag-based alkali-activated materials [24]. 1.5 g of hydrogen peroxide Belox 30 (Belinka, Slovenia) was used for foaming alkali activated pastes and 1.0 g of sodium dodecyl sulfate (sodium salt, pure granular, Acros organics, Malaysia) used as a stabilizing agent.
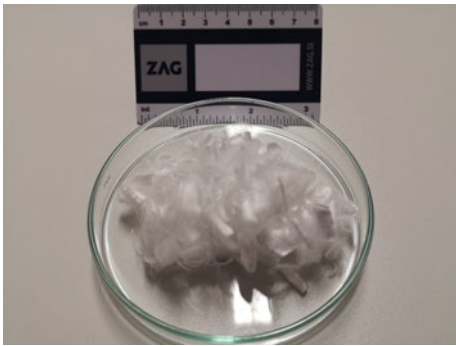
2.2   Fibres

Fibres used in this study were of an elongated shape and comprised different sizes and densities, as shown in Table 1. 0.5 g of fibres were added to the precursor prior to mixing with the alkali activator, stabilizer and foaming agent. The outcome of fibre-reinforcement on the bending and compressive strength of AAFs is presented with microstructure analysis in Fig. 1.

2.3   Sample Preparation

Seven different types of fibres were used for reinforcement of AAFs, as listed in Table 2. Reinforced mixtures were prepared by gradually adding weighed fibres into a mix of ladle and arc furnace slag. The mixture was then stirred with a spatula

Table 1 Properties of the fibres as given by suppliers

Fibre type	Figure	Av. length (mm)	Density (gcm^{-3})
PP		11	0.94
PVA		12	1.19
Basalt		7	3.0
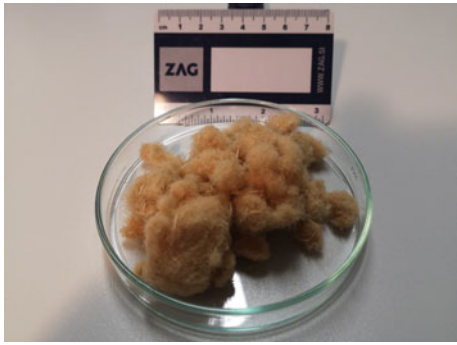
(continued)

Table 1 (continued)

Fibre type	Figure	Av. length (mm)	Density (gcm^{-3})
Cellulose		5	1.5
Steel		12	7.8
Mineral wool		n.a.[*]	n.a.[*]

Table 1 (continued)

Fibre type	Figure	Av. length (mm)	Density (gcm^{-3})
Wood fibres		n.a.*	n.a.*

* n.a. = not added
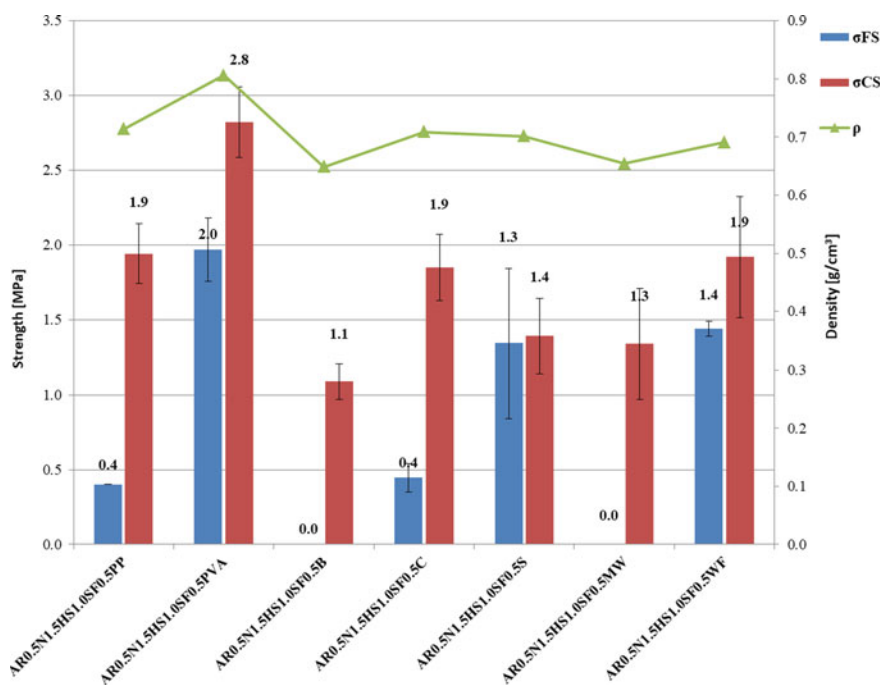
Fig. 1 Values of flexural and compressive strength for different fibre types

Table 2 Mix design (% mass)

Mixture	Slag content (g)	Activator content (g)	Foaming agent content (g)	Stabilizing agent content (g)	Fibre type/ content (g)
AR0.5N1.5HS1.0SF0.5PP	66	33	1.5	1.0	PP/0.5
AR0.5N1.5HS1.0SF0.5PVA	66	33	1.5	1.0	PVA/0.5
AR0.5N1.5HS1.0SF0.5B	66	33	1.5	1.0	Basalt/0.5
AR0.5N1.5HS1.0SF0.5C	64	36	1.5	1.0	Cellulose/ 0.5
AR0.5N1.5HS1.0SF0.5S	66	33	1.5	1.0	Steel/0.5
AR0.5N1.5HS1.0SF0.5 MW	66	33	1.5	1.0	Mineral wool/0.5
AR0.5N1.5HS1.0SF0.5WF	64	36	1.5	1.0	Wood fibres/0.5

until the fibres were equally distributed throughout the whole volume. This dry mixture was then added to the wet mixture of sodium silicate, hydrogen peroxide and sodium dodecyl sulfate. The mixture was further homogenized by hand mixing to obtain a desirable paste. Due to varying properties of the fibres (i.e. capillarity), in some cases the addition of water glass was adjusted from the original calculation. This was the case for wood and cellulose fibres, as shown in Table 2, in order to obtain a more desirably consistency and easier mixing.

Finally the pastes were caste into rubber moulds ($20 \times 20 \times 80$ mm^3) and cured at 70 °C for 3 days in a heating chamber. After the curing, specimens were demoulded and the compressive and bending strengths were measured using a Toninorm instrument (ToniTechnik, Germany) using a 0.05 KN of induced force per second. One part of the specimen was taken for scanning electron microscopy (SEM) image analysis. A selected piece was dried at 40 °C in a vacuum chamber for 24 h and the SEM images were captured using a Jeol JSM-IT500 (Jeol, Japan) with a tungsten filament cathode under high vacuum conditions in backscattered mode.

3 Results

3.1 The Effect of Fibres on Mechanical Properties

The effects of using different fibres on the compressive and bending strengths are shown in Fig. 1. The results show that in most cases flexural and compressive strength is increased when fibres are used to reinforce the matrix. Flexural strength was measurable for samples containing PP, PVA, cellulose, steel and wood fibres but fell below detectable limits for basalt and mineral wool. During preliminary

research flexural strength was also not detectable in specimens mixed without
fibres. Maximum compressive strength was measured for AAFs reinforced with
PVA fibres (2.8 MPa). The lowest density of all samples was 0.65, observed in both
specimens containing basalt (exhibiting a compressive strength of 1.1 MPa) and
wool fibres (with a compressive strength of 1.3 MPa).

3.2 Microstructural Evaluation

The microstructures of AA samples with different fibres are presented in Figs. 2, 3,
4, 5, 6, 7, 8.

PP fibre-reinforced alkali-activated foamed materials from ladle and electric arc
furnace slag are shown in Fig. 2a (low magnification), and in Fig. 2b, where detail
of the boundary between a fibre and the matrix is clearly presented. Figure 2a
shows that PP fibres are evenly distributed throughout the foam, while the detail in
Fig. 2b shows an approximate 1 μm wide gap in some places around the fibre.
Rickard et.al. suggested that this results from shrinkage of the AA gel during the
curing stage [25]. Smaller cracks are presented perpendicular to the fibre whilst
larger cracks are visible at different angles to the fibre or in areas without any fibre
(Fig. 2b). So the cracking and deformations are minimized when PP fibres
are added as reinforcement for alkali-activated foams, as also observed by Mastali
et al. [12].

The uniform size and distribution of PVA fibres is shown in Fig. 3a and the
detail of the fibre incorporation is shown in Fig. 3b. The AAF reinforced with PVA
fibres exhibits the highest compressive and flexural strength. This could be due to a
good embodiment of fibres, with the adhesion preventing excessive cracking during
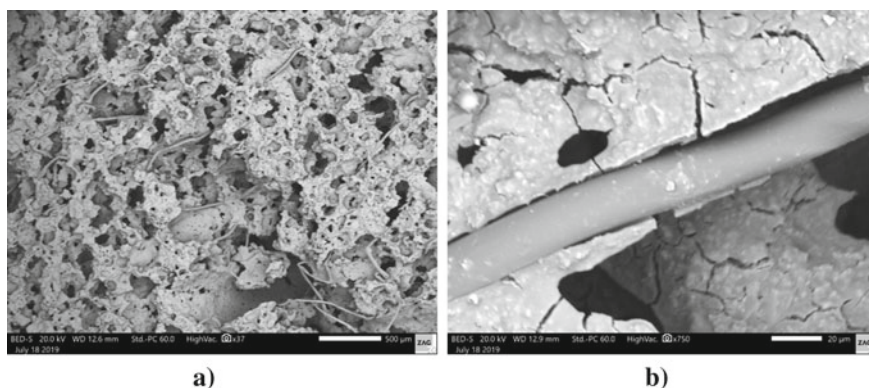the early stages of curing.

a)   b)

Fig. 2 SEM micrographs at 37 and 750-times magnification with capture of sample
AR0.5N1.5HS1.0SF0.5PP reinforced with polypropylene fibres. **a** PP distribution in the matrix;
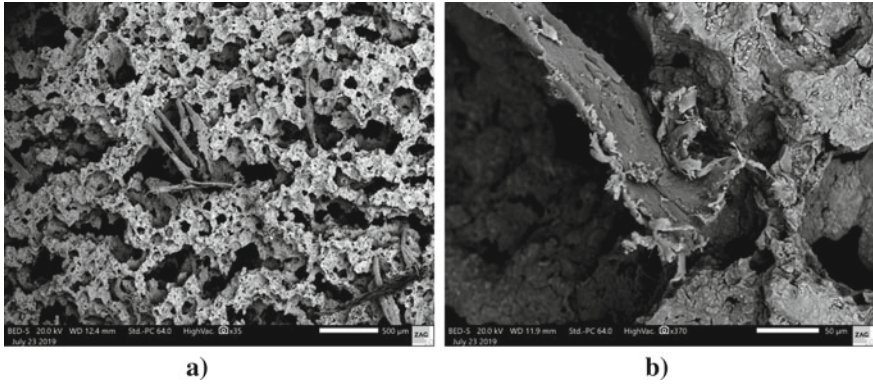**b** boundary between a PP fibre and the matrix

Fig. 3 SEM micrographs at 35 and $\sim$370-times magnification with capture of sample AR0.5N1.5HS1.0SF0.5PVA reinforced with PVA fibres. **a** PVA distribution in the matrix, **b** boundary between a PVA fibre and the matrix
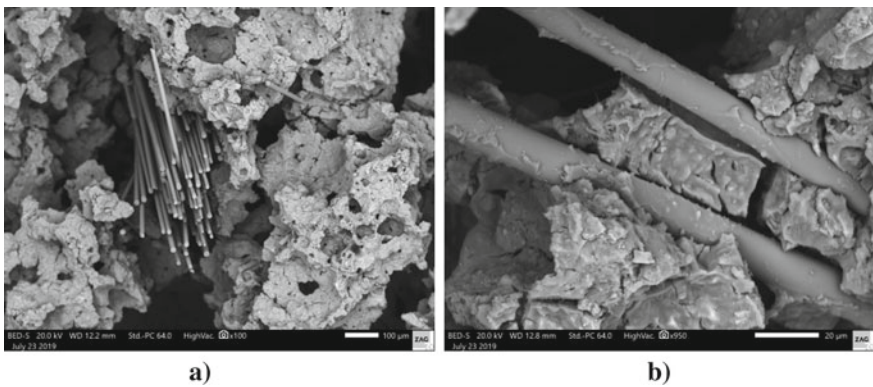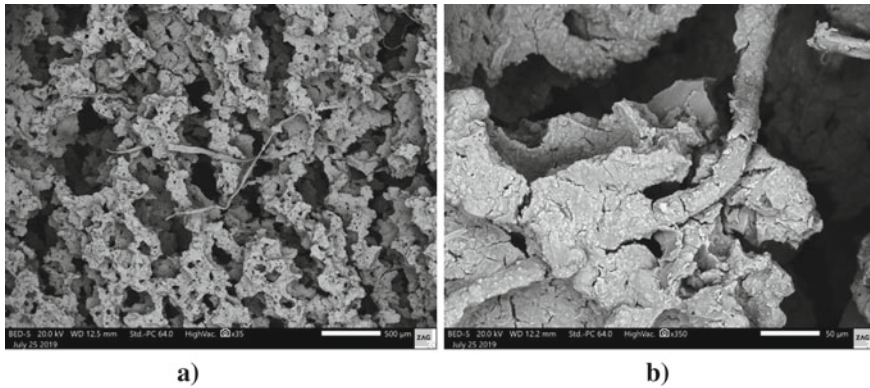

Fig. 4 SEM micrographs at 100 and $\sim$950-times magnification with capture of sample AR0.5N1.5HS1.0SF0.5B reinforced with basalt fibres. **a** Basalt distribution in the matrix; **b** boundary between a basalt fibre and the matrix

Figure 4a shows that basalt fibres are not as well distributed in the matrix as were the PP fibres. Figure 4b shows a boundary between a fibre and the matrix and gaps around the fibres similar to the PP fibres, which could be a consequence of shrinkage (as in the case of the PP fibres).

Cellulose fibres (Fig. 5) are uniformly embedded into the matrix; adhesion between fibres and the matrix appears to be good (Fig. 5b), contributing to an increased flexural strength (0.4 MPa). Cracks or voids are not as evident as in the case of less porous fibres since the porosity of cellulose fibres contributed to a better adhesion.

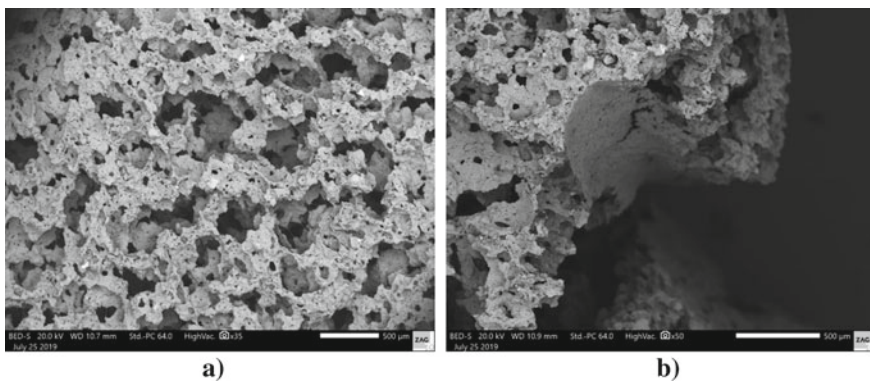**Fig. 5** SEM micrographs at 35 and ∼350-times magnification with capture of sample AR0.5N1.5HS1.0SF0.5C reinforced with cellulose fibres. **a** Cellulose distribution in the matrix; **b** boundary between a cellulose fibre and the matrix

Figure 6a, b show the matrix of steel reinforced AAF. Fibres were not presented in the captures because they were torn from the matrix while cutting and grinding for the SEM analysis. Figure 6b shows the void where the fibre was placed. The low adhesion of the fibre and the matrix reflects the lower compressive strength despite reasonable flexural strength. This could result from a grouping of steel fibres within some areas of the matrix thus increasing the flexural strength.

Figure 7a shows the low magnification of reinforced AAF with wool fibres (MW). These fibres of ground mineral wool are smaller in size so their distribution in the matrix is not clearly visible (Fig. 7a). The detail of their embodiment in the matrix is shown in the higher magnification SEM image in Fig. 7b. The advantage of the smaller fibre size of MW is that they are more easily incorporated into the

Fig. 6 SEM micrographs at 35 and ∼50-times magnification with capture of sample AR0.5N1.5HS1.0SF0.5S reinforced with steel fibres. **a** Steel distribution in the matrix; **b** boundary between a steel fibre and the matrix
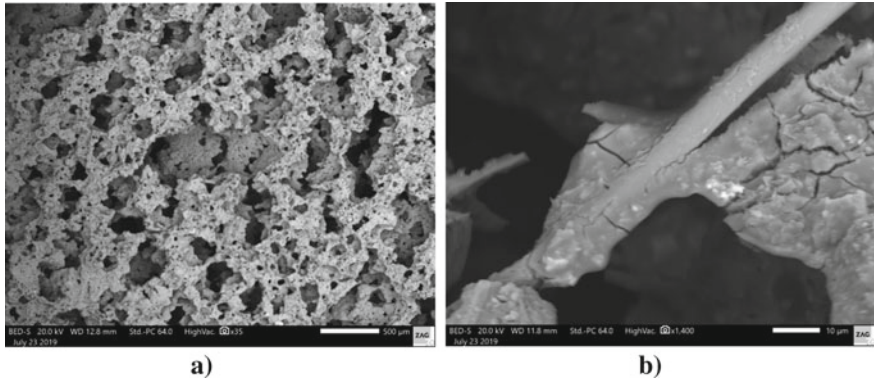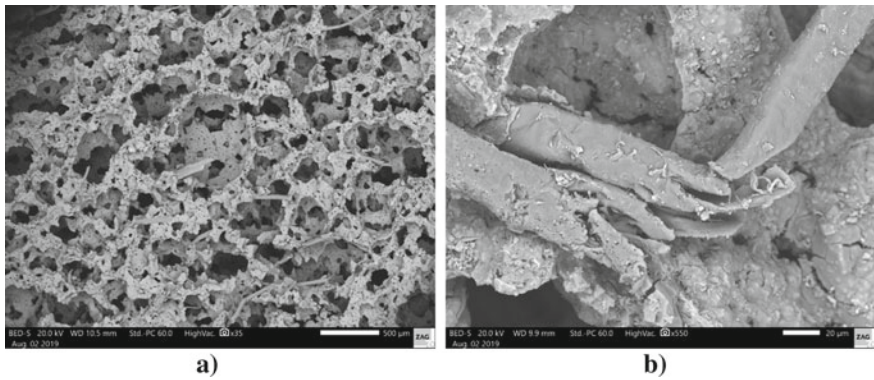
Fig. 7 SEM micrographs at 35 and 1400-times magnification with capture of sample AR0.5N1.5HS1.0SF0.5 MW reinforced with mineral wool fibres (MW). **a** MW distribution in the matrix; **b** boundary between a MW fibre and the matrix

AAF matrix, especially in cell and void boundaries. Despite an improved incorporation of fibres, cracks are still present within the matrix.

Figure 8a shows a uniform distribution of wood fibres in the AAF resulting in a relatively high flexural strength (1.4 MPa). Figure 8b shows the detail of a wood fibre embedded in the AAF matrix. Micro cracks are present around the boundaries where the fibres are placed but are less evident than in other mixtures.

Fig. 8 SEM micrographs at 35 and 550-times magnification with capture of sample AR0.5N1.5HS1.0SF0.5 MW reinforced with wood fibres (FW). **a** WF distribution in the matrix; **b** boundary between a WF fibre and the matrix

4   Conclusions

In order to improve the mechanical properties (fracture resistance followed by flexural strength measurements), seven types of fibres [polypropylene (PP), poly-vinyl alcohol (PVA), basalt (B), cellulose (C), wood (W), ground mineral wool (MW) and steel fibre (S)] were added to selected mixtures and embedded into the AAF matrix. Measurements of flexural and compressive strength show that fibres, especially PVA, improve flexural strength (2 MPa).

Microstructural investigation confirmed that cracking was observed in all samples, but this was less noticeable where fibres were better incorporated into the matrix. Furthermore, good incorporation of the fibres or grouping of the fibres in the matrix cause a force resistance in the axial direction, which subsequently causes an improvement in flexural strength. Where equal size and distribution of fibres was established in the matrix the compressive strength was better. PVA and wool fibres significantly increased flexural strength but there are still opportunities to improve the incorporation of fibres into the matrix by selecting the most suitable curing regime (humidity and temperature) in order to decrease lamination and gap formation.

References

1. Yang, K., Lee, K., Song, J., Gong, M.: Properties and sustainability of alkali-activated slag foamed concrete. J. Cleaner Prod. **68**, 226–233 (2014)
2. Abdollahnejad, Z., Pacheco-Torgal, F., Aguiar, J.B.: Cost-efficient one-part alkali-activated mortars with low global warming potential for floor heating systems applications. J. Euro. J. Environ. Civil. Eng. (2016)
3. Gulatieri, M. Lassinatti, Romagnoli, M., Gulatieri, A.F.: Interactive powder mixture concept for the preparation of geoplymers with fine porosity. J. Euro. Ceram. Soc. **35**, 3167–3178 (2015)
4. Ducman, V., Korat, L.: Characteriazion of geoploymer flay-ash based foams obtained with the addition of AL powder or H_2O_2 as foaming agents. Mater. Charact. **113**, 207–213 (2016)
5. Hajimohamadi, A., Ngo, T., Mendis, P., Nguyen, T., Kashani, A., Van Deventer, J.S.J.: Pore characteristics in one part mix geoplymers foamed by H_2O_2: the impact of mix design. Mat. Des. **130**, 381–391 (2017)
6. Bai, C., Ni, T., Wang, Q., Li, H., Colombo, P.: Porosity, mechanical and insulating properties of geopolymers foams using vegetable oil as stabilizing agent. J. Euro. Ceram. Soc. **38**, 799–805 (2018)
7. Papa, E., Medri, V., Natali Murri, A., Laghi, L., De aloysio, G., Bandini, S., Landi, E.: Characterization of alkali donded expanded perlite. Const. Build. Mat. **191**, 1139–1147 (2018)
8. Jensen, O.M., Hansen, P.F.: Autogenous deformation and RH-change in perspective. Cem. Concr. Res. **31**, 1859–1865 (2001)

9. Nedeljković, M., Li, Z., Ye, G.: Setting, strength, and autogenous shrinkage of alkali-activated fly ash and slag pastes: effect of slag content. Materials **11**, 2121 (2018)
10. Mobili, A., Belli, A., Giosue, C., Bellezze, T., Tittarelli, F.: Metakaolin and fly ash alkali-activated mortars compared with cementitious mortars at the same strength class. Cem. Concr. Res. **88**, 198–210 (2016)
11. Lura, P., Jensen, O.M., Van Breugel, K.: Autogenous shrinkage in high-performance cement paste: an evaluation of basic mechanisms. Cem. Concr. Res. **33**, 223–232 (2003)
12. Mastali, M., Kinnunen, P., Isomoisio, H., Karhu, M., Illikainen, M.: Mechanicanical and acoustic properties of fiber-reinforced alkali-activated slag foam concretes containing lightweight structural aggregates. Const. Build. Mat. **187**, 371–381 (2018)
13. Chen, H., Zhang, W., Wang, X., Eang, H., Wu, Y., Zhong, T., Fei, B.: Effect of alkali treatment on wettability and thermal stability of individual bamboo fibers. J. of Wood Sci. **64**, 398–405 (2018)
14. Li, X., Wang, L., Wang, X.: Compressive and flexural properties of hemp fibre reinforced concrete. Fibres Polym. **5**, 187–197 (2004)
15. Alomayri, T., Shaikh, F.U.A., Low, I.M.: Characterisation of cotton fibre-reinforced geopolymer composites. Composites: Part B **50**, 1–6 (2013)
16. Lin, X., Silsbee, M.R., Roy, D.M., Blankenhorn, P.R.: Approaches to improve the properties of wood fibre reinforced cemetious composites. Cem. Conr. Res. **24**, 1558–1566 (1994)
17. Almeida, F., Cunha, V.M.C.F., Miranda, T., Cristelo, N.: Indirect tensile behaviour of fibre reinforced alkali-activated composites. Fibers **6**(2), 30 (2018)
18. Abdulkareem, M., Havukainen, J., Horttaniainen, M.: How environmentally sustainable are fibre reinforced alkali-activated concrets? J. Clean. Prod. **236**, 117601 (2019)
19. Sivakumar, A., Srinivasan, K.: High performance fibre reinforced alkali activated slag concrete. Int J. Civil Env. Engine. **8**, 1288–1291 (2014)
20. Puertas, F., Gil-Maroto, A., Palacios, M., Ampat, T.: Alkali-activated slag mortars reinforced with ar glassfibre. Performance and properties. Mat. de Const. **56**(283), 79–90 (2006)
21. Wang, L., Tan, X.: Preparation and properties of alkali activated foam cement reinforced with polypropylene fibers. J. Wuhan Uni. Tech.-Mater. Sci. Ed. **26**, 960–964 (2011)
22. Nguyen, H., Kaas, A., Kinnunen, P., Carvelli, V., Monticelli, C., Yliniemi, J., Illikainen, M.: Fiber reinforced alkali-activated stone wool composites fabricated by hot-pressing technique. Mat. Des. **186**, 108315 (2020)
23. Gonclaves, J.R.A., Boluk, Y., Bindiganavile, V.: Crack growth resistance in fibre reinforced alkali-activated fly ash concrete exposed to extreme temperatures. Mater. Struct. **51**, 42 (2018)
24. Češnovar, M., Traven, K., Horvat, B., Ducman, V.: The potential of ladle slag and electric arc furnace slag use in synthesizing alkali activated materials; the influence of curing on mechanical properties. Materials **12**, 1173 (2019)
25. Rickard, W.D.A., Vickers, L., van Riessen, A.: Performance of fibre reinforced, low density metakaolin geopolymers under simulated fire conditions. Appl. Clay Sci. **73**, 71–77 (2013)

Utilization of Biochar as a Multifunctional Additive in Cement-Based Materials

Muhammad Intesarul Haque, Rakibul Islam Khan, Warda Ashraf, and Hemant Pendse

Abstract This article presents an experimental study on the application of processed biochar as a partial replacement of cement. Raw biochar was chemo-mechanically modified to produce super-hydrophobic carbonaceous powder (SHCP). The effects of this SHCP on paste and mortar samples were monitored in terms of compressive strength, hydration products, electrical conductivity, water absorption, and embodied carbon. The performances of the mortar samples were monitored after 7 and 28 days of sealed curing. SHCP primarily worked as inert inclusion and did not significantly affect the cement hydration. Nevertheless, the addition of SHCP as partial replacement of cement was found to decrease the water sorption, increase the electrical conductivity, and decrease the embodied carbon of the mortar samples. As such, this study provided experimental evidence that biochar can be utilized as a multifunctional additive in cement-based composites.

Keywords Biochar · Hydrophobic · Electrical conductivity · Carbon sequestration

1 Introduction

Ordinary Portland Cement (OPC) industry is one of the most energy-intensive manufacturing industries [1]. One ton of cement production is responsible for 0.9 to 1.1 tons of CO_2 emissions to the environment [2, 3]. In addition to this, OPC-based concrete suffers from several durability damages, including freeze-thaw attack, chloride-induced corrosion, etc., which reduce the longevity of this widely used construction material. To promote the development of sustainable infrastructures

M. I. Haque · R. I. Khan · W. Ashraf (✉)
Department of Civil Engineering, Center for Advanced Construction Materials (CACM),
University of Texas at Arlington, Arlington, USA
e-mail: warda.ashraf@uta.edu

H. Pendse
Forest Bioproducts Research Institute (FBRI), University of Maine, Orono, USA

with limited resources, there is a need to focus on alternative pathways that can lead to enhanced longevity and functionality of cement-based composites. Along this line, this article presents the potential application of biochar in cement-based composite to enhance its self-sensing capability, reduced water permeability, and reduced embodied carbon.

Biochar is a co-product of the biomass pyrolysis process where the thermochemical decomposition of biomass occurs at an elevated temperature and without the presence of external oxygen [4]. The pyrolysis of biomass causes water evaporation followed by the release of volatile components, and eventually, a porous-solid product remains with very high carbon content. The volatile components can be extracted as bio-fuel and the remaining solid carbonaceous product is addressed as biochar [5]. Such a pyrolysis process takes place at a wide temperature range of 350–700 °C [5]. Usually, the carbon, hydrogen, and oxygen contents of biochar are within the ranges of 45−60%, 2−5%, and 10−20% by weight, respectively [5].

While biochar mostly used for soil amendment [6], a series of recent researches also focused on the potential application of biochar in construction materials, including asphalt [7] and cement concrete [8]. Biochar can be used to sequester carbon in cement-based material and thus, can reduce the global warming potential (GWP) of concrete [9]. Due to the high water absorption capacity, biochar can also be used as an internal curing agent in high-performance concrete [10]. Nevertheless, in most of the previous studies, biochar was used only in a small amount (i.e., $\sim 2\%$ by weight of cement [9]) which may not offer an effective approach for substantial reduction of the carbon footprint of concrete. Further, the addition of biochar in concrete without adequate surface modification can affect the entrained air content due to the organic carbon present in this material. Accordingly, the goal of this study was to modify biochar in such a way that it can enhance the longevity, sustainability, and electrical properties of cement-based composites. Therefore, this article presents the effort to develop a multifunctional additive for cement-based composites using a low-cost industrial byproduct—biochar.

2 Materials and Mix Design

2.1 Biochar Production and Processing

To achieve the multifunctionality of biochar, a chemo-mechanical modification was followed. The goal was to modify the surface area of biochar, so as to reduce its water absorption. The hydrophobicity of biochar depends on the presence of surface aliphatic groups and can be controlled by the pyrolysis temperature [11]. Nevertheless, for this study, hydrophobicity of biochar was enhanced by using stearic acid ($C_{17}H_{35}CO_2H$). Raw biochar was first mixed with 4% by wt. stearic acid and then ground in a high-shear ball mill for three hours. Stearic acid worked

as a grinding aid resulting in a very fine particle size distribution ($\sim \mu$m) with super-hydrophobic surface characteristics of the biochar. Biochar processed in this way addressed as a super-hydrophobic carbonaceous powder (SHCP) for the remainder of this article (Fig. 1).

2.2 Sample Preparation and Experimental Methods

A total of three mortar batches were prepared to investigate the effects of biochar as a partial replacement of cement. The cement replacement levels with SHCP in these batches were 0% (control batch), 5%, and 10%. The water to binder (cement + SHCP) ratio was 0.42 and the cement to fine aggregate ratio was 2.75 for all the batches. River sand was used as fine aggregate in mortar samples.

Strength. Compressive strengths of 50 mm cubes samples were determined as per ASTM C109 [12] after 7 and 28 days of sealed curing. Sealed curing was achieved by wrapping the mortar samples with plastic sheets and then the samples were stored at a temperature around 23 $\pm$ 2 °C.

Thermogravimetric analysis. The effects of SHCP on cement hydration and microscopic phase formation was determined by performing the thermogravimetric analysis (TGA) of the paste samples after 28 days of curing. Paste samples were prepared by mixing cement and SHCP with water (water to binder ratio = 0.42).
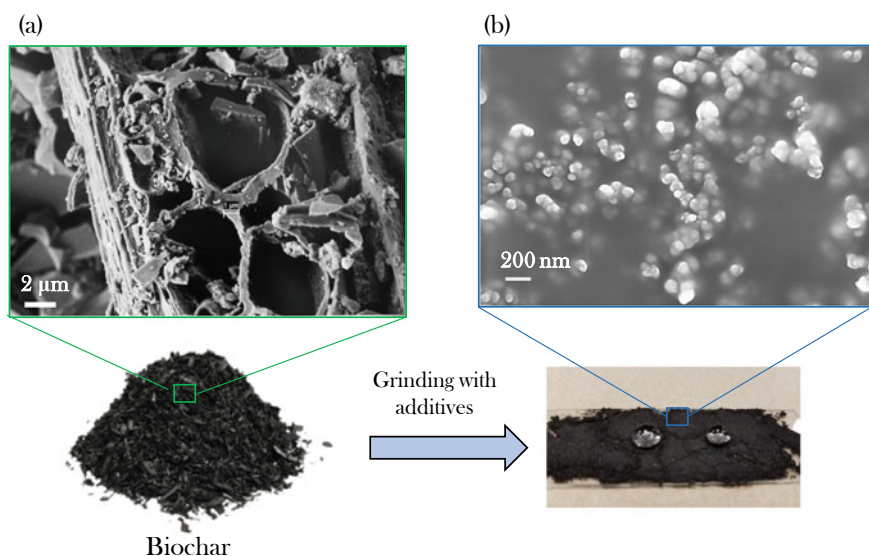

Fig. 1 SHCP preparation from biochar: **a** SEM image showing microstructure of raw biochar, **b** SEM image showing morphology of SHCP

Details of this test procedure can be found elsewhere [13]. Quantitative amounts of chemically bound water in C–S–H and $Ca(OH)_2$ in the hydrated cement paste samples were determined from this test.

CO$_2$ Stored. Replacement of OPC by SHCP in cement-based materials will decrease the total consumption of OPC and thus, reducing the embodied carbon of mortar samples. Further, biochar contains around 40–60% by weight of carbon and using it in cement-based materials ensures sequestration of this carbon which cannot get back to the atmosphere for a long time. Both factors were considered to estimate the relative reduction of carbon footprint due to the usage of biochar as a partial replacement of cement.

Electrical Conductivity. Due to the high carbon content of biochar, it was hypothesized that the addition of biochar in mortar samples will increase the electrical conductivity of these samples. To test this hypothesis, resistivities and conductivities of the mortar cube samples were measured after 7 and 28 days of sealed curing. First, the resistance of the samples was measured as per the two-pole method using a commercially available instrument (Giatec RCON). The resistivity and conductivity of the samples were then calculated using Eq. 1 and Eq. 2, respectively.

$$\text{Resistivity, } \rho = RA/L \tag{1}$$

where, R = resistance, A = cross-sectional area of the sample and L = length between the top and bottom plates for resistance measurement.

$$\text{Conductivty, } \sigma = 1/\rho \tag{2}$$

Water Absorption. Water absorption of mortar samples due to the addition of SHCP was performed as per the modified ASTM C1585 method. This experiment was performed on mortar cube samples, whereas the original test method requires cylindrical concrete samples. After 28 days of sealed curing, the samples were first stored in a 50% RH and 50 °C chamber for 3 days and then it was again stored in another sealed bag for 15 days to stabilize the internal humidity. After this conditioning period, all sides of 50 mm mortar cube samples, except the top and bottom surfaces, were sealed with adhesive tape. Then the bottom surface of the mortar cube was submerged in water (approximate submersion depth = 2.5 mm) and the weight gain of the sample was monitored at a regular interval unto 9 days. The water absorptions of the samples were determined from weight gain using the following equation:

$$\text{Absorption, } I = (M_t - M_0)/Ad \tag{3}$$

where,

M_t = Mass of the sample at a time, t
M_0 = Initial mass of the sample
A = cross-sectional area of the cube sample (50 mm × 50 mm)
d = density of water.

3   Results and Discussion

3.1   Compressive Strength

The compressive strengths of the mortar samples are given in Fig. 2. As observed from this figure, the replacement of cement with SHCP resulted in a reduction of the compressive strength of mortar samples. Specifically, after 7 days of sealed curing the compressive strength of the control batch was around 43 MPa, where the mortar batch containing 10% SHCP resulted in 39 MPa. A similar trend of strength decrease was present even after 28 days of curing. The strength decrease was expected due to the decreased cement content with the increasing SHCP content. Nevertheless, it was apparent that the mortar batch produced with 10% SHCP can still provide more than 85% of the strength of the control batch after 28 days of curing. Whereas, 93% of strength can be achieved even after replacing 5% by weight of cement with SHCP.

Fig. 2 Compressive strength of different mortar batches after 7 and 28 days sealed curing
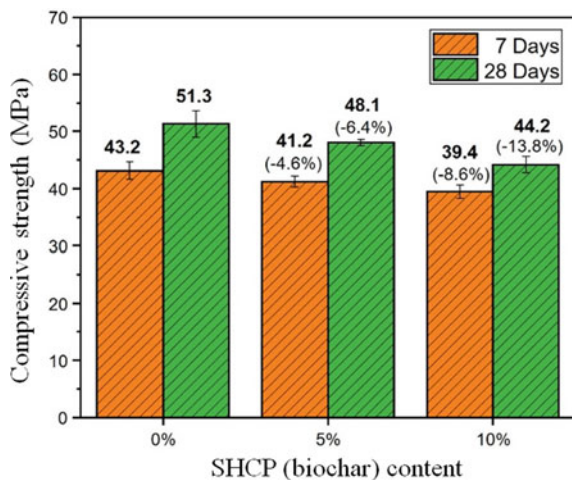
3.2   Thermogravimetric Analysis (TGA)

A typical TGA plot for the cement paste sample containing SHCP is given in Fig. 3a. The weight losses associated with usual cement hydration products including C–S–H, ettringite (AFt), and $Ca(OH)_2$ are marked in this plot as per the literature data [14]. Two additional peaks were observed in the DTG plot of SHCP containing batch, one is around 500 °C indicating a weight gain of the sample and the second one is around 600–800 °C indicating a weight loss. The first peak was attributed to the gas adsorption in biochar particles and the second one is due to the CO_2 released from the oxidation of biochar.

The amount of $Ca(OH)_2$ and chemically bound water of C–S–H present in the hydrated cement paste samples were determined following the approach published elsewhere [13] (Fig. 3b). As it can be observed that at 5% SHCP content, the hydration product was reduced, even though such reduction was not prominent for 10% SHCP content. Moreover, the hydration products per gram of cement were slightly increased at 10% SHCP content. This slight increase in the hydration products at high SHCP content (10%) was attributed to the 'filler effect' of fine biochar particles [8].

3.3   Carbon Footprint Reduction

SHCP helped to reduce the CO_2 emissions by reducing the OPC consumption and by sequestrating carbon in mortar samples. The average fixed carbon content of the SHCP was assumed to be 50% by weight as per the literature data [5]. The fixed carbon was then used to calculate the equivalent CO_2 amount that will be stored
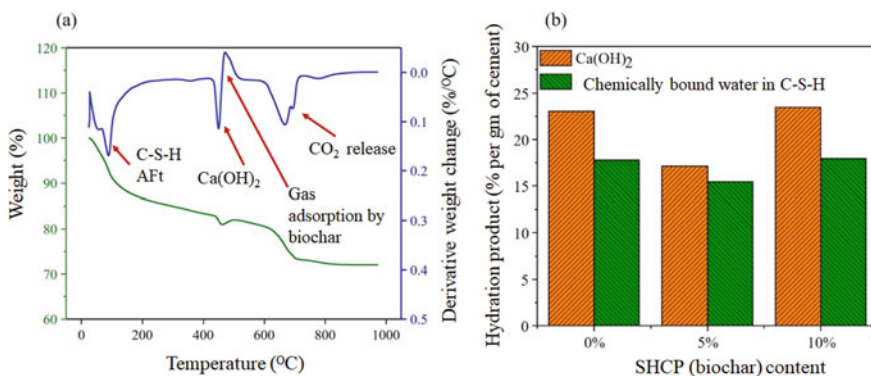

Fig. 3 **a** Typical TGA and DTG plots of cement paste containing SHCP, and **b** cement hydration products in cement paste with different SHCP contents after 28 days of curing

mortar samples due to the use of biochar. Next, a simplified embodied carbon (eCO_2) of the binder mix (cement + SHCP) was calculated considering the control batch as the baseline. The embodied carbon of stearic acid was ignored considering only a small amount of this ingredient used to produce SHCP. The relative embodied carbons (eCO_2) of the binder mix calculated in this approach are given in Fig. 4. Based on this approach, replacing only 5% by weight of cement with biochar can reduce the embodied CO_2 of the binder mixture by more than 14% and for 10% biochar containing batch the reduction was more than 28%.

3.4 Electrical Conductivity

The electrical conductivities of the mortar batches are given in Fig. 5. After 7 days of sealed curing, the electrical conductivities of the mortar batches were enhanced by around 17% and 22% due to the addition of 5% and 10% SHCP, respectively. The electrical conductivities for all batches decreased after 28 days of curing. This is because with the increased degree of hydration the total porosity in the matrix will be reduced, which will then increase resistivity (i.e., decrease conductivity) [15, 16]. The electrical conductivity of the 10% SHCP containing batch was around 33% higher than that of the control batch. Thus, these results indicate that with an adequate amount of biochar, it is possible to enhance the electrical conductivity of the cement-based composite up to an extent that will allow it to use as intrinsic self-sensing construction material [17].
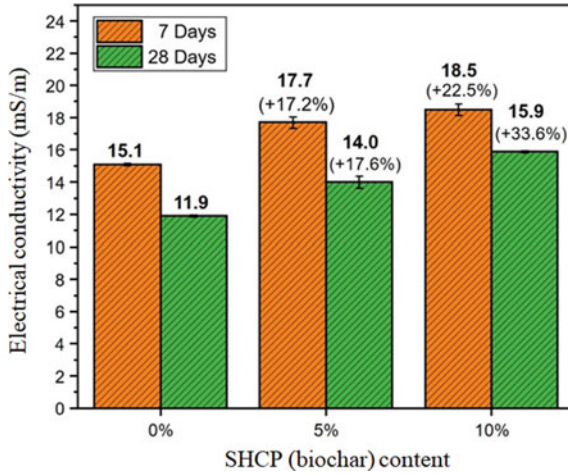
Fig. 4 CO_2 reduction with SHCP content
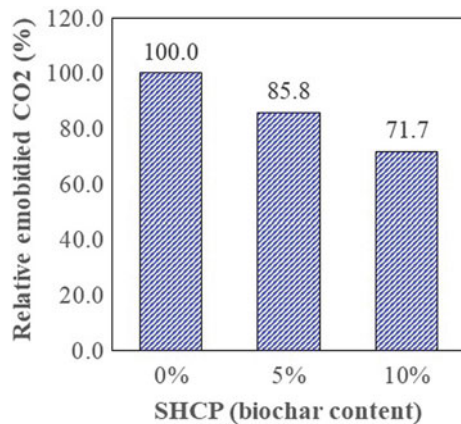
Fig. 5 Electrical conductivity of different biochar batches

3.5 Water Absorption Test

Hydrophobicity is an important physicochemical property that affects the water-retention property of biochar [18]. Biochar has a high internal surface area and a high number of residual pores, where water is retained by capillary force [19]. However, in the case of cement-based materials, lower water permeability is desired to the resistance against freeze–thaw damage, detrimental ionic ingression, etc. As the processed ground biochar is super-hydrophobic, therefore, water absorption of cement-based materials containing this biochar is expected to be lower. To verify this hypothesis and to quantify the effects of adding SHCP, water absorption tests were conducted (Fig. 6).
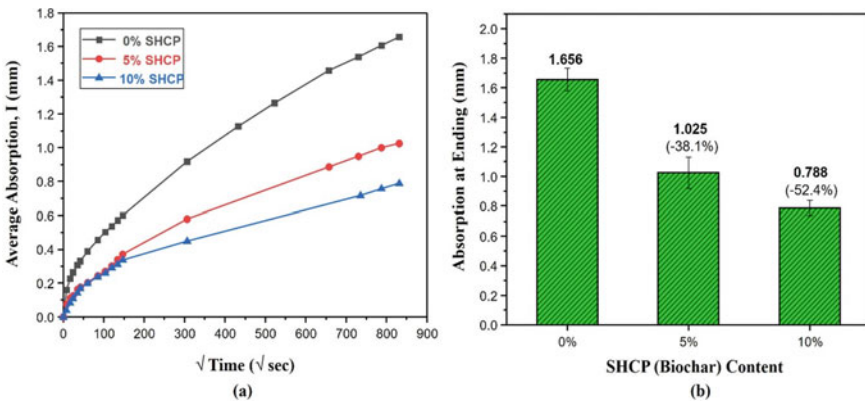
Fig. 6 Water absorption of different biochar batches

It was found that the water absorption was highest for the control batch whereas, the other batches showed relatively lower sorptivity (Fig. 6a). 10% batch showed the least sorptivity as it contained the highest amount of biochar. Specifically, a 10% addition of SHCP reduced the total water absorption by more than 50% at the end of 9 days test duration. Observing the lower water absorption, it is evident that the super-hydrophobic biochar decreased the water permeability of mortar samples.

4   Research Significance and Discussion

The concrete infrastructures often exhibit premature damages due to the durability attacks including freeze-thaw, sulfate attack, reinforcement corrosion. 'Water' is an essential element for all these forms of durability damages; and as such, the damages can be avoided by reducing the moisture transport in concrete. Permeability-reducing admixtures (PRAs [20]) can be used to enhance the performance of concrete. However, commercial PRAs are also known to increase the setting time, decrease the strength of concrete mixes [21, 22] and are less effective in marine environments [23]. The developed SHCP in this study can provide the benefit of reduced water permeability, but at a lower expense as biochar is a byproduct of the biofuel industry. The addition of SHCP reduced the water permeability of mortar samples by inducing surface hydrophobicity and denser microstructure, therefore SHCP acted as a hydrophobic pore blocker. Further, the addition of this processed biochar has shown to enhance the electrical conductivity of cement-based composites by 33%. Electrically conductive concrete has several application sectors including self-sensing composites [24], deicing concrete elements [25], and electromagnetic shielding [26]. For all these applications, processed biochar can be used instead of carbon filler or other carbon nanomaterials. Nevertheless, further study is required to determine the optimum proportion biochar that will result in adequate enhancement of the electrical conductivity of cement-based composites without compromising the strength. Finally, as briefly presented in this article, the utilization of biochar offers an approach of producing cement-based composite with a substantially low CO_2 footprint achieved by sequestering carbon in the matrix.

5   Conclusions

This article presented a methodology to utilize biochar as a multifunctional additive in cement-based materials. Following concluding remarks can be made from this study:

(i)   The addition of SHCP can decrease the water permeability of mortar samples. The total water absorption of mortar was decreased by 53% because of the addition of 10% by weight of SHCP.

(ii) Using SHCP as partial replacement of cement can also enhance the electrical conductivity of the mortar samples. Specifically, 10% by weight of SHCP increased the electrical conductivity by 33%.

(iii) The embodied carbon of a binder mix can be reduced using SHCP. From this work, up to 28% reduction of eCO_2 was achievable by using 10% by weight of SHCP.

(iv) The compressive strength of mortar was decreased with increasing SHCP content. Nevertheless, the reduction of strength was below 14%.

References

1. EIA.: The cement industry is the most energy intensive of all manufacturing industries (2013) https://www.eia.gov/todayinenergy/detail.php?id=11911
2. Golewski, G.L.: Effect of curing time on the fracture toughness of fly ash concrete composites. Compos. Struct. **185**, 105–112 (2018). https://doi.org/10.1016/j.compstruct.2017.10.090
3. Juenger, M.C.G., Winnefeld, F., Provis, J.L., Ideker, J.H.: Advances in alternative cementitious binders. Cem. Concr. Res. **41**, 1232–1243 (2011). https://doi.org/10.1016/j.cemconres.2010.11.012
4. Weber, K., Quicker, P.: Properties of biochar. Fuel **217**, 240–261 (2019)
5. Liu, W.J., Jiang, H., Yu, H.Q.: Development of biochar-based functional materials: toward a sustainable platform carbon material. Chem. Rev. **115**, 12251–12285 (2015). https://doi.org/10.1021/acs.chemrev.5b00195
6. Ali, S., Rizwan, M., Qayyum, M.F., Ok, Y.S., Ibrahim, M., Riaz, M., Arif, M.S., Hafeez, F., Al-wabel, M.I., Shahzad, A.N.: Biochar soil amendment on alleviation of drought and salt stress in plants: a critical review. Environ. Sci. Polut. Res. Int. **24**, 12700–12712 (2017). https://doi.org/10.1007/s11356-017-8904-x
7. Zhou, X., Adhikari, S.: Flow-induced crystallization of biochar in bio-asphalt under various aging conditions. Sci. Total Environ. **695**, 133943 (2019). https://doi.org/10.1016/j.scitotenv.2019.133943
8. Gupta, S., Kua, H.W., Koh, H.J.: Application of biochar from food and wood waste as green admixture for cement mortar. Sci. Total Environ. **619–620**, 419–435 (2018). https://doi.org/10.1016/j.scitotenv.2017.11.044
9. Gupta, S., Kua, H.W., Low, C.Y.: Use of biochar as carbon sequestering additive in cement mortar. Cem. Concr. Compos. **87**, 110–129 (2018). https://doi.org/10.1016/j.cemconcomp.2017.12.009
10. Dixit, A., Gupta, S., Dai, S., Wei, H.: Waste Valorisation using biochar for cement replacement and internal curing in ultra-high performance concrete. J. Clean. Prod. **238**, 117876 (2019). https://doi.org/10.1016/j.jclepro.2019.117876
11. Das, O., Sarmah, A.K.: The love-hate relationship of pyrolysis biochar and water: a perspective. Sci. Total Environ. **512–513**, 682–685 (2015). https://doi.org/10.1016/j.scitotenv.2015.01.061

12. ASTM International: ASTM C109 / C109M - 20b.: Standard test method for compressive strength of hydraulic cement mortars (using 2-in. or [50-mm] cube specimens) Annu. B. ASTM Stand. **04**, 9 (2020)
13. Khan, R.I., Ashraf, W.: Effects of ground wollastonite on cement hydration kinetics and strength development. Constr. Build. Mater. **218**, 150–161 (2019). https://doi.org/10.1016/j.conbuildmat.2019.05.061
14. Scrivener, K., Snellings, R., Lothenbach, B., eds.: A practical guide to microstructural analysis of cementitious materials, 1st edn (2016)
15. Rupnow, T., Icenogle, P.: Surface resistivity measurements evaluated as alternative to rapid chloride permeability test for quality assurance and acceptance. Transp. Res. Rec. (2012). https://doi.org/10.3141/2290-04
16. Azarsa, P., Gupta, R.: Electrical resistivity of concrete for durability evaluation: a review. Adv. Mater. Sci. Eng. (2017). https://doi.org/10.1155/2017/8453095
17. Han, B., Ding, S., Yu, X.: Intrinsic self-sensing concrete and structures: a review. Meas. J. Int. Meas. Confed. **59**, 110–128 (2015). https://doi.org/10.1016/j.measurement.2014.09.048
18. Gray, M., Johnson, M.G., Dragila, M.I., Kleber, M.: Water uptake in biochars: the roles of porosity and hydrophobicity. Biomass Bioenerg. **61**, 196–205 (2014). https://doi.org/10.1016/j.biombioe.2013.12.010
19. Batista, E.M.C.C., Shultz, J., Matos, T.T.S., Fornari, M.R., Ferreira, T.M., Szpoganicz, B., De Freitas, R.A., Mangrich, A.S.: Effect of surface and porosity of biochar on water holding capacity aiming indirectly at preservation of the Amazon biome. Sci. Rep. **8**, 1–9 (2018). https://doi.org/10.1038/s41598-018-28794-z
20. ACI Committee 212, 212.3R-16 Report on Chemical Admixtures for Concrete (2017). https://www.concrete.org/store/productdetail.aspx?ItemID=212310
21. Yurdakul, E.: Concrete pavement mixture design and analysis (mda): evaluation of the fresh and hardened properties of concrete mixtures containing permeability-reducing admixtures to develop a standard testing protocol evaluation of the fresh and hardened properties (2014)
22. Justnes, I.H.: Low water permeability through hydrophobicity 36 (2008)
23. Dao, V.T.N., Dux, P.F., Morris, P.H., Carse, A.H.: Performance of permeability-reducing admixtures in marine concrete structures. ACI Mater. J. **107**, 291–296 (2010). https://doi.org/10.1108/17506200710779521
24. Azhari, F., Banthia, N.: Cement-based sensors with carbon fibers and carbon nanotubes for piezoresistive sensing. Cem. Concr. Compos. **34**, 866–873 (2012). https://doi.org/10.1016/j.cemconcomp.2012.04.007
25. Yehia, S., Tuan, C.Y.: Thin conductive concrete overlay for bridge deck deicing and anti-Icing. Transp. Res. Rec. J. Transp. Res. Board. **1698**, 45–53 (1999). https://doi.org/10.3141/1698-07
26. Yehia, S., Qaddoumi, N., Hassan, M., Swaked, B.: Conductive concrete for electromagnetic shielding applications. Adv. Civ. Eng. Mater. **3**, 20130107 (2014). https://doi.org/10.1520/ACEM20130107

Pore Size Distribution of Cement Based Materials Determined by Dynamic Water Vapor Sorption and Low Temperature Calorimetry

Tian Wang and Min Wu

Abstract In this work, both dynamic water vapor sorption (DVS) and low temperature calorimetry (LTC) methods were adopted to study the pore size distribution of cement pastes prepared by two types of cements CEM I and CEM III. A model porous material, MCM-41, was also included in order to investigate important aspects of the measurement and the data evaluation approaches. As indirect methods for pore structure characterization, important assumptions involved in the data analysis of both methods were highlighted and discussed. In addition, a special attention was paid to the comparison of the results obtained from the two methods. A careful examination of the bases for the two methods for pore structure characterization revealed that a number of matters could affect the obtained results, including sample preparation, possible influencing factors on the measured results, unsolved factors for data analysis, etc. Consequently, the results obtained from one method might differ significantly from the other. Nevertheless, a certain degree of agreement was still found for the pore size distributions determined by the DVS and the LTC methods, despite of the uncertainties involved in each method. Meanwhile, it was concluded that probably none of the two studied methods could deliver the "true" (actual) pore size distribution information at this stage. To further improve the accuracy of the results obtained from the methods, it was highlighted that emphases should be laid on clarifying relevant assumptions made in both measurement and data analysis.

Keywords Pore size distribution · Sorption · Low temperature calorimetry · Cement paste

M. Wu (✉)
Department of Engineering, Aarhus University, 8000 Aarhus, Denmark
e-mail: mnwu@eng.au.dk

T. Wang
Department of Chemical and Biochemical Engineering, Technical University of Denmark, 2800 Lyngby, Denmark

355

1 Introduction

The importance of pore structure to cement and concrete materials can never be overstressed. Apart from being a main parameter which determines the mechanical properties, it is also a major parameter that influences the durability. As is well known, long-term durability is highly desirable for large infrastructures. The design lives for bridge and tunnel structures nowadays typically are longer than 100 years. It should be mentioned that a number of durability problems could be linked to the pore systems of cement/concrete including reinforcement corrosion (e.g. due to the transport of chloride ions and CO_2 gas into the materials) and frost damage, etc. Therefore, accurate characterization of the pore structures can help understand various properties of the concerned materials.

In cement based materials, the pore structures can be rather complicated. Different types of pores with different sizes exist. For instance, mixing and casting often entrap air voids and the sizes can reach millimeters [1]. The sizes of deliberately entrained air voids for frost protection are on the order of 50–100 μm [2]. At the nano-micro scale, "capillary pores" exist, which are the remnants of the interstitial spaces between the unhydrated cement grains [3]. Additionally, there are interlayer spaces, or "gel pores" at the nanometric level, i.e. between the primary particles of the hydration products calcium-silicate-hydrates (C–S–H) [4]. Among the different pores, it has been demonstrated that the transport properties of mature cement based materials are dominated by the so-called "mesopores" [5], with the characteristic sizes between 2 and 50 nm according to the IUPAC definition [6].

Because of the paramount importance, considerable efforts have been devoted to understanding the pore structures of cement based materials. The representative characterization methods include, e.g. nitrogen adsorption/desorption (NAD), mercury intrusion porosimetry (MIP), scanning electron microscopy (SEM), small angle scattering using X-rays or neutrons and nuclear magnetic resonance (NMR) [7]. A brief discussion of the merits and limitations of the typical methods can be found, e.g. in [7].

In this work, dynamic water vapor sorption (DVS) and low (micro-)temperature calorimetry (LTC) were used to investigate the pore size distribution (PSD) of cement based materials, especially at the nanometric level. Compared with traditional methods, e.g., NAD, MIP and SEM, a major advantage shared by the DVS and LTC methods is that the measurements can be conducted on virgin samples without any pre-drying treatment. This is important, since pre-drying treatment may alter the cement pore structures [8]. Advantages of LTC include also the possibility of using short measurement time and it involves a relatively simple sample preparation procedure [9]. By using the DVS instrument combined with data extrapolation processing, the measurement time for obtaining a sorption isotherm can be shortened to make the overall process more effective [10]. However, it should also be mentioned that both DVS and LTC are indirect methods for pore structure characterization. Special attention has to be paid to the measurement and the data analysis procedures, as a number of factors can affect the final results

[7, 10–15]. By including both methods in this work, one intention was to validate if the results obtained from one method can be compared with that from the other. In addition, the comparability of the results may also indicate the accuracy of the two methods to some extent.

2 Important Considerations

2.1 Dynamic Water Vapor Sorption (DVS)

When a porous material is placed into an environment, moisture exchange will occur if there is a gradient on the relative humidity (RH) between the material and the environment until the equilibrium condition is established. The relation between the moisture content and the RH is usually referred to as a sorption isotherm, which may be recorded by a DVS instrument. The sorption behavior is closely related to important properties of the concerned material, e.g. the specific surface area and pore size distribution [16].

For the pore size calculation from the DVS measured results, the BJH model [17] may be adopted. The BJH model assumes two types of water in a pore system, i.e. the adsorbed water and the capillary condensed water. However, the sorption measurement itself cannot distinguish between these two types of water and it only measures the total moisture content at a given RH. That is, the thickness of the adsorbed layer of water, or the so-called t-curve, needs to be determined by some complementing approach in order to make the PSD calculation possible. Several t-curves have been proposed for water vapor. In this work, the Hagymassy et al. curve [18] and the J-BET-curve [19] are used for the calculations. Another important assumption which may significantly affect the obtained PSD results is the assumed meniscus curvature during the capillary condensation processes. It is generally agreed that it is $2/r_k$ during desorption process, while both $1/r_k$ and $2/r_k$ have been proposed for absorption process, where r_k is the Kelvin radius [16]. The impact of the different assumptions will be further illustrated in Sect. 4. Refer to [19] for more details on the calculation.

As an indirect method for pore size characterization, there are quite some limitations and unsolved factors, some of which are summarized in Table 1.

2.2 Low Temperature Calorimetry (LTC)

LTC is a calorimetric method for pore structure characterization by analyzing the transient heat flow during the phase transition processes. The freezing/melting point of water/ice confined in small pores is lower than that of the bulk state. The magnitude of this freezing/melting temperature depression is closely related to the

Table 1 Matters of consideration of the DVS and the LTC methods for the pore structure characterization of cement based materials

Item	DVS	LTC
Sample preparation	The samples must be crushed and/or ground into powders, with the consequence that the pore connectivity becomes seriously affected	Testing samples must be fully saturated. If not, not only the pore volume but also the estimation of the pore sizes will be misinterpreted
Pore size range	(1) Micropores with radii corresponding to a few water molecule's thickness may not be detected. (2) The upper limit of reliable pore radius that can be analyzed is about 30 nm	(1) Pores with radii smaller than that of the un-freezable water layer cannot be detected. (2) The upper limit of reliable pore radius that can be analyzed is about 40–50 nm
Influencing factors on the measured results	(1) The network effect influences the desorption curves. (2) Delayed condensation and possibly advanced absorption affect the absorption curves	(1) Supercooling and network effect influence the heat flow curves of the freezing processes. (2) Advanced melting affects the heat flow curves of the melting processes
Factors not fully solved	(1) The thickness of the adsorbed layer. (2) The meniscus curvature during absorption, i.e. $1/r_k$ or $2/r_k$ (r_k is the Kelvin radius). (3) The computation of pore sizes, especially for the micropores. (4) Applicability of the Laplace equation at the nanometric level	(1) Temperature dependent heat of fusion. (2) The solid–liquid surface tension. (3) The applicability of the thermodynamic parameters at the nanometric level. (4) The thickness of the un-freezable layer, ions effect and thermal lag
Other issues	(1) The pore structure may change at low RHs. (2) A rather long waiting time for the equilibrium conditions at a RH to be established	(1) Homogenous nucleation leads to the pore entry radii smaller than about 2.4 nm not distinguishable. (2) Effects due to frost damage

size of the pores where the phase transition takes place. If a porous material is saturated, the amount of the water confined in the pores can be a measure for the pore volume. Moreover, thermodynamically there is a relation between the freezing/melting temperature of the confined water/ice and the pore sizes. By making some important assumptions, e.g. regarding the surface energies and its geometrical configurations, the pore size corresponding to each freezing/melting temperature can be determined.

To translate the measured heat flow values to PSD results, several steps are needed and important assumptions have to be made, e.g. the thickness of the so-called un-freezable layer. Details of the PSD calculations can be found in [7, 11].

Similar to the DVS method, LTC is also an indirect method for pore size characterization. Typical limitations and unsolved factors of the method are summarized and compared with that for the DVS in Table 1.

3 Experimental and Data Analysis Methods

3.1 Materials

Three materials were studied, i.e. one model mesoporous material MCM-41 and two types of hardened cement pastes. The primary purpose of including the model material was to validate relevant aspects of the measurement and the data evaluation approaches.

With the pore structure in the form of hexagonal arrays of uniform tubular channels of controlled width, MCM-41 is often used as a model material in pore structure studies. The nominal pore diameter of the MCM-41 provided by the producer (Tianjin Chemist Scientific Ltd.) is 3.0 nm and the nominal specific surface area and the total pore volume are reported to be ≥ 800 m^2/g, ≥ 0.70 ml/g, respectively.

Two types of cements, i.e., CEM I 32.5 R and CEM III/B 42.5 N, were used to prepare the paste samples with a water/cement ratio of 0.4. The properties and the chemical compositions of the cements are shown in Table 2. A paddle mixer was used for the mixing. After that, the fresh pastes were cast into plastic vials (ϕ15 50 mm) with proper compaction. After one day of sealed curing at room temperature (about 20 °C) in the plastic vials, the paste samples were demolded. Then, each paste sample was placed into a bigger self-sealable plastic flask filled with saturated limewater for curing at room temperature until the desired testing ages.

Table 2 Properties and the chemical compositions of the cements used in this study

		CEM I (CEM I 32.5 R)	CEM III (CEM III/B 42.5 N)
Density	(g/cm^3)	3.06	2.90
Fineness	(cm^2/g)	2905	4635
Water demand	(%)	26.2	32.3
Initial setting time	(min)	185	270
Loss on ignition	(%)	2.1	1.4
SiO$_2$	(%)	20.6	29.2
Al$_2$O$_3$	(%)	5.6	8.9
Fe$_2$O$_3$	(%)	2.4	1.2
CaO	(%)	63.4	48.0
MgO	(%)	1.6	4.8
SO$_3$	(%)	2.9	2.6
K$_2$O	(%)	0.7	0.6
Na$_2$O	(%)	0.2	0.2
Cl	(%)	<0.1	<0.1

3.2 DVS Measurements

The sample size that can be used in a DVS instrument is relatively small (on the order of milligrams). That is, crushing and/or even grinding of the hardened cement paste samples is needed. After curing for about 6 months, the prepared cylinder paste samples were firstly vacuum saturated with limewater and then the crushing and grinding of the samples was conducted in a carbon dioxide free chamber to avoid carbonation. The RH inside of the chamber was set at 1 (the measured RH was about 0.90–0.95). The sample crushing and grinding was conducted rather quickly (in 30–40 min). Immediately after that, the ground sample powders were placed into plastic flasks containing saturated limewater (for about a week) before the sorption experiments. This procedure was also conducted in the carbon dioxide free chamber.

The measurements were conducted in a climate incubator at 25 °C. The RH was generated into the desired proportions by mixing two airflows, i.e. a totally dry (RH = 0) and a totally saturated (RH = 1) air. The proportions of the two flows can be accurately controlled by the flow regulator devices. The duration time of each RH step in the DVS instrument was controlled by setting the mass change ratio against time, dm/dt at 0.002% (of the initial mass). Then an extrapolation procedure was adopted to estimate the moisture content under the equilibrium condition. This is based on the consideration that practically it is almost impossible to wait for the establishment of the exact equilibrium conditions. More details about the instrument and measurement aspects can be found, e.g. in [19].

3.3 LTC Measurements

The instrument used for this study was a Calvet-type scanning calorimeter (SETARAM). The calorimeter was calibrated and operated to work between 20 and −130 °C. The cooling and heating rate was set to 0.1 °C/min. A freezing and melting cycle consisted the temperature scanning starting from about 20 °C and going down to about −80 °C and then back to about 20 °C again.

For the ease of handling powder MCM-41 samples in the calorimetric measurements, a cylindrical plastic vial was used as a sample holder. The size of the plastic vials ($\phi 14 \times 48$ mm) was chosen to fit the measuring chamber of the calorimeter. The MCM-41 powders were placed into the plastic vials up to about half the volume (the dry weight was about 0.2 g) and then covered with distilled water. In order to saturate the samples, the plastic vials containing powders were placed under a reduced pressure ~ 40 mbar) for about 3 h. After that, the apparent excess bulk water on top of the powders was removed and the samples were stored in closed containers for 2–3 weeks before the calorimetric measurements.

For the cement pastes, powder samples were used for the LTC measurements, i.e. to keep the consistence with the sample type as used in the DVS measurements.

The prepared cylinder samples (as described in Sect. 3.1) were used to obtain the powder samples. The crushing and grinding procedure was similar to that for the DVS sample preparation. The water saturation procedure was the same as that for the MCM-41 samples. The total curing time for the paste samples was about one year when the measurements were performed.

4 Results and Discussions

The PSD curves calculated from the measured DVS and LTC data are compared in this section. Since the choice of water meniscus curvature during the absorption process is somewhat arguable, i.e., $1/r_k$ or $2/r_k$ (Sect. 2), both assumptions are included in the comparison. Due to the occurrence of rather significant supercooling in the freezing process of the LTC measurements, the pore size information that can be obtained from the freezing curve is limited, i.e. between about 2.4 nm to about 5–6 nm. Therefore, only the PSD results calculated from the LTC melting curve are presented.

   The comparison of the determined PSD curves for the MCM-41 is presented in Fig. 1. The R_{max} corresponding to the peak in the calculated PSD curves, i.e. the most frequently occurring pore size, determined from the LTC melting curve and the desorption isotherm is about 1.7 nm and 1.8 nm, respectively. On the other hand, the R_{max} determined from the absorption isotherm is about 1.4 nm and 2.4 nm using the meniscus curvature of $1/r_k$ and $2/r_k$, respectively. It is generally agreed that a LTC freezing curve indicates pore entry sizes, while a melting curve represents the pore interior size information [7]. Then the PSD curve determined from a LTC melting curve should be compared with that determined from the absorption [6]. However, for the studied MCM-41, the result is that the R_{max} from the LTC melting curve (1.7 nm) differs rather significantly from that obtained from the absorption isotherm, i.e., 1.4 nm (assuming curvature as $1/r_k$) and 2.4 nm (assuming curvature as $2/r_k$). In this case, the R_{max} determined from the LTC melting curve is more close to the value obtained from the desorption isotherm (1.8 nm). Similar conclusions can be obtained by using other t-curves in analyzing the sorption data, indicating the calculated PSD curves for the model material MCM-41 is not very sensitive to the different considered t-curves.

   It has been a long debate on which isotherm (desorption or absorption) should be used for the pore size calculation in sorption studies when hysteresis is present. For many years, desorption isotherms were considered to be more thermodynamic stable and therefore, it was thought to be more appropriate to use desorption isotherms to determine the pore size distribution [20]. The drawback of this concept has been demonstrated by taking the network theory into consideration [21], in which it was concluded that desorption isotherms only reflect the pore entry or neck sizes. It was clearly stated in the IUPAC report [6] that it is impossible to provide unequivocal recommendations in the absence of detailed knowledge about the geometry of the pores under study. However, it seems to be more and more
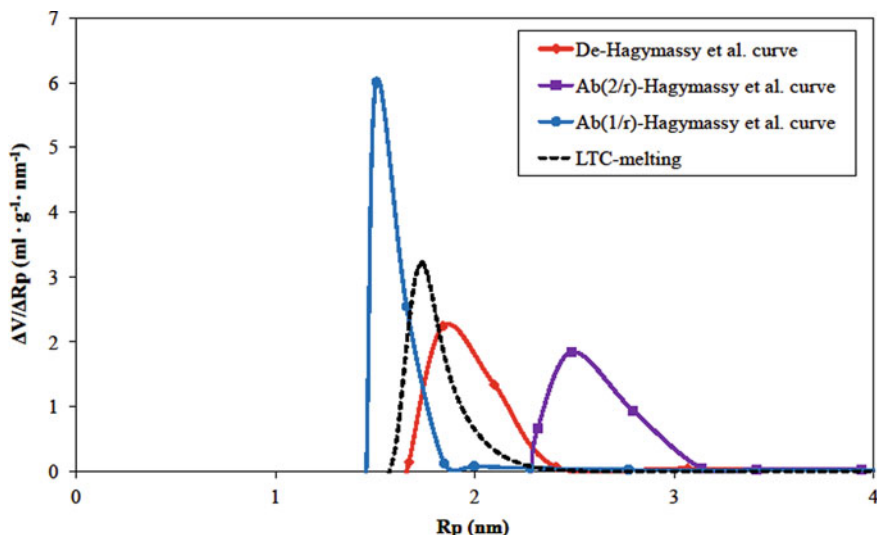
Fig. 1 PSD curves determined from the DVS and LTC methods for the MCM-41. The t-curve used in the sorption PSD calculations is the Hagymassy et al. curve [18]. "De" or "Ab" indicates the desorption or the absorption isotherm is used in the calculation. Ab(1/r) represents that the meniscus curvature during absorption is assumed to be $1/r_k$ and Ab(2/r) represents $2/r_k$

accepted that the calculation using absorption measurements may be more representative for the "true" or pore interior sizes, while the calculation from the desorption isotherms is more related to the network effect (or the pore entry/neck sizes). The results obtained in this study on the MCM-41 seems to support the use of desorption isotherms for interior pore size calculation. However, it should be stressed that this is not conclusive, as many other uncertainties, e.g. the thickness of the un-freezable layer assumed in the LTC analysis [7], may change the picture completely. This is especially true when considering the differences between the R_{max} values obtained from the desorption and absorption isotherms are not that significant.

The comparison of the determined PSD curves for the cement pastes CEM I and CEM III are presented in Figs. 2 and 3, respectively. Hagymassy et al. t-curve [18] was adopted in the calculations. Compared with the results for the MCM-41, the most important difference is that the magnitude of PSD curve corresponding to R_{max} obtained from the desorption isotherms are much higher than that obtained from both the absorption isotherm and the LTC melting curve. Similar to that obtained for the MCM-41, the R_{max} determined from the LTC melting curve (1.7 nm) is more close to that obtained from the desorption isotherm (1.4 nm). In comparison, the values obtained from the absorption isotherm are 1.9 nm (assuming meniscus curvature as $1/r_k$) and 3.2 nm (assuming meniscus curvature as $2/r_k$). In addition, the differences between the specific values of the R_{max}, i.e. that determined the LTC melting curve, the desorption isotherm and the absorption
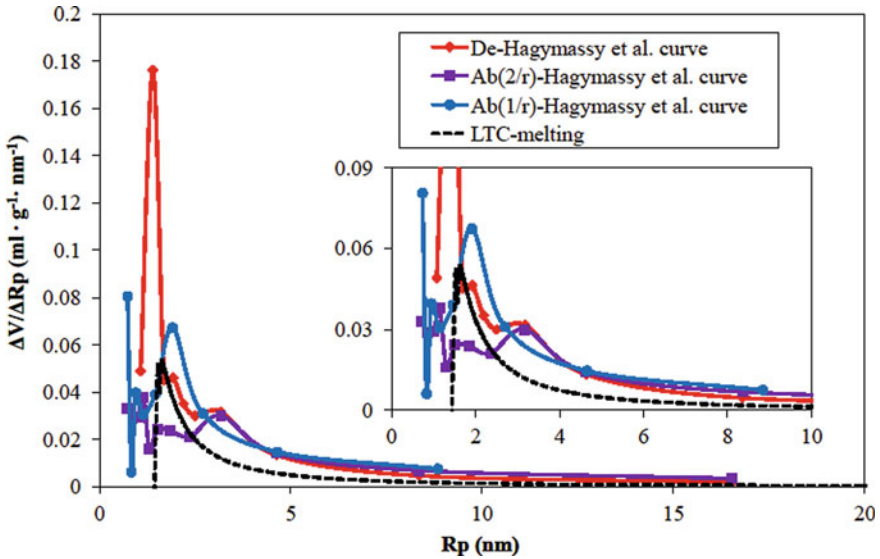
Fig. 2 PSD curves determined from the DVS and LTC methods for the paste CEM I. The t-curve used in the sorption PSD calculations is the Hagymassy et al. curve [18]. "De" or "Ab" indicates the desorption or the absorption isotherm is used in the calculation. Ab(1/r) represents that the meniscus curvature during absorption is assumed to be $1/r_k$ and Ab(2/r) represents $2/r_k$

isotherm are different when compared with that for the MCM-41. Similar conclusions as drawn for the paste CEM I are also applicable for the paste CEM III, except that there is no dominant peak corresponding to R_{max} for the paste CEM III when the meniscus curvature during absorption is assumed to be $2/r_k$ (Fig. 3).

To evaluate the sensitivity of the PSD calculations from sorption data to the assumed t-curves for the cement pastes, the J-BET curve [19] was also used in the calculations. The comparison of the calculated results are presented in Fig. 4 and 5. By using the J-BET curve, the peak corresponding to R_{max} for the paste CEM I becomes less pronounced compared with that obtained using the Hagymassy t-curve. For the paste CEM III, the peak corresponding to R_{max} becomes more well defined compared with that using the Hagymassy et al. t-curve. Other main features of the results obtained using Hagymassy et al. t-curve as discussed above are also applicable to the results obtained using the J-BET t-curve.

Due to the limitations of currently available techniques in pore size characterization, the exact values of the "true" (actual) pore sizes of a concerned material cannot be obtained. By using different measurement techniques, e.g. DVS and the LTC as adopted here, a fitting parameter may be used, e.g. the thickness of the un-freezable layer. Such a fitting parameter can be used to match the pore size distributions obtained from the two separate methods. However, due to the unsolved factors in sorption studies, e.g. the assumed meniscus curvature during the absorption, it may make the adjustment of the thickness of the un-freezable layer
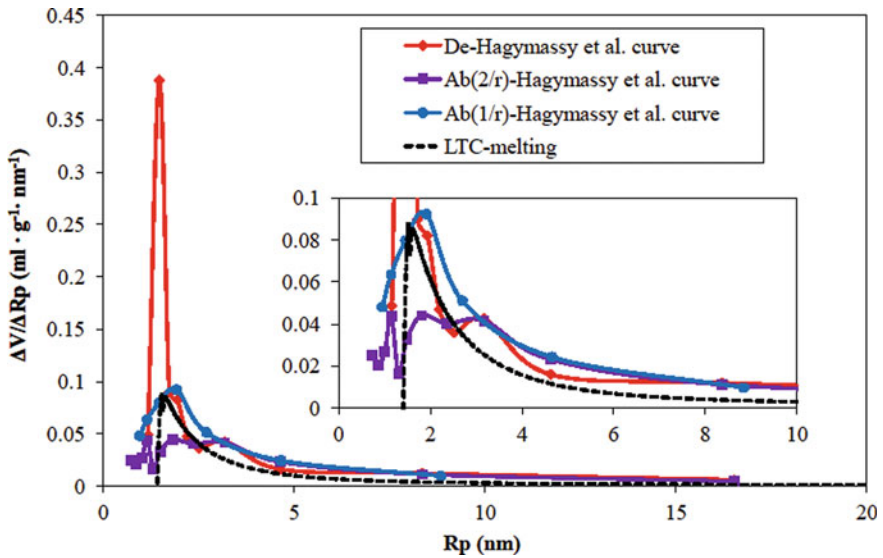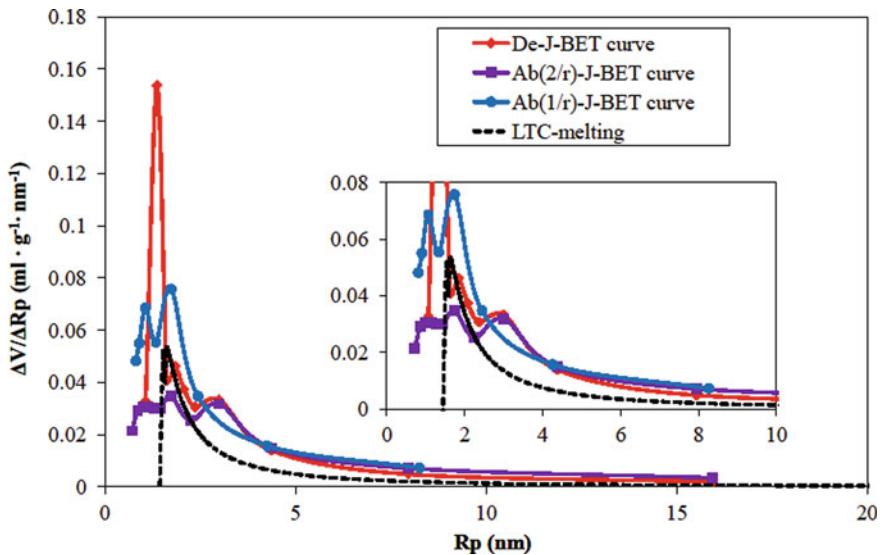
Fig. 3 PSD curves determined from the DVS and LTC methods for the paste CEM III. The t-curve used in the sorption PSD calculations is the Hagymassy et al. curve [18]. "De" or "Ab" indicates the desorption or the absorption isotherm is used in the calculation. Ab(1/r) represents that the meniscus curvature during absorption is assumed to be $1/r_k$ and Ab(2/r) represents $2/r_k$
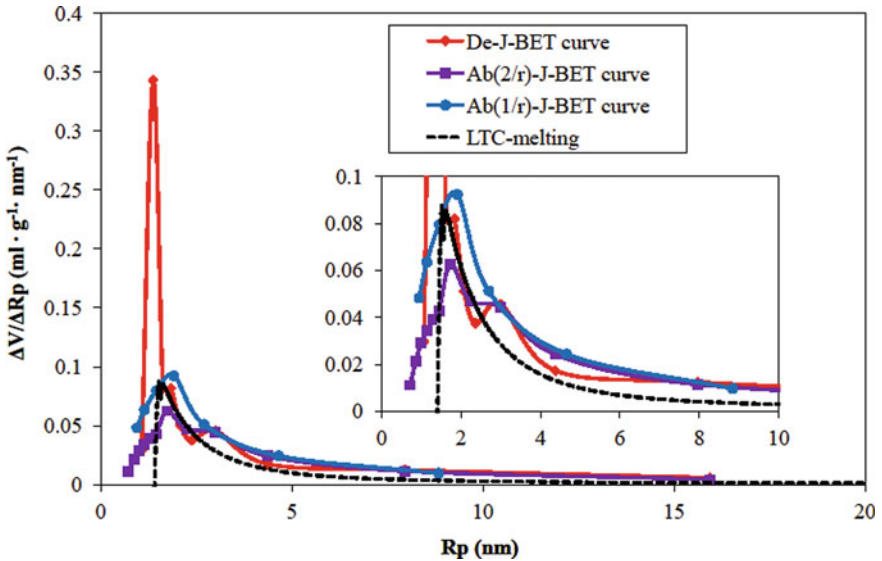

Fig. 4 PSD curves determined from the DVS and LTC method for the paste CEM I. The t-curve used in the sorption PSD calculations is the J-BET curve [16]. "De" or "Ab" indicates the desorption or the absorption isotherm is used in the calculation. Ab(1/r) represents that the meniscus curvature during absorption is assumed to be $1/r_k$ and Ab(2/r) represents $2/r_k$

Fig. 5 PSD curves determined from the DVS and LTC method for the paste CEM III. The t-curve used in the sorption PSD calculations is the J-BET curve [16]. "De" or "Ab" indicates the desorption or the absorption isotherm is used in the calculation. Ab(1/r) represents that the meniscus curvature during absorption is assumed to be $1/r_k$ and Ab(2/r) represents $2/r_k$

little meaning. That is, it is somewhat difficult to make the pore sizes determined by the two methods absolutely fit even for a simple model material (such as the MCM-41). For cement based materials, the pore systems are much more complicated than that of model materials and more unsolved factors come into the picture (Table 1). Of this reason, it becomes even more challenging to make the PSD results determined by the two methods to agree by using parameter fitting only.

5 Conclusions

The current work tried to study the pore size distributions of hardened cement pastes using both DVS and LTC methods. As indirect methods for pore size characterization, it was discussed that a number of matters can affect the obtained results including sample preparation, possible influencing factors on the measured results, unsolved factors for data analysis, etc. Consequently, the results obtained may only be semi-quantitative and remain valuable mainly for comparison purposes.

Nevertheless, a certain degree of agreement was still found for the pore size distributions determined by the two methods, despite of the un-certainties involved in each method. Meanwhile, it should be stressed that probably none of the two

studied methods could deliver the "true" (actual) pore size distribution information based on existing knowledge. To further improve the accuracy of the results, emphases should be laid on clarifying relevant assumptions made in both measurement and data analysis for the concerned methods.

References

1. Kosmatka, S., Panarese, W.: Design and Control of Concrete Mixtures, 14th edn. Portland Cement Association, Illinois, USA (2002)
2. Pigeon, M., Pleau, R.: Durability of concrete in cold climates, 4th edn. Taylor & Francis, Abingdon, UK (1995)
3. Powers, T., Brownyard, T.: Studies of the physical properties of hardened Portland cement paste. ACI J. Proc. **43**, 549–602 (1947)
4. McDonald, P., Rodin, V., Valori, A.: Characterisation of intra-and inter-C-S-H gel pore water in white cement based on an analysis of NMR signal amplitudes as a function of water content. Cem. Concr. Res. **40**, 1656–1663 (2010)
5. Scherer, G., Valenza, I, John, J., Simmons, G.: New methods to measure liquid permeability in porous materials. Cem. Concr. Res. **37**, 386–397 (2007)
6. Sing, K., Everett, D., Haul, R., Moscou, L., Pierotti, R., Rouquerol, J., Siemieniewska, T.: Reporting physisorption data for gas/solid systems. Pure Appl. Chem. **57**, 603–619 (1985)
7. Wu, M., Johannesson, B.: Impact of sample saturation on the detected porosity of hardened concrete using low temperature calorimetry. Thermochim. Acta **580**, 66–78 (2014)
8. Kjeldsen, A., Geiker, M.: On the interpretation of low temperature calorimetry data. Mater. Struct. **41**, 213–224 (2008)
9. Riikonen, J., Salonen, J., Lehto, V.: Utilising thermoporometry to obtain new insights into nanostructured materials (review part 1). J. Therm. Anal. Calorim. **105**, 811–821 (2011)
10. Wu, M., Johannesson, B., Geiker, M.: A study of the water vapor sorption isotherms of hardened cement pastes: possible pore structure changes at low relative humidity and the impact of temperature on isotherms. Cem. Concr. Res. **56**, 97–105 (2014)
11. Wu, M., Johannesson, B., Geiker, M.: Determination of ice content in hardened concrete by low temperature calorimetry: influence of baseline calculation and heat of fusion of confined water. J. Therm. Anal. Calorim. **115**, 1335–1351 (2014)
12. Wu, M., Johannesson, B., Geiker, M.: Impact of heat of fusion of water on the calculated ice content using low temperature calorimetry. In: Proceedings of the Seventh International Conference on Concrete Under Severe Conditions—Environment and Loading, 12, Nanjing, China (2013)
13. Wu, M., Fridh, K., Johannesson, B., Geiker, M.: Influence of frost damage and sample preconditioning on the porosity characterization of cement based materials using low temperature calorimetry. Thermochim. Acta **607**, 30–38 (2015)
14. Wu, M., Fridh, K., Johannesson, B., Geiker, M.: Impact of sample crushing on porosity characterization of hardened cement pastes by low temperature calorimetry: comparison of powder and cylinder samples. Thermochim. Acta **665**, 11–19 (2018)
15. Wu, M., Johannesson, B., Geiker, M.: A preliminary study of the influence of ions in the pore solution of hardened cement pastes on the porosity determination by low temperature calorimetry. Thermochim. Acta **589**, 215–225 (2014)
16. Allen, T.: Powder Sampling and Particle Size Measurement, 1st edn. Elsevier, Amsterdam, The Netherlands (2003)
17. Barrett, E., Joyner, L., Halenda, P.: The determination of pore volume and area distributions in porous substances. I. computations from nitrogen isotherms. J. Am. Chem. Soc. **73**, 373–380 (1951)

18. Hagymassy, J., Brunauer, S., Mikhail, R.: Pore structure analysis by water vapor adsorption: I. t-curves for water vapor. J. Coll. Interface Sci. **29**, 485–491 (1969)
19. Wu, M., Johannesson, B., Geiker, M.: Application of water vapor sorption measurement for porosity characterization of hardened cement pastes. Constr. Build. Mater. **66**, 621–633 (2014)
20. Sing, K.: Adsorption methods for the characterization of porous materials. Adv. Coll. Interface. Sci. **76**, 3–11 (1998)
21. Seaton, N.: Determination of the connectivity of porous solids from nitrogen sorption measurements. Chem. Eng. Sci. **46**, 1895–1909 (1991)

Experimental Investigation on the Influence of Organic Extract from Citrus Sinensis as an Additive in Lime Mortar Preparation

Ben George and Simon Jayasingh

Abstract In the twentieth century, the restoration process in heritage buildings is carried out using cement mortars. From the ongoing study it is found that this can cause extensive damage to the existing structures. In order to avoid consequences of this cement based mortar in the ancient structures, study of lime based mortar is necessary. Many researches are going on to analyses the various strength properties, reactions and the strength factors of lime mortars for different percentages of additives used. Carbonation, which is a slow process, enhances the hardening of the fresh lime mortar and hence increases in its compatibility. For increase in the carbonation rate, various admixtures are added to the lime mortar. It also increases the mechanical strength, weather-resistance and water resistance compared to common lime mortar. This research aims at studying the physical, mechanical and chemical transformations in fresh state and hardened state properties of lime mortar through experimental investigations and for understanding the influence of use of organic extract from Citrus Sinensis (Orange) in lime mortar. Traditional slaking of calcium rich lime was done for various periods of 1, 5, 15 and 30 days. On slaking, quick lime combines with water to form calcium hydroxide which can be used as binder in a mortar. With carbon dioxide from atmosphere, this calcium hydroxide further carbonates to form calcium carbonate. Slaking improves the surface area of the mix. The slaked lime was mixed in the ratio of 1:3 with aggregate, grinded for 0, 5, 10, 15 min and the addition of 5% organic extract. The fresh state properties were obtained based on consistency, workability, and setting time tests. The mechanical property was evaluated by compressive strength test after 28 days of curing. Chemical property of the specimen was evaluated by XRD and FT-IR. Results reveal an increase in the transformation of calcium hydroxide to calcium carbonate in lime mortar with organic addition, enhancing its strength.

Keywords Heritage structures · Lime mortar · Carbonation · Slaking · Organic additive

B. George (✉) · S. Jayasingh
Vellore Institute of Technology, Vellore, Tamil Nadu, India

1   Introduction

In the twentieth century we see that the restoration process in heritage buildings are carried out using cement mortars [1]. From the ongoing study it is found that this can cause extensive damage to the existing structures [2]. The cement based mortars has very high content of soluble salts, which leads to the decay of ancient mortar by crystallization or hydration or by both the process [3]. In order to avoid consequences of this cement based mortar in the ancient structures, study of lime based mortar is necessary. In olden days various organic additives were used along with lime [4]. Many researches are going on to analyze the various strength properties, reactions and the strength factors of lime mortars for different percentages of additives used [2].

There are many advantages of lime mortars which are as follows [5]:

   i. It is very compatible in physical and chemical nature with the ancient mortar due to its similar chemical composition.
  ii. Lime mortar is soft, more deformable, and is able to accommodate movement in masonry structures.
 iii. The price of lime mortar is low.

Slaking occurs when the quicklime hydrates and forms calcium hydroxide. It is a slow process which imparts strength to the lime putty. Many methods were employed during ancient time for slaking the lime which includes addition of lime with water in built basins which acts like a shelter, using plastic or metal barriers in which lime and water is added and subjected to high temperature and pressure conditions causing its expansion, also by spraying water into shallow basins and shifting into barrels containing lime, which is then sieved to get lime putty [6].

Carbonation process in lime mortar is influenced by the diffusion of carbon dioxide into the mortar pore system, by the kinetics of the lime carbonation reaction and by the drying and wetting process in the mortar. Carbonation of lime mortar is

$$Ca(OH)_2 + CO_2 + H_2O \rightarrow CaCO_3 + 2H_2O$$
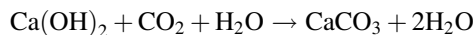
The factors that affect carbonation include temperature rise, relative humidity, amount of water, thickness of walls and its composition. The hardening process of air lime mortars depends on carbonation [7]. The calcium carbonate crystals are formed as the result of carbonation [8].

Several organics were used to improve the properties likeworkability, mechanical strength and durability.During the fourth and sixth century, several kinds of flowers, leaves, beans and pulps from fruits were used for preparing plasters. Adding natural organic compounds like juice of vegetable leaves, sticky rice soup or fish oil greatly improved the performance of lime mortar [9]. Romans used milk, blood and lard while the Europeans used egg white during the Middle Ages. Rice paste, molasses, lacquer, boiled bananas, tung oil was used by the Chinese while in Mesoamerica and Peru, cactus juice and latex were used. Ancient Egyptians used

fruit juices, egg whites, casein, keratin and bullock's blood [10, 11].Various organics such as sticky rice, juice of various plants, seeds etc. are used in lime mortar to find out the various strength properties and carbonation process [12].

Hence the research was done to study the effect of organic additive on the fresh state, carbonation rate and mechanical and durability properties of air lime mortar. This research aims at studying the physical, mechanical and chemical transformations in fresh state and hardened state properties of lime mortar through experimental investigations and for understanding the influence of use of organic extract in lime mortar [13]. The organic used in this study is Citrus Sinensis (Orange) which is widely available, sustainable and economical. Citrus Sinensis contains sugars, carbohydrates, protein and fibers.

The fresh state properties in this study include setting time, consistency and workability. The mechanical property was evaluated by compressive strength test after 28 days of curing. The carbonation test was conducted to evaluate the depth of carbonation. Chemical property of the specimen was examined by X-ray Diffraction (XRD) and Fourier Transform Infra-Red Spectroscopy (FTIR). Therefore, the properties of the mortar are evaluated and it will reveal an increase in the transformation of calcium hydroxide to calcium carbonate in lime mortar with organic addition, enhancing its strength.

2 Materials and Methods

2.1 Raw Materials

Aerial lime passing through 80 micron sieve is used as the binder. This lime was obtained from Edappalayam, Chennai, India, and manufactured by an industrial process.

Grain size distribution is carried out using sieve analysis. River Sand passing through 4.75 mm sieve and retaining on 2.36, 1.18, 0.6, 0.3, 0.15 and 0.08 mm sieves are used as the aggregate. This is done in accordance with the IS: 383 (1970). The specific gravity of sand is tested using pycnometer and is found to be 2.65.

In ancient days various organic additives such as sticky-rice, blood, juice of plants, drying oil were used along with lime for the construction process. Citrus Sinensis is used in this paper as 5% by weight of water added during the casting.

2.2 Slaking

Equal amount of lime and water is mixed and kept in a closed container for 1, 5, 15 and 30 days (S1, S5, S15, S30). Cubes are casted after each slaking period.

2.3 Workability

Workability of lime mortar is carried out in accordance with the IS 6932 (Part 8)—1973. From this we infer that the workability required for our mix is 0.4 to 0.75. The initial flow test is also carried out with reference to thesis from Materials and structures by R. Hanley and S. Pavia.

3 Experimental Work

3.1 Mortar Preparation

The slaked lime putty is used for casting cube specimens. Organics of 5% are added while casting. Binder aggregate ratio of 1:3 is used and $50 \times 50 \times 50$ mm cube specimens are casted. The cubes are demoulded after 7 days.

4 Results and Discussion

4.1 Test on Raw Materials

4.1.1 Lime

Mineralogical composition of air lime is obtained by XRD analysis. XRD patterns of lime shows high intense peaks of portlandite with traces of calcite (Fig. 1).

4.1.2 Sand

The specific gravity of river sand is found to be 2.65 using the pycnometer. The particle size analysis of the river sand was performed and plotted the grain-size distribution curve. The sieve analysis curve conforms to well graded aggregates (Fig. 2).

4.1.3 Organic

Fourier Transform-Infrared Spectroscopy of the Orange fruit indicated the presence of polysaccharides with peaks at 2931.80 and 1049.28 cm^{-1} and proteins at 1631.78 cm^{-1}. The carbohydrates present in the organic changes the microstructure of the lime mortar and the proteins and amides in it impart durability properties (Fig. 3).
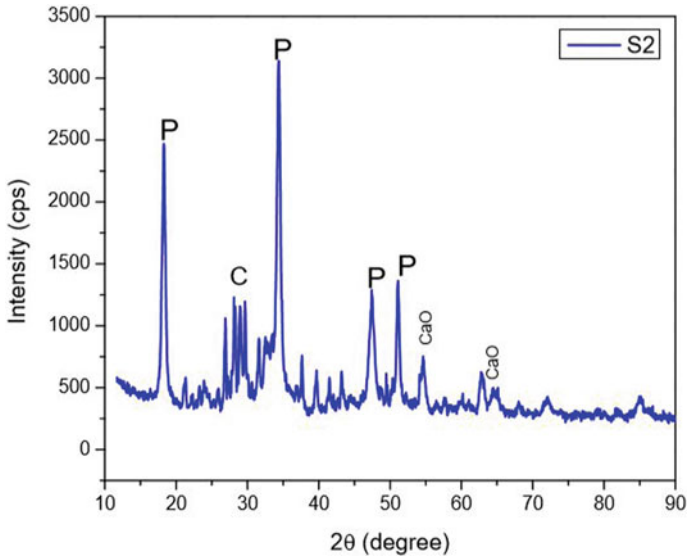
Fig. 1 XRD pattern of lime
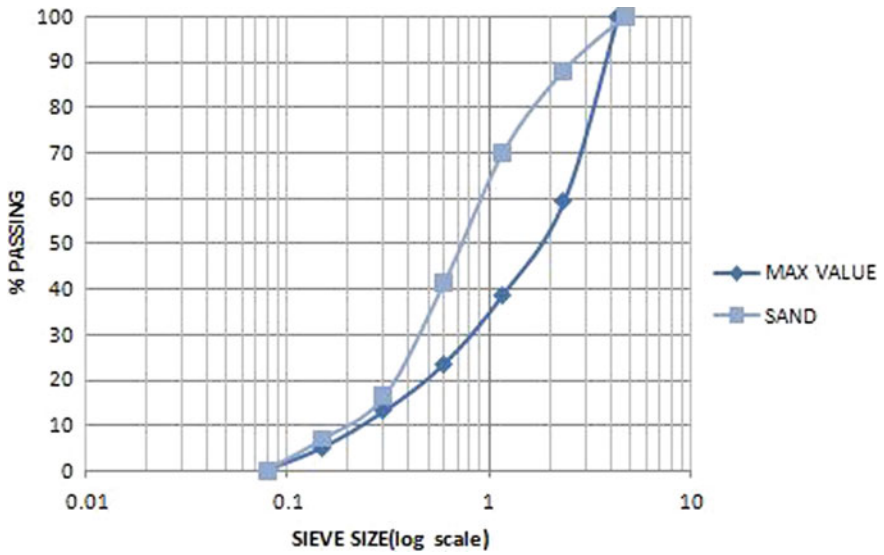
Fig. 2 Grade-size distribution
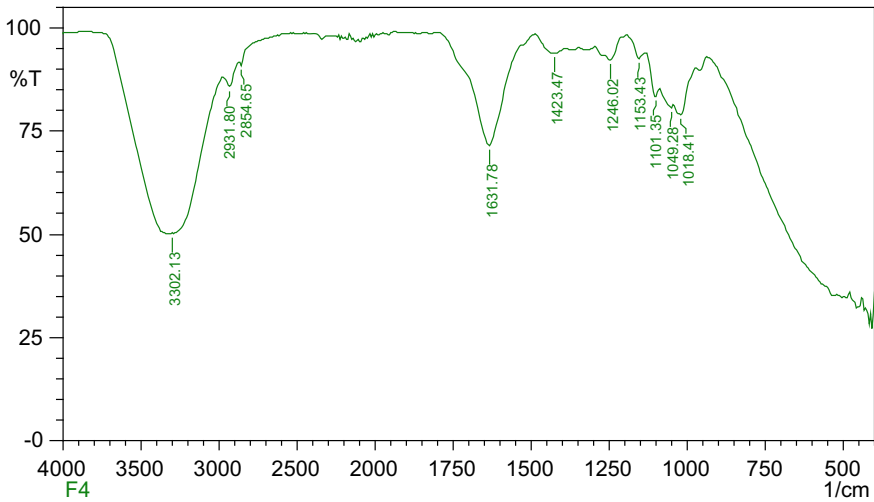
Fig. 3 FT-IR of Orange fruit

4.2 Mechanical Properties

4.2.1 Compressive Strength

After 28 days of air curing compressive strength test is done for cubes. Compressive strength of cubes is done on Electromechanical Universal Testing Machine (Capacity-50 kN) (Figs. 4 and 5).
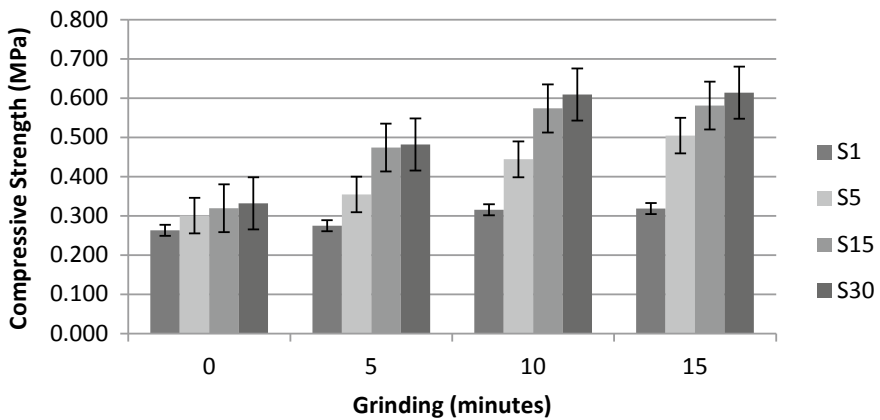

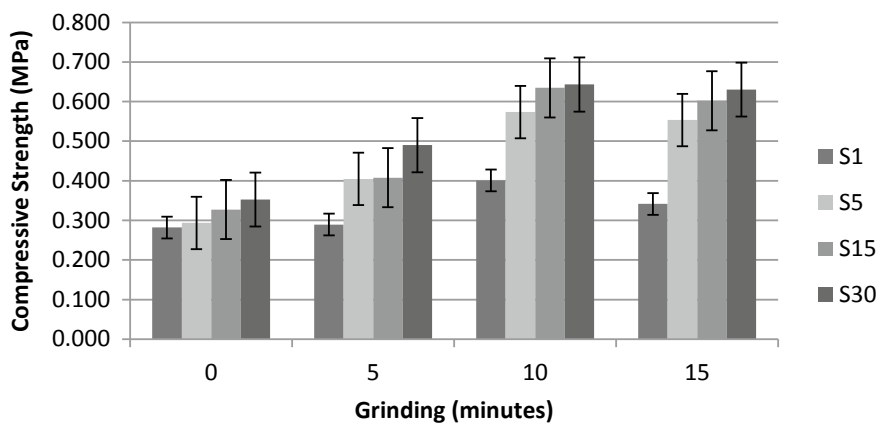**Fig. 4** Compressive strength of specimens without organic at different slaking and grinding periods (Slaking days—S1, S5, S15, S30)

Fig. 5 Compressive strength of specimens with organics (5%) at different slaking and grinding periods (Slaking days—S1, S5, S15, S30)

The process of slaking has a good influence on the compressive strength of hydrated lime mortar. The compressive strength has increased with the slaking periods. The sample undergoing grinding has more strength compared to the samples without grinding. The maximum compressive strength is shown for samples kept for 30 days slaking and grounded for 10 min with organic addition.

4.2.2 XRD—X-ray Diffraction

X-ray diffraction test is carried out to find out the crystalline materials and the analysis of unit cell dimensions. The sample after compression testing is grounded and sieved through 75 micron sieve for obtaining XRD (Fig. 6).

From the XRD results we find that the sample contains Calcite, Quartz, Gypsum, Aragonite, Vaterite, Tricalcium Allite. The highest peak indicates Calcite. It shows the active conversion of portlandite into calcite with an increase in the slaking periods. This enhances the compressive strength of slaked lime mortar samples. These high intense calcite peaks may result from the conversion of calcium hydroxide to calcium carbonate by the process of carbonation, had a good effect on mechanical properties. A vaterite peak was observed in the above pattern, which shows the role of organics in the samples.

4.2.3 FT-IR Analysis

IR spectroscopy (Fig. 7) representing characteristics deeper bands at 999 and 1411 cm^{-1} show the presence of $CaCO_3$ in the samples. But the calcite peak has a lower band at 418.55 and 873.75 cm^{-1}. Bands of polysaccharides at 2981 cm^{-1} and its
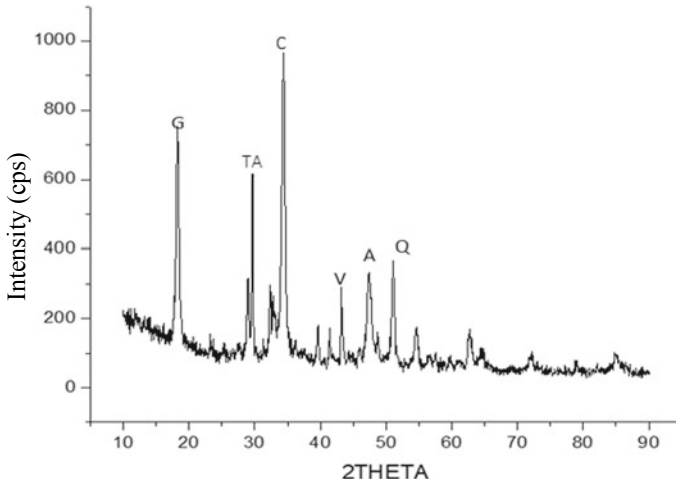
Fig. 6 XRD pattern of S30G10OG5 sample (max compressive value) (S30G10OG5: Slaking 30 (days)—Grinding 10(min)-Organic 5%)
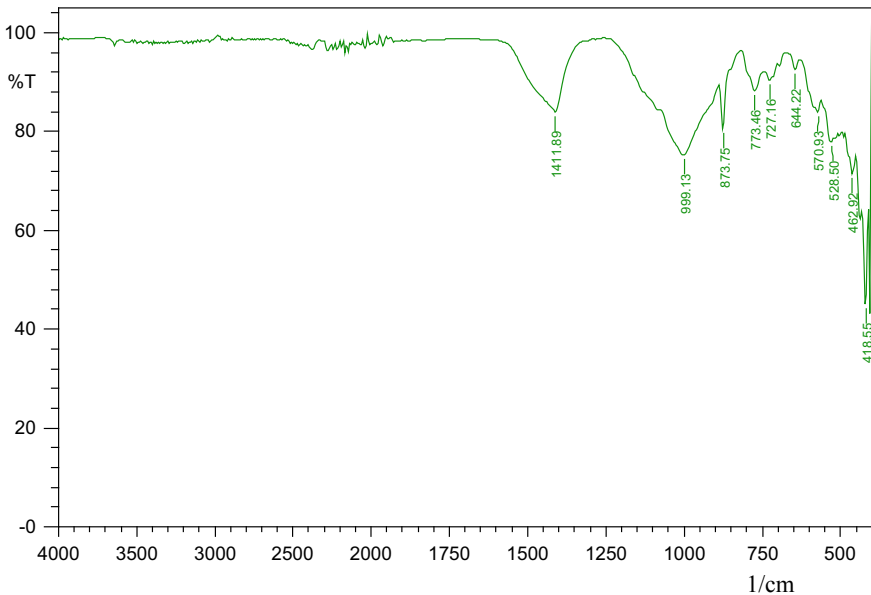

Fig. 7 FT-IR of S30G10OG5 sample (max compressive value)

presence in the admixture make an adherent nature. Polysaccharide in the admixture provides a moist condition, contributed to the enhanced carbonation of mortar samples.

5   Conclusion

The effect of slaking, grinding of aggregates and the impact of organic extract on the fresh-state, mechanical, physical and chemical properties of lime mortar were studied. There is an enhancement in mechanical properties of samples with grounded aggregates and with organic addition.

The moisturizing polysaccharides present in the organic extract facilitates the carbonation process by attracts a greater quantity of carbon dioxide from atmosphere, which indicated in XRD patterns as high intense calcite peaks and strong bands in FT-IR spectrum.

From the results of compressive test we come to a conclusion that the samples with grounded aggregates have more strength compared to the samples without grinding. Also it shows an increasing compressive strength as grinding time changes from 5 to 10 min. The maximum compressive strength is shown for samples kept for 30 days slaking and aggregate grounded for 10 min and also with organic addition.

Hence, it can be concluded that addition of Citrus Sinensis into the slaked lime mortar mix with grounded aggregates could improve the workability, enhance the mechanical properties and offer durability to the lime mortar so that it could well be applied in the conservation of heritage structures.

References

1. Sarah, S., Lawrence, M., Walker, P.: Impact of aggregate type on air lime mortar properties. Energy Procedia **62**, 81–90 (2014)
2. Ventolà, L., Vendrell, M., Giraldez, P., Merino, L.: Traditional organic additives improve lime mortars: new old materials for restoration and building natural stone fabrics. Constr. Build. Mater. **25**, 3313–3318 (2011)
3. Silva, B.A., Pinto, A.P.F., Gomes, A.: Influence of natural hydraulic lime content on the properties of aerial lime-based mortars. Constr. Build. Mater. **72**, 208–218 (2014)
4. Xiao, Y., Xuan, F., Haibing, G., Gao, F., Shaojun, L.: Properties, characterization, and decay of sticky rice–lime mortars from the Wugang Ming dynasty city wall (China). Mater. Charact. **90**, 164–172 (2014)
5. Lanas, J., Alvarez, J.I.: Masonry repair lime-based mortars: factors affecting the mechanical behavior. Cement Concrete Res. **33**(11), 1867–1876 (2003)
6. Hassan, S.A., Zahrani, A.A.: Slaking lime for restoration and conservation of historical buildings and materials, criticism of an Arabic historical manuscripts. Eng. Appl. Sci. **6**, 125–131 (2017)
7. Eleni, D., Thomas, S.,Aurela, S., Frederik, V.: Literature study on the rate and mechanism of carbonation of lime in mortars. In: Proceedings of International Masonry Conference Guimaraes, pp. 1–12 (2014)
8. Balen, K.V.: Carbonation reaction of lime, kinetics at ambient temperature. Cement Concrete Res. **35**, 647–657 (2005)
9. Yang, F., Zhang, B., Pan, C., Zeng, Y.: Traditional mortar represented by sticky rice lime mortar—One of the great inventions in ancient China. Sci. China Ser. E: Technol. Sci. **52**, 1641–1647 (2009)

10. Moropoulou, A., Bakolas, A., Anagnostopoulou, S.: Composite materials in ancient structures. Cement Concr. Compos. **27**, 295–300 (2005)
11. Sickels, L.B.: Organic additives in mortars. Edinburgh Architect. Res. **8**, 7–20 (1981)
12. Thirumalini, S., Ramdoss, R., Rajesh, M.: Experimental investigation on physical and mechanical properties of lime mortar: effect of organic addition. J. Cult. Herit. **31**, 97–104 (2018)
13. Khalid, A.G., Ravi, R., Thirumalini, S.: Revamping the traditional air lime mortar using the natural polymer—Areca nut for restoration application. Constr. Build. Mater. **164**, 255–264 (2018)

A Correlation Between Sorptivity Coefficients of Concrete as Calculated from Relationships of Water Uptake with $t^{0.5}$ or $t^{0.25}$

Yury A. Villagrán-Zaccardi[iD]**, Natalia M. Alderete**[iD]**,**
Alejandra Benítez[iD]**, María F. Carrasco**[iD]**, Patricio Corallo**[iD]**,**
Raúl López[iD]**, Alejo Musante**[iD]**, and Cristian Rios**[iD]

Abstract Sorptivity is a transport parameter widely used for assessing the durable performance of concrete. However, anomalous capillary absorption (or imbibition) is normally reported for cementitious materials, i.e. capillary water uptake evolves non-linearly with $t^{0.5}$. For decades, different methods of dealing with the anomaly have been adopted in different standards. A novel approach based on the hygroscopic nature of cementitious materials has been recently proposed. A linear relationship of water uptake with $t^{0.25}$ (instead of $t^{0.5}$) was proven sound in terms of accurate description of the transport process and fitting with experimental results. For comparative purposes, there is therefore a need for a correlation between the new coefficients and coefficients in the literature computed upon considering an evolution with $t^{0.5}$. In this manner, the potential of sorptivity in the design for durability of concrete structures, previously hindered by the anomalous behaviour of the material, may be further explored. This paper presents a correlation between sorptivity coefficients of concrete as calculated from relationships of water uptake with $t^{0.5}$ and $t^{0.25}$. The data was obtained from the literature and contrasted with own data produced in 6 different laboratories. Samples were pre-dried at 50 °C for a

Y. A. Villagrán-Zaccardi (✉)
LEMIT, CONICET, B1900AYB La Plata, Argentina
e-mail: yuryvillagran@conicet.gov.ar

N. M. Alderete
Department of Structural Engineering and Building Materials, Ghent University, 9052 Zwijnaarde, Ghent, Belgium

A. Benítez · A. Musante
INTI, B1650WAB San Martín, Argentina

M. F. Carrasco
CECOVI-UTN, S3004EWB Santa Fe, Argentina

P. Corallo · C. Rios
Loma Negra-Intercement, C1439DWE Buenos Aires, Argentina

R. López
Holcim, X5000FAN Córdoba, Argentina

limited period of time. With some limits, the obtained relationship is sound. No particular considerations are required with regard to the features of the concrete mixes (e.g. water-to-cement ratio, type of cement, aggregate type, curing).

Keywords Sorptivity · Capillary porosity · Water transport · Imbition · Design for durability

1 Introduction

Among the most common concrete transport properties to measure, capillary water uptake (or imbition) finds numerous potential applications from the correlation with the durable performance in service. In this regard, sorptivity is a useful parameter used to describe the capillary water ingress rate. This parameter describes concrete pore structure in relation to its exposure to aggressive environments, with a low sorptivity value indicating satisfactory properties to guarantee an acceptable life span of a concrete structure [1].

When unsaturated concrete is put in direct contact with water, it absorbs by capillarity due to the action of the adhesion forces of the water molecules to the walls of the pores in the concrete. There are several standard test methods to determine the sorptivity of concrete: IRAM 1871 [2], ASTM C 1585 [3], EN 13057 [4], EN 15801 [5] EN ISO 15148 [6], EN 480-5 [7], with different approaches to attempt the calculation of the sorptivity. Despite most of standards assume the evolution of the water uptake to be proportional to $t^{0.5}$, experimental results demonstrate that this is not exactly the case.

Substantial evidence in the literature confirms the serious limitations of the linear relationship with $t^{0.5}$. Still users have not abandoned it as they seem confident on that it is supported by a solid physical explanation. An in-depth analysis suggests that this perception is incorrect. The earliest solution for the relationship between water uptake by unsaturated porous materials and time is the Lucas Washburn Equation [8], which combines the Laplace relation with Poiseuille's equation of laminar flow. This indicates that the water front and mass versus time follow the relation of $t^{0.5}$ in a small cylindrical capillary.

When the gravitational and inertial terms are neglected, the capillary force is balanced by the viscous force. The solution of this equation can be obtained by considering the initial condition of the dry material, and it is the well-known Lucas Washburn Equation, which relates the height of the water front with $t^{0.5}$. In practice, the gravimetric method is applied, and considering 1-D transport, the height increase is revealed by the corresponding weight increase. The Lucas Washburn Equation has been studied, improved and applied very extensively, but it has several inherent weaknesses and problems when applied to model water uptake of porous materials [9]:

(1) The capillary model considers 1-D flow in straight tubes. It is therefore applicable to 1-D wicking flow only.

(2) The assumption of a bundle of capillary tubes for representing the actual complex microstructure of a porous medium is very simplistic.

(3) There is no consideration of the interconnection of pores.

(4) The distribution of pore diameters cannot be assessed, and only a constant capillary tube diameter is assumed.

(5) The tortuosity is disregarded, and the actual path of the flow is replaced with a straight-line fluid motion.

All these assumptions have been considered in improved models, leading to the inclusion of respective fitting parameters, such as hydraulic diameter, capillary diameter, and tortuosity factors. Pores in cementitious materials are certainly not cylindrical and have no constant radius. Several attempts to adapt the Lucas Washburn Equation for considering the shape and tortuosity have been made [10]. However, these approaches require additional assumptions as they are based on a $t^{0.5}$ evolution. The lack of linearity documented for several materials is therefore considered evidence of the unsuitability of the Lucas Washburn Equation for the description of imbibition in 3-D porous materials [10]. In order to consider the lack of linearity with $t^{0.5}$, a fictional correlation coefficient would have to be included in Lucas Washburn Equation, with no physical meaning and the only purpose of improving the fitting to experimental data. A modified version of this equation to take into account the non-linearity of the process ends up in a completely empirical application. This is because a convenient value for the hydraulic radius needs to be selected with the sole aim of obtaining a good fitting to experimental data. Contrarily, a variable hydraulic diffusivity may be considered in Richards Equation, and depending on its variation, the exponential parameter for the time may adopt different values. The variation of the hydraulic diffusivity can be obtained independently. This is the approach followed in [11], where an improved model based on the Richards Equation is proposed for describing water absorption in cementitious materials, with water uptake increasing with $t^{0.25}$. It is then derived that the Richards Equation is more versatile than the Lucas Washburn Equation as it considers the material as a continuum and defines its properties in accordance.

There are several hypotheses to explain the anomalous sorptivity of cementitious materials that diverges from a linear evolution with $t^{0.5}$. There is no consensus about the causes for the deviation of water uptake from linear evolution with $t^{0.5}$. Numerous theories try to explain the cause of the anomaly: effects of concrete hygroscopicity, gravity, occluded air, heterogeneous distribution of moisture, changes in electroviscosity, or in the chemical composition of the pore liquid, or in the contact angle. According to the model of Pradhan et al. [12] based on the distribution of pore sizes in concrete, when considering a pore structure constituted by idealized cylinders and invariable over time, water uptake should evolve proportionally with $t^{0.5}$. Then, the lack of linearity with $t^{0.5}$ is a clear reflection of a variable pore structure. An analysis of the consistency of these hypotheses can be

found in [11], where the hygroscopicity of the material given by hydrated calcium silicate (C–S–H) and its swelling with increasing moisture content is considered as the most solid explanation.

The effect of swelling of the C–S–H with the moisture content can be translated into a coefficient of hydraulic diffusivity that varies over time. Swelling causes external expansion but also an increase in tortuosity due to the internal restriction to this deformation. Physical evidence of the effect of swelling of C–S–H on sorptivity was presented in Alderete et al. [13], where the developed model leads again to a proportional evolution of water uptake with $t^{0.25}$ instead of $t^{0.5}$.

The proposed approach with $t^{0.25}$ seems very solid, and it compels to establish a correlation between the new coefficients and coefficients in the literature computed upon considering an evolution with $t^{0.5}$. This would allow applying design methods that were originally conceived for the design for durability with values of sorptivity from a relationship with $t^{0.5}$. From a mathematical point of view, a linear transformation can be established for the vectors of each point for transferring from the domain of $t^{0.5}$ to the domain of $t^{0.25}$. Moreover, as several practical procedures cause a divergence of the mathematical correlation, an empirical comparison appears more straightforward at first.

2 Application of the New Approach to Data in the Literature

The Argentine Standard IRAM 1871 establishes a conventional procedure for determining the sorptivity [2]. Since its implementation, numerous laboratories have implemented the procedure and computed a sorptivity index as indicated from the contrast of water uptake and $t^{0.5}$. A literature review of data published during its implementation (2004–2019) [14] resulted in a compilation of results from 84 mixes tested in 8 different laboratories. The comparison of sorptivity indexes S_{05} and S_{025} resulted in Eq. (1), with $R^2 = 0.943$.

$$S_{05} = 0.011934 \cdot (S_{025})^{1.2} \qquad (1)$$

Despite this correlation indicates a significant consistency, it is desirable to account for a correlation obtained from data specifically produced for comparative purposes. This would allow reassuring that the same procedure and data treatment is applied by all the participating laboratories, and that any reduction in the goodness of fit is not due to variations from the standard experimental method.

3 Application of the New Approach to Data from Participating Laboratories

3.1 The Experimental Procedure

The experimental procedure was performed as indicated in IRAM 1871 [2]. Capillary water uptake is tested on three cylindrical samples per series, obtained from the section between 3 and 8 cm from the base of cast concrete cylinders of 10 cm in diameter and 20 cm in height. Concrete specimens are cured for 28 days since casting, and sections are sawed and laterally waterproofed. Then, these samples are saturated under water for 72 h, and put in an oven at 50 °C afterwards. Drying continues until the weight loss is less than 0.1% wt. in a 24 h period. This period generally lasts between 4 and 14 days depending on the features of the mix. After completion of this preconditioning procedure, samples are sealed in plastic bags until tested. For the capillary water uptake test itself, samples are put in contact with water with their bottom face only 3 mm below the water level. Water uptake is computed from the mass increase after exposure times of 0.5, 1, 2, 3, 4, 5, 6, 24 and every 24 h, until weight gain is less than 0.1% wt. in a 24 h period. Water uptake per cross section area is plotted against the square root of exposure time, or the fourth root of exposure time, correspondingly to the type of coefficient aimed. Sorptivity coefficients are obtained as the slope of the fitting line to data. A single value for each coefficient was obtained from a single fitting for each series consisting in the whole group of three samples.

3.2 S_{05} versus S_{025}

The data analysis was produced in six laboratories, testing different mixes. No parametrical study was done regarding the properties of mixes, and values correspond to random features such as diverse water-to-cement ratios, type and content of cement, type of coarse aggregate. No individual tendency is observed for any of the participating laboratories. From the comparison of the best fit to Eq. (1) and considering a fixed value for the exponent equal to 1.2, Fig. 1 shows that the coefficient of proportionality increases from 0.011934 to 0.012549, with 95% confidence interval being (0.01221; 0.01289). A significant divergence from the previous tendency is obtained for very low sorptivity values, as indicated by the relative residues ((S_{05} experimental/S_{05} estimated) − 1) in Fig. 2. In these cases, where the relative residues reach values close to 1 for $S_{025} \sim 20$ g m^{-2} s$^{0.25}$, there is an underestimation of about 50% for this range of values. There are two logical explanations of this result. First, testing is ended prematurely when the capillary rise is very little. As water penetration progresses very slowly, the measurements are ended much earlier than the required period for the capillary rise to reach the top face (many times when it advanced only 1 or 2 cm from the bottom face). Then, the
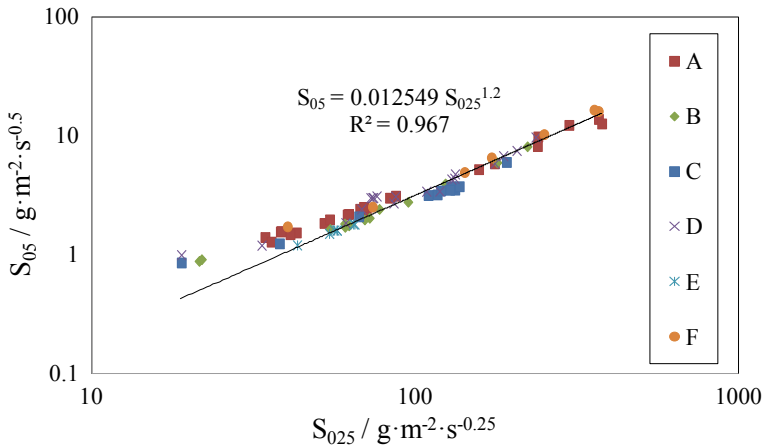
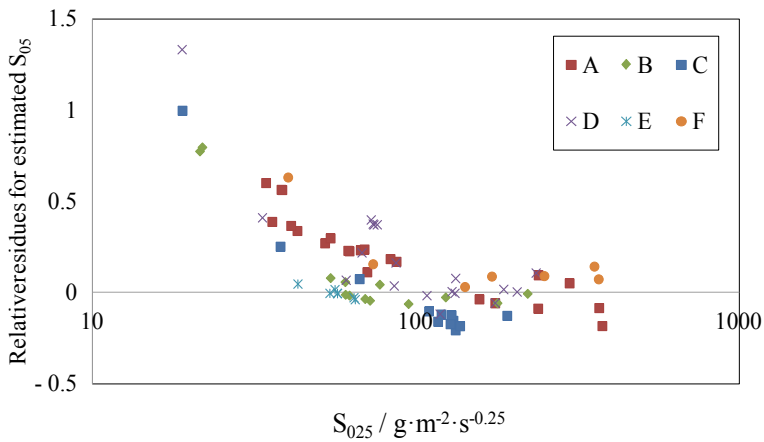**Fig. 1** Comparison of sorptivity indexes S_{05} and S_{025} from labs A to F

Fig. 2 Relative residues for the estimated value of S_{05} versus the corresponding value of S_{025}

first measurement between 0 and 6 h has a higher relative weight for the fitting. In these cases, the difference between the linearity of the two approaches is less marked, so the relationship slightly changes for very low sorptivity values. Second, the potential relationship proposed in Eq. (1) shows a good fitting from an empirical point of view, but it does not fully explain the relationship between both coefficients. Additional examination in this regard is necessary, especially from a theoretical point of view.

4 Conclusions

The anomalous capillary absorption in cementitious materials (lack of linearity with $t^{0.5}$) has been reported in the literature and discussed for quite some time. A possible explanation for continuing to use a linear law with $t^{0.5}$ in standard procedures and regulations is the lack of a theoretical foundation explaining the observed deviation. The sound fitting of experimental data to a law with $t^{0.25}$ when the test is performed according to IRAM 1871 or similar procedures was supported by a theoretical explanation (swelling of the C–S–H) and a mathematical model of the transport phenomenon. Therefore, a potential definite description of the anomalous capillary water uptake may be achieved if the analysis is made considering the evolution with $t^{0.25}$ instead of the evolution with $t^{0.5}$.

To facilitate the transition to the new approach, the present paper presents an equivalence between the coefficients S_{05} and S_{025} with data produced in six laboratories. From the comparison analysis of these results and a previous analysis that considered data in the literature, a consistent correspondence is obtained, which is independent of the composition of the mixes or the features of constituents materials.

Results are however not conclusive. With the presented correlation, increasing underestimations for estimated S_{05} are computed from S_{025} values. The relative residues ((S_{05} experimental/S_{05} estimated) − 1) reach values close to 1 for S_{025} ~ 20 g m^{-2} s$^{0.25}$. This means an underestimation of about 50% for this range of values. Additional research is needed to offer a general equivalence and to determine its limitations.

The simple modification of the treatment of data for computing a sorptivity index is therefore a significant progress for its application to the design of durable concrete structures. It potentially offers new capabilities of this index for performance-based design, the correspondence between S_{05} and S_{025} is a necessary step towards this evolution.

References

1. CIRSOC 201.: Argentine regulation for concrete structures (in Spanish: Reglamento Argentino de Estructuras de Hormigón). INTI, Buenos Aires (2005)
2. IRAM 1871.: Concrete. Test method for determination the water capacity and the capillary suction speed of the hardened concrete (in Spanish: Método de ensayo para determinar la capacidad de succión capilar y la velocidad de succión capilar de agua del hormigón endurecido). IRAM, Buenos Aires (2004)
3. ASTM C 1585.: Standard test method for measurement of rate of absorption of water by hydraulic-cement concretes, ASTM International, West Conshohocken (2004)

4. EN 13057.: Products and systems for the protection and repair of concrete structures, Test methods. Determination of resistance of capillary absorption. CEN, Brussels (2002)
5. EN 15801.: Conservation of cultural property, Test methods. Determination of water absorption by capillarity. CEN, Brussels (2010)
6. EN ISO 15148.: Hygrothermal performance of building materials and products. Determination of water absorption coefficient by partial immersion. CEN, Brussels (2003)
7. EN 480–5.: Admixtures for concrete, mortar and grout—Test methods—Part 5: Determination of capillary absorption. CEN, Brussels (2005)
8. Washburn, E.W.: The dynamics of capillary flow. Phys. Rev. **XVII**, 273–283 (1921)
9. Masoodi, R., Pillai, K.M.: Single-phase flow (sharp-interface) models for wicking. In: Masoodi, R., Pillai, K.M. (eds.) Wicking in Porous Materials Traditional and Modern Modeling Approaches, pp. 31–54. CRC Press, New York (2013)
10. Cai, J., Yu, B.: A discussion of the effect of tortuosity on the capillary imbibition in porous media. Transp. Porous Media **89**, 251–263 (2011)
11. Villagrán-Zaccardi, Y.A., Alderete, N.A., De Belie, N.: Improved model for capillary absorption in cementitious materials: progress over the fourth root of time. Cement Concrete Res. **100**, 153–165 (2017)
12. Pradhan, B., Nagesh, M., Bhattacharjee, B.: Prediction of the hydraulic diffusivity from pore size distribution of concrete. Cem. Concr. Res. **35**, 1724–1733 (2005)
13. Alderete, N.M., Villagrán Zaccardi, Y.A., De Belie, N.: Physical evidence of swelling as the cause of anomalous capillary water uptake by cementitious materials. Cement Concrete Res. **120**, 256–266 (2019)
14. Villagrán-Zaccardi, Y.A., Alderete, N.M., Di Maio, A.A.: Weight gain due to capillary absorption progresses linearly with the fourth root of time (in Spanish: La ganancia de peso por succión capilar progresa linealmente con la raíz cuarta del tiempo), In: Irassar, E.F. et al. (eds.) Proceedings of the VIII International Congress of AATH, pp. 335–343. AATH, Olavarría, Argentina

Numerical Analyses of the Connections Between Representative SFRC Prestressed Rings of Off-Shore Wind Towers

Chandan C. Gowda, Fabio P. Figueiredo, Joaquim A. O. Barros, and A. Ventura-Gouveia

Abstract Off-shore wind towers are the wind farms used to harvest wind energy to generate electricity on water bodies. With the growing need of sustainable production for electricity, off shore wind towers are finding a rapid growth in application. In fact, 4% of European electricity demands will be generated by offshore wind towers by 2020 in European waters. The current project concentrates on development of an innovative structural system using advanced materials for lightweight and durable offshore towers. The present paper discusses the nonlinear finite element modelling of the connections between representative prefabricated rings of off-shore wind towers made by steel fibre reinforced concrete (SFRC) and prestressed by a hybrid system formed by carbon fibre reinforced polymers (CFRP) bars and steel strands. The connection between these two rings are assured by post-tension high steel strength cables and concrete-concrete shear friction of treated surfaces. The model takes into account different types of loads and moments originating from rotor, wind and water currents considering the critical loading conditions. The material nonlinear analyses were carried out in FEMIX V4.0 software, considering a 3D constitutive model capable of simulating the relevant nonlinear features of the SFRC, and interface finite elements for modelling the shear friction of the concrete-concrete surfaces in contact. The SFRC rings are modelled by solid elements, and the longitudinal CFRP bars and steel strands by 3D embedded cables. Parametric studies are carried out in order to assess the influence of different fracture parameters of the SFRC and post-tension level in the cables (steel and CFRP) on the performance of the connection between the two rings.

Keywords Off-shore wind tower · Material nonlinear analyses · Shear frictional · Tied connections

C. C. Gowda (✉) · F. P. Figueiredo · J. A. O. Barros
University of Minho, Guimaraes, Portugal

A. Ventura-Gouveia
Polytechnic Institute of Viseu, Viseu, Portugal

1 Introduction and State of Art

The growing need of energy to increase the quality of life is exhausting the natural resources like oil, natural gas etc., at a more rapid rate than ever. This pushes the mankind for having more sustainable energy production for the future. One of this energy production is by offshore wind tower, which uses the wind blowing from land to water bodies to produce electricity. The first wind farm was installed in Denmark in 1991 [4]. 84% of all offshore wind installations are located in European waters, with remaining 16% mainly in china, followed by Vietnam, Japan, South Korea, U.S and Taiwan [6].

Figure 1 shows the global cumulative offshore wind capacity in 2017, which indicates that the production capacity has increased over 450% from 2011 to 2017 and is continuously growing. This moves the society towards a more productive, cost-efficient and renewable energy production, reducing the carbon dioxide emissions. One of the steps in reducing these costs is by developing innovative structural systems, which is the main aim of the research project. The current concrete towers involve prefabricated concrete rings of high dimensions assembled on site by post-tensioned steel cables.

A small change in design or construction process can have significant impact on these type of constructions in terms of cost and schedule savings [8]. The innovative use of composite materials in construction i.e., in support structures and foundations, will reduce fabrication and transportation efforts, resulting in the most
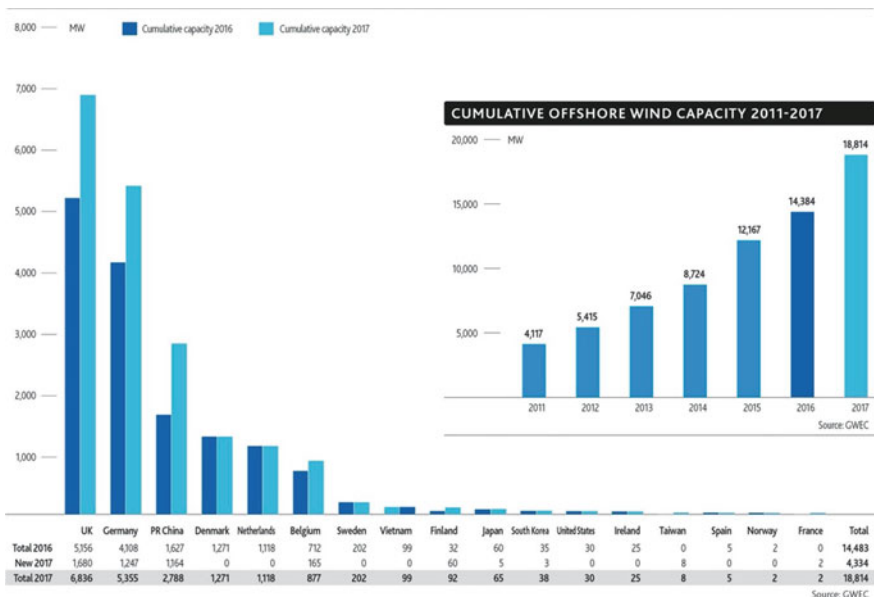

Fig. 1 Global cumulative offshore wind capacity in 2017 [6]

cost effective solutions [7]. The main scope of this paper is to perform material nonlinear analysis of the connection between two representative steel fibre reinforced concrete (SFRC) prefabricated rings (of thin wall and variable diameter) of the structural system developed in the scope of the research project. The steel fibre reinforcement aims to eliminate the conventional steel bars, allowing to reduce the ring's wall thickness. These rings are prestressed with carbon fibre reinforced polymer (CFRP) bars for taking advantage of the no susceptibility of CFRP to corrosion, while post-tensioned steel cables ensure the connection between consecutive rings, providing simple, fast assembling and disassembling process to the tower's construction. However, high stress gradients are expected to occur in these anchoring zones, a concern that promoted the development of the present material nonlinear analysis.

2 Model

2.1 Geometry and Data

The total height of the tower is 110 m, with 90 and 20 m above and below the sea level, respectively. The bottom external radius is 3.6 m (at 0 m height, sea bed) and the radius reduces to 1.8 m (at 110 m height) at the top. The tower consists of 10 rings, with each ring having a height of 11 m. The global analysis is discussed in a separate publication [3], and the current paper analyses the connection between two rings by post-tensioned steel cables, subjected to loads and moments generated through different actions of rotor, wind and water (see Fig. 2). According to the global analysis, the bottom most ring, is subjected to worst combination of forces, as a result the connection between the bottom two rings shown in Fig. 2 i.e., the ring resting on the sea bed and the one above is analysed and discussed in the current paper.

In all the analysis carried out in the present paper, the model consists of the bottom full ring (11 m) and half of the ring above (5.5 m), with a total height of 16.5 m (Fig. 2). The radius at the base of the tower is 3.60 m and the radius at 16.5 m height is 3.33 m. The tower has a wall thickness of 100 mm. Each ring consists of a horizontal rig of 600 mm wide at both the extremes, in the top and bottom, connecting the wall at an inclination of 45 degrees, shown in Fig. 3. It also consists of four stiffeners of 600 mm wide running throughout the length of each ring for 11 m. Post-tensioned steel cables are used to connect the two rings at 12 locations, with four inside the stiffeners and the remaining 8 equally distributed along the perimeter (see Fig. 2). The surface of connection is inclined on both the top and the bottom rings to provide additional shear resistance, shown in Fig. 3. Each ring is prestressed with 16 carbon fibre reinforced polymer (CFRP) bars of 30 mm diameter placed in the centre of the SFRC wall (Fig. 2).
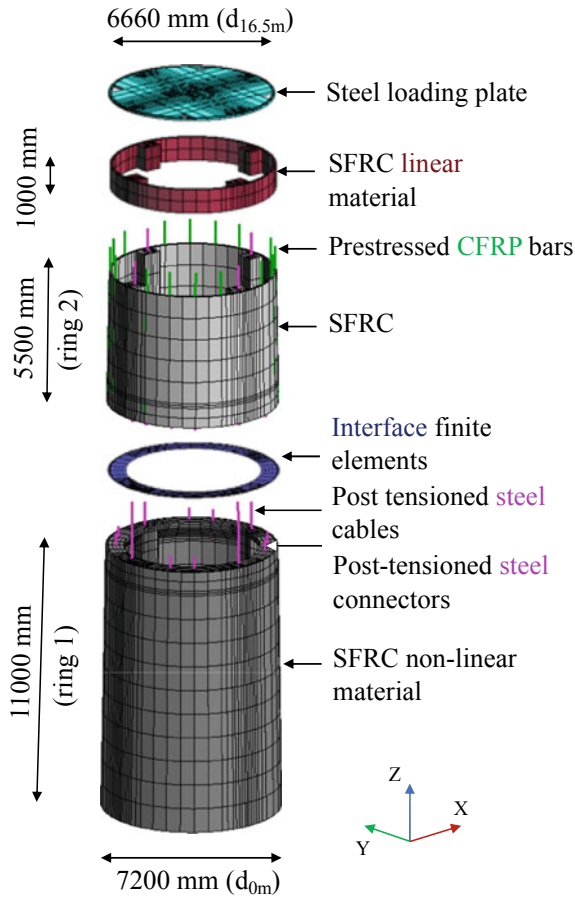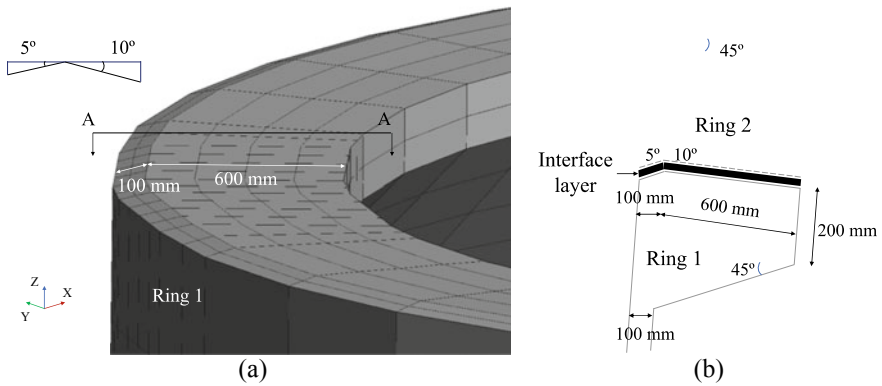
Fig. 2 Model "t_s1" describing different parts

Fig. 3 Geometry of the circumferential rib connecting two rings **a** 3D and **b** 2D, cross section AA

2.2 FEM Attributes and Material Properties for the Constitutive Model

A 3D multidirectional smeared crack model [10] available in FEMIX 4.0 is used for the numerical simulations. GiD software is used as a pre- and post-processor. The Gauss Legendre $2 \times 2 \times 2$ integration scheme allowing a formation of maximum 3 cracks at each integration point is adopted. Modified Newton–Raphson type 1 iterative algorithm is used, where the stiffness matrix is updated only in the first iteration of each load increment. An independent path behaviour is used with a tolerance of 1×10^{-2} in terms of displacement as the convergence criterion.

8-noded solid hexahedra is used to simulate the SFRC, while 2-noded 3D embedded cable is used to simulate CFRP bars and steel cables. The reinforcements are assumed to be perfectly bonded to concrete elements. Interface finite elements of 8 nodes with Gauss-Lobato integration scheme of 2×2 are adopted for modelling the connection between consecutive SFRC rings. In order to avoid the development of severe cracking due to the formation of unrealistic stress fields in the zone of the SFRC ring where loads equivalent to the real tower's loading conditions are applied, an additional linear layer of SFRC (1 m thick) is modelled. Furthermore, a stiff steel plate is added, supporting the extra linear-elastic SFRC layer to receive the equivalent loads and transfer these loads on the structure to be analysed.

The SFRC developed in a parallel research has a compressive strength of 64 MPa (f_{cm}) and tensile strength of 6.77 MPa (f_t), with modulus of elasticity, 42.15 GPa (E_{cm}) obtained in experimental tests. According to technical data sheet of the products, the adopted steel cables (both connectors and cables) have 40 mm diameter, yield strength of 1147 MPa and modulus of elasticity of 191 GPa, while the CFRP cables have 30 mm diameter, a tensile strength of 2400 MPa and a modulus of elasticity of 270 GPa. By inverse analysis of the results obtained in three point notched beam bending tests, the quadri-linear tensile softening diagram shown in Fig. 4a was obtained for modelling the fracture mode I propagation of the SFRC (presented in Table 2 of Sect. 3.2, [1]). The influence of fibre orientation on the post-cracking behaviour of SFRC was assessed by performing three point notched beam bending tests with series of specimens of fibre orientation intervals [0–15°], [15–45°], [45–75°] and [75–90°]. For the present simulations, the fibres were considered to have the best orientation towards the crack planes formed in the tower, which obliges appropriate casting technology for assuring preferential orientation of fibres in the longitudinal axis of a ring. However, the influence of fibre orientation on the response of the tower is assessed in a parametric study described in Sect. 3.2. The crack bandwidth is evaluated as the cube root of the volume of the integration point (IP), being 141 mm in the current case. The tension and compression behaviour of steel reinforcement (cables and connectors) is simulated by the stress–strain diagram represented in Fig. 4b. More details of the material models can be found in Barros et al. [2] and in Gouveia [5]. The constitutive law of the interface finite elements is described in [9]. In the current analysis, the interface
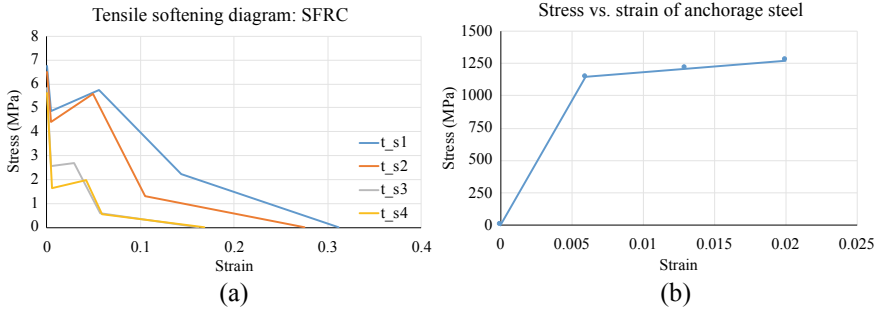
Fig. 4 Numerical model, **a** tensile softening diagram for different fracture parameters of SFRC, **b** non-linear material property of anchorage steel

elements are assigned the following properties: slip at the end of the linear bond-slip relationship is 0.5 mm (s_0), slip at the peak bond stress is 2.5 mm (s_m), material cohesion of 1 MPa, friction angle as 37°, parameter defining pre-peak bond stress-slip relation is $\alpha_1 = 1$, parameter defining post-peak bond stress-slip relation $\alpha_2 = 1$ and a stiffness (K_n) of 6.0×10^7 N/mm.

3 Results

3.1 General Results: Model 't_s1'

As only part of the global model is analysed here, all types of loads acting above the simulated part of the tower, are transformed into the respective forces and moments and applied in the stiff steel plate placed on the top part of the analysed model. The different loads and moments acting on the tower "t_s1" are shown in Table 1, considering the factored loads. More details on the load and moment scenarios arising on the structure are described in Figueiredo and Barros [3].

Figure 5a, shows the graph of force versus displacement of the model, "t_s1" in X-direction. Figure 5b, c, presents the crack pattern at the end of the analysis (100% of F_x), on the bottom and top rings, where the maximum crack width is 0.18 mm (obtained by multiplying the maximum crack normal strain to the crack bandwidth of the integration point where it is being evaluated). The current software (FEMIX 4.0) presents the crack pattern in five different stages i.e., crack opening, closing, reopening, sliding and fully open. Figure 5b, c, presents only crack opening (red colour) and reopening (cyan colour), as other cracks are not formed.

Figure 6 shows the evolution of the strains and stresses along the height of the tower in post-tensioned steel cables (Fig. 6a) and in the steel connectors (Fig. 6b), at different integrations points (IP, black dots on the tower) for the indicated load levels (represented in Fig. 6). According to the results, the stresses and strains are

Table 1 Different loads considered for the analysis

Load description (Force/ Moment)	Notation	Values (kN/kN·m)	
Self-weight	w_g	(calculated by software)	
Water current load	F_{wx}	10,171 kN (0–10 m) 15,946 kN (10–11 m) 17,821 kN (11–12 m) 25,921 kN (12–16.5 m)	
Self-weight from above + dead weight of the rotor	F_z	6513 kN	
Wind force + force due to wind generated by rotor + horizontal force by water current	F_x	1869 kN	
Moment due to wind force + moment due to wind generated by motor + moment due to rotor + moment due to water current	M_y	155,404 kN·m	
Torsional moment due to rotor	M_z	1789 kN·m	

Table 2 SFRC fracture parameters defining stress—strain softening laws

Model	β	α_1 [–]	α_2 [–]	α_3 [–]	ξ_1 [–]	ξ_2 [–]	ξ_3 [–]	f_{ct} [MPa]	G_f^1 [N/mm]
t_s1	0°–15°	0.72	0.85	0.33	0.014	0.18	0.46	6.77	6.00
t_s2	15°–45°	0.68	0.86	0.20	0.014	0.18	0.38	6.50	5.10
t_s3	45°–75°	0.44	0.46	0.10	0.024	0.18	0.35	5.85	2.70
t_s4	75°–90°	0.29	0.35	0.10	0.032	0.25	0.35	5.64	2.70

well within the yield limits (yield stress is 1147 MPa and the yield strain is 0.006). Stress and strain jumps are obtained at certain IP's at later stages due to crack formation (after 77% of F_x) and the respective crack at these locations are shown in Fig. 5b, c. At the interface between the two rings, the expected drastic strain/stress jumps are not taking place, specifying that the provided post-tensioned steel connections are sufficient enough to bear the considered factored loads and moments acting on the structure. However, the stress values at the end of the analysis at the connections are higher than the initially provided post-tension (Fig. 6b).
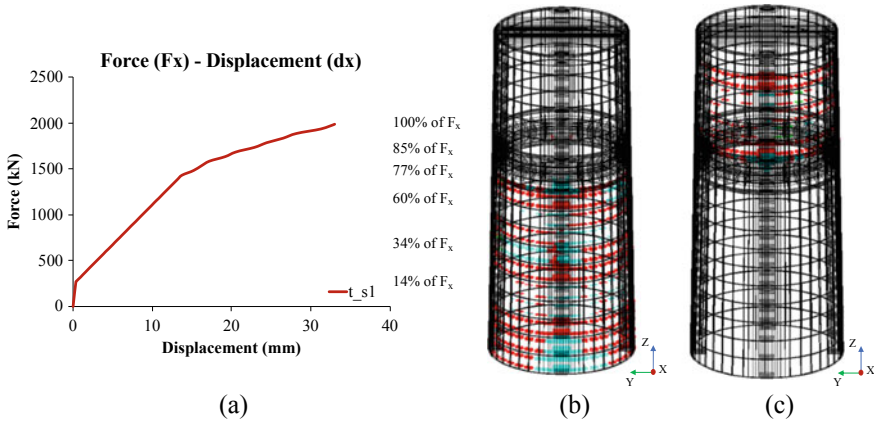
Fig. 5 **a** Force versus deflection; crack pattern, **b** bottom ring and **c** top ring, model "t_s1"

Figure 7 shows the stress distribution in Z-direction (vertical) of the model "t_s1" from two different views. The combination of forces and moments applied in the positive X-direction, generate tensile stresses (positive values, maximum of 104% of f_t) on one half of the tower and compressive stresses (negative values, maximum of 58% of f_{cm} is reached) on the other half. The maximum shear stress variation on the interface layer between the two rings is lesser than 1.9 MPa.

3.2 Parametric Analysis

Two parameters are varied to understand the performance of post tensioned steel connections on prefabricated SFRC rings under different loading conditions on the tower. This includes:

(a) variation of fracture parameters of the SFRC based on fibre orientation and
(b) different pre-stress values for the steel and CFRP reinforcement.

Variation of SFRC Fracture Parameters:

Firstly, the properties of SFRC according to the fibre orientation, based on the experimental research carried out elsewhere [1]. The four different values of softening parameters considered from best to least best, based on the fibre orientation are presented in Table 2 (see also Fig. 4a).

The results of force versus displacement for different fracture parameters of SFRC are shown in Fig. 8a. The performance of SFRC decreases with the increase of fibre orientation angle (less efficient mobilization of the fibre reinforcement mechanisms), leading to higher lateral deflection and the formation of more number of cracks both on the upper and the lower rings in the tower. Comparison of crack
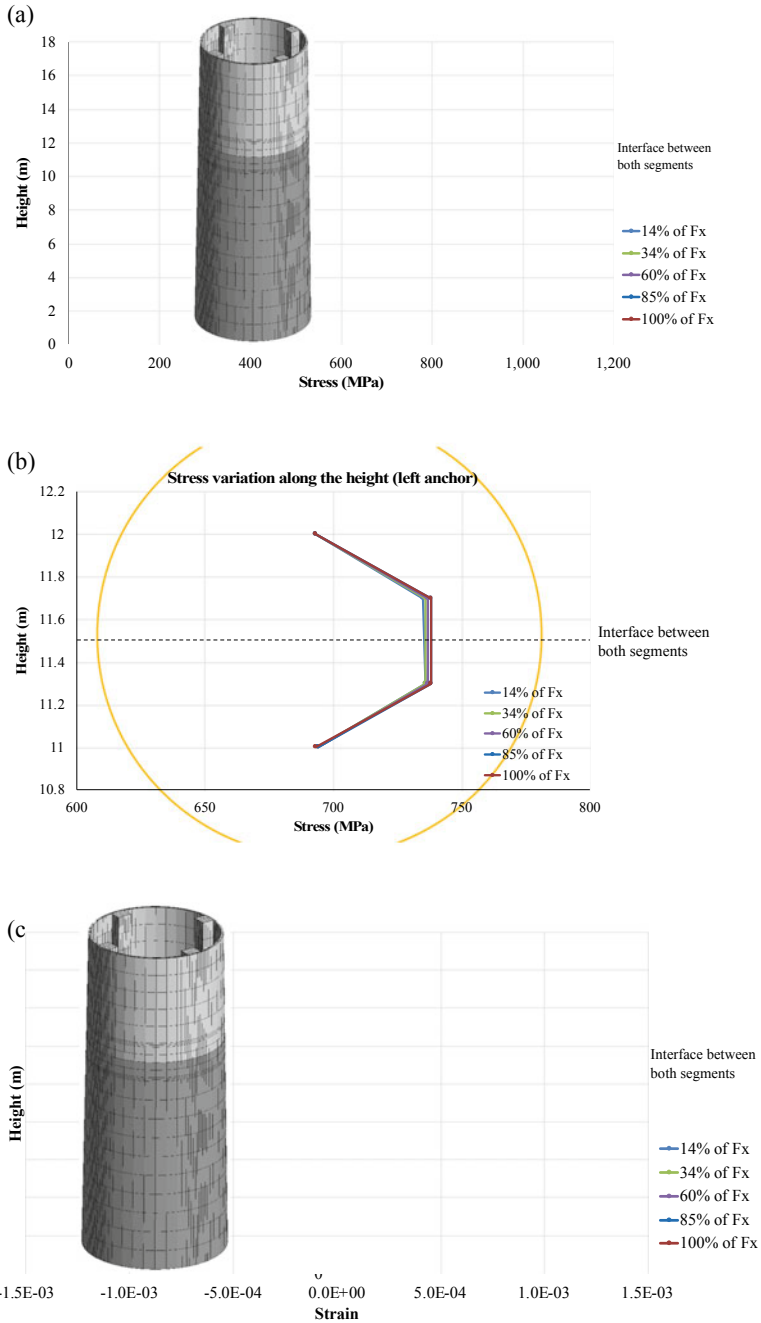
(a)

(b)

(c

Fig. 6 Evolution of steel stress: **a** post-tensioned steel cables, **b** post tensioned steel connectors and **c** strain along the height of the tower in post tensioned steel cables for different load combinations, model "t_s1"
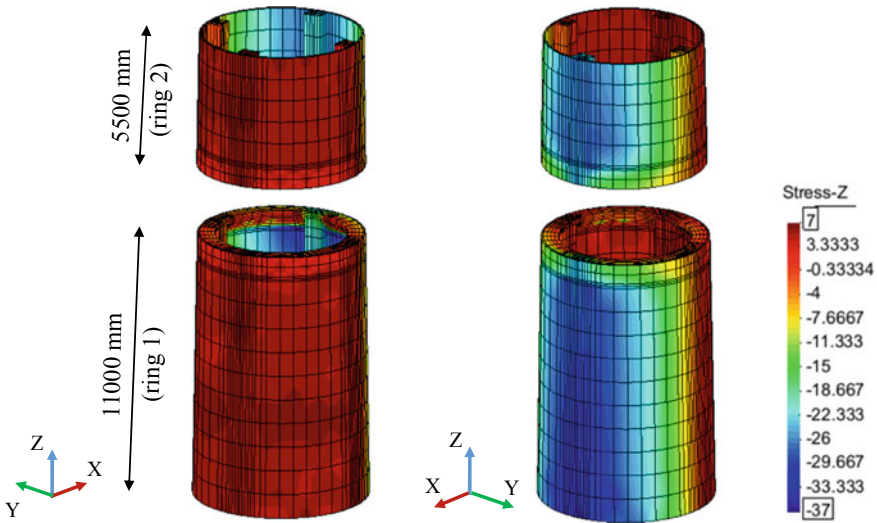
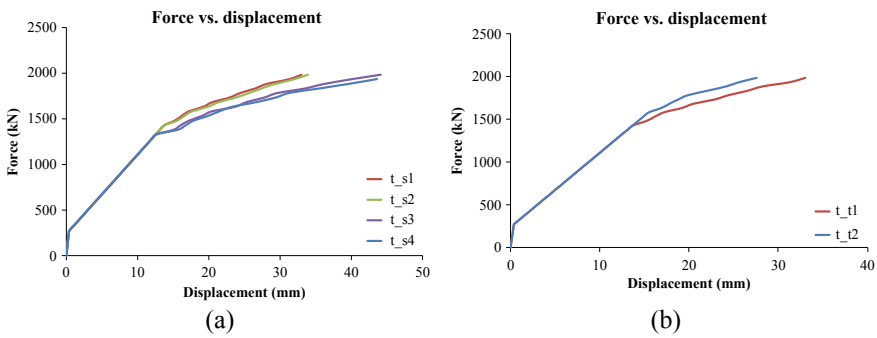**Fig. 7** Stress variation in Z-direction, model "t_s1". Values in MPa

Fig. 8 Influence of the: **a** post-cracking tensile capacity of SFRC (due to preferential fibre orientation angle) and of the **b** pre-stress level on steel and CFRP reinforcements on the force–deflection response of the simulated model

pattern between model "t_s1" (best SFRC property see Figs. 9a and 10b) and "t_s4" (least best SFRC property, see Figs. 9c and 10d), is shown in Fig. 9.

Variation of Pre-stress:

The pre-stress values of steel and CFRP reinforcements are varied according to Table 3. The force versus deflection for both the towers are shown in Fig. 8b. Tower 't_t2' with the increase in 20% pre-stress on steel and 15% in CFRP bars, the
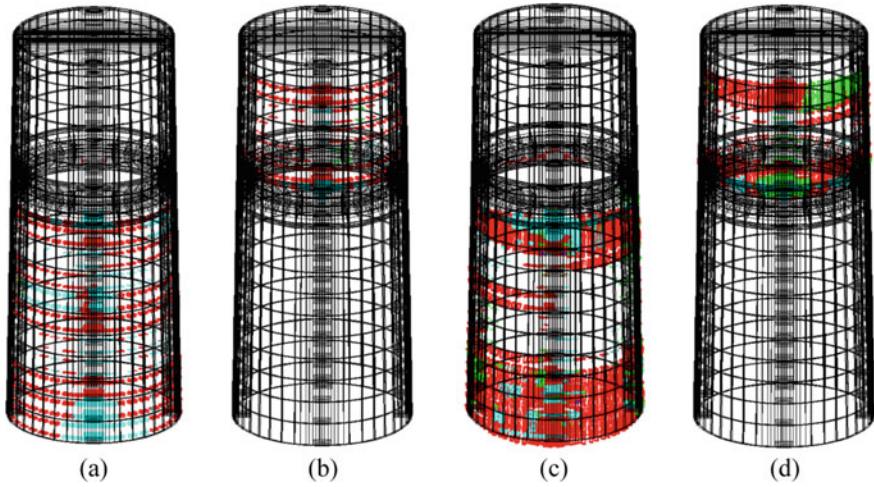
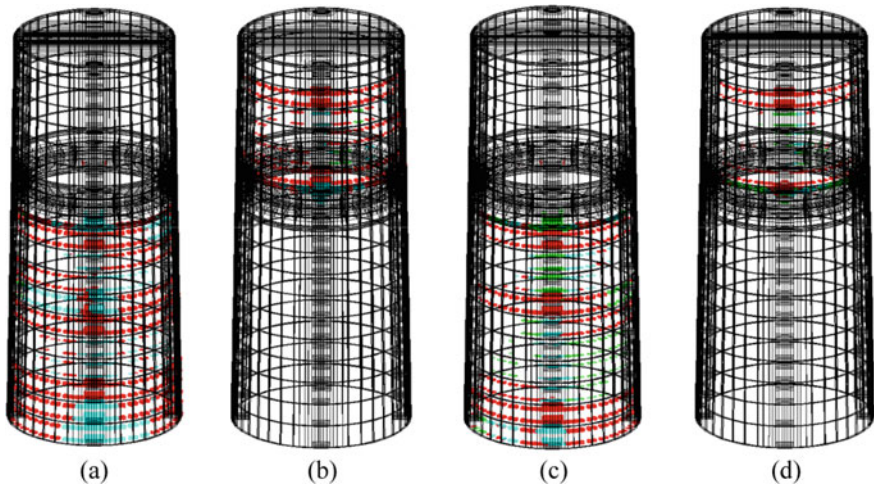**Fig. 9** Crack pattern: **a** and **b** t_s1; **c** and **d** t_s4

Fig. 10 Crack pattern: **a** and **b** t_t1; **c** and **d** t_t2

deflection is reduced by 16.45% and the maximum crack width is reduced by 6.0% in comparison with the tower 't_t1'. The respective crack patterns on the top and the bottom segments of both the towers are shown in Fig. 10a–d. Tower 't_t2' has lower number of cracks of smaller crack width due to higher pre-stress in the reinforcements.

Table 3 Pre-stress percentage and values

Reinforcement/ Tower	't_t1'		't_t2'	
	Pre-stress percentage (%)	Pre-stress (MPa)	Pre-stress percentage (%)	Pre-stress (MPa)
Steel	60	756	75	945
CFRP	40	960	60	1440

4 Conclusions

The following conclusions are obtained based on the results of the FE numerical analysis performed above:

- The proposed material-structural concept of offshore wind tower, combining SFRC, prestressed CFRP bars, post-tensioned steel cables, and post-tensioned steel cables greatly reduces the wall thickness (to 1/6th) with respect to conventional construction;
- The structural behaviour of this tower was assessed by performing material nonlinear analysis and considering some of the most design governing loading conditions, having accomplished the requirements for serviceability and ultimate limit state conditions;
- The maximum crack width obtained in the model with the SFRC of highest post-cracking tensile capacity (due to the consideration of fibre orientation) is 0.18 mm, indicating that no corrosion problems is expected even adopting steel fibres;
- None of the steel reinforcements have yielded nor they are closer to the yielding value, even though some variations are observed at crack locations which are well within yielding limits;
- By managing the prestress level applied to the CFRP bars and steel strands, the stiffness of the response of the tower can be adapted.

References

1. Abrishambaf, A., Barros, J.A.O., Cunha, V.M.C.F.: Time-dependent flexural behaviour of cracked steel fibre reinforced self-compacting concrete panels. Cement Concrete Res. **72**, 21–36 (2015). https://doi.org/10.1016/j.cemconres.2015.02.010
2. Barros, J.A.O., Breveglieri, M., Gouveia, A.V., Dalfré, G.M., Aprile, A.: Model to simulate the behavior of RC beams shear strengthenend with ETS bars. In: FraMCoS-8 Fracture Mechanics of Concrete and Concrete Structures, pp. 505–516 (2013)

3. Figueiredo, F.P., Barros, J.A.O.: Nonlinear analysis of offshore wind towers in prefabricated segments of prestressed fibre reinforced concrete (2020)
4. Giebel, G., Hasager, C.B.: An overview of offshore wind farm design. In: MARE-WINT: New Materials and Reliability in Offshore Wind Turbine Technology. Denmark (2016). https://doi.org/10.1007/978-3-319-39095-6
5. Gouveia, A.V.: Constitutive Models for the Material Nonlinear Analysis of Concrete Structures Including Time-Dependent Effects. University of Minho, Guimaraes, Portugal (2011)
6. GWEC.: GWEC Global Wind 2017 Report—A Snapshot of Top Wind Markets in 2017: Offshore Wind (2017). https://doi.org/10.1021/jp0213102
7. Malhotra, S.: Design and construction considerations for offshore wind turbine foundations. Proc. Int. Conf. Offshore Mech. Arctic Eng—OMAE **5**, 635–647 (2007). https://doi.org/10.1115/OMAE2007-29761
8. Malhotra, S.: Selection, design and construction of offshore wind turbine foundations. In: Wind Turbines (2011). https://doi.org/10.5772/15461
9. Valente, T.D.S.: Advanced Numerical Models for Analysis of the Behaviour of Structures Strengthened with an Innovative Technique". University of Minho, Portugal (2019)
10. Ventura-Gouveia, A., Barros, J.A.O., Azevedo, A.F.M., Sena-Cruz, J.M.: Multi-fixed smeared 3D crack model to simulate the behavior of fiber reinforced concrete structures. In: CCC2008-Challenges for Civil Construction, vol. 11 (2008)

The Effect of Mechanical Load on Carbonation of Concrete: Discussion on Test Methods and Results

Zhiyuan Liu, Philip Van den Heede, and Nele De Belie

Abstract Carbonation of concrete, consuming $Ca(OH)_2$ and lowering concrete alkalinity, will lead to reinforcement corrosion and therefore is one of the major causes of concrete deterioration. Most research mainly focuses on the carbonation of concrete without mechanical load. However, concrete structures will bear load in practice, which has a significant influence on CO_2 transport and carbonation rate. So, studies on carbonation in combination with mechanical load are of great importance for optimizing service life prediction models. In this review paper, it is discussed how imposed load affects the carbonation of concrete and how a dedicated experimental setup is achieved in the lab. The advantages and disadvantages of existing devices are discussed in terms of specimen size, loading frame, method for applying load and stress compensation. Finally, changes in cracks and pore structure induced by compressive loads at different levels are analyzed with respect to gas permeability and carbonation depth.

Keywords Concrete · Carbonation · Mechanical load · Permeability · Stress

1 Introduction

Carbonation of concrete is one of the major causes of reinforced concrete deterioration. When the surface of reinforced concrete is exposed to the atmosphere, CO_2 in the air will penetrate into the concrete through pores and through cracks which are possibly formed during the hydration process which causes shrinkage. In the presence of moisture, CO_2 will dissolve in the pore solution and form HCO_3^- and CO_3^{2-} ions. Then HCO_3^- and CO_3^{2-} ions will react with Ca^{2+} from the hydration products of concrete, such as portlandite $(Ca(OH)_2)$ and calcium silicate hydrates (C–S–H), and form different polymorphs of $CaCO_3$ including calcite, vaterite and aragonite. At high alkalinity, the Ca^{2+} is mainly from the dissolution of portlandite.

Z. Liu (✉) · P. Van den Heede · N. De Belie
Magnel-Vandepitte Laboratory for Structural Engineering and Building Materials, Ghent University, Ghent, Belgium

With the continuous consumption of $Ca(OH)_2$, the alkalinity of concrete will be reduced and lead to the neutralization of concrete and depassivation of steel reinforcement. Finally, reinforcement corrosion may happen, which shortens the service life of reinforced concrete structures. Therefore, as an important issue, the carbonation of concrete has been widely investigated.

The carbonation process is greatly influenced by several factors. Some key factors, including material composition, carbonation condition and curing, determine the carbonation rate and carbonation products. Based on the process from the beginning of CO_2 diffusion to the end of CO_2 reaction, 2 individual processes can be discerned: the physical transport and chemical reaction of CO_2. It should be noted that these 2 processes are not completely independent, for example, the reaction between CO_2 and hydration products also affects the microstructure and hence the subsequent transport [1, 2] of CO_2. All factors influence these 2 processes more or less. For example, material composition is no doubt one of the key factors which determine the rate, reaction products and mechanism of concrete carbonation. A lower water/cement ratio results in a lower capillary porosity and slows down the diffusion of CO_2 [3]. The replacement of cement by supplementary cementitious materials not only changes the porosity of concrete and the tortuosity of the pore system [4] but also reduces the amount of $Ca(OH)_2$. Moreover, when the carbonation process is accelerated in laboratory conditions, by applying a higher CO_2 concentration than in the natural atmosphere, the porosity of OPC decreases and the amount of different carbonation products varies [5].

However, most research mainly focuses on the carbonation of concrete without mechanical load. Concrete structures will bear load in practice, which has a significant influence on CO_2 transport, and thereby has a great impact on carbonation rate. Under different load levels, the concrete microstructure may change and the number, orientation and position of the induced cracks can be different. So, studies on carbonation in combination with mechanical load are of great importance for optimizing service life prediction models.

In this paper, it is discussed how a dedicated experimental setup is achieved for investigating concrete under combined mechanical load and carbonation, through comparison of test methods given in different articles. Then, changes in crack formation and pore structure caused by compressive loads at different levels are analyzed with respect to gas permeability and carbonation depth.

2 Test Method for Carbonation of Concrete Under Compressive Load

There is no standard test method for carbonation of concrete in combination with mechanical load. So different test apparatus and test procedures have been designed to achieve sustained compressive load, and different specimen sizes have been used.

2.1 Specimen Size

Even though a larger specimen size can ensure even distribution of coarse aggregate and a large enough uniformly distributed stress zone, the size of the specimens should not be taken too large. Firstly, the size of specimens is limited by the size of the CO_2 chamber available for accelerated carbonation testing. A strong enough frame designed to transfer uniaxial compressive loads on specimens of size 100 * 100 * 400 mm, may have a total height of over 600 mm. Moreover, during the experiment, specimens may need to be moved out of the CO_2 chamber at certain ages for testing carbonation depth or compensating stress losses. It is difficult for a large CO_2 chamber to maintain the relative humidity and CO_2 concentration, especially for experiments in which a high CO_2 level is required, for example, 20% CO_2 concentration according to the Chinese standard. In most studies, prismatic specimens have been adopted, for example, 100 * 100 * 400 mm [6], 100 * 100 * 300 mm [7] and 40 * 40 * 160 mm [8].

2.2 Loading Devices

The loading frame which provides and maintains sustained load is similar to a post-tensioning system for prestressed concrete. Usually threaded bar tendons are used so compressive stress can be provided. The bar tendons can be designed both inside or outside of the specimens. The typical loading devices for applying uniaxial compressive load [9] and flexural compressive load [10] (3-point bending) by use of external bar tendons are shown in Fig. 1a, b. Such a loading frame with external threaded bar tendons can provide more even and accurate load through adjusting four nuts.

Besides, based on the loading setups mentioned above, some researchers added springs on the bar tendons [14]. In this case, the load is transmitted through the springs and not merely through the bar tendons. So, when inevitable stress losses happen, the applied external load will not decrease too much because of the buffering effect of the spring. Nevertheless, to provide large enough load with a slight strain, very strong springs are required (Fig. 1c), which will greatly increase the total size and weight of the setup. The applied load should never exceed the limit of springs. If the springs are not strong enough, the level of the applied stress is limited [15], especially for compressive stress. In order to keep the total weight as light as possible and allow for a compact design, disc springs (Belleville washers) which can support very large loads with a small installation space are used in several articles (Fig. 1d).

However, the main shortcoming of external bar tendons is that the loading frame may be too large and heavy, which makes it difficult to be manually transported and put into the CO_2 chamber, especially for the loading frames in which springs are added. Therefore, an alternative can be to use internal unbonded bar tendons. As
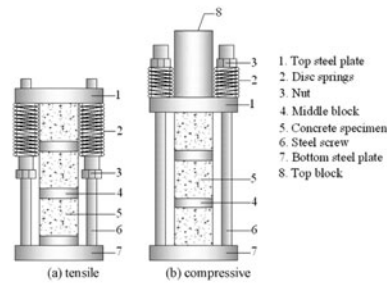
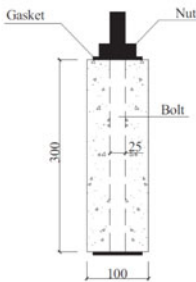(a) Loading frame for applying
compressive load [9]
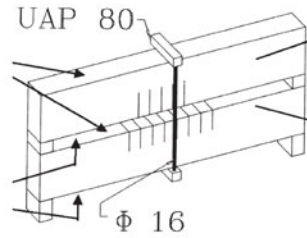
(b) Loading frame for applying 3-point
bending load [10]

(c) Loading frame with coil spring [11]

(d) Loading frame with disc springs [12]

(e) Loading frame with internal bar
tendon [13]

(f) Loading frame developed in Magnel-
Vandepitte Laboratory

Fig. 1 Loading frames developed in different labs (**a–e** are reprinted from [9–13] respectively, with the permission from Elsevier)

shown in Fig. 1e, a circular duct is precast in the concrete for the bar tendon. Obviously, loading with internal bar tendons greatly reduces both the size and weight of the loading setup. But the accuracy and stability of the load still needs further investigation. Besides, Fig. 1f shows a loading frame developed in the Magnel-Vandepitte Laboratory at Ghent University based on the loading frame design in China Building Materials Academy. Disc springs and a sphere are added for reducing the effect of stress loss and load eccentricity respectively.

2.3   Load Application and Compensation

Hydraulics and torque wrenches [16] can be used to apply load. Applying load through hydraulics is more accurate but the operator should pay attention when anchoring with nuts to avoid unexpected prestressing losses. Applying loads through a torque wrench is less accurate because the measured torque is derived from the friction between the nut and screw which highly depends on the nut and screw specifications and even whether it is free of rust and lubricated. But it is still a simple way to apply a relatively low load. Moreover, through gluing strain gauges on the specimen, the operator can also apply the load with a wrench manually according to the resulting strain.

After the load is applied through the loading frame, the load always drops with time. This inevitable phenomenon of stress relaxation is caused by shrinkage, creep and bolt loosening. When the designed stress level is relatively low, regularly releasing the load and reloading is a solution. However, when the load level is over 54% of the failure load, the apparent Poisson's ratio starts to change clearly, which means irreversible plastic deformation happened [17]. In this case, reloading will cause unexpected cracks. Besides, as mentioned before, designed springs can make sure the stress will not drop too much when specimens need to be loaded for a long time.

In the case of prestressed concrete, slightly excessive load (3–5% of designed load) will be applied [18, 19] for the following reasons: first, the stress will decrease greatly after the removal of hydraulics because of the elasticity of the loading frame; second, the shrinkage and creep of concrete will lead to the continuous decrease of stress. Therefore, applying excessive load is essential in prestressed concrete for the structural safety. However, in fact, this can only keep the average stress near or above the design value but not mitigate the effect of shrinkage and creep. Since there is no requirement for structural safety in a loading setup for laboratory tests, more measures are needed to avoid too much stress loss owing to shrinkage and creep. For example, measuring the length variation of springs regularly during carbonation and controlling the length of springs through adjusting the bolts.

3   Effect of Sustained Compressive Load on Carbonation of Concrete

When compressive loads are applied, the microstructure of the concrete may be affected and cracks will change in number, length, width and pattern. The variation in crack pattern and geometry has a great impact on carbonation [20]. A denser concrete structure will slow down the diffusion of CO_2 while a less dense concrete structure contains more pores and cracks which act as flow channels of CO_2 and accelerate the diffusion of CO_2. A larger crack not only makes CO_2 diffusion easier

but also provides more room for carbonation product formation. Several researchers investigated the influence of sustained load on the transport properties and carbonation of concrete.

The effect of applied compressive load on a concrete structure highly depends on the applied stress level. Lim [21] investigated the crack patterns under different stress levels through microscopic observation. According to his research on concrete crack length after compressive load, bond cracks occur at the aggregate-mortar interface when the stress level is above 0.3 times the failure stress and the total crack length increases significantly when the stress level exceeds 0.5. Notable isolated mortar cracks occur at a stress level of 0.7 and interconnect with bond cracks at 0.9 stress level. Although the crack opening displacement reduces after the load is completely removed [22], it is helpful to understand the transport properties of concrete under sustained compressive load.

When the stress level reaches a certain threshold, crack growth goes to another stage and the crack pattern changes greatly. Other researchers also identified a threshold stress level for permeability tests on concrete. Banthia [23, 24] found that the threshold for both plain concrete and fiber-reinforced concrete appears to be approximately 0.3 times the failure stress according to the results of water permeability experiments. In addition to mix proportion, the exact threshold also depends on the age and loading history [25]. Tang found that the gas permeability of unloaded samples obtained through Autoclam method is higher than for samples at 0.3 stress level and lower than for samples at 0.6 stress level (oven dried, air pressure: 500 mBar, specimen size: 100 * 100 * 400 mm) [26], which shows that a threshold for gas permeability may also occur between 0.3 and 0.6 stress level (Fig. 2). For both gas and water permeability, the permeability decreases if the applied compressive stress is below the threshold, while the permeability increases significantly after exceeding the threshold. This phenomenon occurs because the concrete structure becomes denser when a relatively low compressive load is
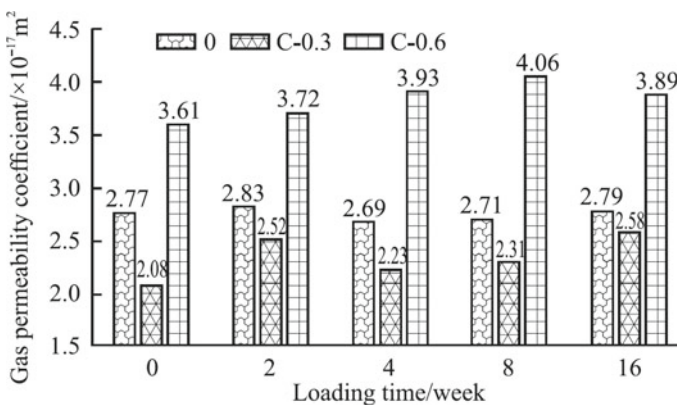

Fig. 2 Gas permeability coefficient under sustained uniaxial compressive loads being 0, 0.3 or 0.6 times the failure load [26]

applied. Some of the cracks and micro-cracks generated during hydration will be closed due to the external stress.

The typical effect of compressive load on carbonation rate is shown in Fig. 3 (CO_2 level: 20%, relative humidity: 70%, specimen size: 100 * 100 * 300 mm). The threshold of the sustained compressive load seems to be higher than the threshold for gas and water permeability. Comparing with unloaded specimens, different authors have found that the carbonation rate under sustained uniaxial compressive load is lower when a fraction of 0.4 [15], 0.5 [27, 28] and even 0.75 [29] of the failure stress is reached. On the one hand, the pressure in the permeability test is much higher than the atmospheric pressure in the carbonation test, which will absolutely cause a discrepancy in the results. On the other hand, carbonation itself may play an important role. The formation of carbonation products caused by the chemical reaction between CO_2 and hydration products of OPC can block the path of CO_2 transport, which has a great impact on CO_2 transport properties in turn. And these are probably the reasons for the difference in threshold between permeability and carbonation.

However, Jinzhi [12] and Koh [9] observed a threshold of sustained compressive load for carbonation at around 0.2 stress level. Interestingly, the size of the specimens (100 * 100 * 50 mm and 100 * 100 * 40 mm respectively and in both cases 100 mm high in the direction of compressive load) in their study is much smaller than the size in the previously described research (usually 100 * 100 * 400 and 400 mm high in the direction of compressive load). The height of 100 mm is usually not large enough to provide a uniform distribution of compressive stress according to the results of finite element analysis. With a lower specimen height, more cracks are generated and may concentrate only on a thin outer layer under compressive load [31], which probably makes the threshold occur at a lower stress level.
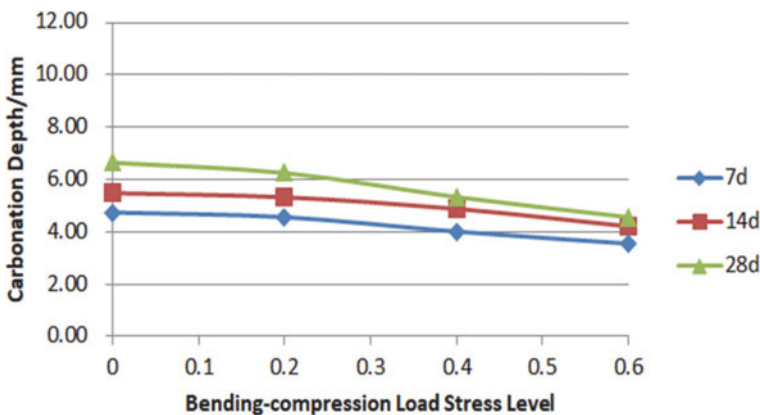

Fig. 3 Typical effect of compressive load on carbonation rate [30]

4   Conclusions

In this paper, the test methods for studying the carbonation of concrete under sustained compressive load are compared and discussed. Then the effect of mechanical load on carbonation is discussed. The applied compressive load can densify concrete at a low loading level. The carbonation rate will be reduced because of the closure of cracks and pores. However, when the applied compressive load exceeds a certain threshold, microcracks connect and the carbonation rate significantly increases.

Future research should be carried out to gain a deeper understanding of the coupled effect of mechanical load and carbonation: The key factors for the threshold load above which the carbonation rate increases, remain uncertain according to existing research. Efforts should be made to determine the threshold stress. It is of great importance for improving the service life of reinforced concrete. Besides, further work is needed to understand how the crack pattern influences CO_2 transport, which is of great help in establishing a theoretical model for service life prediction in practice.

References

1. Auroy, M., Poyet, S., Le Bescop, P., et al.: Impact of carbonation on unsaturated water transport properties of cement-based materials. Cem. Concr. Res. **74**, 44–58 (2015)
2. Claisse, P.A., El-Sayad, H., Shaaban, I.G.: Permeability and pore volume of carbonated concrete. ACI Mater. J. **96**, 378–381 (1999)
3. Shah, V., Bishnoi, S.: Carbonation resistance of cements containing supplementary cementitious materials and its relation to various parameters of concrete. Constr. Build. Mater. **178**, 219–232 (2018)
4. Van den Heede, P., Gruyaert, E., De Belie, N.: Transport properties of high-volume fly ash concrete: capillary water sorption, water sorption under vacuum and gas permeability. Cement Concr. Compos. **32**(10), 749–756 (2010)
5. Van den Heede, P., De Schepper, M., De Belie, N.: Accelerated and natural carbonation of concrete with high volumes of fly ash: chemical, mineralogical and microstructural effects. Royal Soc. Open Sci. **6**(1), 181665 (2019)
6. Liu, X.: Study on Carbonization and Chlorine Ion Penetration Corrosion Regularity of Coastal Concrete Bridge Under Load in Service (in Chinese). Qingdao Technological University (2010)
7. Chen, J., Song, X., Zhao, T., et al.: Service life prediction of lining concrete of subsea tunnel under combined compressive load and carbonation. J. Wuhan Univ. Technol. Mater. Sci. Ed. **25**(6), 1061–1064 (2010)

8. Jin, Z., Sun, W., Zhang, Y., et al.: Study on carbonation of concrete under loading (in Chinese). J. Build. Mater. **8**(2), 179–183 (2005)
9. Koh, T.-H., Kim, M.-K., Yang, K.-H., et al.: Service life evaluation of RC T-girder under carbonation considering cold joint and loading effects. Constr. Build. Mater. **226**, 106–116 (2019)
10. Castel, A., Francois, R., Arliguie, G.: Effect of loading on carbonation penetration in reinforced concrete elements. Cem. Concr. Res. **29**(4), 561–565 (1999)
11. Zheng, J., Huang, L.: Experimental study on carbonation of self-compacting concrete under tensile and compressive stresses (in Chinese). Jianzhu Cailiao Xuebao/J. Build. Mater. **16**(1), 115–120 (2013)
12. Tang, J., Wu, J., Zou, Z., et al.: Influence of axial loading and carbonation age on the carbonation resistance of recycled aggregate concrete. Constr. Build. Mater. **173**, 707–717 (2018)
13. Wang, W., Lu, C., Li, Y., et al.: Effects of stress and high temperature on the carbonation resistance of fly ash concrete. Constr. Build. Mater. **138**, 486–495 (2017)
14. Wan, X., Wittmann, F., Zhao, T.-J.: Influence of mechanical load on service life of reinforced concrete structures under dominant influence of carbonation. Restor. Build. Monuments **17** (2), 103–110 (2011)
15. Wang, Y., Jiang, X., Wang, S., et al.: Influence of axial loads on CO2 and Cl−transport in concrete phases: paste, mortar and ITZ. Constr. Build. Mater. **204**, 875–883 (2019)
16. Carević, V., Ignjatović, I.: Influence of loading cracks on the carbonation resistance of RC elements. Constr. Build. Mater. **227**, 116–583 (2019)
17. Wan, X., Zhao, T., Jiang, F., et al.: Experimental Research on Carbonation Performance of Mechanical Loaded Concrete. In: Proceedings of the Fifth Symposium on Strait Crossings, p. 525 (2009)
18. Wang, H., Lu, C., Jin, W., et al.: Effect of external loads on chloride transport in concrete. J. Mater. Civ. Eng. **23**(7), 1043–1049 (2011)
19. Zhang, Y., Sun, W., Chen, S., et al.: Multi-dimensional carbonation and service life prediction model of fly ash concrete subjected to flexural stress and CO2 attack (in Chinese). J. Southeast Univ. (Nat. Sci. Ed.) **S2**, 226–233 (2006)
20. Van Mullem, T., De Meyst, L., Handoyo, J.P., et al.: Influence of crack geometry and crack width on carbonation of high-volume fly Ash (HVFA) mortar. In: The Third RILEM Spring Convention and Conference, Guimaraes, Portugal (2020)
21. Lim, C., Gowripalan, N., Sirivivatnanon, V.: Microcracking and chloride permeability of concrete under uniaxial compression. Cement Concr. Compos. **22**(5), 353–360 (2000)
22. Wang, K., Jansen, D.C., Shah, S.P., et al.: Permeability study of cracked concrete. Cem. Concr. Res. **27**(3), 381–393 (1997)
23. Bhargava, A., Banthia, N.: Measurement of concrete permeability under stress. Exp. Tech. **30** (5), 28–31 (2006)
24. Banthia, N., Bhargava, A.: Permeability of stressed concrete and role of fiber reinforcement. ACI Mater. J. **104**(1), 70 (2007)
25. Banthia, N., Biparva, A., Mindess, S.: Permeability of concrete under stress. Cem. Concr. Res. **35**(9), 1651–1655 (2005)
26. Tang, G., Yao, Y., Wang, L., et al.: Relation of damage variable and gas permeability coefficient of concrete under stress. J. Wuhan Univ. Technol. Mater. Sci. Ed. **33**(6), 1481–1485 (2018)
27. Tian, H., Li, G., Liu, J., et al.: Experimental research on carbonation of forced concrete specimens (in Chinese). J. Tongji Univ. (Nat. Sci.) **38**(2), 200–204+213 (2010)
28. Wang, M.: Carbonization and Chlorine Ion Erosion Test and Theoretical Analysis of Steamed Prestressed Concrete (in Chinese). Central South University (2012)
29. Luo, X., Zou, H., Shi, Q.: Experimental study on durability of concrete carbonation at different stress states (in Chinese). J. Build. Mater. **21**(2), 194–199 (2012)

30. Liu, Y., Ren, J., Li, Z., et al.: Carbonization resistance of reinforced concrete under bending load. Frattura ed Integrità Strutturale **13**(49), 714–724 (2019)
31. Van Vliet, M.A., Van Mier, J.M.: Experimental investigation of concrete fracture under uniaxial compression. Mech. Cohesive Frictional Mater. Int. J. Exp. Model. Comput. Mater. Struct. **1**(1), 115–127 (1996)

Usefulness of Mercury Porosimetry to Assess the Porosity of Cement Composites with the Addition of Aerogel Particles

Jarosław Strzałkowski and Halina Garbalińska

Abstract Today's need to reduce the energy consumption of buildings makes it necessary to search for new material solutions. Such materials are, for example, cement composites with various types of additives, such as foamed-polystyrene granulates, cenospheres or aerogels, which are intended to reduce the composite's thermal conductivity. The introduction of such additives to concrete composites may be an issue for the assessment of microstructural properties of these materials. This is because the microstructure of concrete and additives are completely different. This problem exist in the mercury porosimetry of cement composites with the addition of aerogel granulate. The Washburn equation, traditionally used in mercury porosimetry, gives false porosity results when applied to aerogels. This paper presents the problems and the method of determining the total porosity and integral and log-differential graphs for cement composites with addition of aerogels. Two types of composites based on lightweight aggregates were tested: expanded clay and sintered fly ash aggregate. In both variants, concrete was made with the addition of aerogel granulate, which accounts for 20% of the total composite volume. Also reference concretes of the same composition, but without aerogel were prepared. The paper presents a method of combining the results of mercury porosimetry using the classic Washburn equation, which is suitable for cement-based materials, and the Pirard equation showing the relationship between the pressure of injected mercury and the diameter of pores in compressed hyperporous materials. The study also provides cumulative and log-differential diagrams of pore distribution in tested concrete with aerogel addition. The values of thermal conductivity in dry state and the compression strength average values for composites after 28 days of curing are also presented.

J. Strzałkowski (✉) · H. Garbalińska
Department of Building Physics and Building Materials, Faculty of Civil Engineering and Architecture, West Pomeranian University of Technology Szczecin, al. Piastów 50, 70-311 Szczecin, Poland
e-mail: jstrzalkowski@zut.edu.pl

1 Introduction

Numerous studies are underway in order to develop new materials characterized by better and better thermal insulation as well as adequate strength. Such materials are, for example, cement composites with various types of additives, such as foamed-polystyrene granulates [1, 2] cenospheres [3–5] or aerogels [6–10] which are intended to reduce the composite's thermal conductivity.

The most promising results were obtained with the use of concrete with the addition of aerogels. Both the pastes [11] as well as mortars and concretes were tested [12–15]. The researchers pointed to the possibility of obtaining composites with significantly improved thermal insulation properties in comparison to other lightweight concretes. Unfortunately, in all the studies, a substantial decrease in the compressive strength of such composites was indicated. Foamed concrete solutions with the addition of aerogels are also tested [16–18]. The insulation properties of the modified materials were even better compared to traditional foamed concrete, but the loss of compressive strength of the materials was no longer as significant as in case of conventional foamed concrete.

The introduction of such additives to concrete composites may be an issue for the assessment of microstructural properties of these materials. This is because the structures of concrete and additives are completely different. This problem exist in the mercury porosimetry of cement composites with the addition of aerogel granulate.

The use of mercury porosimetry to assess the porosity of cement composites is one of the basic methods of microstructural analysis of concrete [19, 20]. Unfortunately, this method has its drawbacks. They result from the complex structure of concrete. For example, the presence of numerous closed pores in the material structure, heterogeneous "T" pores, and random appearance of large pores in the tested sample, that may disturb the evaluation of total porosity [21]. In spite of this, this method is very useful for the comparative assessment of the porosity of different types of concrete composites [20]. Other research methods, such as optical analysis or computed tomography are currently also used [22–25]. However, these methods are characterised by different measurement ranges and other limitations of applications. Therefore, mercury porosimetry remains a frequently used tool for microstructural analysis.

Unfortunately, in the case of cement materials with the addition of aerogel granules, the Washburn equation [26] traditionally used in mercury porosimetry gives erroneous results in assessing the porosity of the materials. In this paper it was decided to present a solution to this problem so that it is possible to determine the correct pore distribution curves using mercury porosimetry.

2 Materials and Methods

The research was carried out on concretes made from lightweight coarse aggregates: sintered fly ash (FA) and expanded clay aggregate (EC). The basic properties of the used aggregates are presented in Table 1.

In the both variants, two mix proportions were prepared using coarse aggregate of 4–8 mm fraction. The first of the mixtures (Ref) was prepared without additives. In the other one (Aero), silicon-based aerogel granules were added in the amount of 20% of the total volume of the mixture. The aerogel granulate of 0.7–4.0 mm fraction of density 120–150 kg/m^3 was used. This aerogel has hydrophobic properties. The thermal conductivity coefficient of the granulate is 0.018 W/(mK), and the porosity exceeds 90%. Performed EDS aerogel tests confirm that the used aerogel is made exclusively of SiO_2.

In the case of sintered fly ash concretes, a super-plasticizer (1.0% of cement mass) was used to maintain proper consistency of the mixture.

The same cement CEM I-42.5R was used in all the variants. The W/C ratio was constant and amounted to 0.55. The constant ratio of 0–2 mm sand to cement, which equalled to 1.2, was also maintained in all the mixtures. The proportions of the individual mixtures are shown in Table 2.

Table 1 Basic properties of expanded clay (EC) aggregate and sintered fly ash aggregate (FA)

Aggregate type:	Water absorbability (%)	Volume density (g/cm^3)		Loose bulk density (g/cm^3)	Porosity (3–300 μm) (%)	Total surface area (m^2/g)
		Hydrostatic	Mercury porosimetry			
FA	22.49	1.31	1.38	0.68	45.72	12.88
EC	28.29	0.56	0.53	0.31	75.09	56.23

Table 2 Mix proportions

Mix symbol	Coarse aggregate (kg/m^3)	Sand (kg/m^3)	Cement (kg/m^3)	Water (kg/m^3)	SP (%)	Aerogel (kg/m^3)	Aerogel (volume %)
FA\Ref	801.9	483.3	402.8	221.5	1.0	0.0	0.0
FA \Aero	641.5	386.7	322.2	177.2	1.0	24.0	20.0
EC\Ref	295.7	511.9	426.6	234.6	0.0	0.0	0.0
EC \Aero	236.5	409.6	341.3	187.7	0.0	24.0	20.0

From each of the mixtures, 4 samples for compressive strength tests with the dimensions of $10 \times 10 \times 10$ cm and 2 samples for porosimetric tests were made. Samples were stored for the first 28 days in a climatic chamber with high humidity. The compression strength (f_{cm}) was tested after 28 days of curing. For each type of concrete, the average value of the strength and the standard deviation have been calculated.

The porosity of individual composites was investigated using mercury porosimetry. After three months of curing and drying, the middle sections were cut out from the cubes. Then, $0.7 \times 0.7 \times 2.0$ cm samples were taken from each of the sections. The surface tension of mercury was established at 0.48 N/m and the contact angle was set at 140 degrees for intrusion. The samples were first subjected to low pressure (up to 0.34 MPa), then the cells with samples filled with mercury were weighed. They were then placed in a pressure chamber and subjected to high pressure (up to approx. 413 MPa). Alongside concrete testing, pure aerogel granules were also tested.

Thermal parameters were studied with the use of Isomet 2104. The device performs the measurement using readings of the heat flux at its transient flow. The thermal conductivity coefficients λ and specific volumetric heat c_v were measured. The tests were carried out after the samples were completely dried at the temperature of 70 °C. The testing was carried out on six samples made from each type of concrete. The samples were $4 \times 14 \times 16$ cm in size, and the analysed area was the base of the sample. The average values of λ and c_v and the standard deviations of the individual results were determined using measurements from all six samples of concrete.

3   Results and Discussion

The traditional method of determining the pore distribution [26] based on the Washburn Eq. (1) is unreliable because of the hyperporous structure [27–29] of the used aerogel.

$$D = \frac{4\gamma \cos \theta}{P} \tag{1}$$

The median pore would be 4.06 μm according to Eq. (1), which does not correspond to the results from SEM microscopy shown in Fig. 1.

For this reason, the assumptions presented in [27, 28, 30] have been used. Low density gels tend to be compressed under the effect of pressure as a result of the influence of injected mercury. The authors described the relationship between the size of the pores and the pressure of the injected mercury with the equation:
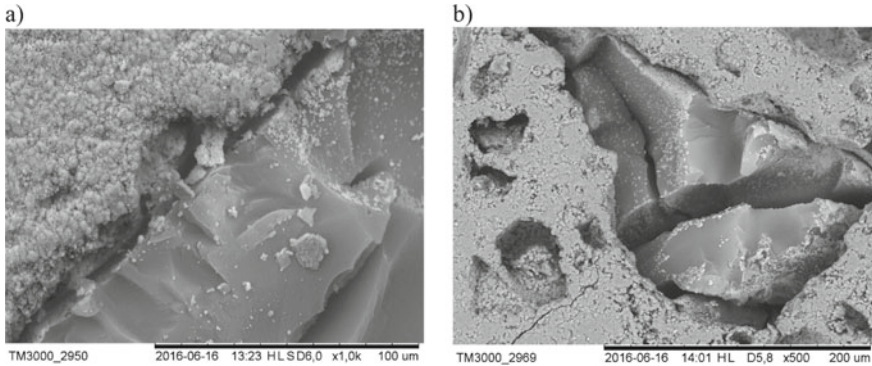
Fig. 1 SEM photos of cross-sections of samples with aerogel particles **a** EC/Aero in $1000\times$ magnification **b** FA/Aero in $500\times$ magnification

$$D = \frac{k_f}{P^{0,25}},\tag{2}$$

where k_f is a coefficient dependent on the transition pressure P_t.

The P_t parameter indicates the value of the pressure at which the mechanism of interaction of the injected mercury with the material changes—below the P_t pressure the material is compressed and above the P_t pressure the mercury is injected into the internal pores of the material.

For the used aerogel, the P_t pressure exceeds the maximum pressure of the used porosimeter, i.e. approx. 413 MPa. This means that the aerogel is compressed and the mercury does not penetrate into the pores within the scope of the experiment. The maximum pressure value of the used porosimeter was therefore used for further calculations. The value of the k_f parameter was calculated from the following formula:

$$k_f = \frac{4\gamma\cos\theta}{P_t^{0,75}}\tag{3}$$

Figure 2 illustrates the log-differential graphs derived for pure aerogel using Eqs. (1) and (2). The Washburn Eq. (1) incorrectly shows a porosity curve in the tested granulate. By applying Eq. (2) according to the guidelines given in [27, 28, 30] it was possible to correctly determine the porosity. The values thus obtained correspond to the data provided by the aerogel manufacturer.

Figure 3 illustrates the log-differential curves of the pore distribution in the tested concrete using the Washburn Eq. (1) only. As with the pure aerogel tests, the results are incorrect. There is a visible increase in porosity in the range from 0.3 to 30 μm when comparing reference concretes without aerogel and their equivalents with aerogel. Such an increase in porosity is completely inconsistent with the specificity of aerogel microstructure.
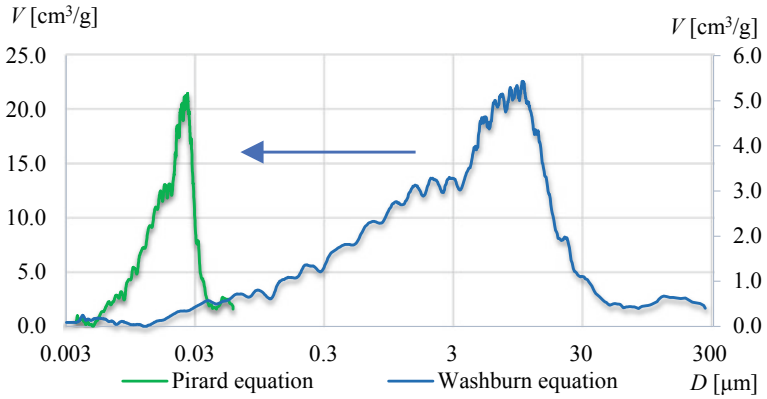
Fig. 2 Log-differential diagrams of pure aerogel obtained with Washburn Eq. (1) and Pirard Eq. (2)
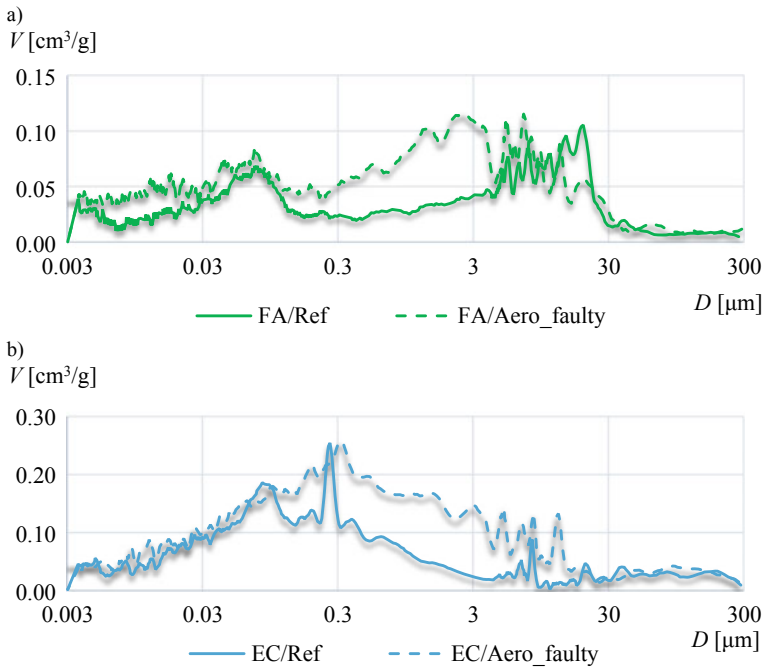

Fig. 3 Log-differential pore size distributions of the composites based on sintered fly ash (**a**) and expanded clay aggregate (**b**) using only Washburn equation

To determine the pore distribution in a cement composite containing aerogel (Aero) in a correct way, the volume of mercury corresponding to the aerogel itself must be extracted by comparing the data with the results for the aerogel-free sample (Ref). The pressure/pore diameter relationship shall then be described separately according to Eq. (1) for the cement matrix and according to Eq. (2) for the aerogel. The data prepared this way can be merged into one graph showing the porosity of the entire composite.

Figures 4 and 5 illustrate the cumulative diagrams of the composites, for which the above mentioned method was applied. In the first step, the volume of mercury corresponding to aerogel granules was extracted from the sample:

$$\text{'Substraction'} = \text{'EC(FA)/Aero\_rawdata'} - \text{'EC(FA)/Ref'} \qquad (4)$$

The cumulative graph obtained in this way was then processed according to Eq. (2) for hyperporous materials, resulting in a graph described as 'Modified substraction'. Then the resulting mercury volume graph corresponding to the aerogel was added to the 'EC(FA)/Aero_fixed' graph, which includes the additional porosity resulting from the use of the aerogel within the normal, expected range of pore size.

Figure 6 illustrates the comparison of the resulting log-differential graphs of composites with and without aerogel. The discrepancy in processed (Fig. 6) and untreated (Fig. 3) results is clearly visible. The porosity of this composite is quite evenly distributed and higher (almost in the whole scope of research) than the porosity of an aerogel-free composite, without taking into account the behaviour of the hyperporous material in the cement matrix.
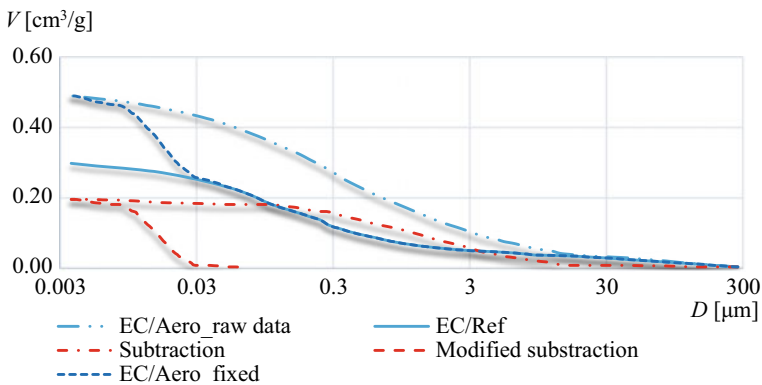

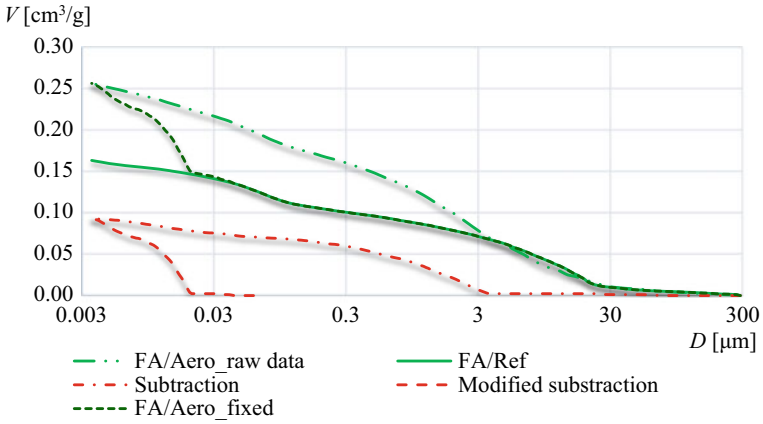**Fig. 4** Cumulative graphs of cement composites with aerogel based on expanded clay aggregate

Fig. 5 Cumulative graphs of cement composites with aerogel based on sintered fly ash aggregate
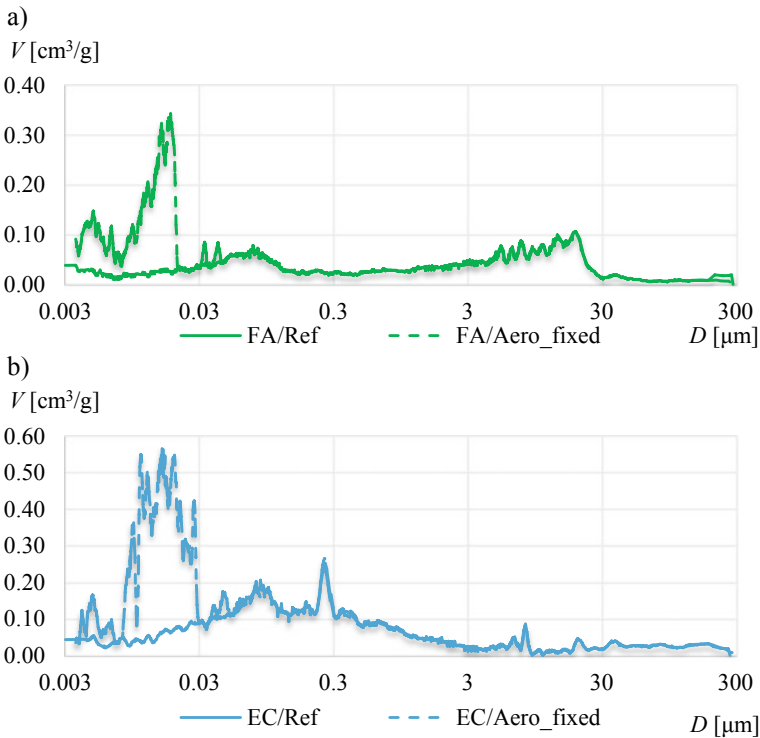

Fig. 6 Correct log-differential pore size distributions of the composites based on sintered fly ash (**a**) and expanded clay aggregate (**b**)

But in reality, the graphs of composites without and with the addition of aerogel should differ only in a small range of porosity, mirroring the porosity of the aerogel itself (about 25 nm). Such an effect was obtained in the processed pore distributions 'FA/Aero_fixed' and 'EC/Aero_fixed'.

Figure 7 illustrates the average compression strength values after 28 days of curing and the volumetric densities of dry concrete. The addition of aerogel in both cases caused a significant decrease in compression strength. In the case of sintered fly ash concrete, the strength decreased by nearly 70% compared to the compression strength of reference concrete. The decrease was 58% in expanded clay aggregate concrete. In both cases, the reduction in bulk density of concrete compared to the reference variants amounted to 18.4%, which corresponds to the fact that the aerogel constitutes 20% of the volume of the tested composites.

Figure 8 illustrates average values of thermal conductivity and volumetric specific heat of concrete in dry state. There is a positive effect of aerogel on the thermal insulation of such a composite. In the case of sintered fly ash concrete, the thermal conductivity decreased by 59% compared to the conductivity of reference concrete, while in expanded concrete the decrease amounted to 42%. The studies also revealed a slight decrease in the volumetric specific heat of concrete by 12% and 6%, respectively.
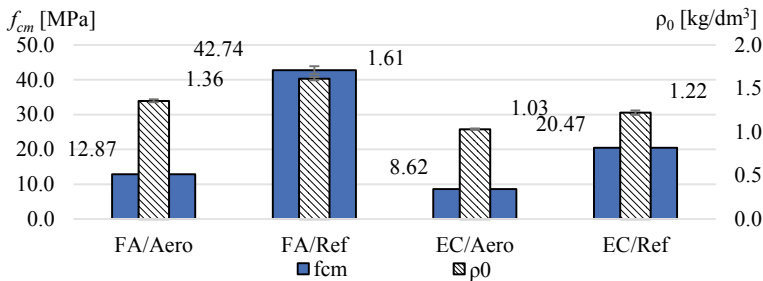

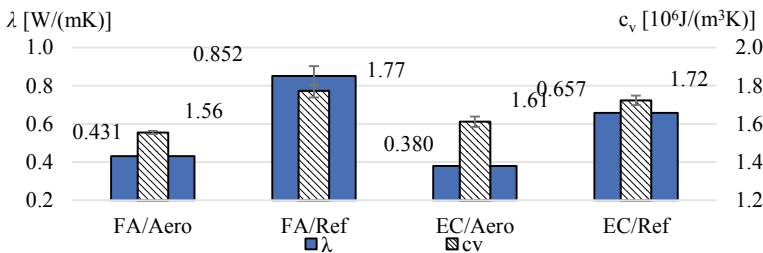**Fig. 7** Average compressive strength f_{cm} of concretes after 28 days of curing and volume densities ρ_0 in dry state

Fig. 8 Average thermal conductivity λ and volumetric specific heat c_v of concrete composites in dry state

4   Conclusions

The paper discusses the findings of studies on the usefulness of mercury porosimetry in the analysis of the porosity structure of cement composites with the addition of aerogel granulate. The results of the studies presented can be summarised by the following conclusions:

- The use of only Washburn equation to analyse the porosity distribution of composites with addition of aerogel granulate results in obtaining incorrect log-differential curves of porosity with abnormal overstated pore ratio in the range from 0.3 to 30 μm.
- The use of Pirard equations for the part of the cumulative curve corresponding to aerogel in modified composites enables the correct determination of the pore ratio in relation to its diameters.
- The method of combining results from both Washburn and Pirard equations presented in the paper makes it possible to determine the full logarithmic-differential curve describing the microstructure of a composite with the addition of aerogel granulate.
- The addition of 20% of the total composite volume of aerogel granulate results in a significant decrease in the compressive strength of concrete based on sintered fly ash and expanded clay aggregate by 70% and 58%, respectively.
- The reduction of the bulk density of concrete in both cases compared to the reference variants amounted to 18.4%.
- The aerogel granulate significantly improves the thermal conductivity of the entire composite. In the case of sintered fly ash concrete, the decrease in conductivity reached 59%, and in expanded concrete 42%.
- The aerogel addition also causes a slight decrease in specific volume heat c_v by 12% for sintered fly ash concrete and by 6% for expanded concrete.

In conclusion, it can be stated that the parallel use of both Washburn equation and the equations proposed by Pirard et al. in the evaluation of porosity of concrete composites with the addition of aerogel granulate enables to obtain proper porosity distributions. This would be impossible by the use of the standard procedure for determining the porosity of these materials with mercury porosimetry.

References

1. Rucińska, T., Kiernożycki, W.: Strain of axially compressed concrete with styrofoam aggregate. Cement, Wapno, Beton **2014**, 33–39 (2014)
2. Rucińska, T., Kiernozycki, W.: Mechanical properties of concrete with foamed styrene aggregate. Cement, Wapno, Beton 289–295 (2010)
3. Liu, F., Wang, J., Qian, X., Hollingsworth, J.: Internal curing of high performance concrete using cenospheres. Cem. Concr. Res. **95**, 39–46 (2017). https://doi.org/10.1016/j.cemconres.2017.02.023
4. Rheinheimer, V., Wu, Y., Wu, T., Celik, K., Wang, J., De Lorenzis, L., Wriggers, P., Zhang, M.-H., Monteiro, P.J.M.: Multi-scale study of high-strength low-thermal-conductivity cement composites containing cenospheres. Cem. Concr. Compos. **80**, 91–103 (2017). https://doi.org/10.1016/j.cemconcomp.2017.03.002
5. Hanif, A., Parthasarathy, P., Ma, H., Fan, T., Li, Z.: Properties improvement of fly ash cenosphere modified cement pastes using nano silica. Cem. Concr. Compos. **81**, 35–48 (2017). https://doi.org/10.1016/j.cemconcomp.2017.04.008
6. Baetens, R., Jelle, B.P., Gustavsen, A.: Aerogel insulation for building applications: a state-of-the-art review. Energ. Build. **43**, 761–769 (2011). https://doi.org/10.1016/j.enbuild.2010.12.012
7. Zhu, P., Brunner, S., Zhao, S., Griffa, M., Leemann, A., Toropovs, N., Malekos, A., Koebel, M.M., Lura, P.: Study of physical properties and microstructure of aerogel-cement mortars for improving the fire safety of high-performance concrete linings in tunnels. Cem. Concr. Compos. **104**, 103414 (2019). https://doi.org/10.1016/j.cemconcomp.2019.103414
8. Wang, L., Liu, P., Jing, Q., Liu, Y., Wang, W., Zhang, Y., Li, Z.: Strength properties and thermal conductivity of concrete with the addition of expanded perlite filled with aerogel. Constr. Build. Mater. **188**, 747–757 (2018). https://doi.org/10.1016/j.conbuildmat.2018.08.054
9. Strzałkowski, J., Garbalińska, H.: Thermal and strength properties of lightweight concretes with the addition of aerogel particles. Adv. Cem. Res. **28**, 567–575 (2016). https://doi.org/10.1680/jadcr.16.00032
10. Garbalińska, H., Strzałkowski, J.: Thermal and strength properties of lightweight concretes with variable porosity structures. J. Mater. Civ. Eng. **30**, 04018326 (2018). https://doi.org/10.1061/(ASCE)MT.1943-5533.0002549
11. Khamidi, M.F., Glover, C., Farhan, S.A., Puad, N.H.A., Nuruddin, M.F.: Effect of silica aerogel on the thermal conductivity of cement paste for the construction of concrete buildings in sustainable cities. **137**, 665–674 (2014). https://doi.org/10.2495/HPSM140601
12. Gao, T., Jelle, B.P., Gustavsen, A., Jacobsen, S.: Aerogel-incorporated concrete: an experimental study. Constr. Build. Mater. **52**, 130–136 (2014). https://doi.org/10.1016/j.conbuildmat.2013.10.100
13. Fickler, S., Milow, B., Ratke, L., Schnellenbach-Held, M., Welsch, T.: Development of high performance aerogel concrete. Energ. Procedia. **78**, 406–411 (2015). https://doi.org/10.1016/j.egypro.2015.11.684
14. Ng, S., Jelle, B.P., Zhen, Y., Wallevik, Ó.H.: Effect of storage and curing conditions at elevated temperatures on aerogel-incorporated mortar samples based on UHPC recipe. Constr. Build. Mater. **106**, 640–649 (2016). https://doi.org/10.1016/j.conbuildmat.2015.12.162

15. Ng, S., Jelle, B.P., Sandberg, L.I.C., Gao, T., Wallevik, Ó.H.: Experimental investigations of aerogel-incorporated ultra-high performance concrete. Constr. Build. Mater. **77**, 307–316 (2015). https://doi.org/10.1016/j.conbuildmat.2014.12.064

16. Liu, S., Zhu, K., Cui, S., Shen, X., Tan, G.: A novel building material with low thermal conductivity: rapid synthesis of foam concrete reinforced silica aerogel and energy performance simulation. Energ. Build. **177**, 385–393 (2018). https://doi.org/10.1016/j.enbuild.2018.08.014

17. Li, P., Wu, H., Liu, Y., Yang, J., Fang, Z., Lin, B.: Preparation and optimization of ultra-light and thermal insulative aerogel foam concrete. Constr. Build. Mater. **205**, 529–542 (2019). https://doi.org/10.1016/j.conbuildmat.2019.01.212

18. Yoon, H.-S., Lim, T.-K., Jeong, S.-M., Yang, K.-H.: Thermal transfer and moisture resistances of nano-aerogel-embedded foam concrete. Constr. Build. Mater. **236**, 117575 (2020). https://doi.org/10.1016/j.conbuildmat.2019.117575

19. Giesche, H.: Mercury porosimetry: a general (practical) overview. Part. Part. Syst. Charact. **23**, 9–19 (2006). https://doi.org/10.1002/ppsc.200601009

20. Ma, H.: Mercury intrusion porosimetry in concrete technology: tips in measurement, pore structure parameter acquisition and application. J. Porous Mater. **21**, 207–215 (2014). https://doi.org/10.1007/s10934-013-9765-4

21. Diamond, S.: Mercury porosimetry: an inappropriate method for the measurement of pore size distributions in cement-based materials. Cem. Concr. Res. **30**, 1517–1525 (2000). https://doi.org/10.1016/S0008-8846(00)00370-7

22. Chung, S.-Y., Abd Elrahman, M., Kim, J.-S., Han, T.-S., Stephan, D., Sikora, P.: Comparison of lightweight aggregate and foamed concrete with the same density level using image-based characterizations. Constr. Build. Mater. **211**, 988–999 (2019). https://doi.org/10.1016/j.conbuildmat.2019.03.270

23. Abd Elrahman, M., Chung, S.-Y., Sikora, P., Rucinska, T., Stephan, D.: Influence of nanosilica on mechanical properties, sorptivity, and microstructure of lightweight concrete. Materials **12**, 3078 (2019). https://doi.org/10.3390/ma12193078

24. Elrahman, M.A., El Madawy, M.E., Chung, S.-Y., Sikora, P., Stephan, D.: Preparation and characterization of ultra-lightweight foamed concrete incorporating lightweight aggregates. Appl. Sci. (Switzerland) **9**, (2019). https://doi.org/10.3390/app9071447

25. Strzałkowski, J., Garbalińska, H.: Porosimetric, thermal and strength tests of aerated and nonaerated concretes. IOP Conf. Ser. Mater. Sci. Eng. **245**, 1–10 (2017). https://doi.org/10.1088/1757-899X/245/3/032017

26. Washburn, E.W.: The dynamics of capillary flow. Phys. Rev. **17**, 273–283 (1921). https://doi.org/10.1103/PhysRev.17.273

27. Pirard, R., Blacher, S., Brouers, F., Pirard, J.P.: Interpretation of mercury porosimetry applied to aerogels. J. Mater. Res. **10**, 2114–2119 (1995). https://doi.org/10.1557/JMR.1995.2114

28. Pirard, R., Rigacci, A., Maréchal, J.C., Quenard, D., Chevalier, B., Achard, P., Pirard, J.P.: Characterization of hyperporous polyurethane-based gels by non-intrusive mercury porosimetry. Polymer **44**, 4881–4887 (2003). https://doi.org/10.1016/S0032-3861(03)00481-6

29. Seraji, M.M., Ghafoorian, N.S., Bahramian, A.R.: Investigation of microstructure and mechanical properties of novolac/silica and C/SiO2/SiC aerogels using mercury porosimetry method. J. Non-Cryst. Solids **435**, 1–7 (2016). https://doi.org/10.1016/j.jnoncrysol.2015.12.021

30. Alié, C., Pirard, R., Pirard, J.-P.: Mercury porosimetry: applicability of the buckling—intrusion mechanism to low-density xerogels. J. Non-Cryst. Solids **292**, 138–149 (2001). https://doi.org/10.1016/S0022-3093(01)00881-X

Calcined Clay-To-Limestone Ratio on Durability Properties of Concrete with Low Clinker CEM II/B-M(Q/LL) Cements

Check for updates

S. Ferreiro, R. Sacchi, L. Frølich, D. Herfort, and J. S. Damtoft

Abstract The present work focuses on the effect of different calcined clay-to-limestone ratios for a clinker replacement level of 35% on durability properties of CEM II/B-M(Q-LL) cements. Two calcined clay-to-limestone ratios, 0.5 and 0.83 expressed as Q/(Q + L), were considered in this investigation. In addition, some specific manufactured batches of finely ground calcined smectite clay and limestone filler with relative high chloride contents were opportunely considered for testing. This was done to investigate the viability of using alternative fuels in clinker, limestone filler and calcined clay productions without compromising the durability of concrete. The durability properties evaluated in concrete specimens with comparable 28-day strength demonstrated that these low clinker cements show a high resistance to chloride penetration, which is independently of calcined clay-to-limestone ratio and chloride content of the cement within the investigated compositions. Moreover, the high reactivity of calcined smectite clay is enough to mitigate ASR even at the cement composition with the lowest Q/(Q + L) and the increased alkalis content derived from calcined clay does not affect the performance in concrete regarding ASR. Nonetheless, it was detected that the increase of the calcined clay at the expense of limestone content in these cement compositions leads to a decrease of the resistance to freeze/thaw.

Keywords Calcined clay · Limestone · Chloride · Freeze/thaw · ASR

1 Introduction

The reduction of clinker content in cement by substitution with supplementary cementitious materials (SCM) is a common practice to reduce CO_2 emissions in cement manufacture. Within the current prescriptive European cement standard EN 197-1, clinker replacement is limited to 35% by wt. in the family of common

S. Ferreiro (✉) · R. Sacchi · L. Frølich · D. Herfort · J. S. Damtoft
Cementir Holding S.p.A., 9220 Aalborg, Denmark
e-mail: sergio.f.garzon@cementirholding.it

cements containing limestone as main constituent (i.e., above 5% by wt.) or in combination with other SCM, such as calcined clay, to manufacture CEM II/B-M (Q-L/LL).

Calcined clays are usually produced in either flash or rotary calciners at a temperature between 600 and 900 °C, significantly lower than needed for clinker production, but still and consequently, some CO_2 emissions result from fuel combustion. Although these emissions can be minimized with the use of alternative fuels that contain biomass, as commonly seen with clinker production, the most suitable clay pits are sometimes located away from cement plants. The distance between clay pits and cement plants normally leads to additional CO_2 emissions associated to transportation. On the contrary, limestone is normally quarried nearby cement plants. Similarly, raw meal dust limestone filler is co-produced along with Portland clinker. Both are suitable sources of limestone L or LL. Certainly, the production of finely ground limestone requires energy for drying and grinding. Yet, it is reasonable to believe that the overall consumption for pre-conditioning the quarried limestone would rarely be higher than analogue processes required in the transformation of wet raw clay into ground calcined clay. Therefore, further CO_2 reduction associated to cement production could tentatively be achieved by increasing the use of limestone at the expense of calcined clay for a given clinker replacement as far as the durability properties of the concrete exposure class are satisfied.

2 Materials and Methods

The chemical composition determined by XRF and physical characteristics of the materials used in this study are shown in Table 1. One calcined smectite clay (Q), two limestone fillers (L_1 and L_2) and one Ordinary Portland Cement (OPC) were used. The calcined clay sample (Q) was manufactured in a rotary kiln by calcination of a smectite clay, which was finely ground in laboratory scale ball mill. The limestone fillers, L_1 is a raw meal dust produced at Aalborg Portland cement plant and L_2 is a high purity Maastrichtian chalk from Rørdal, Northern Denmark. L_2 was a minor additional constituent of one of the two blended cements tested in concrete just to ensure that Cl content is within EN 197-1 requirement. The OPC sample used was a CEM I 52.5N type.

Six blends (A-F) were prepared by mixing OPC, Q and L_1 with different calcined clay-to-calcined clay plus limestone ratio (Q/(Q + L)) as shown in Table 2. This was done to investigate the synergetic effect of combinations of these materials by the determination of compressive strength at 28 days determined according to EN 196-1 but normalized to 2% air content [1]. Then, two extra bulk samples of blended cements (C_1 and C_2) were prepared to evaluate the performance and durability properties of strength class C35/45 concrete. The equivalent alkali and chloride contents of C_1 and C_2 determined according to EN 196-2 are also shown in Table 2.

Table 1 Chemical composition and physical characteristics of the blended cement constituents

Main oxide (%)	OPC	Q	L_1	L_2
SiO_2	19.5	48.3	12.0	3.92
Al_2O_3	5.42	17.7	2.95	0.33
Fe_2O_3	3.99	9.74	1.69	0.14
CaO	63.9	10.2	44.5	53.7
MgO	0.87	2.53	0.55	0.35
K_2O	0.43	2.50	0.76	0.05
Na_2O	0.27	1.04	0.23	0.08
SO_3	3.52	1.35	0.22	0.05
TiO_2	0.29	0.97	0.15	0.02
Cl	0.01	0.13	0.46	0.01
P_2O_5	0.29	0.20	0.17	0.10
Cr_2O_3	0.01	0.02	0.00	0.00
L.O.I	0.68	5.94	35.5	41.8
Density (kg/m^3)	3150	2700	2710	2700
Blaine (m^2/kg)	390	1370	1260	1210

Table 2 Blended cement compositions

Sample ID	OPC (%)	Q (%)	L_1 (%)	L_2 (%)	Q/ (Q + L)	Clinker content EN 197-1 (%)	Na_2Oeq (%)	Cl (%)
A	95.23	–	4.77	–	0	95.0	0.60	0.04
B	66.11	–	33.89	–	0	65.0	–	–
C	66.11	16.94	16.94	–	0.50	65.0	–	–
D	66.11	25.42	8.47	–	0.75	65.0	–	–
E	66.11	29.65	4.24	–	0.875	65.0	–	–
F	66.11	33.89	–	–	1	65.0	–	–
C_1	66.11	16.94	13.51	3.44	0.50	65.0	0.99	0.10
C_2	66.11	28.08	5.81	–	0.83	65.0	1.15	0.08

The mix compositions and performance of the concretes used to determine the resistance to chloride penetration, freeze/thaw and the potential alkali-silica reactivity (ASR) of these combinations of cementitious materials are summarized in Table 3. Slump and air content were determined after mixing in accordance to EN 12350-2 and EN 12350-7, respectively. In addition, air-void parameters of fresh air-entrained concrete (spacing factor and specific surface) were measured with an AVA-3000 from Germann Instruments. The compressive strength at 28 days was assessed in accordance to EN 12390-3 in 3 cylinders (10/20 cm). Table 3 also shows the embodied CO_2 emissions per m^3 of concrete, using the environmental product declaration of the OPC producer [2].

Table 3 Concrete mix compositions

Materials (kg/m^3 concrete)	For Cl penetration and freeze/thaw resistance tests		For ASR tests	
	C_1	C_2	C_1	C_2
C_1	416		416	
C_2		416		416
Quartz sand (0–1 mm)	653	653		
ASR sand (0–4 mm)			653	653
Crushed granite aggregate (4–8 mm)	163	163	163	163
Crushed granite aggregate (8–16 mm)	903	903	903	903
Water	159	166	159	166
Plasticizer	2.9	2.9	2.9	2.9
Air entrainment agent	2.3	2.3	2.3	2.3
Superplasticizer	2.8	4.8	3.9	5.6
w/c	0.398	0.419	0.400	0.420
Slump (mm)	120	110	90	90
Air content (%)	6.6	6.2	4.6	5.1
Specific surface area (mm^{-1})	21	16	15	14
Spacing factor (mm)	0.26	0.34	0.43	0.46
28d strength normalized to 6.5% air (MPa)	49.1	48.2	47.2	46.4
CO_2 (kg/m^3 concrete)[a]	272	281	272	281

[a]The embodied CO_2 of plasticizer, air entrainment agent and superplasticizer has been omitted. The embodied CO_2 of sand and granite is not differentiated across grades

The resistance to chloride penetration was evaluated by NT Build 492 and 443 methodologies. The chloride migration coefficient (NT Build 492) was determined in three concrete specimens per term cured for 28, 56, 91 and 182 days, whilst the effective chloride transport coefficient (NT Build 433) was evaluated in two concrete specimens per term with maturities of 28 and 91 days submerged in saline solution for 35 days.

The freeze/thaw resistance of the concretes was measured in accordance with Swedish standard SS 137244 following the method I-A [3] in four subsamples obtained by sawing concrete cylinders (15/30 cm) cured for 35 ± 1 days. The freeze/thaw resistance of a concrete can be designated on the basis on mass of scaling at 28, 56 and 112 cycles (m_{28}, m_{56} and m_{112}, respectively) following the criteria shown below:

- *Very good*: m_{56} average < 0.10 kg/m^2,
- *Good*: m_{56} average < 0.20 kg/m^2 or,
  m_{56} average < 0.50 kg/m^2
  and m_{56}/m_{28} average < 2 or
  m_{112} average < 0.50 kg/m^2,

- *Acceptable*: m_{56} average < 1.00 kg/m^2
  and $m_{56}/m_{28} < 2$ or
  m_{112} average < 1.00 kg/m^2
- *Unacceptable*: the above is not fulfilled.

The potential alkali-silica reactivity of these combinations of cementitious materials was evaluated in mortar bars in accordance with ASTM C1567 and concrete specimens were tested in a modified TI-B 51 method with an alkali-silica reactive sand (ASR). This sand was graded to prepare the mortar bars in accordance to ASTM C1567 procedure but used as quarried to cast two squared concrete bars $10 \times 10 \times 40$ cm for TI-B 51 test. Analogous concrete mix compositions were used as shown in Table 3, substituting one-to-one by weight the non-ASR quartz sand by the ASR sand. The concrete bars were initially cured for 28 days at 20 °C and then, submerged in a volume of an alkaline solution at 50 °C 4 times the volume of the concrete bar, in accordance to the original TI-B 51 test method. The length change was tracked up to 140 days of exposure. This test procedure was mainly modified to use 1 N NaOH instead of saturated NaCl solution, to avoid any possible interference by Friedel's salt formation. In fact, a more severe alkali environment was considered in the modified method because the sodium concentration in 1 N NaOH solution (40 g NaOH/l) is 1.58 times higher than in a saturated NaCl solution at 50 °C (37 g of NaCl/l).

3 Results

3.1 Synergetic Effect

Figure 1 shows the relative compressive strength at 28 days of five CEM II/B cements (B, C, D, E and F) with 35% clinker replacement and different Q/(Q + L) ratios (0, 0.5, 0.75, 0.875 and 1, respectively) to the control cement CEM I (named as A). The results demonstrated there is a synergetic effect between these calcined clay and limestone in accordance with [4], that provides equivalent or higher performance to CEM I type cement for Q/(Q + L) ratio equal or above 0.7 [5]. It can be also observed that performance follow a linear trendline (dashed line) between 0 and 0.875 and therefore, it can be deducted that the optimum Q/(Q + L) ratio for maximized 28 days strength is not less than 0.875 for 35% clinker replacement.

Though Q/(Q + L) ratio of 0.875 resulted in the highest 28 days strength, two other cements (C_2 and C_1) with Q/(Q + L) ratios (0.83 and 0.5) were prepared (Table 2) and tested in concrete (Table 3). C_2 with Q/(Q + L) of 0.83 overperforming CEM I on 28 days strength was chosen because it is the highest ratio allowed in CEM II/B-M compositions, whilst C_1 with a Q/(Q + L) ratio of 0.5 was selected to investigate an intermediate composition of CEM II/B-M type that underperforms CEM I on 28 days strength.
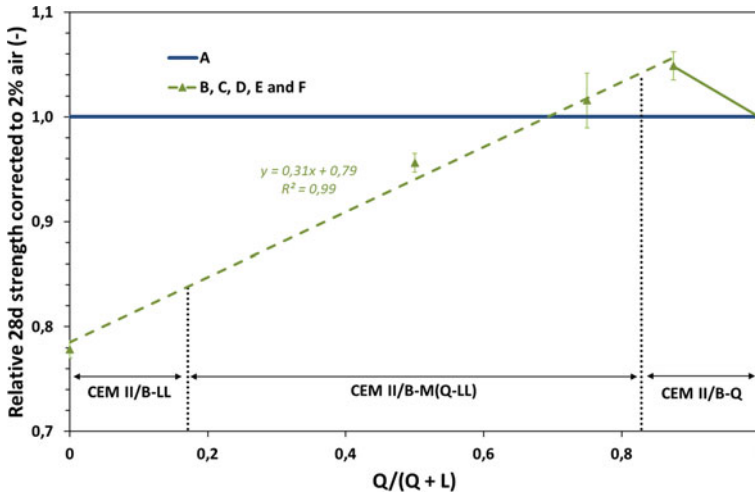
Fig. 1 Relative compressive strength at 28 days of blended cements CEM II/B type including calcined smectite clay and limestone

3.2   Concrete Performance and Durability Properties with Different Combinations of Calcined Clay and Limestone

The concrete mix compositions shown in Table 3 were mainly designed to provide equivalent compressive strength at 28 days in concrete with both CEM II/B-M (Q-LL) cements, but the dosage of superplasticizer (SP) was adjusted for each concrete to achieve acceptable and similar slump and air content after mixing. It is remarkable to notice that the higher calcined clay content of C_2 demanded higher dosages of SP [4], although lower w/c was used in concrete with C_1. It was also observed that the substitution of quartz sand in concrete for ASR tests also increased the SP dosage at around 1 kg/m^3 for both blended cements. The durability properties (resistance to chloride penetration, freeze/thaw and ASR) of two blended cements CEM II/B-M(Q-LL) were evaluated.

Resistance to Chloride Penetration

Though non-steady-state migration coefficients determined by NT Build 492 (Fig. 2) cannot be directly compared with Cl diffusion coefficient obtained from non-steady-state immersion test of NT Build 443 (Fig. 3), both C_1 and C_2 show the same resistance to chloride penetration from 28 to 182 days of hydration. Hence, the amount of calcined clay in C_1 is enough to provide the same effectiveness on chloride binding in concrete as C_2, even though the chloride content of C_1 measured in accordance with EN 196-2 is higher than C_2 (Table 2).
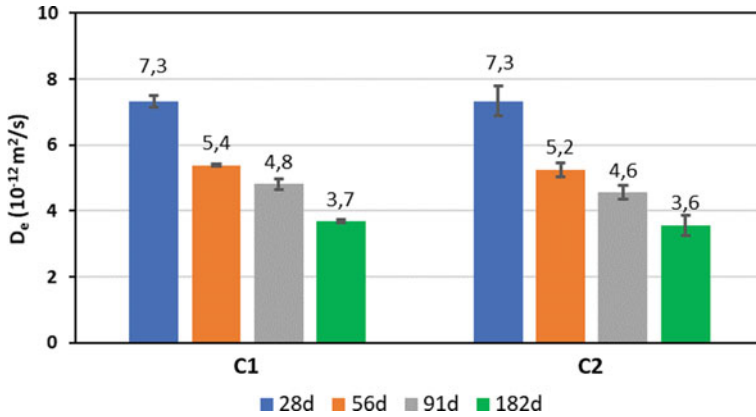
Fig. 2 Chloride migration coefficient determined in accordance with NT Build 492 at maturities of 28, 56, 91 and 182 days
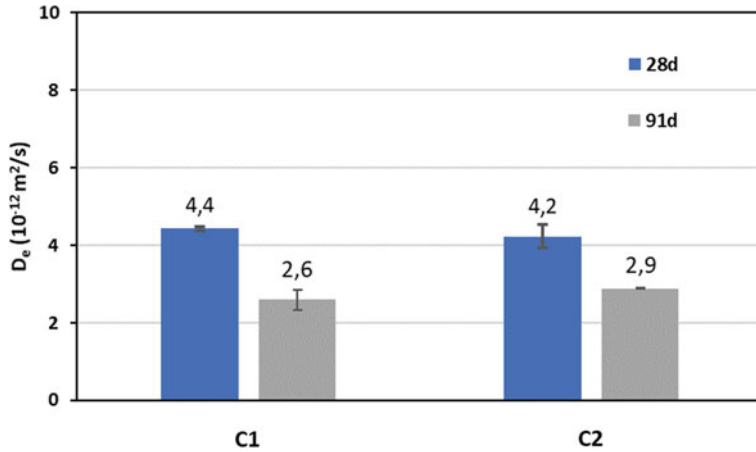

Fig. 3 Effective chloride transport coefficient determined in accordance with NT Build 443 at maturities of 28 and 91 days

Freeze/Thaw Resistance

The average scaling of the specimens shows that there is a significant difference of performance between the two cement compositions up to 56 freeze/thaw cycles (Fig. 4—left). The test was not continued up to 112 cycles because C_1 already demonstrated a "*Good*" resistance (Fig. 4—right), whilst C_2 would result in "*Acceptable*" in best-case scenario in accordance with SS 137244 criteria. However, the extrapolation of the scaling up to 112 cycles (dotted line in Fig. 4—left) clearly indicates that freeze/thaw resistance of C_2 would likely end up being "*Unacceptable*". The lower frost resistance detected at the concrete specimens of C_2
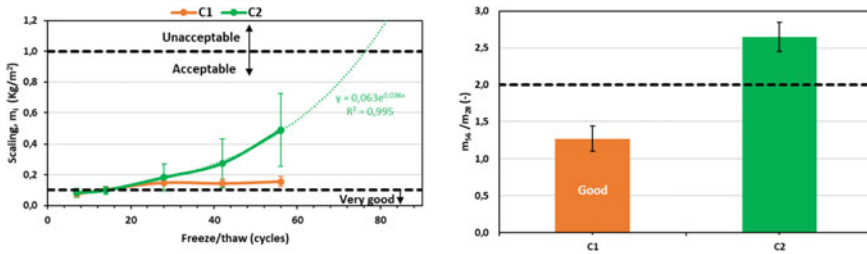
Fig. 4 Scaling of concrete over freeze/thaw cycles (**left**) and m_{56}/m_{28} ratio (**right**)

with a high pozzolan content is in agreement with previous investigations at analogous concrete mix compositions with increased contents of fly ash [6].

Alkali-Silica Reactivity Tests

The potentially deleterious expansion due to alkali-silica reaction (ASR) was firstly tested in accordance to ASTM C1567. The great expansion shown by the cement A (3.5 times higher than requirement) reveals the high potential alkali-silica reactivity of the ASR—sand whether tested with a CEM I without any pozzolan (Fig. 5—left). Inversely, C_2 demonstrated an excellent performance mitigating ASR, whilst the expansion of C_1 slightly above the requirement may be indicative of potentially deleterious expansion.

As recommended by ASTM C1567 whether the expansion is more than 0.10%, the potential for deleterious reaction was reassessed by testing the same combination of materials in concrete (Fig. 5—right). The results of the modified T-B 51 method show that the concrete bars of both C_1 and C_2 have a low expansion up to 14 days, which levels off or even decreased up to 140 days. Contrarily to the results of the accelerated mortar-bar method, C_1 performed better than C_2 mitigating ASR in concrete.

The relative difference on performance of the cements can be explained by the influence of the test conditions on the pozzolanic reaction rate. The better performance of C_2 than C_1 in accelerated mortar-bar method may be ascribed to the high
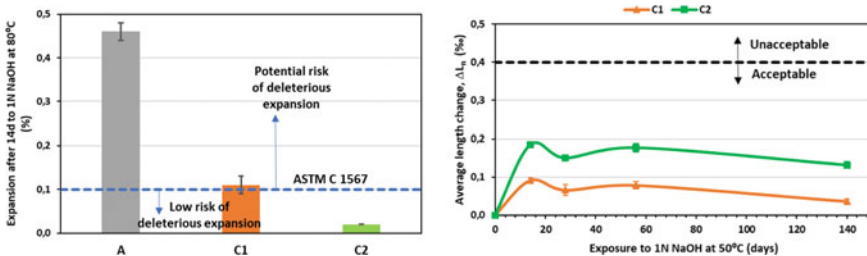

Fig. 5 Expansion of mortar bars in ASTM C1567 test (**left**) and average length change of concrete bars in modified TI-B 51 method (**right**)

temperature (80 °C for 24 h of water curing and subsequent 14 days of NaOH exposure) and water-to-cement ratio of 0.47, which enhance pozzolanic reactivity of the higher calcined clay content of C_2 and uptake in C–S–H, regardless the higher Na_2Oeq content. On the other hand, the lower water-to-cement ratio used in concrete specimens and temperature (20 °C for 28 days of water curing and 50 °C for NaOH exposure) may result in relative higher amount of soluble alkalis with C_2.

4 Conclusion

CEM II/B-M(Q-LL) cements containing two different combinations calcined smectite clay and limestone showed a very good and equivalent resistance to chloride penetration from 28 to 182 days of maturity. Therefore, it can be deducted that the resistance to chloride penetration of these CEM II/B-M type cements in concrete with a given 28 days strength performance is independent of calcined clay-to-limestone ratio within the range of 0.5 to 0.83, expressed as Q/(Q + L). The amount of calcined clay in CEM II/B-M with Q/(Q + L) of 0.5 is also enough to mitigate ASR and increased alkalis content derived from calcined clay does not significantly affect the performance in concrete with ASR sand for any of these two cement compositions. In addition, it is demonstrated that a good frost resistance can be achieved and that the decreasing Q/(Q + L) ratio has not a detrimental effect on frost resistance. These facts prove that a further reduction of CO_2 footprint is possible without compromising the durability properties of the concrete.

References

1. Osbæck, B.: The influence of air content by assessing the pozzolanic activity of fly ash by strength testing. Cem. Concr. Res. **15**, 53–64 (1985)
2. Aalborg, P.: RAPID CEM I 52.5 N (LA)—Environmental Product Declaration (2017). https://www.epd-norge.no/sement/aalborg-portland-rapid-cement-cem-i-52-5-n-la-article1654-324.html
3. SS 137244.: Concrete Testing—Hardened Concrete—Detachment During Freezing. Method I-A (Exposure Surface: Sawn Surface and Freezing Liquid: 3% NaCl Solution) (2005)
4. Herfort D., Damtoft, J.S.: Portland limestone cement with calcined clay. Patent no. DK2429966T3 (2009)
5. Ferreiro, S., Herfort, D., Damtoft, J.S.: Effect of raw clay type, fineness, water-to-cement ratio and fly ash addition on workability and strength performance of calcined clay-limestone Portland cements. Cem. Concr. Res. **101**, 1–12 (2017)
6. Hasholt, M.T., Christensen, K.U., Pade, C.: Frost resistance of concrete with high contents of fly ash - A study on how hollow fly ash particles distort the air void analysis. Cem. Concr. Res. **119**, 102–112 (2019)

A New Dilation Model for FRP Fully/partially Confined Concrete Column Under Axial Loading

Javad Shayanfar, Mohammadali Rezazadeh, Joaquim Barros, and Honeyeh Ramezansefat

Abstract Experimental research has confirmed that the usage of fiber reinforced polymer (FRP) composite materials can be a reliable solution to substantially improve axial and dilation behavior of confined concrete columns. In this regard, FRP partial confinement system is a good compromise from the cost competitiveness point of the view, while the application of discrete FRP strips provides less confinement efficiency compared to full confinement system. Experimental observations demonstrated that the concrete at the middle distance between the FRP strips experiences more transversal expansion compared to concrete at the strip regions. It can result in a considerable decrease in the confinement performance in curtailing concrete transversal expansion, overwhelming the activation of FRP confining pressure. The present study is dedicated to the development of a new dilation model for both full and partial confinement systems, which takes into account the substantial impact of non-uniform distribution of concrete transversal expansion, a scientific topic not yet addressed comprehensibly in existing formulations. For this purpose, a reduction factor was developed in the determination of the efficiency confinement parameter, by considering available experimental results. Furthermore, based on a database of FRP fully/partially confined concrete, a new analytical relation between secant Poisson's ratio and axial strain was proposed. To evaluate the reliability and predictive performance of the developed dilation model, it was applied on the simulation of experimental tests available in the literature. The results revealed that the developed model is capable of predicting the experimental counterparts with acceptable accuracy in a design context.

Keywords FRP confined circular concrete · Partial confinement · Dilation behavior · Axial loading

---

J. Shayanfar (✉) · M. Rezazadeh · J. Barros · H. Ramezansefat
ISISE, Department of Civil Engineering, University of Minho, 4800-058 Guimarães, Portugal

1   Introduction

It is well-known that the application of fiber reinforced polymer (FRP) composite materials to externally confined concrete columns can potentially lead to substantial enhancements in terms of strength, ductility, and energy dissipation, as confirmed by studies [1–10]. Steel hoops ensure a certain concrete confinement in reinforced concrete columns. If not sufficient, concrete confinement can be enhanced by applying FRP strips between the existing steel hoops, resulting in a good compromise in terms of confinement efficiency and cost competitiveness [1–3]. However, the application of discrete FRP strips might pose less confinement efficiency compared to FRP fully confined concrete column (FCCC) as confirmed by [3, 7–10].

To predict the effectiveness of a FRP confining system for the improvement of concrete column responses, several theoretical models have been developed. These models are function of the relationship between axial strain and concrete transversal expansion (known as dilation behavior). Consequently, their predictive performances highly depends on the reliability of this relation. Several analytical models have been proposed to predict dilation behavior of FRP confined concrete. Mirmiran and Shahawy [5] proposed a dilation model to predict the tangential Poisson's ratio (the rate of change of transversal strain with respect to axial strain) vs axial strain relation, depending on the parameter of confinement stiffness (the ratio of confinement pressure over transversal strain). Xiao and Wu [6] derived a relation between secant Poisson's ratio (the ratio between transversal strain and axial strain) and axial strain as a function of unconfined concrete compressive strength and confinement stiffness. Teng et al. [11] and Lim and Ozbakkaloglu [12] proposed transversal strain versus axial strain relations dependent on the level of confinement pressure. In the case of FRP partially confined concrete column (PCCC), Zeng et al. [9] adopted Teng et al. [11]'s dilation model by applying a reduction factor in confinement pressure due to the vertical arching action. It would be noteworthy that the existing dilation models were formulated and calibrated based on FCCC specimens, therefore their applicability in the case of partial confining system is arguable. Furthermore, in the case of PCCC, the concrete at the middle distance between FRP strips, as a critical section, experiences more transversal expansion compared to concrete at the strip regions as confirmed by [7–10]. To the best of the authors' knowledge, the impact of non-uniform transversal expansion on the confinement pressure has not been addressed comprehensibly in the existing formulations. Accordingly, a generalized dilation model applicable for the both FCCC and PCCC, considering the effect of non-uniform expansion, is still lacking.

In this study, by using the results from a database of test results of FCCC and PCCC, a new dilation model with a design framework is developed that considers the FRP confinement stiffness. To account for the effect of the non-uniform distribution of the concrete expansion, a new formulation is also proposed based on the concept of confinement efficiency factor (CEF).

2 Concept of Confinement Efficiency Factor (CEF)

2.1 Original Concept and Its Limitation When Applied to RC Columns Partially Confined with FRP

During axial loading, in a PCCC system, the vertical arching action between the strips can lead to effectively and ineffectively confined concrete regions. Accordingly, the axial stress applied on the confined concrete can be assumed to be carried through two separate components: (1) load carried by ineffectively confined area; (2) load carried by effectively confined area. With the determination of the axial stress versus axial strain relationships of each area, the entire axial stress versus axial strain curve of PCCC can be obtained. On the other hand, for the sake of simplicity, CEF is adopted to reduce confinement stress, f_l, acting on the effectively confined area, so that the reduced confinement pressure is applied on the whole cross-section. The employed reduction CFE factor is generally represented by "K_e". Accordingly, the whole cross-section is uniformly subjected to an effective confinement stress $f_{l,ef} = K_e \times f_l$.

In the case of the confined concrete by transversal steel reinforcements (steel partial system), Mander et al. [13] proposed an equation to calculate K_e as A_{eff}/A_g, where A_{eff} is the effectively confined core area at the critical section (the middle distance between steel hoops) and A_g is the whole cross-section area. Accordingly, assuming a second order parabola curve with the vertical arching angle equal to $45°$, K_e was proposed as:

$$K_e = \frac{A_{eff}}{A_g} = \left(1 - \frac{s'}{2D}\right)^2 \tag{1}$$

where D is the diameter of the column's circular cross section; s' is the clear distance between two adjacent steel hoops. Even though this approach has been adopted for the case of PCCC [14–16], a closer examination of the approach reveals that this model only addresses the effect of the vertical arching action in the determination of K_e. However, in partial confinement strategy, concrete transversal expansion at the critical section would be more than the expansion at mid-plane of consecutive confining systems, resulting in a reduction of confinement pressure [7–10]. Accordingly, in case of PCCC, in addition to the vertical arching action, the impact of concrete transversal expansion should be addressed in the determination of K_e.

2.2 Concrete Lateral Expansion

In the present study, based on the experimental observations of PCCC [7–10], it was assumed that during axial loading, concrete at the critical section experiences

the maximum transversal expansion, $\varepsilon_{l,j}$, as shown in Fig. 1. However, at the mid-plane of the FRP strips, concrete is subjected to lower dilatancy, represented by $\varepsilon_{l,i}$. If k_ε defines the ratio of concrete expansion at the strip mid-plane and at the critical section, FRP tensile strain $\varepsilon_{h,P}$ is equal to $\varepsilon_{l,i} = k_\varepsilon \varepsilon_{l,j}$ (assuming that radial and hoop circumferential strains are identical). In the case of FCCC, due to a uniform distribution of concrete expansion, k_ε is equal to 1, leading to $\varepsilon_{h,F} = \varepsilon_{l,j}$. Accordingly, the ratio of FRP confining stress in PCCC and FCCC named by, f'_f and f_f, respectively, is:

$$\frac{f'_f}{f_f} = \frac{E_f \varepsilon_{h,P}}{E_f \varepsilon_{h,F}} = \frac{\varepsilon_{l,i}}{\varepsilon_{l,j}} = k_\varepsilon \tag{2}$$

As a result, the reduction factor k_ε addresses the impact of the non-uniform distribution of concrete transversal expansion in the determination of FRP confining stress.

The maximum value of this factor ($k_{\varepsilon,max}$) is equal to 1 for FCCC. However, for PCCC, by increasing s_f, k_ε decreases until the minimum value ($k_{\varepsilon,min}$), resulting in extensive damage around the critical section and marginal cracking at strip regions. According to the test data reported by Wang et al. [8], for $s_f/D \geq 1$, k_ε approaches quickly to $k_{\varepsilon,min}$. Assuming a linear relation between k_ε and s_f/D:

$$k_\varepsilon = 1 - \left(1 - k_{\varepsilon,min}\right)\frac{s_f}{D} \quad \text{for} \quad 0 \leq s_f/D \leq 1 \tag{3}$$

To derive $k_{\varepsilon,min}$, it was assumed that concrete at the critical section is unconfined with ultimate secant Poisson's ratio $v_{s,u}$. In addition, at strip zone, concrete behaves with initial secant Poisson's ratio of unconfined concrete, $v_s = v_{s,0}$. Hence, based on the dilation responses of a series of unconfined concrete specimens tested by Osorio
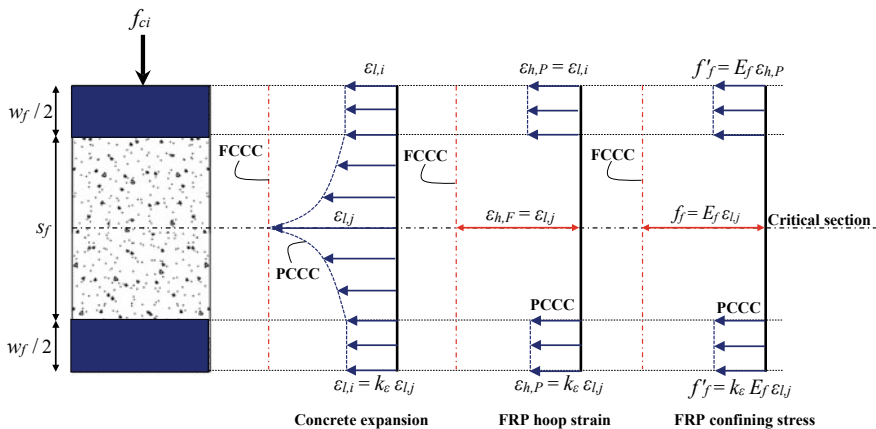

Fig. 1 Dilation behavior in PCCC system

et al. [17], $v_{s,u}$ and $v_{s,0}$ were estimated approximately as 2.5 and 0.2, respectively, therefore $k_{\varepsilon,min}$ can be calculated as:

$$k_{\varepsilon,min} = \frac{\varepsilon_{l,i}}{\varepsilon_{l,j}} = \frac{\varepsilon_c v_{s,0}}{\varepsilon_c v_{s,u}} = \frac{0.2}{2.5} = 0.08 \tag{4}$$

Figure 2 compares the proposed relation between k_ε and s_f/D, with the test results [3, 8–10]. In this figure $v_{s,u}^{exp}$ is the ultimate secant Poisson's ratio at the mid-plane FRP strips, evaluated as the ratio of $\varepsilon_{h,P}^{exp}$ recorded by strain gauge and corresponding axial strain ε_c. It should be noted that the experimental values of k_ε^{exp} are determined as $v_{s,u}^{exp}/2.5$. As shown in this figure, the proposed k_ε seems to provide relatively good agreement with the experimental test data.

2.3 Vertical Arching Action

Figure 3 shows the non-uniform distribution of confinement pressure in a PCCC system. In this study, the reduction factor k_v was defined so that the concrete could be considered to be evenly subjected to a reduced confinement pressure $f_{l,ef} = k_v \times f_{l,i}$.

Here $f_{l,i}$ is the confinement pressure generated by FRP confining stress f_f' at the strip region. Since confinement pressure is a function of the confining stress [13], in case of PCCC, the ratio between $f_{l,i}$ and f_l can be expressed as:

$$\frac{f_{l,i}}{f_l} = \frac{f_f'}{f_f} \rightarrow f_{l,i} = \frac{f_f'}{f_f} \times f_l \rightarrow f_{l,i} = k_\varepsilon \times f_l \tag{5}$$

Fig. 2 Variation of k_ε with s_f/D obtained from Eq. (3) and the test results [3, 8–10]
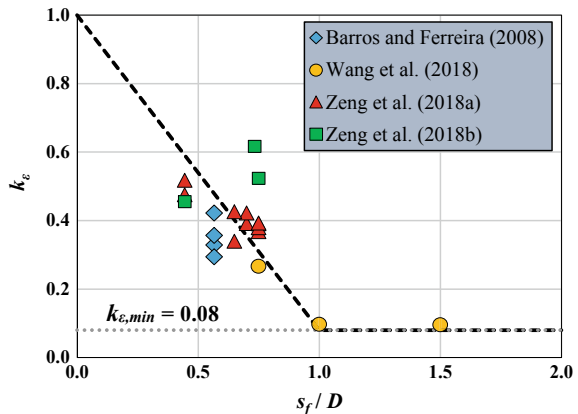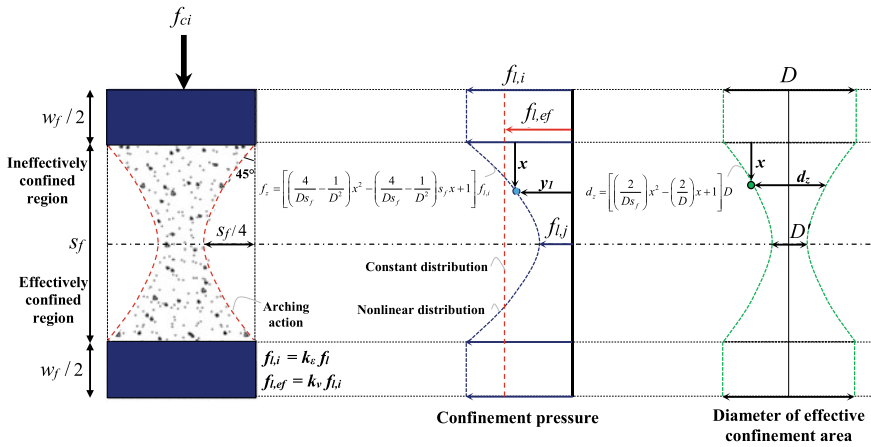
Fig. 3 Distribution of confinement pressure in PCCC

Therefore, the effective confinement pressure $f_{l,ef}$ is obtained from:

$$f_{l,ef} = k_v f_{l,i} = k_v k_\varepsilon f_l = K_e f_l \tag{6}$$

in which

$$K_e = k_v k_\varepsilon \tag{7}$$

where K_e defines the efficiency confinement factor as a function of k_ε and k_v, based on CEF as shown in Fig. 3. Hence, the determination of the reduction factor k_v in Eq. (7) is necessary, as an input parameter. For this purpose, considering the equilibrium of confinement forces in a PCCC results in:

$$k_v f_{l,i}(s_f + w_f)D = 2f_{l,i}\frac{w_f}{2}D + 2\int_0^{s_f/2} f_z d_z dx \rightarrow k_v = \frac{f_{l,i}w_f D + 2\int_0^{s_f/2} f_z d_z dx}{f_{l,i}(s_f + w_f)D} \tag{8}$$

where w_f is the FRP width; f_z and d_z are the functions of FRP lateral pressure and the diameter of effective confinement area, respectively, derived from the geometry constraint as presented in Fig. 3. Then, solving the integration yields:

$$k_v = \frac{w_f + s_f\left(1 - \frac{s_f}{D} + \frac{13s_f^2}{30D^2} - \frac{s_f^3}{15D^3}\right)}{s_f + w_f} \tag{9}$$

Hence, by introducing k_ε and k_v obtained from Eqs. (3) and (9), K_e can be easily calculated by Eq. (7). Based on the preliminary sensitivity analysis of the parameters in K_e, for further simplification, a simplified equation was developed as:

$$K_e = 0.97 + 0.12\frac{w_f}{D} - 1.25\frac{s_f}{D} \leq 1 \quad \text{for} \quad s_f/D < 0.5 \tag{10a}$$

$$K_e = 0.75 + 0.12\frac{w_f}{D} - 0.79\frac{s_f}{D} \geq 0.04 \quad \text{for} \quad 0.5 \leq s_f/D < 1 \tag{10b}$$

$$K_e = 0.04 - 0.02\left(\frac{s_f}{D} - 1\right) \geq 0 \quad \text{for} \quad s_f/D \geq 1 \tag{10c}$$

Figure 4a shows the variation of K_e with s_f/D in a PCCC with $w_f/D = 0.3$ according to Eq. (7). It highlights the mandatory impact of k_ε in the confinement efficiency factor K_e. Moreover, the good agreement between the results obtained from Eq. (7) and the simplified Eq. (10a–10c) confirms the reliability of the simplification. The comparison of K_e obtained from Eq. (1) developed by Mander et al. [13] and Eq. (10a–10c), represented in Fig. 4b, also shows that the proposed model predicts lower values for K_e than Eq. (1). It can be attributed to the consideration of the impact of k_ε, in addition to the vertical arching action, in the determination of K_e.

2.4 Effective Confinement Pressure

In this section, the determination of effective confinement pressure $f_{l,ef}$ based on CEF will be addressed. Once confinement efficiency factor is determined, $f_{l,ef}$ can be calculated using equilibrium of confinement forces as [3]:

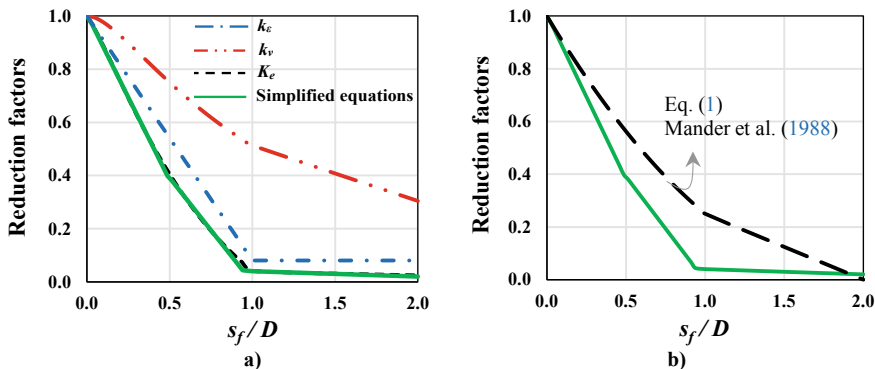$$f_{l,ef} = \frac{1}{2}K_e\rho_f E_f \varepsilon_{l,j} \tag{11}$$

Fig. 4 Variation of K_e with s_f/D for a PCCC system with $w_f/D = 0.3$

in which

$$\rho_f = \frac{4n_f t_f w_f}{(w_f + s_f)D} \tag{12}$$

where ρ_f is the FRP reinforcement ratio; n_f and t_f are the number and thickness of FRP layers, respectively. Considering $\varepsilon_{l,j} = v_s \times \varepsilon_c$, Eq. (11) results:

$$f_{l,ef} = \frac{1}{2} K_e \rho_f E_f v_s \varepsilon_c \tag{13}$$

Accordingly, if ε_c is first specified, then by just addressing the corresponding v_s, effective confinement pressure $f_{l,ef}$ can be calculated from Eq. (13).

3   Determination of v_s-ε_c Relation

In this section, a relation between v_s, corresponding to $\varepsilon_{l,j}$, and the applied axial compressive strain, ε_c, is determined. For this purpose, a large database consisting of 289 test specimens was set. Details of the test specimens can be found in [18]. To predict dilation behavior of both FCCC and PCCC, based on the best curve fit of the test results, the relation between $v_s / v_{s,max}$ and ε_c shown in Fig. 5 was derived, where $v_{s,max}$ is the maximum Poisson's ratio at the critical section corresponding to axial strain $\varepsilon_{c,m}$.

In Fig. 5, c_1, c_2, c_3 and c_4 are non-dimensional empirical coefficients derived based on the experimental results using a back analysis, and $v_{s,0}$ is the initial Poisson's ratio of concrete, determined as suggested by Candappa et al. [19]. The parameter ρ_K, adopted to determine the previous parameters, represents the confinement stiffness index, as suggested by Teng et al. [20] for FCCC. In this study,
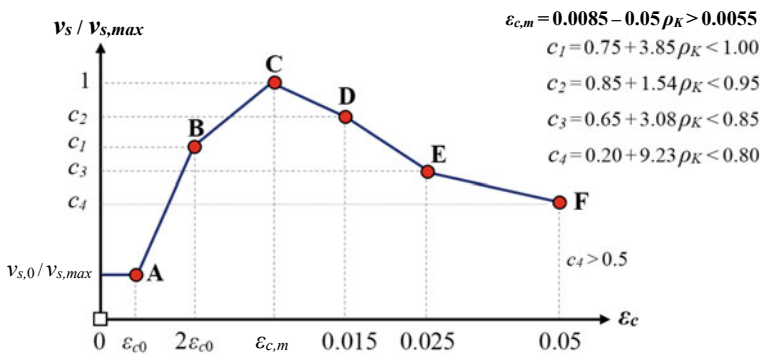

Fig. 5 Relation between $v_s / v_{s,max}$ and ε_c as a function of ρ_K

this non-dimensional parameter index was extended for the case of PCCC by adopting the concept of confinement efficiency factor, as [21]:

$$\rho_K = \frac{f_{l,ef}/\varepsilon_{l,j}}{f_{c0}/\varepsilon_{c0}} = \frac{1}{2}K_e\frac{\rho_f E_f}{f_{c0}/\varepsilon_{c0}} \tag{14}$$

$$\varepsilon_{c0} = 0.0015 + \frac{f_{c0}}{70,000} \tag{15}$$

where ε_{c0} is the axial strain corresponding to f_{c0}. As shown in Fig. 5, the expansion of confined concrete is equal to unconfined concrete up to $\varepsilon_c = \varepsilon_{c0}$(point A) with $v_s = v_{s,0}$. After which, since the development of concrete cracking induces an increase in v_s, the trend enhances from $v_{s,0}$ to $c_1 \times v_{s,max}$, corresponding to $\varepsilon_c = 2\varepsilon_{c0}$ [13], and further up to reach $v_{s,max}$ at $\varepsilon_c = \varepsilon_{c,m}$ (point C), followed by a decrease until ultimate conditions. To examine the reliability of the proposed relation, it was compared with the test results in the different levels of ρ_K, as presented in Fig. 6. There is a good agreement between the experimental and analytical results, confirming the reliability of the proposed design-based relation in Fig. 5.

To formulate the relation between v_s and ε_c, the determination of $v_{s,max}$ as an input parameter is necessary. For this purpose, the following equation was determined by best curve fit of the experimental dilation results provided in the database [18] (Fig. 7):

$$v_{s,max} = \frac{0.155}{(1.23 - 0.003f_c)\sqrt{\rho_K}} \tag{16}$$

To assess its reliability for predicting $v_{s,max}$, the results obtained from Eq. (16) are compared in Fig. 7 to those extracted from the experimental tests. The values of the mean, coefficient of variation, CoV, and mean absolute percentage error, MAPE, reported in Fig. 7 evidences the good predictive performance of the proposed equation to estimate the value of $v_{s,max}$ of both FCCC and PCCC.
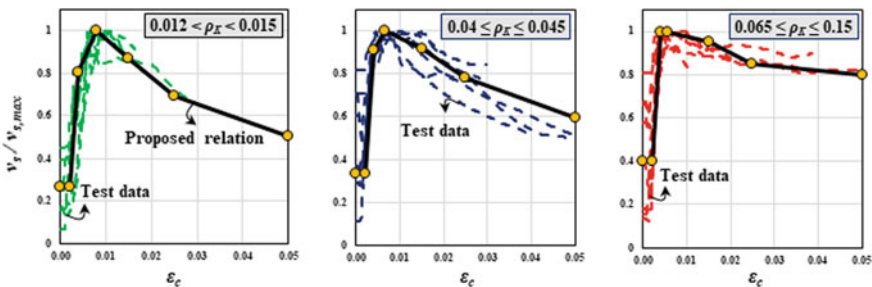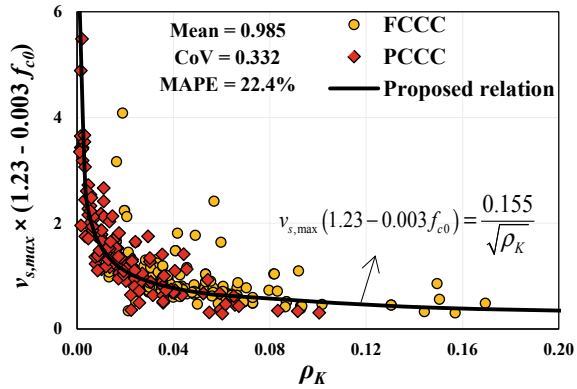

Fig. 6 $v_s/v_{s,max}$ vs ε_c determined analytically and experimentally

4 Verification

The reliability of the proposed confinement model in predicting dilation response of
fully/partially FRP confined circular concrete is assessed, by considering the
experimental results obtained by Zeng et al. [9] in FCCC and PCCC with different
confinement configurations. Complete details of the test specimens can be found in
[9]. The dilation response of the test specimens obtained experimentally and ana-
lytically from the proposed model are compared in Fig. 8, where a good predictive
performance is demonstrated.

5 Summary and Conclusions

A new model with a design framework was developed to predict the dilation
behavior of FCCC and PCCC systems. For this purpose, a relation between the
secant Poisson ratio and the axial strain was proposed, dependent of the confine-
ment stiffness. The confinement stiffness factor proposed by Teng et al. [20] was
modified based on the concept of confinement efficiency factor it order to extend it
to PCCC. In addition to vertical arching action, the effect of the non-uniform
distribution of the concrete expansion was also considered in the determination of
the efficiency confinement factor. To validate the analytical model, it was vastly
applied to predict the behavior of the relevant experimental specimens available in
the literature. The comparison between the model and experimental counterparts
revealed that it is capable of providing an estimation of axial and dilation responses
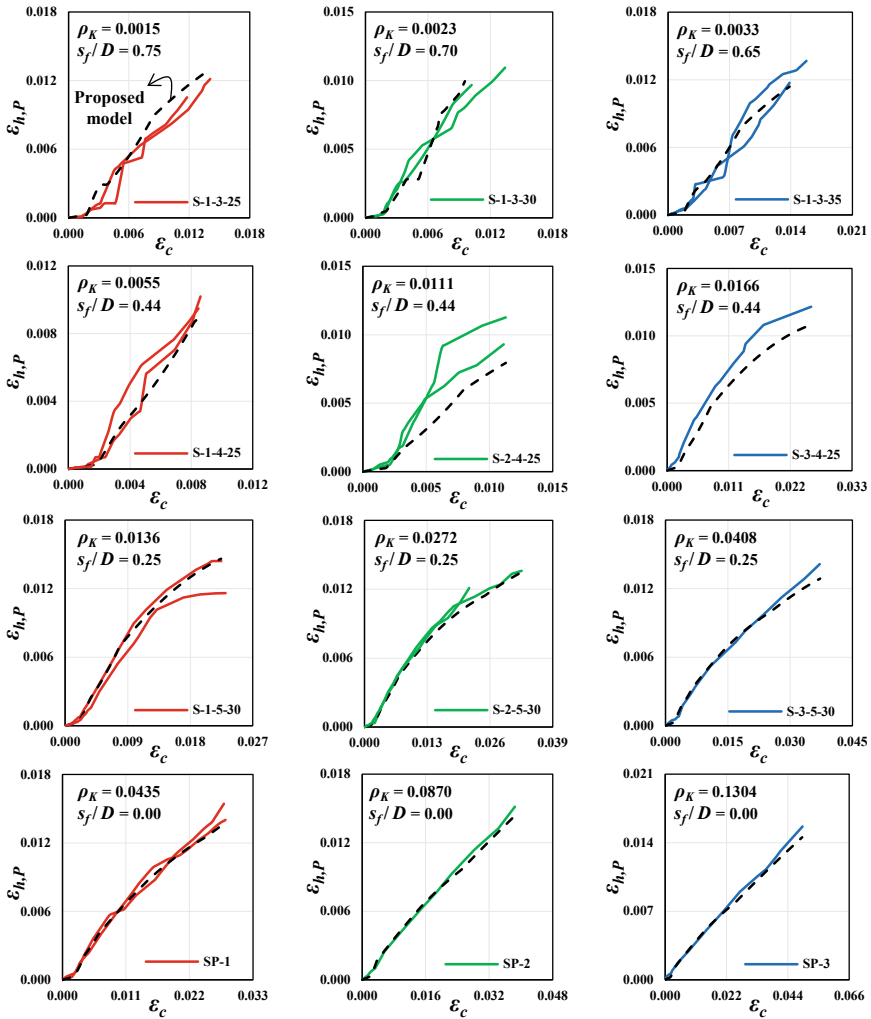with reasonable precision in the design context.

Fig. 8 Analytical versus experimental results in terms of $\varepsilon_{h,P}$ versus ε_c [9]

References

1. Janwaen, W., Barros, J.A., Costa, I.G.: A new strengthening technique for increasing the load carrying capacity of rectangular reinforced concrete columns subjected to axial compressive loading. Compos. B Eng. **158**, 67–81 (2019)
2. Perrone, M., Barros, J.A., Aprile, A.: CFRP-based strengthening technique to increase the flexural and energy dissipation capacities of RC columns. J. Compos. Constr. **13**(5), 372–383 (2009)
3. Barros, J.A., Ferreira, D.R.: Assessing the efficiency of CFRP discrete confinement systems for concrete cylinders. J. Compos. Constr. **12**(2), 134–148 (2008)
4. Shayanfar, J., Bengar, H.A.: A practical model for simulating nonlinear behaviour of FRP strengthened RC beam-column joints. Steel Compos. Struct. **27**(1), 49–74 (2018)
5. Mirmiran, A., Shahawy, M.: Dilation characteristics of confined concrete. Mech. Cohesive-Frictional Mater. **2**(3), 237–249 (1997)
6. Xiao, Y., Wu, H.: Compressive behavior of concrete confined by various types of FRP composite jackets. J. Reinf. Plast. Compos. **22**(13), 1187–1201 (2003)
7. Guo, Y.C., Gao, W.Y., Zeng, J.J., Duan, Z.J., Ni, X.Y., Peng, K.D.: Compressive behavior of FRP ring-confined concrete in circular columns: effects of specimen size and a new design-oriented stress-strain model. Constr. Build. Mater. **201**, 350–368 (2019)
8. Wang, W., Sheikh, M.N., Al-Baali, A.Q., Hadi, M.N.: Compressive behaviour of partially FRP confined concrete: Experimental observations and assessment of the stress-strain models. Constr. Build. Mater. **192**, 785–797 (2018)
9. Zeng, J.J., Guo, Y.C., Gao, W.Y., Chen, W.P., Li, L.J.: Stress-strain behavior of concrete in circular concrete columns partially wrapped with FRP strips. Compos. Struct. **200**, 810–828 (2018)
10. Zeng, J., Guo, Y., Li, L., Chen, W.: Behavior and three-dimensional finite element modeling of circular concrete columns partially wrapped with FRP strips. Polymers **10**(3), 253 (2018)
11. Teng, J., Huang, Y.L., Lam, L., Ye, L.P.: Theoretical model for fiber-reinforced polymer-confined concrete. J. Compos. Constr. **11**(2), 201–210 (2007)
12. Lim, J.C., Ozbakkaloglu, T.: Lateral strain-to-axial strain relationship of confined concrete. J. Struct. Eng. **141**(5), 04014141 (2014)
13. Mander, J.B., Priestley, M.J., Park, R.: Theoretical stress-strain model for confined concrete. J. Struct. Eng. **114**(8), 1804–1826 (1988)
14. Fib Bulletin 14.: Externally bonded FRP reinforcement for RC structures. International Federation for Structural Concrete (2001)
15. ACI-318-08.: Building code requirements for structural concrete, in American Concrete Institute. 2008, American Concrete Institute: Farmington Hills MI (2008)
16. CNR-DT 200.: Guide for the design and construction of externally bonded FRP systems for strengthening existing structures. Italian National Research Council (2004)
17. Osorio, E., Bairán, J.M., Marí, A.R.: Lateral behavior of concrete under uniaxial compressive cyclic loading. Mater. Struct. **46**(5), 709–724 (2013)
18. Shayanfar, J., Rezazadeh M., Barros J. A., Ramezansefat H.: A new theoretical model to predict axial and dilation responses of FRP fully/partially confined circular concrete. Research Report, ISISE, Department of Civil Engineering, University of Minho, Portugal, (2020)
19. Candappa, D.C., Sanjayan, J.G., Setunge, S.: Complete triaxial stress-strain curves of high-strength concrete. J. Mater. Civ. Eng. **13**(3), 209–215 (2001)
20. Teng, J.G., Jiang, T., Lam, L., Luo, Y.Z.: Refinement of a design-oriented stress–strain model for FRP-confined concrete. J. Compos. Constr. **13**(4), 269–278 (2010)
21. Karthik, M.M., Mander, J.B.: Stress-block parameters for unconfined and confined concrete based on a unified stress-strain model. J. Struct. Eng. **137**(2), 270–273 (2010)

Urban Furniture in Fiber Reinforcement Concrete with High Durability

Felipe Melo, Inês Costa, Tiago Valente, Cristina Frazão, Christoph de Sousa, Ana Moreira, and João Sá

Abstract Within the scope of the "NG_TPfib" R&D project, Exporplás and CiviTest have, in the recent past, developed a new typology of polypropylene fibers for the production of urban furniture of high durability by eliminating conventional steel reinforcements susceptive to corrosion. This reinforcement replacement strategy also allows the development of lighter and more elegant urban furniture with complex geometries at competitive costs, giving possibility for new generation of elements of added architectural and sculptural value.

This paper describes the beginning research carried out for the development and production of this type of furniture and presents the main results obtained in the development of the material. In this context, the mechanical properties and some durability indicators of the material were characterized. Due to the prefabrication nature of the production technique adopted for this type of urban furniture, special care was done on the evaluation of the early age properties of this composite, mainly the post-cracking tensile capacity. For this purpose the evolution of the compressive strength and elasticity modulus were evaluated from standard compression tests, while inverse analysis with the results obtained in 3-point notched beam bending tests at different ages have provided the evolution of the post-cracking tensile capacity of this composite. For assessing some relevant aspects of the durability of this composite, its permeability by immersion and by capillarity was evaluated, as well as the influence of the chloride penetration by dry–wet cycles on the its post-cracking resistance. The present paper describes the experimental programs carried out and presents and discusses the relevant results.

Keywords Urban furniture · Polypropylene fibers · Early-age properties · Inverse analysis · Durability

F. Melo (✉) · I. Costa · T. Valente · C. Frazão · C. de Sousa
CiviTest-Pesquisa de Novos Materiais Para a Engenharia Civil, Lda, Vila Nova de Famalicão, Portugal
e-mail: felipesalomao@civitest.com

A. Moreira · J. Sá
Exporplás – Indústria de Exportação de Plásticos, Ovar, Portugal

1   Introduction

In the scope of a R&D project, denominated "NG_TPfib", Exporplás and CiviTest are developing a new typology of polypropylene (PP) fibers for structural reinforcement of concrete elements. The replacement of conventional steel reinforcements by PP fibers in concrete structural elements increases its durability by eliminating the corrosion susceptible steel reinforcements, reduces construction and maintenance costs and decreases construction times. In addition, the use of disperse fiber reinforcements in the concrete elements has the potential to restrain crack opening [1, 2], improve tensile, shear and flexural response of the structural elements [3–7] and improve concrete fire resistance [8, 9].

Within the NG_TPfib R&D project was identified the potential to use the newly developed PP fibers for the reinforcement of urban furniture concrete elements.

In general terms, this type of elements can be characterized by having complex geometry and medium to high volume, being submitted to low to moderate external loads. From the structural point of view, the critical stage of this type of elements usually corresponds to the early ages following the production of the elements, where the concrete cracking risk is at its maximum due to the heat development resulting from cement hydration combined with the low concrete tensile strength.

In order to assess the potential of using PP fibers in urban furniture concrete elements it was identified the need to characterize the evolution of the mechanical properties of the polypropylene fiber reinforced concrete (PPFRC) since early ages, namely the post-cracking residual strength, compressive strength and modulus of elasticity. In addition, an experimental program was defined to characterize some durability aspects of the PPFRC, namely, water absorption by immersion and capillarity, and the post-cracking behavior under chloride attack.

2   Mix Composition of PPFRC

For this study, the PPFRC composition presented in Table 1 was considered. To be noticed that was employed a white Portland cement in the PPFRC mixture, in order to assure additional aesthetic value to the urban furniture elements.

The type of PP fibers under analysis is referenced as DURO54 and are fabricated by Exporplás, S.A. These fibers have 0.7 mm of equivalent diameter, length equal to 54 mm, modulus of elasticity of 6 GPa, and ultimate tensile strength of 500 MPa.

Table 1 PPFRC mix composition

White Portland cement CEM I 52.5R (kg/m³)	Limestone filler (kg/m³)	Aggregate 4/10 mm (kg/m³)	Sand 0/4 mm (kg/m³)	Superplasticizer (l/m³)	Water (l/m³)	Fibers (kg/m³)
380.0	84.0	690.0	900.0	3.1	176.0	6.0

3   Mechanical Properties of PPFRC

In order to characterize the evolution of the mechanical properties of PPFRC that are relevant to assess the cracking risk of urban furniture elements, since early ages, an experimental program was carried out for assessing the determination of the concrete compressive strength, modulus of elasticity and post-cracking residual flexural strength since 6 h after casting up to 28 days of age. The details of this experimental program are summarized in Table 2.

3.1   *Compressive Strength and Modulus of Elasticity*

Since cubes and cylinders were adopted for the determination of the compressive strength of the FRC, a conversion factor based on Eq. (1) was adopted to normalize the maximum compressive stress ($f_{c,cube}$) obtained from the compressive tests of the cubic specimens. In this equation f_c represents the compressive strength in cylinder of 150 mm diameter and 300 mm height.

$$f_c = 0.8 \cdot f_{c,cube} \tag{1}$$

The evolution of the mean compressive strength (f_{cm}) and modulus of elasticity (E_{cm}) of the PPFRC is presented in Fig. 1 and Table 3. As expected, the evolution of the compressive strength and modulus of elasticity increases quickly until the age of 7 days, while the above this age is smooth. From Table 3 it is also possible to denote that the dispersion of results is quite significant for the samples tested up to 9 h.

Table 2   Experimental program for characterization of PPFRC mechanical properties

Mechanical property	Age of testing	Specimens	Testing type	Standard
Compressive strength	at 6 h, 9 h, 12 h, 24 h, 3 days 7 days and 28 days	Cubes and cylinders	Compressive tests	NP EN 12390-3:2009 [10]
Modulus of elasticity		Cylinders		NP EN 12390-13:2013 [11]
Residual flexural tensile strength		Prisms	3-point bending tests	EN 14651:2005 [12]

Fig. 1 Evolution of the compressive strength and modulus of elasticity of the PPFRC
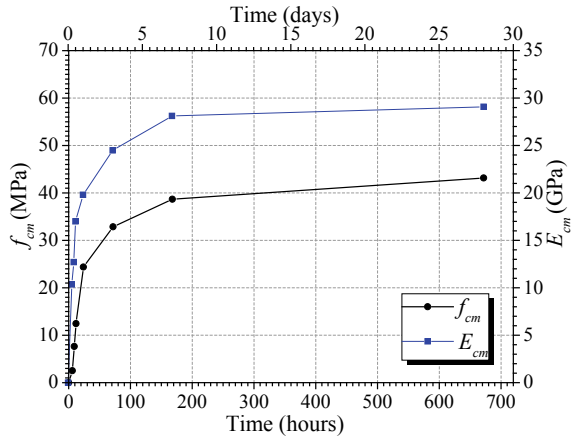
3.2 Post-cracking Residual Tensile Strength

For the characterization of the post-cracking residual tensile strength of the PPFRC, 3-point bending tests (3PBT) of prisms according to EN 14651 [12] were executed at 6 h, 9 h, 12 h, 24 h, 3 days, 7 days and 28 days after casting. Previously to the test, a notch at the midspan position of each specimen was cut in all specimens for promoting crack initiation, except for the specimens tested at 6 h in an attempt of avoiding their premature failure. The test setup is shown in Fig. 2.

The average stress versus midspan deflection obtained from the PPFRC prisms submitted to 3PBT are presented in Fig. 3. From Fig. 3, it is evident that the PPFRC presents a deflection softening behavior for majority of the loading ages under analysis, except for the specimens tested at 6 h where a deflection hardening behavior is noticed.

Table 3 Evolution of the compressive strength and modulus of elasticity of the FRC

Time (h/days)	f_c			E_c		
	N	Average (MPa)	COV (%)	N	Average (GPa)	COV (%)
6 h/0.25d	2	2.52	40.12	3	10.36	18.03
9 h/0.375d	2	7.62	4.58	3	12.70	20.88
12 h/0.5d	2	12.44	6.09	3	17.02	5.61
24 h/1d	4	24.37	9.48	3	19.81	2.10
72 h/3d	3	32.84	5.49	3	24.48	6.54
168 h/7d	3	38.68	3.55	3	28.11	0.28
672 h/28d	3	43.15	4.87	4	29.07	7.02

Legend N—Number of specimens; COV—Coefficient of variation
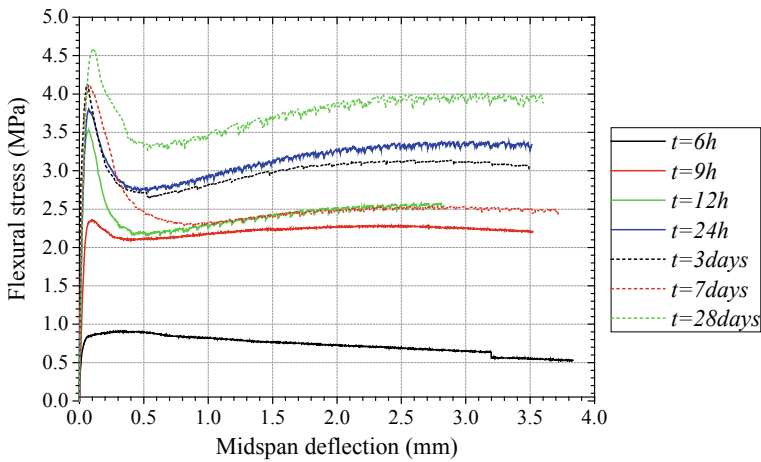
Fig. 2 Setup of the 3-point bending tests

Fig. 3 Average flexural stress versus midspan deflection of the FRC prisms for each loading age

The average values of the post-cracking residual flexural tensile strength of the FRC for each loading age are presented in Fig. 4 and Table 4. As expected, the PPFRC presents a global trend of increasing the post-cracking residual strength with its age. To be noticed that, although the specimens tested at 6 h after casting were tested unnotched, the crack initiation occurred at the midspan cross-section.
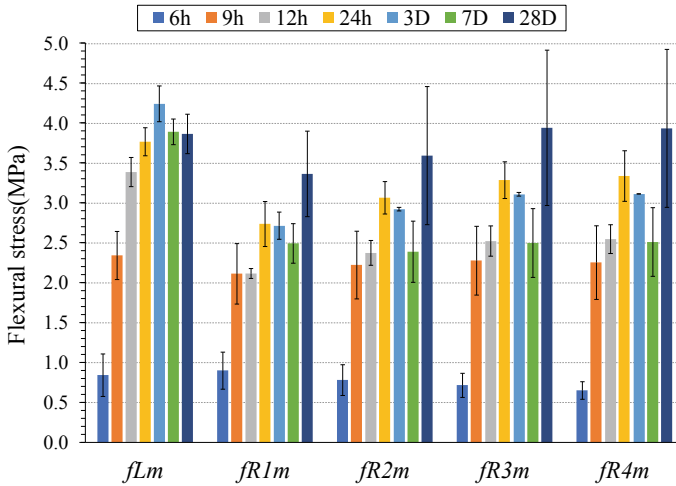
Fig. 4 Average values of the PPFRC post-cracking residual flexural tensile strength parameters

Table 4 Average values of the FRC post-cracking residual flexural tensile strength parameters in MPa

Time [hours/ days]	N	f_{Lm}	f_{R1m}	f_{R2m}	f_{R3m}	f_{R4m}
6 h/0.25d	2	0.84 (31.3%)†	0.9 (26.2%)†	0.78 (24.8%)†	0.72 (21.5%)†	0.65 (17%)†
9 h/0.375d	2	2.34 (12.8%)†	2.11 (17.9%)†	2.22 (19%)†	2.28 (18.9%)†	2.25 (20.5%)†
12 h/0.5d	2	3.39 (5.3%)†	2.12 (2.9%)†	2.38 (6.7%)†	2.52 (7.3%)†	2.55 (6.9%)†
24 h/1d	4	3.77 (4.6%)†	2.74 (10.4%)†	3.07 (6.7%)†	3.29 (7.1%)†	3.34 (9.4%)†
72 h/3d	3	4.25 (31.3%)†	2.72 (6.2%)†	2.93 (0.7%)†	3.11 (0.7%)†	3.12 (0%)†
168 h/7d	3	3.89 (12.8%)†	2.5 (9.9%)†	2.39 (16%)†	2.5 (17.2%)†	2.51 (17.1%)†
672 h/28d	3	3.87 (6%)†	3.37 (16%)†	3.6 (24.2%)†	3.95 (24.7%)†	

Legend N—Number of specimens; †—Coefficient of variation

3.3 Derivation of the PPFRC Post-cracking Tensile Behavior

In order to be capable of simulating the fracture process of FRC under analysis, including its evolution since the early ages of the concrete hardening process, the stress-crack width relationship of the PPFRC was derived by performing an inverse analysis procedure by using the 3PBT results obtained in the experimental tests.

The inverse analysis is performed by conducting numerical simulations of the bending tests considering different sets of parameters that define the stress versus
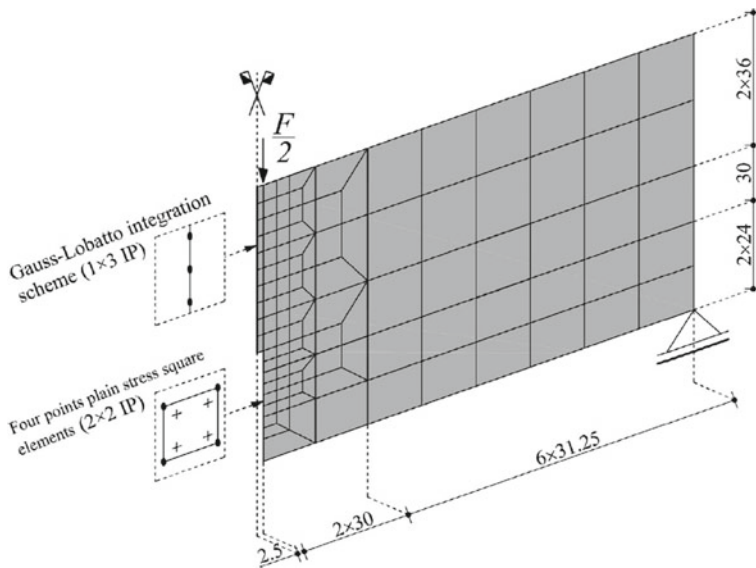
Fig. 5 Finite element mesh, loading and support conditions adopted in the inverse analysis (dimension in mm)

crack width relationship of the FRC. The numerical simulation was conducted in a FEM-based software, FEMIX, considering the finite element mesh presented in Fig. 5, being formed by 240 plane stress quadrilateral elements of four nodes, with Gauss–Legendre 2×2 IP's, while the crack opening in the notch section is simulated with 16 line interface finite elements of four nodes with Gauss–Lobatto 1×3 IP's.

The trilinear diagram presented in Fig. 6a is adopted for simulating the opening component of the constitutive law of the line interface finite elements, by assuming this diagram is capable of reproducing the crack opening propagation of the PPFRC. The remaining quadrilateral plane stress elements are considered in linear isotropic state, admitting the Poisson ratio equal to $v = 0.20$ and Young's modulus with a value according to the results obtained in the tests performed in the experimental program (Table 3). The inverse analysis procedure was only applied for the results of the PPFRC specimens tested at 9 h, 12 h and 24 h after casting. The results of the specimens tested at 6 h after casting were not considered since these specimens were tested unnotched. For each loading age, the parameters of the stress versus crack width model that minimize the deviation between the experimental and numerical force versus midspan deflection response is considered the most accurate set of values that represents the PPFRC post-cracking response at the loading age under consideration. In Fig. 6b and Table 5 are presented the best fits of the stress versus crack width relationship for the loading ages of 9 h, 12 h and 24 h after casting, derived by the inverse analysis procedure. Table 5 also presents the fracture
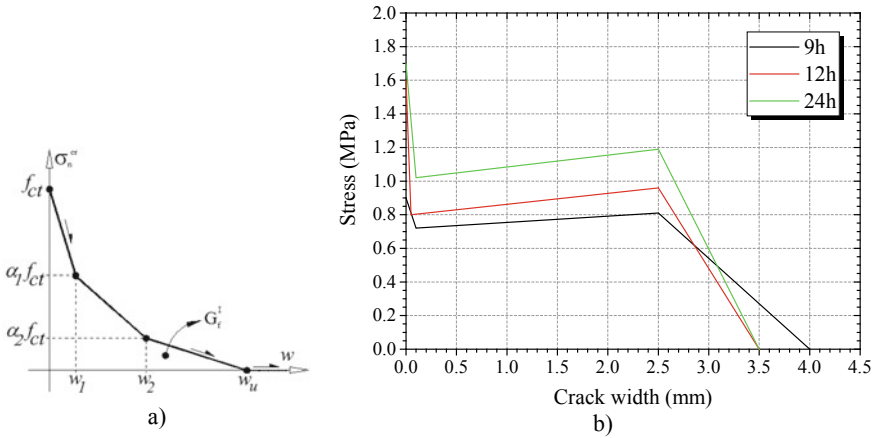
Fig. 6 a Trilinear stress-crack width relationship. **b** Derived stress versus crack width relationship of the PPFRC for the loading ages of 9 h, 12 h and 24 h after casting

Table 5 Parameters of the stress versus crack width diagram of the FRC for the loading ages of 9 h, 12 h and 24 h after casting

Loading age	f_{ct} (MPa)	w_1 (mm)	$\alpha_1 f_{ct}$ (MPa)	w_2 (mm)	$\alpha_2 f_{ct}$ (MPa)	w_u (mm)	G_f (N/mm)
9 h	0.90	0.10	0.72	2.50	0.81	4.00	2.52
12 h	1.60	0.05	0.80	2.50	0.96	3.50	2.70
24 h	1.70	0.10	1.02	2.50	1.19	3.50	3.38

Fig. 7 Comparison between the experimental and numerical force versus midspan deflection
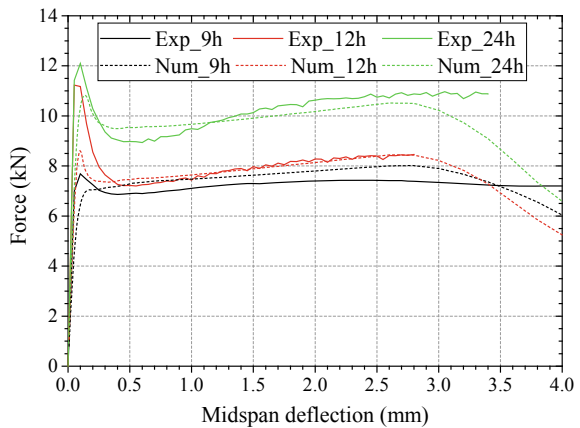
energy (G_f) of the PPFRC at the different loading ages under analysis. Figure 7 presents the comparison between the experimental and numerical force versus midspan deflection for the different loading ages under consideration.

4 Durability Indicators of PPFRC

4.1 Water Absorption by Immersion

The pore structure of concrete is known to be of high importance for the durability of the material. The water absorption by immersion gives an estimation of the total pore volume of the concrete, and in this work was determined according to the Portuguese Standard LNEC E394 [13]. The test consisted in saturating the specimens after drying. First, the specimens were dried in a ventilated oven at a temperature of 100 ± 5 °C until the difference in mass during 24 h was less than 0.1%. The dry mass was called M_d. Afterwards, the specimens were immersed in water until the change in mass during 24 h was less than 0.1%. The obtained saturated mass was called M_s. The water absorption by immersion (W_i) was calculated from the following equation:

$$W_i = \frac{(M_s - M_d)}{(M_d - M_h)} \tag{2}$$

where M_h is the hydrostatic mass of the specimen immersed in water.

The average water absorption by immersion obtained in three cubic specimens of 150 mm was 12.24% with a *COV* of 2.95%. According to the literature, the results obtained of water absorption by immersion indicate that the open porosity of the PPFRC is of the same order of magnitude than other concrete mixtures of similar compressive strength [14, 15].
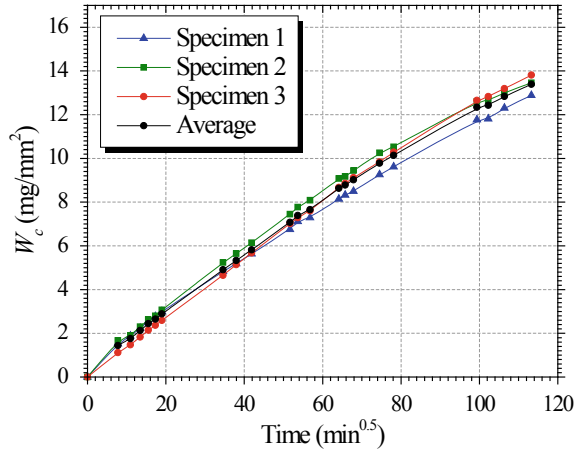
4.2 Water Absorption by Capillarity

Durability of concrete is mainly dependent on its permeability, which is the capacity of a fluid to penetrate the microstructure of the concrete. Low permeability of concrete can improve resistance to the penetration of water, chloride, sulphate and alkali ions, and other harmful substances that cause chemical attack [16]. The water absorption by capillarity was determined according to the Portuguese Standard LNEC E393 [17]. The test consisted in measuring the velocity of water absorption in non-saturated concrete and immersed in a height of 5 ± 1 mm of water. The water absorbed by capillarity, W_c, was determined as the ratio between the increase of the mass specimen by the area of the lower surface of the specimen, Ω_i that was the unique in contact with the water, according the following equation:

$$W_c = \frac{(M_i - M_0)}{\Omega_i} \tag{3}$$

where M_i is the mass of the specimen in contact with water for different times of reading ($\sqrt{t_i}$) and M_0 is the dry mass of the specimen at 100 ± 5 °C.

Fig. 8 Results obtained
of W_c

The results in terms of amount of water absorbed per unit area versus square root of time are presented in Fig. 8. The coefficient of water absorption by capillarity action, which corresponds to the slope of these curves during the initial four hours of testing, is 0.1554 mg/mm^2 × min$^{0.5}$ for PPFRC.

Using the classification recommended by Taywood Engineering Ltd. of the concrete quality as a function of the capillary absorption coefficient determined in tests of 270 min of duration [18], it appears that PPFRP is classified as a medium quality concrete.

4.3 Post-cracking Behavior of PPFRC Under Chloride Attack

For structural elements exposed to chloride environments, chloride ions may penetrate the concrete through one of the four main transport mechanisms: Diffusion, Capillary Suction, Permeation and Migration [19]. The permeation is highly dependent on the concrete cracking process. An increase in the crack width not only produces a highly permeable concrete, but also enhances the possibility of deterioration of the fibers bridging the cracks, with negatives consequences in terms of the mechanical performance of FRC structures.

In the present work, an experimental program was carried out to evaluate the effects of chloride attack on the post-cracking behavior of cracked PPFRC by performing 3PBT. The 3PBT were conducted on notched prisms of PPFRC according to EN 14651 [12]. In order to facilitate the handling and placing process of beams, small PPFRC prisms of 300 × 75 × 75 mm^3 were used, with a notch at midspan with 12.5 mm depth. The influence of the crack width level, w_{cr} was investigated by adopting pre-crack width values of about 0.5 mm for the notched beams. The target pre-crack width was implemented in the beams after 28 days of curing in lab
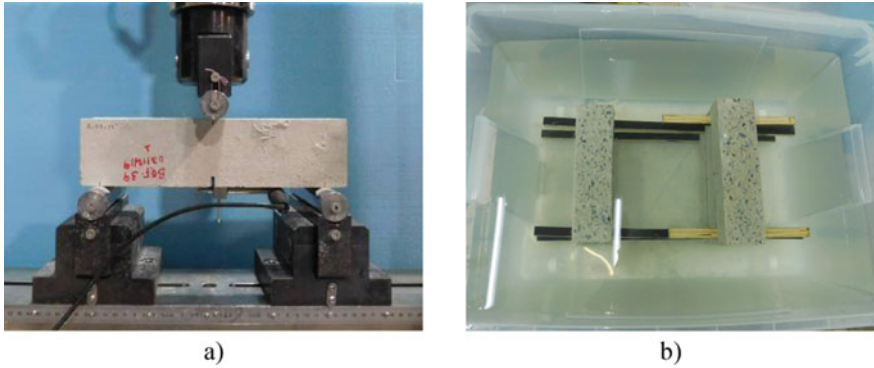
Fig. 9 **a** Test setup for pre-cracking process and final 3PBT. **b** Immersion of PPFRC beams in a 3.5 wt% NaCl solution

environment and before being subjected to chloride environment (Cl⁻). The pre-cracking process consisted of imposing the beams to a load/unload cycle under displacement control by using the test configuration in accordance with the EN 14651 [12] (Fig. 9a). After the pre-cracking process, the pre-cracked beams were subjected to 7 dry–wet cycles (1-day wetting, 2-days drying) in a 3.5 wt% NaCl solution in order to simulate a marine environment (Fig. 9b). For comparison purposes, pre-cracked reference PPFRC beams were considered, immersed in tap water (H_2O) for the same exposure period of chloride exposure. After completing the adopted exposure period, the specimens were submitted to the final 3PBT (Fig. 9a) to assess the influence of chloride attack in the post-cracking behavior of PPFRC.

Figure 10a,b present the stress-crack width responses registered in six pre-cracked beams, during the pre-cracking process (initial load/unload cycle) and after the environmental exposure period (final 3PBT). In these figures are indicated the pre-crack widths, w_{cr} implemented on each beam (after unloading).
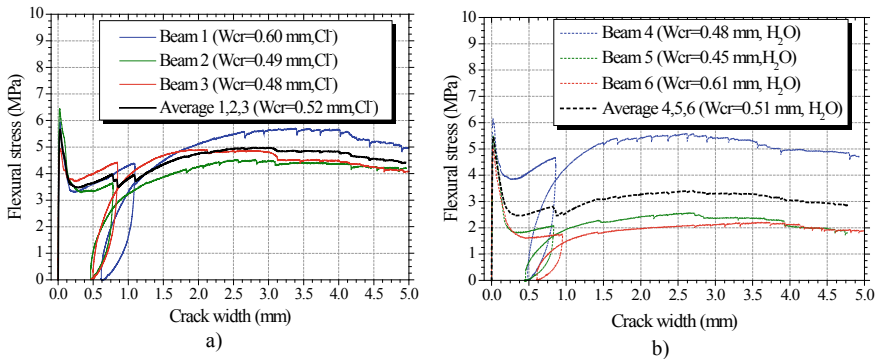

Fig. 10 Stress-Crack width relationships of: Pre-cracked PPFRC beams subjected to: **a** Chloride exposure and **b** Water immersion

According to the results presented in Fig. 10a, b, it appears that the difference between the average flexural stress of cracked PPFRC beams subjected to chloride attack (Fig. 10a) and reference beams (Fig. 10b) is mainly explained by the higher dispersion of results obtained in reference beams, probably due to a non-uniform distribution of the PP fibers at cracked section. After the environmental exposure, the cracked PPFRC beams subjected to chloride attack showed higher average post-cracking behavior than the reference beams, as was observed previously in the pre-cracking stage (Fig. 10a, b), which means than the chloride attack had a negligible effect in the post-cracking behavior of cracked PPFRC. However, in order to better understand the post-cracking behavior of PPFRC in chloride environment, an extensive experimental program with higher number of PPFRC beams in cracked and non-cracked state is being planned and the results will be revealed in future publications.

5   Conclusions

A new type of PP fibers seems to have a high potential to be used for the reinforcement of urban furniture concrete elements. The experimental and numerical findings in the present paper allows to point out the following observations:

1. The compressive strength and modulus of elasticity of PPFRC increased up to 7 days of age after which it remained almost constant up to 28 days of age (43 MPa and 29 GPa, respectively). The post-cracking residual strength of PPFRC of deflection softening behavior, increased with the concrete age (at 28 days, f_{R1} = 3.37 MPa, f_{R3} = 3.95 MPa). Based on inverse analysis procedure of 3PBT results, a numerical model was developed capable of simulating the fracture process of PPFRC since early ages.
2. The water absorption by immersion and capillarity of PPFRC are of the same order of magnitude than other concrete mixtures of similar compressive strength. A negligible effect of the adopted chloride exposure was observed in the post-cracking behavior of cracked PPFRC up to crack width of 0.5 mm.

References

1. Tan, K.-H., Paramasivam, P., Tan, K.-C.: Cracking characteristics of reinforced steel fiber concrete beams under short- and long-term loadings. Adv. Cem. Based Mater. **2**, 127–137 (1995). https://doi.org/10.1016/1065-7355(95)90013-6
2. Altoubat, S.A., Lange, D.A.: Creep, shrinkage and cracking of restrained concrete at early age. Urbana **51**, 61801 (2001)

3. Mohammadi, Y., Singh, S.P., Kaushik, S.K.: Properties of steel fibrous concrete containing mixed fibres in fresh and hardened state. Constr. Build. Mater. **22**, 956–965 (2008). https://doi.org/10.1016/j.conbuildmat.2006.12.004

4. Yazıcı, Ş, İnan, G., Tabak, V.: Effect of aspect ratio and volume fraction of steel fiber on the mechanical properties of SFRC. Constr, Build. Mater. **21**, 1250–1253 (2007). https://doi.org/10.1016/j.conbuildmat.2006.05.025

5. Frazão, C., Barros, J., Bogas, J.A., Pilakoutas, K.: An experimental investigation on the post-cracking behaviour of Recycled Steel Fibre Reinforced Concrete. In: 3rd FRC International Workshop Fibre Reinforced Concrete: from Design to Structural Applications. Desenzano del Garda, Italy, p. 10 (2018)

6. Conforti, A., Minelli, F., Plizzari, G.A.: Wide-shallow beams with and without steel fibres: a peculiar behaviour in shear and flexure. Compos. Part B Eng. **51**, 282–290 (2013). https://doi.org/10.1016/j.compositesb.2013.03.033

7. Kwak, Y.-K., Eberhard, M.O., Kim, W.-S., Kim, J.: Shear strength of steel fiber-reinforced concrete beams without stirrups. ACI Struct. J. **99**, 530–538 (2002)

8. Lourenço, L., Barros, J.A., Santos, S.P.F.: High strength and ductile fibrous concrete of enhanced fire resistance. FEUP, Porto, Portugal (2007)

9. Lourenço, L.: Betão reforçado com fibras: aplicações e técnicas de inspeção e reforço de elementos estruturais afetados pela ação de um fogo. PhD Thesis, University of Minho, Guimarães, Portugal, 267 pages (2013) (in Portuguese)

10. NP EN 12390-3: Testing hardened concrete—Part 3: compressive strength of test specimens. IPQ, Caparica, Portugal (2011)

11. NP EN 12390-13: Testing hardened concrete—Part 13: determination of secant modulus of elasticity in compression. IPQ, Caparica, Portugal (2014)

12. EN 14651 (2005) + A1 (2007) Test method for metallic fibre concrete. Meauring the flexural tensile strength (limit of proportionality (LOP), residual). CEN, Brussels

13. LNEC E394: Concrete. Determination of water absorption by immersion – test at atmospheric pressure. LNEC, Lisbon, Portugal (1993)

14. Frazão, C., Camões, A., Barros, J., Gonçalves, D.: Durability of steel fiber reinforced self-compacting concrete. Constr. Build. Mater. **80**, 155–166 (2015)

15. Pedro, D., de Brito, J., Evangelista, L.: Influence of the Crushing Process of Recycled Aggregates on Concrete Properties. Key Eng. Mater. **634**, 151–162 (2015)

16. Zhang, S.P., Zong, L.: Evaluation of relationship between water absorption and durability of concrete materials. Adv. Mater. Sci. Eng. ID 650373, 8 pages (2014)

17. LNEC E393: Concrete. Determination of water absorption by capillarity. LNEC, Lisbon, Portugal (1993)

18. Coutinho, M.: Melhoria da durabilidade dos betões por tratamento da cofragem. PhD Thesis, FEUP, Porto, Portugal, 392 pages (1998) (in Portuguese)

19. Bertolini, L., Elsener, B., Pedeferri, P., Polder, R.P.: Corrosion of Steel in Concrete—Prevention, Diagnosis, Repair, 1st edn., pp. 21–36. Wiley-VCH, Weinheim, Germany (2004)

Self-healing of Engineered Cementitious Composites at Two Different Maturity Levels

Özlem Kasap Keskin, Kamil Tekin, and Süleyman Bahadır Keskin

Abstract While there are numerous studies in the literature about the application of maturity method to ordinary concrete, strength development mechanism of Engineered Cementitious Composite (ECC) and its effect on self-healing behavior have not been studied in the light of maturity concept. This study aims to apply the maturity method on standard ECC mixture and to compare the self-healing behavior of ECC specimens matured at two different levels. Based on this purpose, datum temperature for temperature–time factor calculation was determined for the standard ECC mixture and maturity indices corresponding to 28 days and 365 days age were calculated. Self-healing assessments of the specimens at low and high maturity levels were carried out by considering the recovery of flexural strengths and ultrasonic pulse velocities and crack closure by visual inspection. In general, it is observed that although ECC exhibits self-healing when the cracks are formed at high maturity level, as the maturity level increases, self-healing capacity of ECC shows some decrement.

Keywords Maturity · Temperature-time factor · Datum temperature · Engineered cementitious composites · Self-healing

1 Introduction

Strength gaining of concrete depends on numerous factors that a producer has control over such as chemical composition and proportioning of ingredients. However, it is not always possible to control the environmental factors affecting the strength development of concrete like ambient temperature at construction site. The maturity method is a non-destructive testing procedure which enables in-situ

Ö. Kasap Keskin (✉) · K. Tekin · S. B. Keskin
Muğla Sıtkı Koçman University, Muğla, Turkey
e-mail: okasapkeskin@mu.edu.tr

S. B. Keskin
e-mail: sbkeskin@mu.edu.tr

applications for strength prediction. This technique requires a detailed correlation study performed in the laboratory by using mixtures having the identical proportioning and ingredients. After the correlations were established in the laboratory, by monitoring the temperature change of the concrete with time at construction site, strength prediction becomes possible for this particular mixture at any time. The method is therefore, valuable to schedule the strength related issues safely and timely at site.

The origins of maturity concept dates back to papers published in 1940s and 1950s [1–3]. Since then several different maturity functions and strength-maturity relations have been proposed in the literature [4]. Among those maturity functions, temperature–time factor [1, 3] and equivalent age concept [5] were widely accepted for the in-situ applications and described in detail in ASTM C 1074 [6].

According to temperature–time factor function which is also known as Nurse-Saul function in the literature, maturity index is calculated by the following equation [6]:

$$M = \sum_{0}^{t}(T_a - T_0) * \Delta t \tag{1}$$

In Eq. (1), M refers to maturity index, T_a refers to average concrete temperature during the time interval Δt, T_0 is the datum temperature, t is the elapsed time and Δt is the time interval. In this equation, datum temperature which is the possible minimum temperature for strength development is the maturity parameter that needs to be determined in order to make precise estimations for concrete strength by maturity method.

On the other hand, equivalent age equation which depends on Arrhenius Law is used to convert the actual age of the concrete to its equivalent at any reference temperature in terms of strength gain. It was proposed by Freiesleben Hansen and Pedersen [5] to eliminate the disadvantages of linear approximation of Eq. (1):

$$t_e = \sum_{0}^{t}e^{-\frac{E}{R}\left[\frac{1}{T}-\frac{1}{T_r}\right]} * \Delta t \tag{2}$$

In Eq. (2), t_e is the equivalent age at the absolute reference temperature T_r, E is the apparent activation energy of the mixture in terms of J/mol, R is the universal gas constant (8.134 J/mol-K), and T is the average absolute temperature of the concrete during interval Δt. In Eq. (2), apparent activation energy (E) is the maturity parameter that defines the relation between the temperature and rate of hydration for the specified mixture.

Despite the fact that, maturity method has been used for strength estimation of ordinary concrete for decades, the application of the method to high performance concrete mixtures is a comparatively new topic. Zhang et al. [7] investigated the apparent activation energy values of high performance concrete and calculated specific activation energy for modulus of elasticity, compressive strength and splitting tensile strength, independently. Maturity method based on equivalent age

function was applied on high performance concrete, synthetic fiber reinforced concrete and metallic fiber reinforced concrete to estimate the compressive strength and it was concluded that the determined activation energy for fiber reinforced mixtures were higher than the mixtures without fiber [8]. Maturity method according to temperature–time factor was used to predict the compressive strength of high performance concrete by Yen et al. [9]. In this study, datum temperature was assumed to be −10 °C for the curing temperature range of 5–43 °C and 4.4 °C for the other curing conditions.

Engineered Cementitious Composite (ECC) is a special type of high performance fiber reinforced cementitious composites that shows strain hardening behavior, high durability performance and autogenous self-healing property [10]. Even though there are studies in the literature researching effect of composite age on the properties of ECC [11, 12], applying the maturity concept to ECC and comparing the effect of age factor in terms of maturity is a new subject.

The aim of this study is firstly to determine the datum temperature of the well-known ECC mixture (M45) [13] for maturity calculation. Secondly, self-healing performance of this mixture was compared by using two different specimen sets having low (corresponds to 28 days curing at 23 °C) and high (corresponds to 1 year curing at 23 °C) maturity levels.

2 Experimental Study

2.1 Materials

In the production of ECC mixture, CEM I 42.5 R type ordinary Portland cement and class-F type fly ash were used as the binders. As the aggregate, silica sand having a particle size range of 0–200 μm was utilized in the mixture. Water, polyvinyl alcohol type fiber and polycarboxylate ether type high-range water reducing admixture were the other ingredients of ECC. Mixture proportioning of ECC used in the study is presented in Table 1.

2.2 Maturity Method

In order to apply maturity method on ECC mixture, first of all maturity parameters should be determined. Datum temperature (T_0) of ECC was determined according

Table 1 Proportions of the standard ECC mixture

Ingredient	Portland cement	Fly ash	Water	Fiber	Sand
Amount (kg/m^3)	560	672	333	26	442

to ASTM C 1074 [6] in this study. For this purpose 50 * 50 * 50 cm cubic specimens were prepared and cured at three different temperatures. Compressive strength values for each curing temperature were obtained as the average of three results at 7 different ages. Compressive strength values for different curing conditions and test ages are listed in Table 2.

As seen in Table 2, compressive strength values were directly affected by curing temperature. At early ages, higher curing temperatures resulted in higher strength values while, at later ages the effect may be adverse. The results given in Table 2, were used to determine the unknown parameters (S_u, t_0 and k) of Eq. (3) according to ASTM C 1074 [6] with the help of a computer program regarding the least-squares regression analysis.

$$S = S_u \frac{k(t - t_0)}{1 + k(t - t_0)} \tag{3}$$

In Eq. (3), S refers to average compressive strength at age t (day) and S_u refers to limiting strength in terms of MPa. Additionally, t_0 is the age in days when strength development is assumed to begin and k is the rate constant in terms of 1/day. Limiting strength (S_u), time for start of strength development (t_0) and rate constant (k) as determined for each curing temperature are given in Table 3.

Among the parameters determined according to Eq. (3), rate constants (k-values) are used to define the maturity parameters of both datum temperature and apparent activation energy of ECC mixture. To detect the datum temperature of ECC, rate constants were plotted with respect to curing temperatures and the best fitting line were established by regression analysis. The interception point of best fitting line with the temperature axis gave the datum temperature (Fig. 1).

Table 2 Compressive strength results for determination of datum temperature

Compressive strength (MPa)			
Age (day)	10 °C	20 °C	40 °C
1	2.8	6.1	20.1
3	12.8	24.2	35.4
7	25.9	35.7	41.1
14	36.8	41.1	50.0
28	42.0	48.0	54.8
56	48.6	53.2	56.0
90	54.2	63.5	58.0

Table 3 Maturity related parameters obtained by Eq. (3)

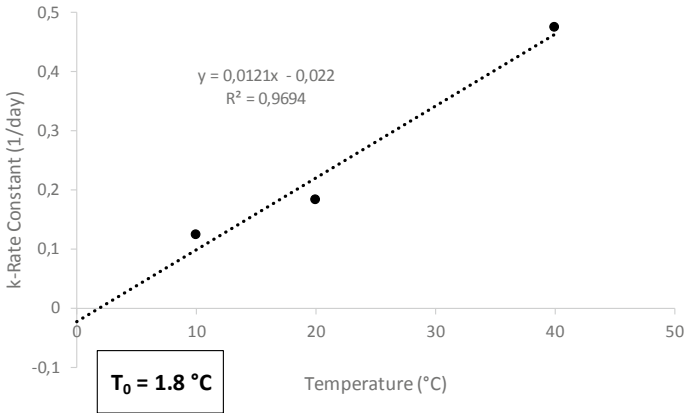| Mix ID	10 °C			20 °C			40 °C		
	S_u	t_0	k	S_u	t_0	k	S_u	t_0	k
F 1.2	57.01	0.58	0.124	61.30	0.18	0.183	58.08	0.00	0.475

Fig. 1 Determination of T_0 for ECC

As seen in Fig. 1, datum temperature was determined as 1.8 °C for standard ECC mixture. Although the traditional value of datum temperature for Portland cement-based materials is generally accepted as −10 °C [14], when the wide range of cement-based materials and the variation in their strength gaining rates are considered, using a constant value for datum temperature would not yield accurate and reliable results [15]. High content of fly ash in the ECC mixture could cause a higher datum temperature value.

After substitution of datum temperature, Eq. (1) is transferred to Eq. (4).

$$M = \sum_{0}^{t} (T_a - 1.8) * \Delta t \tag{4}$$

Using Eq. (4), maturity indices (according to Nurse-Saul Equation) or temperature–time factors for curing temperature of 23 °C were calculated for 28 days and 365 days (1 year)-old specimens as 593.6 °C-day and 7738 °C-day, respectively. Since the concept of the study is basically to compare the self-healing performances of the ECC mixture matured at different levels, low maturity level (LM) refers to 593.6 °C-day and high maturity level (HM) refers to 7738 °C-day in this study.

2.3 Self-healing Tests

For the purpose of comparing self-healing properties of the samples having different maturity indices, 3 different test method were applied; 4-point bending test, ultrasonic pulse velocity (UPV) method and visual inspection. For each maturity level (LM and HM), 18 beam specimens having dimensions of 360 * 75 * 50 mm were prepared. After the completion of casting, the specimens were left in the molds at

23 ± 2 °C and 50 ± 5% relative humidity for 24 h. Following this, the demolded specimens were sealed in plastic bags and kept at 23 ± 2 °C until the preloading time (28 and 365 days).

At the test age, the half of the specimens (9 pieces) were preloaded up to 60% of their deformation capacities to create cracks on the specimens. The other half of the specimens were left sound. Flexural strength and UPV values were determined both for sound and preloaded specimens at the age of preloading process and 30 and 60 days after the preloading process. Hence, the self-healing tests were applied at 28 + 0, 28 + 30 and 28 + 60 days for the specimens preloaded at low maturity level and at 365 + 0, 365 + 30 and 365 + 60 days for the specimens preloaded at high maturity levels. The crack closure was also observed visually 60 days after the crack formation process. The damaged (preloaded) and the sound specimens were kept in water tanks at 23 ± 2 °C till the test ages for self-healing determination. The results obtained for damaged and undamaged specimens were compared to observe the self-healing.

3   Results and Discussion

3.1   Flexural Strength Test Results

Change in flexural strength capacities of the specimens which were preloaded at low (593.6 °C-day) and high (7738 °C-day) maturity levels with time are shown in Fig. 2 for preloading day (PL + 0), and 30 (PL + 30) and 60 (PL + 60) days after the crack formation process. The results for sound specimens were also shown in the same figure.
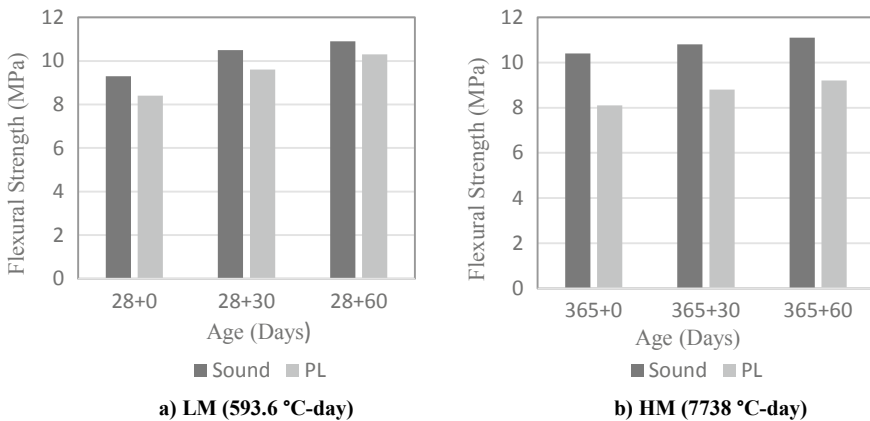

a) LM (593.6 °C-day)   b) HM (7738 °C-day)

Fig. 2 Flexural strength results

As can be seen from Fig. 2, flexural strength increased with time for all cases. However, flexural strength of sound specimens for 28 + 30 and 28 + 60 days were higher than that of sound specimen at 365 + 0. This situation could be occurred due to the moisture curing after preloading. Additionally, preloading process caused reduction in the strength capacities at both maturity levels as expected. Flexural strength values increased in the preloaded specimens with time, however this increase was more significant for the specimens which were preloaded at low maturity level. In other words, the difference between the flexural strength values of sound and preloaded specimens were higher when the specimens were damaged at higher maturity level. Moreover, if the cracks are formed at low maturity levels, flexural strength of damaged ECC specimens could reach the flexural strength of 28 days-old sound specimen (28 + 0) even as early as 30 days after preloading. However, the preloaded specimens with high maturity could not reach the strength values of the sound specimens. Moreover, when the strength values of sound and preloaded specimens are compared for the same test ages, the lowest difference obtained at 60 days after preloading as 0.6 and 1.9 MPa for low and high maturity specimens, respectively in favor of the sound specimens. It can be concluded that none of the specimens experienced a full healing in terms of flexural strength results. On the other hand, at the end of the water curing for 60 days, increases of 1.6 (%17) and 1.9 MPa (%23) was observed respectively for sound and preloaded LM specimens, while those values were 0.7 (7%) and 1.1 MPa (14%) for HM specimens which can be regarded an evidence for the self-healing.

As a result, flexural strength capacities showed that the self-healing performance of the LM specimens were better than that of HM specimens. Since a cementitious composite like ECC contains high amount of unhydrated binder at early ages (low maturity), it tends to heal faster and more sufficiently. However, as the specimens get mature, ongoing hydration reactions consumes the unhydrated binders to some degree which can make the recovery harder. Additionally, the comparatively poor performance of HM specimens could also be attributed to difficulty of controlling crack widths during preloading; same level of loading caused a larger decrease in strength.

3.2 UPV Test Results

The UPV testing is based on assessment of travel time (t) of an ultrasonic pulse wave passed through the concrete. If the distance traveled by the ultrasonic pulse wave (L) is known, UPV is calculated with the formula given in Eq. (5):

$$UPV = \frac{L}{t} \qquad (5)$$

Herein, the path in which waves are transmitted shortens as crack widths decrease and the increase in UPV values becomes more prominent. As a result, the method can be efficiently used as an indicator of self-healing behavior.

The UPV results obtained from the sound and preloaded specimens of both maturity levels are illustrated in Fig. 3 for all test ages.

As seen in Fig. 3, UPV values increased with time in all cases. Highest UPV results were obtained for sound specimens with high maturity levels. It was followed by the sound specimens of low maturity level. Cracks which were introduced by preloading process caused reductions in UPV results for both maturity levels as the ultrasonic pulse waves could not propagate through the cracks but instead travels around the cracks. As the cracks were closed by self-healing, UPV values increased because the total travel path around the cracks became smaller. Throughout the 60 days after preloading, none of the preloaded specimens could reach UPV values as high as the sound ones for both low and high maturity conditions.

Specimens preloaded at low maturity level reached 95% of UPV of their sound specimens in 60 days while the specimens preloaded at higher maturity reached 91% of their sound counterparts within the same duration. This difference is also a sign of better self-healing performance for the early crack formation. When the development of UPV values are considered, for low maturity specimens pre-cracked specimens experienced an increase of 313 m/s corresponding to a 7% at the end of 60 days after preloading whereas, the comparative values for the sound specimens were 215 m/s and 4%. The UPV values of the preloaded specimens converged to those of sound specimens as close as 251 m/s.

On the other hand, high maturity specimens underperformed the low maturity specimens and both the sound and pre-cracked low maturity specimens behaved similarly in terms of UPV values. This can be attributed to the amount of damage induced by preloading as high maturity specimens experienced a higher amount of drop in UPV values upon preloading. It can also be concluded that although similar
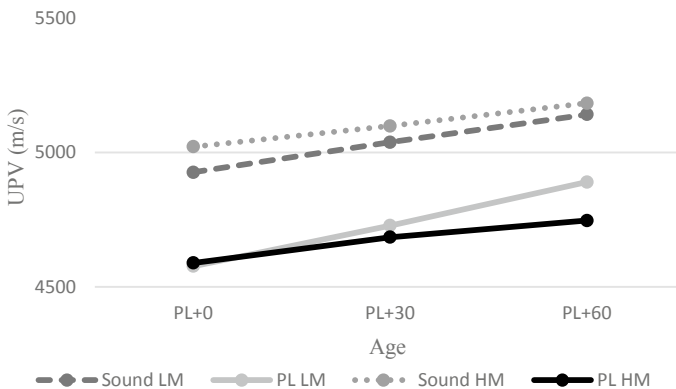

Fig. 3 UPV test results

trends were observed for both flexural strength and UPV tests, high maturity specimens performed a better healing in terms of flexural strength than the UPV tests.

3.3 Visual Inspection Results

The ECC specimens were also inspected visually to evaluate the closure of the cracks. The microscope images of the cracks were taken after the crack formation for two maturity levels. Images of the same cracks were also observed 60 days after the self-healing period for both cases. The microscope images are given in Fig. 4.
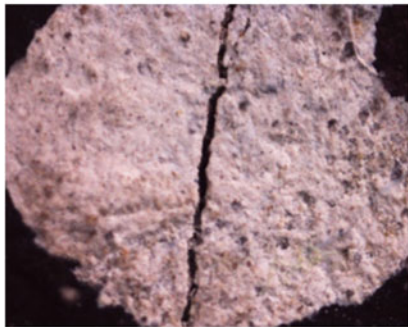
As seen from Fig. 4, both specimens exhibited self-healing at different extends in terms of crack closure. At the end of 60 days following the preloading, cracks of the specimens subjected to preloading at 28 days were closed completely (Fig. 4b). On the other hand, although a good crack closure performance was shown by
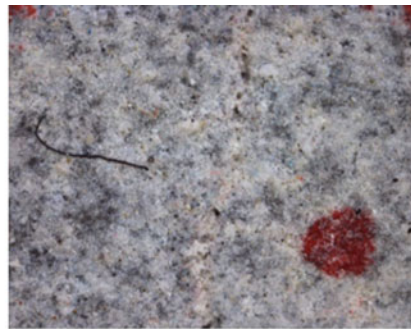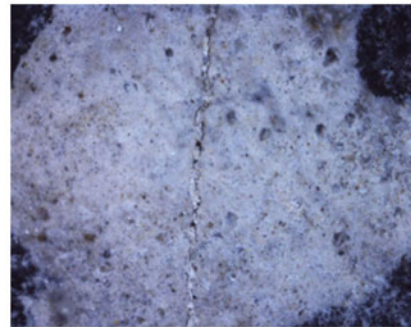

a) 28 + 0 (LM)   b) 28 + 60 (LM)

c) 365 + 0 (HM)   d) 365 + 60 (HM)

Fig. 4 Microscope images taken from the cracks of LM and HM specimens

specimens subjected to preloading at 365 days, it was still possible to observe some gaps on the crack surface (Fig. 4d). Additionally, the crack width obtained at higher maturity level (Fig. 4c) is larger than the crack width obtained at lower maturity level (Fig. 4a) under the same level of loading. Therefore, the closure of crack occurred at high maturity became harder. These images also supported the flexural strength results obtained by 4-point bending test and UPV test results.

4   Conclusion

This study was carried out to study the effect of maturity on the self-healing performance of the standard ECC mixture. In this regard, maturity method was applied on ECC specimens according to ASTM C 1074 in order to calculate maturity indices as temperature–time factor. Maturity indices of specimens cured at standard conditions for 28 and 365 days were calculated. In order to compare the self-healing capability of ECC mixture damaged at low and high maturity levels, flexural strength and UPV values were determined on sound and precracked specimens at 0, 30 and 60 days after the preloading process. The results revealed that ECC specimens showed self-healing performance regardless the damaging age. However, it was observed that as the maturity of ECC specimen during the crack formation increases, self-healing performance affected adversely due to the decrease in unhydrated binder amount and increase in crack widths.

References

1. Saul, A.G.A.: Principles underlying the steam curing of concrete at atmospheric pressure. Mag. Concr. Res. **2**(6), 127–140 (1951)
2. McIntosh, J.D.: Electrical curing of concrete. Mag. Concr. Res. **1**(1), 21–28 (1949)
3. Nurse, R.W.: Steam curing of concrete. Mag. Concr. Res. **1**(2), 79–88 (1949)
4. Kasap. O.: Effects of Cement Type on Concrete Maturity. M.Sc. thesis, Middle East Technical University, Ankara, Turkey (2002)
5. Hansen, P.F., Pedersen, J.: Maturity computer for controlled curing and hardening of concrete. Nordisk Betong **1**, 19–34 (1977)
6. ASTM C 1074: Practice for estimating concrete strength by the maturity method. ASTM Standards, West Conshohocken, PA (2017)
7. Zhang, J., Cusson, D., Monterio, P., Harvey, J.: New perspectives on maturity method and approach for high performance concrete applications. Cem. Concr. Res. **38**, 1438–1446 (2008)
8. Benaicha, B., Burtschell, Y., Alaoui, A.H.: Prediction of compressive strength at early age of concrete—application of maturity. J. Build. Eng. **6**, 119–125 (2016)

9. Yen, T., Pann, K.S., Huang, Y.L.: Strength development of high performance concrete at early ages. In: Zingoni, A. (ed.) Structural Engineering, Mechanics and Computation, vol. 2, pp. 1349–1356 (2001)
10. Li, V.C.: On engineered cementitious composites (ECCs): a review of the material and its applications. J. Adv. Concr. Technol. **1**, 215–230 (2003)
11. Yıldırım, G., Khiavi, A.H., Yeşilmen, S., Şahmaran, M.: Self-healing performance of aged cementitious composites. Cement Concr. Compos. **87**, 172–186 (2018)
12. Yıldırım, G., Öztürk, O., Al-Dahawi, A., Ulu, A.A., Şahmaran, M.: Self-sensing capability of engineered cementitious composites: effects of aging and loading conditions. Constr. Build. Mater. **231**, 117–132 (2020)
13. Li, V.C.: From micromechanics to structural engineering the design of cementitious composites for civil engineering applications. J. Struct. Mech. Earthq. Eng. **10**(2), 37–48 (1993)
14. Carino, N.J., Lew, H.S.: The maturity method: from theory to application. Structures Congress and Exposition, pp. 1–19. American Society of Civil Engineers, Washington D.C. (2001)
15. Jin, N.J., Seung, I., Choi, Y.S., Yeon, J.: Prediction of early-age compressive strength of epoxy resin concrete using the maturity method. Constr. Build. Mater. **152**, 990–998 (2017)

Comparison of Chloride-Induce Corrosion of Steel in Cement and Alkali-Activated Fly Ash Mortars

Antonino Runci and Marijana Serdar

Abstract The aim of this paper is to make an initial evaluation of chloride-induced corrosion behaviour of steel in alkali-activated fly ash and compare it to behaviour of classical cement mortar. Fly ash used in this research was obtained from regional production and was activated with sodium silicate and sodium hydroxide. Setup for evaluating corrosion behaviour consisted of structural steel plate covered with mortar layer under tap water or simulated seawater solutions. Corrosion behaviour of structural steel plates was monitored by Open Circuit Potential (OCP) and Linear Polarization (LP). The mortars have been additionally characterized by their mechanical properties, pore structure obtained by mercury intrusion porosimetry (MIP), electrical resistivity and chloride migration according to NT BUILD 492.

Keywords Alkali-activated fly ash · Corrosion · Chloride · Linear polarisation · Chloride diffusion · Migration

1 Introduction

Alkali-activated materials (AAMs) are alternative type of binder based on an alkali activator and an aluminosilicate powder, which is generally a by-product of other industrial activities [1]. AAMs are recently finding high interest due to the enormous demands for production of concrete, especially in developing countries, and the urgent need for a reduction of CO_2 emissions in industrial activities. According to McLellan et al. [2] AAMs can save in term of greenhouse gas emission around 44–64% in Australia, coming mostly from activators production and transportation and pretreatment of precursors.

Despite different studies indicating good performance of AAMs, there are still not enough studies in the literature about long-term durability performance related to chloride ingress and corrosion of embedded steel. The knowledge available on

A. Runci · M. Serdar (✉)

Faculty of Civil Engineering, Department of Materials, University of Zagreb, Zagreb, Croatia

e-mail: marijana.serdar@grad.unizg.hr

corrosion of steel in ordinary Portland cement cannot be directly transferred to AAMs, due to their significantly different chemical and physical properties. Furthermore, AAMs have displayed wide variability due to the changeable chemical and physical properties of by-products used and types and ratios of activators, which makes any generalization about these systems practically impossible.

The corrosion of steel embedded in concrete is the first cause of degradation and poor durability in reinforced concrete ($\sim$70–90% of times) [3]. The cause of embedded steel corrosion is the breakdown of the protective passive layer at the steel–concrete interface formed at high pH. The carbonation process and/or chloride ingress drive the activation of steel surface lowering the pH and the precipitation of corrosion product at the interface [4].

This paper presents results of a study on durability of alkali-activated mortar based on fly ash compared to the OPC. The aim of the study was to evaluate the applicability of this systems in aggressive environment and characterize the diffusion and microstructural behavior.

2 Experimental Program

2.1 Materials and Mix Design

The alkali-activated formulation (labelled hereafter FA) used was based on fly ash class F coming from Elektroprivreda BiH, TE Kakanj, Bosnia & Hercegovina. The formulation was adopted from RILEM TC 247-DTA round robin test studies [5]. In present study, fly ash was activated with sodium silicate Geosil 34,417 from Woellner with Ms = 1.68 and NaOH solution. The aggregate was local limestone sand with granulometry of 0–4 mm. The binder/aggregate used for FA mix was 0.375. FA was mixed with 16.5 sodium silicate/fly ash ratio and 5.9 NaOH/fly ash ratio. The reference mortar mix (labelled hereafter OPC) was prepared with CEM I from CEMEX, Croatia and with a water/binder ratio 0.5. Table 1 shows the chemical composition of fly ash and OPC.

Mortar samples of OPC were prepared according to EN 196-1. FA mortar was prepared using following procedure: dry powders and aggregate were mixed for a minute, and then again for 6 min adding continuously activators; the mixing was paused for a minute and then again mixture was mixed for additional minute. Samples were demolded after one day and were then tightly wrapped to prevent moisture loss for continued sealed curing until testing.

Table 1 Chemical composition of used materials

	CaO	SiO$_2$	Al$_2$O	Fe$_2$O	MgO	K$_2$O	Na$_2$O	SO$_3$
Fly ash	13.04	51.10	20.58	5.39	2.15	1.99	0.89	1.72
OPC	64.04	19.32	4.86	2.94	1.83	0.82	0.23	2.75

2.2 Methods

The compressive strength of mortar specimens was determined on prisms $4 \times 4 \times 16$ cm according to EN 196-1 with a loading rate of 2400 kN for compressive strength at 28 days of curing. Mercury Intrusion porosimetry (MIP) was used to provide information regarding the pore size distribution and pore volume of the mortars [6]. Specimens for MIP were immersed in isopropanol for 14 days and then vacuum dried. Autopore IV 9510 was used for MIP measurement and the pore size ranging from 350 to 0.007 µm were detected.

To detect the alkaline condition of mortar the pH was measured per each specimen every 7 days. From each testing 5 g of mortar powder was collected and mixed with 5 ml dis-tilled water for 24 h at room temperature. pH of the obtained leachate solution was deemed to be an acceptable approximation of the pH of the mortar pore electrolyte [7].

The non-steady-state chloride migration was conducted according to NT Build 492. Three specimens per mix with 100 mm diameter and 50 mm height were tested after 28 days of curing. $AgNO_3$ colorimetric analysis was applied at the end of the test. Chloride penetration was measured as the visible boundary between white precipitation of AgCl when chloride is present in sufficient quantities and precipitation of brown Ag_2O otherwise. An important parameter for this test is the chloride concentration at which the colour changes (c_d). The NT BUILD 492 recommends the value of 0.07 N for cd for OPC concrete. However, for alkali-activated fly ash $c_d = 0.21$ was applied [8, 9] to take into account hydroxide ions (pH value).

The monitoring of the corrosion of steel in mortar was carried out using an unconventional three-electrode cell suggested by Šoić et al. [10] with a PAR VMP2 potenciostat/galvanostat. The samples were prepared using carbon steel plate as working electrodes, which simulated the reinforcement inside the concrete. Carbon steel plates were polished until even metallic surface was obtained. On top of the steel plate, a polymeric cylinder was glued with silicon. This cylinder was used as a mold for the prepared mortar. A graphite stick was placed inside the solution to act as the counter electrode, and saturated calomel electrode (SCE) was positioned to act as the reference electrode (Fig. 1).

Samples were cured for 7 days, after which 0.130 ml of tap water for the reference specimens and 0.130 ml of 3.5% NaCl were added to each cell (3 per mixes). Samples were covered with plastic foil to prevent electrolyte evaporation in the period between measurements. Open-circuit potential (OCP) and linear polarization resistance (LPR) were performed approximately every 7 days, respectively for 15 and 1 min. For LPR measurements, the steels were polarized to ± 10 mV of corrosion potential (E_{corr}) at a scan rate of 0.166 mV/s. The polarisation resistance (R_p) was calculated using the modified Stern-Geary equations. Corrosion current densities were calculated from the measured R_p values, using theoretical value of Tafel constant B = 52 mV.
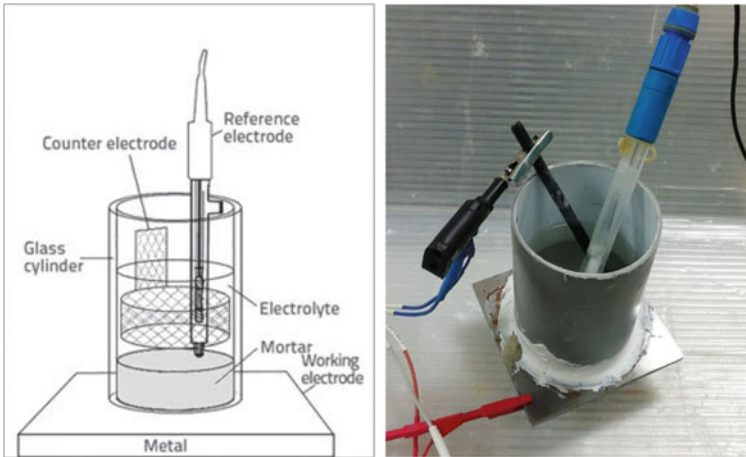
Fig. 1 Three-electrode electrochemical cell with steel plate as working, graphite stick as counter and saturated calomel as reference electrode

3 Results and Discussion

Table 2 displays slump and strength results for OPC and FA after 28 days of humidity chamber curing for OPC and sealed curing for FA. Despite the higher slump value, FA mix was sticky and less workable due to the high activator content. FA mix showed higher compressive strength than OPC mix. FA mix also showed better performance than average value from RILEM TC 247 [5].

The pH is the main factor influencing the stability of passive film on steel. Figure 2 shows the pH values of OPC and FA mixes at 7, 14, 21 and 28 days of curing compared with resistivity values.

OPC data were almost stable throughout the testing period. However, values for FA mix showed a slow reduction from 12.12 until 12.04. Monticelli et al. [11] showed that pH of OPC has higher stability after 11 weeks of wet-dry cycles rather than FA mortars. The difference between the two systems could be attributed to an early carbonation of alkali-activated mix, which was earlier reported in the literature [12]. The resistivity of mortars was increasing with the time. After 14 days, OPC stabilized, while FA values sharply increased at 28 days.

Compared to OPC, FA showed a drastically higher resistance to migration under a forced chloride penetration. Van Deventer et al. [13] demonstrate a congruent

Table 2 Consistency and compressive strength for FA and OPC mix

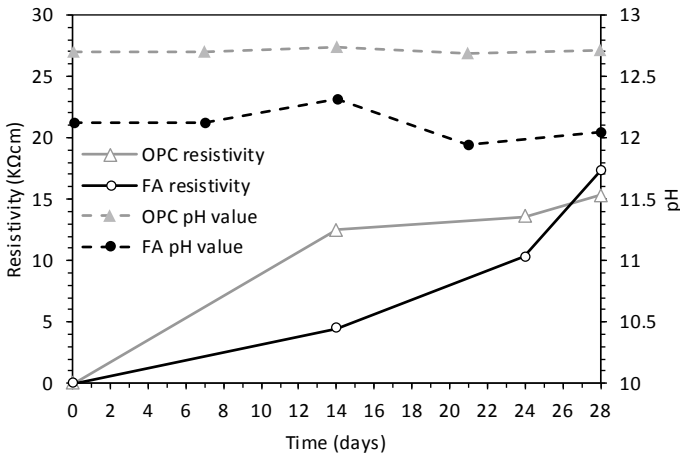|	Consistency by slump (mm)	Compressive strength (MPa)
OPC	160	59.48
FA	175	77.38

Fig. 2 Evolution of resistivity (full line) and pH (dotted line) of FA and OPC mix

behavior with alkali-activated slag and slag-fly ash systems [9]. The high resistivity and the low migration are probably connected to the lower porosity (Fig. 3) of FA systems that reduce the diffusion through the pores [14].

In OPC, there are two peaks in the differential curve (Fig. 4), corresponding to two pore systems: gel pores and capillary pores. The gel pores are formed within the formation of the CSH gels; their pore size diameter ranges is from 0.5 nm to 0.01 µm. The capillary pores refer to the space left by the water which did not react during the hydration reaction; the capillary pore sizes range from 0.01 to 10 µm.

Similarly, FA shows two peaks (Fig. 4): the first peak reflecting pore sizes with diameter in the range of several nm to 0.04 µm, corresponding to the gel pore; and a second peak corresponding to pore size ranges of 0.1–1 µm, representing the 'capillary pores' [15]. Differently than the paste from Ma et al. [16], FA mortar shows at the same condition a lower total porosity than OPC. The highest gel porosity of FA is probably an overstimation due an 'ink-bottle' effect. This effect is due to the cavities left by fly ash particles dissolution and have dimension to the capillarity pores. These pores difference form OPC capillarity pores because they do not show a continuous network; rather, they are connected to extern with fines pores network [17].

Fig. 3 Colorimetric analysis with AgNO$_3$ on specimen of OPC and FA mix after chloride migration testing according to NT BUILD 492
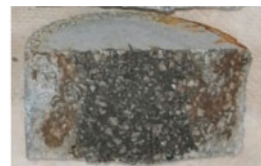
$D = 14 \times 10^{-12}$ m^2/s $D = 3 \times 10^{-12}$ m^2/s
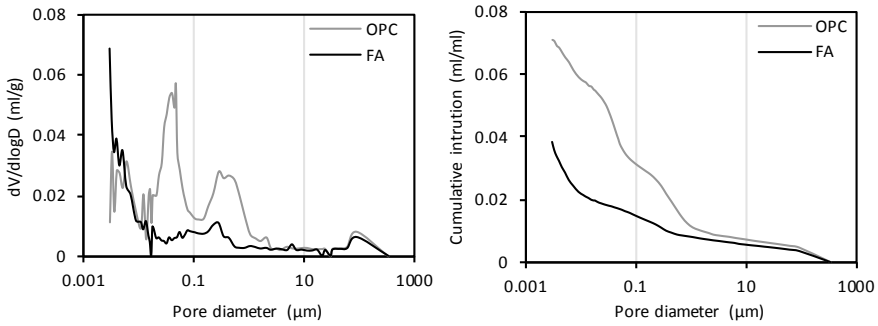
Fig. 4 Pore size distribution for OPC and FA mix obtained by MIP

Corrosion potential (E_{corr}) is the most common corrosion index, it is only a qualitative parameter and does not necessarily correlate with corrosion corrent density (i_{corr}), which describes the rate of dissolution of steel. Figure 5 shows the trend of the elctrochemical parameters in reference and corrosion environment. The more negative potential value (E_{corr}) for FA is not necessarily indicative of a higher risk of corrosion, but it may be consequence of several factors: the lower pH value of FA (as seen on Fig. 2) and the finer porosity which decreases the permeability of oxygen in cathodic areas which leads to more negative corrosion potential values (as seen on Fig. 3) [18, 19].

The corrosion current density (i_{corr}) of steel in FA was higher than steel in OPC, although the difference is not as significant. The deviation of FA in corrosion environment indicates the initiation stage of corrosion. Despite the observation of lower porosity in alkali-activated fly ash compared to OPC, confirmed also by a lower chloride migration coefficient and higher resistivity (as seen on Figs. 2 and 3), the electrochemical measurement shows an initial corrosion after 100 days of measurement. This behavior may be influenced by the microstructure evolution of FA. Ma et al. [16] demonstrated through MIP measurement that the capillaries pores in alkali-activated fly ash still exist after several months of curing; rather in OPC the hydration products continuously fill the cavities till vanishing the peak corresponding to the capillary pores. However, to further investigate this hypothesis, additional measurements should be performed.

4 Conclusion

This study showed comparison between OPC and alkali-activated fly ash mortar under chloride environment. Alkali-activated fly ash showed higher compressive strength, significantly lower chloride migration coefficient and electrical resistivity. Improved properties of FA mix compared to OPC mix can be attributed to finer pore size distribution, as evident form MIP presented in the paper. However,
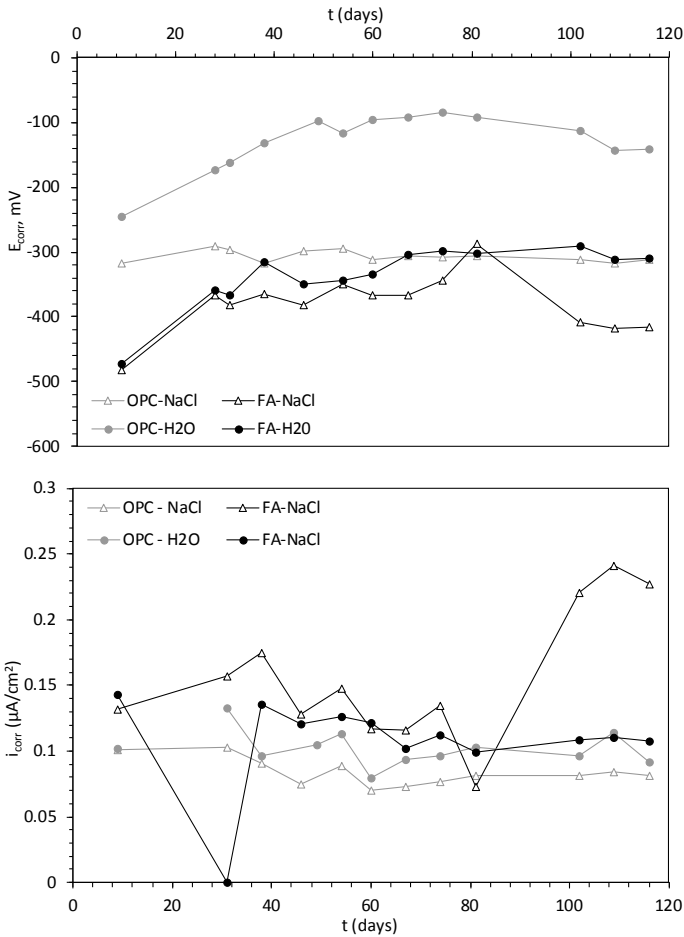
Fig. 5 Corrosion potential and current of steel in OPC and FA mortar exposed to tap water and to 3.5% NaCl solution

regardless of this lower chloride migration coefficient and finer pore size distribution, corrosion did occur in FA system sooner than in the OPC system. Reasons for sooner corrosion initiation in this specific system are focus of current research.

References

1. Provis, J., van Deventer, J.: Alkali Activated Materials: State-of-the-Art Report, RILEM TC 224-AAM, vol. 13. Springer, Dordrecht (2014)
2. Mclellan, B.C., Williams, R.P., Lay, J., Van Riessen, A., Corder, G.D.: Costs and carbon emissions for geopolymer pastes in comparison to ordinary portland cement. J. Clean. Prod. **19**(9–10), 1080–1090 (2011)
3. Angst, U.M.: Challenges and opportunities in corrosion of steel in concrete. Mater. Struct./ Materiaux et Constr. **51**(1), 1–20 (2018)
4. Ahmad, S.: einforcement corrosion in concrete structures, its monitoring and service life prediction—a review. Cem. Concr. Compos. **25**(4–5) SPEC, 459–471 (2003)
5. Provis, J.L., et al.: RILEM TC 247-DTA round robin test: mix design and reproducibility of compressive strength of alkali-activated concretes. Mater. Struct. **52**(5), 1–13 (2019)
6. Scrivener, K., Snellings, R., Lothenbach, B.: A Practical Guide to Microstructural Analysis of Cementitious Materials (2015)
7. Räsänen, V., Penttala, V.: The pH measurement of concrete and smoothing mortar using a concrete powder suspension. Cem. Concr. Res. **34**(5), 813–820 (2004)
8. Noushini, A., Castel, A., Aldred, J., Rawal, A.: Chloride diffusion resistance and chloride binding capacity of fly ash-based geopolymer concrete. Cem. Concr. Compos. 103290 (2019) (no. May 2018)
9. Ismail, I., et al.: Influence of fly ash on the water and chloride permeability of alkali-activated slag mortars and concretes. Constr. Build. Mater. **48**, 1187–1201 (2013)
10. Šoić, I., Martinez, S., Lipošćak, I., Mikšić, B.: Development of method for assessing efficiency of organic corrosion inhibitors in concrete reinforcement. Gradjevinar **70**(5), 369–375 (2018)
11. Monticelli, C., et al.: A study on the corrosion of reinforcing bars in alkali-activated fly ash mortars under wet and dry exposures to chloride solutions. Cem. Concr. Res. **87**, 53–63 (2016)
12. Fernández Bertos, M., Simons, S.J.R., Hills, C.D., Carey, P.J.: A review of accelerated carbonation technology in the treatment of cement-based materials and sequestration of CO2. J. Hazard. Mater. **112**(3), 193–205 (2004)
13. Van Deventer, J.S.J., et al.: Microstructure and durability of alkali-activated materials as key parameters for standardization. J. Sustain. Cem. Based Mater. **4**(2), 120–134 (2015)
14. Provis, J.L., Myers, R.J., White, C.E., Rose, V., Van Deventer, J.S.J.: X-ray microtomography shows pore structure and tortuosity in alkali-activated binders. Cem. Concr. Res. **42**(6), 855–864 (2012)
15. Zhou, J., Ye, G., van Breugel, K.: Characterization of pore structure in cement-based materials using pressurization-depressurization cycling mercury intrusion porosimetry (PDC-MIP). Cem. Concr. Res. **40**(7), 1120–1128 (2010)
16. Ma, Y., Hu, J., Ye, G.: The pore structure and permeability of alkali activated fly ash. Fuel **104**, 771–780 (2013)
17. Bastidas, D.M., Fernández-Jiménez, A., Palomo, A., González, J.A.: A study on the passive state stability of steel embedded in activated fly ash mortars. Corros. Sci. **50**(4), 1058–1065 (2008)
18. Babaee, M., Khan, M.S.H., Castel, A.: Passivity of embedded reinforcement in carbonated low-calcium fly ash-based geopolymer concrete. Cem. Concr. Compos. **85**, 32–43 (2018)
19. Holloway, M., Sykes, J.M.: Studies of the corrosion of mild steel in alkali-activated slag cement mortars with sodium chloride admixtures by a galvanostatic pulse method. Corros. Sci. **47**(12), 3097–3110 (2005)

Correction to: Proceedings of the 3rd RILEM Spring Convention and Conference (RSCC 2020)

Isabel B. Valente, António Ventura Gouveia, and Salvador J. E. Dias

Correction to:
I. B. Valente et al. (eds.), *Proceedings of the 3rd RILEM Spring Conventionand Conference (RSCC 2020)*, **RILEM Bookseries 33,** https://doi.org/10.1007/978-3-030-76551-4

The original version of the book was published with incorrect initial of the editor "Salvador J. E. Dias" has been corrected.

The book have been updated with the change.

The updated version of the book can be found at
https://doi.org/10.1007/978-3-030-76551-4